OMIEC beyond side chain glycolation



JUNFU TIAN
Hertford College

Supervisor: Professor Iain McCulloch
Department of Chemistry
University of Oxford

A thesis submitted in partial fulfilment of the requirements for the degree of Doctor of Philosophy in Chemistry

Oct 2025

Declaration of Originality

I declare that unless otherwise mentioned, all results included in this thesis are my own work.

Junfu Tian, 2025

Abstract

Organic electrochemical transistors (OECTs) have spanned many different applications like biosensors, flexible electronics and neuromorphic computing. Over the years, many high-performance materials, be it p-type or n-type, continue to burgeon under countless effort from the research community. Many state-of-the-art materials, such as PgBTTT and P-75, adopt side-chain glycolation. While this proves effective in improving ionic affinity in aqueous supporting electrolyte, synthesis and optimization of the materials can be challenging and cumbersome. This thesis hence aims to investigate alternative molecular architectures for OMIEC design, with a focus on conjugated rod-coil block copolymer and conjugated backbone with polar alcohol pendant groups.

Chapter 2 and 3 each explores the synthesis and characterization of P3DOT-based rod-coil block copolymers, with a focus on synthetic methodology and material properties, respectively. This work features P3DOT backbone with competitive figure-of-merit against many side-chain glycolated design and highlights how incorporation of coil fragment in its block copolymer improves the ionic transport properties of the polymer film. More importantly, μC* of rod-coil block copolymers exhibit strong negative correlation with the active swelling of polymer film, which sheds light towards future designs. In Chapter 4, we demonstrate on-film chemical treatment of PgBTTT-OTBS to yield an alcohol-terminated conjugated backbone, featuring an excellent μC* of 1036 $Fcm^{-1}V^{-1}s^{-1}$. In Chapter 5, we reset our focus on conjugated rod-coil block copolymers using backbones like F8BT and explore alternative applications like photochemical hydrogen evolution reaction. A second part of this chapter is dedicated to further exploration in synthesis of precisely functionalized P3DOT backbone, using alternative, more general Suzuki-Miyaura Catalyst Transfer Polymerization (SCTP).

Acknowledgement

This acknowledgement is dedicated to everyone who had accompanied me throughout my PhD journey in Oxford, whom I owe a debt of gratitude to.

Firstly, I would like to express my utmost gratitude to Prof. Iain McCulloch for accepting me into the group and introducing me to the wonderful world of organic semiconductor and OECT. Iain, thank you for the support and supervision you had given me over the course of my DPhil, without which I would not have developed as a scientist and person as I am today.

Petruta and Adam, thank you for patiently teaching me the ropes, which had benefited me greatly throughout the later days of my PhD, and it is a pity that you had not stayed longer.

I would also like to express my sincerest thanks to all past and present members in the McCulloch Group, including: Ben, Cath, Flo, Sophie, Maryam, Helen, Xiaolei, Weimin, Huchen, Luvian, Yuanbao, Ellen, Guanru, Yu, Yunseul, Christina, Wanpeng, Jin, Zeinab, Elena, Andi, Tomaž, Rachael and Qingpei, whom I have learnt many important, useful knowledge and skills. Thank you all for also fostering a caring and supportive environment in the group, without which my Oxford experience would have never been so memorable.

I would also like to thank my amazing collaborators, including Silan (Cambridge), Wentao (KAUST) and Bob (MIT). It has been a great pleasure working with you all and your perspectives from a different angle had significantly enriched my understanding in device and material characterization. More importantly, this educates me how it takes more than polymer chemistry to develop into mature, effective semiconductor technologies.

I am also grateful to my friends from A*STAR: Aik Seng, Hui Jia, Edward, Garrick and Zhang-He, Aristotle in Hertford College: Simon and Jingxuan, across the globe: Siyang, Jeff, Sean, Jeck, Anlong, Weihao, Jit as well as all the fun neighbours in CRL, who made my days in Oxford extremely enjoyable.

Lastly, I would like to express my warmest gratitude to my mum, dad and my wife-to-be, Xin, who are always there to share my happiness for every successful breakthrough and emotionally support me when encountering frustrating barriers. I would love you for the rest of my life.

List of Abbreviations

AC	As-casted
AFM	Atomic force microscopy
ATRP	Atom transfer radical polymerization
BET	Brunauer-Emmett-Teller
BHJ	Bulk heterojunction
C*	Volumetric capacitance
CPE	Conjugated polyelectrolyte
CuAAC	Copper(I)-catalyzed azide-alkyne cycloaddition
CV	Cyclic voltammetry
DMF	*N,N'*-Dimethylformaldehyde
DMSO	Dimethyl sulfoxide
DP	Degree of polymerization
DSC	Differential scanning calorimetry
EGOFET	Electrolyte-gated field-effect transistor
EIS	Electrochemical impedance spectroscopy
ESR	Electron spin resonance
eV	Electron volt
GIWAXS	Grazing incidence wide-angle X-ray scattering
g_m	Transconductance
GPC	Gel-permeation chromatography
HER	Hydrogen evolution reaction
HH	Head-to-head
HOMO	Highest occupied molecular orbital
HT	Head-to-tail
IP	Ionization potential
ITO	Indium tin oxide

KCTP	Kumada catalyst transfer polymerization
LCAO	Linear combination of atomic orbitals
LUMO	Lowest unoccupied molecular orbital
MALDI-TOF	Matrix-assisted laser desorption/ionization-time of flight
MIDA	N-methyliminodiacetic acid
MS	Mass spectrometry
MSA	Methanesulfonic acid
NMR	Nuclear magnetic resonance
NMRP	Nitroxide-mediated radical polymerization
º	Degree
OECT	Organic electrochemical transistors
OEG	Oligoethylene glycol
OFET	Organic field-effect transistor
OLED	Organic light-emitting diodes
OMIEC	Organic mixed ionic–electronic conductor
OPV	Organic photovoltaics
OWS	Overall water splitting
P3AOT	Poly(3-alkoxythiophene)
P3AT	Poly(3-alkylthiophene)
P3DOT	Poly(3-decoxythiophene)
P3HT	Poly (3-hexylthiophene)
PCBM	Phenyl-C61-butyric acid methyl ester
PCE	Power conversion efficiency
PCL	Polycaprolactone
PE	Polyethylene
PEG	Polyethylene glycol
PESA	Photoemission spectroscopy in air

PhMe	Toluene
PLLA	Poly(*L*-lactide)
PMDETA	*N,N,N',N'',N''*-Pentamethyldiethylenetriamine
PMMA	Poly (methyl methacrylate)
PS	Polystyrene
RAFT	Reversible Addition-Fragmentation chain Transfer
SCTP	Suzuki-Miyaura Catalyst Transfer Polymerization
TA	Thermally annealed
TAD	1,1,5,5-tetramethyl-3-azapentane-1,5-diol
TBAF	Tetra(n-butylammonium) fluoride
TBAPF6	Tetra(n-butylammonium) hexafluoride
TBD	Triazabicyclodecene
TBS	Tributylsilyl
Tg	Glass transition temperature
THF	Tetrahydrofuran
Tm	Melting temperature
TMSBr	Trimethylsilyl bromide
TT	Tail-to-tail
V_G	Gate voltage
V_T	Threshold voltage
XPS	X-ray photoelectron spectroscopy
μ	Mobility

Table of contents

Abstract 3

Acknowledgement 4

List of Abbreviations 6

CHAPTER 1 Introduction 13

1.1 Introduction to organic electronics 14

1.2 Conjugated polymer as organic semiconductors 18

1.2.1 Introduction to semiconductors 18

1.2.2 Electronic structure of organic semiconductors 21

1.2.3 Charge transport in organic semiconductor transistor device 26

1.3 Design considerations for organic thin-film transistors 28

1.3.1 Organic Thin-film transistors: OFET and OECT 28

1.3.2 Design principle of OECT: side chain engineering 33

1.3.3 Effective OMIECs without glycol substituents 36

1.4 Novel OMIECs architectures beyond glycolated conjugated polymers 39

1.4.1 Motivation 39

1.4.2 Block copolymers and conjugated block copolymers 40

1.4.3 Conjugated backbone with alternative polar side chains 46

1.5 Thesis objectives and research questions 48

CHAPTER 2 Synthesis of P3AOT-based block copolymers 51

2.1 General information and attributions 52

2.2 – Introduction 52

2.3 – Kumada catalyst transfer polymerization 57

2.3.1 P3HT and Kumada catalyst transfer polymerization 57

2.3.2 Synthetic considerations in Kumada catalyst transfer polymerization 58

2.3.3 Termination in Kumada catalyst transfer polymerization 62

2.3.4 Strategies of rod-coil block copolymers from P3AT 62

2.4 Motivation of block copolymer design 64

2.5. Optimising end-group controlled synthesis of poly(3-alkoxythiophene) (P3AOT) 64

2.6 Post-functionalization of H/Br P3DOT 69

2.6.1 CuAAC approach 69
2.6.2 Suzuki cross-coupling approach 72
2.6.3 Knoevenagel cross-coupling approach 75
2.7 Conclusion 80
CHAPTER 3 Understanding P3AOT-based block copolymers: Structure, morphology and OECT 81
3.2 Optoelectronic properties 84
3.2.1 Energy of frontier orbitals and band gap 84
3.2.2 Electrochemical doping behaviour of PEG Series 86
3.3 Morphological properties 91
3.3.1 Grazing incidence wide-angle X-ray scattering (GIWAXS) 91
3.3.2 Atomic force microscopy (AFM) imaging 93
3.4 Thermal properties 95
3.5 Swelling characteristics 98
3.5.1 Water vapour Brunauer-Emmett-Teller (*BET*) isotherm 98
3.5.2 Electrochemical quartz crystal microbalance with dissipation monitoring 99
3.6 OECT performance 101
3.6.1 Figure-of-merit 101
3.6.2 Deconvoluting figure-of-merit 105
3.6.3 Effects of thermal treatment on OECT performance 109
3.6.4 Effect of varying side chain on main-chain PEGylated block copolymers 110
3.7 Conclusion and outlook 111
3.8 Future work 113
3.8.1 Investigating alternative self-assembly behaviour through annealing 113
3.8.2 Nanoporous OECT through on-surface chemical cleavage 114
CHAPTER 4 A minimalist design to high-performance OECT 121
4.1 General information and contributions 122
4.2 Introduction 122
4.3 Polymer synthesis 125
4.4 Polymer characterization 127

4.4.1 Optoelectronic properties of PgBTTT-OTBS before etching 127
4.4.2 Optoelectronic properties of PgBTTT-OTBS after etching – TBAF treatment 128
4.4.3 Optoelectronic Properties of PgBTTT-OTBS after etching – TMSBr treatment 132
4.5 Conclusion and outlook 136
CHAPTER 5 Other block copolymers: Structure and functions 138
5.1 Motivation and introduction 139
5.2 Synthesis of PEG-b-F8BT-b-PEG and nano-precipitable photocatalysts for 141
5.2.1 Brief introduction to photocatalytic hydrogen evolution from polymer 141
5.2.2 Synthetic design of PEG-b-F8BT-b-PEG 145
5.2.3 Hydrogen evolution reaction with PEG-b-F8BT-b-PEG nanoparticles 147
5.2.4 Concluding remarks 149
5.2.5 In-situ polymerization with mono-halogenated macroinitiator 150
5.3 Towards the future: Suzuki catalyst transfer polymerization (*SCTP*)..... 151
5.3.1 Motivation 151
5.3.2 Design of heterofunctional monomer and synthesis optimization .. 153
5.3.3 Optimization of SCTP 158
5.3.4 Chemical properties of P3DOT with SCTP 160
5.3.5 Investigation of SCTP on other 3-alkoxythiophene substrates..... 164
5.3.6 Concluding remarks and future works 166
5.4 Conclusion and outlook 167
CHAPTER 6 Outlook and future work 169
CHAPTER 7 Experimental procedures 174
7.1 General Methods 175
7.1.1 Materials for synthesis and purification 175
7.1.2 Instrument for general characterizations of chemical products 175
7.1.3 Cyclic Voltammetry 176
7.1.4 Ultraviolet-Visible (UV-Vis) Spectroscopy 177
7.1.5 Spectro-electrochemistry 177

7.1.6 Photoemission Spectroscopy in Air (PESA) 177
7.1.7 Water vapour adsorption Isotherm 177
7.1.8 Grazing Incidence Wide-Angle X-Ray Scattering 178
7.1.9 Organic electrochemical transistor fabrication 178
7.2 Synthetic Procedures 179
7.2.1 Synthetic Procedure for Chapter 2 and 3 179
7.2.2 Synthetic Procedure for Chapter 4 254
7.2.3 Synthetic Procedure for Chapter 5 265
CHAPTER 8 References 302

CHAPTER 1

Introduction

1.1 Introduction to organic electronics

We live in a world where countless incredible technologies are powered by semiconductors. Arrays of simple transistor combine to create very-large scale integration integrated circuits, which have become an indispensable part of modern electronics. A world without digital revolution would be foreign and unimaginable for many people. Industries and lifestyles have been reshaped by advancements in computing and communication. Daily entertainment has transformed from reading newspaper headlines to surfing the internet and playing with mobile apps, even research across the globe would not be as fast paced without easy access to online journals. Semiconductors have been together with us for nearly a century, bringing a radical makeover to human societies, and they continue to evolve.

In February this year, The Semiconductor Industry Association (SIA) had announced a total global semiconductor sale of $627.6 billion in 2024. Compared to 2023, this had increased by an astonishing 19.1%, while a continuing double-digit market growth is projected for 2025.[1] Many factors have contributed to the rapid growth of semiconductor industries in the recent years. Notably, accelerating advancements in artificial intelligence integration, internet of things and next-generation medical devices have led to increasing demands for semiconductor products, generating countless lucrative business opportunities.[2] At the national level, major global powers have recognized the importance of bolstering domestic semiconductor manufacturing and committed significant financial investment. The UK government had unveiled the National Semiconductor Strategy, investing up to $1 billion in the next decade to empower infrastructure and research in the area. In the United States, CHIPS and Science Act implemented in August 2022 had catalysed nearly $400 billion private investment and created about 115 thousand jobs in the sector over the past two years[3].

Traditionally, inorganic semiconductors based on silicon and other metal-based materials have formed the fundamental cornerstone of modern electronics and are indeed the primary targets of these governmental initiatives. However, in recent years, the rapidly expanding research and development in organic semiconductor technology is projected to drive robust growth in the global market. In 2023, the organic semiconductor market value was estimated to be approximately $120 billion[4–8]. This amounts to about 19% of the total semiconductor market and is estimated to reach 30% by 2030[2,5].

Growing demand for bioelectronic and increasing adoption of flexible electronics are two key factors driving the rise of organic semiconductor market. While inorganic materials are still widely adopted due to their high efficiency, stability and durability, they are less eco-friendly and biocompatible compared to their organic counterparts. In addition, their manufacturing often requires complex, energy-intensive processes, making their scalable production less cost-effective.

Conversely, organic semiconductors offer several distinct advantages for design of next-generation wearable electronics: their plastic nature leads to excellent mechanic flexibility, while solution-processability enables large-scale fabrication on substrates that can be customized in shape and sizes to suit specific demands. This is exceptionally important for applications such as wearable sensors, which must interface directly with skin or soft tissue for continuous, real-time, non-invasive monitoring of bio-analytes. To minimize discomfort when worn and maintain structural integrity under human motion, polymeric material is a more attractive option compared to inorganic semiconductors because they are flexible, stretchable and light weight. In addition, because organic semiconductors can function under low operating voltage in devices such as organic electrochemical transistors (OECT), they are not only energy-efficient,

but dissipate little heat under bias, enabling safer operation when in contact with human body.

Besides being an integral part of bioelectronic devices, organic semiconductor also plays an essential role in flexible displays, which have been extensively utilized in curved OLED TVs and foldable smartphones. More commonly known as organic light-emitting diodes, these materials have proliferated as the leading technology for display panels and exhibits remarkable features such as wide colour gamut, rapid response time and large viewing angle.[9] There had been enormous amount of research work dedicated to enhance the materials, performance and lifetime of OLED[10] and its commercialization remains one of the most successful among all organic semiconductor devices. To date, the global OLED market was valued about $50 billion[11], accounting for more than 70% of the total revenue share, which undoubtfully dominates the overall display market.[12]

Organic semiconductors have also been instrumental in sustainable fuel and energy applications. In order to address the growing concern over global warming and climate change, conventional energy supply based on fossil fuel combustion must be curbed. In 2015, 196 nations had adopted the Paris Agreement, a legally binding international treaty, sets the global goal of achieving net-zero emissions by 2050 and limits temperature increase to 1.5 ºC above pre-industrial levels.[13] Organic photovoltaics (OPV) and organic photocatalysts for hydrogen fuel production are two key research areas that aim to tackle these issues. Since organic semiconductor materials are carbon-based, they can be manufactured in scale from abundant and non-toxic organic materials. In addition, as they can be processed based on solution-based printing techniques, less energy would be necessary for fabrication of device, further reducing carbon footprint. Moreover, since the band structure of organic semiconductors could

be easily tuned through structural design, they can be engineered to be semi-transparent, which are ideal for building-integrated photovoltaics such as solar windows and facades.

The intermittence of regional solar energy supply necessitates the development of energy storage technology to regulate its supply and demand over different timescale. Combustion of hydrogen gas is one of the most eco-friendly processes for energy harvesting. Because only water is produced during the process, hydrogen fuel is an ideal source of clean energy which garnered significant global attention. The EU Hydrogen Strategy aims to install 40 GW of electrolyzer capacity by 2030 for green hydrogen production from renewable energy. Germany had committed €9 billion in 2020 for hydrogen infrastructure and industrial decarbonization, while the United States had initiated the Inflation Reduction Act in 2022 to incentivize hydrogen production with tax credits. Despite lagging behind in term of energy efficiency and lifespan compares to its inorganic counterparts, organic photocatalysts still stand out due to superior sustainability and lower carbon footprint for production. To date, there had been many conjugated polymer based system which achieves high-performance hydrogen evolution[14–16].

There are many other applications of organic semiconductors, such as electrocatalysis, carbon dioxide reduction photocatalysis and water splitting, but they would only be mentioned in brief. Overall, the organic semiconductor is a fascinating area holding great promises for shaping a sustainable future in energy, electronics and beyond. Over the past decades, there have been enormous amounts of research on structural design of organic semiconductors. These efforts better clarified our understanding of the general structure-activity relationships and inspired many innovative and novel material designs. However, much of these works are based on single polymer or their blend mixture, underscoring the importance of material processing in shaping a desirable

morphology, while works on novel molecular architectures, such as block copolymer, remains overlooked, particularly owing to the challenges in the reliable and controlled synthesis of these materials. The scope of this PhD work hence aims to address the shortcomings in this research area, beginning with a discussion of synthetic consideration for block copolymer coupling, followed by a detailed understanding of the structure-activity relationships of these materials.

1.2 Conjugated polymer as organic semiconductors

1.2.1 Introduction to semiconductors

First, we should briefly review the atomic structure and electronic properties of semiconductors. As the name suggests, these materials present an electrical conductivity between that of a conductor and an insulator. In a periodic solid crystal, an enormous number of atoms contribute their orbitals for overlap. Instead of discrete energy levels, the resulting linear combinations of these orbitals form molecular orbitals with such minuscule energy differences that they merge into near-continuous bands. Therefore, the electronic structure of semiconductors is commonly described as two bands, namely the valence band, where the occupied electrons reside and the conduction band, a continuum of vacant unoccupied states.

Electrons are fermions and their distribution of energy follows Fermi-Dirac statistics (Equation 1). Because of Pauli exclusion principle, no two fermions can possess identical quantum number. Therefore, only two electrons with opposing spins can occupy the same energy level. An important concept associated with the distribution of electron energy level is the Fermi energy, which is defined as the total chemical potential, μ, at absolute zero temperature. At this energy, the Fermi function equals 0.5. A rough interpretation of its physical picture is that 50% of the electron population

would occupy at this energy level or below. Nonetheless, it must be noted that such an energy level could be hypothetical, which means that there does not necessarily exist a corresponding electronic state.

$$f(\varepsilon) = \frac{1}{e^{(\varepsilon-\mu)/(k_B T)}+1}$$ (Equation 1)

where f(ε) is the probability density of Fermi Dirac Density for given energy ε, μ and T are the chemical potential and temperature of the system, respectively.

The energy gap between the two bands, commonly known as the band gap, is an essential quantity correlated with the electrical conductivity of the material. Due to interaction of electrons from different atoms within the crystal lattice, the energy level of the semiconductor splits, forming a forbidden energy gap separating the valence and conduction band, which arose due to constructive and destructive interference of the electronic wavefunctions. This is the minimum energy required to excite an electron into free movement under an external bias. In a conductor, the valence band and conduction band overlap to form an energy continuum. When a current is applied through the conductor, the injected electron could move freely between the valence band and the conduction band, rendering the material high electrical conductivity. Conversely, insulators possess large band gaps, which are generally greater than 3 – 4 eV. The next available vacant states are hence too high in energy to accommodate injected charges. Consequently, insulators are poor conductor of electricity.

Semiconductors possess band gap between that of a conductor and an insulator. At 0 K, semiconductors are electronically insulating. However, at the temperature which device operates at, a small portion of electrons in the valence band possesses sufficient kinetic energy to be thermally agitated into the conduction band. Therefore, semiconductor intrinsically exhibit electrical conductivity orders of magnitude higher than insulator

but are poorer than conductor to similar extent. On the other hand, the conductivity of semiconductors can be easily modified with the introduction of chemical impurities, in a chemical process known as doping.

In conventional silicon-based materials, doping involves the partial displacement of crystal lattice with phosphorous or boron atoms. The prior possesses one additional valence electron compared to silicon atom, which can be donated into the lattice. This process is known as n-type doping, and results in a significant impact to the electronic properties of the material. In an intrinsic semiconductor at thermal equilibrium, the concentration of electrons and holes is equivalent. However, addition of dopant shifts this balance towards a single type of charge carriers. In the case of n-type dopant, additional occupied energy states close to the conduction band are introduced, elevating the Fermi level of the material. This corresponds to a higher population of electrons which can be thermally excited into the conduction band at ambient temperature, creating free charges and leading to a substantial increase of the electric conductivity. Similarly, incorporating p-type dopants introduces additional low-lying vacant states close to the valence band. This reduces Fermi level and facilitates hole formation by facile excitation of valence electrons into these unoccupied electronic states.

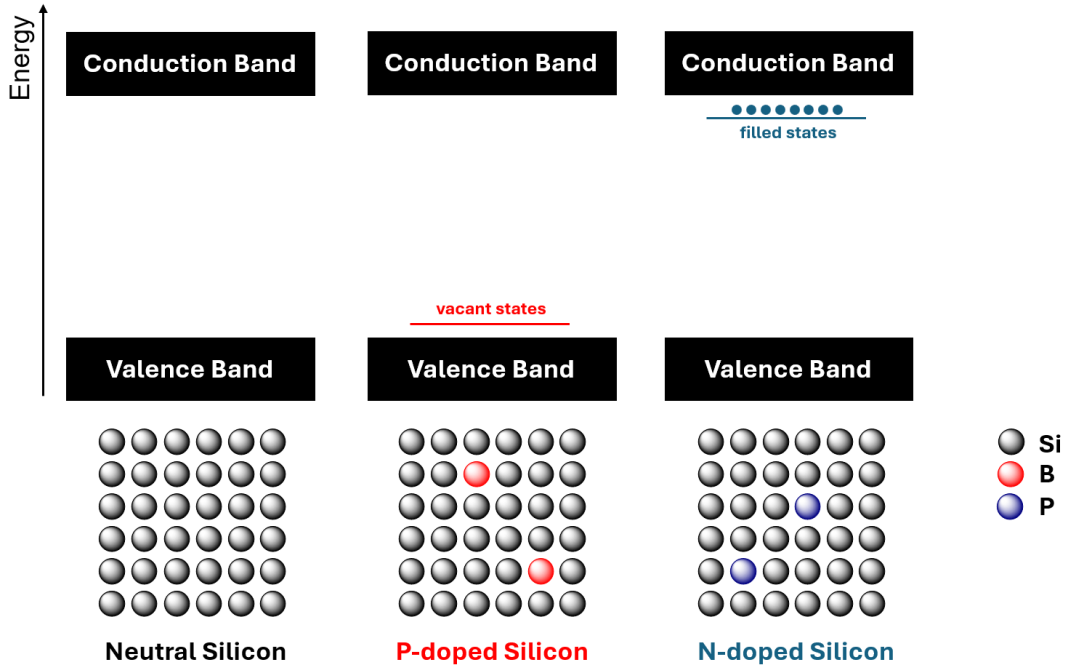

Figure 1.1 Schematic Diagram of p-doping and n-doping in Si-based semiconductors

1.2.2 Electronic structure of organic semiconductors

There are a few notable differences between organic semiconductors and their inorganic counterparts. Besides being made up of predominantly carbon, hydrogen and heteroatoms such as sulphur, oxygen and nitrogen, organic semiconductors are extrinsic semiconductors. This implies that charges are generally injected from electrodes, via electrochemical doping or through optical excitation of coulombically attracted electron-hole pairs. Common materials used in organic semiconductors include conjugated small molecules and polymers. Unlike the three-dimensional covalent network in the case of a semiconducting silicon, these organic compounds exhibit extended aromatic systems along their backbone and are held together by intermolecular π-π stacking. Hence, charge transport generally takes place intramolecularly through the delocalized π-electron system and intermolecularly via hopping between the chains. The anisotropic nature of these molecular interactions

results in remarkably different charge mobilities along face-on or edge-on directions. As a result, the electronic properties of organic materials can be heavily influenced by morphological control, where different processing methods can lead to substantial difference in charge transport behaviour even for identical materials.

Despite the remarkable difference in molecular interaction, electronic structure of organic semiconductors in the solid state or a thin film also exhibits band-like behaviour. They can hence be similarly described with valence and conduction band. However, there are stark differences over how these energy continuums arise. Fundamentally, this boils down to the π-electrons extensively delocalized over the conjugated backbone, which endues organic semiconductors with many remarkable optoelectronic properties, such as colour and conductivity.

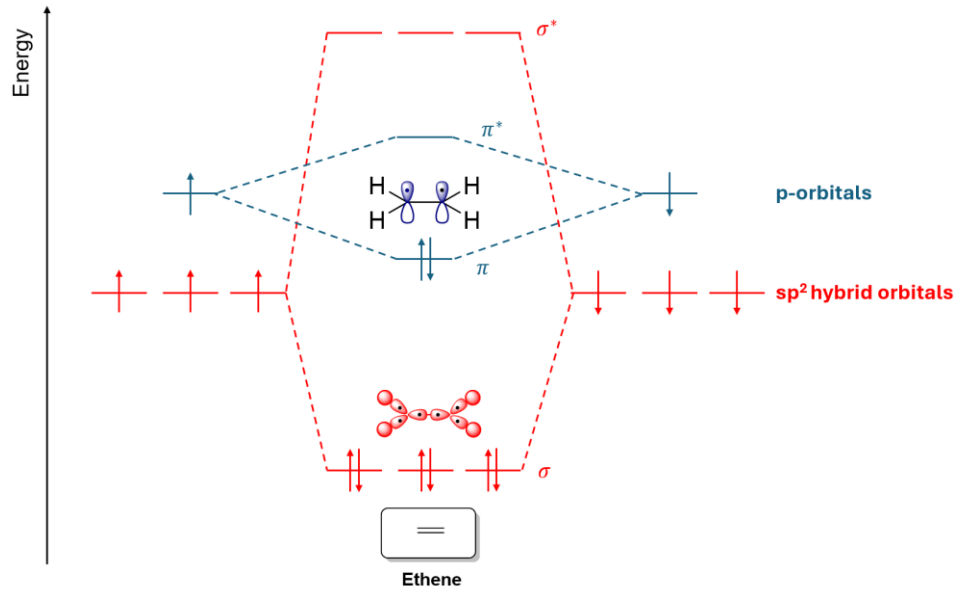

Figure 1.2 Molecular orbital diagram outlining bonding in ethene

To understand this phenomenon, we must first get down to the basis of conjugation. A simple conjugated system to begin with is an ethylene-like repeating unit. This moiety is made up of two sp^2-hybridized carbon atoms, where a σ-bond forms between two

sp^2-hybrid atomic orbitals in an end-to-end overlap. On top of this, a pair of 2p-orbital overlaps side-to-side to form a π-bond but is usually weaker compared to σ-bonds. In a molecular orbital diagram, this translates to a lower energy splitting from π-orbital formation, facilitating charge extraction and injection from the pair of bonding π-orbital and antibonding π*-orbitals, respectively.

When several simple π-systems are oriented adjacent to one another, further orbital overlap occurs, leading to greater delocalization of π-electrons and an increase in conjugation length. A direct consequence of this phenomenon is the reduction of energy difference between the frontier orbitals. This can be quantitatively evaluated with Hückel method, where all molecular orbitals in the π-system are approximated by linear combinations of atomic orbitals (*LCAO*, Equation 2).

$$\psi_i = \sum c_{ij}\phi_j \quad \text{(Equation 2)}$$

Herein, ψ_i is the wavefunction of the i_{th} molecular orbital, φ_j is the wavefunction of j_{th} atomic orbital in the linear combination, with c_{ij} as its coefficient. There are many comprehensive sources on solving the expected molecular orbital energy under Hückel approximation, so the mathematics involved would only be discussed in brief. For a linear system containing 2N orbitals, a general solution for energy of k_{th} molecular orbital exists and can be given by Equation 3.

$$E_k = \alpha + 2\beta \cos\left(\frac{(k+1)\pi}{2N+1}\right) \quad \text{(Equation 3)}$$

Where E_k is the energy of k_{th} molecular orbital, $\alpha = \int \phi_i \hat{H} \phi_i d\tau$, the energy of the carbon 2p orbital in the conjugated system, $\beta = \int \phi_i \hat{H} \phi_j d\tau$, physically representing the stabilization energy between overlapping neighbouring p-orbitals.

Several qualitative chemical interpretations could be inferred from Equation 3. For instance, considering the energy difference between two energy levels, which exhibit a local maximum near the frontier orbitals, the density of state is more diffuse. The highest occupied molecular orbital (HOMO) and the lowest unoccupied molecular orbital (LUMO) in such a system would be N-1_{th} and N_{th} LCAO, respectively. The energy difference between the fronter orbitals could be employed to evaluate the band gap, ΔE (Equation 4), which is consistent with the chemical intuition that an increase in conjugation length leads to a reduction of band gap.

$$\Delta E = 4\beta \sin\left(\frac{\pi}{2(2N+1)}\right) \qquad \text{(Equation 4)}$$

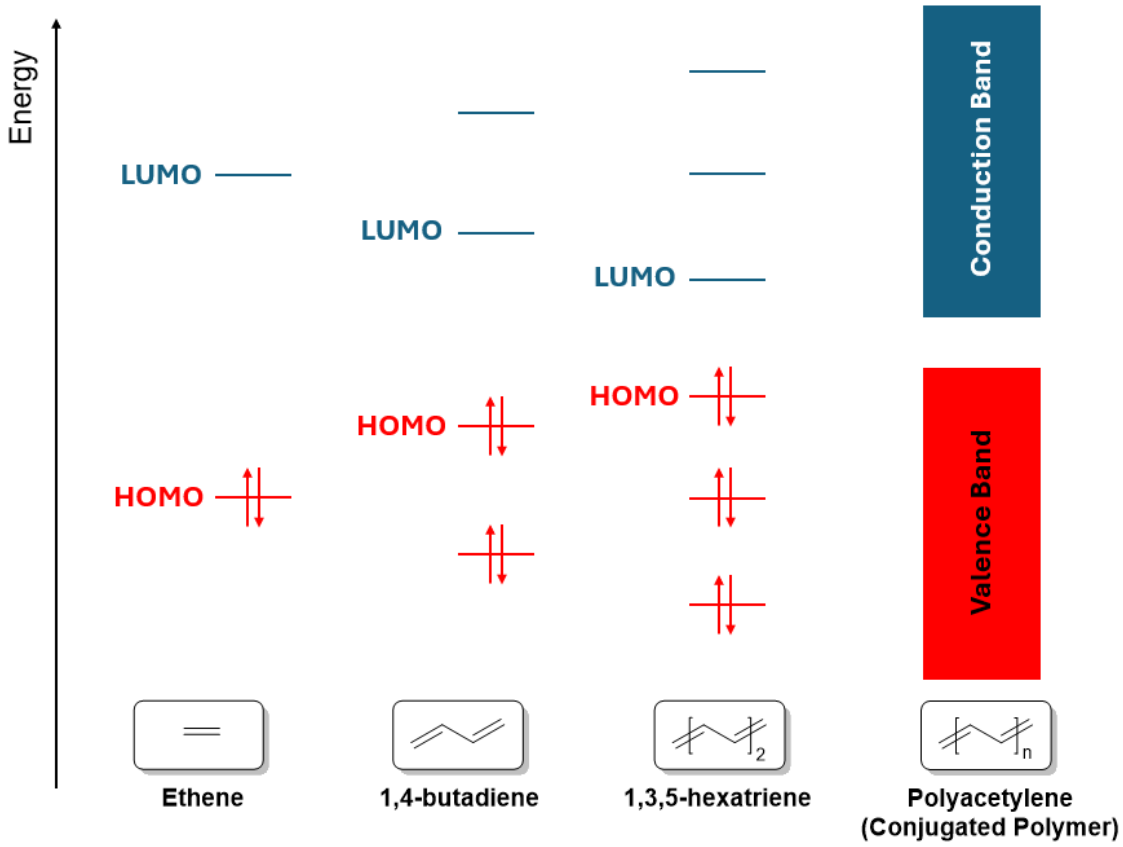

Figure 1.3 Molecular orbital diagram illustrating the impact of increasing conjugation on energy levels

While Huckel model for a linear polyene provides a simple approximation for band structure of organic semiconductors, the actual electronic picture is more complicated.

In a real conjugated polymer sample, since the molecular mass distribution usually deviates from mono-dispersity, these varied-length chains each present distinct energy states and result in a more densely filled electronic bands.

Despite this resemblance to the previously discussed electronic structure from inorganic semiconductors, the charge carrying species in conjugated polymers are not free electrons or holes. Polymer chains usually do not form highly ordered crystalline lattice. Instead, they are held together by weak interchain van der Waals interactions to form semicrystalline or amorphous aggregates. In addition, they are "soft" - the geometric structure of the molecules can be strongly influenced by local charges. This means that charge injection into polymer chains leads to molecular relaxation around the charge carriers, which are quasi-particles known as polaron or soliton, where a coupled charge-lattice deformation usually takes place. These charge-bearing species form localized electronic states within the band gap, which are electronically like p-doping or n-doping of organic semiconductors. Under electrochemical doping, these polaronic species can be further pinned by an injected counter-ion to maintain overall charge neutrality.

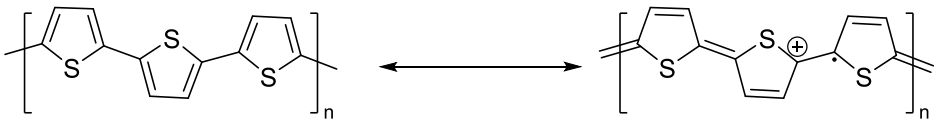

Figure 1.4 Aromatic and quinoidal resonance structure of poly(thiophene)

An example of charge-lattice deformation during polaron formation had been well-established in poly(thiophenes). In simplified bond-line notation, removal of an electron pair forms stabilized ionised quinoid structure around polaron centre (Figure 1.4). A more realistic picture would involve a gradual change in bond alternation from the position of the polaron. Since quinoid-like structures are usually higher in energy compared to the aromatic ones, a thiophene unit closer to the polaron formed will

possess higher quinoidal character, while one further away will be more aromatic in nature. Quinoidal heteroarene motif may also exhibit different C-C bond length compared to the aromatic ones, which also explains the potential mechanical strains during lattice relaxation. At higher doping level, a balance will be established between Coulombic repulsion between the polarons and the concentration of mechanical defect, singly occupied polarons with opposing spin may then pair up to form a doubly charged, spinless quasi-particle known as bipolarons.

1.2.3 Charge transport in organic semiconductor transistor device

To understand the charge transport behaviour through organic semiconductors, we must interpret the mechanism behind how charge carriers move within a material. Charge flow in a semiconductor can be driven by diffusion and drift. For instance, photogenerated excitons diffuse down concentration gradient, before being harnessed for electricity or photocatalysis. Diffusion is also significant in highly ordered crystalline inorganic semiconductors such as silicon or gallium arsenide. Due to high mobility of these materials, charge carriers could move freely through ballistic band transport, and a small concentration gradient is often sufficient to drive substantial current flow.

In transistors, organic semiconductors tend to transport charges through drift. Drift refers to the movement of charge carriers driven by an external applied electric field. In conjugated polymers, weak intermolecular van der Waals interaction and more disordered molecular structure result in formation of defect and localized states, trapping charge carriers and hindering diffusion. Moreover, these materials are extrinsic semiconductors, resulting in low intrinsic carrier concentration in the absence of

dopants. This leads to low concentration gradient, rendering diffusive transport ineffective.

It was widely accepted that charge flow in organic semiconductors operates through polaronic transport[17,18]. However, the exact model describing their charge transport continues to be a topic of controversy, possibly owing to their complicated behavior at different conditions and mobilities. In the two dichotomous extreme cases, polaronic movement can be modelled by band-like or hopping-like transport where complete delocalization and localization of the charge carriers occur respectively[19]. In most conjugated polymers, weak phonon-polaron coupling allows electrons to sufficiently relax to the ground state in the charge-transfer process, leading to localization of polaron in specific molecular sites[20]. This is also often tied closely with the reorganization energy (λ) of the conjugated system, which is defined by Marcus theory as the energy required for the backbone to adopt an equilibrium geometry following charge injection[21]. The total reorganization energy depends on the sum of internal and external contributions. The prior constitutes the energy needed to distort a neutral structure on the polymer to its ionic state, while the latter, in addition, takes account of intermolecular polarization from surrounding polymer or solvent[22]. Achieving high-performance transistors require careful structural optimization of polymers to reduce λ, because large λ hinders charge transport due to over-localization and formation of deep charge traps, whereas smaller λ would involve minimal geometry relaxation following charge transfer, leading to faster charge hopping.

Ideal band-like transport in organic semiconductors is rare and often only observed in highly ordered single crystal materials such as rubrene and C_8-BTBT[23] The intrinsic mobility of organic materials can also be compromised by presence of contact resistance[24], grain boundaries and step edges. In the cases of polymeric semiconductor,

many other factors such as polydispersity, thermal lattice vibrations and poorer packing efficiency also contribute to higher molecular disorder. Therefore, in classical organic field-effect transistors (*OFET*) as well as organic electrochemical transistors (*OECT*), charge transport through polymeric materials predominantly undergoes a hopping mechanism, where polaronic carriers are transiently localized and migrate through closely located empty sites with similar energy levels.

1.3 Design considerations for organic thin-film transistors

1.3.1 Organic Thin-film transistors: OFET and OECT

In Section 1.1, we had briefly outlined the burgeoning development of organic semiconductors to enable future electronic products such as flexible integrated circuit, biosensors and displays. These organic active materials exhibit many promising properties such as low energy and scalable processability, tuneable electronic properties, mechanical flexibility and biocompatibility.

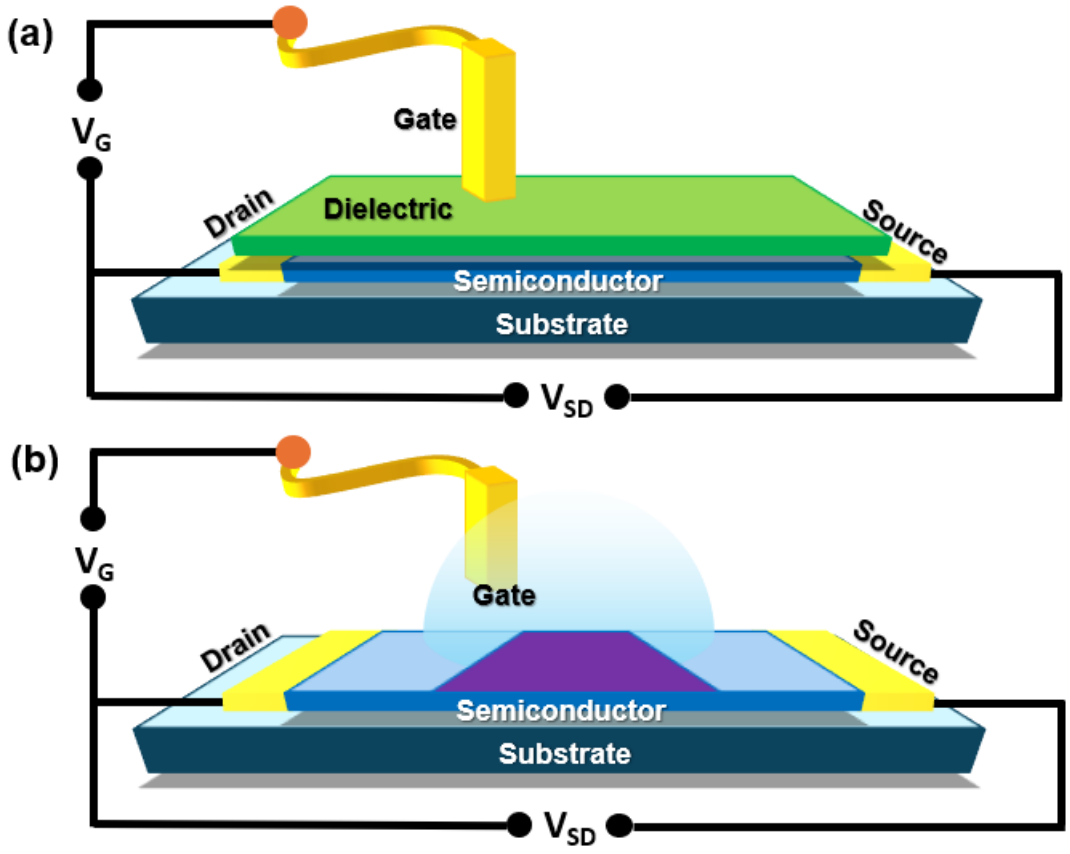

Figure 1.5 Schematic Diagram outlining structure of (a) Top-gate bottom-contact OFET (b) OECT

Fundamentally, realizing manufacturing of these devices involves integration of countless organic thin-film transistors, which are the basic building blocks for flexible electronics. These transistors structurally comprise a three-electrode system with a central channel fabricated from organic semiconductors. Conductivity through the semiconducting active material can be tuned through electrochemical doping. In the case of a field-effect transistor, this is mediated through the gate dielectric via an applied gate bias. The dielectric layer usually composes highly capacitive materials such as silicon oxide or PMMA. When a gate voltage is applied, the electric field induces charge carrier formation at the dielectric-organic semiconductor interface. This results in the formation of a conducting channel and modulates conductivity through the active layer. For instance, in an accumulation-mode p-type OFET, a negative gate bias induces

hole polaron formation at the dielectric-semiconductor interface, hence amplifying the output current between the source and drain electrodes.

Organic electrochemical transistor (OECT) is an alternative type of thin-film transistor demonstrating promising performance in applications like biosensing and neuromorphic computing[25,26]. Unlike its field-effect transistor counterpart, application of gate bias does not modulate channel conductivity through a gate dielectric layer. Instead, the channel material is immersed in an electrolyte solution. Aqueous sodium chloride or potassium chloride is commonly employed for OECT to mimic biological media while other electrolytes such as tetra(n-butyl)ammonium hexafluorophosphate and ionic liquid are used in neuromorphic computing. When a gate bias is applied, electrolyte ions are injected into the active layer, stabilizing the induced polaronic charge carriers. A key difference between OECT and OFET is that the entirety of channel active layer can be electrochemically doped during operation, resulting in a large current gain under low gate bias, rendering the device more suitable for biomedical-related applications.

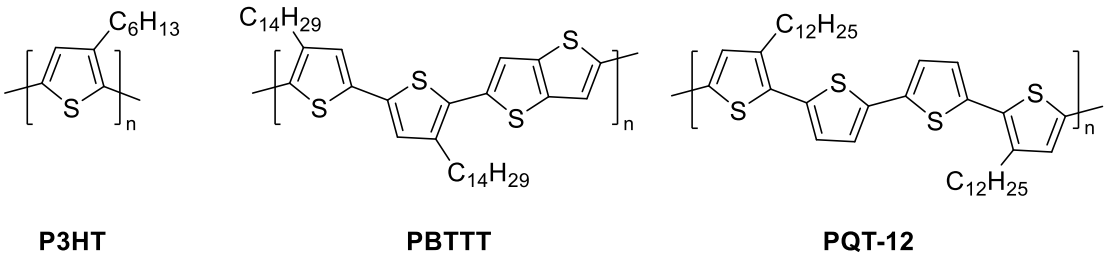

Figure 1.6 Skeletal structure of P3HT, PBTTT and PTQ-12

The difference in device operation between OFET and OECT results in distinct channel material design principles. A high-performance OFET material generally requires long-range organisation of its molecular structure, which is favoured by formation of crystalline domains. Amorphous materials, on the other hand, usually exhibit low

carrier mobility. Thus, highly ordered conjugated polymer such as regio-regular poly(3-hexylthiophene) (P3HT), poly(4,4″-didodecyl[2,2′:5′,2″:5″,2‴-quaterthiophene]-5,5‴-diyl) (PQT-12), poly[2,5-bis(3-tetradecylthiophen-2-yl)thieno[3,2-b]thiophene] (PBTTT) (Figure 1.6)[27], as well as crystalline films of small-molecule materials like pentacene often result in large carrier mobility. In addition, optimal thermal annealing which enhances molecular ordering and granular arrangement of the active layer films have been reported to improve device performance[28,29]. Conversely, design of a high-performance OECT material involves several additional considerations. Since aqueous electrolyte counterions are necessary to stabilize charge carriers, an efficient OECT channel material must be highly conductive upon doping and allows facile penetration of hydrated ions under gate bias. Ion infiltration therefore leads to electrochemical doping of the bulk material. These materials are hence termed organic mixed electronic/ionic conductor (OMIEC), as the channel conductivity is modulated by both electronic and ionic transport through the material.

Transconductance (g_m) is commonly used to describe the device performance of a single transistor. In OFET, both transconductance in the linear and saturated regime depends on the charge mobility (μ), which is thereby commonly extracted as the figure of merit for OFET materials. In the case of OECT, operation through bulk doping means that the material performance depends on both electronic and ionic transport through the channel[30]. Hence, a popular figure of merit benchmarking the steady-state efficiency of OMIEC is given by the product of charge carrier mobility (μ) and volumetric capacitance (C*)[31]. This value can be extracted by normalizing g_m by the ratio of channel dimensions and the difference between operating gate bias (V_G) and threshold voltage (V_T), as depicted in Equation (5). Here, W, L, d represents the channel width, length and film thickness respectively.

$$g_m = \frac{Wd}{L}\mu C^*(V_T - V_G) \qquad \text{(Equation 5)}$$

The operating principle of OECT hence dictates that performance of channel material no longer only depends on its charge carrier mobility[32]. Due to bulk doping of OECT material under bias, materials with small charge mobility could exhibit large transconductance given sufficient volumetric capacitance. A high-performance OECT material hence requires a careful optimization of ionic and electronic transport properties simultaneously. For instance, regio-regular poly(3-hexylthiophene) (rr-P3HT), a reference material in OFET with a high hole mobility, was generally deemed unsuitable for OECT devices with aqueous potassium chloride electrolytes due to high operating voltage and threshold bias. Furthermore, μC* reported previously is strongly influenced by minute deviation in threshold voltage[33], which may also come at the expense of reversibility and response time. This can be attributed to the strong hydrophobicity and crystallinity of P3HT, impeding ion infiltration. On the other hand, this phenomenon can be strongly associated with the identity of electrolyte pairs used. Biologically important chloride anions in saline electrolytes are small and less polarisable and hence penetrate polymer film with a hydrated solvent shell. As this is repelled by hydrophobic material, a greater onset bias will be necessary to drive electrochemical doping. Nonetheless, larger, more polarisable anions are less hydrated and could more easily permeate hydrophobic films[34–36]. This may find many useful synaptic applications in neuromorphic computing, where interaction with a biological interface is not necessary. On the other hand, enable device operation with saline supporting electrolytes necessitates specific principles in structural design.

1.3.2 Design principle of OECT: side chain engineering

Grafting aliphatic side chains onto the polymer backbone is a widely adopted strategy to tune its photophysical properties, hydrophilicity and solution processability. To facilitate uptake of hydrated ions in the polymer film, polar oligoethylene glycol side chains are installed for better ionic transport in aqueous electrolytes. This can be attributed to the increased number of oxygen atoms present on the chain, which could interact effectively with the aqueous environment as a hydrogen bond acceptor. This greatly enhances hydrophilicity of the polymer and had been demonstrated in many previous reports to enhance device performance of OECT devices[32].

There are several further implications and differences following replacing an alkyl chain with a glycol one[37]. Beside higher polarity and ionic conductivity, glycol chains are also more flexible due to reduced steric hindrance around oxygen atoms, thereby reducing energy barrier for rotation along C-O bond. In solid state, this could account for the closer π-π stacking observed in some glycolated conjugated polymers when compared with their alkylated analogue. The greater flexibility of OEG side chains promote adoption of a favourable conformation that minimizes steric clash when the conjugated chains are in proximity. In some cases, this may lead to more compact polymer backbones, enhances crystallinity and promotes charge transport. However, it must be emphasized that this depends heavily on the structural alignment of the side chains. For instance, scanning tunnelling microscopy analysis of pgBTTT against its alkylated derivatives leads to several conflicting implications[38]. In this case, self-assembly of both polymers was governed by interactions of side chain, driving formation of conformation resembling polyethylene (PE) and polyethylene glycol (PEG) respectively. Based on this argument, the lack of dipole along alkyl side chain in fact results in more uniform van der Waals interactions. The alkyl side chains adopt all-

trans extended conformation, leading to more extended, regular and crystalline domains. On the other hand, oxygen atoms on glycol side chain introduces competing electrostatic interactions, creating conformational variability. Glycol side chains hence display twistedorientations due to stereo-electronic gauche effect between C-O bond. This causes PEG to be innately helical in structure. This hence suggests that the functional versatility of glycol side chain came alongside microstructural disorder, but it would be possible to improve overall ordering by optimizing side chain separation, which forms a more uniform, interdigitated side chain network.

Many previous works hence attempt to optimize ionic and electronic transport of OECT material via side chain engineering. For instance, chain length[39–41]. While an increase in glycol chain length should reflect enhanced ionic affinity and in theory, greater volumetric capacitance, the increment is not always monotonic. In p(g2T-T) series, C^* increases from 8 F cm^{-3} in p(g2T2-T) to a peak value of 211 in p(g3T2-T), which then decreases to 192 in p(g4T2-T). C^* of the longest p(g6T2-T) is not reported due to significant delamination. This reduction is attributed to lack of additional ion stabilization in p(g4T2-T) compared to p(g3T2-T), while mass percent of electroactive backbone is reduced. There are a few drawbacks with increasing side chain length excessively. (i) This leads to higher torsional freedom and reduces consistence length, thereby compromising mobility. (ii) This results in over-swelling and delamination, hindering device stability upon repeated cycling. (iii) It also may disrupt the proportion of polymers adopting preferential edge-on orientation and leads to a more disordered morphology[39].

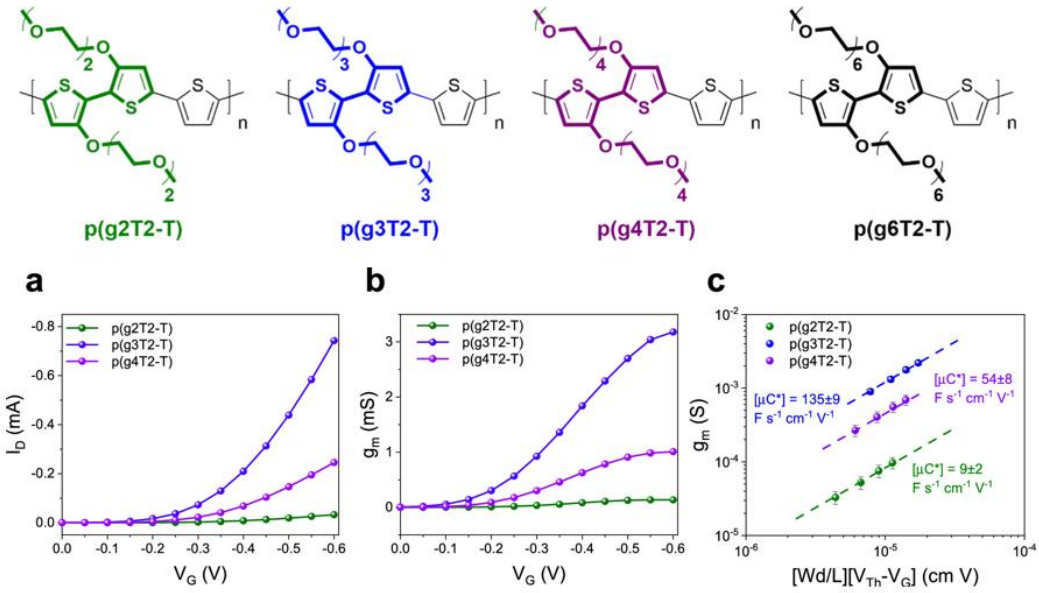

Figure 1.7 (top) Structures of p(g2T2-T), p(g3T2-T), p(g4T2-T), p(g6T2-T) (bottom) output, transfer and OECT characteristic of p(g2T2-T), p(g4T2-T) and p(g6T2-T)

In order to better control swell-ability of the material and its crystallinity upon ion uptake, several effective strategies are developed beyond tuning of chain length. One such method is given by side chain redistribution to improve the device performance of p(g3T2). This involves sequential increase of ethylene glycol on one bithiophene moiety, followed by simultaneous reduction by equal number of repeating units on the successive bithiophene unit[40]. Compare to p(g3T2), all side-chain distributed derivatives led to a substantial lowering of active swelling. This demonstrates a strong inverse relationship with the operational stability and charge carrier mobility of the material, highlighting how this strategy could improve device performance through a structural modification of swelling capability. Alternative strategies include employing a hybrid of glycol and alkyl side chains[42–44], which could optimize charge carrier transport, self-assembly and processability under a judicious design. A similar method involves inserting an alkyl spacer between the glycol moiety and the conjugated backbone[45–48], which had reported several advantages such as reduced active swelling, lowered charge pinning on the backbone, enhanced volumetric capacitance and

improved operational stability. Branching of glycol substituents could also dramatically impact the electrochemical behaviour of conjugated polymers. For instance, incorporating 2,2'-bis(3,4-ethylenedioxythiophene) (biEDOT) and 3,4-propylenedioxythiophene (ProDOT) with asymmetric branched OE side chains enables solution processing from benign solvents like acetone, while most other high-performance OMIECs with linear chains generally requires toxic chlorinated solvents. In addition, these branched copolymers exhibit better ion transport, reduced aggregation issues and improved film morphology, without significantly compromising the charge carrier mobility[49].

1.3.3 Effective OMIECs without glycol substituents

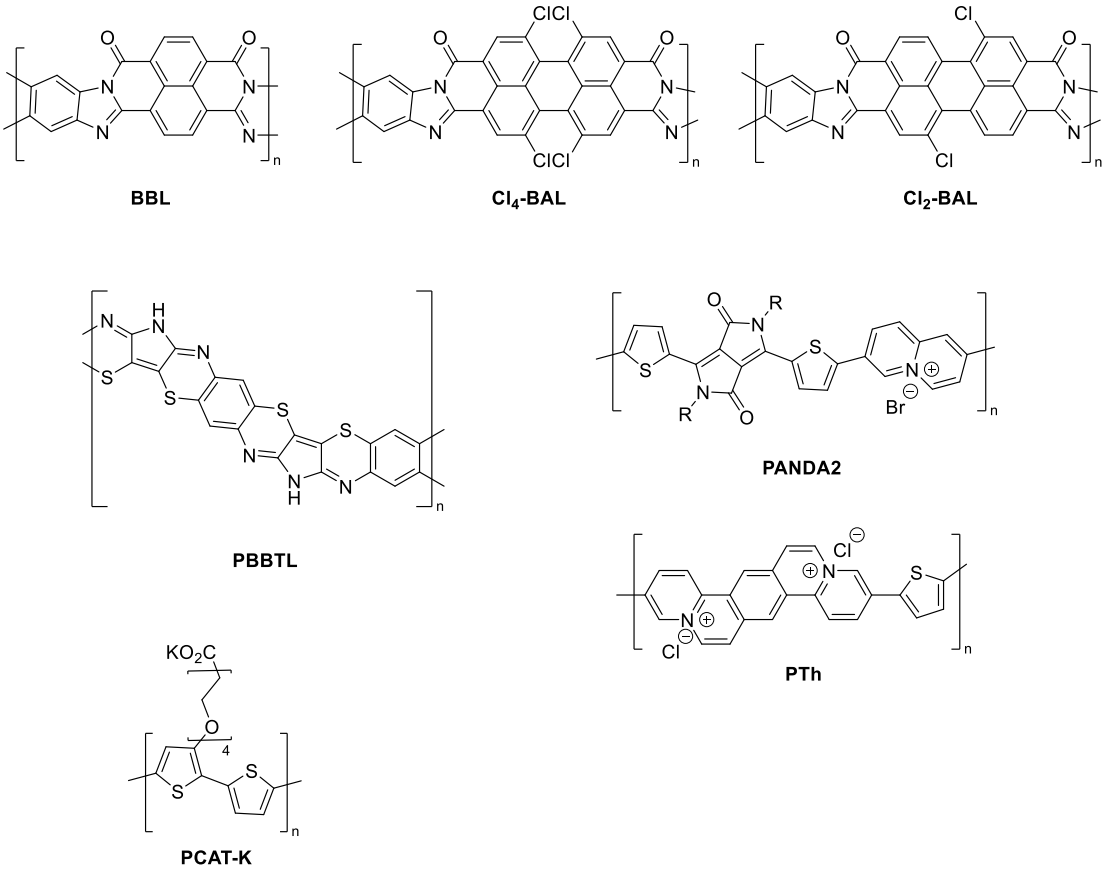

Figure 1.8 All addressed structures of *OMIEC*s without side chain

Despite the widespread use of glycolated, conjugated polymers as effective OECT active layer materials, many high-performance OMIECs without glycol substituents have proven to be promising alternatives. Poly-(benzimidazobenzophenanthroline) (BBL)[50,51] is one such remarkable material extensively studied, featuring high figure-of-merit of 25.9 $Fcm^{-1}V^{-1}s^{-1}$ and an impressive volumetric capacitance of 589 Fcm^{-3}, despite the lack of hydrophilic, solubilizing side chain. This interesting phenomenon could be attributed to an irreversible hydration of the material driven by the initial electrochemical doping cycle. This leads to a subsequent lamellar expansion with retention of water molecules which persist over the electrochemical cycles, creating an embedded hydrophilic environment which favours the transport of kosmotropic ions[52]. In addition, the rigid backbone and lack of side chains in BBL results in higher crystallinity and improved operational stability, as water and ion uptake does not significantly alter and degrade the ordering of polymer film[52]. One notable drawback commonly associated with BBL is its poor processability, since a solution-based fabrication could only be achieved from organic acids like methanesulfonic acid. This also poses difficulties in characterizing the molecular weight, making viscosity measurement the only effective approach in making an effective estimation[53]. This problem of poor solubility had been mitigated in more recent reports with addition of dopants like poly(ethyleneimine) (PEI)[54] and PCAT-K[55] (Figure 1.8), creating highly conductive polymer ink soluble in ethanol and water, respectively.

Possibly owing to its outstanding performance and facile synthesis[32], structural variants of BBL remains relatively unexplored until more recently[56–62]. One key modification involves π-extension of its backbone into a perylene-derived structure[59,62], creating four additional substitution sites for further functionalization. This improves the versatility in tuning optoelectronic properties. For instance, in Cl_4-BAL[59], tetra-chlorination of the

polymer backbone leads to a deep LUMO of -4.83 eV, resulting in remarkable air-stability upon n-doping. This bay substitution also creates a twisted perylene core with a twist angle of 37°, giving rise to excellent solubility in methanesulfonic acid (MSA). Reducing Cl-substitution on perylene core proves effective in enhancing device performance in an n-type OECT. In this case, Cl_2-BAL features an eightfold improvement in μC* compared to Cl_4-BAL. The lower Cl-substitution reduces twisting around the perylene bay position, enforcing backbone planarity and resulting in lower π-π stacking distance. In addition, Cl_2-BAL presents exclusive edge-on substitution, which better promotes electron transport compared to Cl_4-BAL[58]. Interestingly, Cl_2-BAL also possesses antiambipolar transfer characteristics and could be used in an OECT-based inverter with p(g1T2-g5T2) as pull-up channel[62]. P-type ladder polymers such as PBTTL[56,60,61] exhibit μC* lagging slightly behind the state of the art materials, but still presents potentials to be developed into promising OMIECs. These materials feature enhanced thermal stability, making them good candidates as active layer in thermoelectric applications.

Beside ladder polymers, conjugated backbone with cationic hydrophilic building blocks also garnered increasing attention over the recent years. A first report of poly (pyridinium phenylene) in 2008 aimed to simultaneously increase the solubility of the material in water and deepen its LUMO energy level[63]. This key innovation was brought up again more than a decade later, shedding the light for a library of new high-performance OECT material, featuring PANDA2 with a μC* of 62 $Fcm^{-1}V^{-1}s^{-1}$[64]. Recently, a record-high μC* of 225.71 $Fcm^{-1}V^{-1}s^{-1}$ was achieved from high-molecular-weight polymers from side-chain-free ionenes[65]. Similarly, this design strategy inspires the invention of many high-performing materials in related optoelectronic application such as semiconducting hydrogels[66] and thermoelectric[67]. Their excellent processability

in water or alcohol enabled fabrication of electronic devices from green-solvents, paving the way in building safe, biocompatible interface for bioelectronic applications.

1.4 Novel OMIECs architectures beyond glycolated conjugated polymers

1.4.1 Motivation

While the previously outlined OMIEC design principles provide a systematic framework for developing new materials, each approach has its inherent limitations, and a universal design blueprint remains elusive. For instance, incorporation of extended glycol chain can improve solution processability[68] and enhances ordering in film morphology[69]. However, disruption of interconnectivity between crystalline domains have been previously reported[70], not to mention that these aliphatic fragments were intrinsically insulating. An excessively extended glyme substituent incorporated without judicious considerations, as in in p(g6T2-T), deteriorates device performance and results in films with poor mechanical stability[39]. Although balancing ionic and electronic transport through further side-chain engineering remains a feasible optimization strategy, greater complexity in structural design associates with more cumbersome synthesis, limiting scalability and increasing production cost.

In comparison, ladder-type conjugated polymers are synthesized from structurally simpler precursors. However, their fabrication often requires strong organic acids, which raises concerns about in vivo biocompatibility for biomedical applications. Furthermore, the harsh condition employed for polymer synthesis demand specialized, chemically resistant reactor vessels. From the perspective of structural design, the versatility of this approach is also restricted by the relatively limited number of reported processable, high-performing conjugated backbones.

In light of these, the intrinsic limitations in these widely adopted approaches dictate that investigating alternative molecular architecture for OMIEC design is not just relevant, but necessary. The exploration of novel paradigm in structural design may provide solutions that circumvent these existing compromises and brings about a fresh perspective in delivering next-generation high-performance OMIECs.

1.4.2 Block copolymers and conjugated block copolymers

Block copolymers form a versatile class of materials which rapidly developed over the past 60 years[71]. Stemming from macromolecular counterparts of molecular surfactants, these materials present unique self-assembly behaviours both in-solution and on-surface, facilitating control over the nanostructures of the materials. A general understanding of block copolymer morphology on-surface was discussed in many prior reviews based on phase diagrams of an ideal diblock copolymer, which was estimated based on self-consistent mean-field theory. The morphology of the assemblies was governed by three factors – the polymer degree of polymerization (N), Flory-Huggins parameter (χ) and the volume ratio of the component blocks (f)[72,73]. In most cases, χ reflects the degree of incompatibility between different blocks, with a positive and large χ entropically favouring microphase separation. To sum up the overall thermodynamic incompatibility from all monomers in each sub-block, this is scaled by the degree of polymerization (N), giving rise to segregation product (χN). This is used to quantify the extent of microphase separation, with an estimated minimum value of 10.5 necessary for the formation of ordered nanostructure. The exact morphology is further influenced by the volume fraction of each block. To minimize interfacial contact, curvature between the segregated nanodomain decreases as the block ratio tends to unity. In an ideal, monodisperse diblock copolymer system, order-to-order transition progresses

from body-centered cubic spheres to hexagonally packed cylinders, to bicontinuous gyroid, to lamellae networks as the block ratio increases[74–76]. These morphology profile became more complicated when polydispersity is taken into account. For instance, the melt of polymer with higher PDI contains larger chains which acts as an effective compatibilizer stabilizing the interface between different blocks, this lowers q*, the spatial frequency of the dominant composition fluctuation, which translates to greater domain spacing compare to a monodisperse polymer with identical average M_n[77,78]. On the other hand, this improved interfacial stabilization promotes ordering of the block copolymer, lowering the segregation product required for microphase separation. An alternative interpretation can be given from a thermodynamic standpoint – more polydisperse polymer composition intrinsically exhibits higher configurational entropy, thereby reducing the free energy penalty over mixing of polymer chains with different length[77].

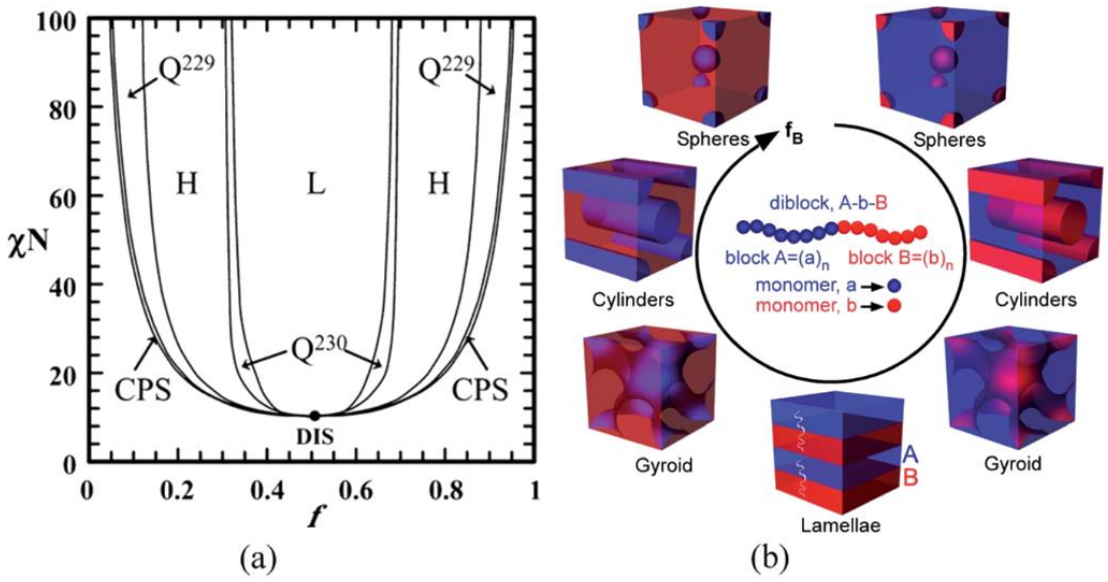

Figure 1.9 a) Phase diagram of diblock copolymer predicted by SCMF theory. In this diagram, H and L refers to hexagonally packed cylinders and lamellae, respectively. Q_{229} is body centred spheres while Q230 is double-gyroid phase. CPS is closed-packed spheres and DIS is disordered phase. b) Various microdomain organization patterns of a linear AB diblock copolymers[76]. reproduced under Creative Commons Attribution licence 4.0 International

The versatility of block copolymer to adapt different morphology with varying molecular composition provides a new mean for nanostructure engineering. This finds useful applications in pattern transfer during nanolithography[79]. For instance, to prepare a nanoporous polystyrene (PS) template, a well-ordered film of PS-b-PMMA following thermal annealing could be treated with deep UV irradiation to remove the photolabile PMMA block, revealing ordered pore structure in the remaining PS film. The resulting pore size could be controlled by varying molecular weight of the block copolymer while maintaining similar composition[80,81]. An alternative method to enlarge the nanopores involve incorporating small amount of PMMA homopolymer, which increases the size of the PMMA domain during self-assembly[82]. Similar nanoporous templates could be prepared from PS-b-PLLA through air plasma treatment[83] or base-mediated hydrolysis [84,85]. The nanostructure of the resulting porous PS could be transferred in many different

ways. For instance, in preparation of ordered <100> Si nanorod[86,87], the nanoporous PS template was fabricated over a thin layer of Si_3N_4, which acts as a hard mask for the Si substrate underneath. Following reactive ion etching, the pattern on the nanoporous polystyrene was directly transferred to the Si_3N_4 hard mask, which then underwent further HBr etching to leave regular Si nanorods.

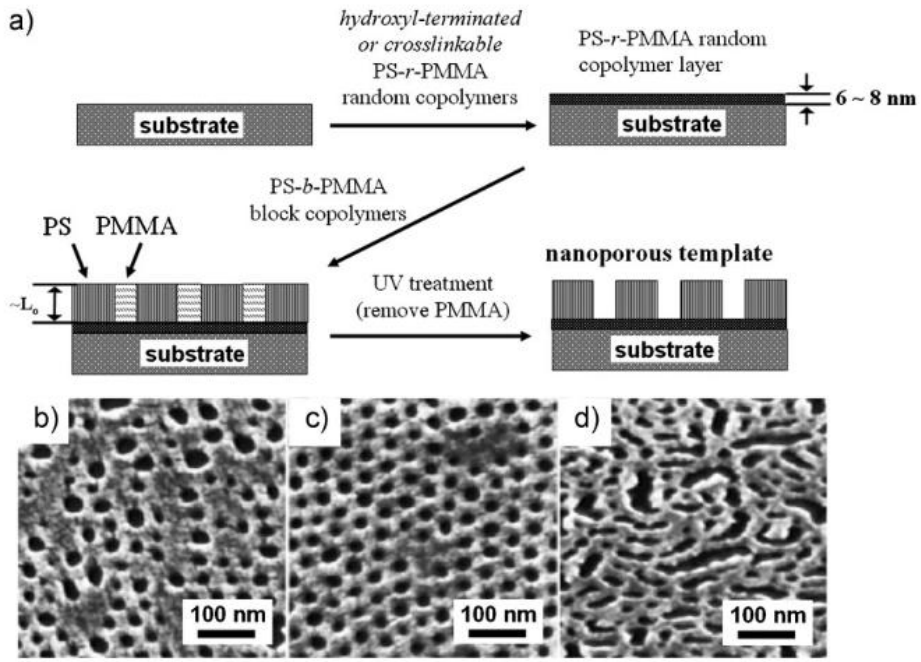

Figure 1.10 a) Schematics to prepare the nanoporous template from PS-b-PMMA thin film The SEM images of nanoporous template after UV irradiation. The thickness of templates is: (b) 31 nm, (c) 42 nm, and (d) 51 nm.[87] reprinted with permission from. (K. W. Guarini, C. T. Black, S. H. I. Yeung, Adv. Mater. 2002, 14, 1290) Copyright 2002, Wiley-VCH.

Beside forming unique nanopatterns through on-film self-assembly, block copolymers can also aggregate into micelles of different shapes in solution. For instance, polaxomers, a class of amphiphilic block copolymers with a hydrophobic polypropylene glycol core sandwiched between two polyethylene glycol fragments[88]. Their intrinsic capability to undergo sol-gel transition under heating had been extensively studied[89]. In aqueous solution, polaxomers like Pluronic 127 is solvated by a hydration layer and therefore exist as low-viscosity injectable fluid (sol). When the

temperature is raised, individual Pluronic 127 unimers micellize and stack together into organized networks, which is associated with dehydration driven by the entropy gain from aggregation of PPG chains, leading to gelation. This features many useful biomedical applications such as tissue regeneration[90], drug delivery and antimicrobial therapy[91].

Conjugated block copolymer forms a distinctive subset of block copolymers. As the name suggests, one or more comprised subcomponent is fully conjugated in nature. The rigidity of these molecular structures favours strong π-π interaction between individual backbones and are termed "rod" to reflect their conformational dissimilarity from other flexible polymers like PEG and PS, which are referred to as "coil". This stark disparity leads to large value of χ in a rod-coil block copolymer. However, the propensity of rod block to crystallize under rod-rod interaction can complicate the overall morphology, leading to deviation from the ideal self-assembled nanostructures discussed previously.

To date, there exists countless conjugated building blocks which can be assembled into polymer chains. Contrarily, only a limited number of backbones are suitable for rod-coil coupling. This can be attributed to the relatively narrow scope of monomers that can be harnessed to yield an end-group precise polymer fragment. This is unsurprising, considering that a suitable condition must be simultaneously highly efficient to drive effective polymerization and present sufficient chain-growth character for better end-group control.

The quasi-living character of KCTP[92] on P3AT leads to a vast array of poly(thiophene)-based rod-coil block copolymers. These materials find useful during early development of P3HT:PCBM-based bulk heterojunction (BHJ) photovoltaics[93], which had been shown to improve the device performance in several distinct ways. For instance,

compare to a blended mixture of P3HT:PCBM, P3BT-b-fullerene featured better microphase separation with less domain size, favouring exciton diffusion. Alternatively, these block copolymers could be added to P3HT:PCBM blend as compatibilizer, reducing interfacial tension between the two phases and hence the size of each domain. These had been shown[94,95] to improve the overall PCE significantly. While these materials do not prove competitive against the current state-of-the-art, they offered an interesting strategy to tune BHJ morphology, which can be employed in modern organic photovoltaic designs to further improve device performance.

In addition, the self-assembly behaviour of rod-coil block copolymers was employed to improve device performance in OFET. For instance, the presence of PS block in P3HT-b-PS strengthened chain packing between P3HT backbones. The optimal charge mobility was achieved with the block copolymer with 85 wt% P3HT, which exhibits a crystalline nanoribbon nanostructure and presents twofold mobility increase compared to P3HT homopolymer. This was attributed to the ordering of P3HT domain from optimal interfacial stabilization of the PS coil block[96]. Another interesting example was given by P3HT-b-Poly(PyMA). In this case, instead of the conventional morphologies discussed previously, 6-(pyren-1-yloxy)hexyl methacrylate (abbreviated as PyMA), a discotic liquid crystalline mesogen, stacked together to promote long-range π–π interactions and ordering of P3HT block. This is supported by the formation of uniform microdomains under Atomic Force Microscope (AFM), achieving improved field-effect mobility[97]. Beside improving carrier mobility, incorporation of flexible coil fragment also proved effective in increasing stretchability and reducing elastic modulus, featuring several P3HT-based block copolymers which remains effective OFET following hundreds of strain-release cycle, and are therefore applicable in future flexible electronics[98–100].

Overall, conjugated rod-coil block copolymers feature improved functionalities through controlled formation of unusual and complex nanostructures[101]. In fact, through post-treatment such as crystallization-driven self-assembly (CDSA) or air-liquid interface self-assembly (ALISA), it is possible to prepare 1D or 2D micellar nanoparticles, such as nanoribbon[102], nanofiber[99,103,104] or nanoplatelets[105–107]. Nevertheless, the library of applicable conjugated structures for rod-coil coupling remains scarce. This proves problematic in some applications requiring special electrochemical considerations. For instance, in OECT, poly(3-alkylthiophene) is deemed relatively unsuitable, due to its strong hydrophobicity and HOMO energy level not shallow enough to drive effective electrochemical doping. A prior investigation with block copolymers of P3HT reveals high threshold voltage over 0.8 V, raising concerns regarding its redox stability[33].

Therefore, in order to explore the applicability of rod-coil block copolymer as effective OECT active material, we should adopt a backbone with higher HOMO. Achieving this requires novel chemistry to develop a new shallow-HOMO conjugated backbone with precisely controlled end group, and a method leading to the corresponding block copolymer with judiciously incorporated coil fragment. Addressing these problems found the first cornerstone of this thesis, which attempts to investigate the use of poly(3-alkoxythiophene)-based rod-coil block copolymer as a novel paradigm for OMIEC design.

1.4.3 Conjugated backbone with alternative polar side chains

Despite the abundance of side chain glycolation in OECT active materials, a substantial amount of early developed OMIECs is non-glycolated derived. For instance, conjugated polyelectrolytes based on sulfonate pendant group[108] have been applied as

p-type accumulation OECT material even before the benchmarking figure-of-merit, μC* was established[31], as well as the first introduction of glycolated polymer[109]. In the recent decade, many OMIECs with alternative polar side chains were also investigated in parallel [41,108,110–114]. However, many of these ideas did not receive further development, under reasons not limited to: (i) uncompetitive figure-of-merit compare to the state-of-the-art materials at the time, which are abundantly glyme-derived; (ii) inability of the pendant group to sufficiently solubilize the yielded polymer, especially the ones prepared from structurally bulky building blocks. On the other hand, these materials are more atom-economic than the glyme-grafted counterparts. For instance, the introduction of a single alcohol moiety on side chain results in comparable volumetric capacitance to that of a tetraethylene glycol[41]. Others reveal low active swellability[113], which had been shown to benefit charge carrier mobility[40]. An alternative method to exploit the above advantages, while mitigating undesirable issues associated with processability would be discussed. Herein, we would show how polymer film with short hydroxyl termini could achieve excellent OECT performance, following a post-fabrication treatment strategy to mitigate issues associated with processability.

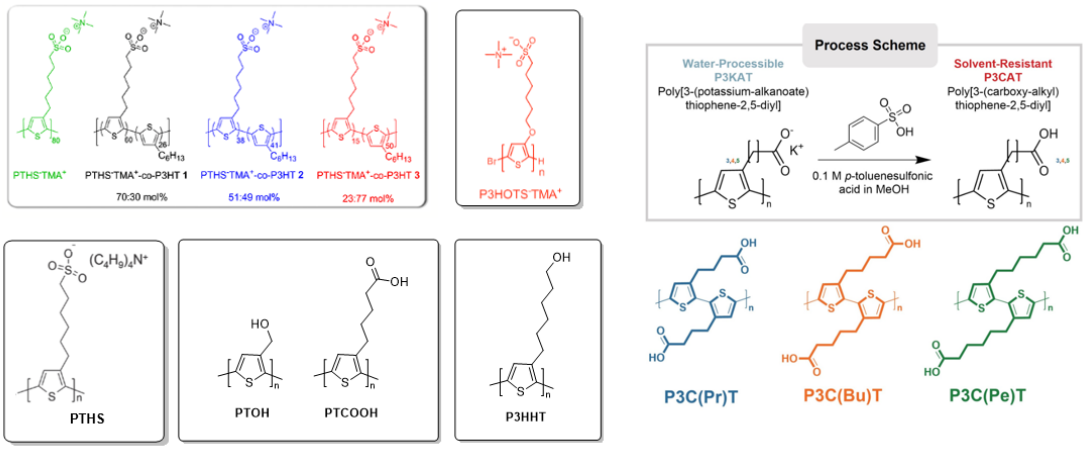

Figure 1.11 All addressed structures of conjugated polymers with non-glycolated, polar side chains

1.5 Thesis objectives and research questions

In this chapter, we have provided an overview of the approaches and considerations in structural design of conjugated polymers, with a focus on improving OECT performance. While side-chain glycolation remains a dominant paradigm, several drawbacks could be identified, such as cumbersome preparation of monomer incorporating structurally complex side chains. Notably, anchorage of pendant group can happen at a relatively early stage of synthesis [39,40,109], compromising the divergence of the chemical synthesis. Considering that optimization of glyme-derived OMIECs requires judicious control over side-chain properties, cumbrous synthesis work would be involved before the material could be actually screened and characterized. Since the role of glycol side chain is primarily to modulate ionic transport in the device channel, an interesting approach would be to explore paradigms with alternative fragments serving similar functionalities.

Hence, a central theme of this thesis involves investigation of two such designs in OMIECs – P3AOT-based rod-coil block copolymers and conjugated polymers with alcohol terminus.

In Chapter 2, we provide a comprehensive discussion of the novel chemistry required for the synthesis of P3AOT block copolymers. The goal of this strategy is to segregate electronic conduction (rod block) and ionic transport (coil block) of the material, offering a modular platform for optimization of charge and ion mobility. The solutions to two important subproblems are presented in chronological order: a novel synthesis of end-group precise poly(3-dodecoxythiophene) (P3DOT) is first presented, alongside the reasoning behind condition optimisation achieving this goal. Subsequently, three different rod-coil coupling schemes are addressed, eventually concluding with a novel Knoevenagel-type reaction which successfully synthesizes the series of block copolymers.

Chapter 3 builds upon the work in the previous chapter. A library of block copolymer series was prepared. The electrochemical properties of which are investigated with cyclic voltammetry, UV-Vis spectroscopy and spectroelectrochemistry, while the morphology is mapped with AFM. The device performance of P3DOT-based block copolymer is then evaluated. Interestingly, incorporation of a short PLLA fragment achieves the highest figure-of-merit, which was rationalized based on swelling and scattering experiments. The scope of P3AOT block copolymers is then expanded to include two derivatives with branched and partially glycolated side chains, respectively. These are characterized with spectroelectrochemical analysis and contrasted against P3DOT to understand the interplay between side-chain and main-chain glycolation.

Chapter 4 seeks to explore poly(thiophene) with short alcohol terminus as OMIEC. Limited by the poor solubilizing ability of these side chains, direct deposition of such material is practically impossible. Hence, the alcohol functionality is masked with a bulky silyl protecting group, which renders the polymer lipophilic enough for solution processing. The uniform film fabricated on OECT device is then chemically treated to

unmask the alcohol terminus, achieving excellent OECT figure-of-merit of 1036 $Fcm^{-1}Vs^{-1}$.

Finally, Chapter 5 presents the alternative investigations conducted by the author in finding a general procedure for conjugated rod-coil block copolymer synthesis. Herein, block copolymers with alternative rod block, such as PEG-b-F8BT-b-PEG, were fabricated into nanoparticles following nano-precipitation, achieving improved HER efficiency. The chapter is concluded with preliminary explorations in SCTP for poly(3-alkoxythiophenes), which presents remarkable difference from its KCTP counterpart discussed in Chapter 2 and 3.

CHAPTER 2

Synthesis of P3AOT-based block copolymers

2.1 General information and attributions

The project was first conceptualized by Dr. Iuliana P. Maria and Prof. Iain McCulloch. All development and analysis of polymer, cyclic voltammetry, UV-Vis spectroscopy, PESA and spectro-electrochemistry was conducted by Junfu Tian, under the supervision of Dr. Iuliana P. Maria, Dr. Christina Koussef and Dr. Sophie Griggs. GIWAXS was similarly conducted by Junfu Tian at Diamond Light Source at Beamline I07 with the help of Dr. Jonathan Rawle (Diamond Light Source, UK), under the lead of Dr. Jin Yang. BET analysis was conducted by Yuyun Yao and Dr. Wanpeng Lu. Analysis of GIWAXS was conducted by Dr. Andreas Erhardt. DSC analysis was conducted by Rachael Found. AFM was conducted by Dr. Xian E Li, Dr. Elena Chulanova and Bob Zhang (Massachusetts Institute of Technology). OECT testing was performed by Rachael Found and Wentao Shan (King Abdullah University of Science and Technology).

2.2 – Introduction

Among all conjugated polymers used in organic electronics, poly(thiophene) stands out as one of the most important classes of material. It had been utilised in a wide range of applications, such as transistors, batteries and LEDs. Despite its prominence, the development of poly(thiophene) dates back only a few decades, with its first successful synthesis reported in 1980[115]. Compared to other conducting polymers like polyacetylene, poly(thiophene) exhibits superior thermal stability, inertness to oxygen and versatility for chemical functionalization[115]. Furthermore, the abundance and affordability of thiophene monomers make scalable industrial production feasible, further solidifying its role as a key building block for material design.

The conductive nature of poly(thiophene) stems from both the electronic structure of the monomers and the molecular ordering of the polymer chain. While these macromolecules are intrinsically insulating and generally possess band gap of a few eV, charge transport can be induced through electrochemical charge injection. These charge carriers, commonly described as polarons, are quasi-particles comprising an injected charge coupled with a structural deformation of the polymer chain. Depending on their polarity, they are further classified as p-type and n-type.

The aromatic system of thiophene is considered electron-rich due to conjugation of high-energy nonbonding lone pair from the sulphur heteroatom. In the scope of this chapter, our discussion focuses on poly(thiophene) with shallow HOMO levels, which are predominantly p-type in nature. Charge transport in these materials is facilitated by hole-polaron, which forms when a π-electron is removed from the conjugated backbone. These charge carriers tend to delocalize extensively across the polymer chain due to favourable Coulombic interaction with the π-system as well as enhanced planarity induced by polaron-phonon coupling[116,117]. For instance, p-type doping causes charge induced relaxation in poly(thiophenes), transforming its aromatic building block into quinoid-like structures. This structural change shortens bonds between each thiophene unit and reinforces planarity along the polymer backbone, thereby facilitating intra-chain charge transport. Conversely, charge transfer between the polymers takes place through hopping of the hole polarons, which is enhanced by the strong π-π stacking of the ordered polymer chains[116].

While it is intuitive that increased molecular order and structural rigidity of conjugated backbone strengthens both intra- and inter-chain charge transport, these benefits often come at the expense of polymer solubility. This trade-off poses significant challenges for processability and fabrication of the material in device applications. Indeed, early

attempts to prepare “unsubstituted thiophene polymers” through acid-catalysed condensation[115,118–120] primarily yielded oligomers rather than true polymers, leading to degree of polymerization less than 10, alongside substantial amounts of insoluble products following Soxhlet extraction. This phenomenon can be attributed to the precipitation of the long, insoluble polymer chain from the reaction mixture. This causes further propagation to become kinetically hindered, thereby leading to premature termination of the polymerization process.

To improve optoelectronic properties of these materials, two families of thiophene-containing compounds were simultaneously studied: oligomers and polymers grafted with side chains. Due to better molecular ordering and synthetic reproducibility, the former offers advantages over their polymeric analogue for the manufacturing of electronic devices. Unsubstituted linear thiophene-containing oligomers can be synthesized with high purity up to 8 monomer units long[121–123]. However, similar to the unsubstituted poly(thiophene)s, the strengthening of π-π stacking interactions renders these materials increasingly insoluble with greater number of repeating units. For instance, octithiophene is a completely insoluble crystalline powder[121]. This lack of processability requires extensive purification efforts. In the case of octithiophene, despite the highest reported mobility in OFET compared to its lower oligomeric homologues[124], the device performance is highly dependent on the thermal treatment, and more importantly, the purity of the thin film[125–127]. Trace amounts of equally insoluble α,β- and β,β- coupled side-products were extremely difficult to remove[121] and the presence of these impurities can lead to significant reduction of charge mobility.

To address these challenges, α,ω-functionalization of thiophene oligomers has been widely investigated as a strategy to improve their solution processability[121]. Many works focus on the end-chain engineering of these compounds, particularly alkyl

substitution, which has garnered considerable attention due to the ability to induce liquid crystalline-like behaviour. The presence of these alkyl substituents influences the molecular assembly of materials, aligning their long axis perpendicular to the substrate underneath[121,123,126]. This molecular ordering in turn impacts their electronic behaviour in OFETs. This is particularly evident in α,ω-dimethyl and α,ω-dihexyl oligomers[121,128] where the short alkyl chains exhibit minimal solubilizing effect but instead promote the reordering of their molecular assembly upon deposition. Extending these end functionalities to longer dodecyl tail[129] allows these compounds to be soluble in hot chlorinated solvents, improving solution processability.

Beyond alkyl substituents, various other moieties are incorporated into the oligothiophene core to introduce alternative functionalities. For instance, fluorocarbon end-capping of the oligothiophene molecules transforms the material into an electron-transporting semiconductor, while maintaining film morphology and molecular microstructure comparable to the alkyl-substituted analogue[128]. Another interesting approach involves incorporation of thermally labile ester moieties on the termini. Because these saturated substituents are inherently electron-insulating, their removal following fabrication can enhance the charge carrier mobility of the device. Annealing the solution-processed film cleaves these end-cappers, increasing mobility by three orders of magnitude[130]. Interestingly, the attachment of ethylene glycol units[131,132] to oligothiophenes was reported even before the rise of organic electrochemical transistor. While enhancing ionic transport and hydrophilicity does not directly improve FET mobility, these designs leverage the solubilizing capabilities and self-organising behaviour of the glycol substituents, yielding sexithiophene lamellae that are both conductive and highly solution processable. Similar principles of molecular design were recently employed in developing small-molecule p-type OECT[133]. This approach

involves end-grafting of a triethylene glycol tail onto an oligomeric bithiophene or bis-3,4-ethylenedioxythiophene core. In aqueous environments, the combination of a highly electron-rich backbone with hydrophilic end chain significantly enhances electrochemical charge injection. While μC* of the best-performing device still falls behind many state-of-the-art polymeric materials, these substituted oligothiophenes represent the first small molecules suitable as active material in a p-type OECT. This hence establishes a novel OMIEC architecture and design framework, paving the way for further development of small-molecule active materials in the field.

Among conjugated polymers, poly(3-alkylthiophene) is one of the most representative classes of materials studied. Presence of 3-alkyl substituents strongly enhances solubility and processability. Under appropriate polymerization techniques, such as Grignard Metathesis polymerization (GRIM)[92,134,135] or metal-catalysed oxidative polycondensation[136], high-molecular-weight conjugated polymers can be synthesized. The GRIM method, in particular, offers the added advantage of producing polymers with high regioregularity. This structural precision reduces the band gap, improves on-film crystallinity and promotes molecular ordering, significantly improving electrical conductivity of the fabricated devices[137,138].

Similar to the use of functionalized end chains to tailor material behaviour in oligothiophenes, the past decade has seen significant advancement in side-chain engineering for poly(thiophene)s. For instance, glycolation of conjugated polymer has been extensively utilized to design high-performance active material for OECT, as detailed in Section 1.3. Herein, we aim to preserve the strong microstructural order of alkylated conjugated polymers while achieving the high hydrophilicity required for efficient charge injection in aqueous electrolyte. A direct approach involves constructing a rod-coil block copolymer from an alkylated polymer core. Coil

fragments such as PEG, PCL and PLLA can be introduced via chain-end incorporation. This integration of both side-chain and end-chain engineering not only expands the chemical space for functional material design but also unveils unprecedented self-assembly behaviours.

2.3 – Kumada catalyst transfer polymerization

2.3.1 P3HT and Kumada catalyst transfer polymerization

Due to the strong nucleophilicity of its aromatic ring, thiophene is highly susceptible to oxidation. Early design of P3AT synthesis hence involves an oxidative polymerization using a $FeCl_3$ oxidant[136], which does not generate undesirable 2,4-coupling product[139]. While M_n of these polymers correlate positively with the amount of chemical oxidant used, they exhibit a broad polydispersity[140,141] and poor reproducibility. Moreover, the asymmetric nature of 3-hexylthiophene monomer raises further concern on regioregularity of the polymer. Since oxidative polymerization of 3-hexylthiophene takes place via coupling of the oxidized cationic radical, possible head-to-head (HH) and tail-to-tail (TT) dyad structures form simultaneously alongside desired head-to-tail (HT) ones. While steric repulsion between the alkyl chain may favour the latter slightly, oxidative polymerization with $FeCl_3$ results in HT couplings ranging from 58% to 80%[139,141,142]. Other synthesis such as electropolymerization[143] also suffers from similar problems.

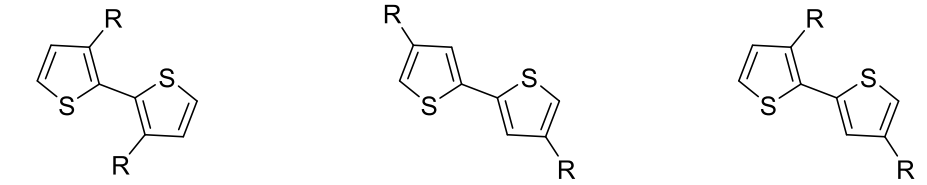

Figure 2.1 Structures of HH, TT and HT dyad

In P3AT, presence of HH structure brings pairs of alkyl side chains in proximity and this unfavourable steric repulsion disrupts planarization of polymer backbone, hindering π-π stacking and impeding transport of charge carriers. Additionally, irregularly placed side chain obstructs proper backbone alignment, impeding ordered self-assembly in both solution and solid states. Elimination of these defect can hence result in improved charge carrier mobility, leading to better electrochemical and photonic properties[144–148]. This synthetic challenge is addressed by Kumada catalyst transfer polymerization (KCTP)[92].

2.3.2 Synthetic considerations in Kumada catalyst transfer polymerization

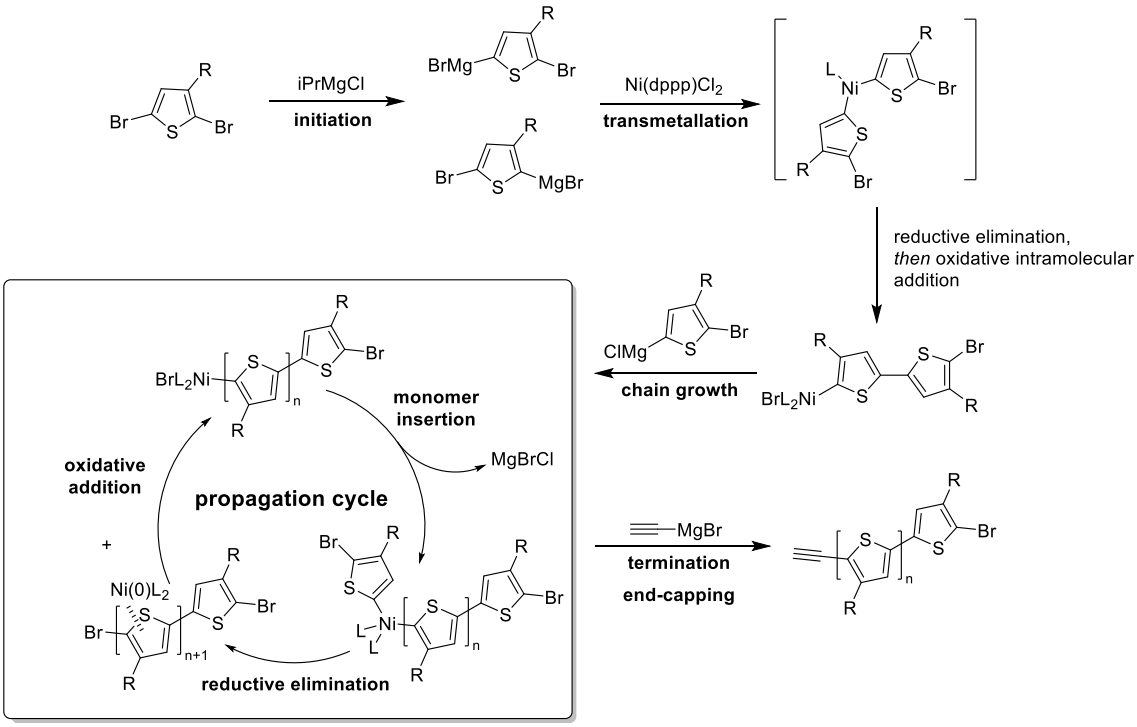

Figure 2.2 Reaction Mechanism of Kumada Catalyst Transfer Transfer (KCTP)

KCTP is widely accepted take place via a chain-growth mechanism. Compared to uncontrolled alternating copolymerization with bi-functionalized monomers, there are several interesting design considerations for KCTP featuring remarkable controls in the polymerization process. Notably, KCTP is more than simple polycondensation between

heterofunctional compounds, because competitive step-growth mechanism should prevail otherwise. KCTP results in polymers with controllable molecular weight, narrow dispersity and under special design, controlled end-group functionality. While its mechanism remains controversial, a chain-growth model through catalyst transfer propagation is widely accepted and presented in Figure 2.1.

To form the active catalyst, Ni(II) precatalyst is first transmetallated by two Grignard monomers, which then undergoes reductive elimination to form a π-complex. In this process, the metal centre remains associated with the dimer formed, which isomerizes and oxidatively adds to the terminal halide, completing formation of the initiator. This is supported by many several previous mechanistic studies[92,149], where reaction with two stoichiometric equivalence of monomer to catalyst predominantly forms the tail-to-tail initiator following acid quenching. The strongly electron-donating magnesium halide moiety impedes oxidative addition at the halogen terminus of other unreacted monomers, allowing propagation to selectively take place on the initiated backbones with Ni reaction centre. Then, monomers in the reaction mixture sequentially adds to the Ni reaction centre following transmetallation and is eventually covalently linked to the chain by reductive elimination.

"Ring-walking" of Ni(0) centre is a key step during propagation which distinguishes catalyst transfer polymerization from simple polycondensation[150]. Following reductive elimination, the metal centre migrates and associates itself non-covalently with the terminal thiophene monomer, before oxidative insertion into the halogen terminus takes place. Therefore, only one metal centre should remain associated with extending chain in an ideal, living catalyst transfer polymerization. The average degree of polymerization can hence be controlled by varying monomer-to-catalyst ratio.

The reactivity and stability of the π-complex and catalyst are essential properties determining the living and chain-growth nature of the polymerizations. For instance, Ni catalysts often exhibit higher polymerization kinetics compared to their Pd analogues[150]. This can be ascribed to stronger reactivity from smaller atomic radius of Ni, enabling faster oxidative addition and transmetallation. In addition, stronger donor ancillary ligand like NHC promotes efficiency of ring-walking. Considering that Ni(0) complexes exhibit unique three-center-four-electron bonding interactions[151], a stronger donor ligand can stabilize the reaction intermediate better by favouring π-backbonding from metal to thiophene chain.

In addition, KCTP yields polymer with significantly higher regioregularity. In the classical synthesis of P3AT, the Grignard intermediate is prepared via transmetallation of dibromo-substituted alkyl thiophene monomer. While the presence of alkyl side chain sterically hinders formation of 2-substituted precursor, it is still formed as a minor product with 15% yield. This phenomenon of achieving >95% HT regioregularity from an 85:15-ratio mixture of regioisomeric Grignard precursor stems from the different kinetics in HH, TT and HT coupling[92]. In particular, competition experiments of alkyl-substituted thiophene monomers reveal that HH coupling is sterically disfavoured and significantly slower compared to TT and HT couplings.

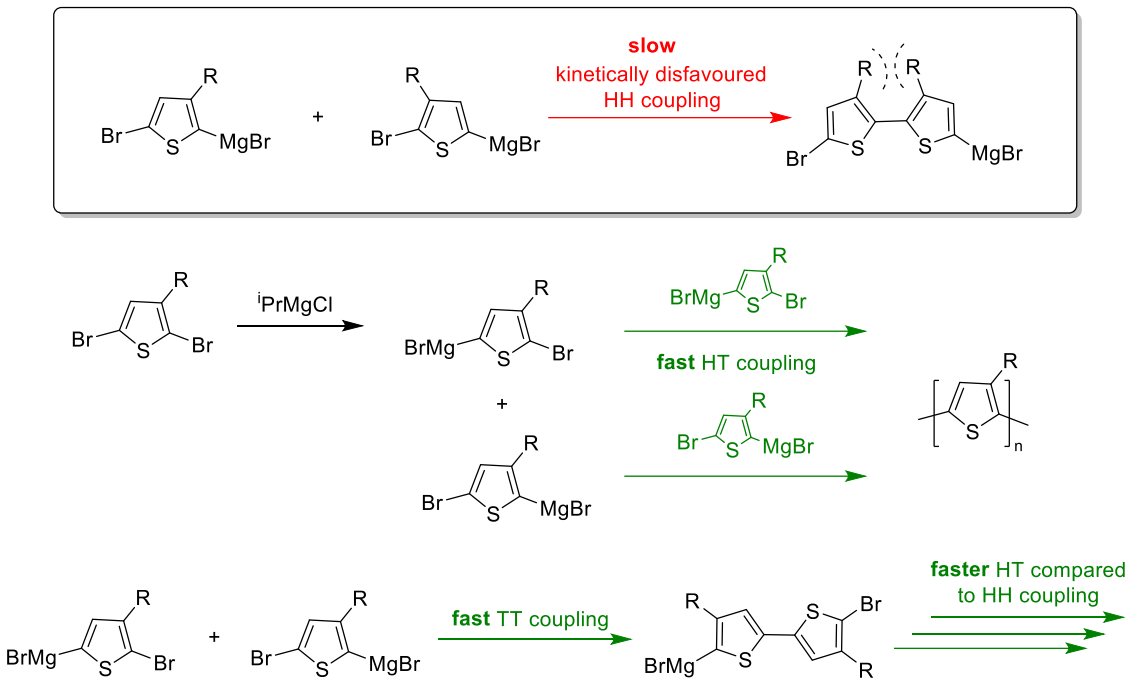

Figure 2.3 Reaction Scheme outlining the kinetics of the possible step reactions during KCTP

As shown in Figure 2.2, despite forming a regioisomeric mixture, each isomer favourably reacts with its own kind, leading to predominant HT coupling. An alternative fast side reaction involves cross-coupling between the two different regioisomers tail-to-tail. However, after this initial TT coupling, both alkyl substituents orient outwards. Since HH coupling is kinetically disfavoured, subsequent propagation must take place in a head-to-tail fashion, leaving one TT defect in an almost regioregular backbone. In both cases, KCTP takes place in a highly regioselective manner, achieving excellent regioregularity.

2.3.3 Termination in Kumada catalyst transfer polymerization

To establish control over end-group functionality of the polymer chain, an in-situ strategy will involve quenching the polymerization mixture with a suitable Grignard reagent. Ethynyl and ethenyl magnesium chloride are commonly used, which mono-functionalize P3AT chains with high selectivity[152]. In addition, ethynyl terminus can be modularly coupled with azide-functionalized counterparts, while an ethenyl substituent forms an excellent masking group for functionalities such as hydroxyl to facilitate further post-polymerization chain extension.

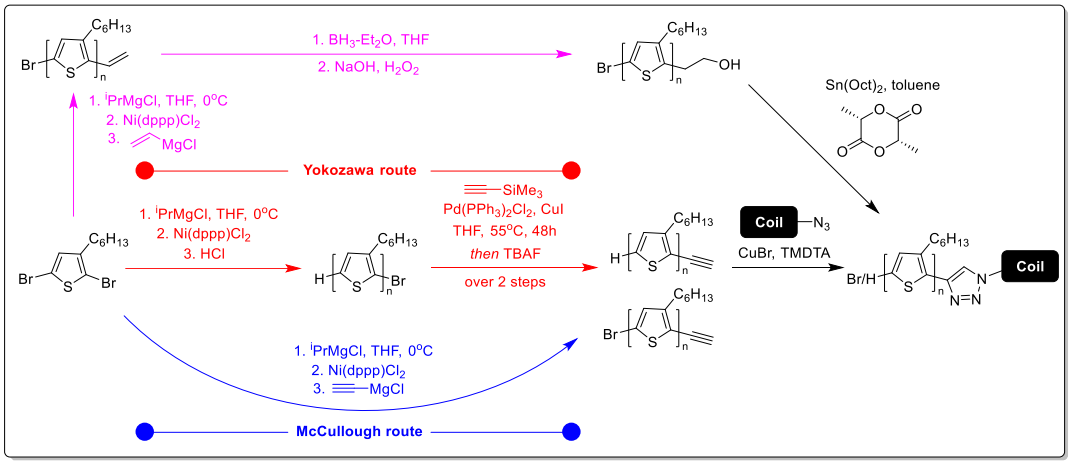

Figure 2.4 Reaction Scheme for examples of synthetic strategies for P3HT-based block copolymers

2.3.4 Strategies of rod-coil block copolymers from P3AT

A summary of most mainstream rod-coil block copolymers strategies was listed in Figure 2.3. For coil fragments like polylactide and polycaprolactone, which were accessible through cationic or anionic polymerization, coil extension starts from a hydroxyl terminated macroinitiator[153,154]. Analogous strategy also involves nitroxide-mediated radical polymerization (*NMRP*)[155], atom transfer radical polymerization (*ATRP*)[97,156,157] or Reversible addition−fragmentation chain-transfer polymerization (*RAFT*)[94,158]. While this strategy allows for facile removal of monomer and oligomeric

impurities, reaction in glovebox is often required for control of polydispersity. In addition, while *P3AT* possesses excellent solubility in common lipophilic solvents, this strategy might prove difficult for more insoluble or viscous macroinitiators.

An alternative strategy involves modular coupling through copper-catalysed azide–alkyne cycloaddition (*CuAAC*) between ethynyl terminated P3AT and azide-terminated coil block[159–161]. For P3AT, the McCullough route[152] is synthetically simpler than Yokozawa route[162], but the latter demonstrates better extensibility to other macroinitiator and results in better specificity towards mono-capped macroinitiator. The complementary coil fragments with an azide-terminus can be easily prepared from the corresponding small-molecule initiator or were commercially available.

An intrinsic limitation of polymer-polymer modular coupling lies in the precise determination of reactant stoichiometry. Because estimation of molecular weight based on *GPC* is calibrated from hydrodynamic volume of randomly coiled polystyrene standards, the molecular mass of conjugated polymers, which are more structurally rigid, tends to be overestimated[163]. Conversely, *MALDI-TOF-MS* distribution is often skewed towards low molecular weight fragments, which more readily desorbs and ionizes, leading to an underestimation of M_n. Considering these, end-group analysis through ^{1}H *NMR* will be ideal for measuring relative stoichiometry.

To promote complete formation of rod-coil block copolymer, a stoichiometric excess of coil fragment was used. This could account for any underestimation of coil fragment stoichiometry due to systematic uncertainties. To remove excess coil blocks in the reaction mixture, their relatively higher solubility due to better structural flexibility could be utilized, allowing them to be removed easily from the reaction mixture through a selective Soxhlet extraction procedure.

2.4 Motivation of block copolymer design

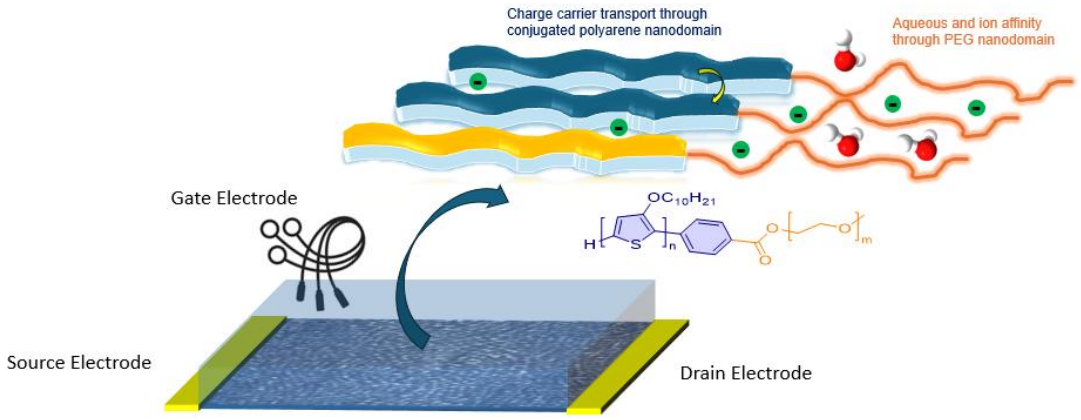

Figure 2.5 Schematic drawing demonstrating the motivation of main-chain PEGylation

In Section 1.4, a brief introduction of block copolymers in organic optoelectronics had been provided. However, to date, a systematic assessment of main chain functionalization on *OECT* performance of rod-coil block copolymers is lacking. In the scope of this thesis, polar coil fragment is attached to the conjugated backbone to enhance its ionic transport properties, with *PEG* depicted as an example in Figure 2.4.

2.5. Optimising end-group controlled synthesis of poly(3-alkoxythiophene) (P3AOT)

Despite being a workhorse p-type material in *OFET*s, being hydrophobic in nature, *P3HT* is generally rendered unsuitable for *OECT* using saline supporting electrolyte. It had been previously reported to only exhibit steady-state saturation behaviour near an applied gate bias of 0.8 V[33]. Compared to *P3HT*, *P3AOT* has a significantly lower ionization potential due to the presence of a conjugatively donating oxygen lone pair adjacent to the thiophene monomer. This raises the *HOMO* energy level of the aromatic system, facilitating charge injection. To further demonstrate that incorporating

functional coil fragments can enhance device performance—even for hydrophobic polymers—we selected poly(3-decoxythiophene) (*P3DOT*) as the target backbone.

KCTP of various alkoxylated[164,165] and glycolated thiophenes[42,166] have been reported previously. Without exception, these procedures followed the same conditions used for classical P3HT polymerization. While these syntheses resulted in conjugated polymers with narrow polydispersity, their end-group distribution was not characterized with *MALDI-TOF* analysis. Achieving high end-group fidelity is crucial, since this strongly influences the reactivity of rod-coil coupling. Moreover, since the resulting polymers exist as a distribution of conjugated chains with different length, distinguishing backbones with different chain-end would be extremely challenging through chromatography. This leads to two considerations required during reaction optimization: (i) The unit coupling reaction must be high-yielding for efficient polymerization, (ii) this reaction must also lead to high end-group fidelity following polymerization. A further implication of criterion (ii) is that, thermal agitation should be avoided if possible to minimize the occurrence of side reactions such as chain transfer. Thus, catalyst transfer polymerization should ideally proceed at room temperature.

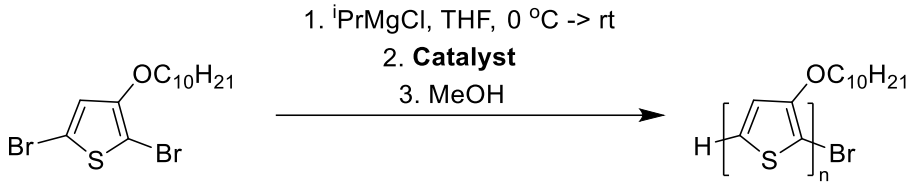

Entry	Catalyst	Condition	M_n/kDa	PDI	Yield
1	$Ni(dppp)Cl_2$	rt, 30 mins	7.0	1.4	29%
2		reflux, 30 mins	10.7	1.5	33%

3		reflux, overnight	9.4 (D = 1.3), 57.6 (1.1)	Bimodal distribution	49%
4		rt, 30 mins, end capper applied	10.8	1.4	35%
5	Ni(dppf)Cl2	rt, 30 mins	4.2	1.5	18%
6	Pd-PEPPSi-IPr	rt, 30 mins	6.4	1.4	33%
7		rt, overnight	7.3	1.4	31%
8	$Ni(IPr)(PPh_3)Cl_2$	rt, 30 mins	15.7	1.4	61%

Table 2.1 Summary of reaction conditions resulting in successful polymerization of *P3DOT*

Different catalytic conditions were screened and summarized in Table 2.1. Initial investigation replicates conditions used for P3HT polymerization[92]. However, a few unique challenges were encountered. Unlike its alkyl analogue, 2-bromo-3-alkoxythiophene moiety autopolymerizes with acid present[167], resulting in the formation of highly insoluble solid following quenching, possibly arising from further polymerization or acid-mediated cross-linking. On the other hand, in-situ end-capping with ethynyl magnesium bromide resulted in minimal conversion, as shown in Figure 2.5. Using $Ni(dppf)Cl_2$, quenching the polymerization with alcohol results in low molecular weight oligomers with a mixture of H/H, H/Br, Br/Br termini. Raising the reaction temperature did not significantly increase the molecular weight. Instead, it activates undesirable side reaction pathway such as capping of isopropyl functionalities and eventually leads to further end-group scrambling.

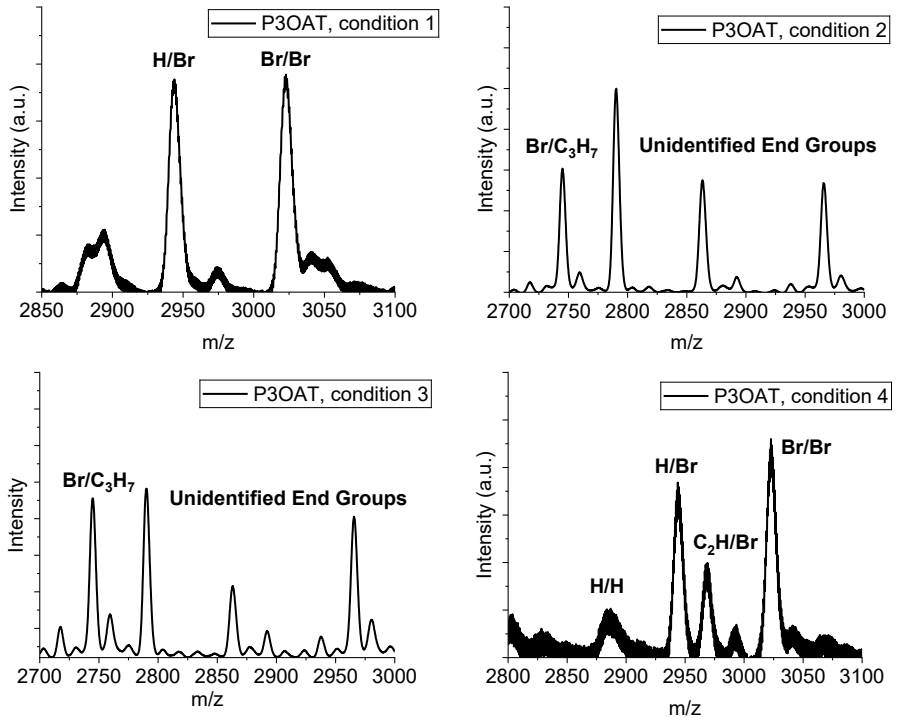

Figure 2.6 End group analysis of *P3DOT* prepared with condition 1 – 4 with *MALDI-TOF*.

Despite being efficient for polymerization of alkylthiophenes, Ni(dppf)Cl_2 was proven unsuitable for the synthesis of *P3DOT* with precise end-group functionalities. In *KCTP*, narrow polydispersity is achieved if the metal catalyst remains associated with the polymer chain throughout propagation. Prior computational studies reveal that the strength of such catalyst-polymer association is governed by a three-center, four-electron interaction between the ligand, metal, and thiophene ring, with electron density donated into the π-system of the thiophene from the metal catalyst[151]. Hence, we hypothesized that the electron-rich alkoxythiophene unit weakens this interaction, promoting early chain termination after catalyst dissociation, as evidenced by the predominance of Br/Br-terminated chains previously observed.

Seeking to prolong the catalyst association and improve living characteristic of the chain-growth polymerization, several catalysts were screened. Among which, Ni(IPr)(PPh_3)Cl_2 resulted in *P3DOT* with the highest monomodal molecular weight and

a narrow polydispersity. As shown in Figure 2.6, each polymer chain exhibited predominantly H/Br termini following precipitation. This optimized condition was effective for synthesizing alkoxylated and glycolated poly(thiophene) with high end-group fidelity. However, in-situ termination with Grignard end-cappers remained ineffective, leading us to instead build block copolymers from a *P3DOT* macroinitiator with H/Br termini. This provides a robust foundation for developing block copolymers via post-polymerization coupling.

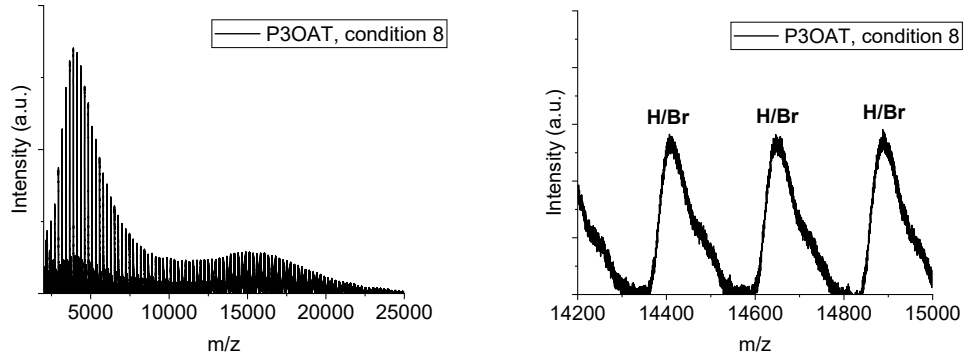

Figure 2.7 End group analysis of *P3DOT* prepared with optimal condition with *MALDI-TOF*.

2.6 Post-functionalization of H/Br P3DOT

2.6.1 CuAAC approach

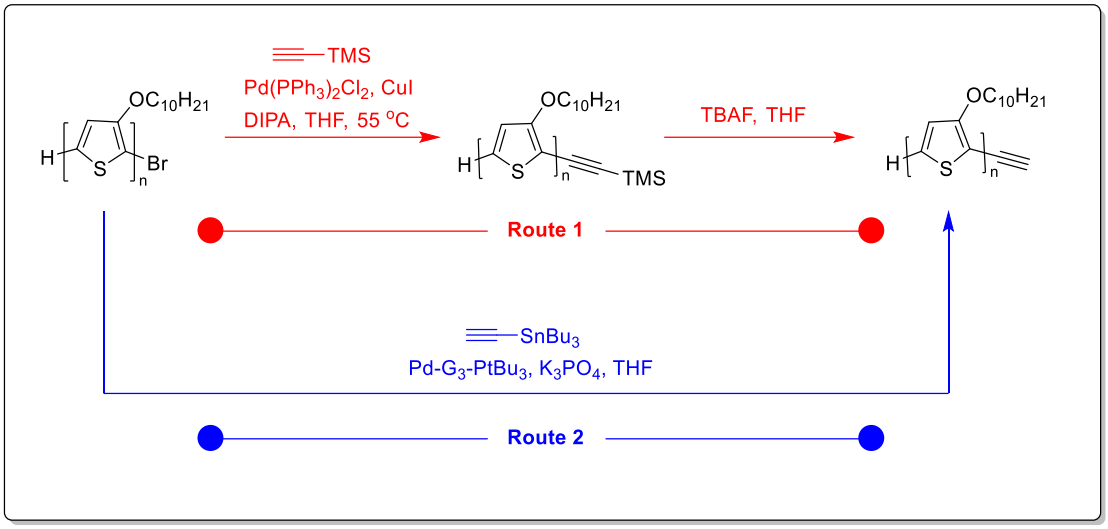

Figure 2.8 Reaction scheme of two routes attempted for alkyne-terminated *P3DOT*. Route 1 involves Sonogashira with diisopropylamine (DIPA) as base, followed by deprotection of trimethylsilyl (TMS) group with tetra(n-butylammonium) fluoride (TBAF). Route 2 is faster with Stille coupling.

To obtain a rod fragment suitable for *CuAAC*, two distinct ethynylation strategies were investigated, as illustrated in Figure 2.7. Initial effort employed an approach similar to the previously reported post-polymerization ethynylation of *P3HT*[162]. This approach aimed to install a trimethylsilyl protected alkyne handle via Sonogashira coupling, followed by *TBAF* deprotection. While this is the best route available at the time, it suffers from a few limitations: (i) n-type conjugated polymers had been reported several times[168,169] to be chemically doped by *TBAF*, making subsequent rod-coil coupling synthetically difficult and thereby limiting the procedure to p-type backbones. (ii) This two-steps synthesis introduced persistent impurities, which could be hardly removed without chromatographic separation.

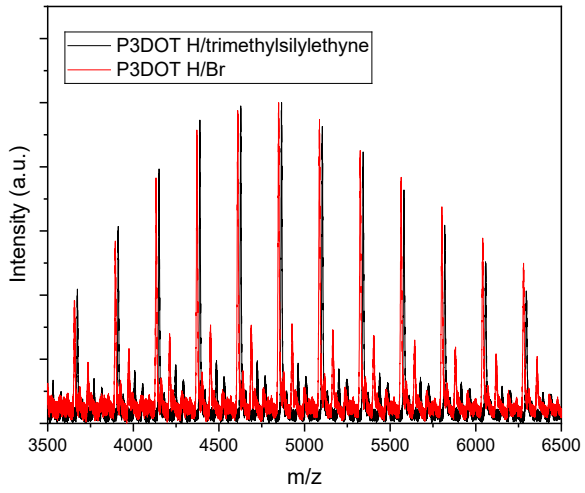

Figure 2.9 *MALDI-TOF* Spectrum of trimethylsiylethyne-terminated *P3DOT* from Route 1

To circumvent these issues, a streamlined Stille cross coupling protocol (Figure 2.7, Route 2) was developed. A mild catalytic system with Pd-G_3-P^tBu_3/K_3PO_4 achieved nearly quantitative conversion to the corresponding alkyne with minimal dehalogenation and no observable molecular weight artifacts, therefore completing the rod block without further protecting-group manipulations.

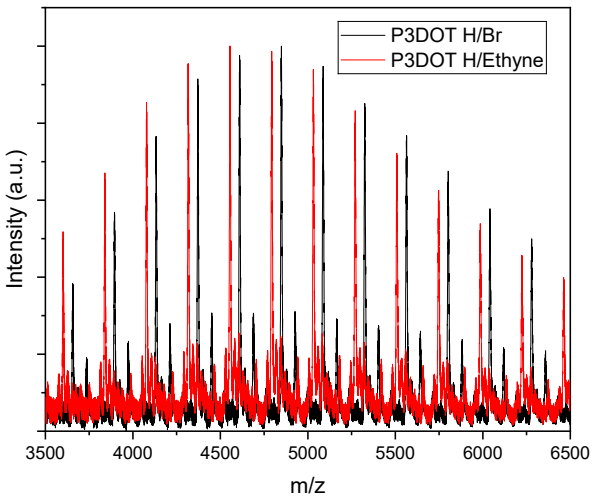

Figure 2.10 *MALDI-TOF* Spectrum of ethyne-terminated *P3DOT* from Route 2

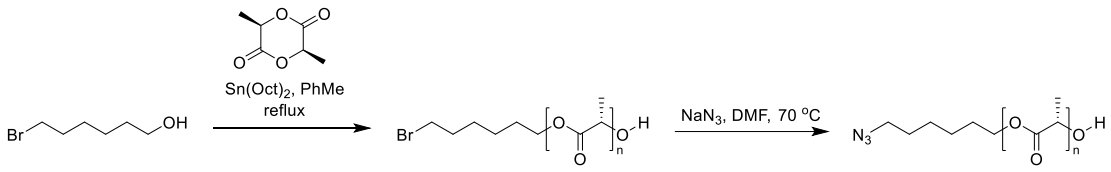

Figure 2.11 Reaction scheme for preparation of azide-terminated *PLLA*

While commercial azido-*PEG* and azido-*PLLA* were available, their fixed molecular weights preclude systematic studies of block length effects. Hence, preparation of azide-terminated coil block, particularly PLLA, was attempted using cationic ring-opening polymerization with $Sn(Oct)_2$ Lewis acid, as shown in Figure 2.10. The acid sensitivity of azide moiety led us to first mask it as a halogen handle. A bromo-terminated *PLLA* was thereby prepared with 6-bromo-1-hexanol as an initiator, which was subsequently converted to the desired azido-terminated coil fragment with sodium azide.

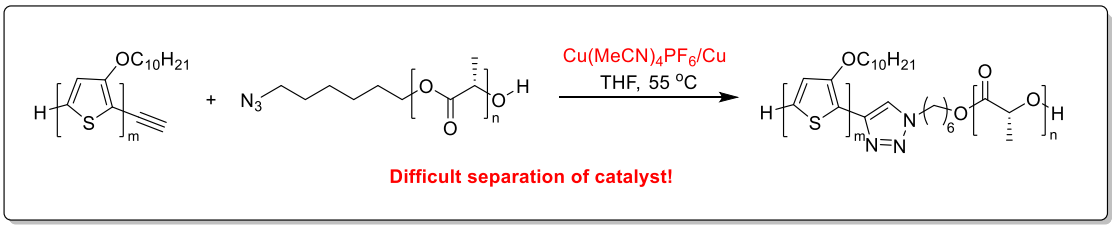

Figure 2.12 Reaction scheme for *CuAAC* of *P3DOT* and *PLLA*

Rod-coil block coupling was then carried out through *CuAAC*. Unfortunately, conventional catalytic system $CuBr(PPh_3)_2$/*PMDETA* failed to yield desired product. On the other hand, using $Cu(MeCN)_4PF_6$ with Cu powder as cocatalyst led to successful coupling. Nonetheless, removal of copper removal necessitated alumina chromatography, which is proven problematic due to poor scalability and substantial product loss in the stationary phase. Given these synthetic challenges—multistep fragment synthesis, metal contamination risks, involvement of toxic azide reagent and low yields—alternative conjugation strategies were prioritized for subsequent studies.

2.6.2 Suzuki cross-coupling approach

To facilitate the efficient synthesis of block copolymer, we outline several design principles derived from previous observations. Firstly, number of end-group conversions should be minimized for both rod and coil fragments to reduce synthetic complexity. Crucially, modification of coil block terminus should prioritize over that of rod block. Coil blocks are structurally more flexible and hence more processible in ambient solvent. Extraction or even silica column chromatography could be used for purification to separate undesired persistent impurities.

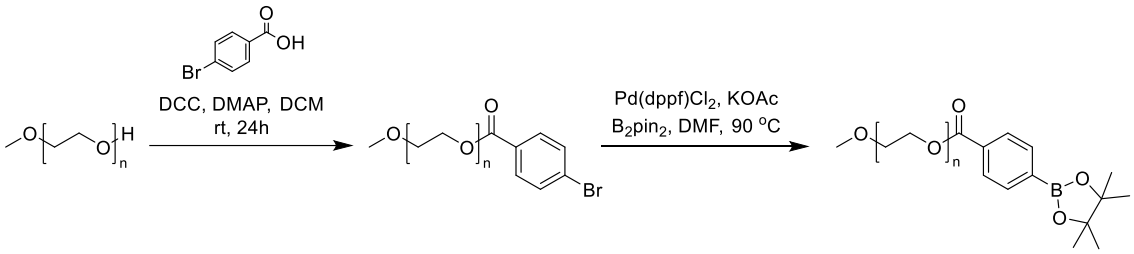

Figure 2.13 Reaction scheme for preparation of boronic ester-terminated *PEG*

The high efficiency of backbone functionalization achieved through Stille coupling inspired us to explore an alternative block copolymerization strategy, which directly couples coil fragment with the halogen-terminated rod block. This approach was supported by a recently reported tandem Suzuki-Miyaura functionalization of *P3HT* with boronate ester (Bpin)-terminated coil block[170]. As a proof-of-concept, we first prepared Bpin-terminated *PEG* through a two-step process involving (1) Steglich esterification to install an aryl halide handle, followed by (2) Miyaura borylation to generate the corresponding pinacol boronic ester. The corresponding coil fragment was then anchored to the bromo-terminated rod using Pd-G3-P^{t}Bu$_3$/K$_3$PO$_4$. The success of this reaction eliminates the need to further functionalize the rod fragment before coupling, establishing metal-catalyzed cross-coupling as a viable alternative to *CuAAC* in block copolymer synthesis.

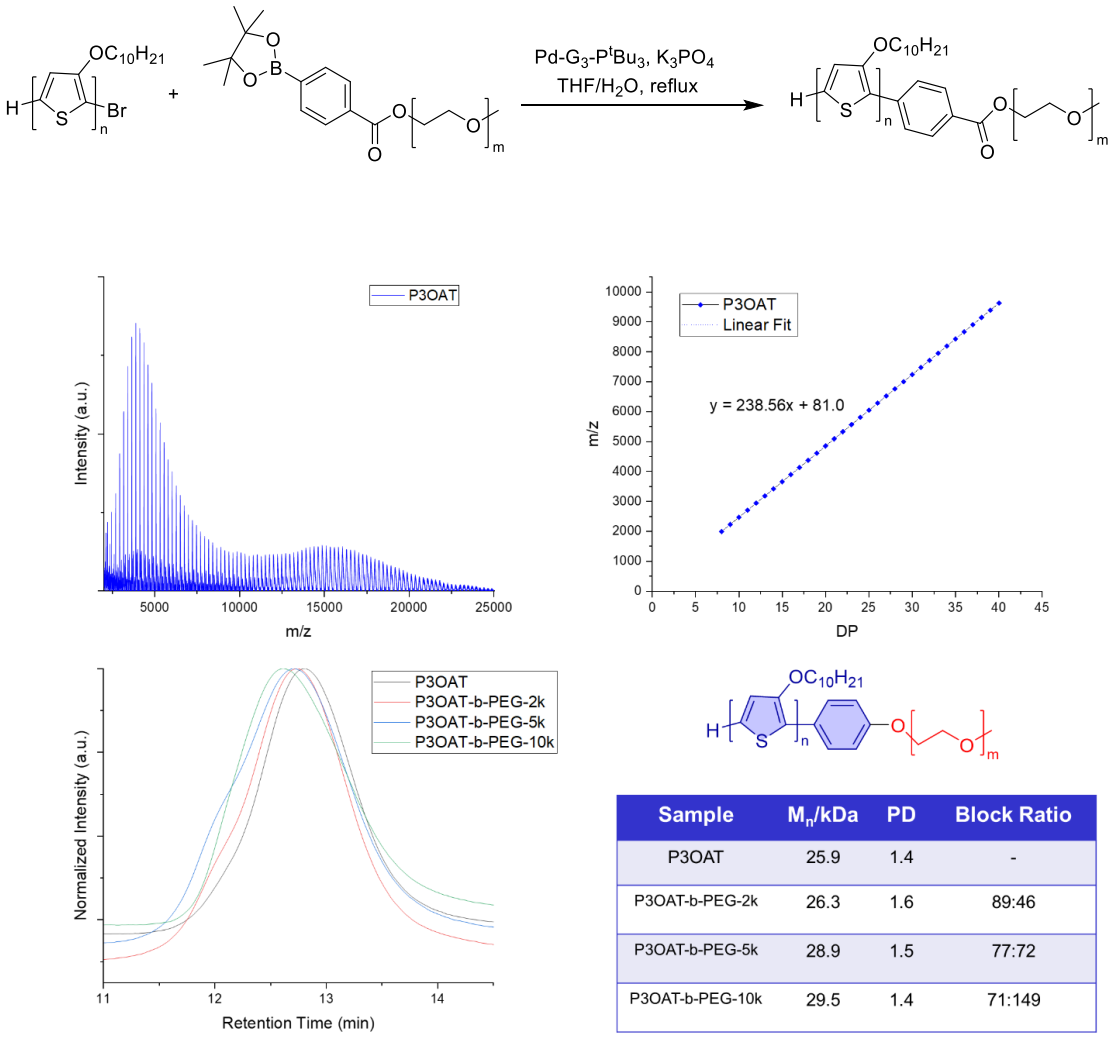

Sample	M_n/kDa	PD	Block Ratio
P3OAT	25.9	1.4	-
P3OAT-b-PEG-2k	26.3	1.6	89:46
P3OAT-b-PEG-5k	28.9	1.5	77:72
P3OAT-b-PEG-10k	29.5	1.4	71:149

Figure 2.14 Reaction scheme for preparation of (top) P3DOT-*b*-PEG through Suzuki-Miyaura Approach (mid, left) MALDI-TOF of P3DOT H/Br (mid, right) linear regression to determine the formula mass of end-group, (bottom, left) GPC of P3DOT-*b*-PEG (bottom, right) GPC mass of the block copolymers

Successful coupling of both fragments was confirmed by a pronounced shift in *GPC* retention time (Figure 2.13), consistent with the increment in M_n. Quantitative ^{1}H *NMR* analysis of *PEG* content showed reasonable agreement with theoretical stoichiometric values. However, this coupling scheme also presents a few limitations. Firstly, halogen end group on the rod block could not be effectively monitored with ^{1}H *NMR*, making it hard to accurately determine the amount of coil fragments required for rod-coil coupling. In addition, the reaction proves incompatible with *PLLA* due to possible base-

induced scission. *PLLA* was observed to slowly degrade even in strictly anhydrous *THF* in the presence of K_3PO_4 base. To circumvent concerns on hydrolytic degradation of *PLLA*, rod-coil coupling was also attempted with *PLLA* functionalized with tributylstannyl terminus through Stille cross-coupling. Nonetheless, all reactions without base addictive failed, revealing Pd-G_3-P^tBu_3/K_3PO_4 as the optimal condition. Maximum coupling efficiency was achieved at 16 hours, with declining rod-coil ratio following prolonged reaction times, likely owing to *PLLA* degradation. This time-sensitive balance between coupling and base-mediated degradation complicates reaction optimization. Moreover, progressive coil-block cleavage may result in poor reproducibility.

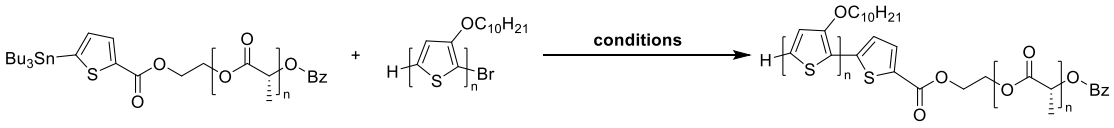

Entry	Catalyst	Solvent	t	[Monomer]	Temperature	Final block ratio (P3DOT:PLLA)
1	$Pd(PPh_3)_4$,	DMF/ PhMe	**16h**	0.3 mM	110^oC	9:1
2	Pd_2dba_3, P^tBu_3	**THF**		**1mM**	**70^oC**	didn't couple
3	**Pd-G_3-**					**2:1**
4	**$PtBu_3$,**		4h			**4:1**
5	**Cs_2CO_3**		8h			**4:1**
6			24h			**3:1**
7			48h			**9:1**

8	Pd_2dba_3, P(o-tol)$_3$, 48h	DMF/ PhMe			110°C	5:1
9	$Pd(PPh_3)_4$					9:1

Table 2.2 All reaction conditions attempted for rod-coil coupling of P3DOT-*b*-PLLA

In conclusion, the preparation of PEGylated poly(3-alkoxythiophene) was successful with the Suzuki-based coupling approach, but the scope of the method is severely limited by stability issues associated with hydrolytically sensitive group. This leads to questionable block ratio for block copolymers with a PLLA coil. To circumvent these challenges, the reaction condition must be as mild as possible to be compatible with *PLLA*. In addition, termini of both fragments should be re-designed to be trackable by ^{1}H NMR, allowing their coupling to be easily monitored.

2.6.3 Knoevenagel cross-coupling approach

The inability to reliably monitor reaction progress by ^{1}H NMR is a persistent problem in both *CuAAC* and Suzuki-based rod-coil coupling. This difficulty arises due to similar chemical shift between the end-group proton with either aromatic protons on the backbones or α-protons on the side chains. To overcome this, a suitable end-group must exhibit a chemical shift well-resolved from these interfering signals. Aldehydic proton, with its characteristically de-shielded resonance, serves as an ideal reaction handle and is anchored to the rod block. To complement this reactivity, the coil fragment is functionalized with rhodanine moiety, which is featured in many prior studies[171,172] to present highly efficient Knoevenagel coupling.

The feasibility of the idea was tested with *P3HT* backbone. Bis-formylated *P3HT* was prepared in accord to previous reports[173,174]. Decaethylene glycol monomethyl ether was end-capped with rhodanine moiety via Steglich esterification. After screening several combinations of solvent and base, we found out that piperidine/chloroform system could quantitatively convert *P3HT* dialdehyde to its corresponding *PEG*-terminated triblock copolymer. This was marked by the complete quenching of aldehydic resonance, with the concomitant emergence of a new peak at 8.00 ppm (Figure 2.16), which corresponds to the alkene proton signals. Further purification of the reaction mixture through Soxhlet extraction eliminates the chemical shift associated with the α-protons on the rhodanine carbonyl moiety. The relative integral of *P3HT* aromatic proton to that on the *PEG* fragment and the interlinking end groups is in close agreement with the expected block ratio, strongly supporting the complete formation of PEG-*b*-P3HT-*b*-PEG triblock without any residual macroinitiator precursors.

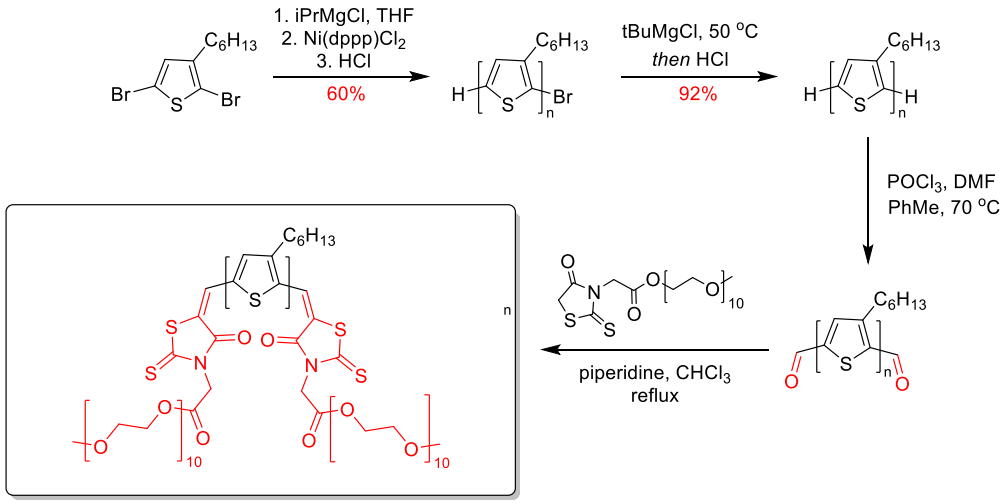

Figure 2.15 Reaction Scheme for Test Reaction for Knoevenagel coupling

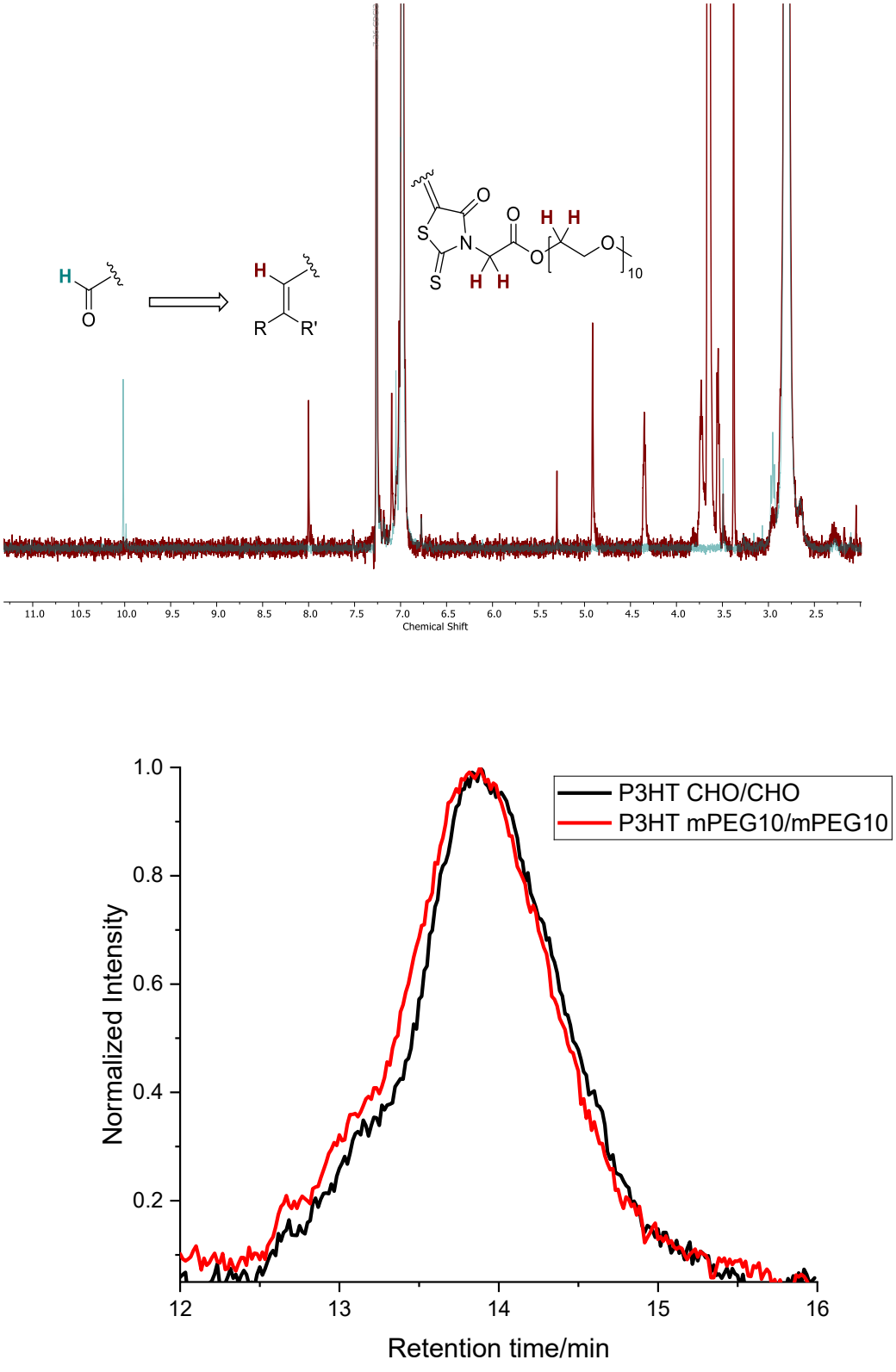

Figure 2.16 (top) ^{1}H *NMR* of polymer (bottom) GPC trace of polymer sample before and after Knoevenagel coupling

Entry	Coil block	Reaction conditions	End-group conversion (%)	Coil block stability
1	PEG[a]	NEt_3, $CHCl_3$, reflux, 24 h	36	✔
2		NEt_3, PhCl, 90 °C, 24 h	51	✔
3		Piperidine, $CHCl_3$, reflux, 24 h	100	✔
4	PCL[b]			✔
5	PLLA[b]		100	✘
6		DIPEA, $CHCl_3$, reflux, 24 h	27	✔
7		Pyridine, $CHCl_3$, reflux, 24 h	0	✔
8		Morpholine, $CHCl_3$, reflux, 24 h	0	✘
9		DBU, $CHCl_3$, reflux, 24 h	100	✘
10		2,2,6,6-tetramethylpiperidine, $CHCl_3$, reflux, 24 h	85	✔
11		2,2,6,6-tetramethylpiperidine, $CHCl_3$, reflux, 48 h	100	✔

Table 2.3 Reaction conditions explored for rod-coil coupling of P3HT

The generality of this method was further investigated with several other coil fragments such as PLLA and PCL. In order to monitor the stability of the polyesters under basic condition, benzyl moiety was anchored on the opposite terminus of rhodanine coupling group. This group was referred to “safety pin” in our design. Any undesired side reactions compromising the integrity of the polyester chain, regardless the extent, reduces the ^{1}H NMR signal of the benzyl protons. Thus, the stability of polyester coil following rod-coil coupling would be reflected from the resonance intensity of the benzyl protons.

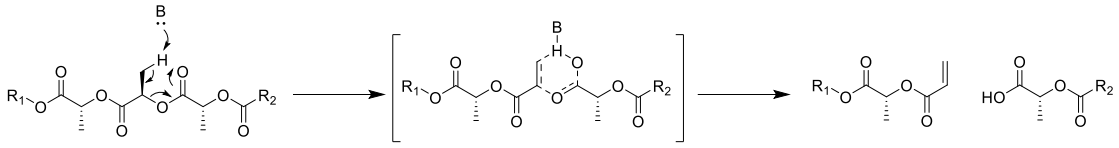

Figure 2.17 Proposed degradation pathway for *PLLA* coil block with piperidine

The optimized procedure proceeds smoothly with the *PCL* block. However, degradation of *PLLA* still occurs. The mechanism of base-mediated scission was proposed in Figure 2.17, possibly driven by a stabilized six-membered transition state. After screening several bases, we found out that all successful Knoevenagel condensations required a secondary amine base with pKa_H around 10. Weaker base such as morpholine would not lead to successful rod-coil coupling but still result in the degradation of *PLLA*. This problem was solved by using a non-nucleophilic base like 2,2,6,6-tetramethylpiperidine. Unfortunately, the steric hindrance around the active catalyst also reduces the rate of Knoevenagel condensation, resulting in a longer reaction time necessary for full conversion to the corresponding block copolymer.

2.7 Conclusion

In this chapter, we explored the synthesis and optimization of poly(3-alkoxythiophene)-based rod-coil block copolymers. Three different strategies were evaluated, with their design principle and limitations discussed in detail. To complete the synthesis of rod-coil block copolymer, besides the high reaction efficacy of rod-coil coupling, both rod and coil block precursor must possess high end-group fidelity. The prior was achieved with a modified KCTP under judicious catalyst selection. After reaction screening, $Ni(IPr)(PPh_3)Cl_2$, where the metal centre is both sterically shielded and electron-rich, proves optimal for polymerization of P3DOT.

Several different approaches were investigated for rod-coil coupling. Among which, Knoevenagel condensation was identified to be the most robust method, featuring compatibility with sensitive polyester coils using a non-nucleophilic base.

Overall, this work expands the scope of controllably synthesized conjugated polymer to include poly(3-alkoxythiophenes). This work can be further extended to develop rod-rod donor-acceptor blocks from the corresponding bromo-terminated macroinitiator, which may find its uses in photovoltaics[175–177]. By controlling their self-assembly behaviour, the size of different domains could be optimized for exciton diffusion. Ultimately, this methodological study sets the foundation for preparation of *P3DOT* rod-coil block copolymers, which will be further investigated for applications in *OECT*.

CHAPTER 3

Understanding P3AOT-based block copolymers: structure, morphology and OECT

3.1 Polymer Synthesis

P3AOT block copolymer synthesis discussed in Chapter 2 proved generalizable to a broad substrate scope, including both linear (P3DOT) and branched (P3AOT-C_2C_6) substituents. Additionally, P3AOT-G_1C_7, where the polymer side chain is partially glycolated, could be prepared with high end-group precision. Interestingly, P3TEG, where alkoxy substituent of P3AOT was completely replaced by a methoxy triethylene glycol substituent, reveals significantly dehalogenated chain-ends. This signifies increased chain-transfer side reactions, which likely arises because chain-walking of catalyst is disrupted by interactions from the glycol side chains. All the prepared P3AOT macroinitiators and their corresponding block copolymers were listed in Figure 3.1 and 3.2, respectively.

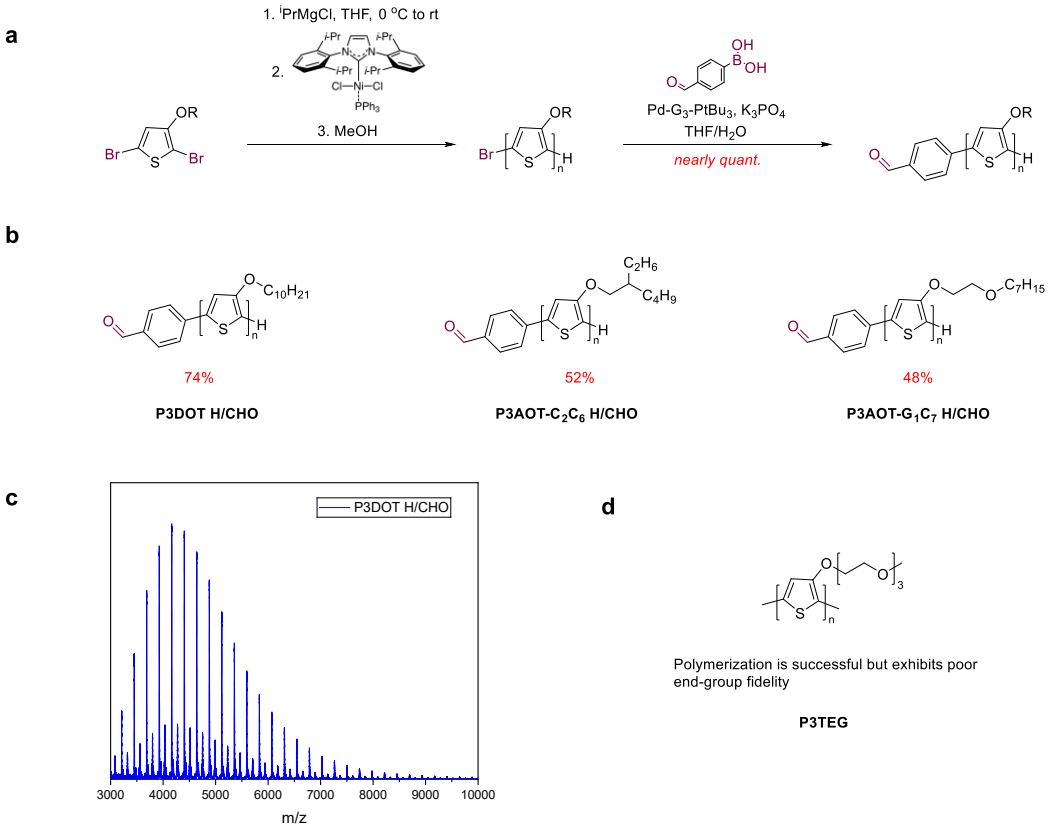

Figure 3.1 (a) Synthetic scheme of *P3AOT* rod precursor (b) Reaction yield of all *P3AOT* derivatives explored (c) MALDI-TOF of *P3DOT* rod precursor (d) Structure of *P3TEG*

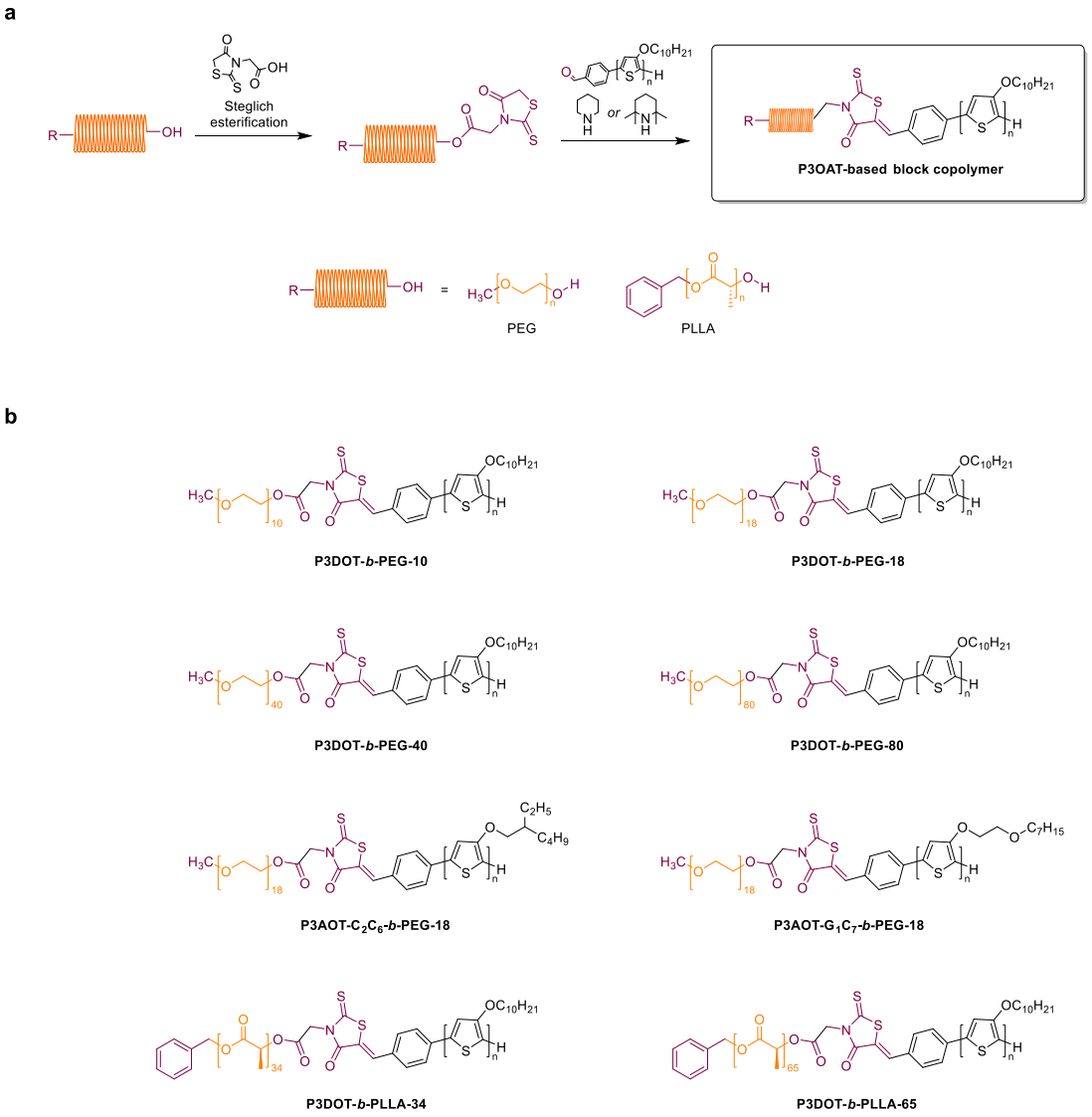

Figure 3.2 (a) Reaction scheme of rod-coil coupling (b) Scope of all block copolymers prepared

Interestingly, the reaction yield of P3AOT macroinitiator reduces with increased branching and glycolation of side chain. This associates with the increased solubility in common lipophilic solvent due to poorer π-π stacking, leading to higher proportion of removed oligomers during Soxhlet extraction.

The success of rod-coil block copolymer is marked with a significant reduction of retention time in GPC, as depicted in Figure 3.3, as well as the emergence of ^{1}H NMR signal from corresponding coil block following purification.

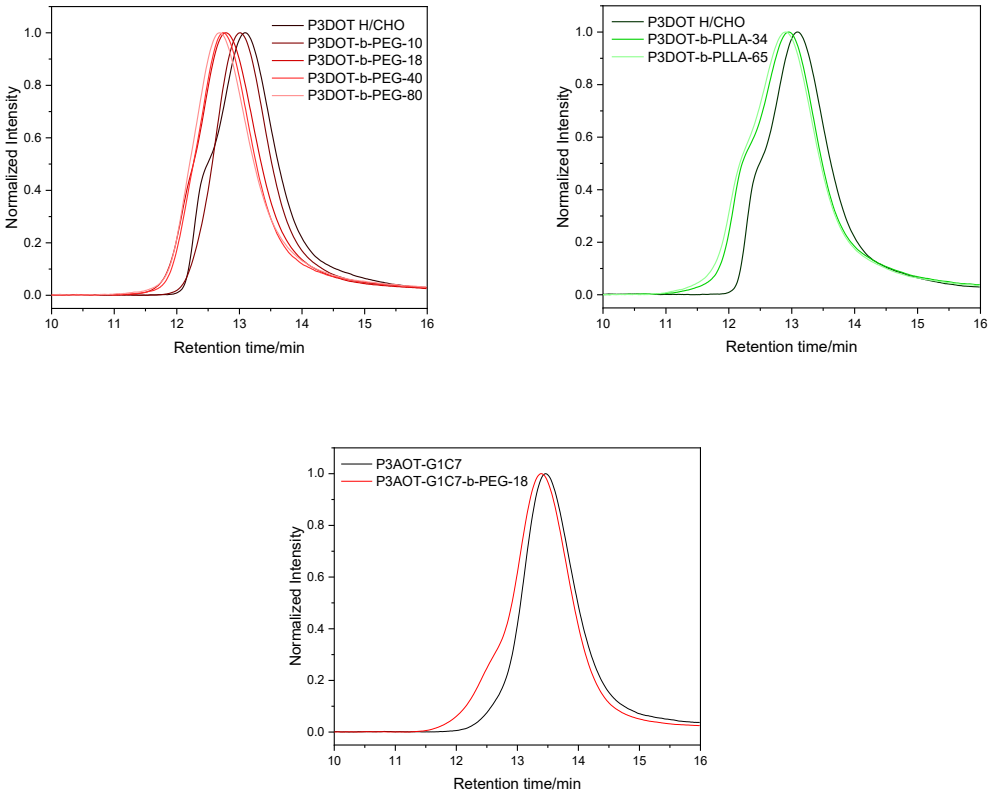

Figure 3.3 GPC trace of all block copolymers

In Figure 3.2, the P3OAT block copolymers could be broadly classified into two categories: PEG-series, which comprises all block copolymers with PEG coil blocks, and are synthesized to investigate the role of enhanced hydrophilicity associated with main-chain PEGylation, as well as PLLA-series, which similarly include block copolymers with PLLA fragment.

3.2 Optoelectronic properties

3.2.1 Energy of frontier orbitals and band gap

The energy levels of the frontier orbitals for a polymer thin-film could be estimated by both PESA and cyclic voltammetry in acetonitrile solution of $TBAPF_6$ electrolyte. The optical band gap of all P3DOT-based block copolymers was determined by UV-Vis Spectroscopy to be 1.57 eV from the onset of π-π* absorption. Collectively, these allow

us to evaluate both HOMO and LUMO of the block copolymers. The energy level of frontier orbitals from P3DOT-based block copolymer are tabulated in Figure 3.4, with similar HOMO around -4.8 eV determined by PESA, revealing minimal variation across the series. Cyclic voltammograms in acetonitrile with 0.1 M TBAPF6 supporting electrolyte showed that all block copolymers shared a similar first oxidation onset around -0.3 V and an addition oxidation peak around 0.5 V, which was later found to correspond to the oxidation of disordered domain (Section 5.3.4). In addition, all block copolymers in the polyester series exhibit an additional oxidation peak around 0.7 V.

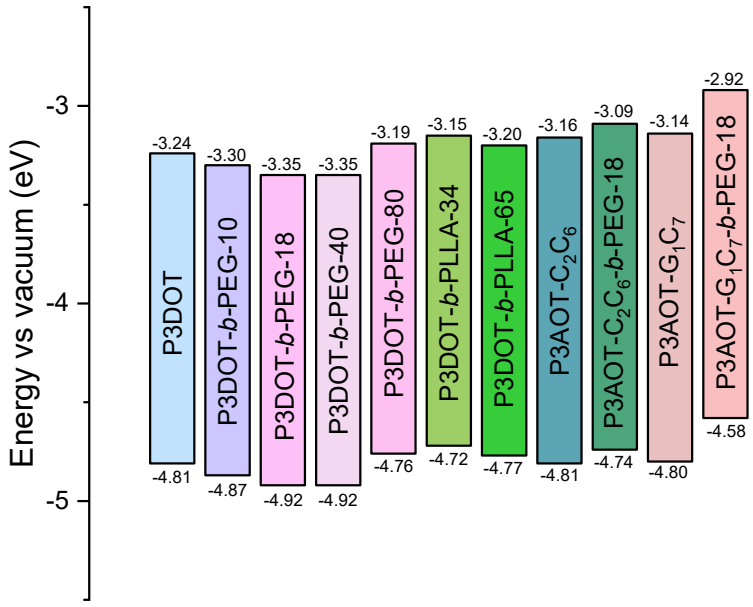

Figure 3.4 Energy level profile of all block copolymers

Despite the presence of coil block, they would interact weakly, if at all, with the π-system of P3DOT backbone due to their electronically insulating nature. These findings are further supported by the similarity in energy level for all block copolymers.

Consequently, any differences in electrochemical properties of the materials must be ionic and morphological in origin, rather than opto-electronically related.

3.2.2 Electrochemical doping behaviour of PEG Series

To study the electrochemical doping behaviour of P3DOT-b-PEG series, spectro-electrochemical measurement was performed in 0.1 M aqueous NaCl solution. UV-Vis spectroscopy depicts two absorption peaks centred around 650 and 700 nm, as shown in Figure 3.6, which corresponds to π-π* absorption of P3DOT and its aggregation shoulder respectively. Considering the low IP of all the block copolymers, they exhibit a propensity to spontaneously oxidize under ambient condition and therefore must be negatively biased for complete de-doping prior to measurement. After the complete dedoping of the block copolymers, electrochromic response was taken with an increasing applied bias from -0.2 to 0.7 V, as depicted in Figure 3.7. Notably, an external voltage around 0.3 V induces an absorption around 960 nm, which was attributed to the formation of polaron. This is simultaneously accompanied by the gradual diminishing of the optical absorptions in the neutral state, which can be reverted with a reverse bias of -0.2 V, revealing excellent electrochemical stability. An isosbestic point was found around 760 nm. Surprisingly, despite the more extended PEG chain, all the block copolymers in the PEG-series show similar threshold voltage. This implies less significant impact of main-chain PEGylation on the ease of ion injection into polymer film, compare to conventional side-chain glycolation.

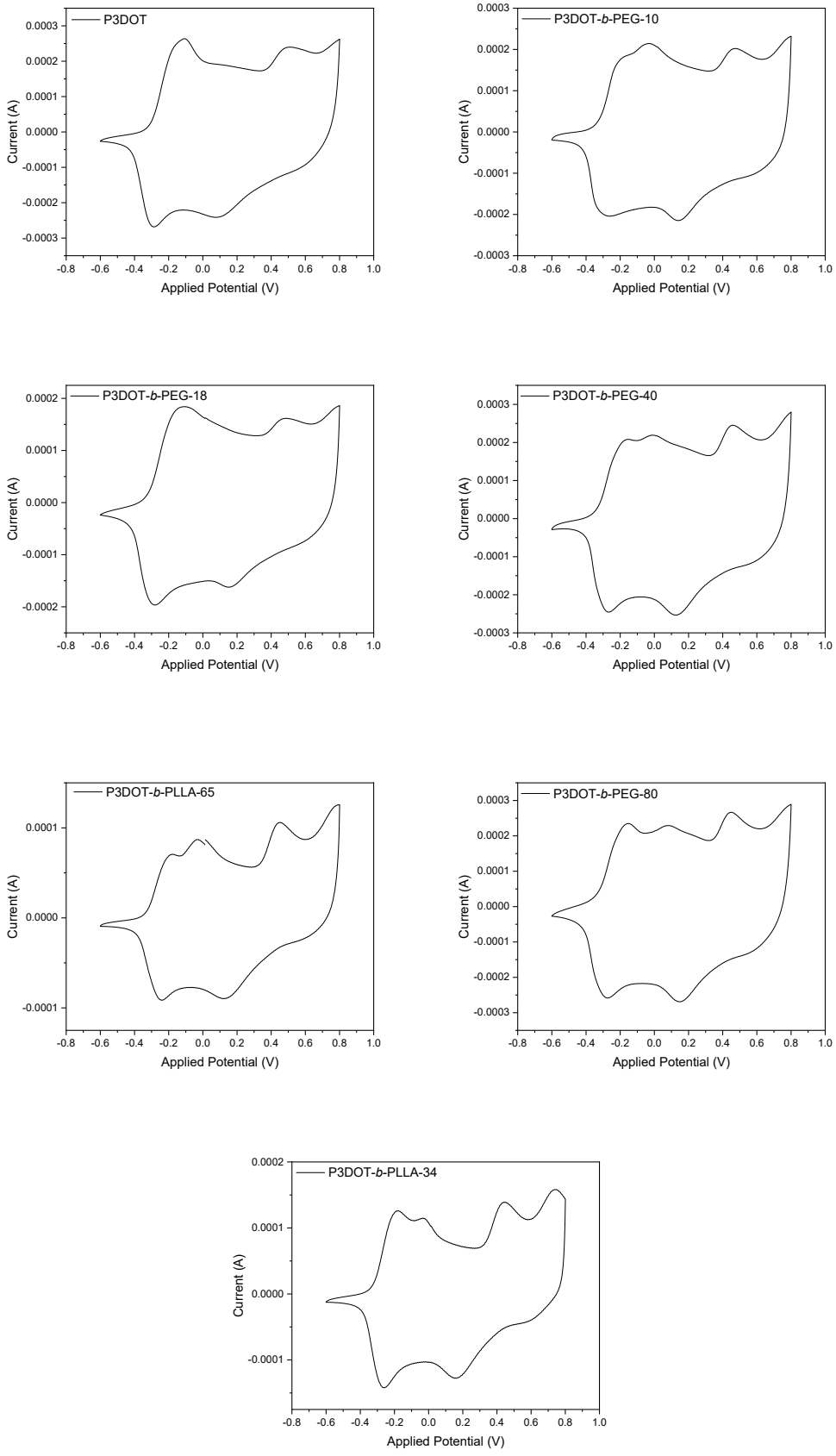

Figure 3.5 Cyclic voltammogram of block copolymers in MeCN solution with 0.1 M TBAPF6 supporting electrolyte at a scan rate of 100mV/s.

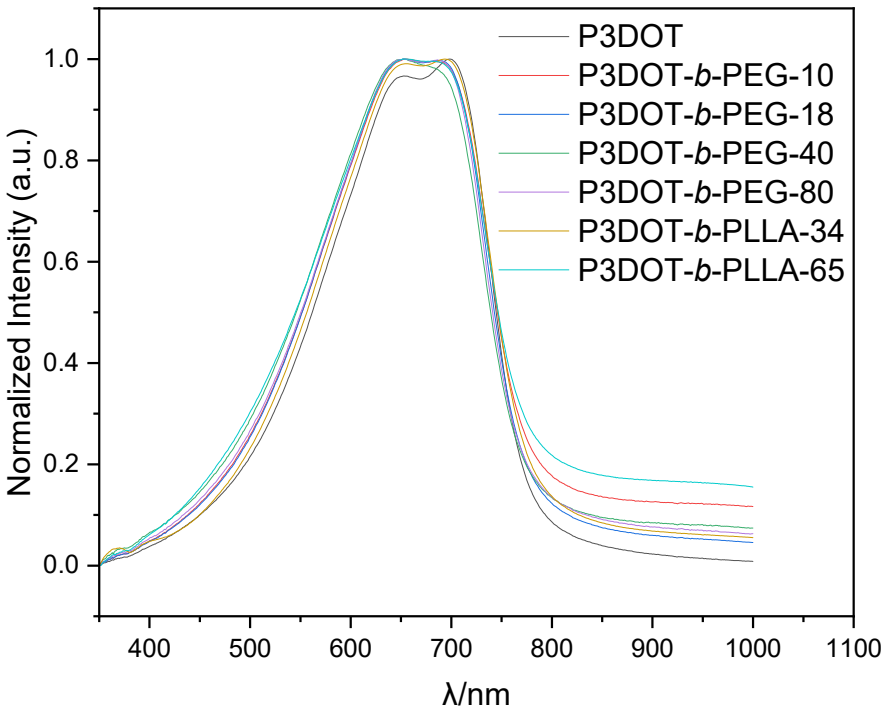

Figure 3.6 UV-Vis Absorption Spectra of all block copolymers

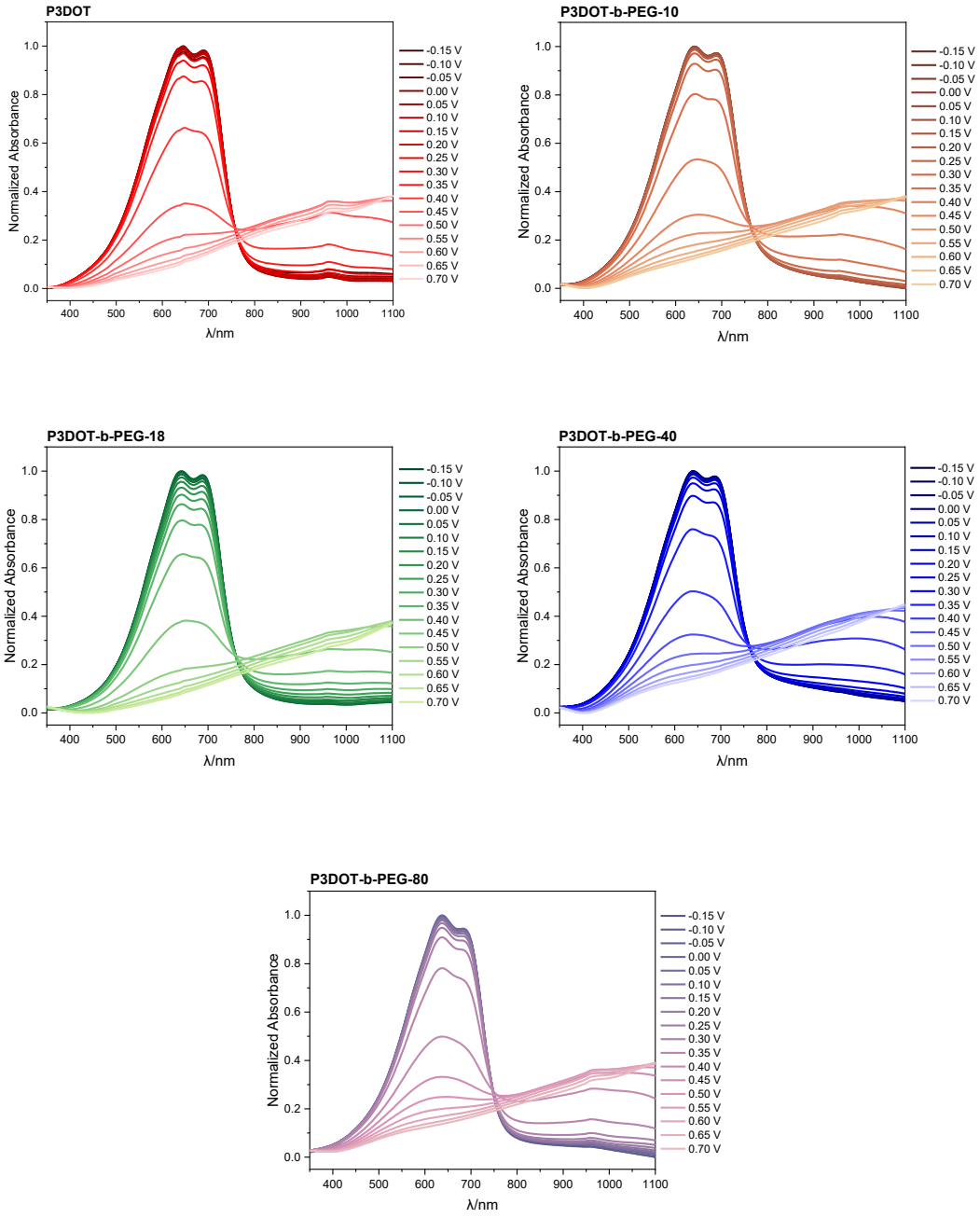

Figure 3.7 Spectro-electrochemistry Plots of P3DOT-*b*-PEG

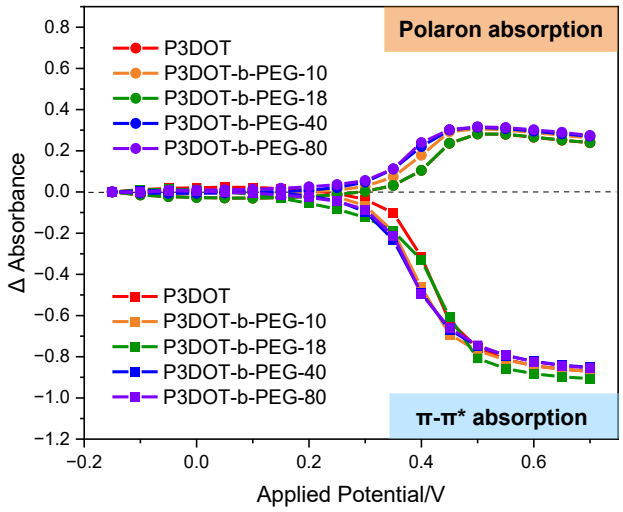

Figure 3.8 Plot of normalized absorbance of P3DOT-*b*-PEG against applied bias, illustrating the onset voltage and relative intensity in electrochromic response

In 0.1 M aqueous NaCl solution, cyclic voltammogram of the P3DOT-*b*-PEG thin-films on *ITO* substrate reveals increasingly capacitive nature with more extended *PEG* length, as evidenced from the greater enclosed area from charging/discharging process. This is also accompanied by a decrease in onset potential, which can be associated with the improved ion affinity from the more extended PEG chains, facilitating ion permeation through favourable hydrogen bond with the hydrophilic, hydrated ions. On the other hand, the peak current density of the polymer film initially increases from *P3DOT* to P3DOT-*b*-PEG-18 but does not change significantly with further increase of *PEG* length. This could be correlated with increased ion injection after several electrochemical cycles. In P3DOT and P3DOT-b-PEG-10, it is possible that electrochemical doping is still incomplete upon completion of cyclic voltammetry, resulting in lower measured current density.

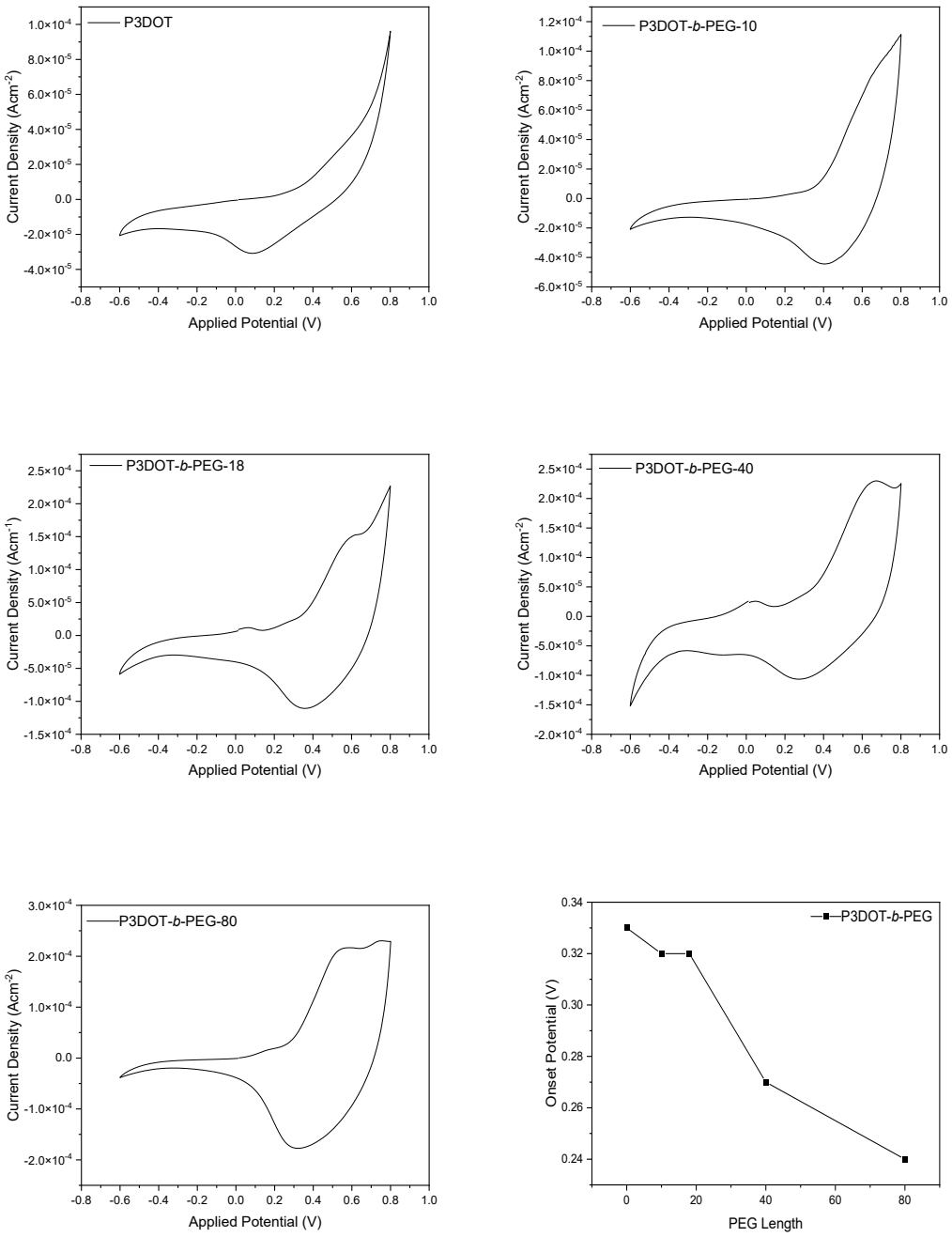

Figure 3.9 Cyclic voltammogram of P3DOT homopolymer and P3DOT-b-PEG in aqueous solution with 0.1 M NaCl supporting electrolyte.

3.3 Morphological properties

3.3.1 Grazing incidence wide-angle X-ray scattering (GIWAXS)

To better understand the nanostructural properties of the block copolymers, the thin films, both as-casted and thermally annealed, were studied with GIWAXS. The two-

dimensional GIWAXS maps of the on-casted P3DOT are presented in detail in Figure 3.10. All block copolymers exhibit a series of intense lamellar scattering peaks in the out-of-plane direction (q_z), with three orders of (h00) clearly observed for all as-casted films. A (010) reflection was prominent on the in-plane-direction (q_r) for both P3DOT homopolymer and P3DOT-b-PEG, and is attributed to π-π stacking, revealing a predominantly edge-on orientation. This scattering is however less prominent in P3DOT-b-PLLA, suggesting weakening of π-π interaction.

Incorporating coil fragment did not introduce additional scattering features. In PEG series, all P3DOT-b-PEG shows very similar interlamellar spacing. This could be correlated with the amorphous nature of PEG at ambient temperature, with a low T_g of -60 ^oC[178]. This implies that the PEG chains exhibit some degree of molecular mobility at ambient temperature and is therefore more flexible. This lower stiffness resulted in minimal disruption to interlamellar stacking between the P3DOT backbone. Contrarily, this change in lamellar distance is more pronounced in P3DOT-b-PLLA. For instance, P3DOT-b-PLLA features the minimum interlamellar distance of 28.2 Å, approximately corresponding to the length of two extended decoxyl substituents. This can be similarly rationalized base on the higher rigidity of PLLA microphases due to higher T_g at 60 ^oC[179]. This means that PLLA chains will adopt a glassy state at room temperature, which translates to lower molecular mobility and is therefore harder and stiffer. This mechanically forces the P3DOT backbones into proximity in the lamellar direction, resulting in tightened interlamellar spacing. The d-spacing following thermal annealing was also evaluated. In all block copolymer films, without exception, a further lamellar contraction of 20 – 25 % was observed.

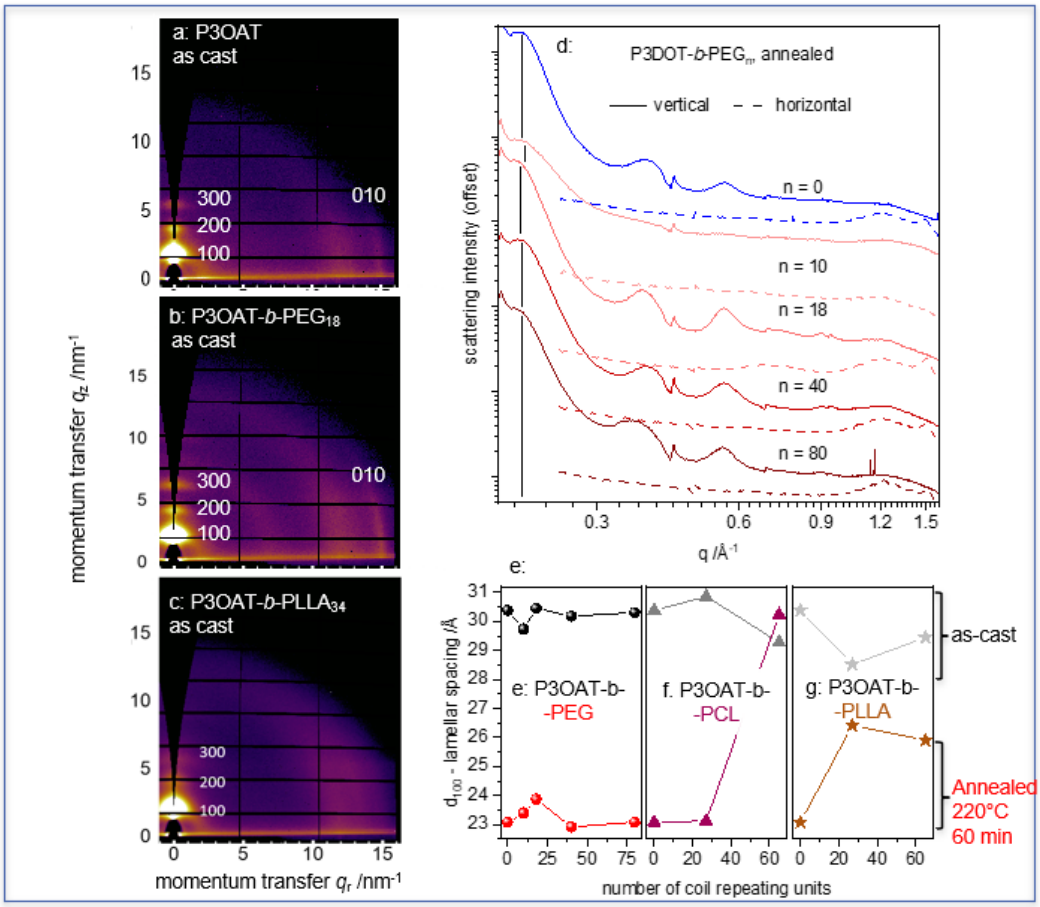

Figure 3.10 2D GIWAXS of as-casted (a) P3DOT (b) P3DOT-b-PEG-18 (c) P3DOT-b-PLLA-34 (d) In-plane 1D Line-cut of P3DOT-b-PEG series (e) Lamellar spacing of P3DOT-b-PEG series and P3DOT-b-PLLA series

3.3.2 Atomic force microscopy (AFM) imaging

To better understand the film morphology of the block copolymers, dry as-casted films were evaluated with AFM. Given that the polymer films were fabricated over glass-supported device during OECT measurement, all films were deposited on cut glass slides with 1 cm x 1 cm dimensions through spin-coating to better present their morphology when casted on device. The topological height and phase images of the block copolymers are presented in Figure 3.11. The increase in PEG length across the series leads to significant topological variation. In P3DOT homopolymer, the film features high surface uniformity, evidenced by the homogeneous phase plot.

Introduction of short PEG-10 coil block roughens the phase distribution profile. In P3DOT-b-PEG-18, both height and phase profile feature self-assembly into thicker, microfibril-like structures, which dissolves upon further PEG extension and leads to a smoother phase profile. Overall, all as-casted block copolymers beside P3DOT-b-PEG-18 did not present significant variation in height profile, adopting a random distribution of globular features, with less frequent occurrence of aligned microfibers.

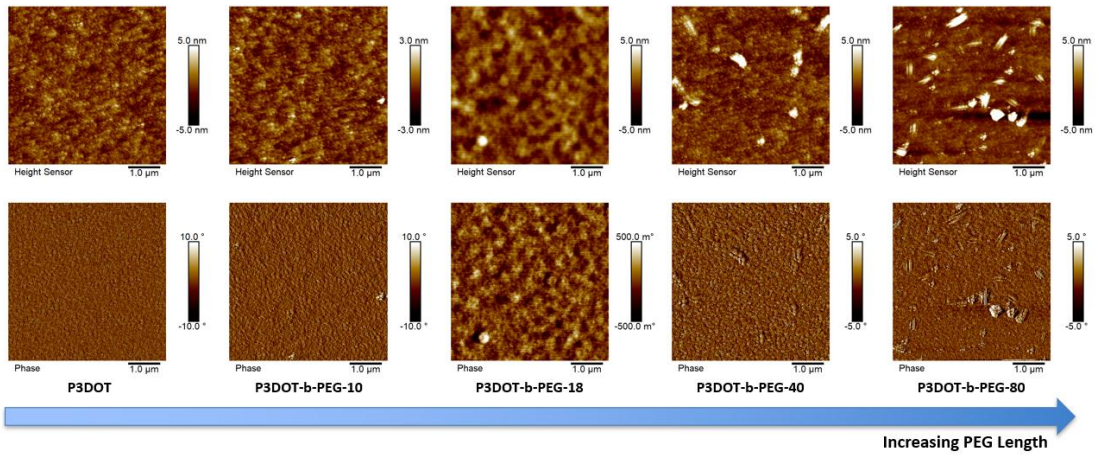

Figure 3.11 *AFM* height and phase topography of P3DOT-*b*-PEG

The surface morphology of P3DOT-b-PLLA was then screened with PeakForce Tapping AFM, where differences in chemical composition was not reflected from changes in phase but rather on the mechanical properties. Indentation profile, which is plotted base on the maximum displacement reached following a nanoscale indentation process, is used instead. In P3DOT-b-PLLA-34, indentation profile revealed needle-shaped crystallite-like features, which became less pronounced but is accompanied with the concomitant formation of long fiber-like feature in P3DOT-b-PLLA-65. This morphological analysis demonstrated that varying chemical identity and composition of coil block could impact the surface profile of block copolymer thin film significantly.

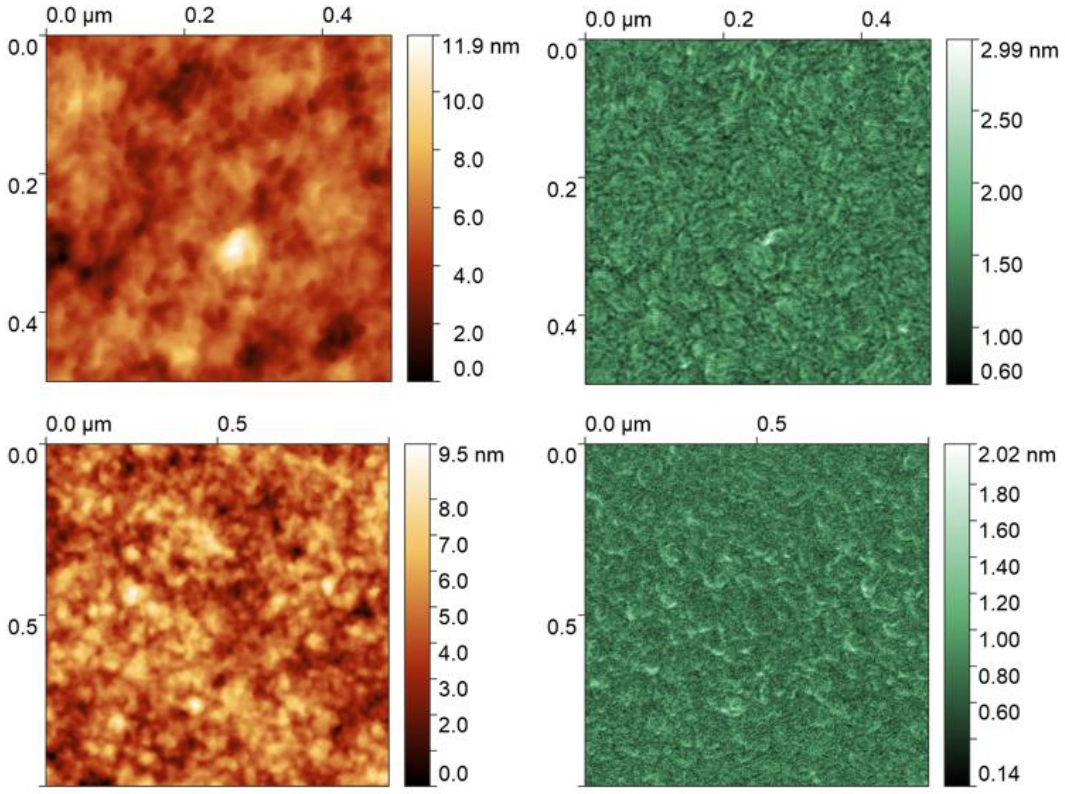

Figure 3.12 Peakforce *AFM* height and indentation profile of (top) P3DOT-*b*-PLLA-34 (bottom) P3DOT-*b*-PLLA-65

3.4 Thermal properties

Differential scanning calorimetry (DSC) was performed to measure the thermal properties of the block copolymers. Shown in Figure 3.13, all DSC curves feature good thermal reversibility with no significant change in melting endotherm and crystallization exotherm following heating to 260 ºC. Nonetheless, raising the maximum temperature to 300 ºC results in disappearance of crystallization isotherm. Further optical analysis following DSC results in blueshift of absorption maximum with widening of optical band gap, and is attributed to the degradation of polymer backbone (Figure 3.14).

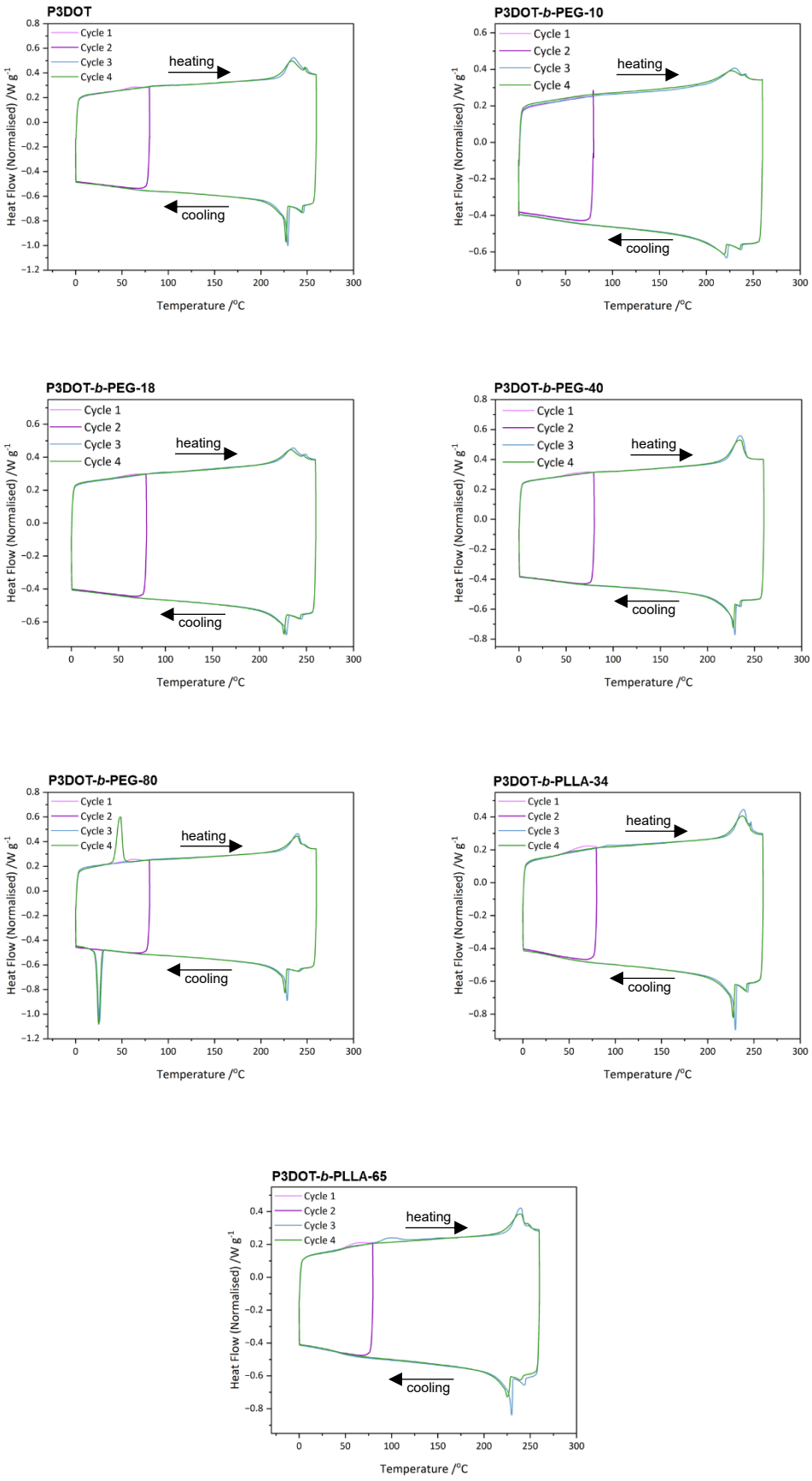

Figure 3.13 DSC Curves of all block copolymers

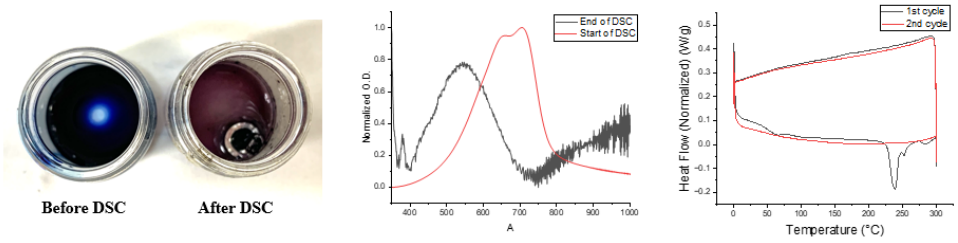

Figure 3.14 (left) Photo and (middle) UV-Vis absorption spectrum of *P3DOT* homopolymer before and after *DSC;* (right) DSC Calorimogram of *DSC* homopolymer

The enthalpy of fusion and melting temperature of the block copolymers were extracted from the second thermal cycle of each calorimetric curve and summarized in Table 3.1. Compare to P3DOT homopolymer, T_m is depressed slightly upon incorporation of short PEG-10, which could be ascribed with the packing frustration[180] that disrupts molecular ordering in the solid state. This is alleviated with the lengthening of PEG chains, which could extend and stack together to improve the overall ordering of the block copolymers in the solid state, leading to increased T_m. Similar trend is also depicted in P3DOT-b-PLLA.

Notably, P3DOT-b-PEG-80, crystallization of PEG domain appeared following initial annealing, while PEG domains remained vitrified in the remaining block copolymers. This shows that in these block copolymers, the crystallization in the solid state is dominated by the P3DOT domain. In the case of P3DOT-b-PEG-80, however, the longer coil length facilitates self-assembly and molecular ordering upon annealing, thereby leads to the appearance of both crystallization exotherm for P3DOT and PEG domains in the second cycle.

Sample	Enthalpy of fusion (J/g)	T_m (^oC)
P3DOT	15.44	233
P3DOT-*b*-PEG-10	12.28	227
P3DOT-*b*-PEG-18	10.31	233
P3DOT-*b*-PEG-40	14.97	234
P3DOT-*b*-PEG-80	11.86	239
P3DOT-*b*-PLLA-34	14.04	237
P3DOT-*b*-PLLA-65	11.49	238

Table 3.1 Enthalpy of fusion and T_m of all block copolymers

3.5 Swelling characteristics

3.5.1 Water vapour Brunauer-Emmett-Teller (*BET*) isotherm

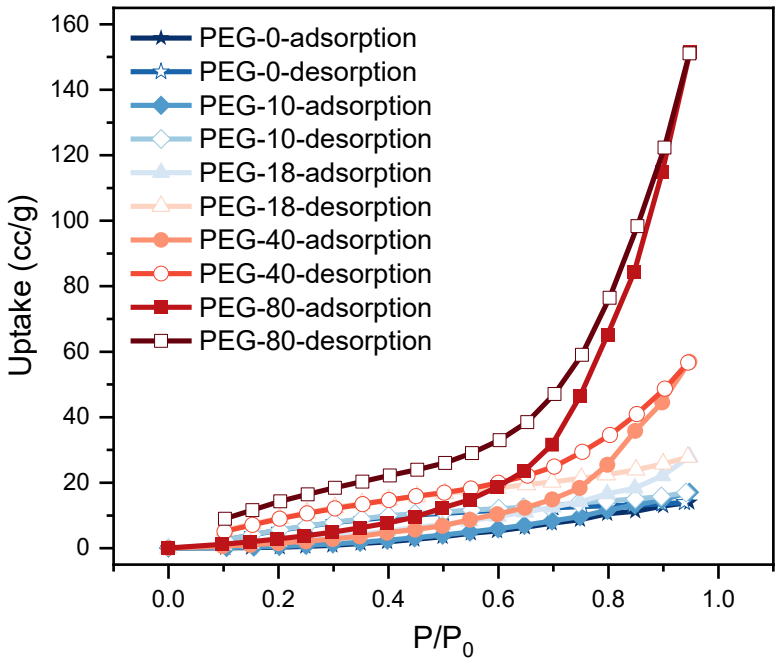

Figure 3.15 Water vapour BET Isotherm of P3DOT-*b*-PEG

The hydrophilicity of the P3DOT-b-PEG was studied by water vapour BET. In all cases, the absorption process revealed a Type III isotherm[181], arising from clustering of water

vapour around more hydrophilic surfaces on the nonporous particles[182]. Water uptake near saturation of atmosphere increased with longer PEG coil, consistent with greater hydrophilicity. This was also depicted in the adsorption-desorption hysteresis profile, favouring formation of film-like adsorbate multilayer, which desorbed more readily compared to nanodroplets[182]. Interestingly, P3DOT-b-PEG-40 and P3DOT-b-PEG-80 desorbed incompletely at the end of the cycle, likely caused by trapped moisture content within the irreversibly swelled volume.

3.5.2 Electrochemical quartz crystal microbalance with dissipation monitoring (*EQCM-D*)

The structural response of block copolymer film following electrochemical doping is evaluated by EQCM-D with QSense Analyzer. All tests were performed with as-casted polymer film in degassed 0.1 M aqueous NaCl electrolyte, with Pt counter and Ag/AgCl reference electrodes. The shift and dissipation of 1st, 3rd, 5th, 7th, 9th and 11th frequency harmonics were measured, and the best fitted harmonics are selected for quantitative analysis. All block copolymers present rigid thin-film property from their low dissipation factor. The passive swelling of P3DOT-b-PEG increases with longer coil chain, likely arising from higher hydrophilicity. Interestingly, active swelling under an external bias of -0.8 V reduces to a minimum at P3DOT-b-PEG-18, with thickness of the polymer film changing by <10% upon charging. A possible rationalization of this could link back to the outstanding self-assembly pattern presented under AFM. The film expansion is completely restored after relaxation, and is similarly featured in P3DOT-b-PEG-40. In contrast, P3DOT-b-PEG-80 depicts a significantly higher passive and active swelling, with thickness changing by 18% and 27% respectively. This is consistent with the three-fold increase of moisture uptake for P3DOT-b-PEG-80

compared to P3DOT-b-PEG-40 in water vapour BET isotherm, suggesting a significantly higher propensity to swell under humidity.

Interestingly, both block copolymers in PLLA series exhibit such low passive swelling that it is lower than the P3DOT homopolymer. This is consistent with the tightening of interlamellar distance illustrated with GIWAXS mapping (Figure 3.10), where more densely distributed alkyl side chains hinder film expansion following uptake. Moreover, compare to PEG, PLLA block intrinsically exhibits lower water diffusivity coefficient. These are determined in a previous spectroscopic studies[183] to be 1.4 x 10^{-9} and 4.2 x 10^{-8} cm^2s^{-1}, for PLLA and PEG respectively.

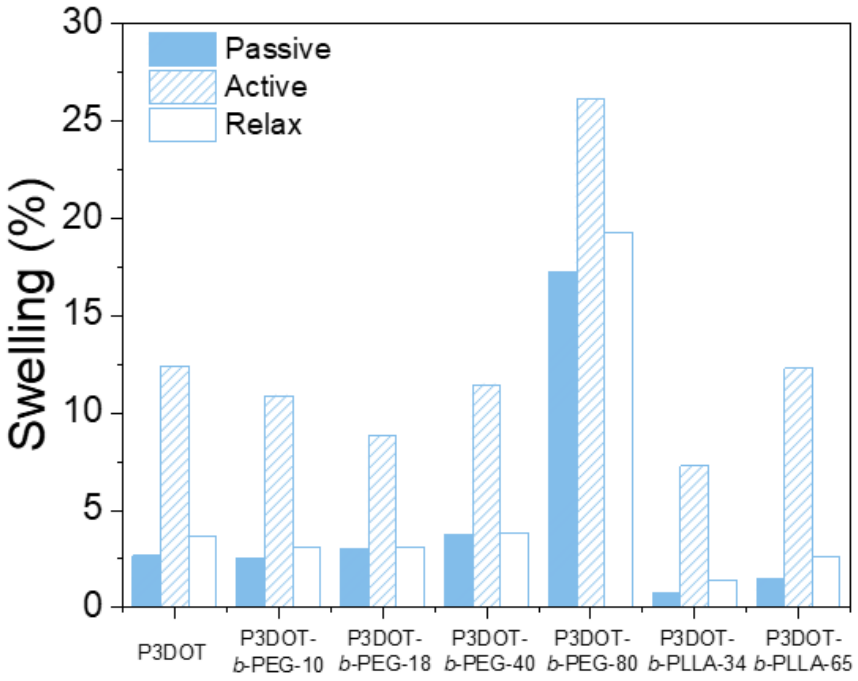

Figure 3.16 Quantitative profile of passive, active swelling and relaxation on block copolymer thickness

3.6 OECT performance

3.6.1 Figure-of-merit

The characterizations of *P3DOT*-based block copolymers lead to several important conclusions from different angles. The spectro-electrochemical measurements prove that under external bias, all block copolymers could be doped stably and reversibly in aqueous electrolytes. On the other hand, covalent linking of coil fragment with varied length and chemical identity did not result in significant deviation in optoelectronic properties, but these differences were more exemplified in their surface and swelling properties, which were rationalized base on the hydrophilicity and stiffness of the coil fragment. Overall, these materials fulfilled the criteria for an effective *OMIEC*. Therefore, these materials are applied in an *OECT* device with a channel width (W) and length (L) of 100 and 10 μm, respectively to benchmark their respective electronic performance. Several previous literatures reported the specific details of device fabrication[108,109], after which each block copolymer was spin-coated from a chloroform solution. The figure-of-merit was then evaluated with a 0.1 M NaCl as supporting electrolytes.

The I-V and transfer curves of the block copolymers were listed in Figure 3.17 and further summarized in Table 3.2. All block copolymers operate in accumulation mode and could be turned on under a negative gate bias around -0.4 V. Despite the similar V_{TH}, incorporation of coil block reduced the potential required by around 0.05 V, which could be rationalized by the high polarity of both *PEG* and *PLLA* microphases, facilitating ion penetration.

	d (nm)	V_{TH} (V)	g_m (mS)	$g_{m,\,norm}$ (Scm^{-1})	μC^* ($Fcm^{-1}V^{-1}s^{-1}$)	C^* (Fcm^{-3})	μ_{OECT} ($cm^2V^{-1}s^{-1}$)
P3DOT	47	0.42	2.33	49.6	130	0.915	142
P3DOT-*b*-PEG-10	45	0.39	0.676	15.0	62.6	6.99	8.96
P3DOT-*b*-PEG-18	38	0.36	2.34	61.6	153	7.56	20.2
P3DOT-*b*-PEG-40	38	0.37	0.649	17.1	51.8	6.95	7.45
P3DOT-*b*-PEG-80	47	0.37	0.756	16.1	40.0	67.8	0.590
P3DOT-*b*-PLLA-34	45	0.36	4.88	108	243	1.31	185
P3DOT-*b*-PLLA-65	35	0.38	2.27	64.8	154	2.52	61.1

Table 3.2 Summary of steady-state *OECT* performance of all block copolymers

Hydrophobic, alkoxylated backbone had been overlooked as *OMIEC* since the first use of p(g2T-TT)[109]. Until now, there had not been many reports on their usage in *OECT* devices with aqueous supporting electrolytes. Two notable exceptions[33,184] demonstrated *P3HT* core to exhibit good transconductance. However, a large threshold voltage around -0.80 V was necessary to turn on the device. The small difference between operating and threshold voltage led to a large gradient in the transfer curve. Hence, despite the relatively high transconductance, these devices suffered from less competitive saturation current, as well as a large operating voltage near the redox stability window of water.

Interestingly, *P3DOT* homopolymer featured a large μC^* of 130 $Fcm^{-1}V^{-1}S^{-1}$, which proved competitive against many glycolated counterparts[32,185,186]. Additionally, this material presented a V_{TH} of -0.42 V, which is lower and similarly comparable to that of

glycolated derivatives. Conversely, this polymer revealed a slow response, requiring a slow sweep rate to complete a doping-dedoping cycle and reach the steady state of the device. This was also accompanied with a significant hysteresis in the transfer curve. Likely, the hydrophobic thin film impeded ion egress under reverse bias, leading to slower doping kinetics.

With the exception of *P3DOT* homopolymer, all block copolymers presented a close correlation between active swelling and figure-of-merit. Previous result in this group had established a negative correlation between the extent of active swelling and OECT charge carrier mobility[40]. To interpret the pattern of μC^* shown, both active swelling and composition of insulating block should be considered simultaneously. In the case of P3DOT-*b*-PEG-10, despite reduced passive and active swelling with respect to *P3DOT* homopolymer, the nuance in figure-of-merit could be rationalized due to first introduction of electronically insulating PEG coil component, lowering overall electronic conductivity. Additionally, the short PEG block is unable to improve ionic transport significantly, leading to a reduced μC^* of 63 $Fcm^{-1}V^{-1}S^{-1}$.

Extension of PEG fragment resulted in an increase of μC^* to 153 $Fcm^{-1}V^{-1}S^{-1}$ for P3DOT-*b*-PEG-18, which exhibited the minimum active swelling among the PEG series. Further lengthening the PEG block incurred a reduction of μC^* to 52 $Fcm^{-1}V^{-1}S^{-1}$ and 40 $Fcm^{-1}V^{-1}S^{-1}$, for P3DOT-*b*-PEG-40 and P3DOT-*b*-PEG-80 respectively. This is associated with both higher active swelling, as well as greater composition of insulating coil component in block copolymer film, which compromises μ significantly. On the other hand, extension of PEG fragment reduces the hysteric behaviour of the polymer films. This is in agreement with the enhanced hydrophilicity and active swelling, leading to faster ion movement following biasing, which translates to faster kinetics of doping-dedoping.

This correlation between active swelling and charge carrier mobility was further shown in the PLLA series. P3DOT-*b*-PLLA-34, which features the minimum active swelling among all the block copolymers, achieves the maximum μC^* of 253 $Fcm^{-1}V^{-1}S^{-1}$. Furthermore, P3DOT-*b*-PLLA-65 also demonstrated a remarkable μC^* of 154 $Fcm^{-1}V^{-1}S^{-1}$, which is significantly higher than its PEG counterparts with similar *DP* in coil component.

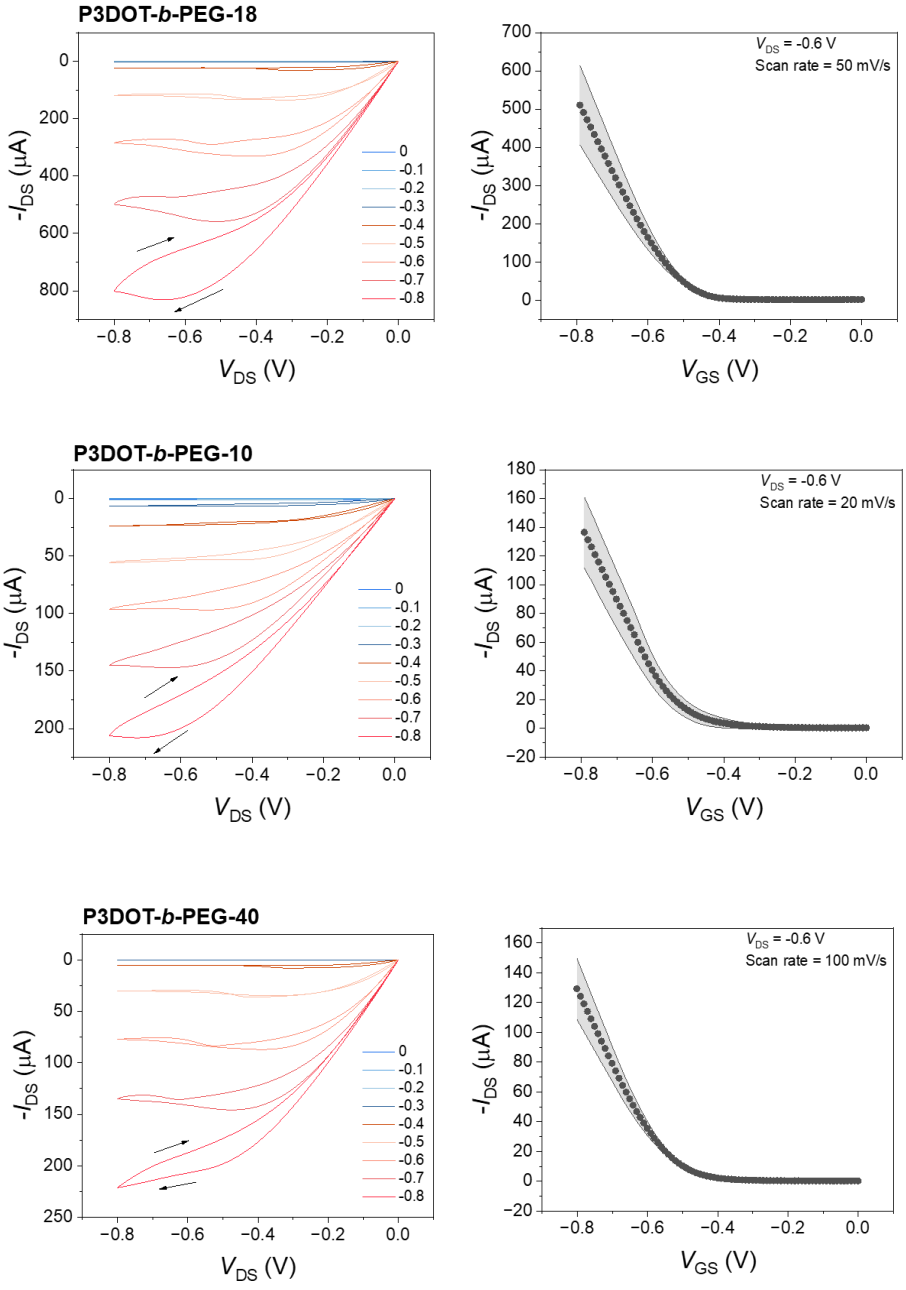

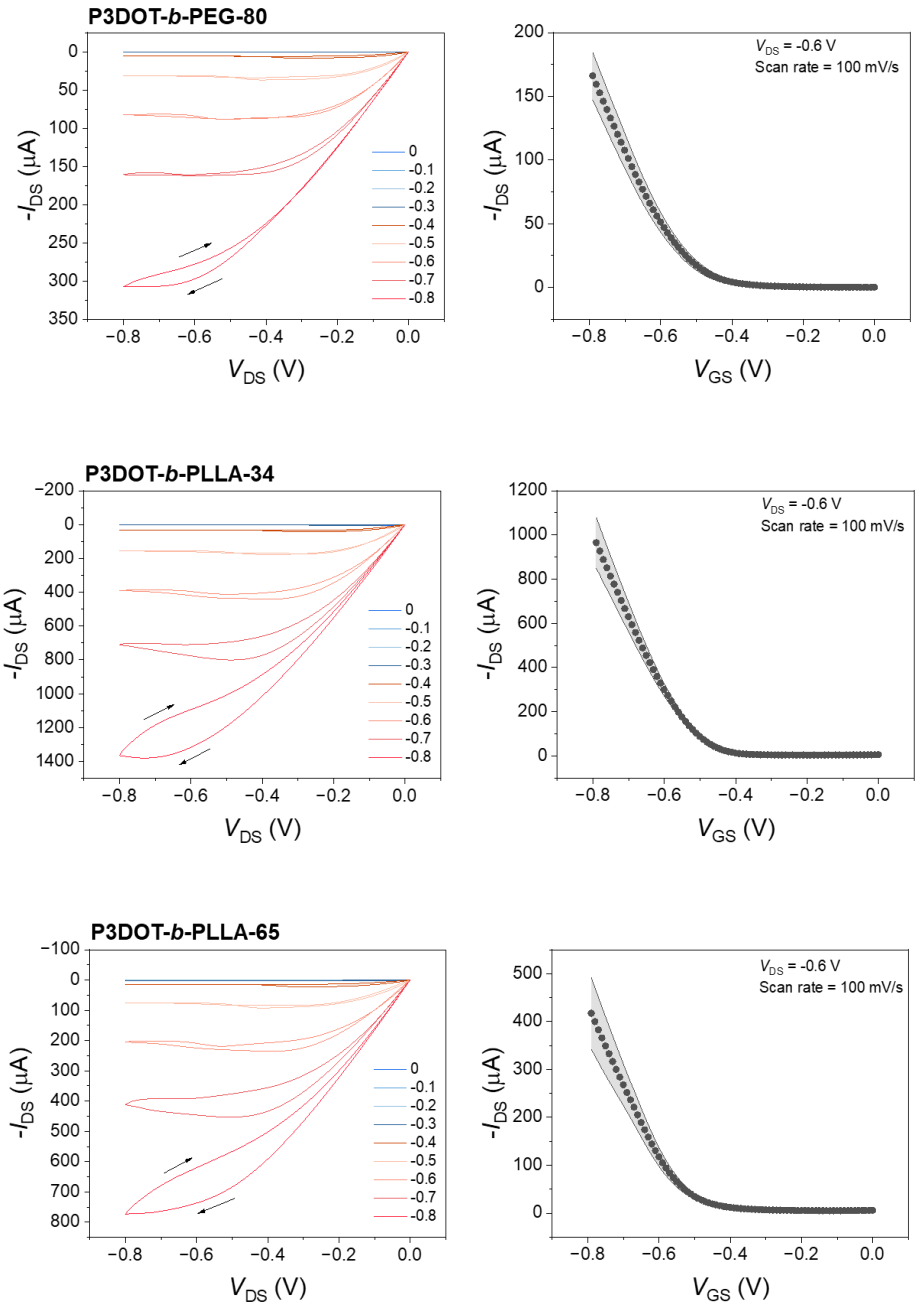

Figure 3.17 Output and transfer characteristics of all block copolymers

3.6.2 Deconvoluting figure-of-merit

For a better understanding on the underlying reason behind the performance of the block copolymers, the volumetric capacitance of the OMIEC-coated device was further evaluated with Electrochemical Impendence Spectroscopy (EIS). Herein, an increasing gate voltage was applied on the active channel in aqueous 0.1 M NaCl electrolyte

solution. The C* was then extracted by normalizing the capacitance by the volume of the active polymer film, under the gate bias associated maximum measured transconductance ($g_{m,\,max}$).

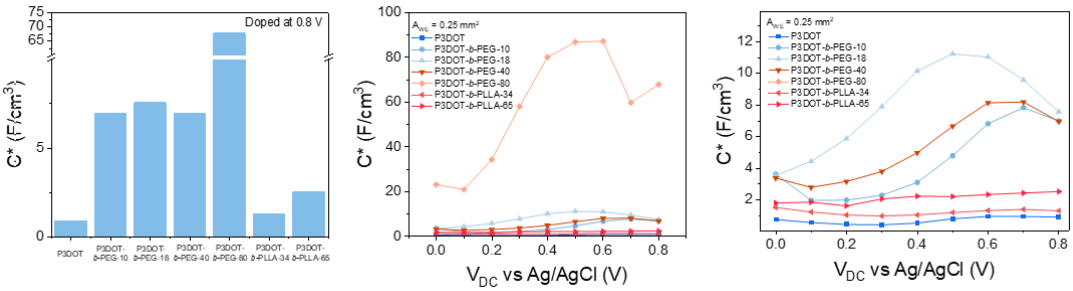

Figure 3.18 (left) Volumetric capacitance of all block copolymers (middle) *C** of all block copolymer measured as a function of applied gate voltage (right) *C** of all block copolymer measured as a function of applied gate voltage, for all block copolymer except P3DOT-*b*-PEG-80

From Figure 3.18, we noticed that the volumetric capacitance of all block copolymers, with the exception of P3DOT-b-PEG-80, is about an order of magnitude lower than that from side-chain glycolated analogues. C* of P3DOT-b-PLLA is slightly higher than that of P3DOT homopolymer, and replacing the coil fragment with more hydrophilic PEG increases this value further to around 8 Fcm^{-3}. Given that the coil fragments are anchored to the end of P3DOT backbone, it's possible that ion ingress concentrates on coil microphases. Doping-dedoping would occur most effectively near the interfacial area between rod and coil microphases due to better compensation of polaronic charge carriers with the electrolyte ions. It is hence more difficult for ion uptake to take place near the centre of the P3DOT domain. Moreover, the hydrophobic nature of alkoxy side chain also resists ion penetration. This less propensity towards ion permeation therefore leads to lower capacitance of the polymer film. Hence, while incorporating short, or less hydrophilic coil block proves effective in improving ionic transport properties of the material, it is possible that the device operates somewhere in between the interfacial

doping regime (OFET), where the capacitance is that of an electrical double layer, and the bulk doping regime in OECT. In the case of P3DOT-b-PEG-80, higher PEG content results in more effective electrochemical doping, leading to higher volumetric capacitance comparable to common OMIECs. Therefore, P3DOT-b-PEG-80 operates in the bulk doping regime.

The volumetric capacitance and the charge carrier mobility in an OECT device are hence deconvoluted and similarly summarized in Table 3.2. Beside P3DOT-b-PEG-80, which features an OECT charge carrier mobility resembling other OMIECs[40], all remaining materials present values orders of magnitude higher, which ties back to the mixed mode of device operation.

To measure the operational stability of the OMIECs, the fabricated devices are cycled through 200 cycles of continuous biasing pulses between "ON" and "OFF" states and benchmarked base on the percentage retention of the drain current. Following 200 rounds of continuous electrochemical addressing, the pristine P3DOT homopolymer retains 65% of its initial drain current. In comparison, P3DOT-b-PEG-18 and P3DOT-b-PLLA-65, which feature higher μC*, also achieve better operational stability, retaining 83 and 87% of initial current, respectively. P3DOT-b-PEG-10 also proves stable with a percentage retention of 80%. The remaining block copolymers show percentage retention less than 60%, but still demonstrates significantly higher operating stability compared to previously reported OECT devices fabricated from P3HT-based block copolymers[33].

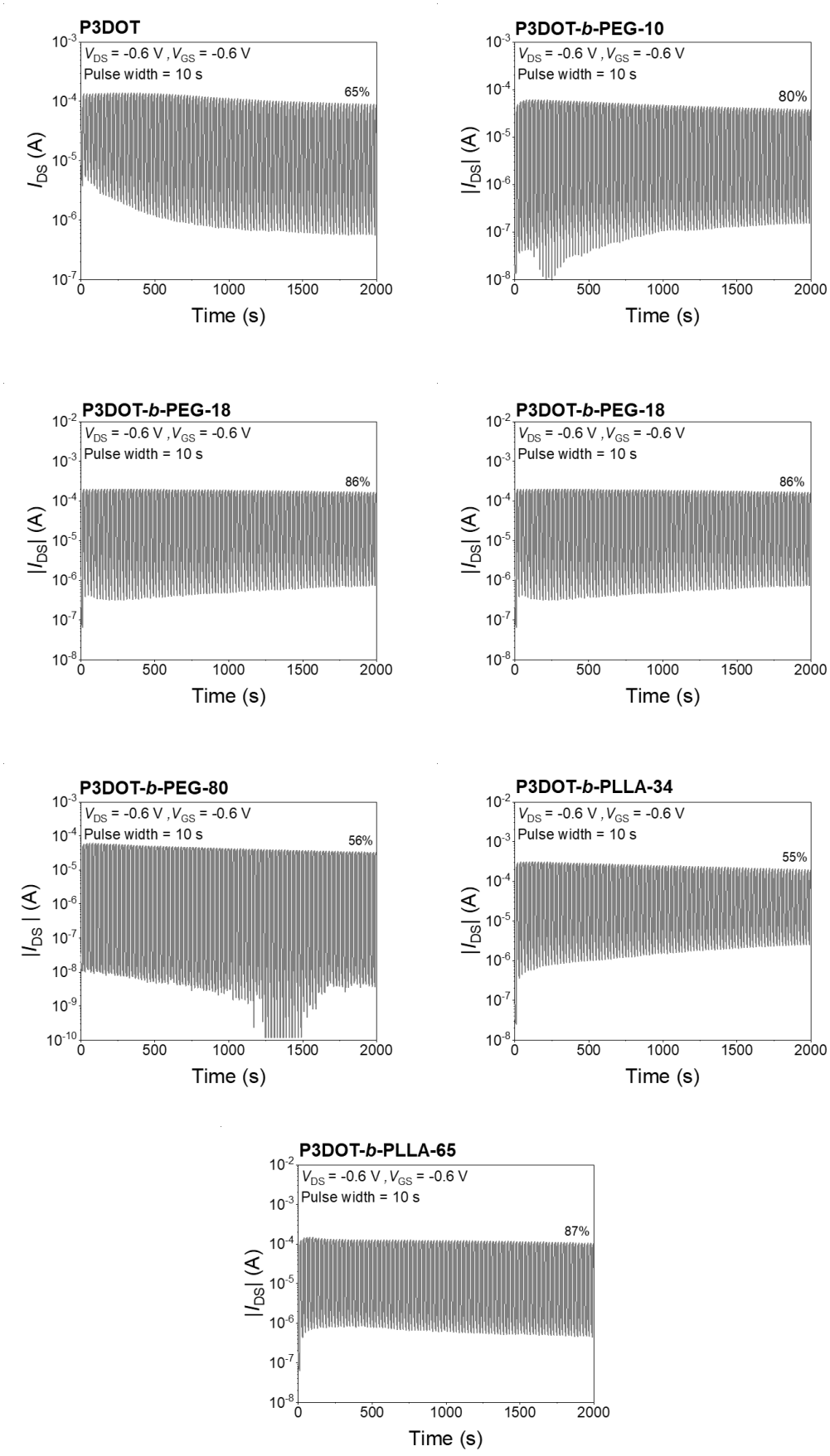

Figure 3.19 Electrochemical stability of all block copolymers after 200 cycles

3.6.3 Effects of thermal treatment on OECT performance

To examine how annealing could impact the device performance of the block copolymers, all OECTs were heated at 150 ºC for 30 minutes in a N_2-filled glovebox and cooled to room temperature before measurements were made. As shown in Table 3.3, all block copolymers demonstrate inferior normalized transconductance and higher threshold voltage following annealing. This can be correlated with the lamellar contraction revealed in the GIWAXS map of block copolymers following annealing, which further impedes ion infiltration, reducing μC* by compromising volumetric capacitance. On the other hand, annealing leads to better percentage retention in drain current and demonstrates less hysteric behaviour in P3DOT-b-PEG-40 and P3DOT-b-PEG-80, but these benefits could hardly compensate for the loss in device performance.

	V_{th} (V)	g_m(mS)	$g_{m,norm}$ (Scm^{-1})	μC* ($Fcm^{-1}V^{-1}s^{-1}$)
P3DOT AC	0.42	2.33	49.6	130
P3DOT TA	0.42	1.80	38.4	173
P3DOT-*b*-PEG-10 AC	0.39	0.676	15.0	62.6
P3DOT-*b*-PEG-10 TA	0.41	0.213	4.74	16.6
P3DOT-*b*-PEG-18 AC	0.36	2.34	61.6	153
P3DOT-*b*-PEG-18 TA	0.36	1.24	32.6	116
P3DOT-*b*-PEG-40 AC	0.37	0.649	17.1	51.8
P3DOT-*b*-PEG-40 TA	0.37	0.306	8.06	18.8
P3DOT-*b*-PEG-80 AC	0.37	0.756	16.1	40.0
P3DOT-*b*-PEG-80 TA	0.37	0.184	3.92	9.02
P3DOT-*b*-PLLA-34 AC	0.36	4.87	108	243
P3DOT-*b*-PLLA-34 TA	0.41	1.87	41.6	108
P3DOT-*b*-PLLA-65 AC	0.38	2.27	64.8	154

P3DOT-*b*-PLLA-65 TA	0.39	2.07	59.2	146

Table 3.3 V_{TH}, g_m, normalized g_m and μC^* of all block copolymer, *AC* denotes as-casted films and *TA* denotes thermally annealed films.

3.6.4 Effect of varying side chain on main-chain PEGylated block copolymers

In addition to altering the chemical identity and composition of the coil fragment, the impact of varying side chain on the P3AOT backbone is also investigated. The dodecoxy moiety is first replaced with a branched ethylheoxy counterpart (P3AOT-C_2C_6). This aims to weaken the hydrophobicity between the conjugated backbones, as we reason that side-chain branching may disrupt interlamellar ordering, favouring ion ingress, leading to better electrochemical doping. Unfortunately, contrary to our expectations, this chemical modification increases V_{TH} to -0.53 V and significantly lowers the μC* to 3.08 $Fcm^{-1}V^{-1}S^{-1}$. Including a coil block of PEG-18 slightly increases the figure-of-merit to 4.84 $Fcm^{-1}V^{-1}S^{-1}$. Base on these experimental outcomes, it is likely that branching simultaneously leads to two negative consequences: (i) disruption of molecular ordering in polymer backbone compromises charge carrier transport; (ii) Less linear pendant groups may have increased the difficulty for effective ion ingress, leading to poor electrochemical properties.

Alternatively, we seek to increase the hydrophilicity of the pendant group slightly, in the hope that this will favour bulk doping in the fabricated device. To achieve this, a glycol unit is introduced on the side chain (P3AOT-G_1C_7). In this case, while V_{TH} is reduced to -0.26 V, the homopolymer presents μC* of 77.9 $Fcm^{-1}V^{-1}S^{-1}$, which is lower than that of P3DOT homopolymer. This can be reasoned base on the increased flexibility of the pendant moiety, which have been shown to weaken charge carrier transport in previous reports[44]. Moreover, introducing PEG-18 coil block leads to

reduced μC* of 51.5 $Fcm^{-1}V^{-1}S^{-1}$. A possible explanation is that, in addition to weakening charge carrier mobility, partial side-chain glycolation also leads to significant increase in ionic transport properties. This overwhelms the volumetric capacitance contributed by main-chain PEGylation, leading to more significantly reduced charge carrier mobility due to greater insulating nature.

3.7 Conclusion and outlook

In this chapter, we report on the characterization of block copolymers from several different angles, including optoelectronic, thermal and morphological properties, followed by an evaluation of their OECT performances. Water vapour BET isotherm reveal that increased PEGylation results in greater moisture uptake. However, this leads to less reduction in V_{TH} compared to side-chain glycolation. In addition, all block copolymers exhibit very similar optoelectronic properties. This shows that any variation in device performance is minimally influenced by the differences in energetics of the block copolymers.

P3DOT homopolymer features a high μC* of 130 $Fcm^{-1}V^{-1}S^{-1}$, which is higher than many glycolated counterparts. However, the hydrophobic nature of P3DOT core leads to hysteric transfer characteristic due to slow kinetics of electrochemical de-doping. Among P3DOT-b-PEG, P3DOT-b-PEG-18 achieves the best μC* of 153 $Fcm^{-1}V^{-1}S^{-1}$ and features the minimum active swelling. In fact, the figure-of-merit of all P3DOT-b-PEG exhibits negative correlation with the extent of active swelling. This agrees with previous literatures reporting similar trend[33,40]. However, care should be taken to compare the two because the swelling properties of these block copolymers are still much lower than that of the side-chain glycolated derivatives. P3DOT-b-PLLA exhibits similar pattern, with P3DOT-b-PLLA-34 presenting the highest μC* of 243 $Fcm^{-1}V^{-1}S^{-}$

[1] among all block copolymers tested. The presence of PLLA block leads to lower passive swelling and active swelling compare to coil block with similar chain length. This could be accounted by lower water diffusivity, leading to less kinetic and capacity of water uptake. Notably, these block copolymers also present lower passive swelling than the P3DOT homopolymer. This can be rationalized base on the lower interlamellar distance between these backbones. Since PLLA possesses a higher T_g at 60 °C, a possible rationalization for the differences in molecular packing stems from the glassy state of the coil fragment at ambient temperature, illustrating greater stiffness of the microphase domain.

EIS measurements reveal that incorporating coil fragment improves C* of the material. However, they are an order of magnitude lower than side-chain glycolated OMIECs. This shows that while incorporation of short coil block can result in higher figure-of-merit, it is possible that these devices operate in between interfacial and bulk doping behaviour. That is, they present a mode of operation in between OECT and that of an OFET. Using a long, hydrophilic PEG-80 improves C*, matching that of glycolated OMIECs. However, this results in a poor μC* due to the insulating nature of the extended coil block.

Overall, this work presents the application of a novel molecular architecture for OMIEC design, but demonstrates many differences to popular state-of-the-art. For instance, the high figure-of-merit of P3DOT demonstrates that there exists such hydrophobic material which could lead to larger transconductance than some glycolated derivatives, through thin-film EGOFET-like behaviour. Given the strong correlation between active swelling and μC*, optimal figure-of-merit is presented by P3DOT-b-PLLA-34, which exhibits the minimum active swelling. However, this material still suffers from low volumetric capacitance and significant hysteric electrochemical behaviour, while the

higher C* of P3DOT-b-PEG-80 sacrifices electronic conductivity to attain an OECT-like behaviour. Collectively, these phenomena show that to optimize electrochemical transport of block copolymers, the coil fragment must not incur excessive active swelling and possess moderate chain length to not significantly compromise electronic conductivity of the thin film. Additionally, the greater C* of all block copolymers compare to P3DOT homopolymer highlights the role played by coil fragment in enhancing ionic transport, decoupling the ionic affinity from the conjugated backbone. In light of this, future development of coil fragment should seek better ion uptake. We demonstrate that rational design could be made by selecting polar, moderate-length coil fragment with low active swelling properties, leading to the development of better OMIEC on top of hydrophobic, conjugated backbone, hence providing fundamental insight for the development of next-generation material for OECT.

3.8 Future work

3.8.1 Investigating alternative self-assembly behaviour through annealing

The end of this chapter is dedicated to discuss some future directions in light of the current works. Due to the cumbrous synthesis and the characterizations of the on-casted film to understand the underlying structure-activity relationship, self-assembly of the block copolymers under post-fabrication treatment had been overlooked. For instance, all P3DOT-b-PEG other than P3DOT-b-PEG-18 did not demonstrate well-defined, prominent nanostructure and the structural correlation between that and electrochemical performance remains elusive.

The idealized phase diagram of diblock copolymer was introduced in Section 1.4, with polydispersity and greater χ favouring ordering of microphases. In addition, recent studies have shown that phase-separated material with crystalline, conjugated units

favour the formation of lamellar morphology, as predicted by crystal lattice analysis[187]. This inspires us to investigate thin-film treatment driving self-assembly, such as solvent-vapour annealing.

Preliminary work in this group has shown that, annealing under saturated chloroform vapour enhances phase separation order of the material. Gradual deswelling of the block copolymer film by slowly lowering the vapour pressure results in most well-defined lamellar nanostructure. This is demonstrated in Figure 3.19, where AFM phase-profile of solvent-vapour annealed P3DOT-b-PEG-18 and P3DOT-b-PEG-40 are presented, marking clear difference compared to that of the as-casted film. (Section 3.3.2). Subsequent work seeks to explore if this treatment could influence the morphology of block copolymer in the OECT channel area in an identical way, and whether promoting the formation of lamellar nanostructure benefits the device performance in any way.

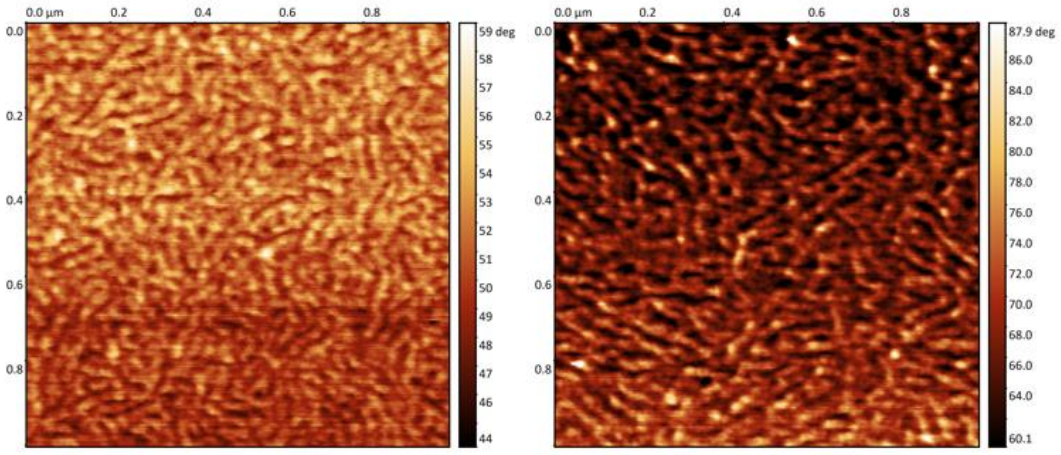

Figure 3.20 *AFM* phase profile of P3DOT-*b*-PEG-18 and P3DOT-*b*-PEG-40 after solvent vapour annealing

3.8.2 Nanoporous OECT through on-surface chemical cleavage

It is important to note that despite enhancing ionic transport, PEG tail is intrinsically insulating. Hence, this may limit the peak overall electronic conductivity a block

copolymer can attain. On the other hand, the ionic transport behaviour can be further enhanced if accessible channels or voids are present for better ion penetration. Incorporation of mesopores to conjugated polymer film through breath figure self-assembly had been previously reported[184], which showed that porous poly(thiophene)-based OECT with alkyl side chain generally outperformed their dense analogue. However, these pores are usually large with irregular and uncontrolled size. On the other hand, rod-coil block copolymers hold promise for better control in surface porosity. To achieve this, semiconducting polymer backbone could be covalently linked with a sacrificial polymer chain, which are then etched following fabrication to prepare porous films uniformly segregated by microphases.

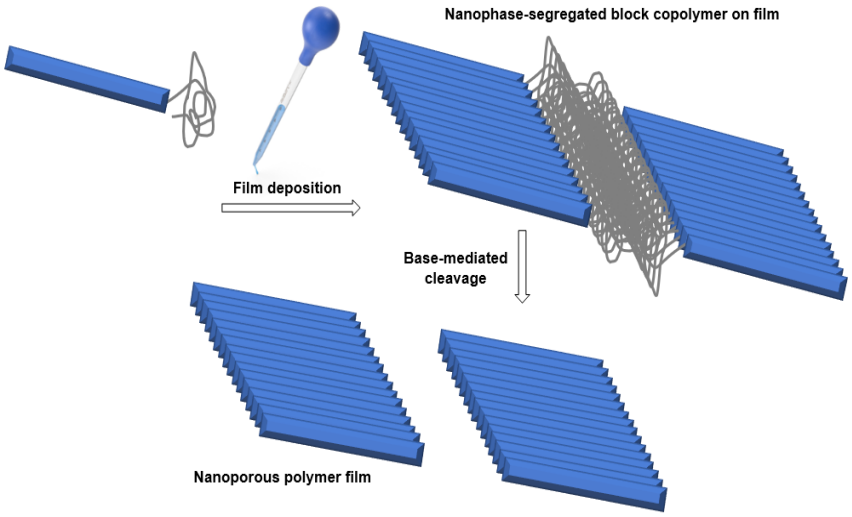

Figure 3.21 Schematic drawing demonstrating the chemical cleavage of conjugated rod-coil block copolymer to introduce nanoporosity.

Base-mediated hydrolysis of polyester is one such reported, viable strategy to create porosity[154,188,189]. A solution of sodium hydroxide in an alcohol-water mixture was commonly employed, leading to complete cleavage of poly(L-lactide) following 72 hours. Nevertheless, water-induced delamination of polymer coating severely challenged mechanical stability of the materials on-film[190], leading to loss of adhesion

through several different mechanisms, such as a change in physical and chemical environment at the polymer-substrate interface[190–192]. We found that immersing the block copolymer films for extended duration increases the risk of delamination. Moreover, since the reported etchant involves sodium hydroxide near saturation concentrations, these ionic compounds can form microcrystals in the polymer film, deteriorating its electrochemical properties.

Organocatalyzed methanolysis is an alternative method used for polyester upcycling[193], recycling common plastics such as Polyethylene terephthalate (PET). Prior reports usually involve an amidine superbase catalyst such as triazabicyclodecene (TBD)[194], which readily dissolves in most common organic solvents and could be used with a wide range of alcohols (i.e. MeOH, EtOH, BuOH), achieving full degradation of poly(L-lactide) in minutes[195]. Herein, TBD promotes degradation of polyester fragment through a dual activation mechanism. In the transition state, the organocatalyst binds an alcohol molecule in proximity with the carbonyl moiety on a polyester through hydrogen-bonds, lowering the activation barrier of nucleophilic substitution, thereby facilitating depolymerization.

This motivated us to explore selective cleavage of the polyester block by immersing the block copolymer thin films in an alcoholic solution of TBD. Compared with conventional hydrolysis, this approach offers three key advantages: (i) Organocatalyst and alcohol molecules can better penetrate the block copolymer thin films in an organic medium, thereby accelerating heterogeneous depolymerization; (ii) the lower surface tension of alcohol reduces the risk of nanopore collapse[196] and film delamination; (iii) the trans-esterified depolymerization products are also highly soluble in common lipophilic solvents, allowing their simultaneous removal alongside TBD by rinsing the polymer film with an organic anti-solvent.

The feasibility of the approach was investigated with a polymer-film of PCL-b-P3HT-b-PCL deposited on a glass substrate via drop-casting. This ensures that the mass of polymer applied could be accurately quantised. Following cleavage, the polymer film is re-dissolved, and the molecular weight is measured by GPC (Figure 3.22). Three different conditions were screened. Encouragingly, compare to hydrolysis, both methanolysis conditions reveal complete depolymerization within 24 hours, with the retention profile of etched polymer in approximate agreement with the P3HT precursor. Herein, MeCN was added as an addictive to promote permeation of etchant into the polymer film, but this did not significantly improve etching efficiency.

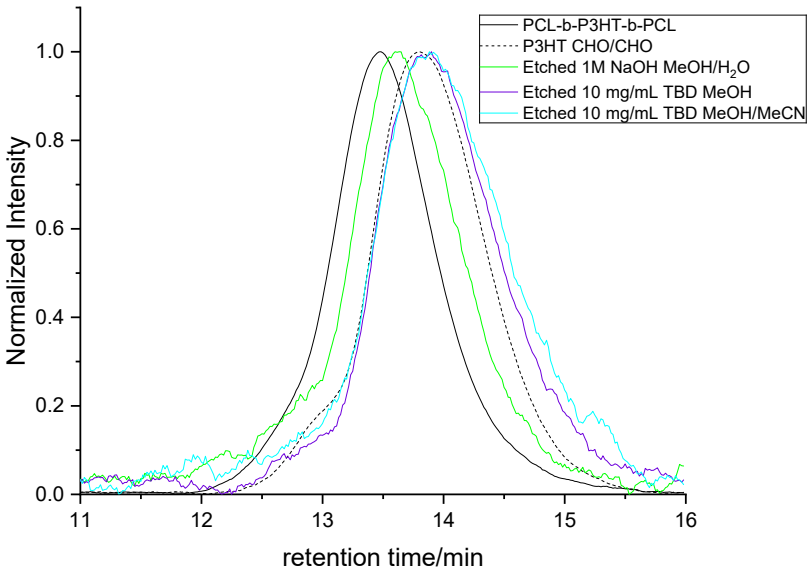

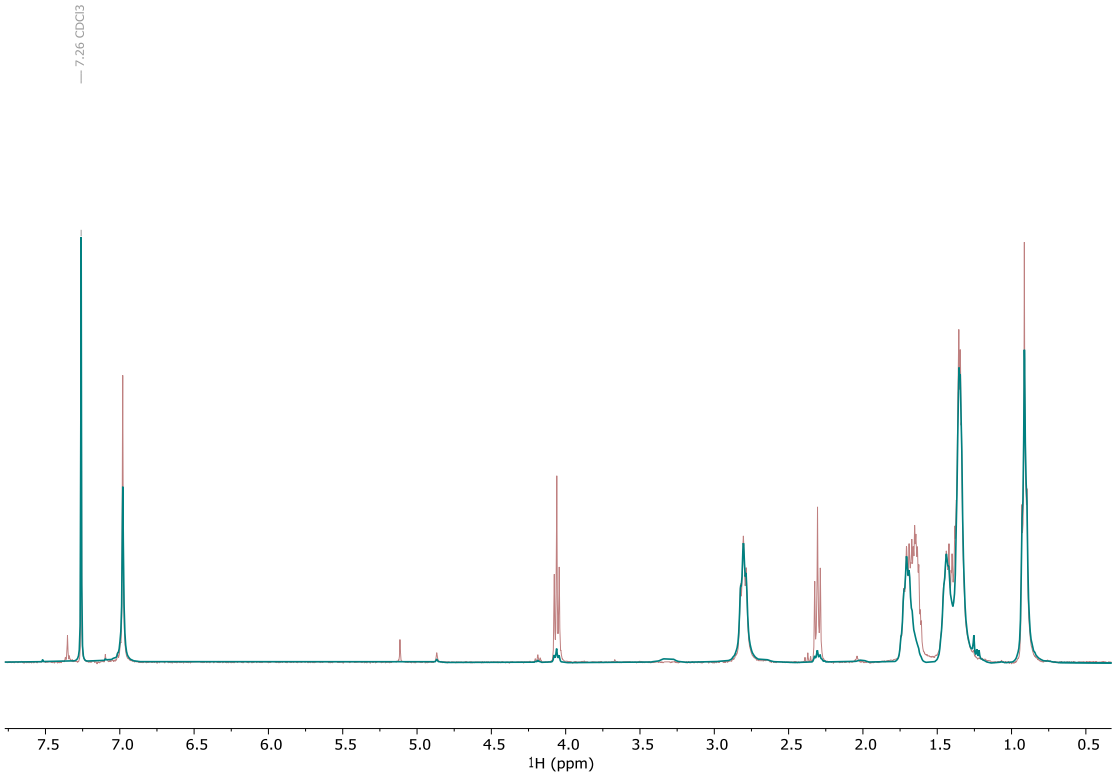

Figure 3.22 (top) *GPC* trace of PCL-b-P3HT-b-PCL (bottom) ^{1}H *NMR* before (maroon) and after etching (green)

The complete removal of the PCL block was further supported by ^{1}H NMR and the topography of the film following etching was screened with PeakForce AFM (Figure 3.22) with height and adhesion profile. The presence of pore-like feature was clearly more prominent following etching.

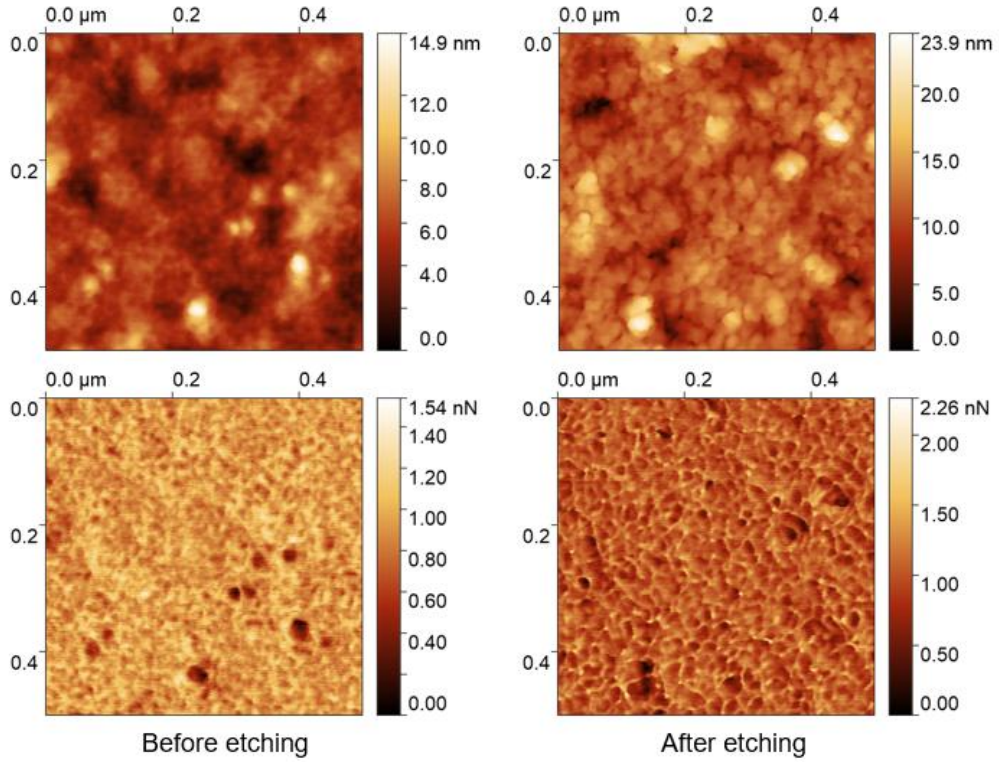

Figure 3.23 PeakForce *AFM* height profile of PCL-*b*-P3HT-*b*-PCL (a) before etching (b) after etching and adhesion profile of PCL-*b*-P3HT-*b*-PCL (c) before etching (d) after etching

This treatment also proves highly effective to P3DOT-b-PLLA, where similar pore-like feature emerges following etching under PeakForce AFM (Figure 3.23 and 3.24).

Herein, we have demonstrated two methods to alter the morphology of the as-casted film. A structure-activity relationship over how these nanostructures could correlate to OECT performance would provide a more in-depth understanding in application of these materials as OMIEC, far beyond the scope discussed in the main text of this chapter.

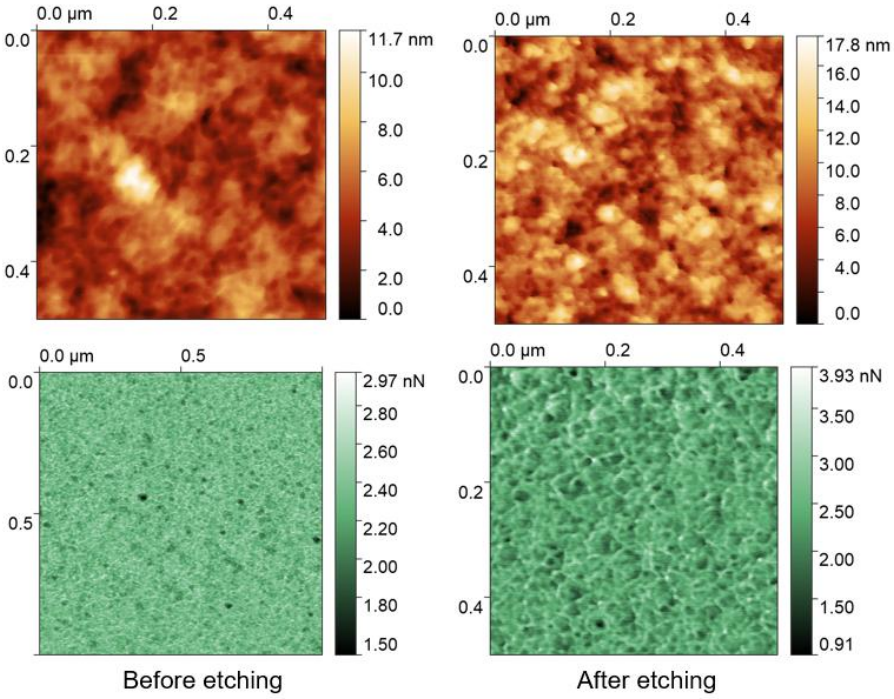

Figure 3.24 PeakForce *AFM* height profile of P3DOT-*b*-PLLA-34 (a) before etching (b) after etching and adhesion profile of P3DOT-*b*-PLLA-34 (c) before etching (d) after etching

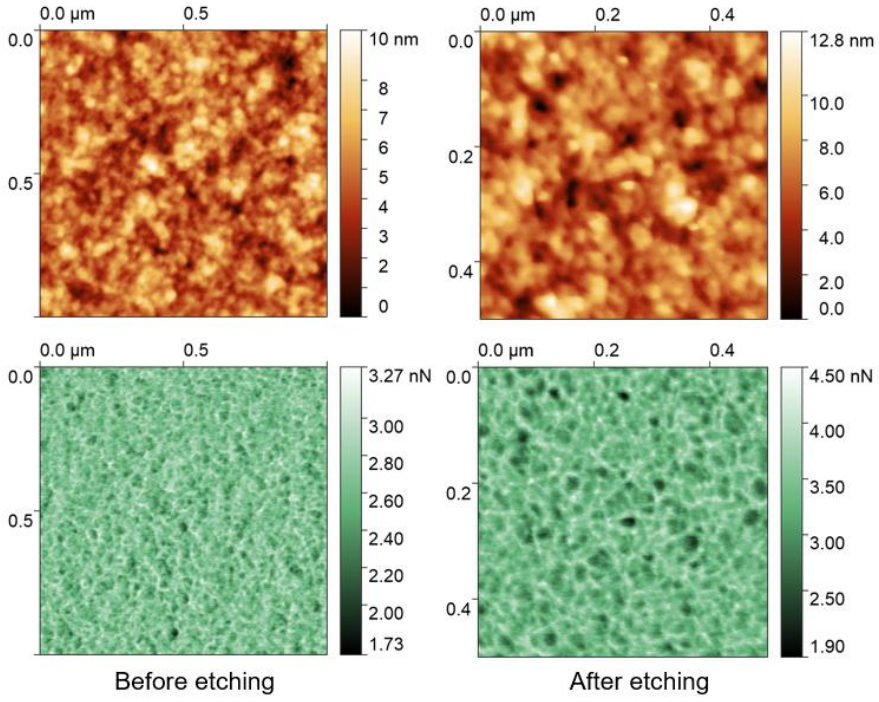

Figure 3.25 PeakForce *AFM* height profile of P3DOT-*b*-PLLA-65 (a) before etching (b) after etching and adhesion profile of P3DOT-*b*-PLLA-65 (c) before etching (d) after etching

CHAPTER 4

A minimalist design to high-performance OECT material

4.1 General information and contributions

The project was conceptualized by Junfu Tian and Prof. Iain McCulloch, inspired by the work by Dr. Benjamin Willner[197]. All polymer analysis, cyclic voltammetry, UV-Vis spectroscopy, PESA and spectro-electrochemistry was conducted by Junfu Tian. Polymer deposition and post-fabrication treatment were carried out by Junfu Tian with the help of Yuyun Yao and Rachael Found. OECT testing was performed by Dr. Silan Zhang (University of Cambridge).

4.2 Introduction

Organic electrochemical transistor (OECT) has emerged as a transformative class of devices, significantly advancing bioelectronics in the past decade. By employing organic mixed ionic-electronic conductor (OMIEC) as channel material, OECTs efficiently transduce ionic signal from biological systems into measurable electronic output[25]. The soft and pliable nature of OMIECs further facilitates seamless interfacing with biological surface. These synergistic features establish OECT as a versatile cornerstone technology for next-generation bioelectronics, enabling diverse applications ranging from biosensors to wearable electronics and neuromorphic computing[198].

A detailed explanation of working mechanism and device structure of OECT had been previously discussed in Chapter 1, where it was also explained how side-chain glycolated conjugated polymers form a dominant category of OMIECs, but also suffer from challenging synthesis and material optimization, as well as poor atom economy. To explore alternative molecular architectures for OMIEC design, the synthesis and characterization of P3DOT-based rod-coil block copolymer was reported in Chapter 2 and 3, respectively.

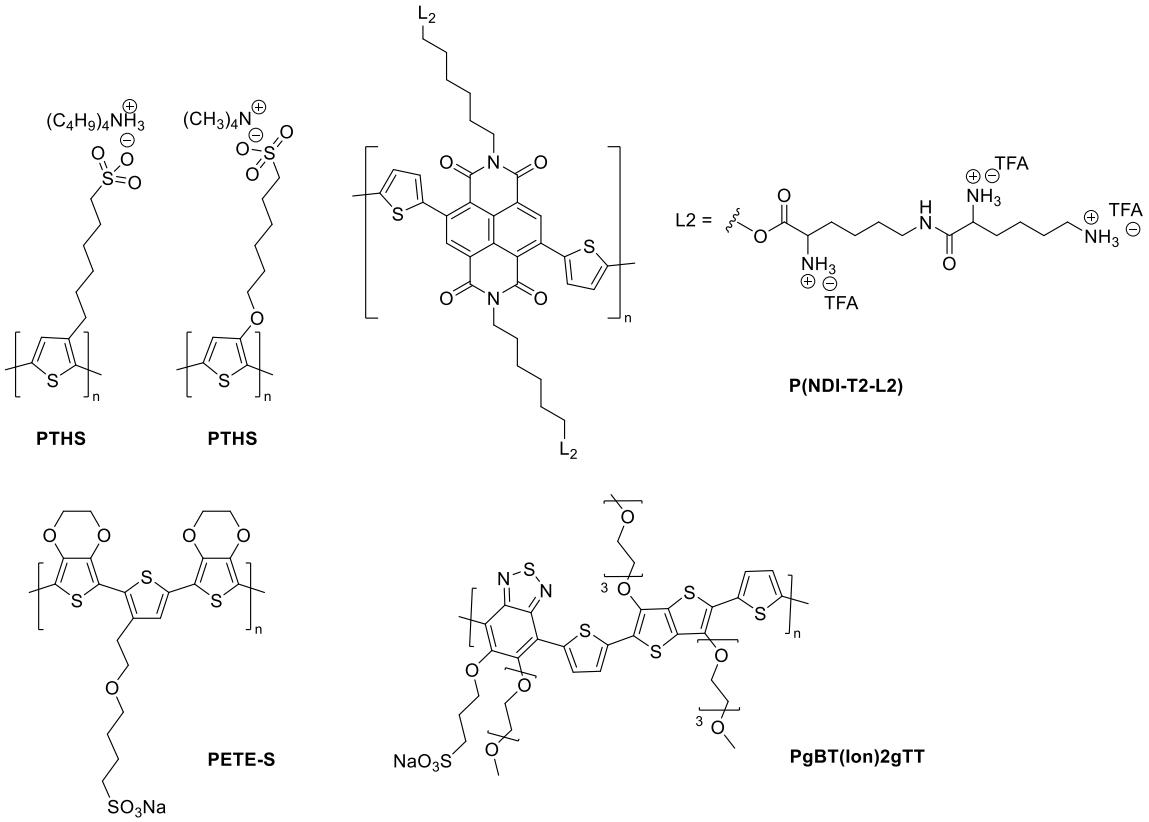

Figure 4.1 Examples of conjugated polymers incorporating alternative polar side chains

The first use of conjugated polymers with polar side chains as OMIEC[108] dates earlier than the invention of glycolated conjugated polymers[109]. Initial designs usually incorporated charged pendant moieties, such as PTHS[108] p(NDI-T2-L2)[110], PETE-S[111], PgBT(Ion)2gTT[112] and P3HOTSTMA[114]. These were inspired by the high transconductance achieved by PEDOT:PSS OECT, which exhibited state-of-the-art bioelectronics at the time[199], where the use of conjugated polyelectrolyte (CPE) not only features competitive hole mobility, but highly favours ionic transport, making them promising material for OMIECs. In addition, incorporation of anionic side chain with positive mobile counterion demonstrated enhanced cation dynamics in its charging mechanism[36]. However, positioning of charged moieties close to the conjugated backbones was also shown to hinder charge transport[200], where the polaronic carriers could be electrostatically pinned. Alternatively, some CPE also present self-doping properties, requiring a positive bias to de-dope the material completely and resulting in a poor ON-OFF ratio.

Investigation of alternative non-ionic polar side chains, such as esters, alcohols and carboxylic acids, was pioneered by Katz et al. and demonstrates that their inclusion in the pendant side chain features a large shift to lower V_{TH} and increases in drain-current in OECT at steady-state[201]. The use of alcohols[113] and carboxylic acids[202] were further developed, presenting lower active swelling, which was correlated with higher OECT charge mobility both in previous reports and earlier chapters of this thesis. In addition, the presence of alcohol-substituted side chains was shown to result in volumetric capacitance comparable to that of a tetraethylene glycol substituents[41]

Given that oligoethylene glycol functionalities are fully saturated and intrinsically insulating in nature, it would be interesting to explore whether their replacement with structurally simpler, more atom-economic substituents like alcohols or carboxylic acids could improve OECT performance. However, some prove less competitive in figure-of-merit comparisons to their glycolated counterparts[41,201]. This can be rationalized based on the inclusion of excessive spacer to aid solubility of the material, but this simultaneously increased the hydrophobicity and insulating nature of the conjugated backbone. On the other hand, a short alkyl spacer will render the material not solution-processable, making their fabrication into a uniform thin-film practically challenging.

To simultaneously benefit from the high ionic affinity of simple polar functionalities and improved charge carrier mobility from shortening of alkyl spacer, the conventional method of direct solution-processing must be disregarded. An alternative approach to avoid these problems, is to synthesize a conjugated polymer bearing a solubilizing side chain for better processability and morphology control, which could crucially be cleaved post-fabrication to expose a sufficiently polar group, to simultaneously enhance hydrophilicity and conductivity. Such post-fabrication treatment had been described in the previous chapter to prepare nano-porous polymer thin-film from block copolymer precursor. Alternative approaches include thermal deprotection of carbamate-substituted poly(thiophene)s[203] or decarboxylation of poly(thiophene) esters by acid catalysis[204]. However these strategies require high-temperature

thermal treatment, which compromises device stability. Interestingly, a prior work in the group attempted the preparation of alcohol-substituted polymers with intrinsic porosity (PIMs) through deprotection of processable silyl ether-grafted polymer precursor. This method proves highly versatile as the length of alkyl chains on the silyl protecting group can be tuned to accommodate better solubility. This strategy inspired the development of an on-film post-fabrication treatment base on silyl ether-protected polymers. Herein, a design based on gBTTT backbone[205], the state-of-the-art p-type OMIEC at the time, was chosen. The device performance of these polymer films after alcohol de-protection is then evaluated.

4.3 Polymer synthesis

The synthesis of the silyl ether-protected PgBTTT-OTBS is shown in Figure 4.2. In this pathway, a key intermediate is monomer 4.1, where an alkyl spacer 4 carbons long is positioned between the conjugated backbone and the alcohol terminus. The choice in length of the spacer is based on practical concerns. When truncated to 2 carbons long, the 3-alkoxythiophene precursor prepared in the initial step of the synthesis became highly unstable and underwent auto-polymerised upon formation. Tributylsilyl protecting group (TBS) was chosen to provide sufficient processability but not introduce excessive steric hindrance, which may disrupt π- π stacking significantly.

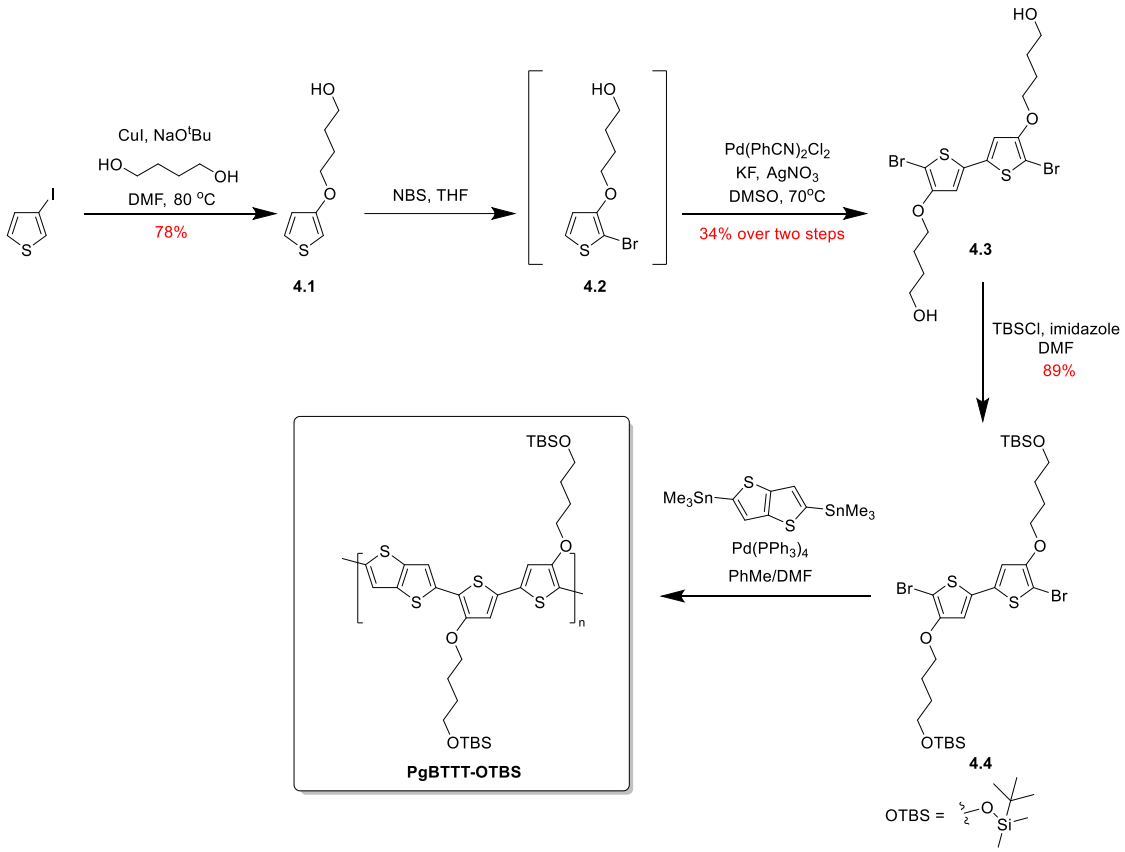

Figure 4.2 Reaction scheme for the synthesis of PgBTTT-OTBS

Mono-bromination of the 3-alkoxythiophene also proved challenging. Following chromatographic separation, it was important that the purified monomer 4.2 to not be dried completely At high concentration, 2-bromo-3-alkoxythiophene derivative is highly unstable and auto-polymerizes spontaneously, compromising the overall yield of the process. Serendipitously, subsequent dimerization through oxidative C-H homocoupling[206,207] used *DMSO* solvent, allowing volatile solvent impurities in the previous step to be removed under reduced pressure. The bithiophene 4.3 following homocoupling is photosensitive and should be contained in a covered vessel as far as possible and will form green oligomerized impurities otherwise. The protected bithiophene, monomer 4.4, too, should be handled in similar manner.

Having successfully synthesized monomer 4.4, PgBTTT-OTBS could be obtained following Stille cross-coupling polymerization with 2,5-bis(trimethylstannyl)thieno[3,2-b]thiophene, with good reaction yield of 63%.

4.4 Polymer characterization

PgBTTT-OTBS presents moderate processability in chlorobenzene. However, a uniform polymer film required hot deposition from a solution with concentration 5 mg/mL. GPC in chlorobenzene revealed a M_n of 3.9 kg/mol. However, this was likely an underestimate because more insoluble, higher molecular-weight polymer chains were filtered before elution of the polymer solution. More reliable estimates require GPC analysis with more solubilizing eluents such as trichlorobenzene, which is more lipophilic and can operate at a higher temperature. The polymeric nature of the material can be supported by ^{1}H NMR (Section 7.2.2), which features broad resonance signals.

4.4.1 Optoelectronic properties of PgBTTT-OTBS before etching

As shown in Figure 4.6, the as-cast UV-Vis absorption spectrum of PgBTTT-OTBS featured two absorption maxima at 601 and 648 nm, resembling that of PgBTTT[205] with a slight redshift. The peaks present relatively well-resolved vibronic features, which could be attributed to the 0-0 and 0-1 transitions, respectively. Notably, the absorption near 650 nm is more intense compare to its glycolated counterpart, suggesting a higher degree of structural order.

The ionization potential of PgBTTT-OTBS was determined by PESA to be 4.9 eV, which is slightly deeper than that of PgBTTT, with a value of 4.7 eV[205]. Because both conjugated polymers present a similar optical band gap, this lowering in HOMO is likely not related to differences in backbone planarity and coherence length of the π-system. Instead, given the shallow HOMO and greater hydrophilicity of PgBTTT, under ambient air exposure, it is more favourable for moisture-induced p-doping to take place due to oxygen diffusion[208], accounting for the reduced ionization potential measured.

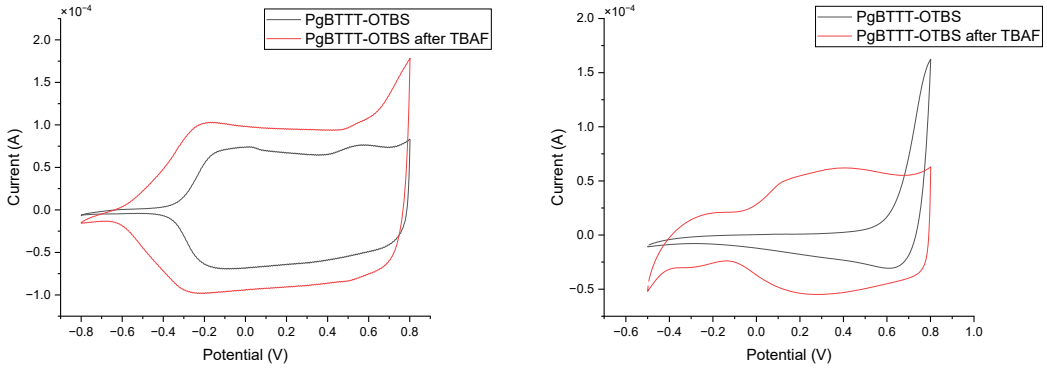

Figure 4.3 Cyclic voltammogram of PgBTTT-OTBS in (left) acetonitrile with 0.1 M $TBAPF_6$ supporting electrolyte and (right) 0.1 M aqueous NaCl electrolyte solution, with a scan rate of 100 mV/s. The potential was referenced with Ag/AgCl electrode.

The cyclic voltammograms of PgBTTT-OTBS in organic and aqueous electrolyte solution are presented in Figure 4.3. With 0.1 M $TBAPF_6$ supporting electrolyte in acetonitrile, PgBTTT-OTBS exhibits similar CV trace and onset potential compared to PgBTTT, suggesting similar HOMO level around 4.5 eV. Contrarily, the highly lipophilic, bulky silyl group on the pendant side chain renders the backbone strongly hydrophobic, leading to a large onset potential of 0.63 V in 0.1 M aqueous NaCl solution.

4.4.2 Optoelectronic properties of PgBTTT-OTBS after etching – TBAF treatment

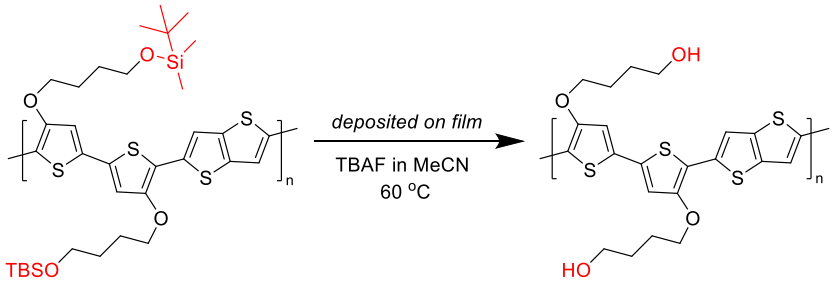

Figure 4.4 Reaction Scheme of on-film deprotection with TBAF

Chemical cleavage of silyl group was performed with tetrabutylammonium fluoride (TBAF) in acetonitrile, which the film was sufficiently permeable in but not soluble. Complete deprotection of the backbone was supported by XPS, where a significant increase in Si binding energy is observed. This was consistent with the formation of Si-F bond on the silyl protecting

group following reaction, indicating that all TBS moieties had been unmasked. However, the reduction of Si/S ratio by only 20% suggested significant amount of TBAF impurities present in the polymer film.

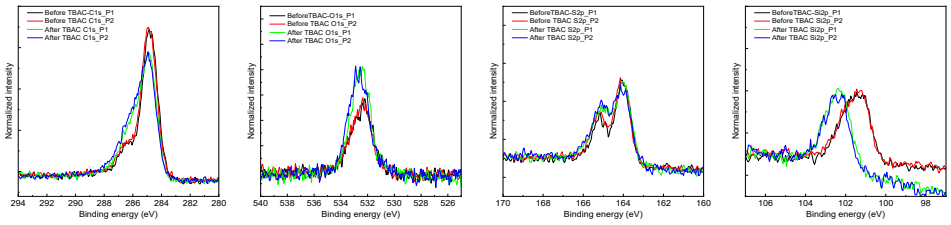

Figure 4.5 XPS Spectra of PgBTTT-OTBS before and after TBAF treatment by elements

The optical and electrochemical properties of PgBTTT-OTBS following deprotection with TBAF were compared against the untreated polymer in Figure 4.3 and 4.6, respectively. As shown in Figure 4.6, UV-Vis spectrum did not present significant change in absorption maximum but instead led to a diminishing of the peak corresponding to 0-1 transition.

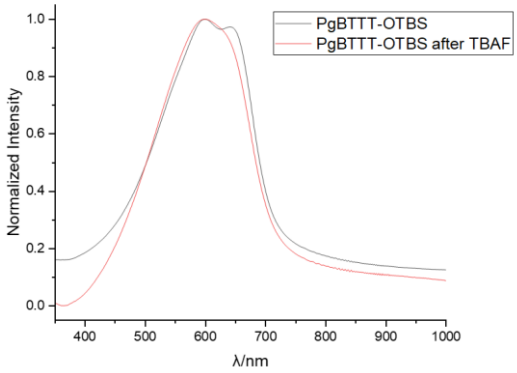

Figure 4.6 UV-Vis Absorption Spectra of PgBTTT-OTBS before and after TBAF treatment

The electrochemical response of the material under external applied bias was evaluated with cyclic voltammetry. As shown in Figure 4.3, we noticed a significant reduction in onset potential to -0.04 V with increase in capacitive nature with 0.1 M aqueous NaCl supporting electrolyte, corresponding to improved hydrophilicity, which is consistent with the presence of

exposed alcohol moieties following deprotection. Interestingly, the cyclic voltammogram with 0.1 M $TBAPF_6$ supporting electrolyte in acetonitrile (Figure 4.3) revealed reduced IP, and was further supported by the same trend observed in PESA (Figure 4.7). The IP of the materials estimated based on their onset potential in CV with organic electrolyte and determined by PESA are listed in Table 4.1, respectively.

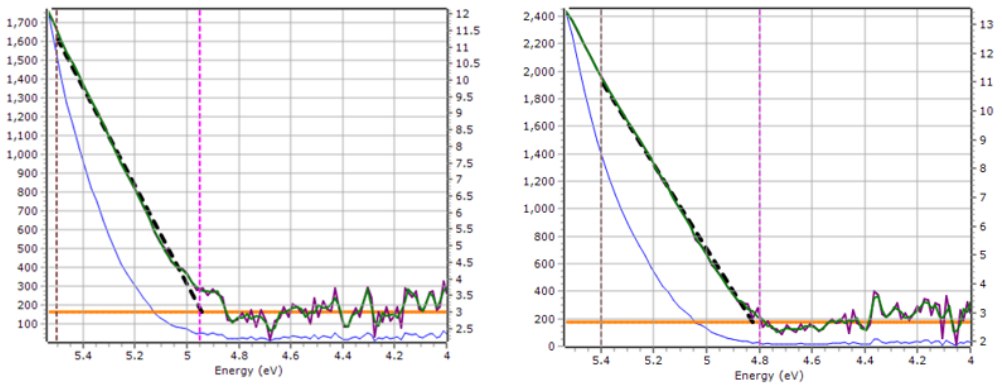

Figure 4.7 PESA of PgBTTT-OTBS before and after TBAF treatment

Sample	**$IP_{CV, org}$/eV**	**IP_{PESA}/eV**
PgBTTT-OTBS	4.48	4.94
PgBTTT-OTBS after TBAF treatment	4.31	4.82

Table 4.1 Ionization Potential of PgBTTT-OTBS before and after TBAF treatment, determined by cyclic voltammetry and PESA

The reversible and stable electrochemical doping featured by PgBTTT-OTBS following chemical treatment rendered the material suitable for OMIEC, which was then fabricated from a chlorobenzene solution. Importantly, deposition from a hot solution promotes the formation of a uniform film. The fabricated device was immersed in 0.1 M TBAF in MeCN and warmed to 60 ^{o}C in a sealed chamber for 24 hours. The surface was cleaned by gentle rinsing with clean acetonitrile and the device was operated in 0.1 M aqueous NaCl electrolyte solution with an Ag/AgCl gate electrode. Importantly, the chemical treatment should be performed before peeling off the parylene C insulating layer, because exposure to TBAF led to erosion of gold

electrode over time. The I-V and transfer characteristics of the devices were summarized in Figure 4.8.

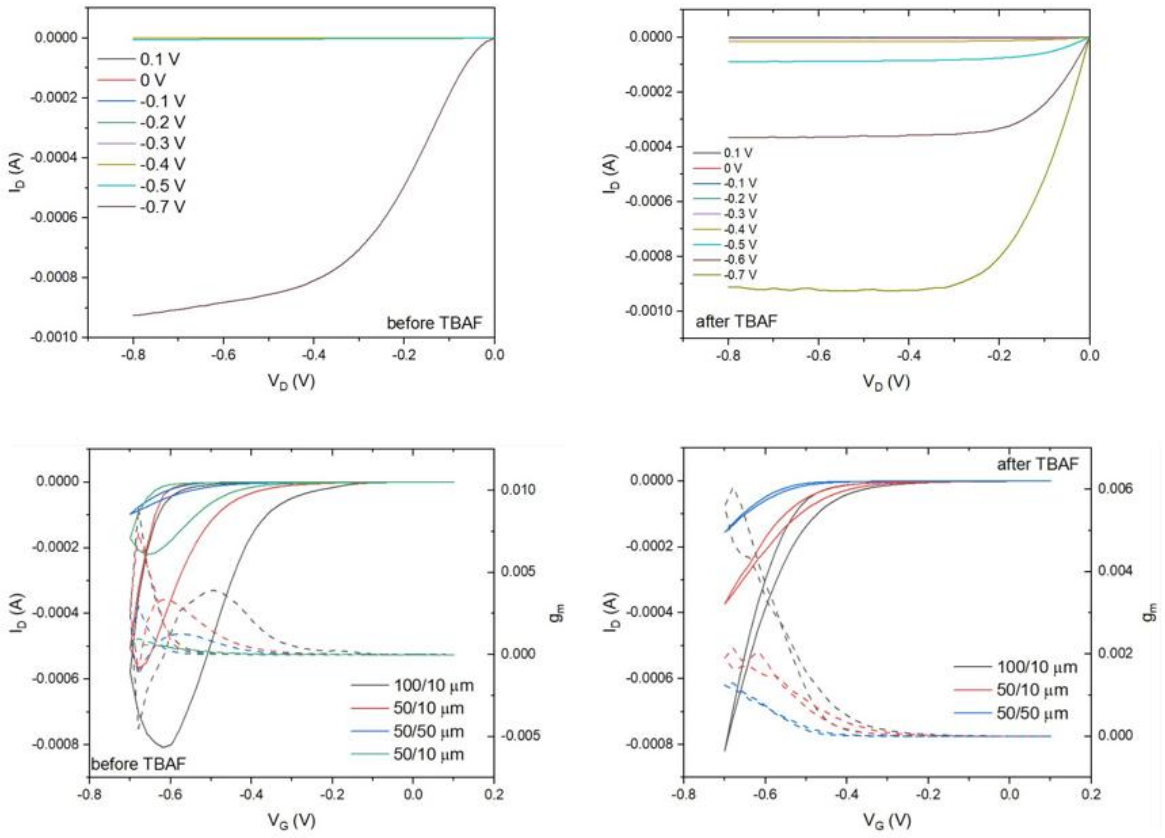

Figure 4.8 Output and transfer characteristics of PgBTTT-OTBS before and after TBAF treatment

Evidently, before cleavage, the strong hydrophobicity of the PgBTTT-OTBS backbone resulted in a large V_{TH}, which only exhibited p-type accumulation behaviour under gate bias around 0.7 V, and was associated with strongly hysteric behaviour. The improved hydrophilicity following chemical cleavage was reaffirmed by the reduced V_{TH} to 0.45 V, as featured in Figure 4.9. Collectively, these result in a µC* of 543 $Fcm^{-1}Vs^{-1}$, which was slightly better that reported value for PgBTTT of 502 $Fcm^{-1}Vs^{-1}$. However, both devices exhibited similar steady-state current upon activation, the influence of the chemical treatment to improve the overall device performance was not prominent. We attributed this loss of mobility due to presence of salt impurity. Considering this and the practical difficulty associated with device fabrication, an alternative chemical cleavage procedure was investigated.

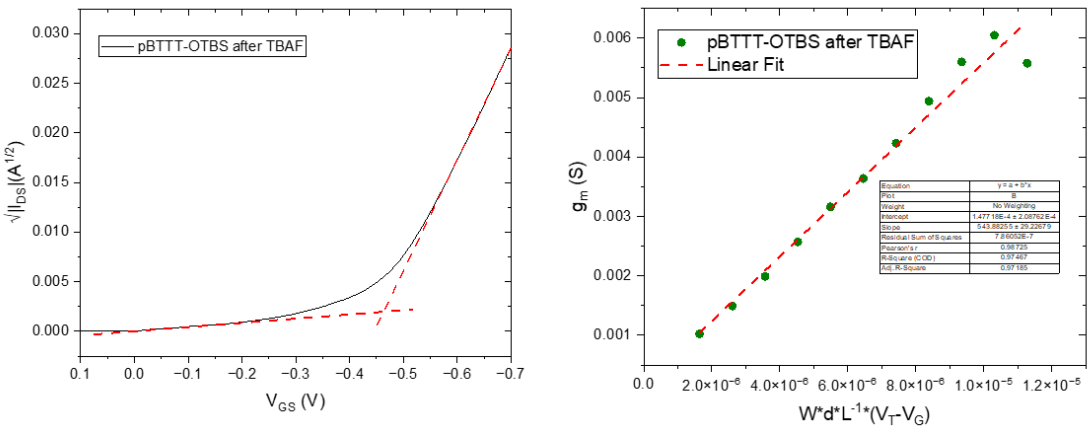

Figure 4.9 V_{TH} and μC^* of PgBTTT-OTBS after TBAF treatment

4.4.3 Optoelectronic Properties of PgBTTT-OTBS after etching – TMSBr treatment

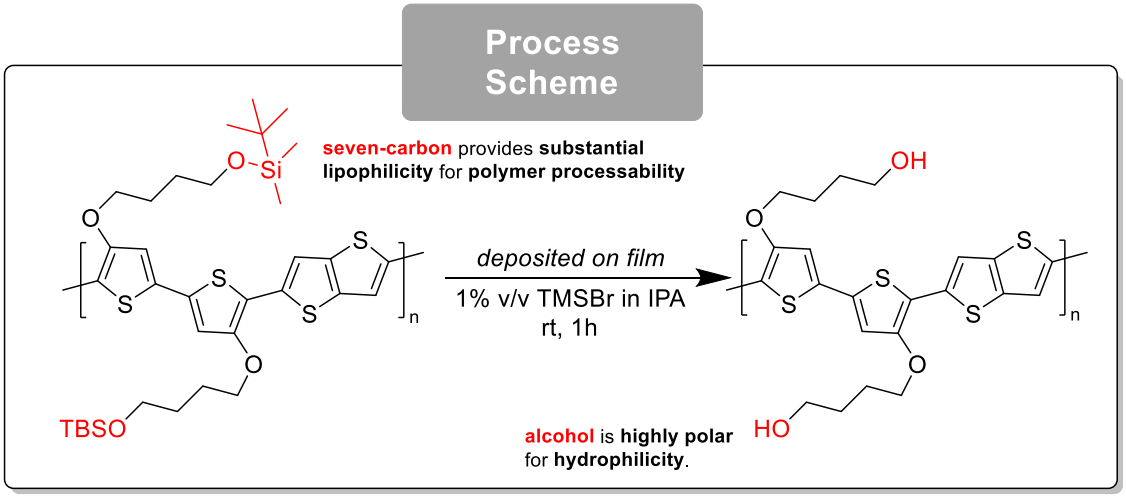

Figure 4.10 Reaction Scheme of on-film deprotection with TMSBr

An alternative more mild deprotection procedure of TBS-protected aliphatic alcohol was investigated, based on a reported procedure (Figure 4.10)[209]. This reaction features large scope of usable solvent, alongside faster reaction, high yield with catalytic amount of TMSBr necessary (compared to stochiometric TBAF in the previous method), and shows good tolerance to a range of chemical functionalities. In addition, prolonged exposure did not lead to erosion of gold electrodes. The effectiveness of deprotection was featured by a dramatic change

in cyclic voltammogram with 0.1 M aqueous NaCl supporting electrolyte, depicting reduced onset potential with more capacitive nature.

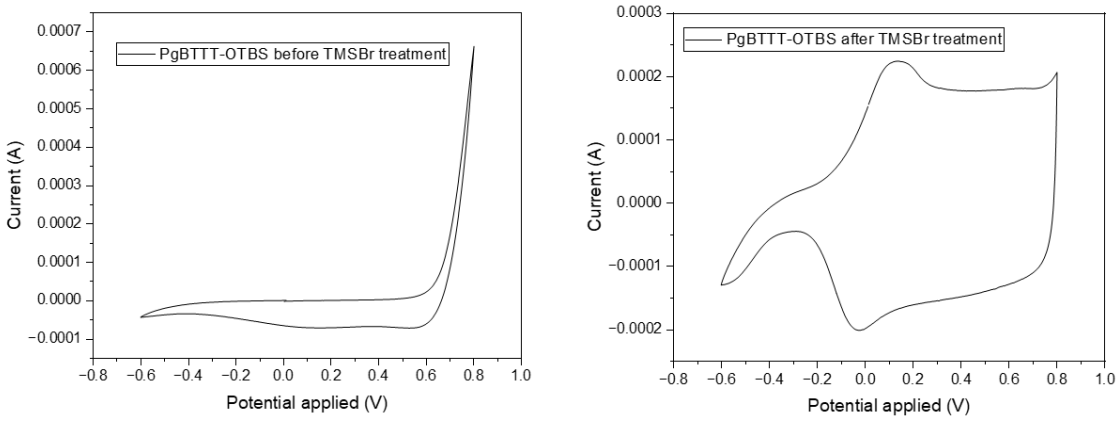

Figure 4.11 Cyclic voltammograms of PgBTTT-OTBS in 0.1 M aqueous NaCl electrolyte solution before and after TMSBr treatment

The electrochemical doping of the material was further studied with spectro-electrochemistry. In Figure 4.12, UV-Vis absorption spectra similar to PgBTTT-OTBS following TBAF treatment was shown, without significant difference in absorption maximum but exhibiting reduced intensity in 0-1 transition. The electrochromic response of PgBTTT-OTBS was marked by the emergence of a new absorption peak centred at 963 nm, which was ascribed to the formation of polaronic carriers. This was associated with the concomitant diminishing of the absorption peaks around 601 and 648 nm, which was reversible upon application of reverse bias.

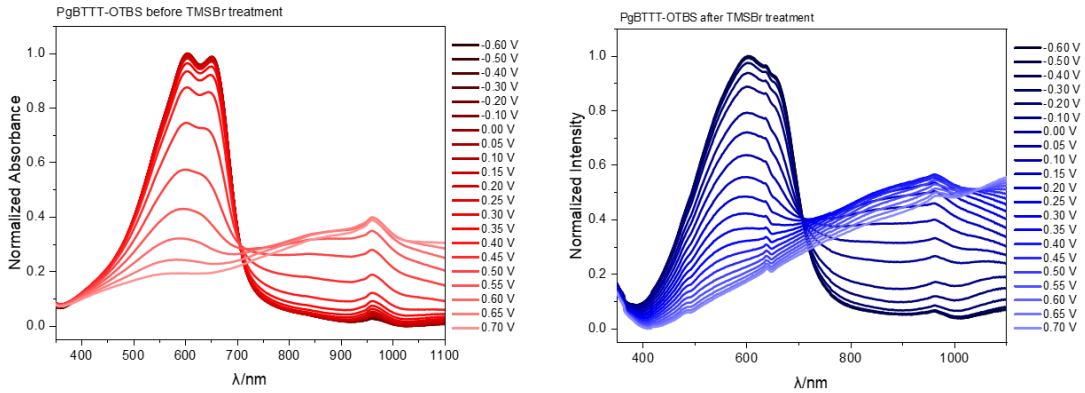

Figure 4.12 Spectro-electrochemistry of PgBTTT-OTBS in 0.1 M aqueous NaCl electrolyte solution before and after TMSBr treatment

Notably, both spectra exhibit an isosbestic point at 714 nm. However, the absorption intensity at this wavelength experienced significant reduction under further forward bias. The relationship between the intensity of π-π transition, polaronic absorption and that at 1100 nm with applied bias was shown in Figure 4.13. Interestingly, following chemical treatment, the formation of polaronic carrier in PgBTTT-OTBS occured at less negative external bias, and is marked by higher normalized maximum intensity. Interestingly, the intensity of polaronic absorption decreases with greater applied potential, but the absorption at 1100 nm continues to increase. This phenomenon is more significant following TMSBr treatment, where a second isosbestic point at 1044 nm emerged. This was attributed to the formation of a lower energy absorption feature at wavelength beyond 1100 nm, but could unfortunately not be detected due to limited wavelength range of the photodetector in the UV-Vis spectrophotometer. Further spin characterization of the material, such as ESR, would be necessary to determine if this absorption is bipolaronic in nature.

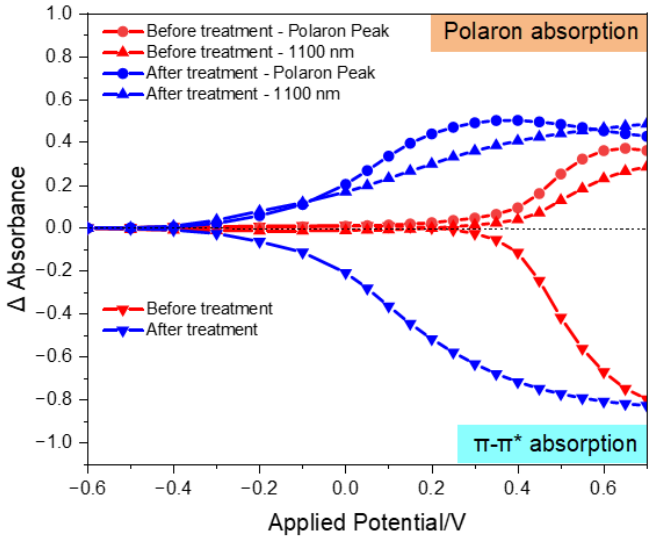

Figure 4.13 Plot of normalized absorbance of PgBTTT-OTBS against applied bias before and after TMSBr treamtment, illustrating the onset voltage and relative intensity in electrochromic response

All OECT measurements were conducted with an initial applied potential of 0.1 V to confirm the absence of electrochemical doping under neutral bias. The output and transfer characteristics of the polymer film following chemical treatment was presented in Figure 4.14.

The device presents p-type accumulation-mode behaviour with no output current under neutral bias. Interestingly, a maximum steady-state current of 14 mA was attained for a thin-film with a thickness of 65 nm, which also exhibits a threshold voltage of -0.08 V.

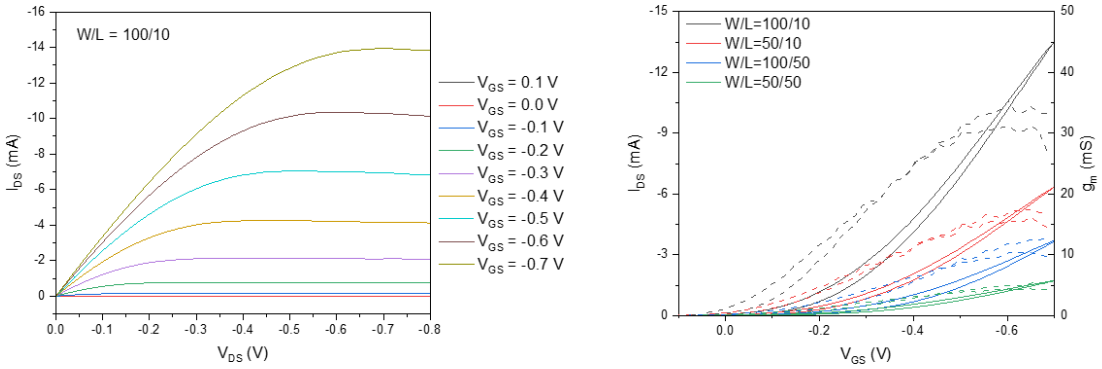

Figure 4.14 Output and transfer characteristics of PgBTTT-OTBS after TMSBr treatment

As shown in Figure 4.15, this device results in a normalized transconductance of 531 Scm^{-1} and a ten-fold increase in thickness-normalized drain current compare to PgBTTT-OTBS before chemical cleavage. The figure-of-merit was extracted in Figure 4.16 averaging over several different device geometries, leading to a μC* of 1036 $Fcm^{-1}Vs^{-1}$, which proves competitive among the best p-type accumulation-mode materials, surpassing its side-chain glycolated counterpart, PgBTTT by a large margin.

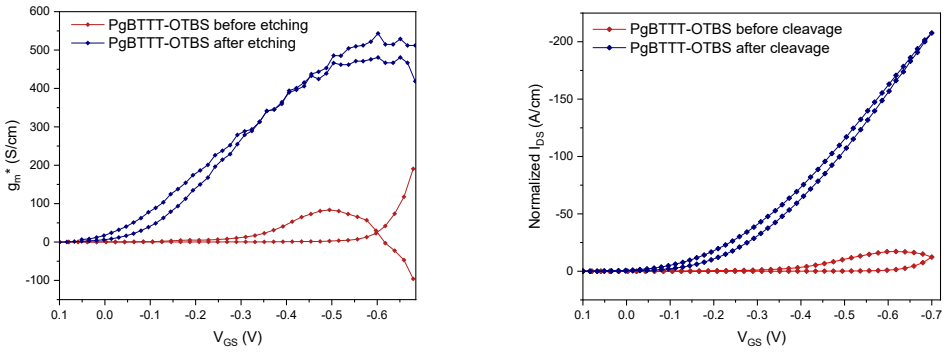

Figure 4.15 Normalized transconductance and drain current of PgBTTT-OTBS before and after TMSBr treatment

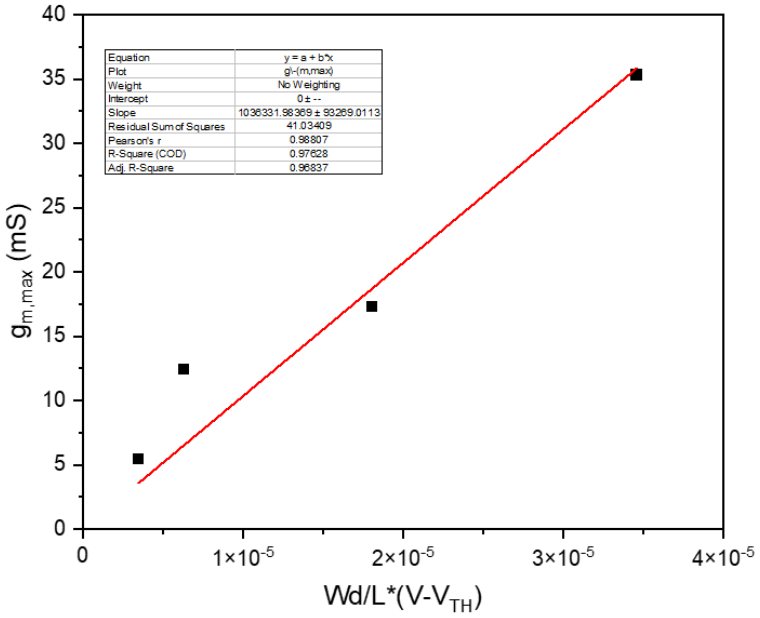

Figure 4.16 μC^* of PgBTTT-OTBS after TMSBr treatment

4.5 Conclusion and outlook

In this chapter, we presented the development post-fabrication surface deprotection to prepare uniform film from conjugated polymer with short, alcohol-terminated side chain, which proves insoluble and unprocessable from direct, solution-based deposition. It was also highlighted that the device performance is highly dependent on the deprotection reaction, which possibly arises due to different, if any, side product remains in the thin film.

In contrast to a previous report[41], it was demonstrated that deprotection of PgBTTT-OTBS with 1% v/v TMSBr in isopropanol resulted in a highly competitive μC* of 1036 $Fcm^{-1}Vs^{-1}$, which is greater than its side-chain glycolated counterpart. This device also featured high operational stability, with a percentage retention in drain current of % after 12000 cycles.

However, for a deeper understanding of the device performance, further studies over its microstructure following GIWAXS would be necessary, with EIS measurement to deconvolute the contribution of electronic and ionic transport. More importantly, to establish this method as a general, versatile platform for OMIEC design, the scope of conjugated polymer films prepared through this procedure must be broadened to generalize this approach. However,

overall, we have demonstrated the feasibility of this approach to achieve high-performance OMIEC without the need of side-chain glycolation, shedding light to the development of novel polymer architecture for next-generation materials in OECT.

CHAPTER 5

Other block copolymers: structure and functions

5.1 Motivation and introduction

In Chapter 2 and 3, we have introduced a novel Knoevenagel approach to the preparation of P3AOT-based block copolymers and characterized their optoelectrical, morphological and device properties respectively. We have demonstrated how judiciously designed conjugated rod-coil block copolymers could decouple charge carrier and ionic transport properties between rod and coil fragments and introduced three ways that the incorporation of these fragments could improve the device performance. However, to date, the field of conjugated polymer synthesis with precise end-group functionality remains underdeveloped. While P3AOT with precise end-group functionality could be prepared with the improved KCTP involving NHC-chelated Ni catalyst, the generality of this method remains limited. For example, synthesis of common alternating copolymers such as N2200 and p(DPP-T2) with precise end functionalities remain challenging under the existing methodology. Therefore, the remaining works in this thesis seek to expand the current scope of synthesis.

Step-growth polymerization from Stille or Suzuki cross-coupling reactions presents a logical heuristic to approach this synthetic challenge. Like end-capping strategies in KCTP, selective quenching of polymer chains with complementary functional end-cappers is a seemingly plausible strategy. However, this suffers from the lack of control during chain propagation. In an ideal scenario, chain extension through successive cross-couplings would proceed indefinitely; however, termination typically occurs for two primary reasons: (i) limited solubility of the growing polymer chain in the reaction solvent, hindering further reactivity, or (ii) undesired side reactions that chemically modify the chain terminus, rendering it inactive toward further cross-coupling.

The former issue was frequently observed with highly rigid and insoluble comonomers such as dibenzothiophene sulfone, often leading to gelation of reaction mixture. Nonetheless, polymerization could still proceed slowly following saturation in the reaction medium. For instance, following precipitation, the high-molecular weight fragment from the crude polymer may become insoluble in the original solvent. The latter termination pathway arises from the minor side reactions inherent to cross coupling, such as dehalogenation and demetallation.

Dehalogenation generally takes place through two pathways: (i) Following oxidative addition, the Pd(II) intermediate may acquire a hydride ligand through oxidation of protic substrates like alcohols, subsequently undergoing reductive elimination to form Ar-H[210]. The prevalence of this side reaction depends on the arene substrate but becomes more significant upon depletion of coupling partners. Compared to the halogenated species, trialkylstannyl and boronic acid functionalities are less stable. While rate of demetallation is substrate-dependent, using aryl boronic esters instead of free boronic acids allows better control over effective concentration. Reaction conditions (e.g., base choice, moisture levels) can further fine-tune this process.

The unpredictability of end-group functionalities due to competing side reactions complicates post-polymerization end-capping. To mitigate this, sequential monomer addition under controlled conditions has been employed in rod-rod block copolymer synthesis[211–217]. Typically, this one-pot polymerization strategy begins with reaction of acceptor block monomers for short duration. Then, the donor block monomers were introduced to the mixture, and the reaction was left for extended duration. While the success of sequential polymerization was justified with a reduction in GPC retention time, precise, structural characterization remains challenging, as the product may contain impurities such as multiblock components, pre-terminated donor or acceptor

fragments. For instance, a previously reported synthesis of multiblock rod-rod copolymer uses purified di-functionalized macromonomers[218], prepared from monomers under a slight stoichiometric imbalance. However, considering the similarity in reaction time to the previously mentioned rod-rod block copolymers, in-situ formation of multiblock species is highly likely. Alternative method involves an one-pot polymerization with addition of mono-halogenated end-capping species[175,219]. This method ensures that a significant portion of the rod chain could be end-capped with the designed terminus but requires high polymerization efficiency with minimal pre-termination. Additionally, these end-capped block copolymers are limited by Carothers equation in degree of polymerization, with a substantial quantity of coexistent un-capped and bi-capped impurities.

Despite the distinct limitations of these methods, their applicability in rod-rod systems provides a useful entry point for synthesizing rod-coil block copolymers. In the subsequent sections, we will demonstrate how these strategies from construction of rod-rod-systems could be adapted to address similar synthetic challenges faced in rod-coil architectures.

5.2 Synthesis of PEG-b-F8BT-b-PEG and nano-precipitable photocatalysts for hydrogen evolution reaction based on post-polymerization approach

5.2.1 Brief introduction to photocatalytic hydrogen evolution from polymer nanoparticles

The exploitation of fossil fuels has powered technological revolutions, but their environmental cost demands sustainable alternatives. To date, combustion of these non-renewable and carbon-rich resources have significantly accelerated global warming, which is becoming an menacing nemesis with increasing risks of environmental degradation, natural disasters, extreme weathers and many more devastating

consequences[220]. In 2020, the gravity of the situation was assessed by many scientists across the globe and referred to as climate crisis[221].

The solution to alleviate the growing climate emergency resides in the development of an alternative sustainable and abundant energy source. A major driving force of this global energy transition is solar power. For instance, global solar installation had experienced impressive growth of 33% in the past year[222], with significant expansions in Asia-Pacific regions, leading to proliferation of solar energy market. While these achievements greatly motivated the global decarbonisation initiatives, it is pivotal to recognize the intermittency of sunlight due to factors like the rotation of Earth, influence of weathers and seasons. Therefore, to ensure that this inexhaustible energy source could be readily available, design of energy storage system is highly necessary.

One such useful process is featured by the conversion of solar energy into hydrogen fuel source. H_2 is the lightest combustible gas and possesses a very high gravimetric energy density, roughly thrice that of gasoline and diesel. Conventional green production of hydrogen involves alkaline electrolysis of water[223], but this would require a preliminary transformation into electrical power. Overall water splitting (OWS) is a challenging process requiring a thermodynamic energy input of 1.23 V, but an overpotential significantly higher than this is necessary to overcome the kinetic barriers. Photochemical OWS presents an alternative, direct method to harness hydrogen fuel from sunlight. These photocatalysts operate through photoexcitation of electrons in the conduction band. Subsequent charge separation results in the formation of an electron and hole charge carriers, which then migrate to the active sites for hydrogen and oxygen evolution reactions to take place, respectively. In the case of hydrogen evolution, thermodynamics dictate that at pH 7, the valence band of the photocatalysts must exhibit a minimum absolute energy level of -4.0 eV with respect to vacuum[224]. In this

case, platinum is frequently used as a metal cocatalyst for proton reduction. An additional sacrificial donor such as ascorbic acid is sometimes included in the reaction mixture to scavenge the photogenerated holes. This allows hydrogen evolution to take place without completing the thermodynamically challenging water oxidation half-reaction.

Compared to their inorganic counterparts, organic semiconductors feature improved band gap tunability, low-cost and greater scalability. However, their hydrogen evolution rates (HER) usually could not match the inorganic materials, which explains why attention in this field only dramatically increased in the recent decade[225]. Soluble conjugated polymers are a class of materials which open countless opportunities for photocatalyst design. Notably, they can be processed into sophisticated structures beyond insoluble precipitates. One such example is polymer nanoparticle, which can be prepared through two main methods: namely mini-emulsion and nano-precipitation. Mini-emulsion, as the name suggests, comprises nano- to micro-sized lipophilic polymer droplets stabilized by surfactant molecules. To induce its assembly, a mixture of water and polymer dissolved in an immiscible organic solvent is agitated with high-energy ultrasonication. Stabilized nanoparticles are formed following removal of organic solvent. An advantage of this method is the broader scope of organic solvent utilizable for polymer processing. However, its scalability is intrinsically limited by the high-energy mixing process. Additionally, the charge-generating polymeric species are encapsulated by a layer of surfactant molecules, which are often electrochemically insulating.

Alternatively, nano-precipitation forms nanoparticles by rapidly mixing a dilute solution of polymer in a water-miscible solvent with water, aided by vigorous stirring or ultrasonication. Compare to mini-emulsion, absence of surfactant shell can lead to

shorter induction period and more effective adsorption of cocatalyst and substrate. Nonetheless, solvent used for polymer processing is limited to polar organic solvents, which many hydrophobic polymers are not compatible with. Additionally, the hydrophobic nature of polymer backbone can compromise the stability of the nanoparticles, which leads to aggregation, gradually forming large and less photocatalytic polymer aggregates, owing to their much-reduced interface area with aqueous electrolyte.

Increasing hydrophilicity of the polymer backbone is an effective strategy to improve the photocatalytic efficiency of polymer nanoparticle formed via nano-precipitation. Its better affinity towards aqueous medium leads to improved stability. This can also reduce the diameter of nanoparticles, decreasing volume of optical dead zone. Optical dead zone is the region inside semiconductor particles at depts greater than the optical density of the material permits significant light penetration. This region is essentially unpredictive volume where light harvesting and charge separation and transport to the surface cannot take place. Therefore reducing particle size such that a greater proportion of the semiconductor exists outside of this dead zone improves the efficiency of the photocatalyst[226]. In addition, infiltration of water molecules into the nanoparticle leads to higher dielectric constant in the surrounding environment of polymer backbone, improving charge separation and overall photocatalytic efficiency[227]. Effective strategies to enhance polymer hydrophilicity includes side chain glycolation[16] and the incorporation of hydrophilic photocrosslinkers[228].

Herein, an alternative solution based on PEGylation of hydrophobic conjugated backbone is explored. To the best of our knowledge, this strategy remains unexplored due to synthetic challenge of preparing rod-coil block copolymers with reliable and precise end-group. Serendipitously, we discover that poly(9,9-dioctylfluorene-

alt-benzothiadiazole) (F8BT) with predominantly Br/Br-termini could be prepared following a controlled Suzuki-Miyaura polycondensation, providing anchoring points for post-polymerization backbone functionalization.

5.2.2 Synthetic design of PEG-b-F8BT-b-PEG

Conventional preparation of high-molecular weight F8BT involves a high-temperature Suzuki-Miyaura polymerization between boronic ester-substituted fluorene and halogen-substituted benzothiazole[229,230]. To minimize end-group scrambling due to dehalogenation and protodeboronation, the temperature of polymerization is kept close to room temperature. To achieve this, we adapted the catalytic condition base on a previously reported Suzuki-Miyaura polycondensation condition driven by the Buchwald precatalyst Pd-G_2-P^tBu_3[231]. Immediately upon completion of polymerisation, reflected by darkening of polymer solution, MALDI-TOF-MS revealed that most F8BT fragments possess Br/Br termini. However, extended reaction duration is highly detrimental to end-group distribution of polymers, resulting in increased likelihood of dehalogenation. Moreover, this effect is heavily influenced by the scale of reaction. Currently, consistent anchorage of Br/Br functionalities could only be successfully achieved with monomer loading of 0.05 mmol. It is likely that a balance in reaction rate of boronic ester hydrolysis and propagation through Suzuki-Miyaura coupling is consequential to end-group distribution of resulting polymers. This is not only dependent on stoichiometry and concentration of the reactants, but can also be significantly affected by geometrical shape the reaction medium is contained in.

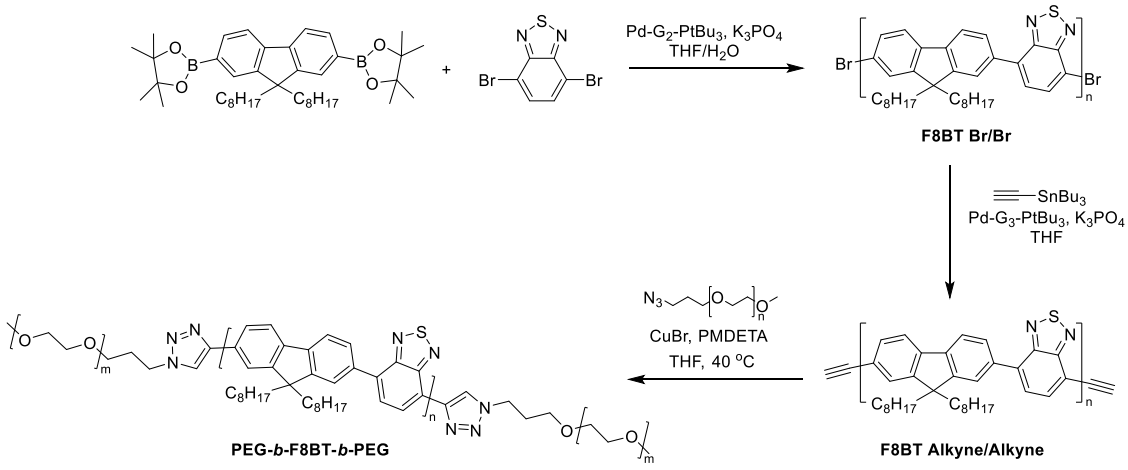

Figure 5.1 Reaction scheme for the synthesis of PEG-*b*-F8BT-*b*-PEG

After polymerization, Br/Br-termini of F8BT was further functionalized through ethynylation through Suzuki-Miyaura coupling previously described in Section 2.5.1. Complete end-group conversion was reflected by MALDI-TOF-MS with simultaneous change of F8BT fragment mass. A slightly increase in M_n is observed, likely due to Glaser coupling side-reactions, leading to further oligomerization of the ethynyl-terminated F8BT fragments.

Following installation of ethynyl handle, F8BT backbone was PEGylated through CuAAC with a stoichiometric excess of azide-terminated PEG. This functionalization resulted in a substantial increase in M_n. Substantially improved hydrophilicity also leads to enhanced solubility in THF, facilitating subsequent nanoparticle assembly via nano-precipitation.

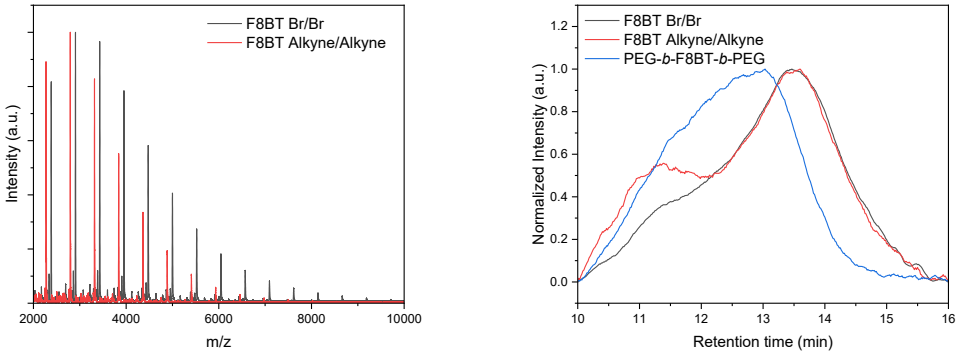

Figure 5.2 (left) MALDI-TOF of F8BT precursors (right) GPC trace of F8BT Br/Br, F8BT Alkyne/Alkyne and PEG-*b*-F8BT-*b*-PEG

5.2.3 Hydrogen evolution reaction with PEG-b-F8BT-b-PEG nanoparticles

A major difference between PEG-b-F8BT-b-PEG and F8BT is the stability of the nanoparticles produced from polymer solution at same concentration. A dilute THF solution of PEG-b-P8BT-b-PEG at concentration of 1 mg/mL is readily miscible with water under ultrasonication, forming aqueous nanoparticle solution with stability lasting months to years, where minimal aggregation is observable. On the other hand, a THF solution of F8BT with identical concentration, upon immediate addition to water, exhibits substantial precipitation. Considering that F8BT backbone comprises a large density of hydrophobic alkyl side chain, it is challenging for the polymer chain to fold and twist into a configuration such that a sufficiently hydrophilic surface can be formed to stabilize nanoparticle assembly. In contrast, hydrophilic PEG fragment of PEG-b-F8BT-b-PEG could interact favourably with the aqueous environment and assemble into an outer shell encapsulating the photoactive F8BT core, facilitating formation of stable nanoparticles via nano-precipitation.

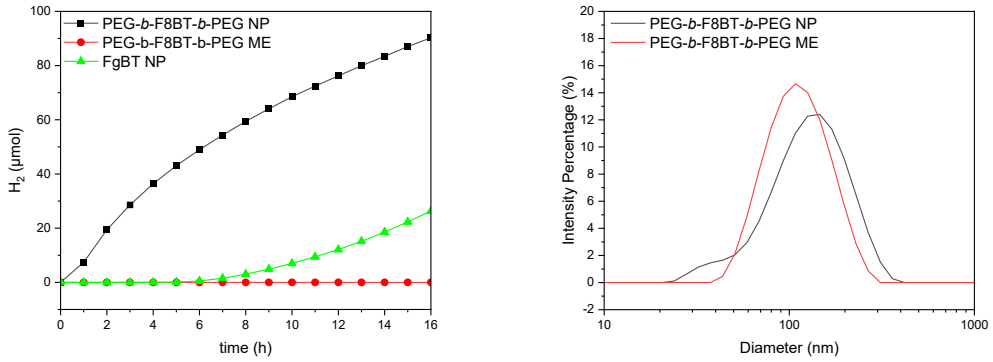

Figure 5.3 (left) H_2 production of PEG-b-F8BT-b-PEG through nano-precipitation (NP), mini-emulsion (ME) and FgBT through NP (right) Diameter of PEG-*b*-P8BT-*b*-PEG through nano-precipitation (NP) and mini-emulsion (ME)

Nanoparticles of PEG-b-F8BT-b-PEG through both mini-emulsion and nano-precipitation were prepared and their hydrogen evolution reaction rates were measured with 0.8 wt% H_2PtCl_6 and 0.2 M ascorbic acid loaded as cocatalyst and hole scavenger respectively. Evidently, the block copolymer nanoparticles prepared through mini-emulsion did not yield any H_2, while that of nano-precipitation showed a significantly higher reaction rate of 2.5 $mmolg^{-1}h^{-1}$. Notably, hydrogen evolution took place in the initial hour without any detectable induction period. We attribute this observation to the rapid permeation of water molecule through the PEG layer. Moreover, these hydrophilic molecules likely swell and trap water molecules within, creating an environment with high effective reactant concentration for the photocatalysts. This is also shown by the average particle size of 134 nm measured by Dynamic Light Scattering (DLS), which is larger than that in the mini-emulsion solution of 118 nm (Figure 5.3).

While the emulsion solution of PEG-b-F8BT-b-PEG with sodium dodecyl sulphate did not yield detectable amount of H_2, greater extent of photobleaching is also observed in the mini-emulsion solution. This can be attributed to the strong redox reactivity of the excitonic species, which if not transported and dissipated at the reaction centre, accumulates on the F8BT backbone, causing photodegradation after extended

duration[232]. mini-emulsion, the surfactant molecules build up an insulating barrier between the conjugated polymers and the Pt catalysts, thereby further hindering charge transport and compromising photochemical stability of the nanoparticle.

The effectiveness of this strategy was then compared against side-chain glycolation. A nanoparticle solution of FgBT, a chemical derivative of F8BT where the octyl side chains are replaced with diethylene glycol analogues, was prepared through nano-precipitation. Under identical reaction conditions with equivalent mass of polymers loaded, FgBT demonstrated a HER rate of 1.4 $mmolg^{-1}h^{-1}$, about 56% that of PEG-b-F8BT-b-PEG.

5.2.4 Concluding remarks

In this section, we have demonstrated how PEGylation of photoactive conjugated polymer could result in stable, nano-precipitated nanoparticles as effective single component HER photocatalysts. The preparation of block copolymer is synthetically facile, presenting nearly ideal cross-coupling reactivity with minimal interference of side reaction. Nevertheless, the criteria required for reliable preparation of block copolymers with Br/Br terminus remains unclear. Considering that the block copolymer can only be consistently prepared on a limited scale, it is probable that the shape of the reaction container also influences end-group control during polymerization. Additionally, three structural variants of F8BT, namely F8FBT, F8-sulfone and F8T2 were prepared. These polymers possess completely distinct end-group distribution despite identical catalytic condition and scale adopted. It is postulated that a suitable balance should be established between the rate of each unit reaction during propagation, which will be impacted by more sophisticated factors beyond stoichiometry, concentration and reaction condition. This opens up opportunities for further

investigation which may clarify the principles of reliable end-group control behind Suzuki-Miyaura polymerization.

5.2.5 In-situ polymerization with mono-halogenated macroinitiator

Beside F8BT, room-temperature polymerization of P(NDI-2OD-T2), also known as N2200, had been previously reported through Stille cross-coupling polycondensation[233] with Buchwald precatalyst Pd-G_3-P^tBu_3. Additionally, similar systems had been reported to polymerize effectively with stoichiometric imbalance of monomers, implying that naphthalene diimide (NDI) system might promote selective intramolecular catalyst transfer with thiophene comonomers[234]. Two end-cappers marked by a terminal trimethylsilyl moiety were prepared, and were functionalized with bromo and tributylstannyl moiety respectively. After one hour of polymerization, the bromo-terminated end capper was added and stirred for 12 hours. The tributylstannyl functionalized end capper was then added in a stoichiometric excess to quench any leftover bromo-terminated counterparts. Surprisingly, ^{1}H NMR did not reveal any detectable trimethylsilyl functionalities following post-polymerization functionalization, while MALDI-TOF-MS is too complicated for end-group resolution. Similar to the cases listed in Section 4.2.4, this may indicate a pronounced interference from side reactions, leading to loss of end-group functionalities.

Introducing end-capper at the start of polymerization is an effective strategy to retain the proportion of end-group functionalities following polymerization. This, however, comes with an intrinsic statistical trade-off – the fundamental limitations of Carothers's equation. For instance, to implement this method, PEG and PCL with a single 2-bromothiophene terminal moiety are prepared, which are then stirred together with the monomers during polymerization. Monte Carlo simulation from a similar system

previously shows that the bis-functional polymer to be the major product[219], but this assumes a propagation process continuing infinitely given the right complementary moieties. Carother's equation also dictates that in this ideal situation, a high-molecular-weight polymer is achieved with minimal macroinitiator added. Conversely, from a practical standpoint, this would lead to increased formation of unsubstituted polymers formed. In addition, incorporation of a flexible coil fragment increases polymer solubility, resulting in significant loss of desired product during Soxhlet extraction. Altogether, these factors result in the polymer product with much less coil block terminus than expected, motivating the exploration of an alternative pathway.

5.3 Towards the future: Suzuki catalyst transfer polymerization (*SCTP*)

5.3.1 Motivation

In Chapter 2 and 3, we have demonstrated how KCTP could yield rod fragment with a precise terminal bromo handle. Its quasi-living nature allows us to mitigate most synthetic problems addressed in Section 4.2, resulting in excellent end-group control with careful optimization of catalyst. On the other hand, the involvement of an in-situ generated Grignard intermediate imposes strict limitations over functional group compatibility of the monomer. In other words, propagation in KCTP could be quenched by common moieties like esters and amides. Additionally, considering that the best catalytic condition requires both efficient polymerization and high end-group fidelity following termination, reaction optimization is synthetically very sophisticated. Optimal condition for each different monomer could hence be a serendipitous encounter. This is best illustrated through the unsuccessful adaptation of classical P3HT synthesis to 3-alkoxythiophene monomer, suggesting limited substrate generality for each catalytic system. In addition, following polymerization, the introduced halogen handle

must be further functionalized to necessitate rod-coil coupling. It is possible that even a nearly quantitative conversion may result in trace amount of incorrectly terminated polymer chain hardly resolvable by MALDI-TOF. Moreover, since this Suzuki-Miyaura coupling leads to significant loading of residual palladium metal into the polymer mixture, synthetically cumbersome metal scavenging must be carried out to minimize the electrochemical influence of these impurities.

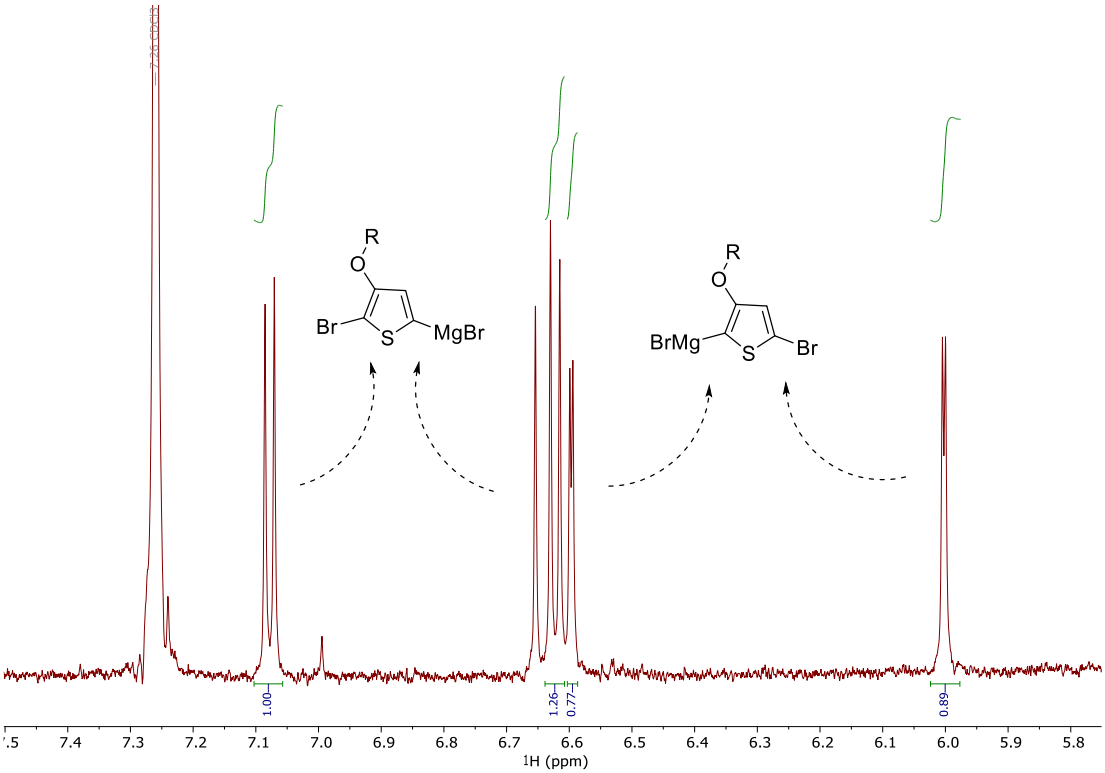

Figure 5.4 Crude ^{1}H *NMR* of 2,5-3-alkoxythiophene following deprotonation with isopropyl magnesium chloride, depicting the relative ratios of the isomer

To simultaneously incorporate the desired end functionalities during catalyst transfer polymerization, utility of an external initiator was previously reported[235]. In this design, the oxidative addition complex of Ni catalyst with a desired functional group for end-capping was isolated. During propagation, the terminal functional group on the external initiator remained covalently attached to every growing chain, leading to in-situ end-group introduction. However, a similar chemical compatibility problem was

encountered – this terminal group must be stable throughout polymer propagation. To put it in another way, functional groups intolerable to Grignard intermediate remain unusable. Unfortunately, this includes several key players in rod-coil coupling, such as aldehyde and alkyne.

A recent breakthrough beyond KCTP was the development of SCTP. Replacing the reactive Grignard functional group with a suitably designed boronate ester significantly broadened the scope of applicable monomers and external initiators. In fact, several previous reports[236–239] have established an in-situ preparation of initiation complex through a base-mediated oxidative addition of Buchwald precatalyst with an iodo-substituted initiator molecule, mitigating sensitivity issues of handling Ni(0) and Pd(0) complexes. When using an asymmetric monomer, SCTP also offers the additional benefit of control over regioregularity. In KCTP, transmetallation of asymmetric di-halogenated monomers usually lead a mixture of regioisomers. In the case of 2,5-dibromo-3-dodecoxythiophene, ^{1}H NMR analysis revealed an approximate 4:6 distribution (Figure 5.4) and its consequence on regioregularity remains unclear. NMR analysis did not depict distinct resonance peaks in the aromatic region. It is possible that the planarization due to S…O interaction[240] reduces the difference in chemical environment between HH, TT and HT conformers. On the other hand, in SCTP, halogen and boronic ester moieties were precisely placed during monomer preparation, leading to uniform orientation in the resulting polymer. In this section, we will hence explore the synthesis of P3AOT through SCTP, comparing its differences with that from KCTP.

5.3.2 Design of heterofunctional monomer and synthesis optimization

Realizing an effective end-group precise polymerization through SCTP requires careful design of heterofunctional monomer. In Section 4.2, we briefly discussed how end-

group precision is strongly influenced by the rates of boronate ester hydrolysis and cross-coupling. This consideration is crucial for SCTP: a high concentration of hydrolysed monomer bearing boronic acid functionality can lead to intensified protodeboronation, thereby impeding chain propagation. To tune reactivity, various boronic ester derivatives, such as MIDA ester, can be emplyed in place of Bpin, although their synthesis and purification are typically more demanding.

In 3-alkoxythiophene, the boronic ester group could be installed at either the 2- (M1) or the 5-position (M2), with each regioisomer requiring a distinct synthetic route. For instance, preparation of M2 necessitates a 2-bromo-3-alkoxythiophene intermediate, which exhibits a strong propensity for autopolymerization when concentrated and purified[167]. This sensitivity of this monomer limits both the scope and scalability of subsequent functionalization. Furthermore, during polymerization, the terminal halogen atom located para- to the alkoxy substituent (P2) is particular more prone to protonlysis, increasing likelihood of premature termination. Therefore, targeting M1 is more advantageous: in this case, the propagating polymer chain (P1) retains a more chemically stable halide terminus, thereby enhancing the livingness of SCTP.

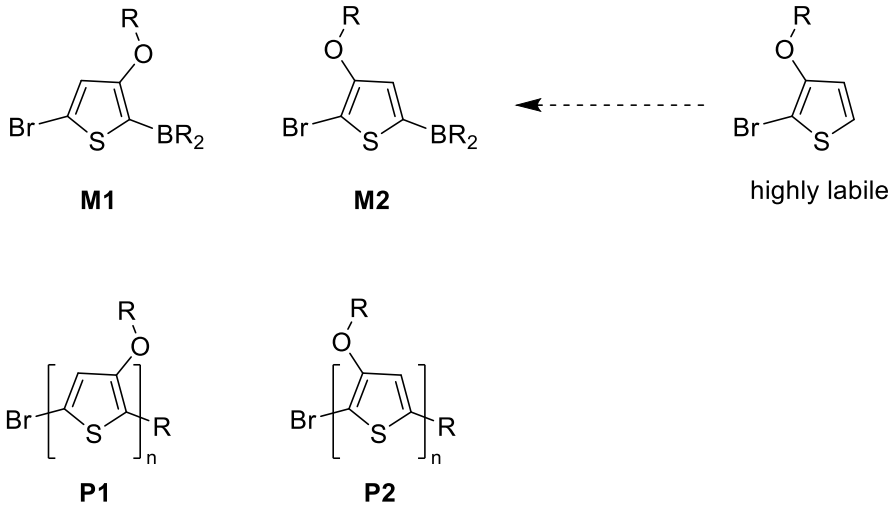

Figure 5.5 Structures of possible 3-alkoxythiophene heterofunctional monomer and the structure of propagating chain

The previously reported success in ProDOT monomer[239] motivates us to synthesize 4,4,8,8-tetramethyl1,3,6,2-dioxazaborocane (Me4DABO) 3-alkoxythiophene. These N-coordinated boronates cannot be directly obtained via lithiation-borylation of the di-halogenated precursor. Instead, synthesis must proceed through a more reactive boronic ester intermediate, which is subsequent transesterified with 1,1,5,5-tetramethyl-3-azapentane-1,5-diol (TAD) (Figure 5.7).

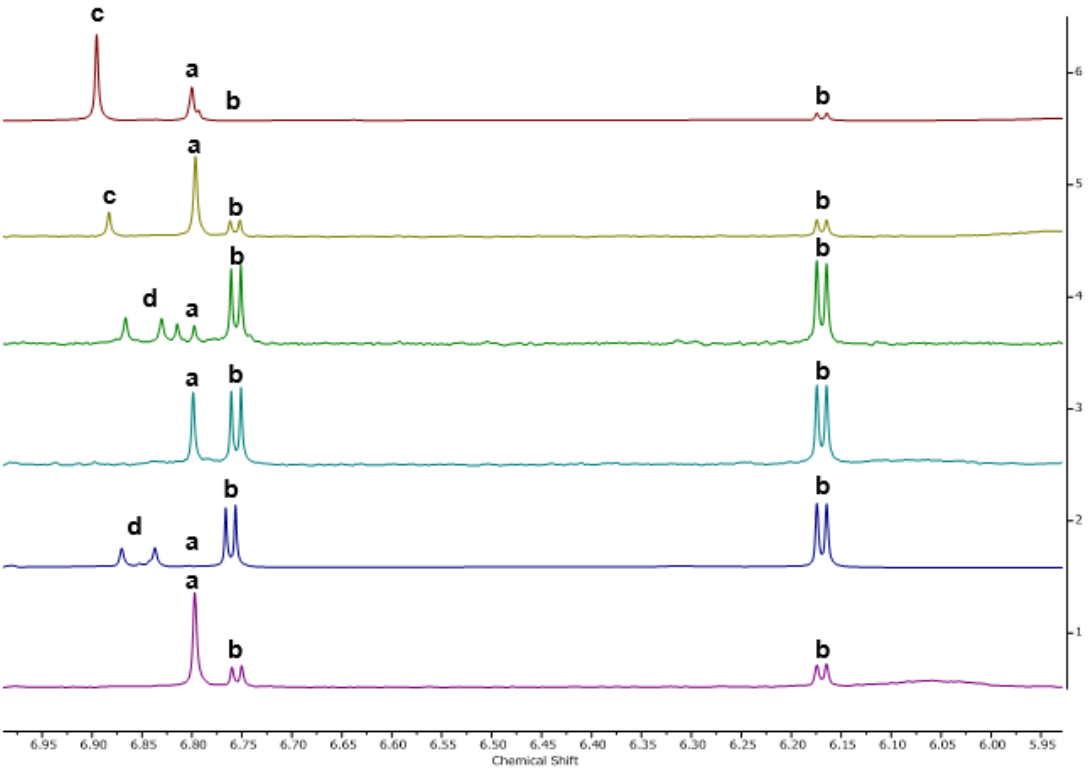

Figure 5.6: ^{1}H NMR (CD_2Cl_2, 200 MHz) of crude mixture (1 mmol scale) under attempted reaction conditions. Signals correspond to (a) product (b) protodeborylated species (c) Starting materials (d) Unidentified side products

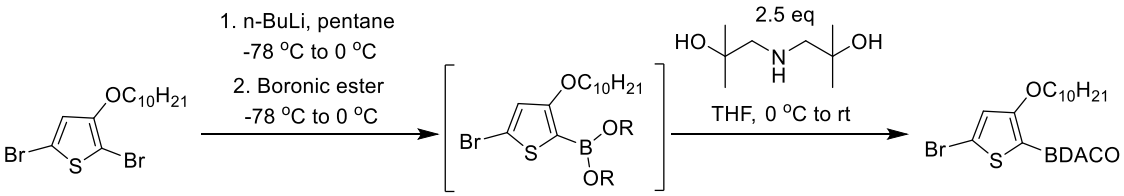

Figure 5.7 Reaction Scheme for the preparation of heterofunctional thiophene monomer by using reactive boronic ester, including $B(OBu)_3$, $B(OiPr)_3$, $B(OMe)_3$ and $B_2(neop)_2$

Entry	Boronic Ester	Product (%)	Protodeborylated Species (%)
1	1.5 eq $B(OBu)_3$	75	25
2	1.5 eq $B(OiPr)_3$	0	100
3	1.5 eq $B(OMe)_3$	38	62
4	1.5 eq $B_2(neop)_2$	11	89

Table 5.1 Yield of product and protodeborylated species for the preparation of heterofunctional thiophene monomer by using reactive boronic ester

Lithiation-borylation of 2,5-dibromo-3-decoxythiophene was examined with several boronates. Boronic esters chelated only by mono-dentate ligand, or by bidentate neopentyl glycolato ligand lacking α-alkyl substituents, proved highly susceptible to hydrolysis, undergoing complete protodeboronation during aqueous workup. In these reactions, excess TAD ligand in anhydrous THF was added, yielding mixtures of transesterified product with significant protodeboronated impurities.

In contrast, pinacol boronic ester-substituted alkoxythiophene could be purified through aqueous workup. although the monomer decomposed on silica gel within seconds via protodeboronation. When the intermediate was used without purification, a large stoichiometric excess of TAD ligand was required for efficient transesterification, likely owing to residual isopropyl pinacol ester in the mixture, which disfavoured equilibrium towards TAD substitution. Removal of this impurity by vacuum distillation afforded nearly quantitative TAD substitution.

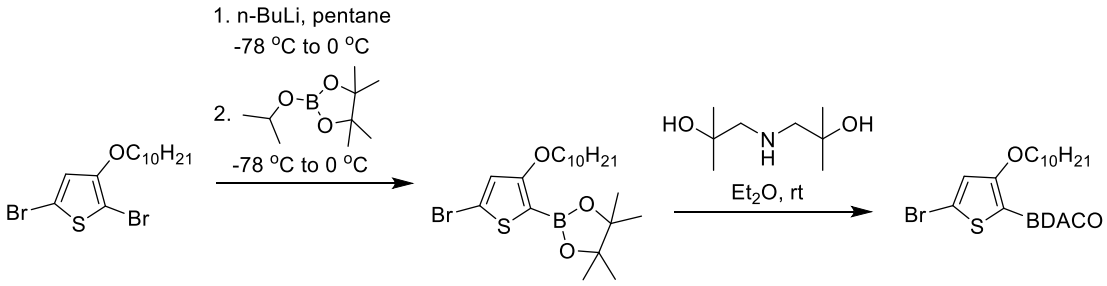

Figure 5.8 Reaction Scheme for the preparation of heterofunctional thiophene monomer by using isopropyl pinacol boronic ester

Entry	TAD eq	Remaining Intermediate (%)	Product (%)	Protodeborylated Species (%)
5	6	17	64	19
6	1	66	22	12

Table 5.2 Yield of product and protodeborylated species for the preparation of heterofunctional thiophene monomer by using isopropyl pinacol boronic ester

Although functionalization of 2,5-dibromo-3-decoxythiophene proved effective, the scope of compatible monomer was intrinsically limited by the solvent during lithiation. For instance, glycolated derivatives, being less lipophilic, exhibited low solubility in pentane under cryogenic conditions. Solvent screening reveals that, while ethereal solvents (e.g. diethyl ether, THF) effectively solubilized all alkoxythiophenes, lithiation at 5-position, previously unobserved, became significant. This likely arises because ethereal solvents actively stabilize organolithium intermediates[241]. In their absence, lithiation at 2-position is strongly directed by the alkoxy substituent, while 5-position lithiation faces a much higher activation barrier and is kinetically inaccessible under cryogenic condition. In contrast, ethereal solvation reduces this barrier, diminishing regioselectivity. Considering these factors, we found that non-chelating, aromatic solvent such as toluene provided significantly improved solubility while preserving stereospecific lithiation at 2-position.

With the optimized conditions, a reliable, we achieved a reliable and scalable synthesis of heterofunctional monomer for SCTP. The scope of substrates investigated is summarized in Table Z. In practice, monomers with adequate chemical tolerance towards organolithium, as well as good solubility in both toluene and diethyl ether, could afford satisfactory conversion.

5.3.3 Optimization of SCTP

Having established the transformation of dibrominated precursor to the corresponding heterofunctional monomer, we turn to optimizing SCTP for the in-situ preparation of conjugated backbone with precise end-group functionalities. A central challenge in this process lies in balancing chain propagation with the hydrolysis of boronic esters. Previous studies on SCTP of P3AT[242] identified Pd-G_3-RuPhos and Pd-G_3-SPhos as

highly effective catalysts, affording polymers with high molecular weight, narrow polydispersity, excellent yield and regioregularity. These conditions are therefore selected as the initial basis for further reaction optimization.

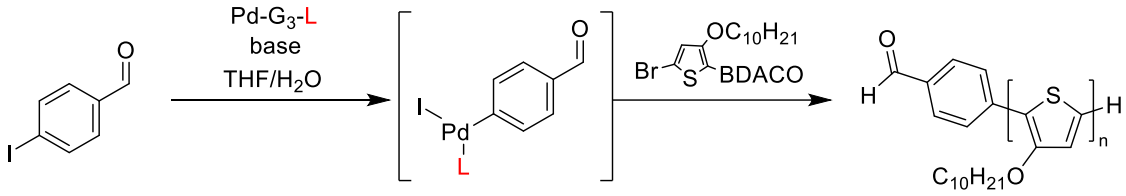

Figure 5.9 Reaction Scheme for the preparation of P3DOT through SCTP

Herein, we targeted the synthesis of P3DOT with benzaldehyde terminus (Figure 5.9). Despite their close structural resemblance to ProDOT, application of Pd-G_3-RuPhos and Pd-G_3-SPhos[239] with potassium phosphate base resulted in a substantial fraction of chains terminated with H/H end-groups, indicating considerable chain transfer during propagation. Nevertheless, MALDI-TOF-MS reveals that, when using Pd-G_3-RuPhos with a weaker potassium carbonate base with less water content affords P3DOT with predominant H/CHO termini. Unsurprisingly, this modified reaction significantly reduces the rate of boronic ester hydrolysis, leading to lower concentration of boronic acid species during propagation. Because of this controlled release, a large ratio of propagating chain against boronic acid monomer arises. These active monomers hence exhibit greater propensity to insert into the propagating chain than to couple to another small-molecule partner. Therefore, most long-chain polymers would contain the moiety associated with the initiator complex upon termination, while short chain-transfer oligomers can be removed by Soxhlet extraction.

Entry	Catalyst	Base	THF/H_2O	CHO/H (%)
1	Pd-G_3-SPhos	K_3PO_4	30	29
2	Pd-G_3-RuPhos	K_3PO_4	30	44
3		K_2CO_3	99	91

Table 5.3 Yield and end-group fidelity of P3DOT under different catalytic condition

5.3.4 Chemical properties of P3DOT with SCTP

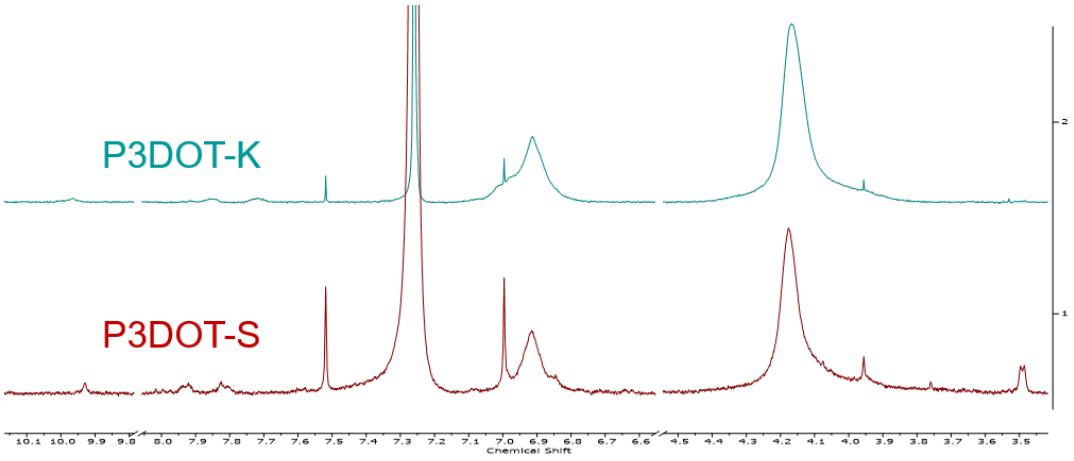

Figure 5.10 ^{1}H NMR of P3DOT-K and P3DOT-S

Herein, P3DOT prepared through KCTP and SCTP will be denoted as P3DOT-K and P3DOT-S, respectively. The regiochemistry of both backbones are assessed by ^{1}H NMR. Compare to P3DOT-K, P3DOT-S exhibits a narrower, bell-shaped resonance of aromatic thiophene proton at 6.9 ppm. The corresponding signal in P3DOT-K is broader, with an intense, secondary shoulder around 7.0 ppm, likely corresponding to chemical environments from structural defects like head-to-head or shoulder-to-shoulder coupling. Similar signs in uniformity of thiophene chemical environment were further supported by sharper resonances from α-protons on the alkyl side chain (4.2 ppm), the terminal aromatic aldehyde proton (9.9 ppm), and phenyl protons (7.8, 7.9 ppm), which

also exist as a pair of coupling doublets. Collectively, these chemical signatures imply a more regio-regular, less-defective P3DOT-S backbone compared to P3DOT-K.

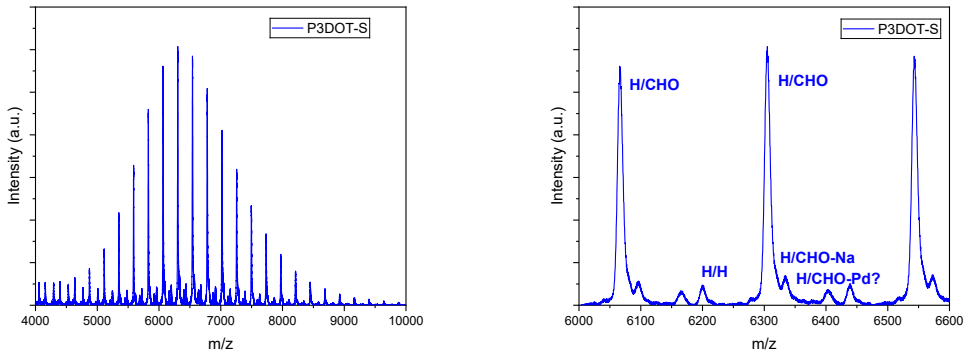

Figure 5.11 (left) *MALDI-TOF* of P3DOT-K (right) zoomed-in *MALDI-TOF* with each peak labelled with corresponding end-group

Compare to P3DOT-K, the prepared P3DOT-S is less in molecular weight. MALDI-TOF-MS depicts a monomodal, gaussian weight distribution with dominant benzaldehyde terminus. Despite the shorter polymer chains, P3DOT-S exhibits considerably lower solubility in solvents like chloroform and chlorobenzene at room temperature, with complete dissolution necessitated by prolonged heating. This greater propensity towards aggregation is further shown by prominent shoulder present in its GPC trace, likely owing to high regio-regularity, which results in more ordered, regular packing of polymer chain with stronger π-π interaction.

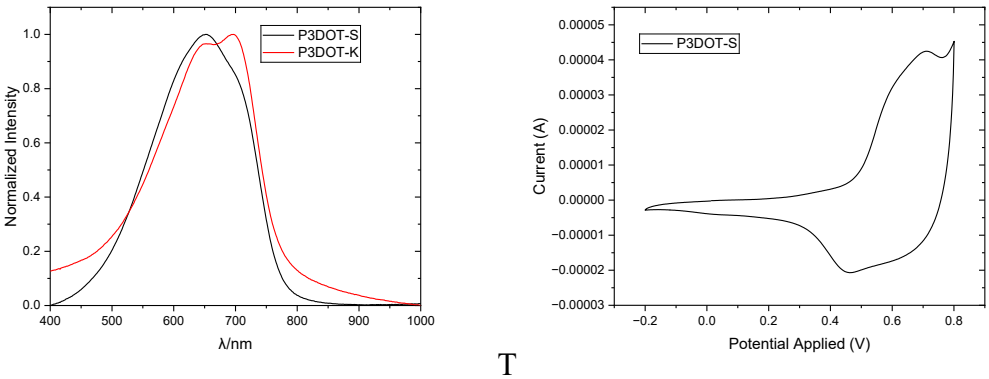

T

Figure 5.12 (left) UV-Vis absorption spectra of P3DOT-K and P3DOT-S (right) Cyclic voltammogram of P3DOT-S in 0.1 M aqueous NaCl electrolyte solution

The combined impact of lower molecular weight and higher structural rigidity in P3DOT-S leads to pronounced differences in electrochemical properties. For instance, P3DOT-S possesses a more blue-shifted absorption spectrum. However, both films exhibit similar optical band gap, consistent with nearly identical HOMO measured by PESA. Despite this, P3DOT-S coated ITO film shows greater onset voltage during cyclic voltammetry in 0.1 M NaCl solution, revealing greater impedance towards electrochemical doping. This is consistent with better regio-regularity of P3DOT-S, where the more orderly aligned alkyl side chains form an organized hydrophobic lamellar network between polymer backbones. This hinders permeation of hydrated ion into the polymer film, resulting in higher applied potential necessary for electrochemical doping. Cyclic voltammogram of P3DOT-S in 0.1M acetonitrile solution of $TBAPF_6$ electrolyte is similar to that of P3DOT-K but lacks an oxidation peak around 0.5 V, which likely arises from disordered, structurally defective domains in P3DOT-K.

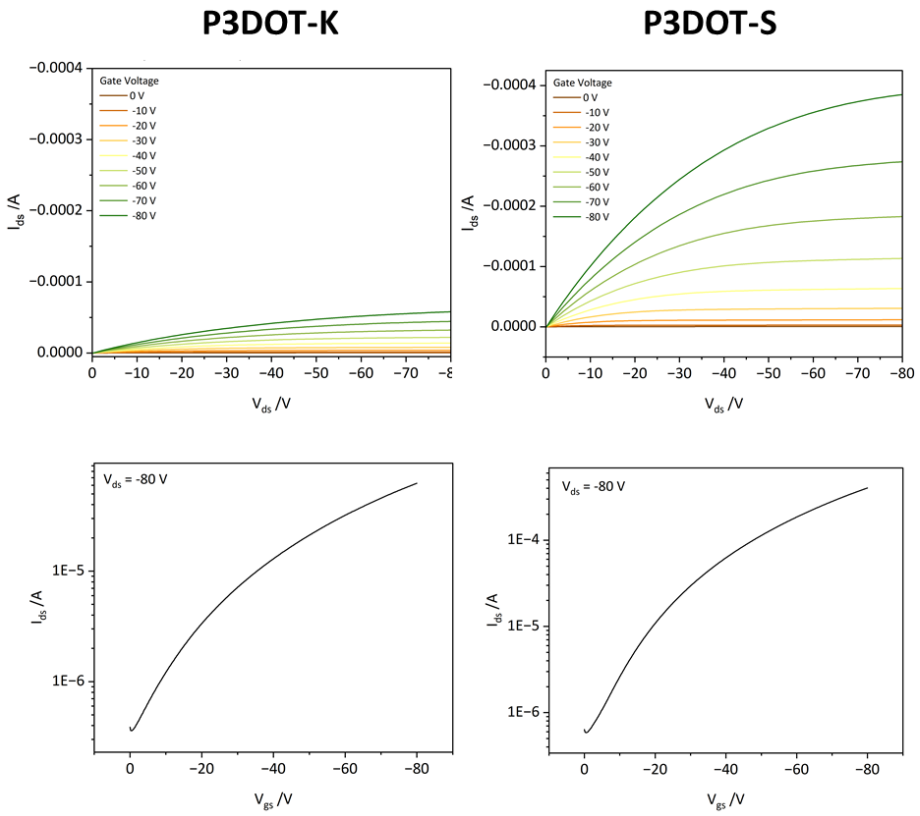

Figure 5.13 output and transfer characteristics of P3DOT-K and P3DOT-S

Material	As cast (AC) or annealed (TA) at 150 ℃ for 10 min	μ_{sat} / cm² V⁻¹ s⁻¹	V_T /V
P3DOT-K	AC	1.02 x 10^{-4}	-48.9
	TA	3.29 x 10^{-3}	-8.5
P3DOT-S	AC	4.16 x 10^{-3}	-15.8
	TA	2.77 x 10^{-2}	-10.6

Table 5.4 Summary of threshold voltage and charge carrier mobility of P3DOT-K and P3DOT-S

To study the differences in device performance, both P3DOT-S and P3DOT-K were fabricated on a bottom-gate bottom-contact OFET substrate with silicon dioxide dielectric layer with coated octadecyltrichlorosilane (ODTS) SAM. The mobility of the

OFET devices were measured with the polymers as-cast or thermally annealed at 150 °C for 10 minutes. For both materials, thermally annealed device leads to a saturated charge mobility an order of magnitude higher than that as-casted, consistent with improved crystallinity following thermal treatment. This impact is more significantly demonstrated in P3DOT-K, where annealing resulted in a thirty-fold increment in charge mobility and a significant reduction of V_{TH} from -48.9 V to -8.5 V. A possible explanation can be given by reorganization of defective disordered domain in the P3DOT-K polymer, resulting in significant improved film quality and passivating trapped states. Notably, P3DOT-S possesses an forty- and eightfold higher charge mobility compare to P3DOT-K when as-casted and thermally annealed, repectively. This further demonstrates its higher regio-regularity, featuring better interlamellar stacking between polymer chains and better crystallinity, leading to improved charge transport.

5.3.5 Investigation of SCTP on other 3-alkoxythiophene substrates

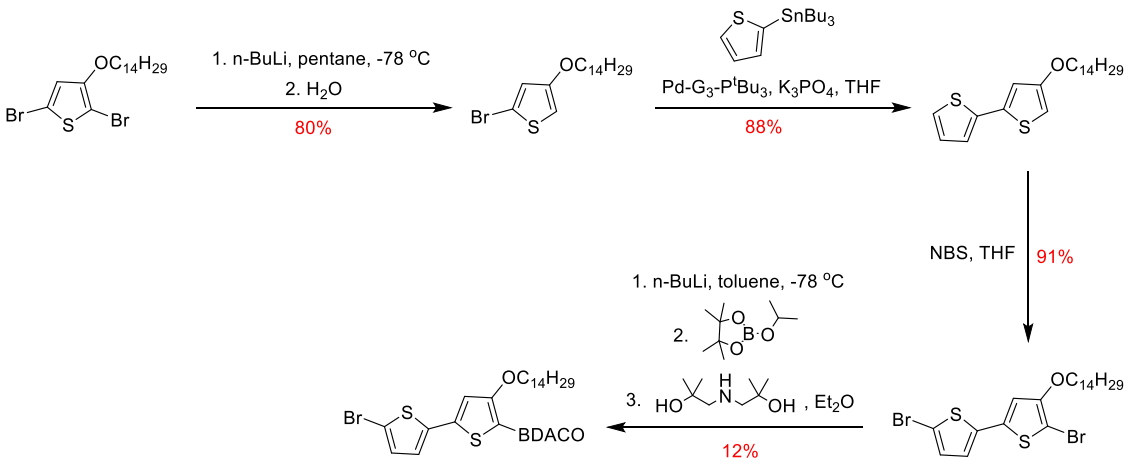

Figure 5.14 Reaction scheme for synthesis of P(3TOT-T)

To demonstrate the applicability of our developed method, we targeted the synthesis of a heterofunctional bithiophene monomer following Figure 5.12. A thiophene spacer was

introduced between each 3-alkoxythiophene, with the goal of enhancing backbone crystallinity. Furthermore, considering that an optimal side-chain separation of ~4.5 Å facilitates lamellar interdigitation between adjacent backbones[38], reducing side chain density was expected to promote this interchain alignment, leading to a more ordered conformation.

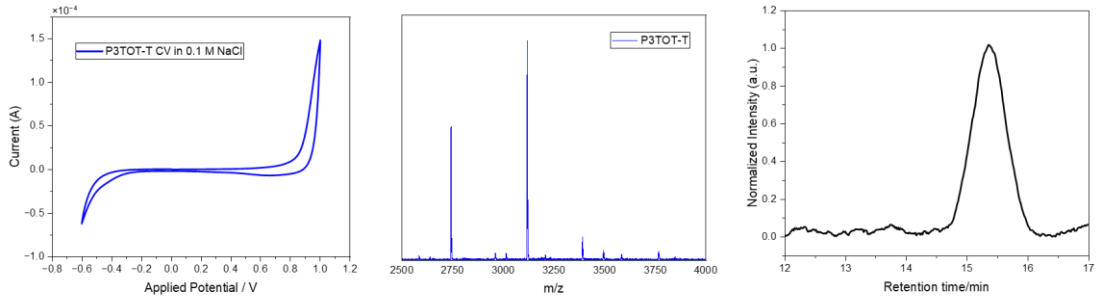

Figure 5.15 (left) Cyclic voltammogram in 0.1 M aqueous NaCl electrolyte solution, (mid) *MALDI-TOF*, (right) *GPC* of P(3TOT-T)

Using SCTP, we successfully obtained a purple conjugated polymer (P3TOT-T) after two days of reaction. Further purification revealed that while high-molecular weight polymer chains exhibited limited solubility, the low-molecular-weight fractions were processible in hot chlorobenzene. MALDI-TOF-MS analysis confirmed the presence of well-defined H/CHO-terminated backbones with degrees of polymerization (DP) of 8 and 9, in agreement with GPC data indicating a M_n of 2.9 kDa. Cyclic voltammetry of polymer films in 0.1 M aqueous NaCl solution revealed a high onset potential of 0.82 V.

These findings underscore that a precise chain-growth polymerization of conjugated polymers with more complex repeating units could be achieved through SCTP. In this case, it is likely that the poor solubility arises because of the strong aggregation behaviour promoted by side-chain interdigitation. While the large onset voltage may render this material unsuitable for OECT operation, the synthetic protocol could be

adapted to accommodate analogous regio-regular poly(thiophene)s with glycol side chain, inspiring novel OMIEC design involving regio-regular conjugated polymers with asymmetric repeating units.

5.3.6 Concluding remarks and future works

Overall, we have demonstrated how SCTP procedure could be optimized to successfully synthesize conjugated polymers with precise end-groups. Compared to KCTP, to balance rates of boronic ester hydrolysis and cross-coupling, more variables such as the boronic ester involved, moisture content, type and stoichiometry of base used have to be considered on top of catalyst selection. Encouragingly, this creates additional dimensions in the chemical space for reaction optimization, increasing the likelihood of finding a suitable protocol simultaneously achieving effective polymerization with correct terminal functionalities.

Next, we investigated the key differences in P3DOT synthesized through SCTP and KCTP. Despite the similarity in optoelectronic properties, P3DOT-S features higher charge mobility in OFET, which is associated with greater regio-regularity and crystallinity of the polymer film. Conversely, P3DOT-S displays greater resistance towards electrochemical doping in aqueous electrolyte, which is consistent with more ordered interlamellar stacking between hydrophobic alkyl chains. To demonstrate the generality of the procedure, a more structurally complex polymer P3TOT-T is successfully prepared with high end-group fidelity.

SCTP offers many synthetic benefits against KCTP – better functional group tolerance, broader chemical space for optimization and more specific end-group introduction not needing a preliminary halogen handle. Nonetheless, optimization of reaction procedure is more sophisticated. This is evidenced by the unsuccessful end-group control in the

partially glycolated derivatives of 3-alkoxythiophenes. In this case, the optimized conditions still result in significant formation of chains with H/H terminus. Further catalyst screening and reaction optimization are hence necessary for high end-group fidelity.

5.4 Conclusion and outlook

In this chapter, we extended beyond P3AOT-based systems discussed in the previous chapters, aiming to identify more generalizable strategies for precise end-group control and functionalization. Conventional step-growth approaches were first assessed, highlighting how the predictability over end-group functionalities could be hampered by intrinsic limitations like poor solubility and side reactions. Despite these, precise end-group control was achieved for F8BT following polymerization, post-polymerization end-group modification and a subsequent rod-coil coupling. This provides a valuable entry point for general construction of rod–coil systems, although structural ambiguities and impurities remain a persistent challenge for alternative monomers employed.

PEGylation of hydrophobic F8BT effectively enables stable nanoparticle assembly through nanoprecipitation, establishing novel material architecture with direct application in hydrogen evolution reaction. The resulting nanoparticles exhibited superior stability, reduced induction periods, and significantly enhanced photocatalytic activity compared to both F8BT and FgBT. These results underscore the value of block copolymer in controlling solubility and molecular assembly in aqueous environment, enabling a novel design in improving photocatalytic efficiency.

Conversely, several key challenges persist. For instance, the sensitivity of end-group fidelity in Suzuki–Miyaura polymerization towards reaction scale, container geometry,

and delicate kinetic balances limits reproducibility and scalability. Alternative strategies, such as in-situ polymerization with macroinitiators, were constrained by statistical trade-offs and side-reaction pathways. Collectively, these findings highlight the inherent chemical limitations associated with conventional cross-coupling polymerization and motivates the transition toward catalyst transfer polymerization with broader monomer compatibility to overcome the current bottlenecks. However, the wider chemical space of SCTP for reaction modification associates with more sophisticated optimization. This not only leads to longer development cycle to improve end-group fidelity but also results in greater complications in understanding the underlying mechanisms.

Overall, the studies presented in this chapter highlight both the opportunities and synthetic challenges associated with generalizing existing block copolymer design. Unfortunately, a general solution to precision polymer chemistry, which is very important to unlock the potential of rod-coil block copolymer development, remains lacking. Encouragingly, in the recent years, the flourishing developments in catalyst transfer polymerization[237,239,242–246] have provided a better understanding of the ambiguities and complications associated, paving the way for a general platform in designing next-generation materials with precise functionalities.

CHAPTER 6

Outlook and future works

Herein, we developed the use of conjugated rod-coil block copolymers and in-situ on-film deprotected conjugated polymer with alcohol pendant group to complement side-chain glycolated OMIECs. The investigation into these materials present several interesting findings. For instance, the feasibility of thin-film hydrophobic homopolymer as OMIECs with competitive μC* was demonstrated. Given a judiciously designed coil block, the figure-of-merit could be enhanced further with improved volumetric capacitance. Considering the strong correlation between OECT charge carrier mobility and the active swelling of the block copolymer thin films, an optimal coil fragment should feature moderate water diffusivity and stiffness, with P3DOT-b-PLLA-34 demonstrating the best performance. In addition, we illustrated how a successive in-situ on-surface deprotection of PgBTTT-OTBS, which unmasked the alcohol side chains, could achieve an p-type accumulation-mode OECT with μC* amongst the best materials reported to date, outperforming PgBTTT by a large margin.

To envision the future of these novel architectures in OMIEC design, it is important to understand their current limitations. In the case of rod-coil block copolymers, to date, a general polymerization scheme to prepare conjugated backbone with precisely functionalized end group remains elusive. Broadening the scope of rod block hence continues to be synthetically challenging. Furthermore, while benchmarking the electrochemical performance of P3DOT-based block copolymers base on current model[31] resulted in a good figure-of-merit exceeding many side-chain glycolated backbones, the low volumetric capacitance, alongside a hysteric output and transfer behaviour, suggested EGOFET-like behaviour, which limits the reversibility and overall transconductance of the device channel.

While these indicate that the practical use of P3DOT-based block copolymers as OECT channel materials may come with reservations, the research featured in **Chapter 2 and 3** shed light towards future designs for OMIECs adopting such architectures. Importantly, a judiciously designed coil fragment must possess higher hydrophilicity and feature lower active swelling to provide better interfacial stabilization under gate bias. Possible candidates fulfilling such criteria include hydrogel-forming polymers like polyvinyl alcohol (PVA) or polyacrylamide (PAM). An alternative strategy could target incorporating aromatic moieties in the coil fragments, which was partly inspired by previous work by Salleo et al, which demonstrated that inclusion of aromatic rings facilitate long-range tunnelling in a conjugated polymer-insulator blend, featuring minor decrease in charge mobility in p(4-MeOS) for same weight of non-conductive component compared to aliphatic insulators such as PEG[247]. This allows for greater coil component in the block copolymer, presenting opportunities to better improve ionic transport without compromising overall electronic response.

The greatest bottleneck limiting further development of rod-coil block copolymer in OMIEC is lack of a polymerization scheme with precise end-group control. As presented in **Chapter 5**, SCTP, which presents more tuneable chemical parameters in reaction design, highlighting better controllability. Therefore, broadening the chemical space of expandable rod block requires collective optimization of monomer, catalyst and solvent parameters, featuring further opportunities in design of block copolymer materials. For instance, instead of completely deconvoluting ionic transport to coil block, judicious incorporation of fragments which structurally inhibit active swelling of target polymer film, such as PLLA, can improve the electrochemical response of side-chain glycolated OMIECs.

Further opportunities in rod-coil block copolymer in OMIECs, or more broadly in the field of organic optoelectronics, also exist from a non-synthetic perspective. Given the versatility of rod-coil block copolymer morphology to post-treatment, a correlation between microphase separation in the polymer thin-film with its electrochemical behaviour will prove beneficial to design of next-generation OMIECs, but remains elusively understood. As remarked in the final section of **Chapter 3**, since solvent-vapour annealing favours the self-assembly of P3DOT-b-PEG into lamellar microstructures, the impact of such post treatment on OECT response will benefit further understanding of such structure-activity relationship. Integrating with a suitable surface etching procedure to remove labile coil block, this work could be further extended to the development of nanoporous conjugated material presenting different ordered morphology.

In solution-phase, conjugated rod-coil block copolymers also prove effective in nanoparticle fabrication through facile nano-precipitation. As shown in **Chapter 5**, this presents opportunities beyond OMIECs, in areas like hydrogen evolution reaction, which is highly important in the chemical storage of solar energy. Moreover, recent burgeoning development of crystallization-driven self-assembly[248,249] had illustrated how block copolymers could be self-assembled into a wide range of ordered, hierarchical micellar nanostructures like fibers and platelets. Future studies could hence harness the potential of these molecular assembly in photochemical hydrogen conversion, which could help us to understand the principles to design materials with fast conversion turnover.[15]

Finally, in **Chapter 4**, we demonstrated how on-film deprotection of a silyl-ether masked PgBTTT-OTBS could achieve a figure-of-merit which far exceeds its side-

chain glycolated counterpart. This encouraging result could be further developed to prepare a broader scope of conjugated backbone as high-performance active material in OECT, thereby generalizing this work into a versatile strategy for OMIEC design.

Overall, in this thesis, we have focused on the development of block copolymers and backbones with alcohol pendant group as effective channel material in p-type accumulation OECT. Given satisfactory figure-of-merit in both cases, we have demonstrated the feasibility of this alternative molecular architecture in OMIEC design, indicating how side-chain glycolation is no longer the exclusive strategy to build high-performance OECT materials. However, like how steady-state performance of the n-type materials lag behind their counterpart, extending these strategies towards structurally more sophisticated n-type building blocks is synthetically more difficult. Achieving these challenging research goals hence requires further development of the chemistry and design principles reported herein. It is hoped that the findings within the scope of this will not only benefit design and development of future OMIECs, but also present opportunities to advance research in other organic semiconductor-related areas, wherein new ideas could be inspired with these molecular architectures.

CHAPTER 7

Experimental Procedures

7.1 General Methods

7.1.1 Materials for synthesis and purification

Reagents and chemicals were purchased from commercial suppliers, including Sigma-Aldrich, FluoroChem, Alfa Aesar, Acros Organics, Manchester Organics, Insight Biotechnology Ltd, Ambeed Inc and were used as supplied unless stated otherwise. Anhydrous chlorobenzene and tetrahydrofuran was purchased from Sigma Aldrich while all remaining dry solvents were collected from a MBraun SPS800 solvent drying systems. Prior to usage, all glassware was oven dried at 120°C and then cooled to room temperature under reduced pressure. Thin layer chromatography (TLC) was performed on Merck aluminium silica gel 60 F254 precoated plates. Plates were visualized under an ultraviolet lamp (λmax = 254nm or 365nm) and/or by staining with iodine suspended on silica, potassium permanganate solution or phosphomolybdic acid. Column chromatography was carried out on Merck Geduran Silicagel 60 (230 – 400 mesh).

7.1.2 Instrument for general characterizations of chemical products

^{1}H and ^{13}C nuclear magnetic resonance (NMR) spectra were taken on a Bruker AVIII HD 400 or AVIII HD 500 spectrometer. Chemical shifts are quoted in parts per millions (ppm) with multiplicities of the spectra recorded as the following: s, singlet; d, doublet; t, triplet; q, quartet; p, quintet; m, multiplet; br, broad; dd, doublet of doublets et cetera. Coupling constants (J) are given in Hertz (Hz) and rounded to the nearest 0.1 Hz. High resolution ESI mass spectra were recorded on a Bio-Accord LC-MS system, m/z values are reported in Daltons (Da) and high-resolution values are calculated to four decimal places from the molecular formula, with all found values in a tolerance of 5 ppm. MALDI spectra were taken on Autoflex MALDI-TOF/TOF instrument with linear mode unless stated otherwise. Analytical GPC was taken on either (chloroform, via RI-

detector and UV-detector with polystyrene standard) was performed on either Agilent 1200 Series GPC-SEC system using HPLC chloroform eluent at 40 °C or Agilent 1260 Infinity II using HPLC chloroform eluent at 80 °C. Preparative GPC, if necessary, was performed by first filtering crude polymer through celite with chloroform. The polymer solution was then concentrated under reduced pressure to a volume of ca. 5mL, then passed through a short size-exclusion column (Bio-Beads S-X1, chloroform) to remove residual metal salt.

7.1.3 Cyclic Voltammetry

Cyclic voltammetry measurements were carried out under ambient air pressure and temperature using AutoLab PGSTAT101 machine with Metrohm Autolab NOVA software version 2.1. A three-electrode configuration was used for all measurements, with a polymer-deposited ITO substrate as working electrode and a platinum mesh wire as counter electrode. For measurement conducted in 0.1 M aqueous NaCl supporting electrolyte, a BASi Ag/AgCl (3M NaCl) Reference Electrode (MF-2052) was used as reference electrode. For measurement in 0.1 M $TBAPF_6$ supporting electrolyte in acetonitrile, a BASi Ag/Ag^+ nonaqueous reference electrode (MW-1085) filled with 0.01 M $AgNO_3$ and 0.1 M $TBAPF_6$ solution was used and calibrated against ferrocene/ferrocenium redox couple (Fc/Fc^+). All cyclic voltammograms were recorded with a scan rate of 100 mVs^{-1}. Ionization potentials were estimated base on **Equation 7.1**.

$$IP = 4.8\,V + E_{ox} - E_{Fc/Fc^+}$$

Herein, E_{ox} refers to the oxidation onset potential of polymer film with 0.1 M $TBAPF_6$ supporting electrolyte in acetonitrile and and $E_{Fc/Fc+}$ is the half-wave potential of the ferrocene/ferrocenium couple in identical organic electrolyte solution.

7.1.4 Ultraviolet-Visible (UV-Vis) Spectroscopy

Ultraviolet-Visible (UV-Vis) absorption spectra were collected under ambient air atmosphere and temperature on a UV-1800 Shimadzu Spectrophotometer machine, with UV-Probe 2.42 software. Thin-film UV absorption was taken from polymer-coated glass substrates with a detector wavelength ranging from 350 to 1100 nm. Optical band gap was evaluated based on the wavelength of the onset absorption.

7.1.5 Spectro-electrochemistry

Spectro-electrochemistry was conducted in a "Cappuccino PEC Cell" placed in UV-1800 Shimadzu Spectrophotometer machine. A three-electrode configuration identical to that used in cyclic voltammetry was connected in the cell. During each measurement, a uniform, continuous potential was applied by AutoLab PGSTAT101 machine for 10 seconds on the polymer-coated ITO working electrode for equilibration, before the optical absorption was recorded.

7.1.6 Photoemission Spectroscopy in Air (PESA)

PESA spectra were recorded on a KP Technology APS02 system over wavelengths of ca. 180 – 280 nm, over a polymer-coated glass slide. All photoemission measurements were taken under applied bias of -70 V. The ionization potential is evaluated from the onset energy level with respect to the cubic root of photoemission intensity.

7.1.7 Water vapour adsorption Isotherm

Hydrophilicity of the materials were evaluated from volume of water vapour uptake per unit mass using Adsorption Isotherm with H_2O adsorption gas. ca. 50 mg of the polymer sample was loaded into an Anton Paar Autosorb iQ-XR gas sorption analyser. The

materials were heated at 110 ºC for 18 hours under vacuum on the apparatus before the measurement to remove moisture present in the sample. The water sorption isotherm was measured at 25 ºC in a water bath.

Six classic types of adsorption isotherms were described previously (https://pubs.acs.org/doi/10.1021/ja01864a025) and would not be discussed in detail here. Instead, we focus on Type III adsorption, which is featured in all P3DOT-*b*-PEG as shown in Chapter 3. This depicts multilayer adsorption, where the strength of strong intermolecular H-bond between H_2O gas is competitive with the physio-adsorption of the gas molecules with the substrate surface. Consequently, high water vapour pressure is required to facilitate significant moisture uptake.

7.1.8 Grazing Incidence Wide-Angle X-Ray Scattering

Two dimensional GIWAXS map was acquired from polymer-coated silicon wafer substrates. Scattering measurements were carried out on I07 Beamline at Diamond Light Source with beam energies at 12.5 keV and sample detector distance of 609 mm. Data analysis was carried out using either IgorPro version 6.37 or Data Analysis Workbench 2.32.

7.1.9 Organic electrochemical transistor fabrication

OECTs were fabricated following previously reported photolithographic procedure[251]. Polymer films were spin-coated onto the substrate. In the case of P3DOT block copolymers, polymer solution in chloroform (5 $mgmL^{-1}$) was used. In the case of PgBTTT-OTBS, hot deposition from polymer solution in chlorobenzene (5 $mgmL^{-1}$) was used and subsequently dried in vacuum oven at 50 ºC for 1 hour. The device was immersed in a sealed jar with 5 mL of 1% v/v TMSBr in IPA for 1 hour, then washed

with IPA, before being dried in vacuum oven at 50 ºC for another hour. In the case of TBAF etchant, the device was similar immersed in 5 mL of 0.1 M TBAF in MeCN and warmed to 60 ºC in a sealed jar overnight, before washed with MeCN and then dried in vacuum oven at 50 ºC for another hour.

Following the deposition of materials in the active channel, the sacrificial Parylene C layer was peeled-off. The device performance was evaluated with 0.1 M aqueous NaCl supporting electrolyte under ambient air atmosphere and temperature. An Ag/AgCl pellet electrode (World Precision Instruments, EP1) was used as the gate electrode and a Keithley 2602A SourceMeter machine was used to measure the output and transfer characteristics of the device.

7.2 Synthetic Procedures

7.2.1 Synthetic Procedure for Chapter 2 and 3

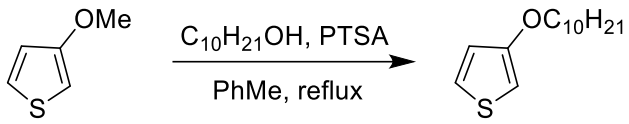

*Preparation of **3-(decyloxy)thiophene***

Under N_2, 3-methoxythiophene (4.00 g, 35.0 mmol, 1 eq) was dissolved in toluene (40 mL). Then, 1-decanol (8.31 g, 10.0 mL, 52.5 mmol, 1.5 eq), followed by p-toluenesulfonic acid monohydrate (603 mg, 3.50 mmol, 0.1 eq) was added and the reaction mixture was heated to reflux overnight. Upon completion of reaction, the reaction mixture was diluted with diethyl ether (160 mL) and washed with saturated sodium bicarbonate solution (150 mL), water (150 mL x 2) and dried over anhydrous sodium sulphate. The crude product was further purified by column chromatography (petroleum ether) to yield the product as a colourless oil. (6.90 g, 82%). ^{1}H NMR (400

MHz, CDCl3) δ 7.17 (dd, J = 5.2, 3.1 Hz, 1H), 6.76 (dd, J = 5.2, 1.5 Hz, 1H), 6.23 (dd, J = 3.1, 1.5 Hz, 1H), 3.94 (t, J = 6.6 Hz, 2H), 1.88 – 1.67 (m, 2H), 1.52 – 1.40 (m, 2H), 1.40 – 1.19 (m, 12H), 0.96 – 0.81 (m, 3H). ^{13}C NMR (101 MHz, $CDCl_3$) δ 158.2, 124.6, 119.7, 97.1, 70.4, 32.0, 29.7, 29.7, 29.5, 29.5, 29.4, 26.2, 22.8, 14.3. HRMS (ESI): calcd for $C_{14}H_{24}OS$, 240.1542; found 240.1544 (M+, 0.7 ppm).

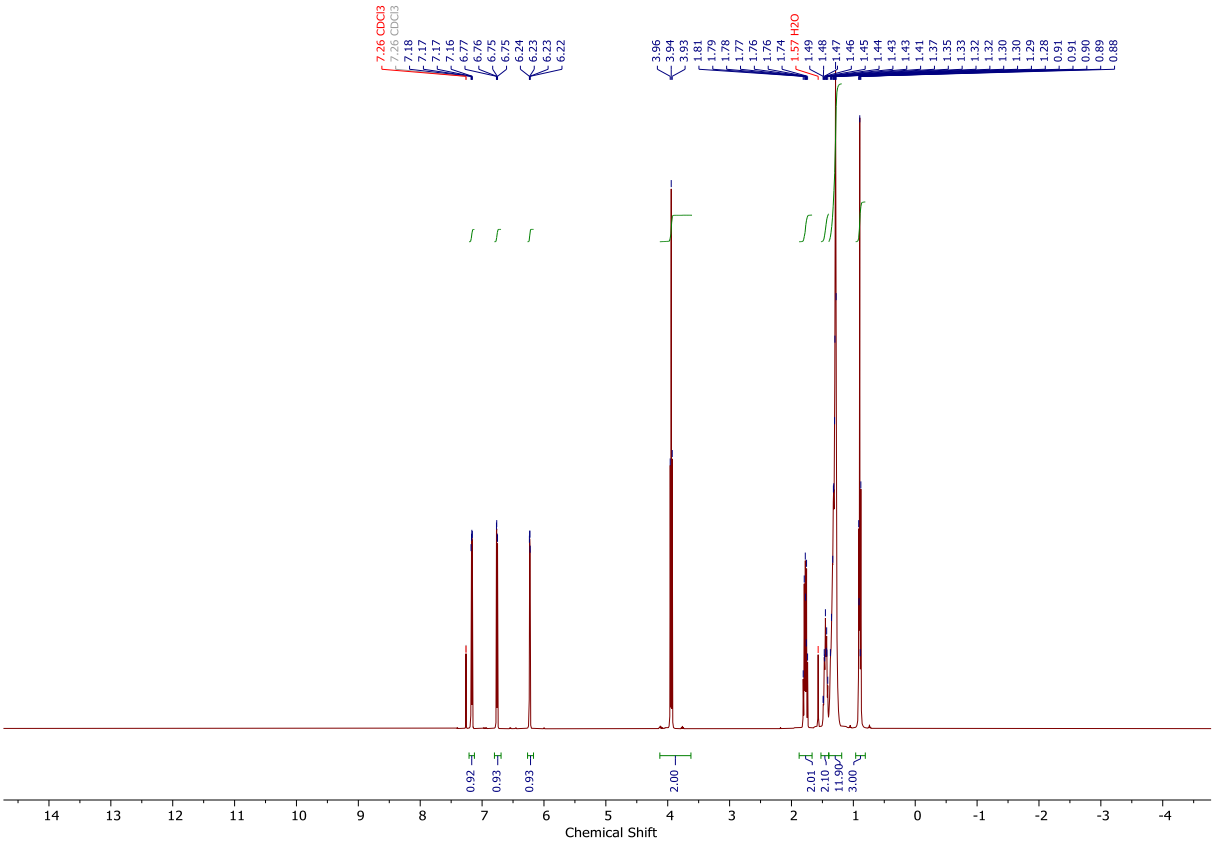

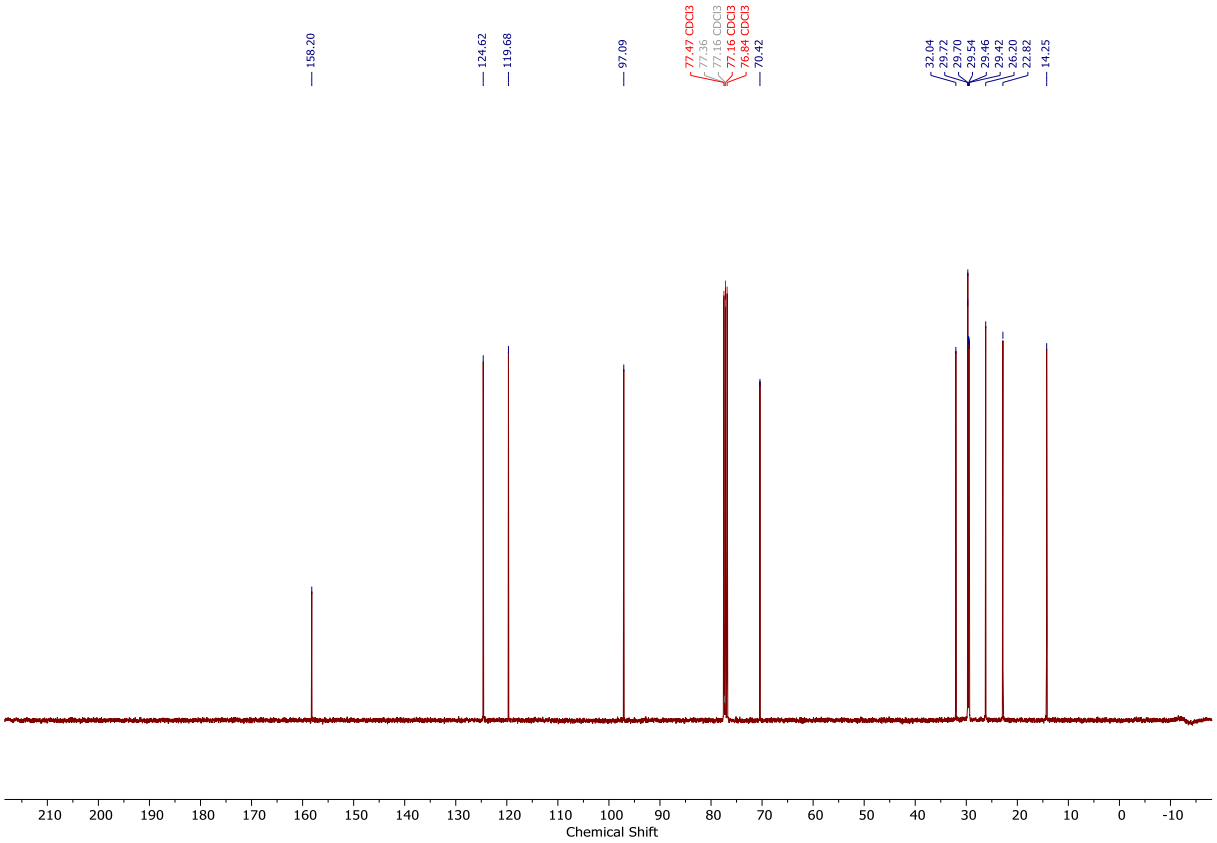
158.20
124.62
119.68
97.09
77.47 CDCl3
77.36
77.16 CDCl3
77.16 CDCl3
76.84 CDCl3
70.42
32.04
29.72
29.70
29.54
29.46
29.42
26.20
22.82
14.25
210 200 190 180 170 160 150 140 130 120 110 100 90 80 70 60 50 40 30 20 10 0 -10
Chemical Shift

Expanded Spectrum RT 0.11, NL 413261, Peak [1], Target Mass 240.1542

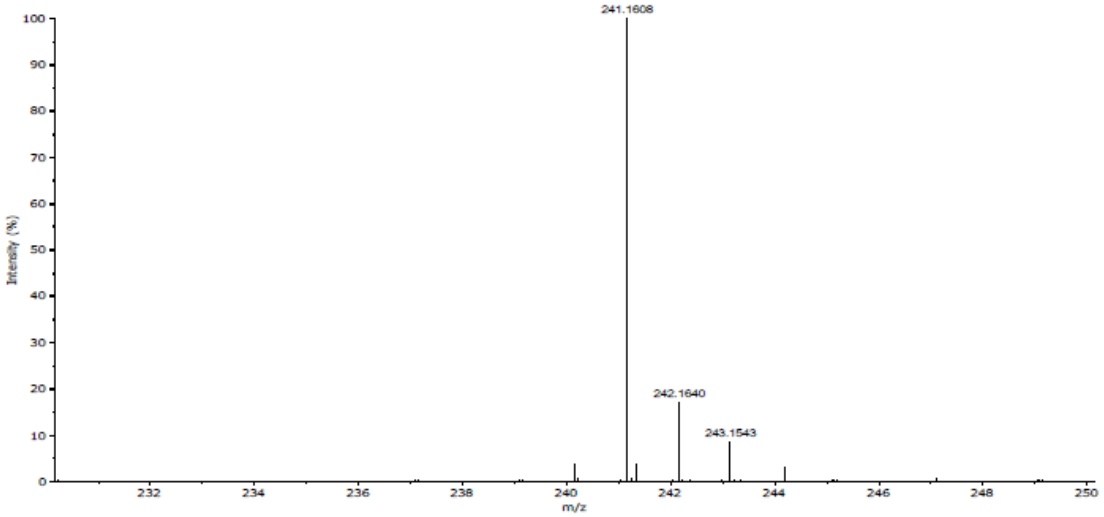

Theoretical Spectrum for C14H24OS, Minimum Abundance 0.01%

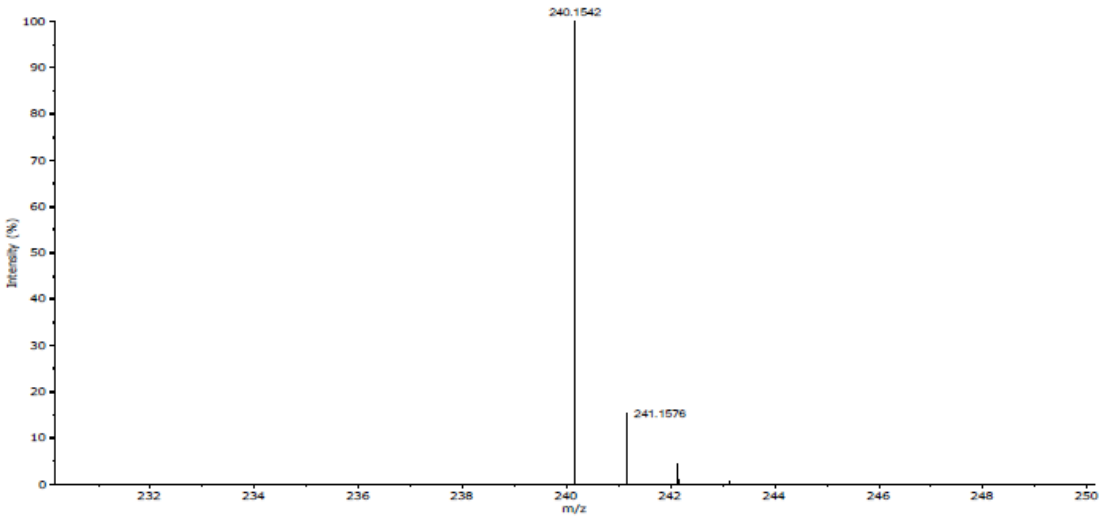

Measured Mass	Calculated Mass	Error (mDa)	Error (ppm)	Formula $[M]^+$	Response
240.1544	240.1542	0.16	0.67	$C_{14}H_{24}OS$	79279

The measured m/z value is consistent with your proposed formula for this sample.

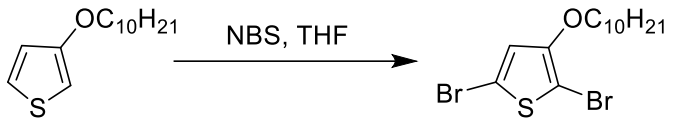

Preparation of ***2,5-dibromo-3-(decyloxy)thiophene***

Under N_2, 3-(docyloxy)thiophene (2.20 g, 9.15 mmol, 1 eq) was dissolved in anhydrous THF (20 mL) and was cooled to 0 ºC. Then, N-Bromosuccinimide (3.58 g, 20.13 mmol, 2.2 eq) was added. The reaction mixture was protected from light with aluminium foil and left to stir at room temperature for 3 hours. Upon completion of reaction, the reaction mixture was diluted with diethyl ether (180 mL) and washed with saturated sodium bicarbonate solution (150 mL), water (150 mL x 2) and dried over anhydrous sodium sulphate. The crude product was further purified by column chromatography (petroleum ether) to yield the product as a colourless oil. (2.80 g, 77%). ^{1}H NMR (400 MHz, $CDCl_3$) δ 6.76 (s, 1H), 3.99 (t, *J* = 6.6 Hz, 2H), 1.73 (dq, *J* = 8.2, 6.6 Hz, 2H), 1.44 (td, *J* = 8.1, 4.9 Hz, 2H), 1.42 – 1.25 (m, 12H), 0.92 – 0.84 (m, 3H). ^{13}C NMR (101 MHz, $CDCl_3$) δ 154.0, 121.0, 109.7, 90.7, 72.7, 32.0, 29.7, 29.5, 29.5, 29.4, 25.9, 22.8, 14.3. HRMS (ESI): calcd for $C_{14}H_{23}Br_2OS$, 396.9831; found 396.9835 (M+H+, 1.0 ppm).

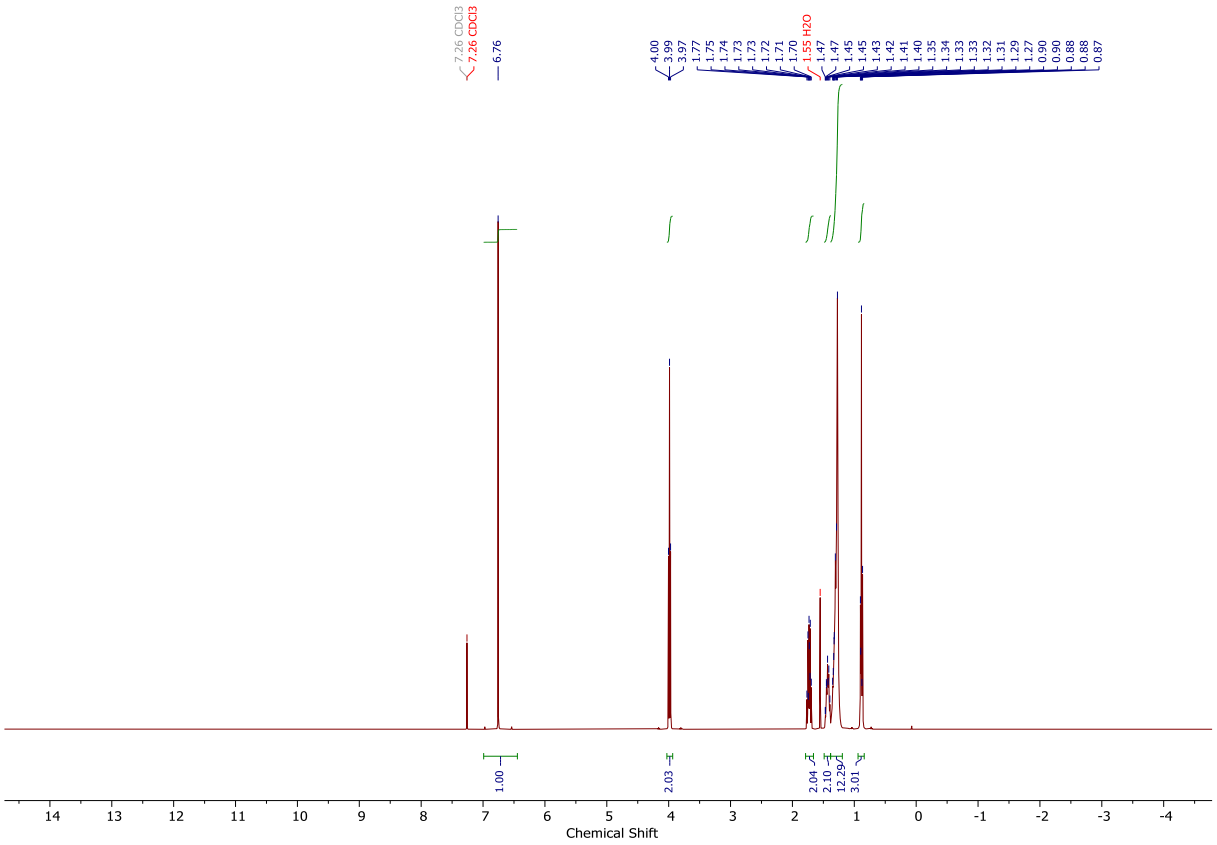
7.26 CDCl3
7.26 CDCl3
6.76
4.00
3.99
3.97
1.77
1.75
1.74
1.73
1.72
1.71
1.70
1.55 H2O
1.47
1.47
1.45
1.45
1.43
1.42
1.41
1.40
1.35
1.34
1.33
1.33
1.32
1.31
1.29
1.27
0.90
0.90
0.88
0.88
0.87
1.00
2.03
2.04
2.10
12.29
3.01
14 13 12 11 10 9 8 7 6 5 4 3 2 1 0 -1 -2 -3 -4
Chemical Shift

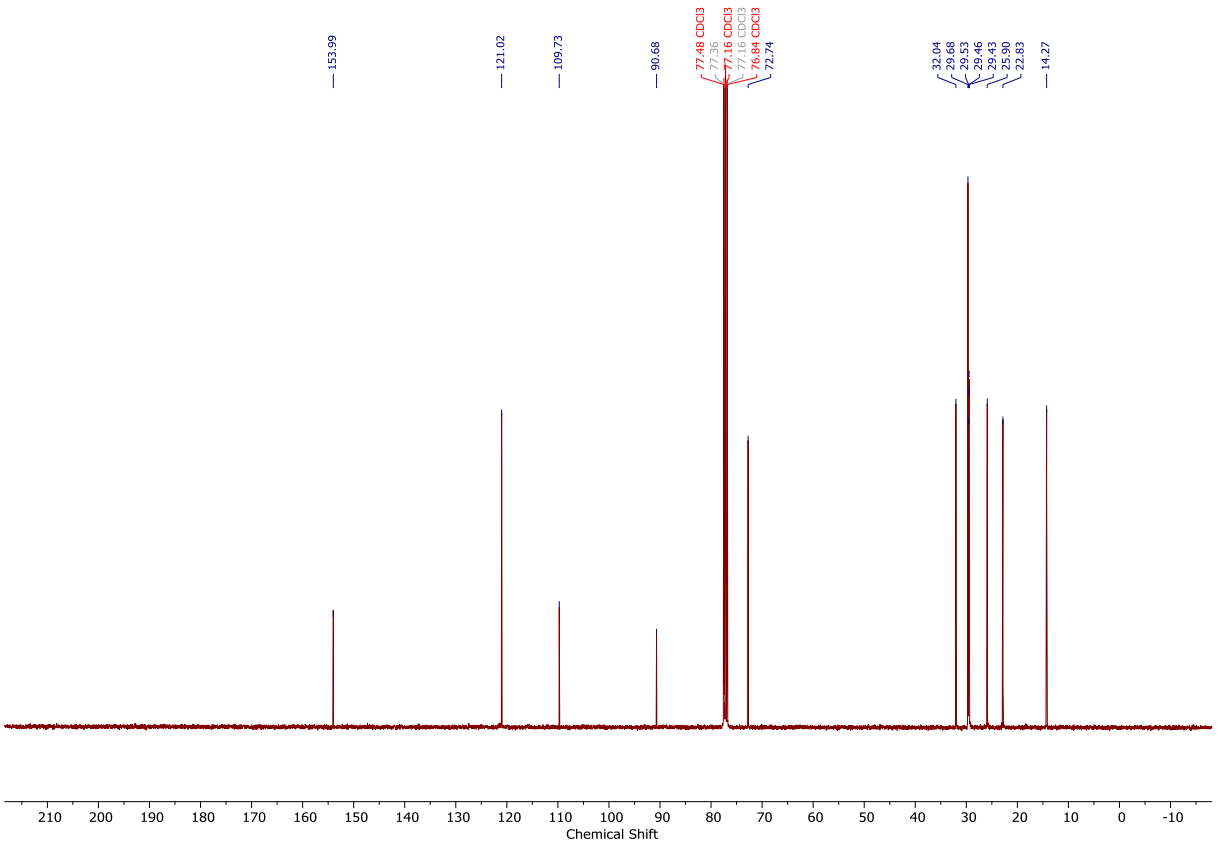
153.99
121.02
109.73
90.68
77.48 CDCl3
77.36
77.16 CDCl3
77.16 CDCl3
76.84 CDCl3
72.74
32.04
29.68
29.53
29.46
29.43
25.90
22.83
14.27
210 200 190 180 170 160 150 140 130 120 110 100 90 80 70 60 50 40 30 20 10 0 -10
Chemical Shift

Expanded Spectrum RT 0.08, NL 2062380, Peak [1], Target Mass 396.9831

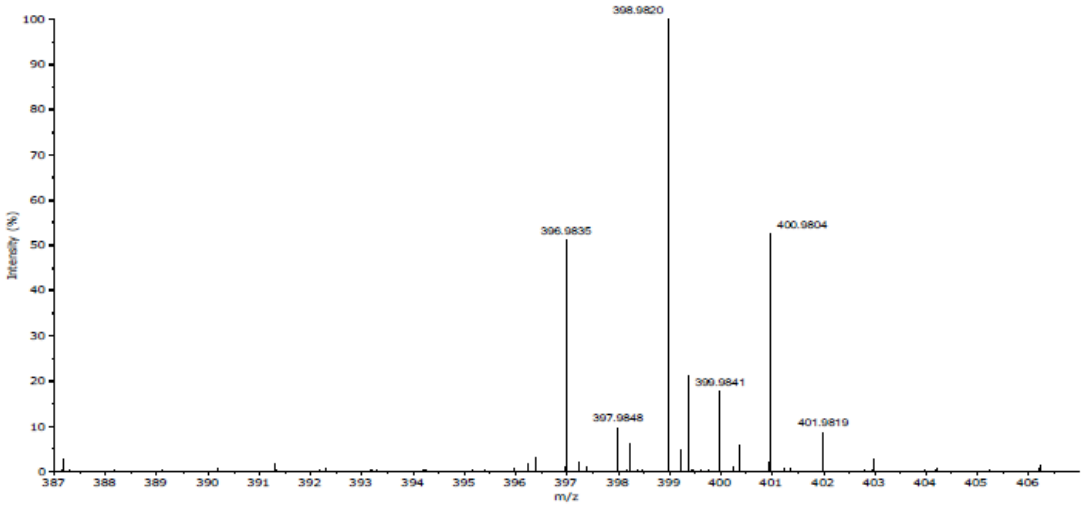

Theoretical Spectrum for C14H23Br2OS, Minimum Abundance 0.01%

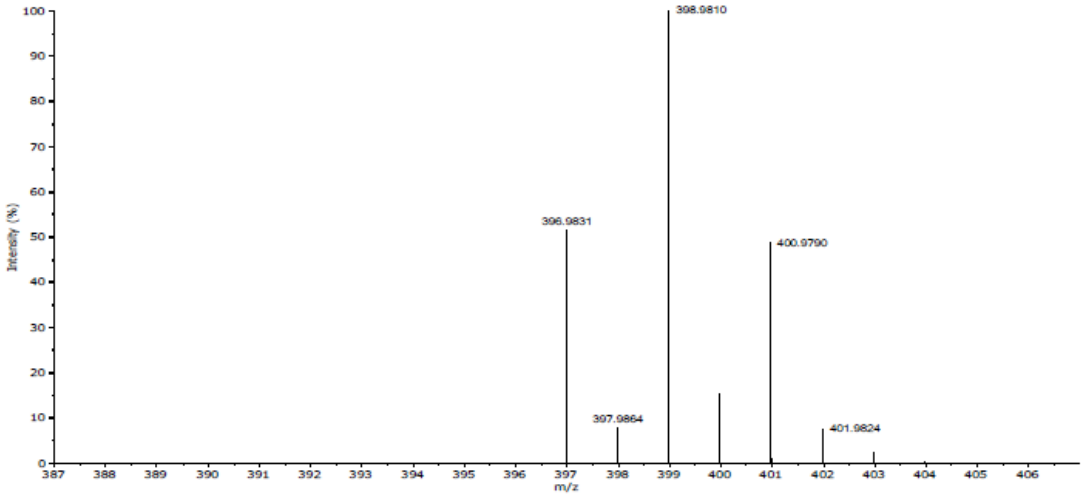

Measured Mass	Calculated Mass	Error (mDa)	Error (ppm)	Formula $[M+H]^+$	Response
396.9835	396.9831	0.41	1.04	$C_{14}H_{23}Br_2OS$	952306

The measured m/z value is consistent with your proposed formula for this sample.

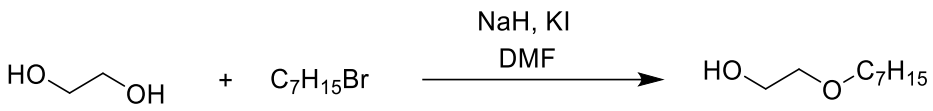

Preparation of ***2-(heptyloxy)ethan-1-ol***

Under N_2, ethylene glycol (41.90 g, 675 mmol) was dissolved in anhydrous DMF (250 mL) and cooled to 0 ºC. Then, sodium hydride (9.0 g, 225 mmol) was added in portions over an hour. Then, the reaction mixture was left to stir at room temperature for an hour and cooled to 0 ºC again. Potassium iodide (24.9 g, 150 mmol) and heptyl bromide (26.9 g, 150 mmol) was added and the reaction mixture was left to stir at room temperature overnight. Upon completion, the reaction mixture was added to water (1.0 L) and extracted with ethyl acetate (400 mL x 3), which was washed twice with water (400 mL x 2), brine (400 mL) and then over anhydrous sodium sulphate. The crude product was further purified by column chromatography (hexane/ethyl acetate 9/1) to yield a pale-yellow oil. (15.5 g, 64%). ^{1}H NMR (500 MHz, $CDCl_3$) δ 3.74 – 3.69 (m, 2H), 3.54 – 3.50 (m, 2H), 3.46 (t, *J* = 6.7 Hz, 2H), 2.08 (s, 1H), 1.63 – 1.53 (m, 2H), 1.39 – 1.19 (m, 8H), 0.92 – 0.82 (m, 3H). ^{13}C NMR (126 MHz, $CDCl_3$) δ 71.9, 71.6, 62.0, 31.9, 29.8, 29.3, 26.2, 22.7, 14.2. HRMS (ESI): calcd for $C_9H_{20}O_2Na$, 183.1356; found 183.1356 (M+Na+, 0.3 ppm).

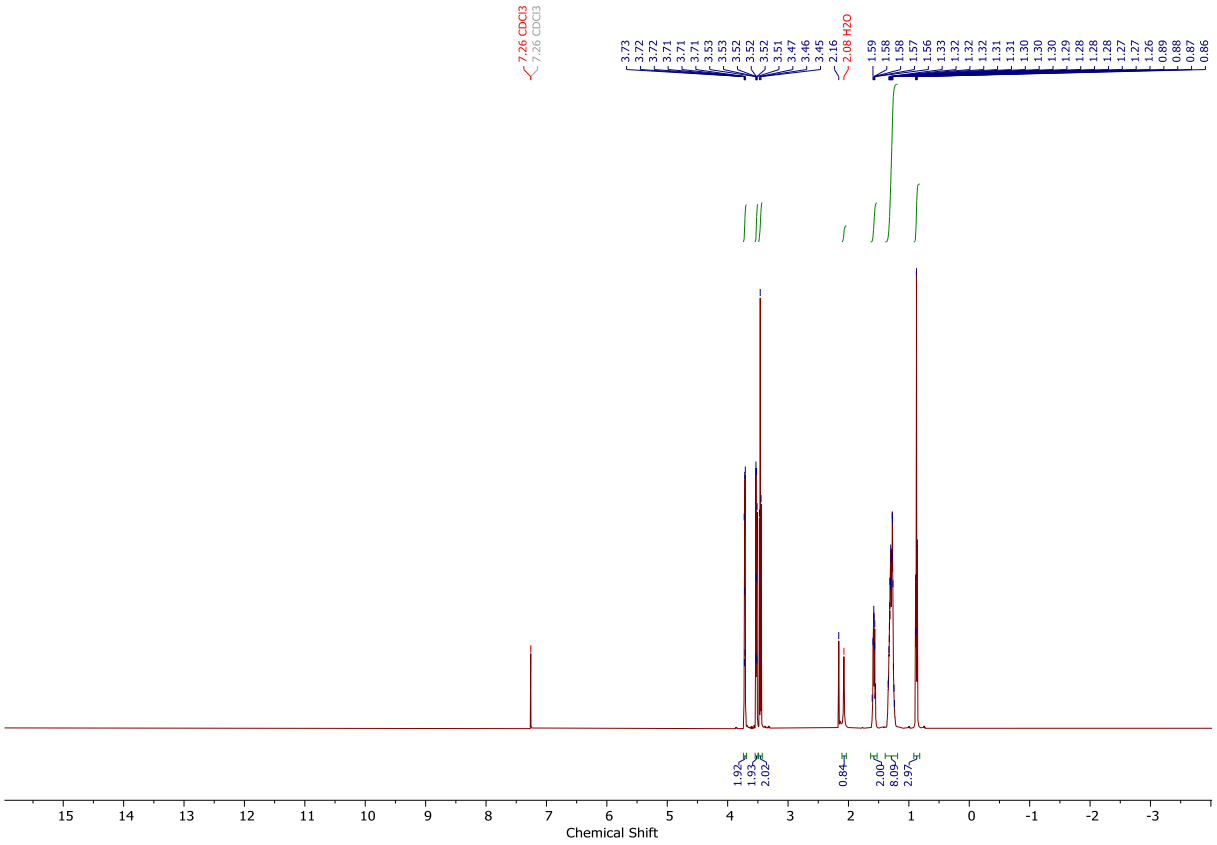
7.26 CDCl3
7.26 CDCl3
3.73
3.72
3.72
3.71
3.71
3.71
3.53
3.53
3.52
3.52
3.52
3.51
3.47
3.46
3.45
2.16
2.08 H2O
1.59
1.58
1.58
1.57
1.56
1.33
1.32
1.32
1.32
1.31
1.31
1.30
1.30
1.30
1.29
1.28
1.28
1.28
1.27
1.27
1.26
0.89
0.88
0.87
0.86
1.92
1.93
2.02
0.84
2.00
8.09
2.97
15
14
13
12
11
10
9
8
7
6
5
4
3
2
1
0
-1
-2
-3
Chemical Shift

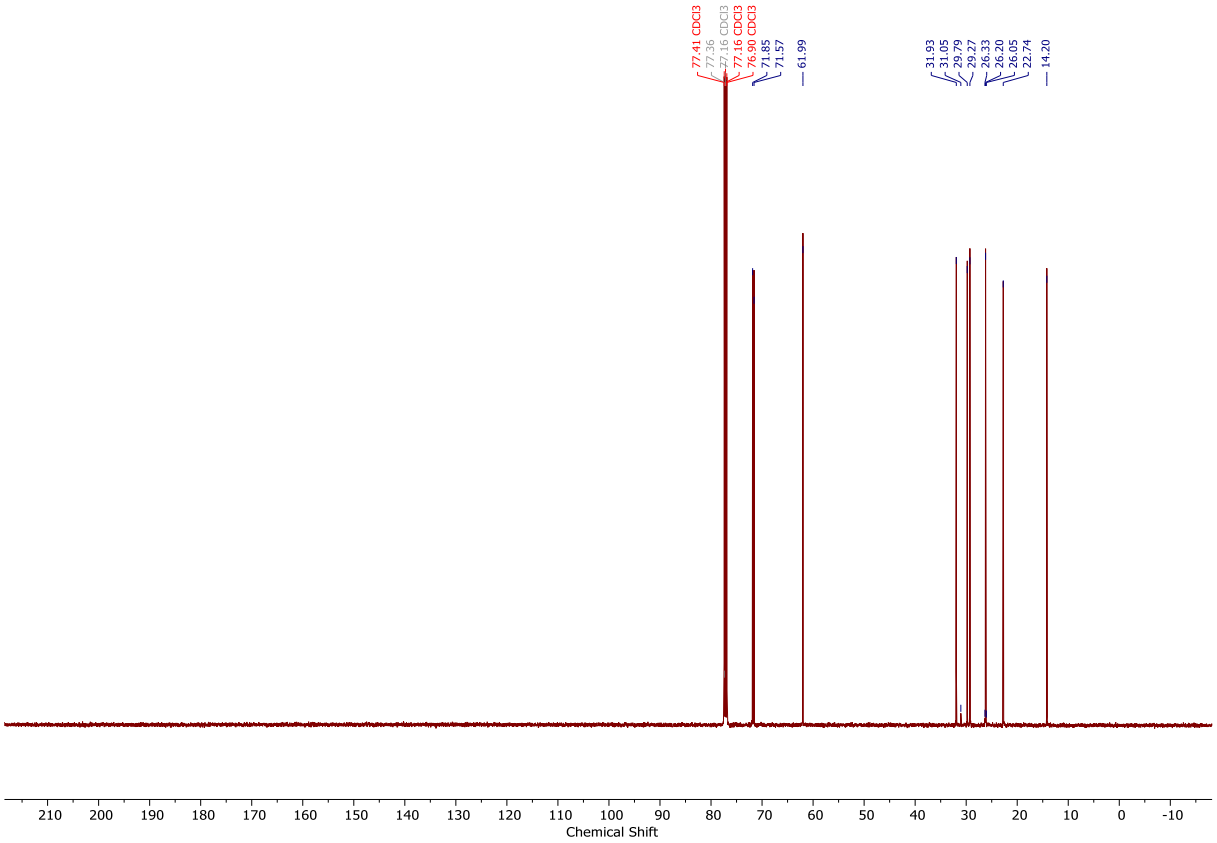
77.41 CDCl3
77.36
77.16 CDCl3
76.91
76.66 CDCl3
71.85
71.57
61.99
31.93
31.05
29.79
29.27
26.33
26.20
26.05
22.74
14.20
210 200 190 180 170 160 150 140 130 120 110 100 90 80 70 60 50 40 30 20 10 0 -10
Chemical Shift

Expanded Spectrum RT 0.10, NL 3513529, Peak [1], Target Mass 241.1621

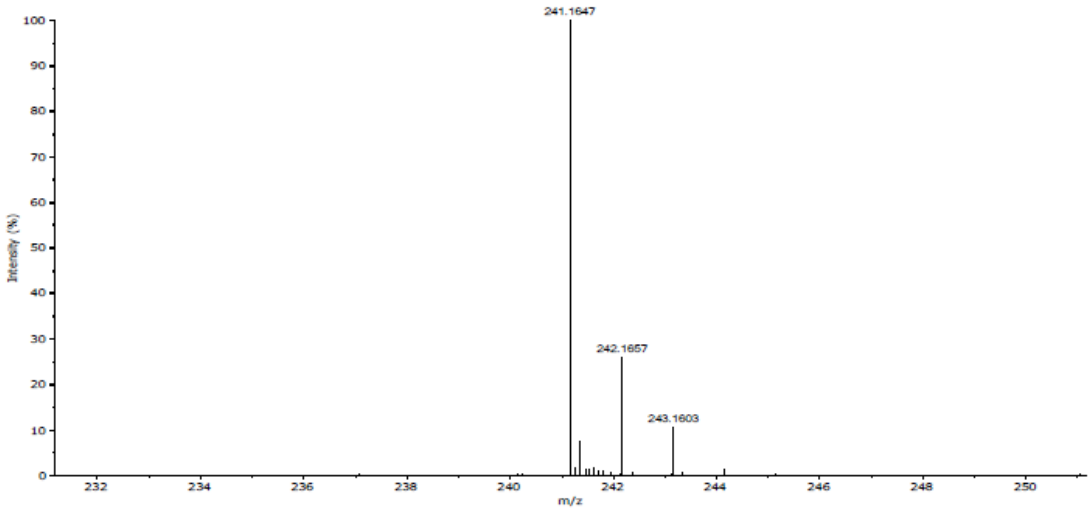

Theoretical Spectrum for C14H25OS, Minimum Abundance 0.01%

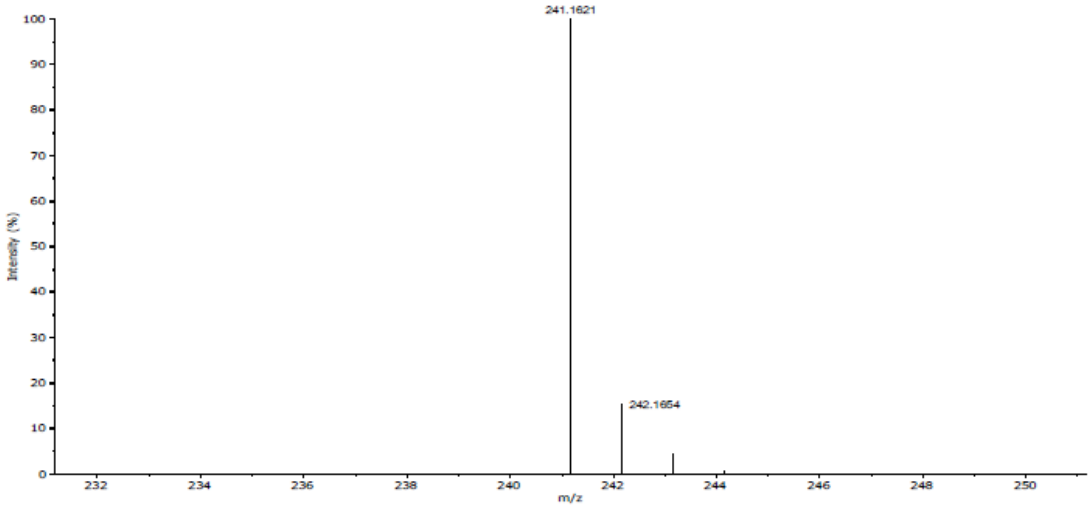

Measured Mass	Calculated Mass	Error (mDa)	Error (ppm)	Formula $[M+Na]^+$	Response
183.1356	183.1356	0.05	0.27	$C_9H_{20}O_2Na$	1218065

The measured m/z value is consistent with your proposed formula for this sample.

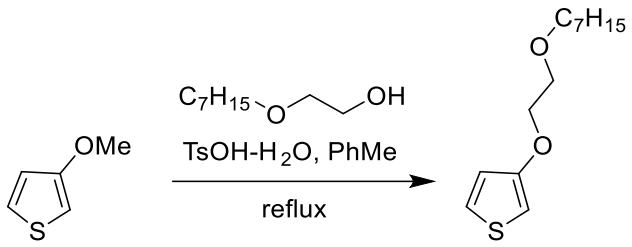

Preparation of ***3-(2-(heptyloxy)ethoxy)thiophene***

Under N_2, 3-methoxythiophene (5.15 g, 45.11 mmol) was dissolved in anhydrous toluene (40 mL). Then, 2-(heptyloxy)ethan-1-ol (10.84 g, 67.67 mmol, 1.5 eq) was added, followed by p-toluenesulfonic acid monohydrate (858 mg, 4.51 mmol). The reaction mixture was refluxed overnight. Upon completion of reaction, the reaction mixture was diluted with diethyl ether (160 mL) and washed with saturated sodium bicarbonate solution (150 mL), water (150 mL x 2) and dried over anhydrous sodium sulphate. The product was further purified by column chromatography (hexane -> hexane/diethyl ether 30/1) as a pale-yellow oil (8.30 g, 76%). ^{1}H NMR (500 MHz, $CDCl_3$) δ 7.16 (dd, *J* = 5.2, 3.1 Hz, 1H), 6.79 (dd, *J* = 5.3, 1.6 Hz, 1H), 6.26 (dd, *J* = 3.1, 1.5 Hz, 1H), 4.17 – 4.02 (m, 2H), 3.83 – 3.68 (m, 2H), 3.51 (t, *J* = 6.8 Hz, 2H), 1.60 (dt, *J* = 8.2, 6.6 Hz, 2H), 1.43 – 1.18 (m, 8H), 0.99 – 0.78 (m, 3H). ^{13}C NMR (126 MHz, $CDCl_3$) δ 157.8, 124.7, 119.8, 97.6, 71.8, 69.7, 69.2, 32.0, 29.8, 29.3, 26.2, 22.7, 14. 2. HRMS (ESI): calcd for $C_{13}H_{22}O_2SNa$, 265.1233; found 265.1235 (M+Na+, 0.9 ppm).

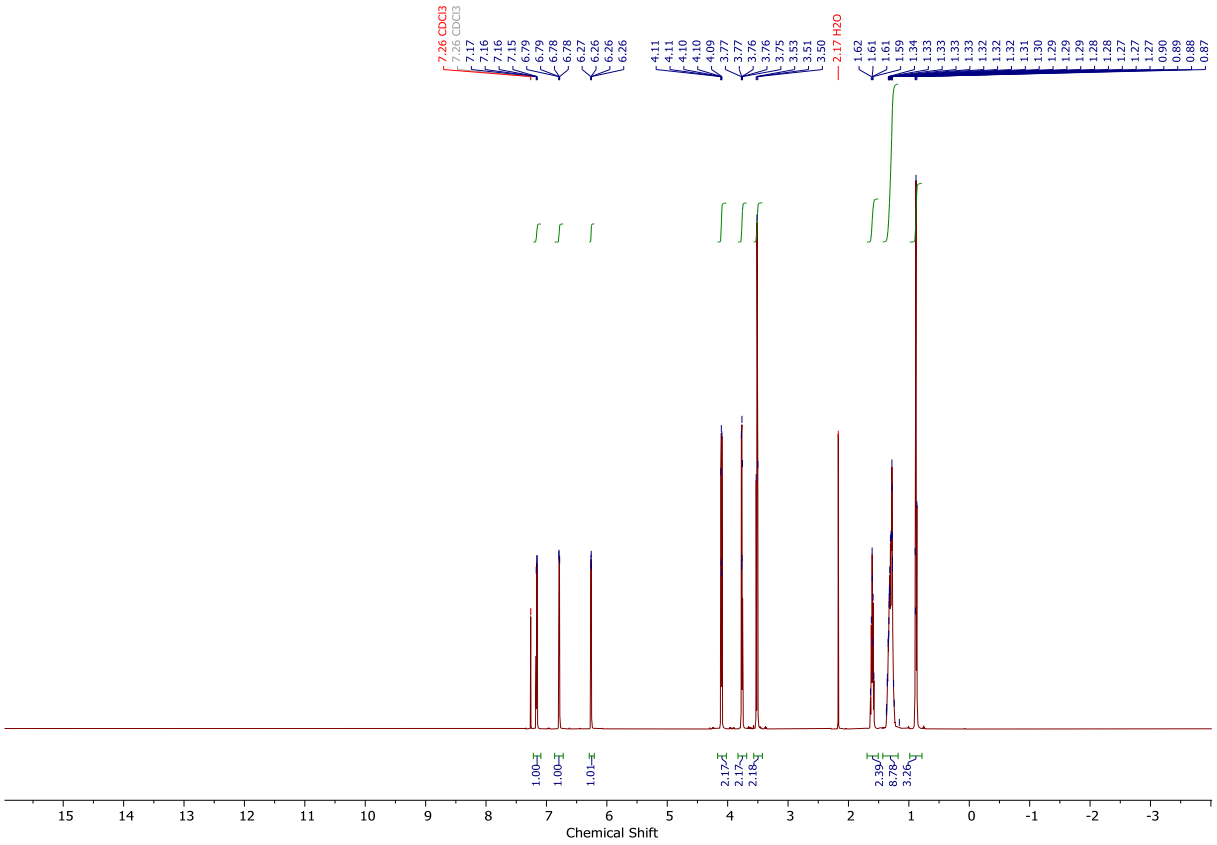
7.26 CDCl3
7.26 CDCl3
7.17
7.16
7.16
7.15
6.79
6.79
6.78
6.78
6.27
6.26
6.26
6.26
4.11
4.11
4.10
4.10
4.09
3.77
3.77
3.76
3.76
3.75
3.53
3.51
3.50
2.17 H2O
1.62
1.61
1.61
1.59
1.34
1.33
1.33
1.33
1.33
1.32
1.32
1.32
1.31
1.30
1.29
1.29
1.29
1.28
1.28
1.27
1.27
1.27
0.90
0.89
0.88
0.87
1.00
1.00
1.01
2.17
2.17
2.18
2.39
8.78
3.26
15
14
13
12
11
10
9
8
7
6
5
4
3
2
1
0
-1
-2
-3
Chemical Shift

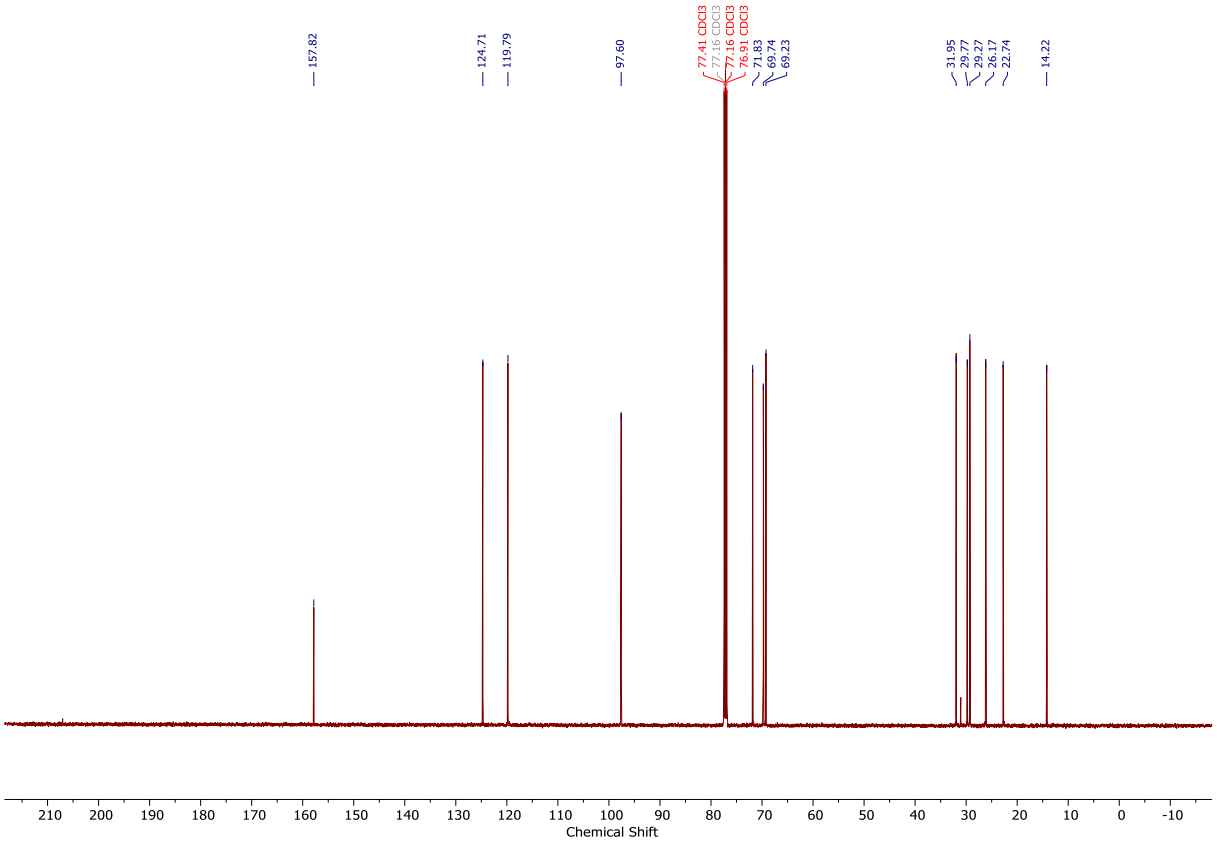
157.82
124.71
119.79
97.60
77.41 CDCl3
77.16 CDCl3
76.91 CDCl3
71.83
69.74
69.23
31.95
29.77
29.27
26.17
22.74
14.22
210 200 190 180 170 160 150 140 130 120 110 100 90 80 70 60 50 40 30 20 10 0 -10
Chemical Shift

Expanded Spectrum RT 0.16, NL 3718993, Peak [2], Target Mass 265.1233

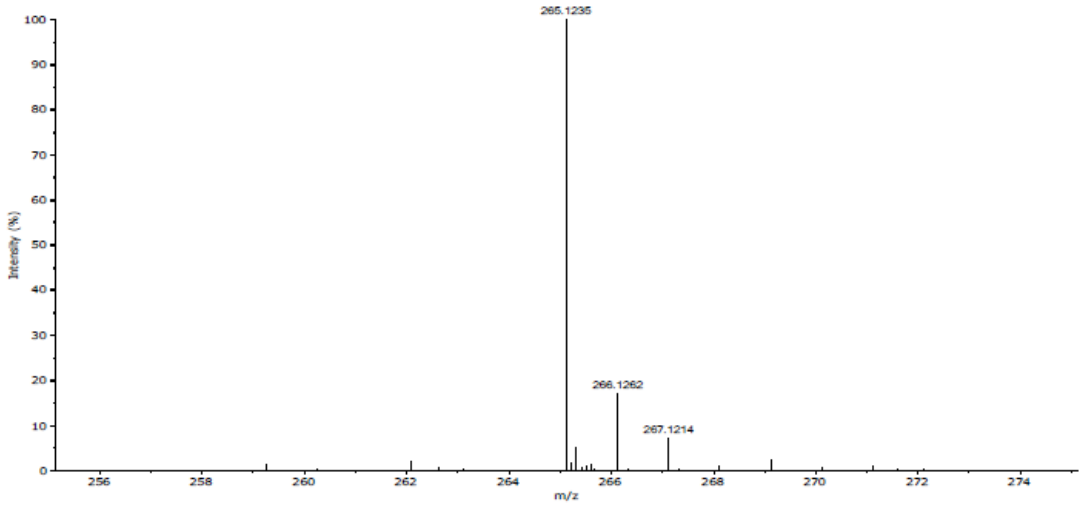

Theoretical Spectrum for C13H22O2SNa, Minimum Abundance 0.01%

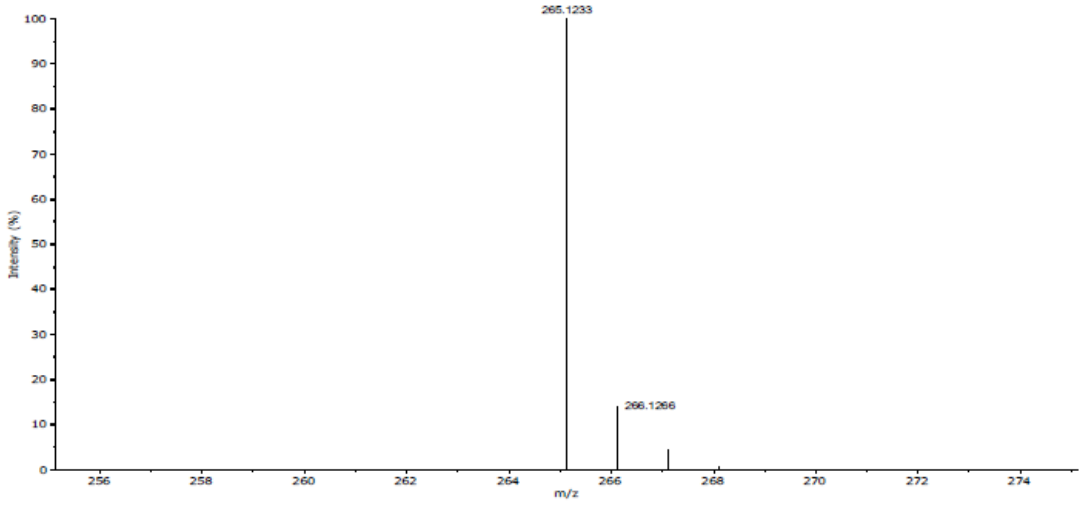

Measured Mass	Calculated Mass	Error (mDa)	Error (ppm)	Formula $[M+Na]^+$	Response
265.1235	265.1233	0.23	0.85	$C_{13}H_{22}O_2SNa$	10738098

The measured m/z value is consistent with your proposed formula for this sample.

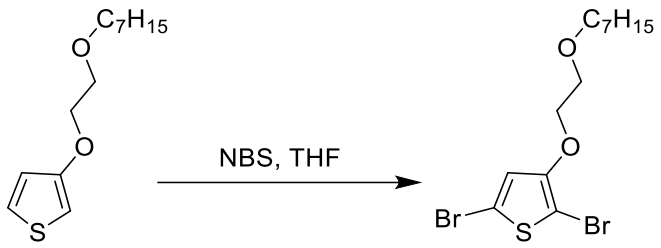

Preparation of ***2,5-dibromo-3-(2-(heptyloxy)ethoxy)thiophene***

Under N_2, 3-(2-(heptyloxy)ethoxy)thiophene (7.106 g, 29.32 mmol) was dissolved in anhydrous THF (90 mL) and cooled to 0 °C. Then, the reaction mixture was protected from light and N-Bromosuccinimide (11.5 g, 2.2 eq) was added. Then, the reaction mixture was stirred at room temperature for 2 hours, then diluted with diethyl ether (300 mL) and washed with saturated sodium bicarbonate (200 mL), water (200 mL x 2) and dried over anhydrous sodium sulphate, before being further purified by column chromatography (hexane -> hexane/diethyl ether 25/1) as a pale-yellow oil (9.8 g, 84%). ^{1}H NMR (500 MHz, $CDCl_3$) δ 6.81 (s, 1H), 4.22 – 4.07 (m, 2H), 3.77 – 3.65 (m, 2H), 3.50 (t, J = 6.7 Hz, 2H), 1.65 – 1.48 (m, 2H), 1.40 – 1.19 (m, 8H), 0.98 – 0.74 (m, 3H). ^{13}C NMR (126 MHz, CDCl3) δ 153.9, 121.7, 109.7, 91.5, 72.2, 71.9, 69.4, 32.0, 29.8, 29.3, 26.2, 22.8, 14.2. HRMS (ESI): calcd for $C_{13}H_{20}Br_2O_2SNa$, 420.9443; found 420.9438 (M+Na+, 1.2 ppm).

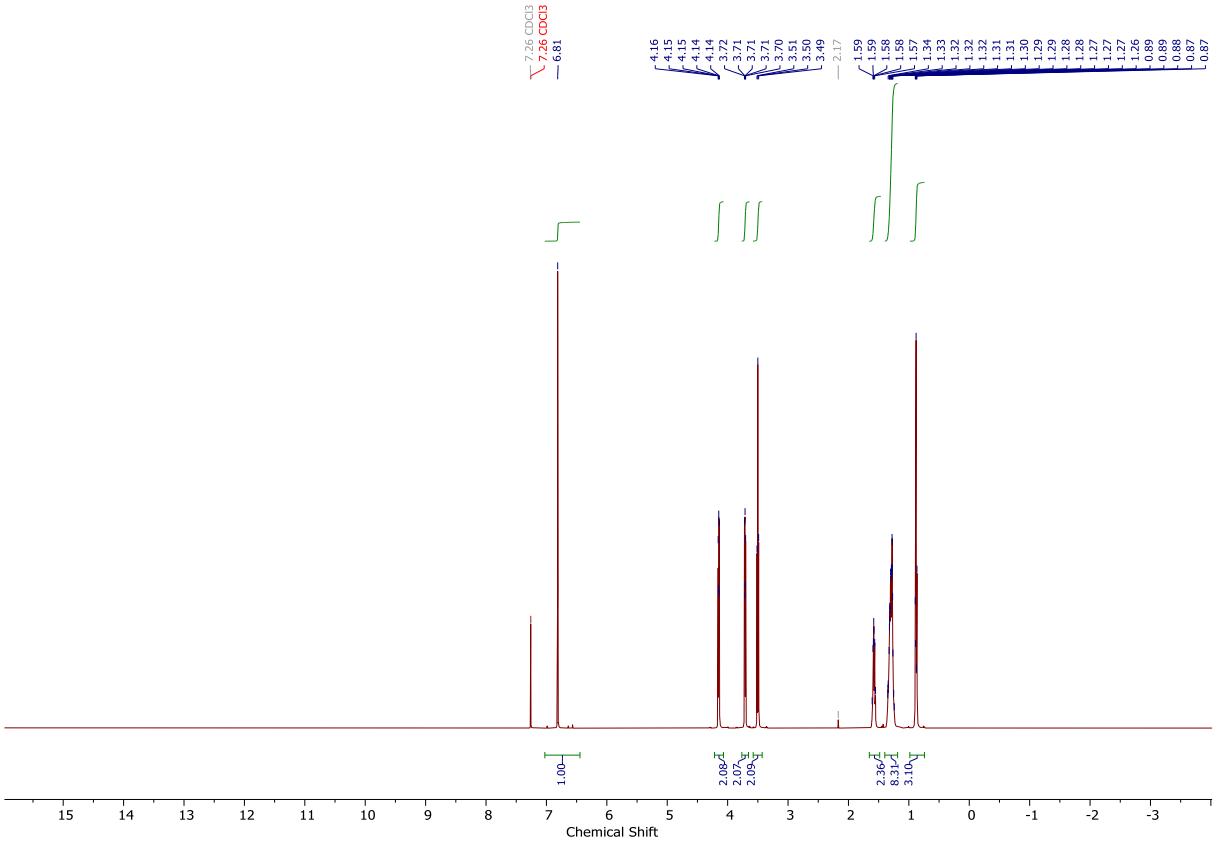
7.26 CDCl3
7.26 CDCl3
6.81
4.16
4.15
4.15
4.15
4.14
4.14
3.72
3.71
3.71
3.71
3.70
3.51
3.50
3.49
2.17
1.59
1.59
1.58
1.58
1.58
1.57
1.34
1.33
1.32
1.32
1.32
1.31
1.31
1.30
1.29
1.29
1.28
1.28
1.27
1.27
1.27
1.26
0.89
0.89
0.88
0.87
0.87
1.00
2.08
2.07
2.09
2.36
8.31
3.10
15
14
13
12
11
10
9
8
7
6
5
4
3
2
1
0
-1
-2
-3
Chemical Shift

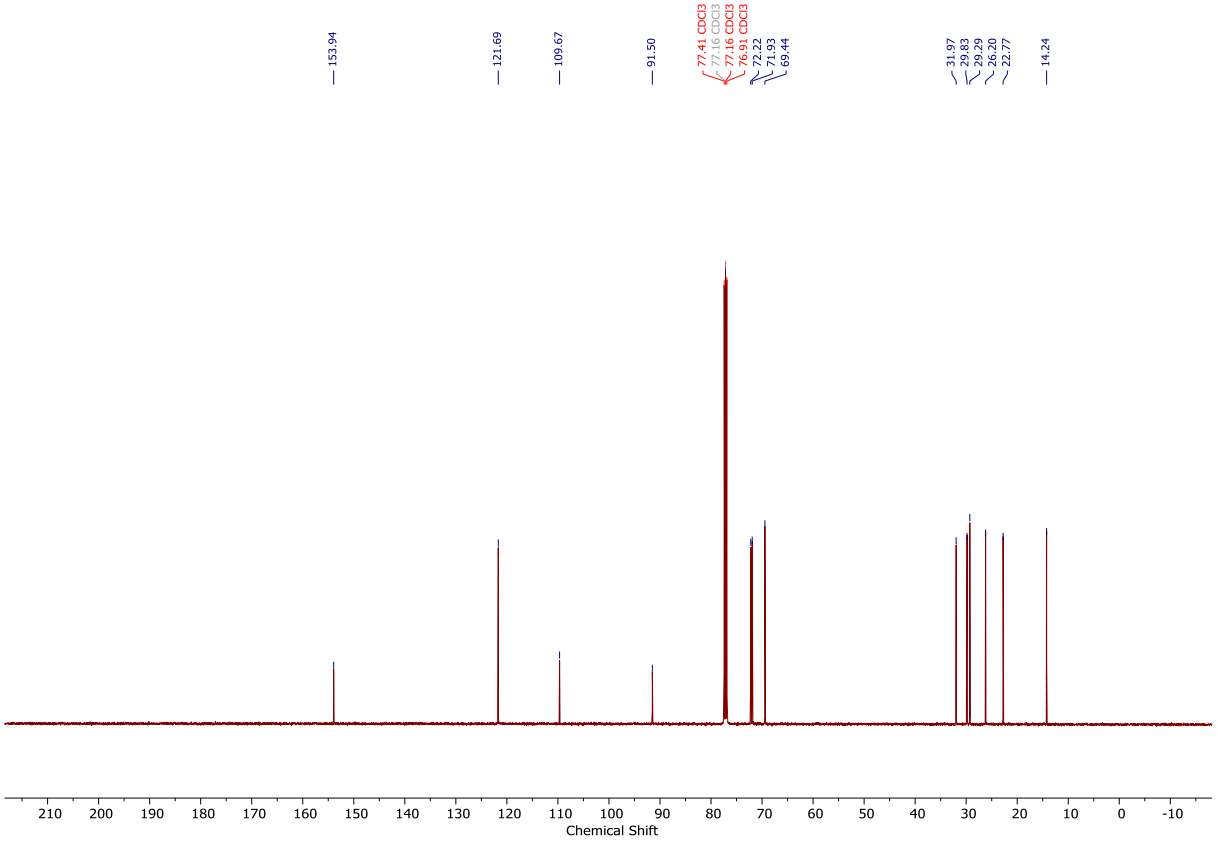
153.94
121.69
109.67
91.50
77.41 CDCl3
77.16 CDCl3
76.91 CDCl3
72.22
71.93
69.44
31.97
29.83
29.29
26.20
22.77
14.24
210
200
190
180
170
160
150
140
130
120
110
100
90
80
70
60
50
40
30
20
10
0
-10
Chemical Shift

Expanded Spectrum RT 0.18, NL 14540961, Peak [2], Target Mass 420.9443

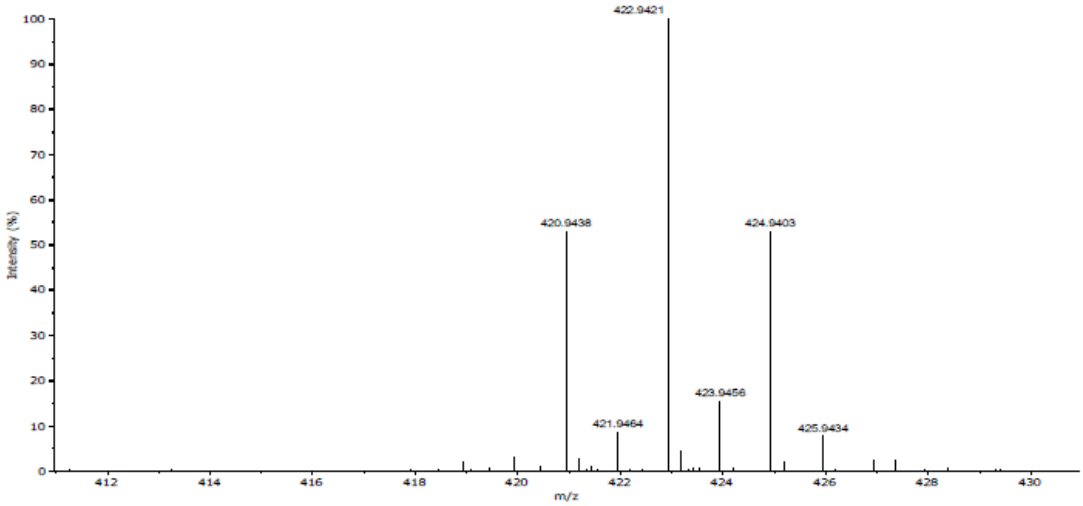

Theoretical Spectrum for C13H20Br2O2SNa, Minimum Abundance 0.01%

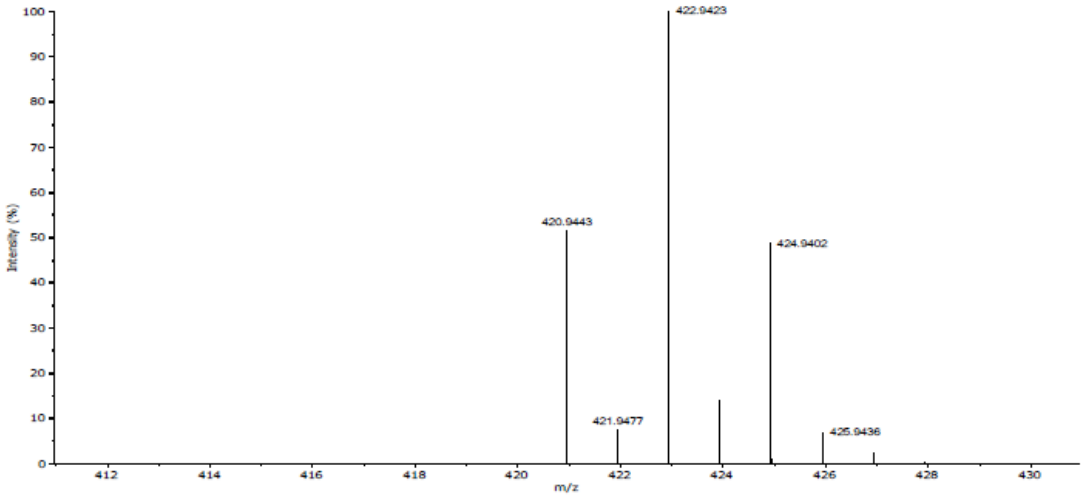

Measured Mass	Calculated Mass	Error (mDa)	Error (ppm)	Formula $[M+Na]^+$	Response
420.9438	420.9443	-0.50	-1.18	$C_{13}H_{20}Br_2O_2SNa$	30552468

The measured m/z value is consistent with your proposed formula for this sample.

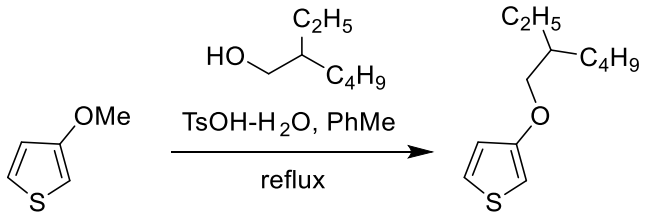

*Preparation of **3-((2-ethylhexyl)oxy)thiophene***

Under N_2, 3-methoxythiophene (5.15 g, 45.11 mmol) was dissolved in anhydrous toluene (40 mL). Then, 2-ethyl-1-hexanol (8.81 g, 67.67 mmol, 1.5 eq) was added, followed by p-toluenesulfonic acid monohydrate (858 mg, 4.51 mmol). The reaction mixture was refluxed overnight. Upon completion of reaction, the reaction mixture was diluted with diethyl ether (160 mL) and washed with saturated sodium bicarbonate solution (150 mL), water (150 mL x 2) and dried over anhydrous sodium sulphate. The product was further purified by column chromatography (hexane) as a pale-yellow oil (4.98 g, 52%). ^{1}H NMR (400 MHz, $CDCl_3$) δ 7.17 (dd, J = 5.2, 3.1 Hz, 1H), 6.76 (dd, J = 5.2, 1.5 Hz, 1H), 6.23 (dd, J = 3.2, 1.5 Hz, 1H), 3.83 (dd, J = 5.8, 1.1 Hz, 2H), 1.71 (hept, J = 6.1 Hz, 1H), 1.54 – 1.26 (m, 8H), 1.00 – 0.83 (m, 6H). ^{13}C NMR (101 MHz, $CDCl_3$) δ 158.5, 124.6, 119.8, 96.9, 72.9, 39.6, 30.7, 29.2, 24.0, 23.2, 14.2, 11.3. HRMS (ESI): calcd for $C_{12}H_{21}OS$, 213.1308; found 213.1300 (M+H+, 3.6 ppm).

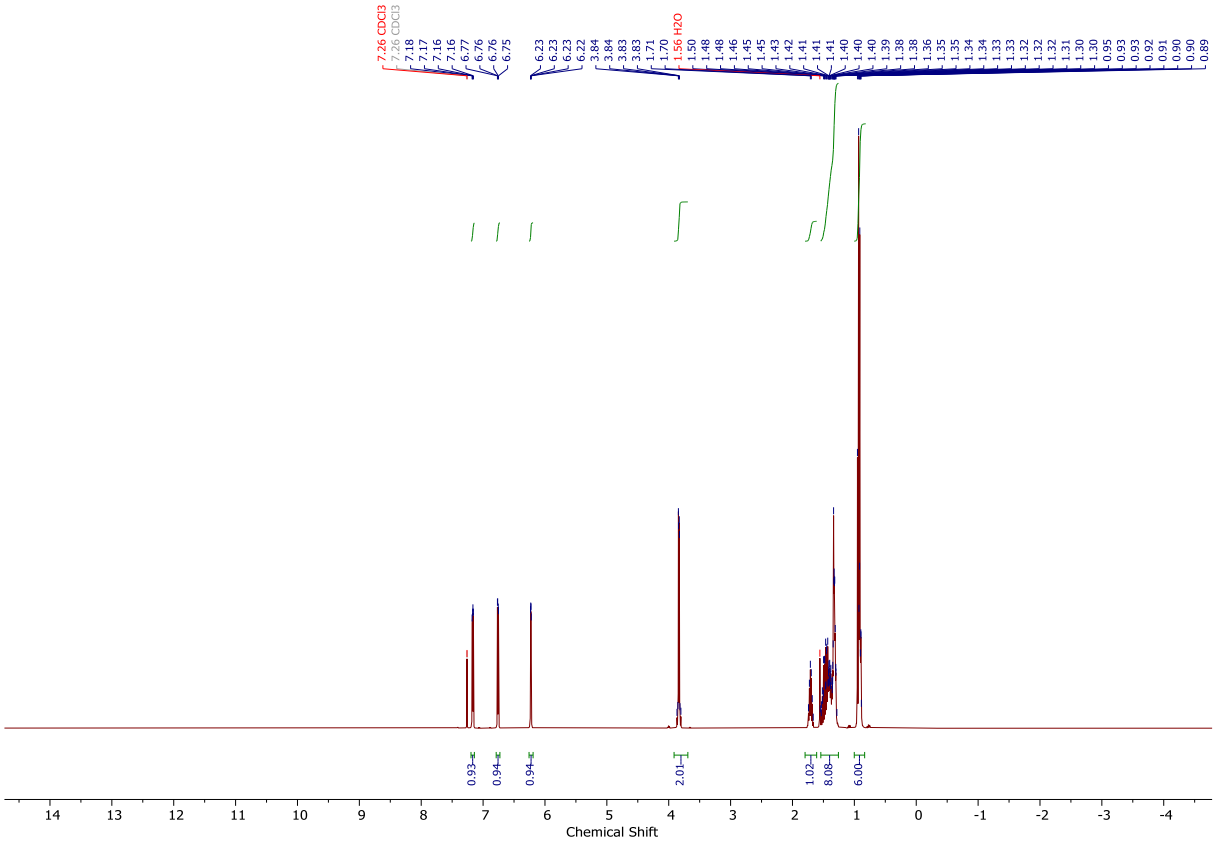
7.26 CDCl3
7.26 CDCl3
7.18
7.17
7.16
7.16
6.77
6.76
6.76
6.75
6.23
6.23
6.23
6.22
3.84
3.84
3.83
3.83
1.71
1.70
1.56 H2O
1.50
1.48
1.48
1.46
1.45
1.45
1.43
1.42
1.41
1.41
1.41
1.40
1.40
1.40
1.39
1.38
1.38
1.36
1.35
1.35
1.34
1.34
1.33
1.33
1.32
1.32
1.32
1.31
1.30
1.30
0.95
0.93
0.93
0.92
0.91
0.90
0.90
0.89
0.93
0.94
0.94
2.01
1.02
8.08
6.00
Chemical Shift

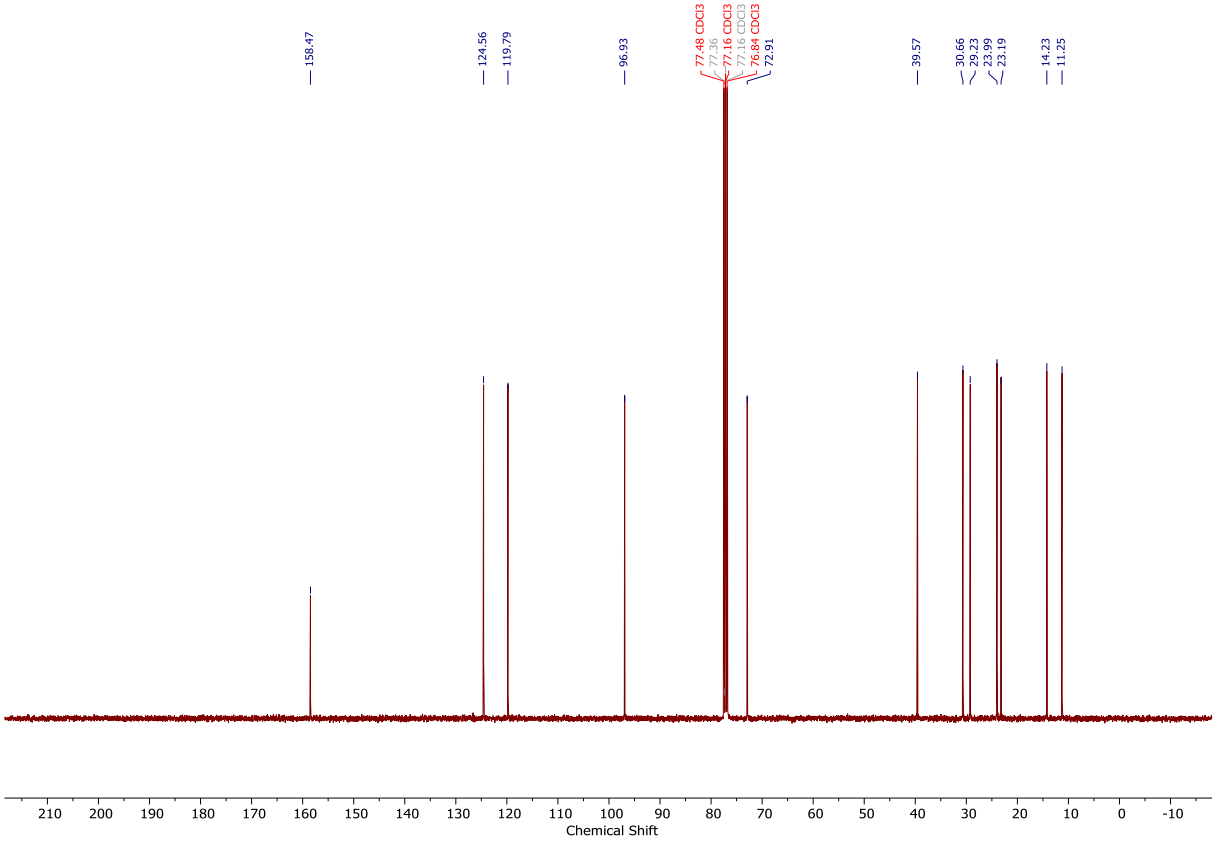
158.47
124.56
119.79
96.93
77.48 CDCl3
77.36
77.16 CDCl3
77.16 CDCl3
76.84 CDCl3
72.91
39.57
30.66
29.23
23.99
23.19
14.23
11.25
Chemical Shift

Expanded Spectrum RT 0.13, NL 434530, Peak [1], Target Mass 213.1308

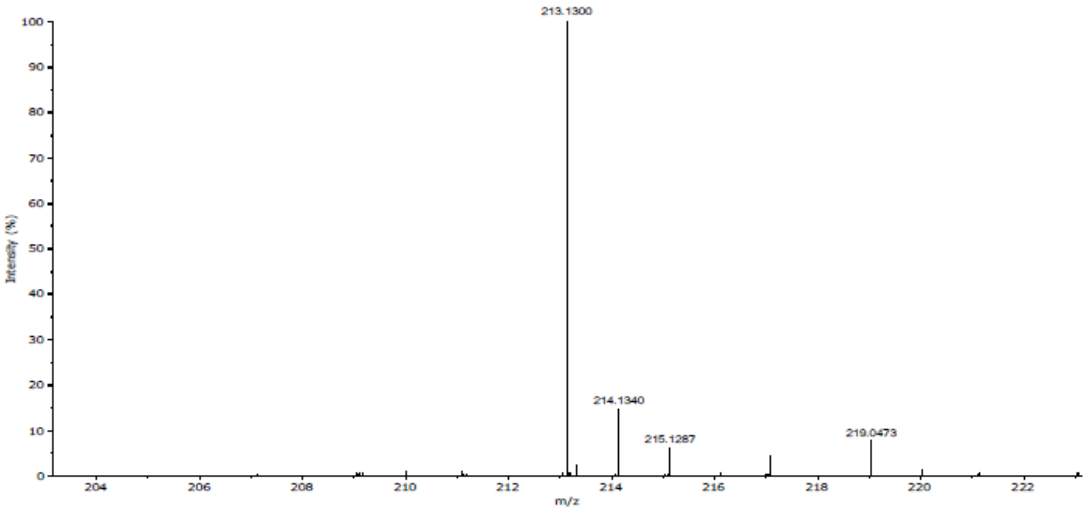

Theoretical Spectrum for C12H21OS, Minimum Abundance 0.01%

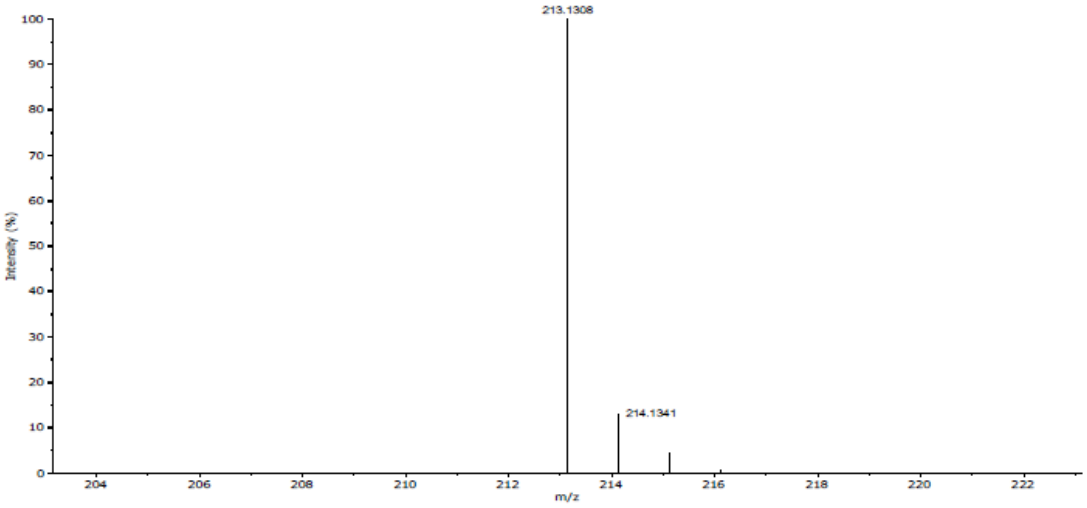

Measured Mass	Calculated Mass	Error (mDa)	Error (ppm)	Formula $[M+H]^+$	Response
213.1300	213.1308	-0.76	-3.58	$C_{12}H_{21}OS$	815792

The measured m/z value is consistent with your proposed formula for this sample.

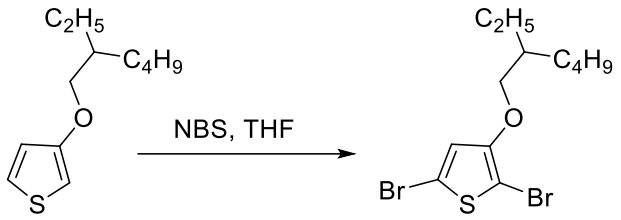

Preparation of ***2,5-dibromo-3-((2-ethylhexyl)oxy)thiophene***

Under N2, 3-((2-ethylhexyl)oxy)thiophene (4.247 g, 20.00 mmol) was dissolved in anhydrous THF (70 mL) and cooled to 0 °C. Then, the reaction mixture was protected from light and N-Bromosuccinimide (7.83 g, 2.2 eq) was added. Then, the reaction mixture was stirred at room temperature for 2 hours, then diluted with diethyl ether (300 mL) and washed with saturated sodium bicarbonate (200 mL), water (200 mL x 2) and dried over anhydrous sodium sulphate, before being further purified by column chromatography (hexane) as a pale-yellow oil (5.19 g, 70%). ^{1}H NMR (400 MHz, $CDCl_3$) δ 6.76 (s, 1H), 3.88 (d, J = 5.8 Hz, 2H), 1.68 (hept, J = 6.1 Hz, 1H), 1.55 – 1.27 (m, 8H), 1.02 – 0.84 (m, 6H). ^{13}C NMR (101 MHz, $CDCl_3$) δ 154.2, 121.0, 109.7, 90.5, 75.2, 39.7, 30.4, 29.1, 23.8, 23.2, 15.4, 14.2, 11.2. HRMS (ESI): calcd for $C_{12}H_{19}Br_2OS$, 365.9518; found 365.9514 (M+H+, 1.0 ppm).

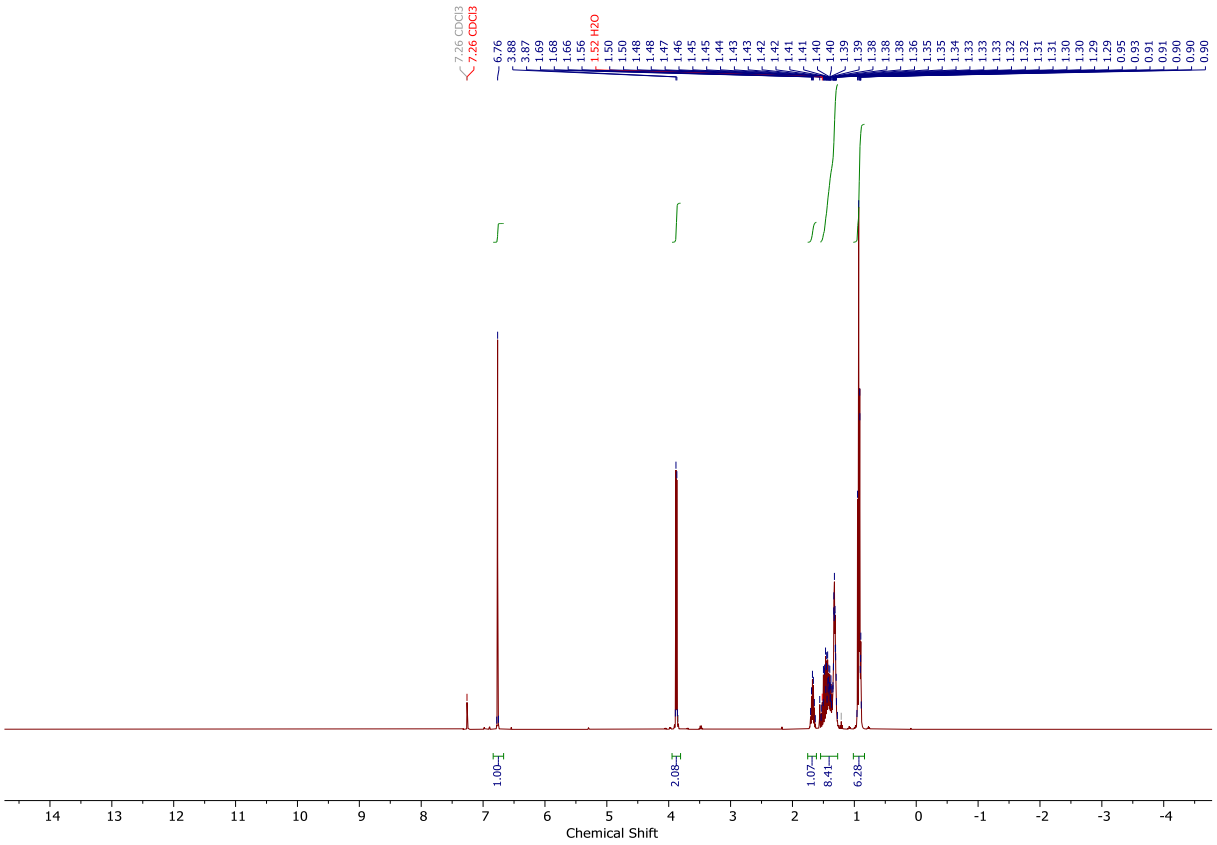
7.26 CDCl3
7.26 CDCl3
6.76
1.52 H2O
1.00
2.08
1.07
8.41
6.28
Chemical Shift

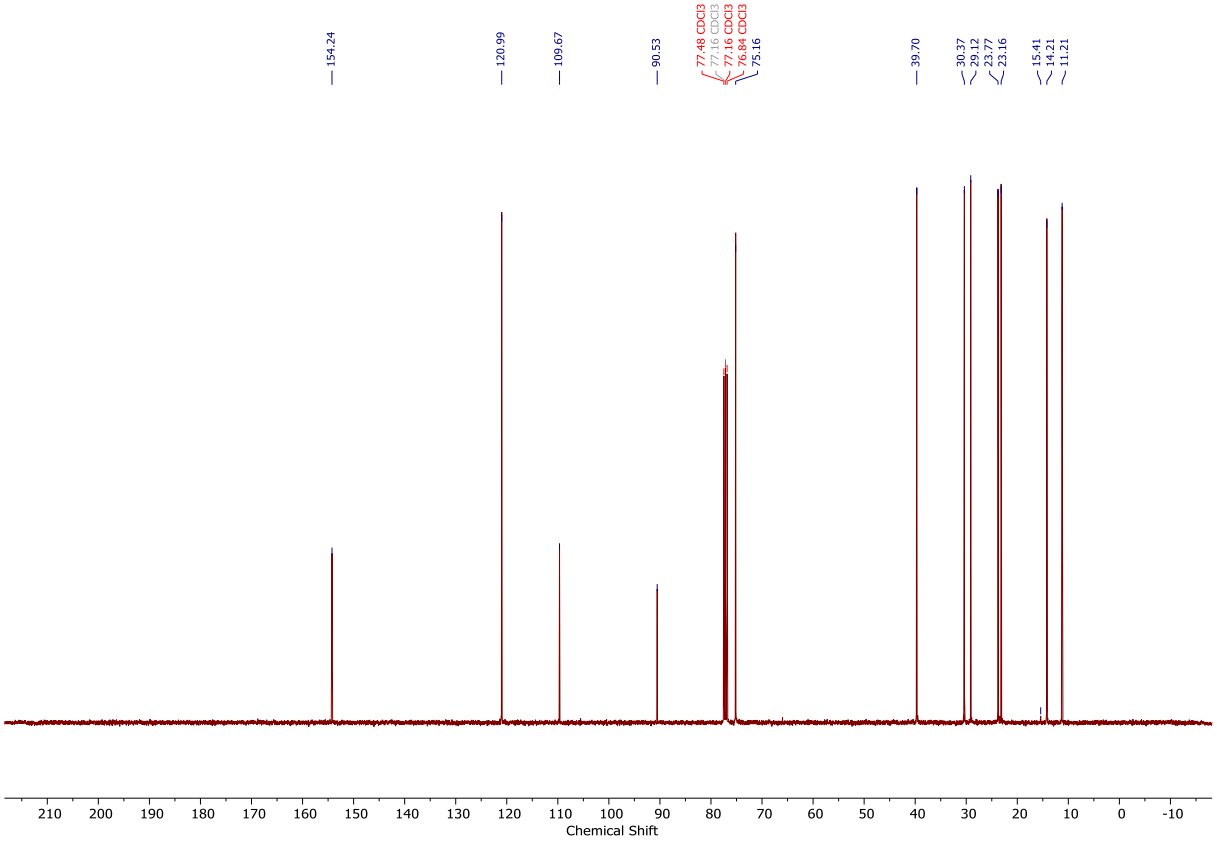
154.24
120.99
109.67
90.53
77.48 CDCl3
77.16 CDCl3
77.16 CDCl3
76.84 CDCl3
75.16
39.70
30.37
29.12
23.77
23.16
15.41
14.21
11.21
Chemical Shift

Expanded Spectrum RT 0.08, NL 892318, Peak [1], Target Mass 368.9518

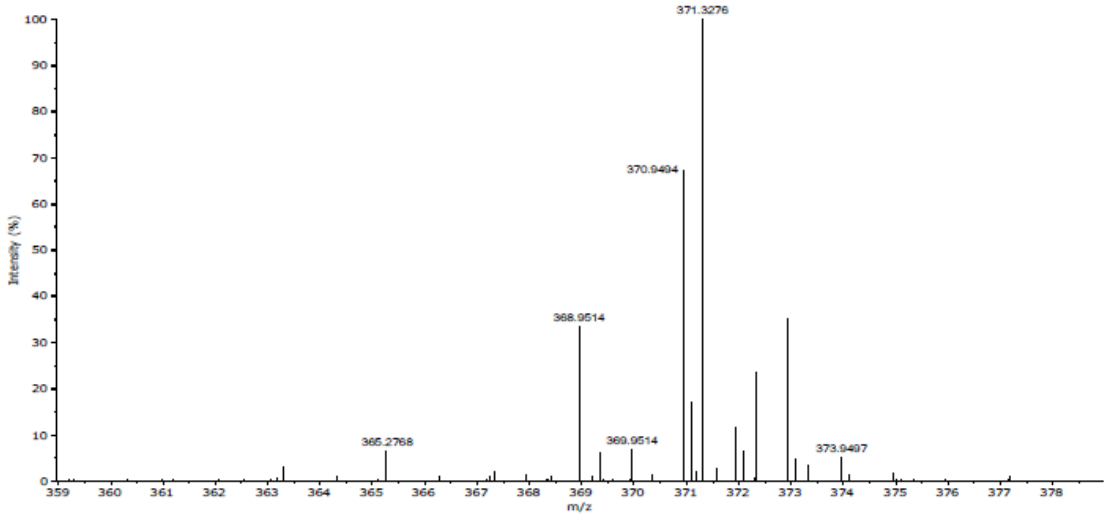

Theoretical Spectrum for C12H19Br2OS, Minimum Abundance 0.01%

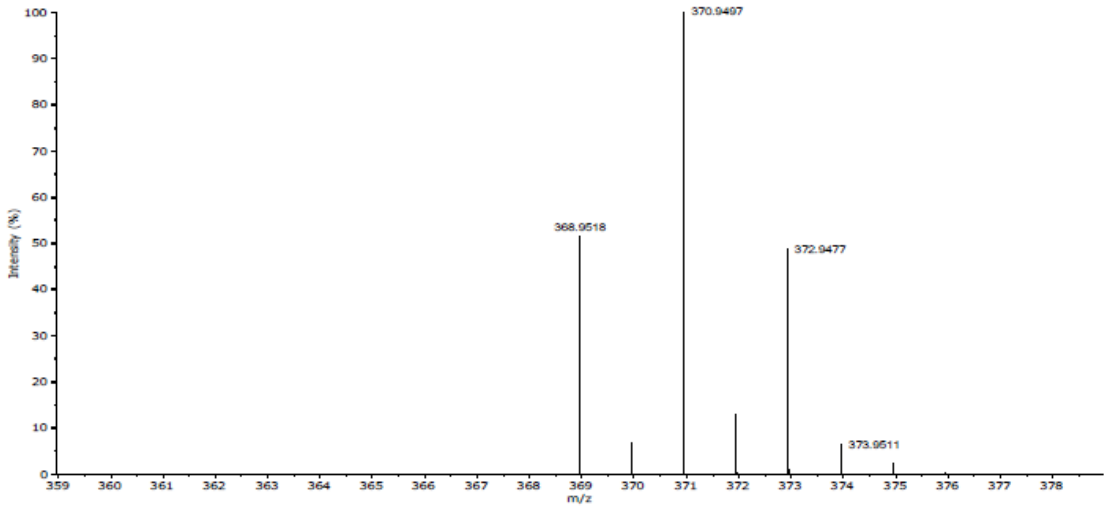

Measured Mass	Calculated Mass	Error (mDa)	Error (ppm)	Formula $[M+H]^+$	Response
368.9514	368.9518	-0.39	-1.04	$C_{12}H_{19}Br_2OS$	630964

The measured m/z value is consistent with your proposed formula for this sample.

General procedure A for the synthesis of H/Br terminated poly(3-alkoxythiophene):

2,5-dibromo-3-(decyloxy)thiophene was evacuated under vacuum for 30 minutes and dissolved in anhydrous THF to a concentration of 0.1M. The reaction mixture was cooled to 0 ºC and isopropyl magnesium solution (0.90 eq) was added dropwise. The reaction mixture was stirred at 0 ºC for another 10 minutes, before being left at room temperature for another 50 minutes. Then, an anhydrous solution of [1,3-Bis(2,6-diisopropylphenyl)imidazol-2-ylidene]triphenylphosphine Nickel(II) dichloride ($Ni(IPr)(PPh_3)Cl_2$ in THF (0.88 mol%) was injected at once. The reaction mixture was stirred at room temperature for 30 minutes, where a dark blue viscous liquid was formed. The reaction mixture was precipitated in methanol and filtered to yield the polymer product, which was further purified by Soxhlet extraction (acetone -> hexane -> chloroform) to yield the pure polymer.

Example Procedure: Preparation of ***poly(3-decoxythiophene) (P3DOT) H/Br***

Under N_2, 2,5-dibromo-3-(decyloxy) thiophene (1820 mg, 4.57 mmol) was dissolved in anhydrous THF (45.7 mL). Then, the solution was cooled to 0 ºC and $^{i}PrMgCl$ (2.06 mL, 2.0M, 0.9 eq) was added. The reaction mixture was cooled to 0 ºC for 10 minutes, before being left at room temperature for another 50 minutes. After which, an anhydrous solution of $Ni(IPr)(PPh_3)Cl_2$ (2.00 mL, 20 mg/mL in THF) was added. The reaction mixture was stirred at room temperature for 30 minutes, before being precipitated in methanol. The crude polymer was filtered and further purified by Soxhlet extraction in acetone (4 hours), hexane (4 hours) and finally extracted in chloroform. The chloroform fraction was concentrated in vacuo and precipitated once more in methanol to yield a dark blue solid (825 mg, 74%). ^1H NMR (400 MHz, $CDCl_3$) ^1H NMR (400 MHz,

$CDCl_3$) δ 6.92 (s, 1H), 4.16 (s, 2H), 1.89 (s, 2H), 1.59 (s, 2H), 1.27 (s, 12H), 0.86 (s, 3H). GPC (PhCl): M_n = 15.9 kDa, M_w = 20.9 kDa.

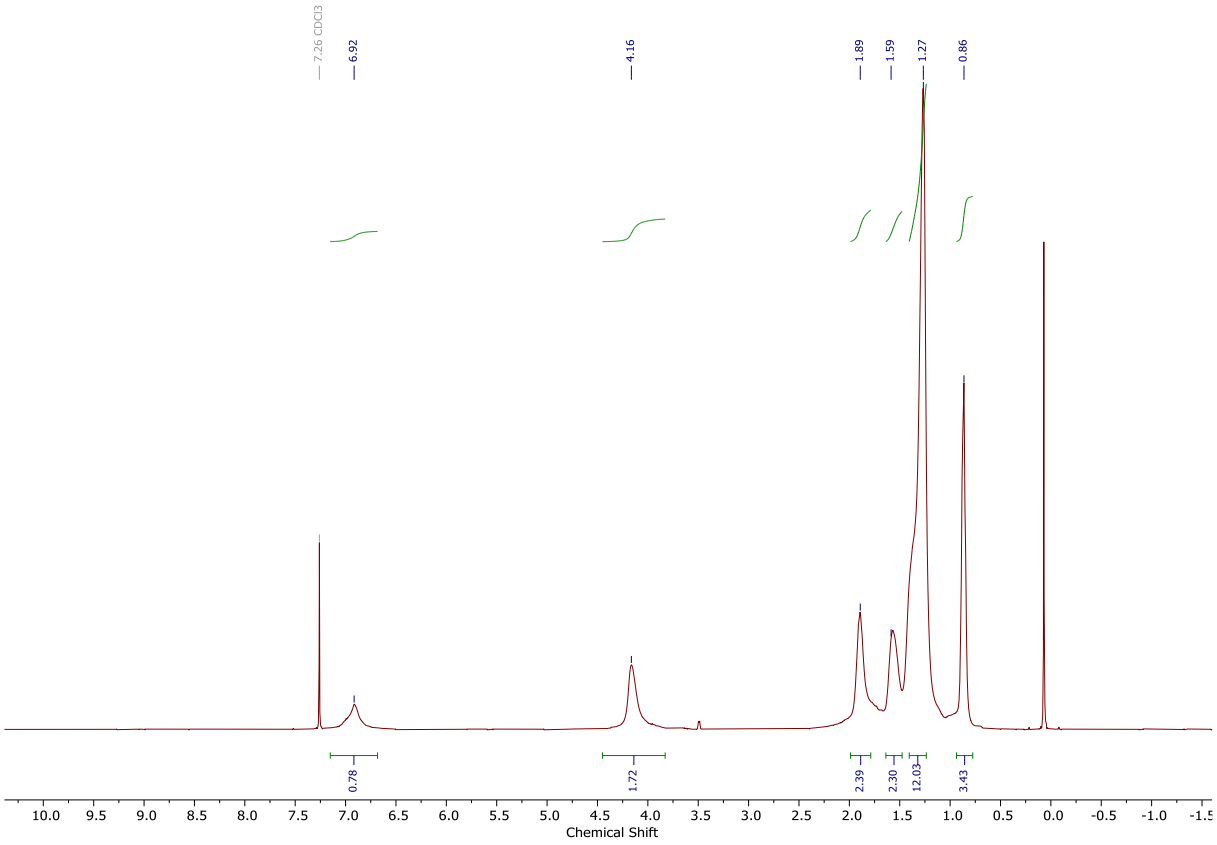

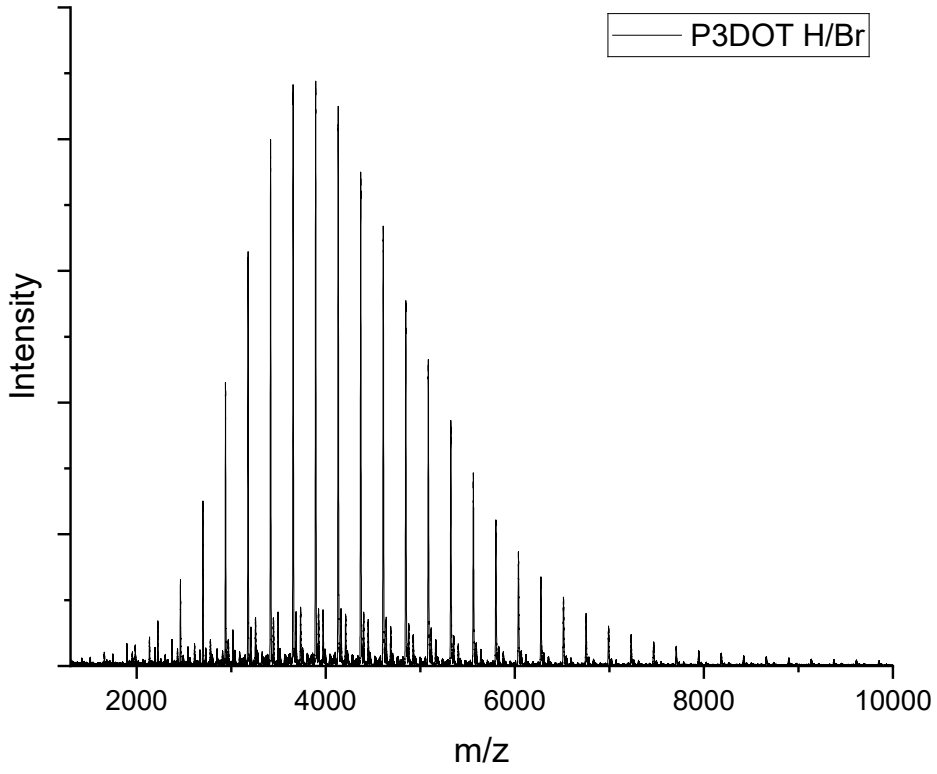

Molecular Weight Averages

Peak	Mp (g/mol)	Mn (g/mol)	Mw (g/mol)	Mz (g/mol)	Mz+1 (g/mol)	Mv (g/mol)
Peak 1	19212	15874	20895	25723	30872	20202

PD
1.316

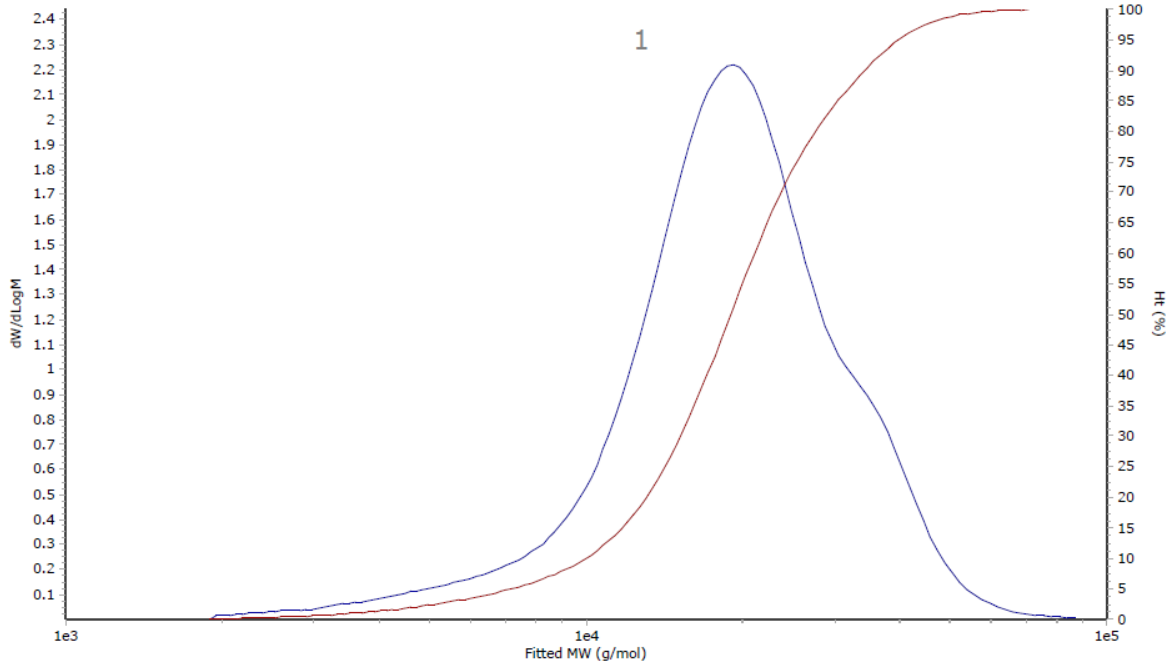
1
dW/dLogM
HL (%)
Fitted MW (g/mol)
1e3
1e4
1e5

Preparation of ***poly(3-alkoxythiophene)-G1C7 H/Br***

2,5-dibromo-3-(2-(heptyloxy)ethoxy)thiophene (1130 mg, 2.82 mmol), anhydrous THF (28.2 mL), iPrMgCl (1.27 mL, 2.0M, 0.9 eq) and Ni(IPr)(PPh3)Cl2 (0.99 mL, 20 mg/mL in THF) was used to polymerize P3AOT-G_1C_7 following General Procedure A. A dark blue solid (321 mg, 48%) was collected as product. ^{1}H NMR (400 MHz, $CDCl_3$) δ 6.95 (s, 1H), 4.32 (s, 2H), 4.02 – 3.74 (m, 2H), 3.59 (m, 2H), 1.75 – 1.55 (m, 2H), 1.53 – 1.11 (m, 8H), 0.84 (t, J = 7.2 Hz, 3H). GPC (PhCl): M_n = 12.7 kDa, M_w = 14.9 kDa

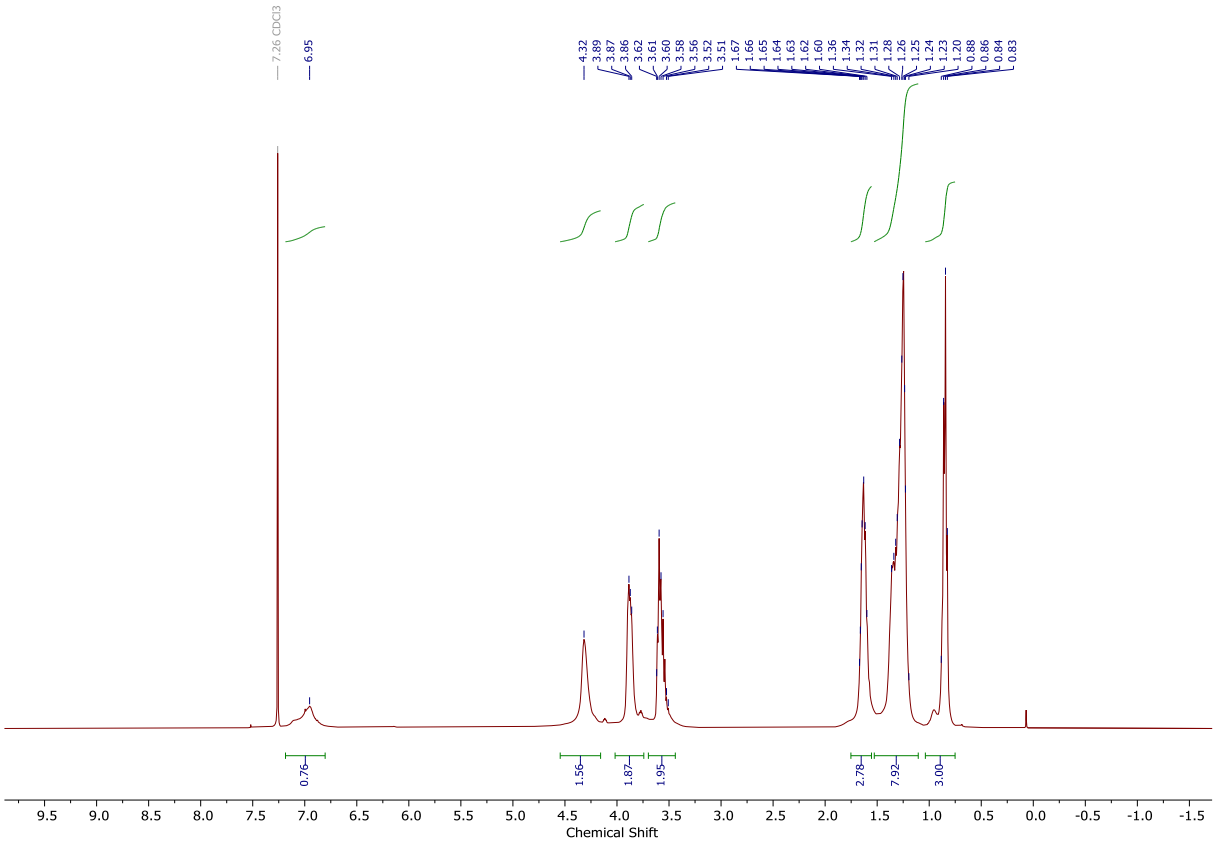

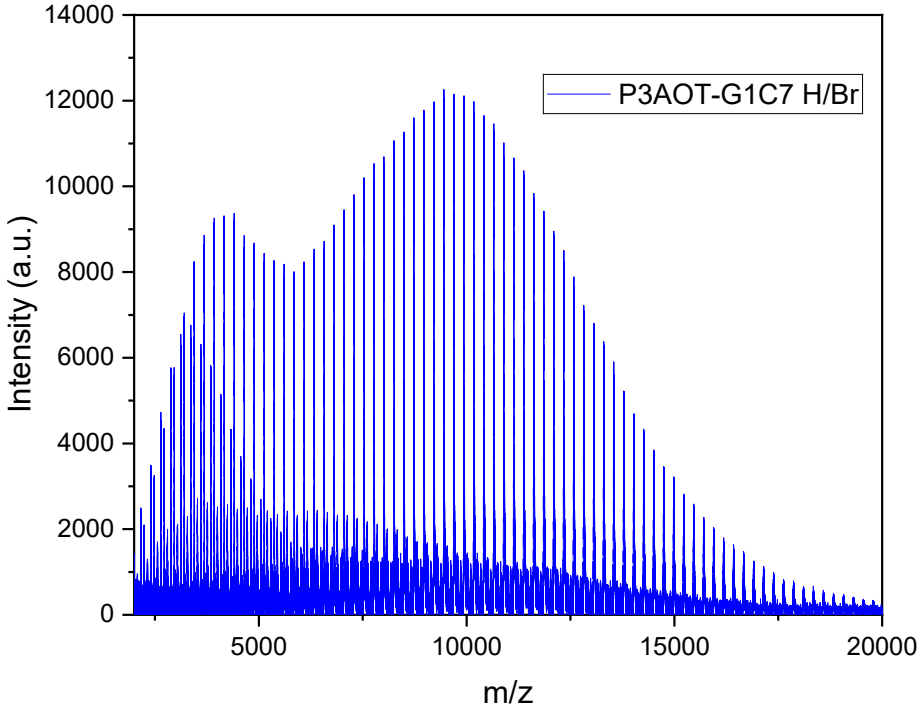

Molecular Weight Averages

Peak	Mp (g/mol)	Mn (g/mol)	Mw (g/mol)	Mz (g/mol)	Mz+1 (g/mol)	Mv (g/mol)
Peak 1	14542	12744	14897	17249	20194	14575

PD
1.169

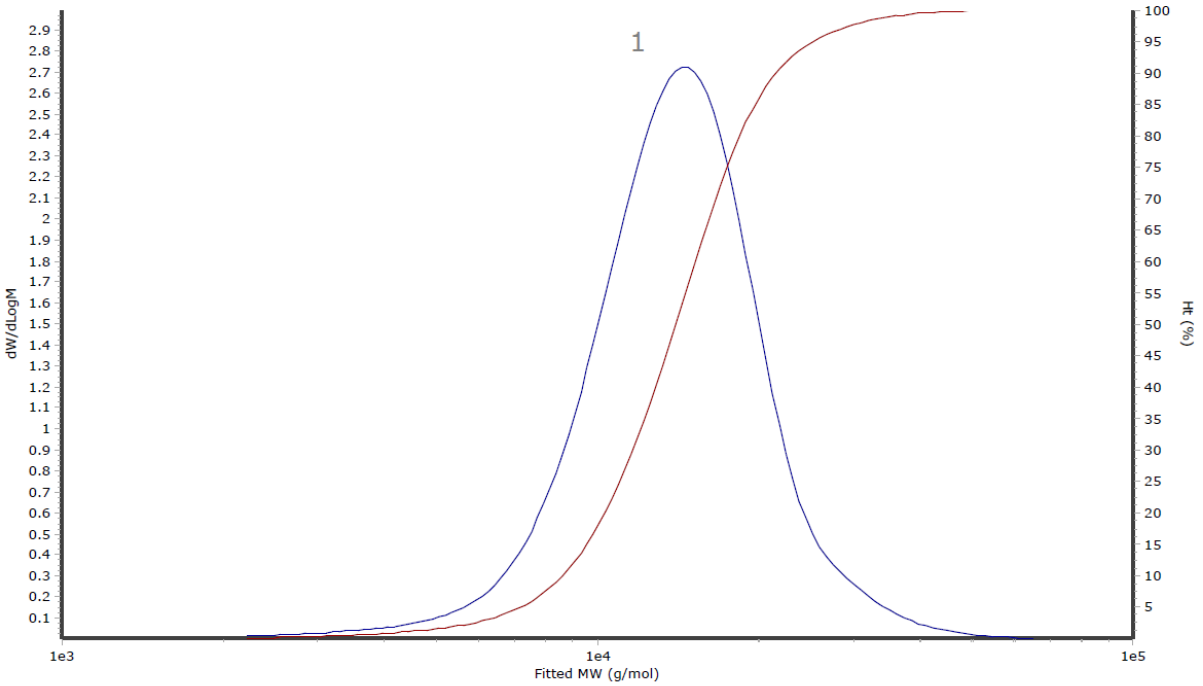

Preparation of ***poly(3-alkoxythiophene)-C2C6 H/Br***

2,5-dibromo-3-((2-ethylhexyl)oxy)thiophene (1112 mg, 3.00 mmol), anhydrous THF (30.0 mL), ^{i}PrMgCl (1.35 mL, 2.0M, 0.9 eq) and Ni(IPr)(PPh_3)Cl_2 (1.31 mL, 20 mg/mL in THF) was used to polymerize P3AOT-C_2C_6 H/Br following General Procedure A. A dark blue solid was collected as product. (325 mg, 52%). ^{1}H NMR (400 MHz, $CDCl_3$) δ 6.86 (s, 1H), 4.04 (s, 2H), 2.00 – 1.08 (m, 9H), 1.08 – 0.72 (m, 6H). GPC (PhCl): M_n = 16.7 kDa, M_w = 19.5 kDa.

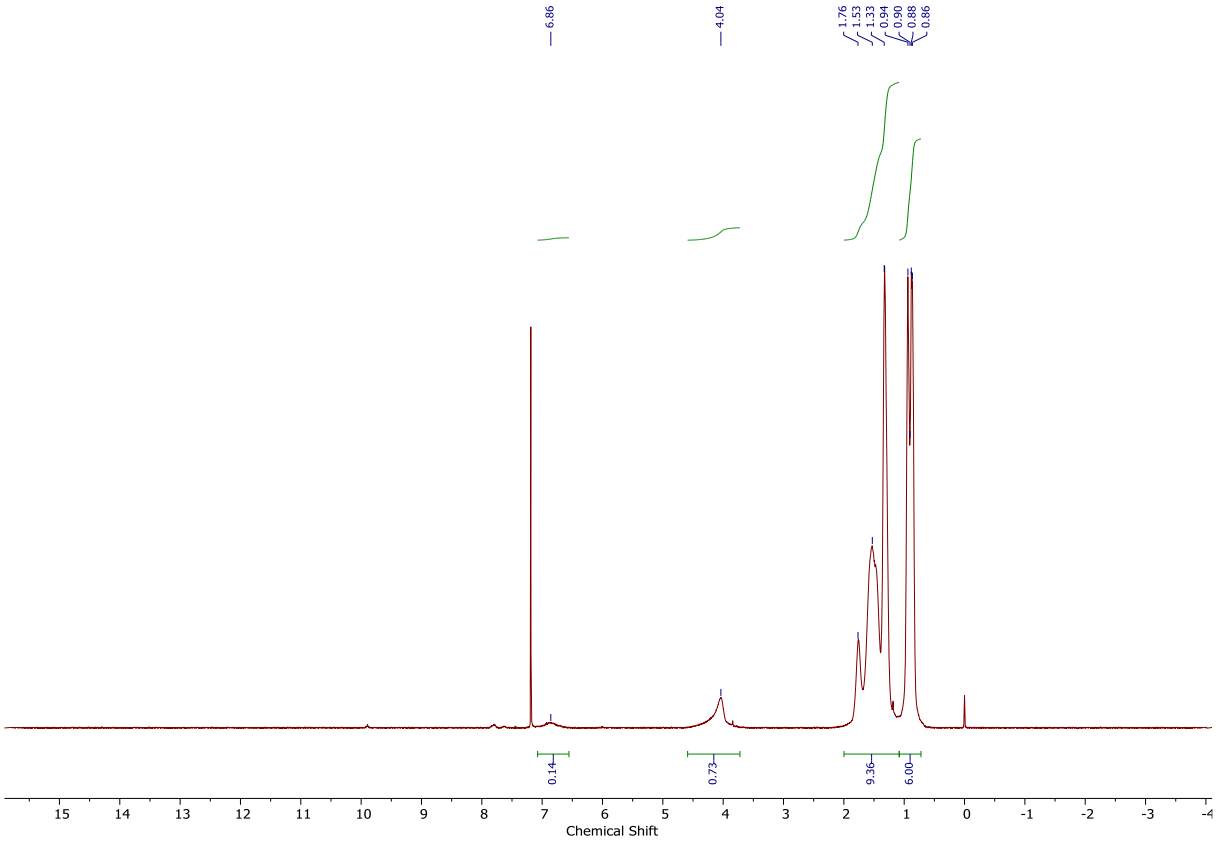

Molecular Weight Averages

Peak	Mp (g/mol)	Mn (g/mol)	Mw (g/mol)	Mz (g/mol)	Mz+1 (g/mol)	Mv (g/mol)
Peak 1	21842	16683	19473	21800	23878	19108

PD
1.167

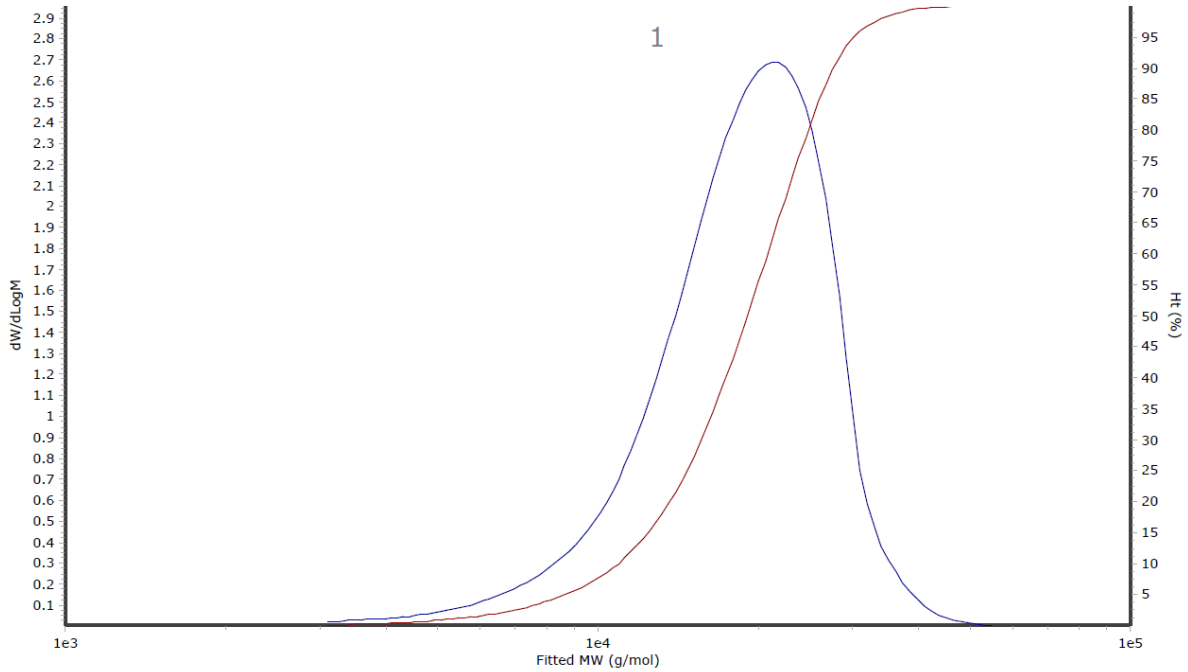

General procedure B for the synthesis of H/CHO terminated poly(3-alkoxythiophene)

Example Procedure: Preparation of ***poly(3-decoxythiophene) (P3DOT) H/CHO***

Reaction and workup P3DOT H/Br (800 mg, 0.053 mmol), (4-formylphenyl) boronic acid (160 mg, 1.06 mmol, 20 eq), Pd-G_3-P^tBu_3 (45.76 mg, 0.080 mmol, 1.5 eq) and anhydrous potassium phosphate (900 mg, 4.24 mmol, 80 eq) was dissolved in degassed THF (80 mL) and water (1.60 mL). The reaction mixture was warmed to reflux overnight, then precipitated and further purified by Soxhlet extraction (methanol -> acetone -> chloroform). The extractant from chloroform is concentrated in vacuo to about 150 mL in volume.

Palladium scavenging Sodium diethyldithiocarbamate (1.50 g) was dissolved in water (150 mL) and added to the chloroform extractant. Then, the biphasic mixture is stirred to reflux for 24 hours and cooled to room temperature. The layers are separated and the organic layer washed with water twice (150 mL x 2). Then, more solution of sodium diethyldithiocarbamate (1.50 g) in water (150 mL) was added to the chloroform extractant and the Pd scavenging process was repeated for another two times, before the cleaned organic layer was finally concentrated and precipitated in methanol, then purified further by Soxhlet extraction with methanol overnight to remove sodium diethyldithiocarbamate remaining in the organic phase. The product was finally extracted with chloroform, concentrated and precipitated in methanol to yield the cleaned P3DOT H/CHO solid (783 mg, 98%). ^{1}H NMR (400 MHz, $CDCl_3$) δ 9.84 (t, *J* = 6.9 Hz, 1H), 6.91 (s, 53H), 4.17 (s, 128H), 1.89 (d, *J* = 13.0 Hz, 123H), 1.54 – 1.26 (m, 768H), 0.87 (dt, *J* = 7.2, 3.5 Hz, 163H).

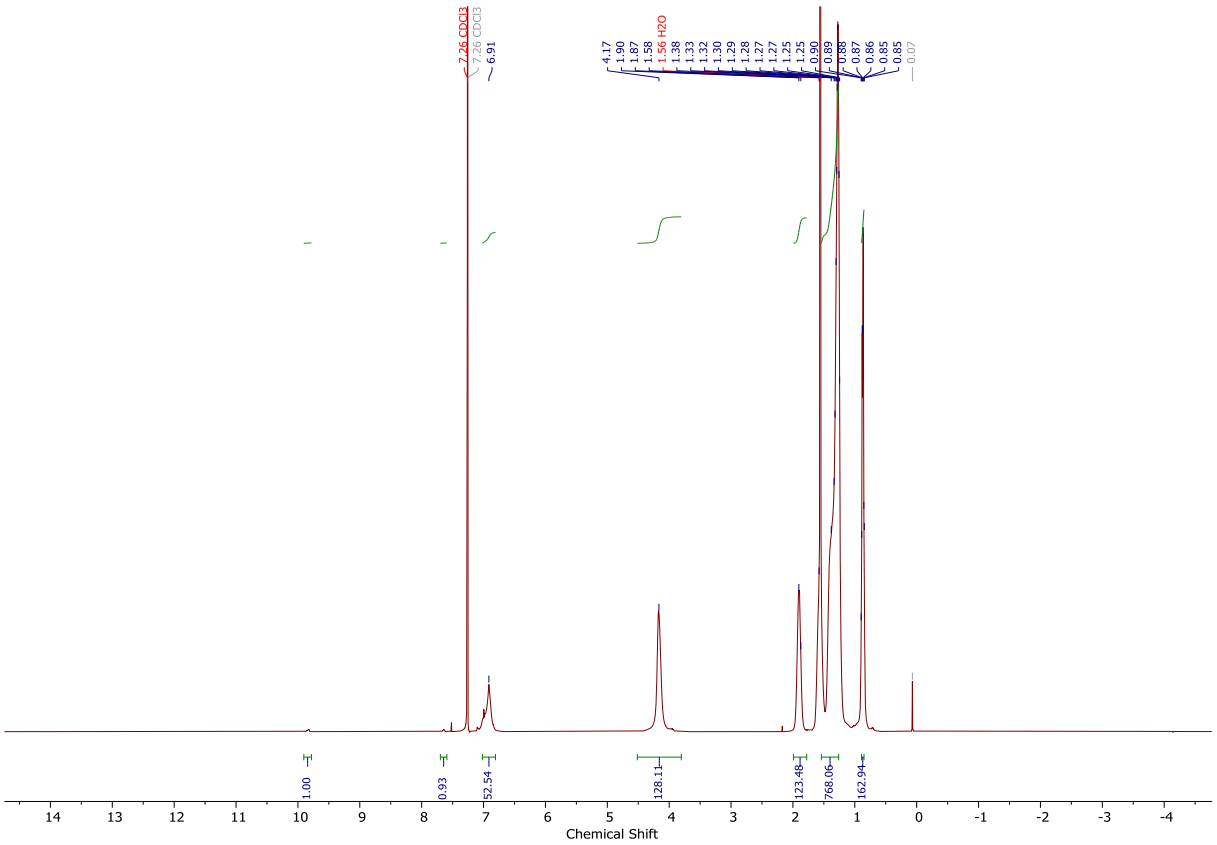
7.26 CDCl3
7.26 CDCl3
6.91
4.17
1.90
1.87
1.58
1.56 H2O
1.38
1.33
1.32
1.30
1.29
1.28
1.27
1.27
1.25
1.25
0.90
0.89
0.88
0.87
0.86
0.85
0.85
0.07
1.00
0.93
52.54
128.11
123.48
768.06
162.94
14 13 12 11 10 9 8 7 6 5 4 3 2 1 0 -1 -2 -3 -4
Chemical Shift

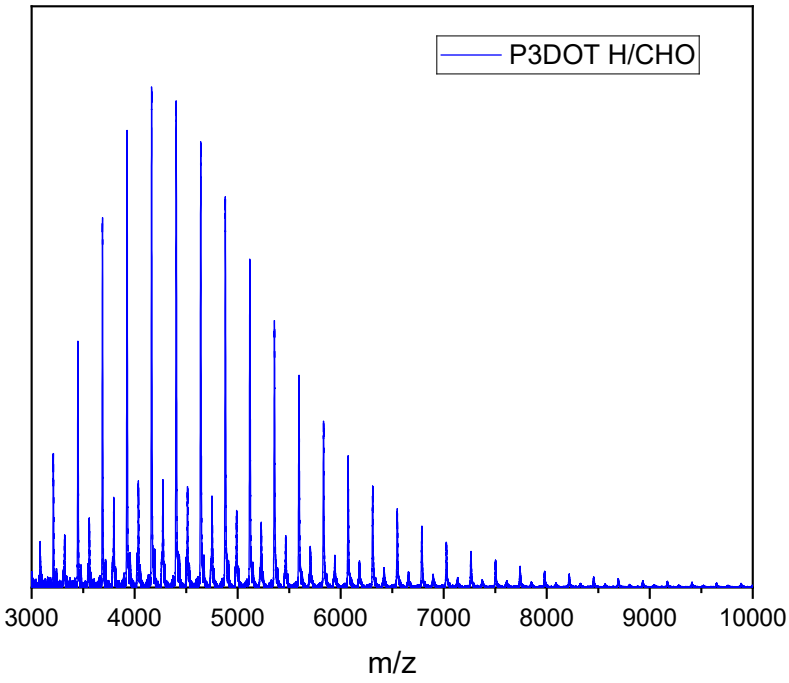
P3DOT H/CHO
3000 4000 5000 6000 7000 8000 9000 10000
m/z

Molecular Weight Averages

Peak	Mp (g/mol)	Mn (g/mol)	Mw (g/mol)	Mz (g/mol)	Mz+1 (g/mol)	Mv (g/mol)
Peak 1	19486	15087	19674	23467	26762	19083

PD
1.304

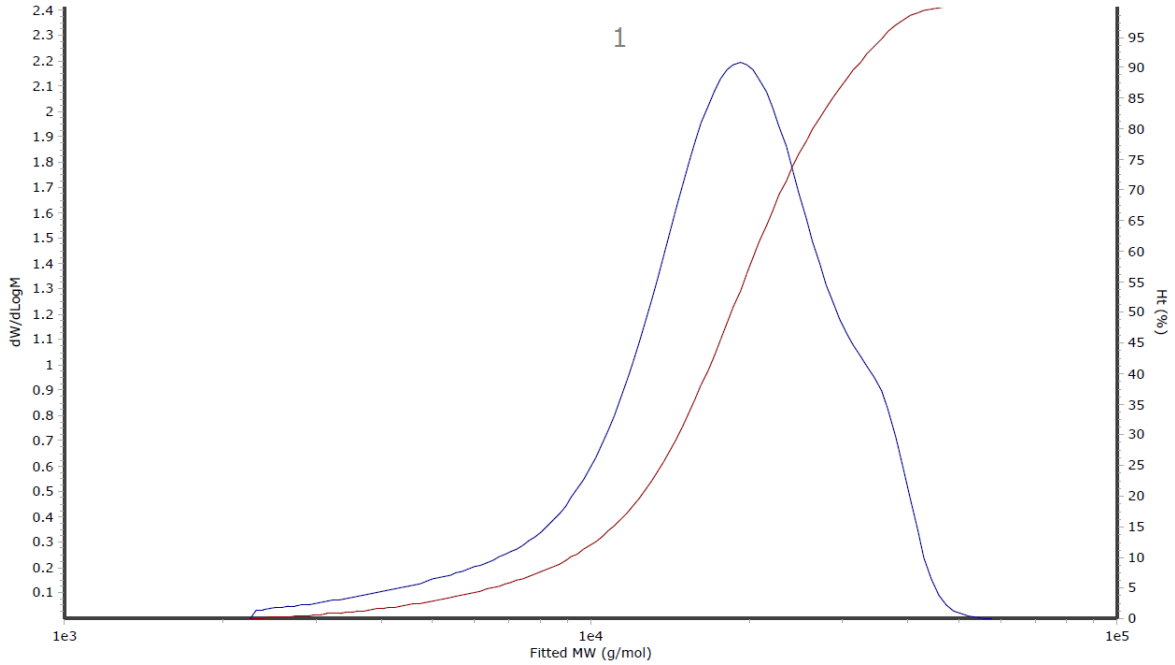

Preparation of ***poly(3-alkoxythiophene)-G1C7 H/CHO***

P3AOT G_1C_7 (305 mg, 0.024 mmol), (4-formylphenyl) boronic acid (71.97 mg, 0.48 mmol, 20 eq), Pd-G_3-P^{t}Bu$_3$ (20.59 mg, 0.036 mmol, 1.5 eq), anhydrous potassium phosphate (408 mg, 1.92 mmol, 80 eq), degassed THF (38 mL) and water (0.80 mL) was used to prepare P3AOT G_1C_7 H/CHO following General Procedure B. P3AOT-G_1C_7 H/CHO (300 mg, 98%) was yielded as a dark blue solid. ^{1}H NMR (400 MHz, $CDCl_3$) δ 9.96 – 9.84 (m, 1H), 7.85 – 7.72 (m, 2H), 7.70 – 7.59 (m, 2H), 7.15 – 6.56 (m, 47H), 4.56 – 3.97 (m, 122H), 3.81 (dq, *J* = 10.3, 4.5 Hz, 144H), 3.60 – 3.20 (m, 141H), 1.64 – 1.42 (m, 308H), 1.40 – 0.99 (m, 579H), 0.78 (dd, *J* = 8.5, 5.4 Hz, 214H). GPC (PhCl): M_n = 11.8 kDa, M_w = 14.1 kDa.

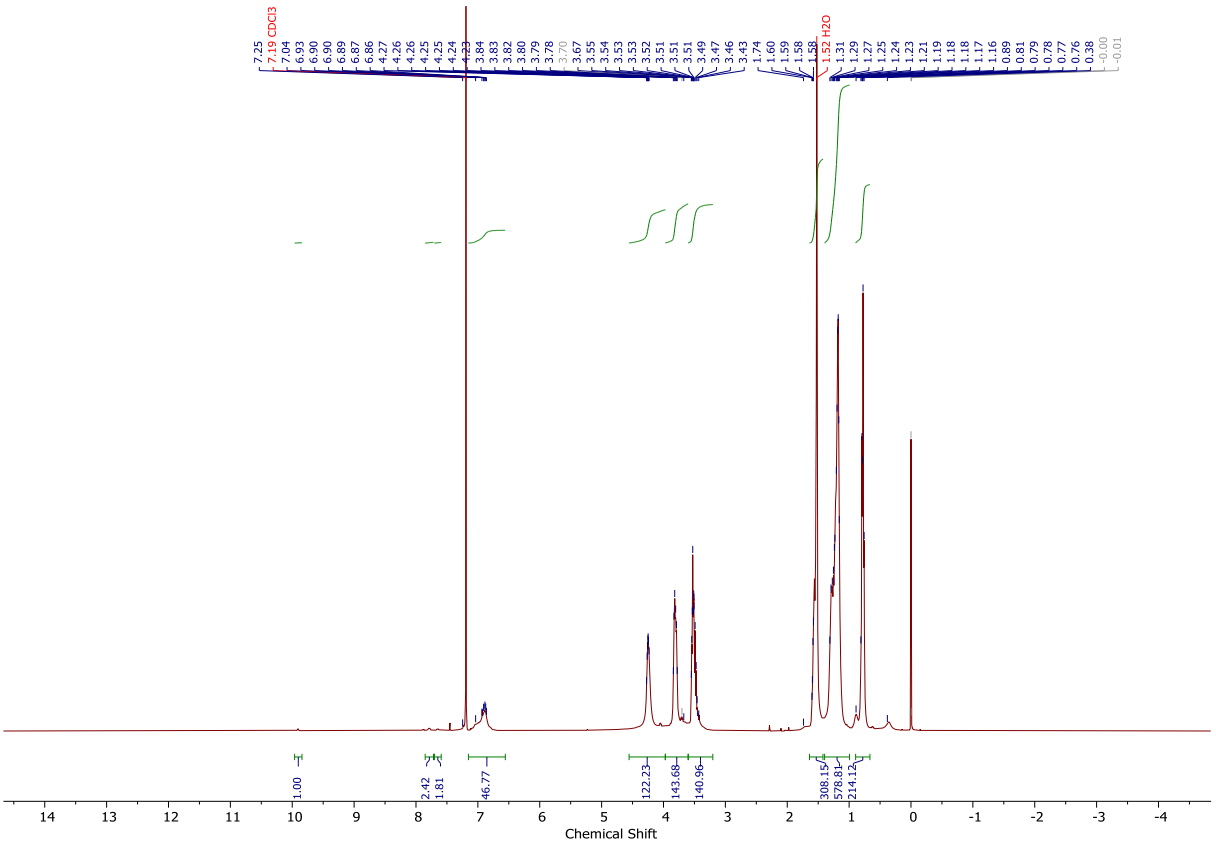

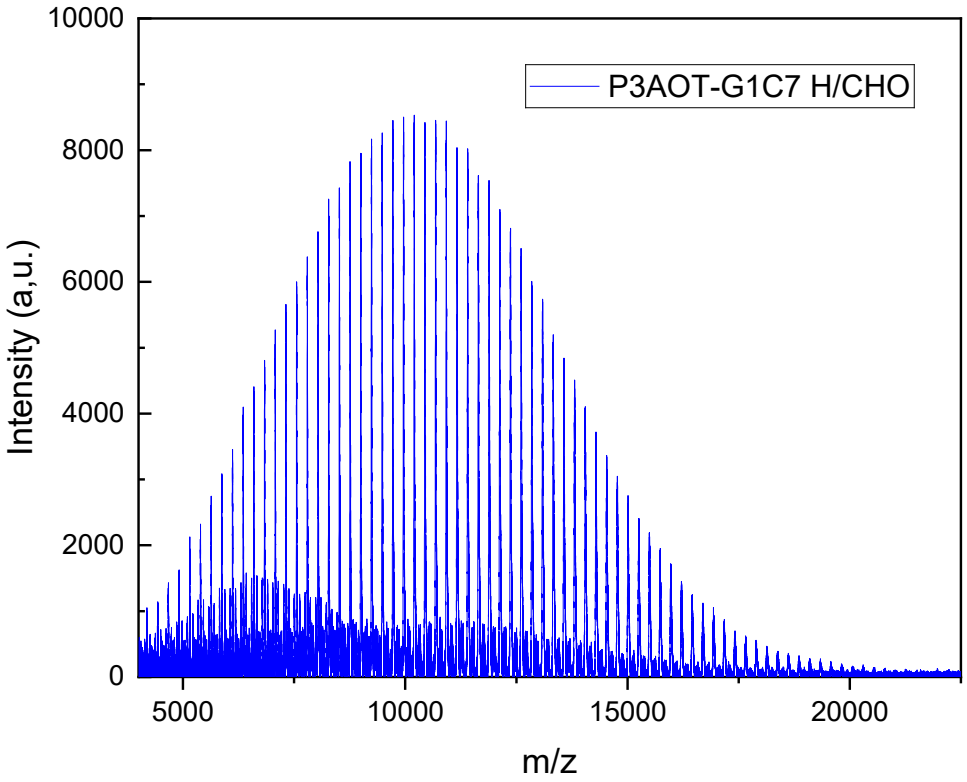

Molecular Weight Averages

Peak	Mp (g/mol)	Mn (g/mol)	Mw (g/mol)	Mz (g/mol)	Mz+1 (g/mol)	Mv (g/mol)
Peak 1	14148	11848	14095	16368	18877	13770

PD
1.19

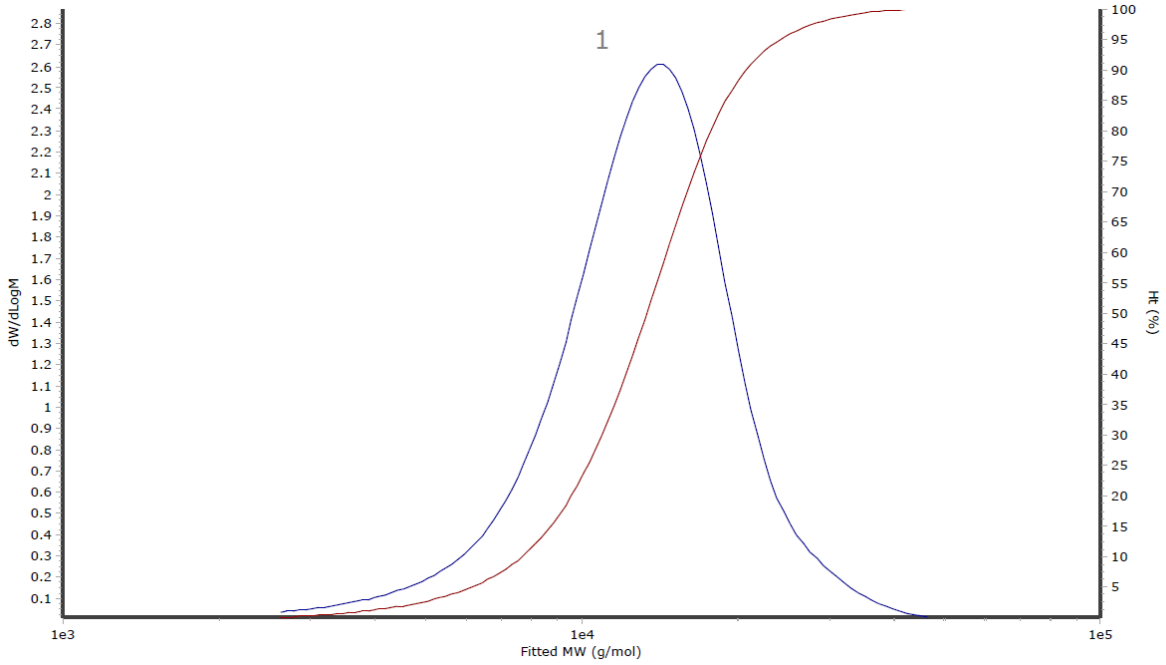

Preparation of ***poly(3-alkoxythiophene)-C2C6 H/CHO***

P3AOT C_2C_6 H/Br (240 mg, 0.015 mmol), (4-formylphenyl) boronic acid (945.0 mg, 0.30 mmol, 20 eq), Pd-G_3-P^tBu_3 (12.9 mg, 0.0225 mmol, 1.5 eq), anhydrous potassium phosphate (255 mg, 1.2 mmol, 80 eq), degassed THF (24 mL) and water (0.48 mL) was used to prepare P3AOT-C_2C_6 H/CHO following General Procedure B. P3AOT-C_2C_6 H/CHO (235 mg, 98%) was yielded. ^{1}H NMR (400 MHz, $CDCl_3$) δ 9.97 (s, 1H), 7.87 (s, 2H), 7.70 (s, 2H), 6.92 (s, 19H), 4.12 (s, 74H), 1.97 – 1.25 (m, 766H), 1.12 – 0.81 (m, 502H). GPC (PhCl): M_n = 16.1 kDa, M_w = 19.3 kDa.

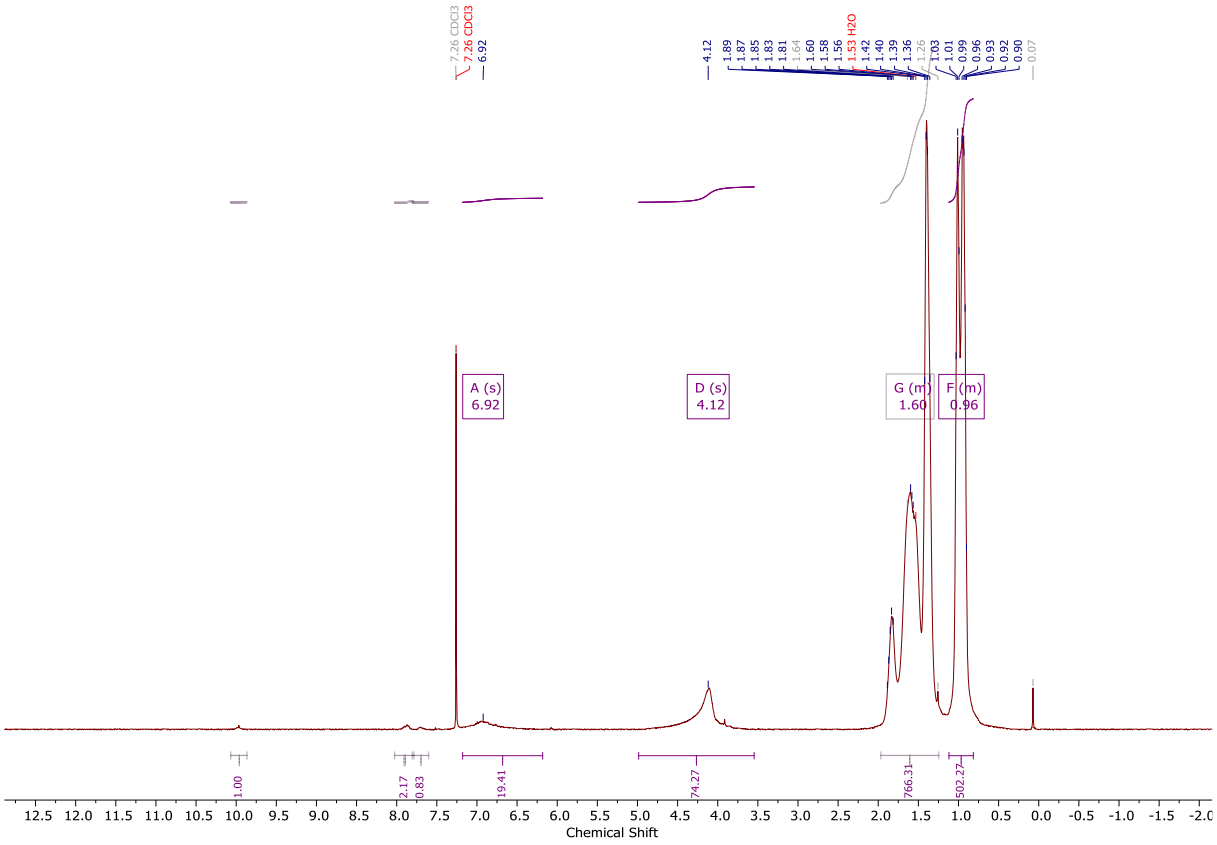

Molecular Weight Averages

Peak	Mp (g/mol)	Mn (g/mol)	Mw (g/mol)	Mz (g/mol)	Mz+1 (g/mol)	Mv (g/mol)
Peak 1	21531	16117	19308	21922	24421	18902

PD
1.198

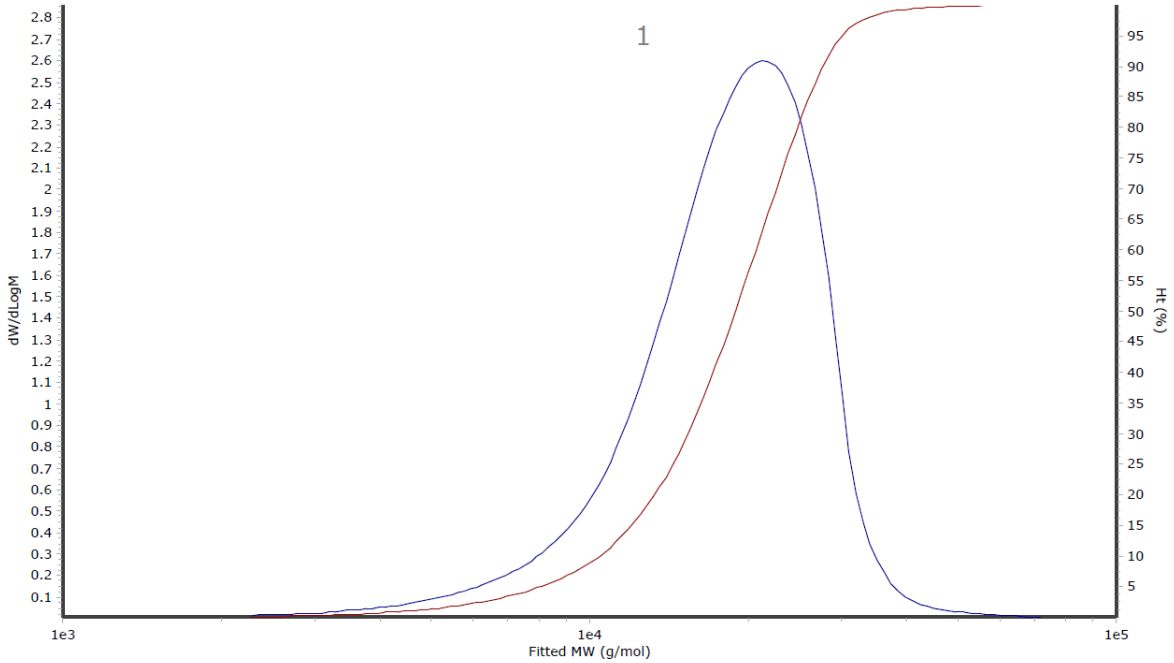

General Procedure C.1 for Synthesis of rhodanine-terminated polyethylene glycol

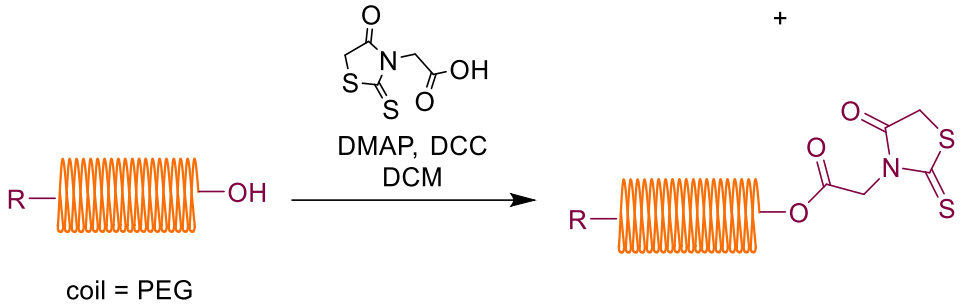

Under N_2, Alcohol-terminated PEG and 2-(4-oxo-2-thioxothiazolidin-3-yl)acetic acid (2.0 eq) was dissolved in anhydrous DCM (to a concentration of 100 mg/mL w.r.t. coil precursor). Then, DMAP (0.2 eq), followed by DCC (2.0 eq) was added and the reaction mixture was stirred at room temperature for 16 hours. Then, ethanol (2.0 eq) was added to convert any unreacted acid to the corresponding ester and DCC to DCU respectively. The reaction mixture was then diluted with acetonitrile 10 times the volume, cooled to 0 ^{o}C for 1 hour, before filtered and washed with additional cold acetonitrile, then dried in vacuo. This process is repeated 2 – 3 times until no visible precipitation of DCU following solvent removal. Then, the crude polymer is further purified by column chromatography.

Note: Polymer of around 5-6 kDa is around the highest molecular weight polymer which can pass through silica column chromatography.

Example Procedure: Preparation of PEG-Rh-4k

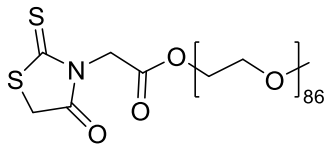

Polyethylene glycol monomethyl ether (5k, commercially available, a mixture of 4 kDa and 8 kDa) (1875 mg, 0.38 mmol), 2-(4-oxo-2-thioxothiazolidin-3-yl)acetic acid (107 mg, 0.75 mmol) was dissolved in anhydrous DCM (19 mL). Then, DMAP (9.15 mg, 0.075 mmol), followed by DCC (116 mg, 0.75 mmol) was added and the reaction mixture was stirred overnight. Completion of reaction was monitored by MALDI-TOF-MS. The product was diluted with acetonitrile, then repeatedly filtered, concentrated, diluted as described in General Procedure 2. The product was further purified by column chromatography (chloroform/methanol 19/1 -> chloroform/methanol 85/15) to yield a white solid (823 mg, 44%). ^{1}H NMR (400 MHz, $CDCl_3$) δ 4.76 (s, 2H), 4.31 (t, J = 4.7 Hz, 2H), 4.11 (s, 2H), 3.64 (s, 342H), 3.46 (t, J = 5.0 Hz, 2H), 3.38 (d, J = 1.1 Hz, 3H). GPC ($CHCl_3$): M_n = 5.5 kDa, M_w = 7.3 kDa

Note: Increasing the eluent ratio beyond chloroform/methanol 4/1 starts to elute PEG-Rh-8k.

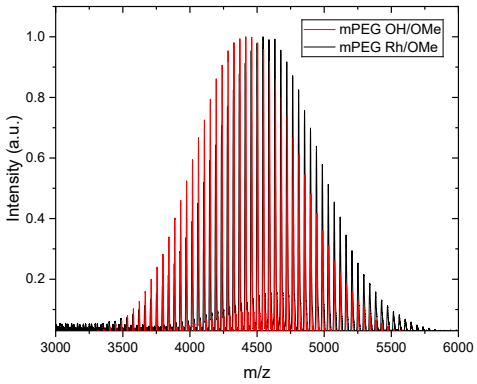
mPEG OH/OMe
mPEG Rh/OMe
Intensity (a.u.)
1.0
0.8
0.6
0.4
0.2
3000
3500
4000
4500
5000
5500
6000
m/z

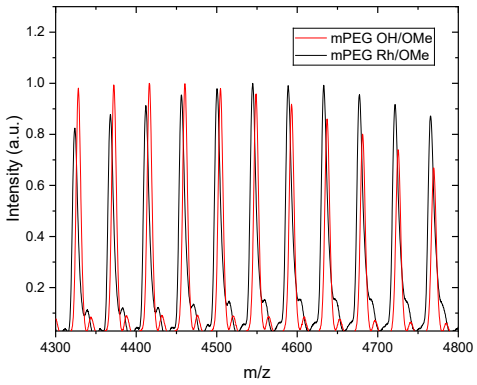
mPEG OH/OMe
mPEG Rh/OMe
Intensity (a.u.)
1.2
1.0
0.8
0.6
0.4
0.2
4300
4400
4500
4600
4700
4800
m/z

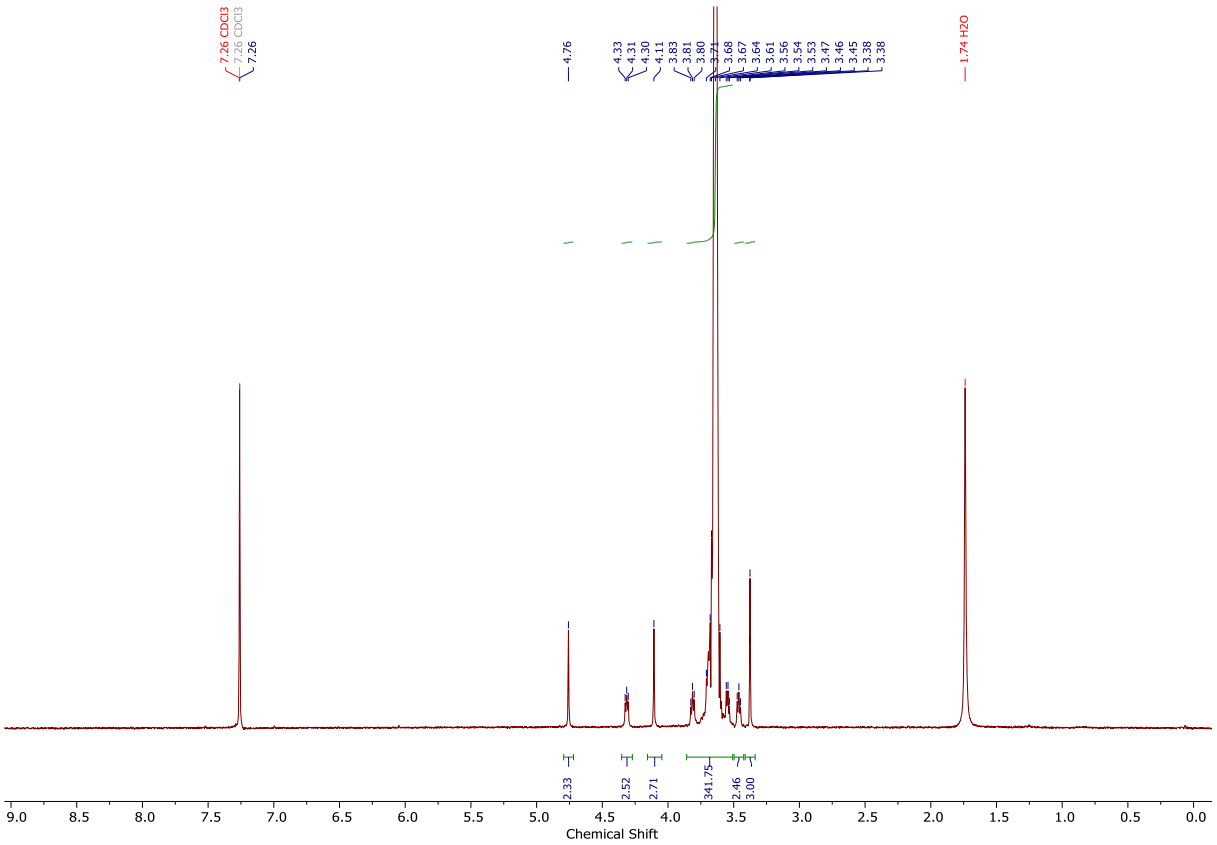
7.26 CDCl3
7.26 CDCl3
7.26
4.76
4.33
4.31
4.30
4.11
3.83
3.81
3.80
3.71
3.68
3.67
3.64
3.61
3.56
3.54
3.53
3.47
3.46
3.45
3.38
3.38
1.74 H2O
2.33
2.52
2.71
341.75
2.46
3.00
9.0 8.5 8.0 7.5 7.0 6.5 6.0 5.5 5.0 4.5 4.0 3.5 3.0 2.5 2.0 1.5 1.0 0.5 0.0
Chemical Shift

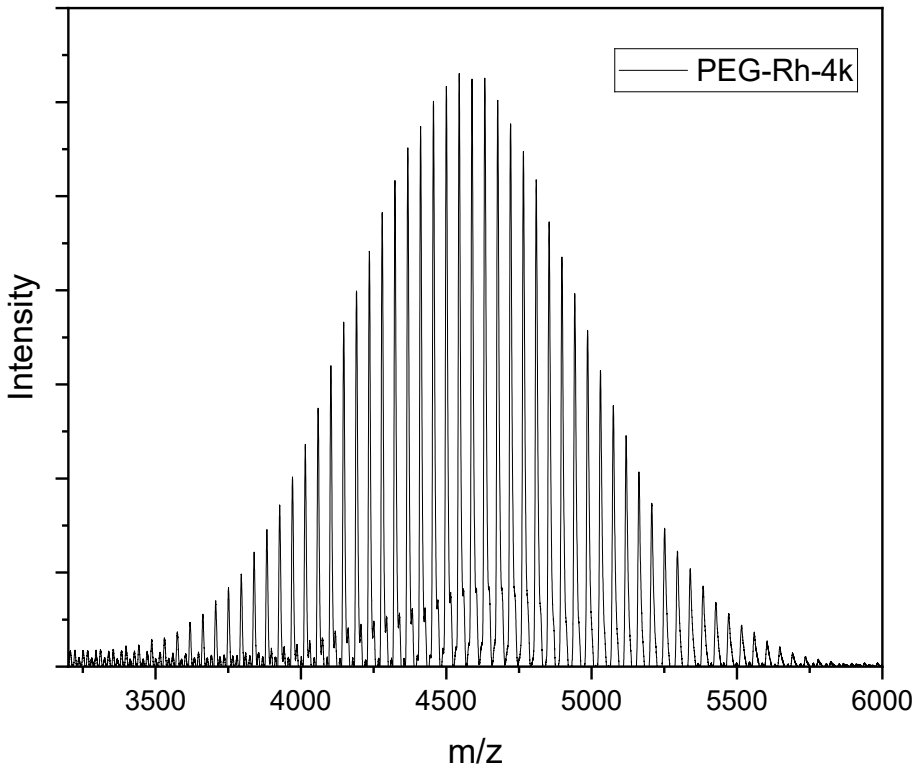
PEG-Rh-4k
Intensity
3500 4000 4500 5000 5500 6000
m/z

Molecular Weight Averages

Peak #	RT (min)	Mp (g/mol)	Mn (g/mol)	Mw (g/mol)	Mz (g/mol)	Mz+1 (g/mol)	PD
1	16.469	7666	5552	7314	9302	12249	1.317363

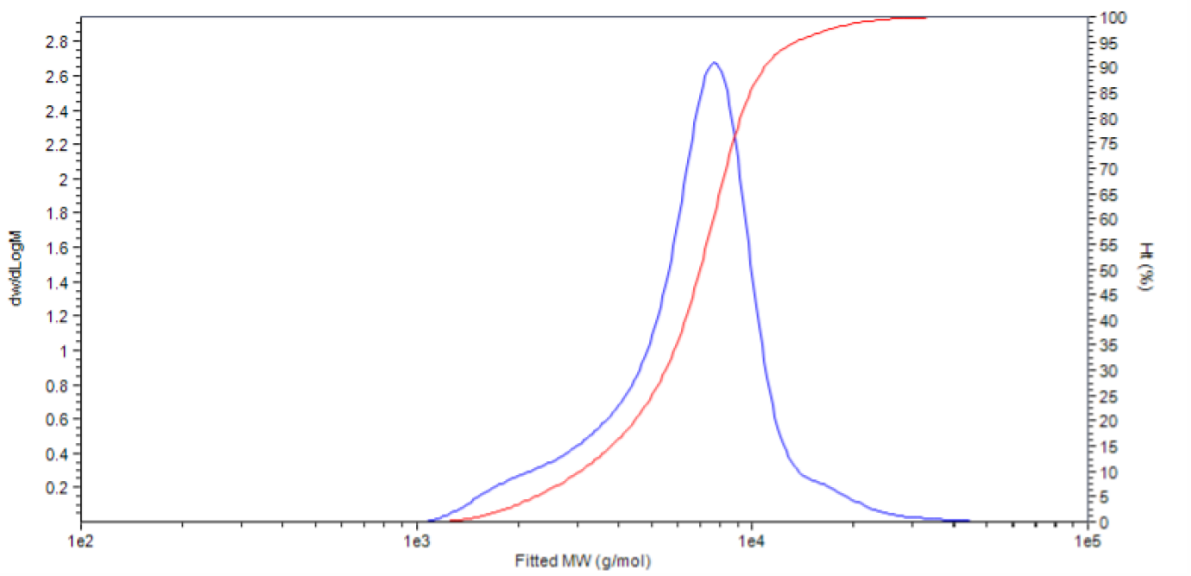

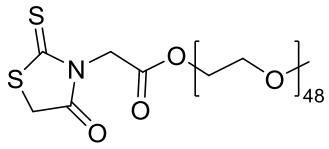

Preparation of PEG-Rh-2k Polyethylene glycol monomethyl ether (2k, commercially available) (1500 mg, 0.75 mmol), 2-(4-oxo-2-thioxothiazolidin-3-yl)acetic acid (215 mg, 1.50 mmol), DMAP (18.3 mg, 0.15 mmol), DCC (232 mg, 1.50 mmol) and DCM (17 mL) were used. The crude product was purified by column chromatography (chloroform/ethanol 39/1 -> chloroform/ethanol 37/3) to yield the product as a white solid. (1159 mg, 77%). ^{1}H NMR (400 MHz, $CDCl_3$) δ 4.76 (s, 2H), 4.34 – 4.28 (m, 2H), 4.11 (s, 2H), 3.85 – 3.77 (m, 1H), 3.64 (s, 188H), 3.50 – 3.43 (m, 1H), 3.38 (s, 3H). GPC ($CHCl_3$): M_n = 2.1 kDa, M_w = 2.7 kDa

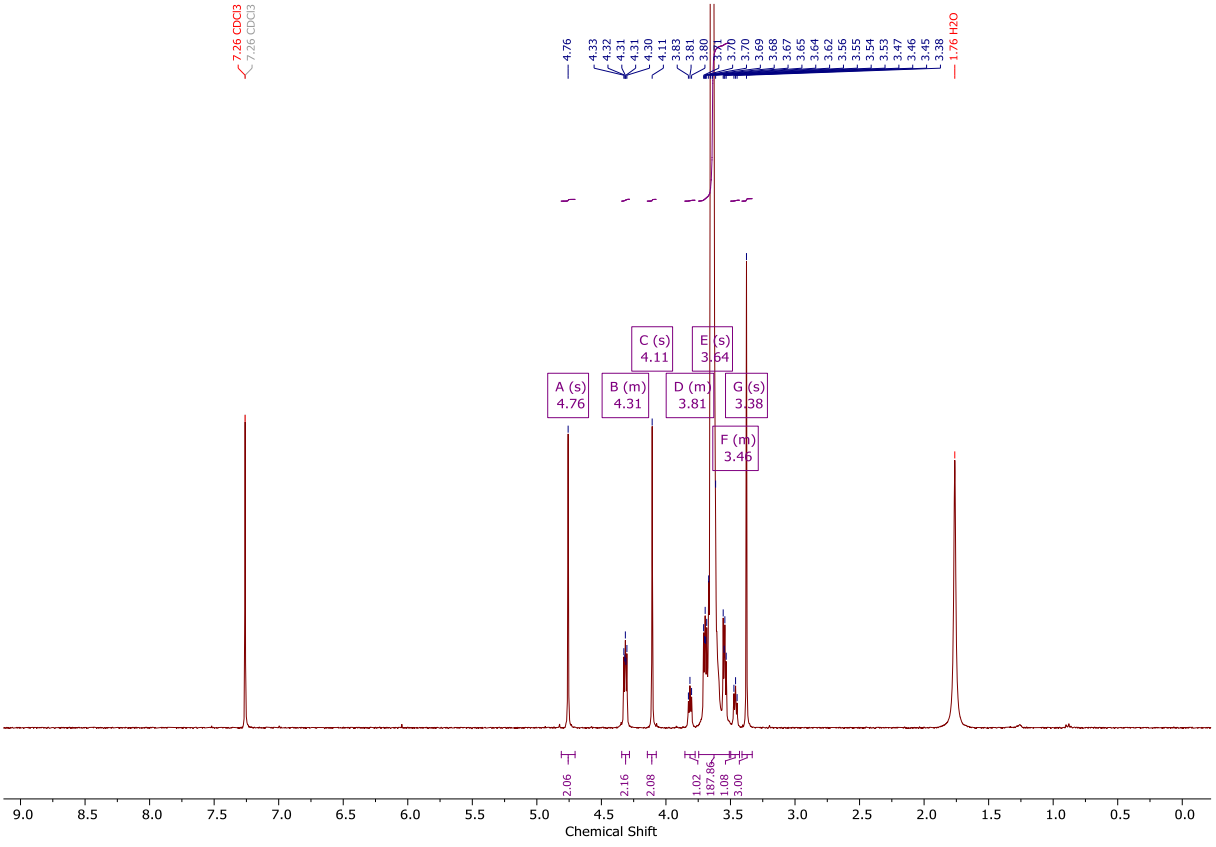

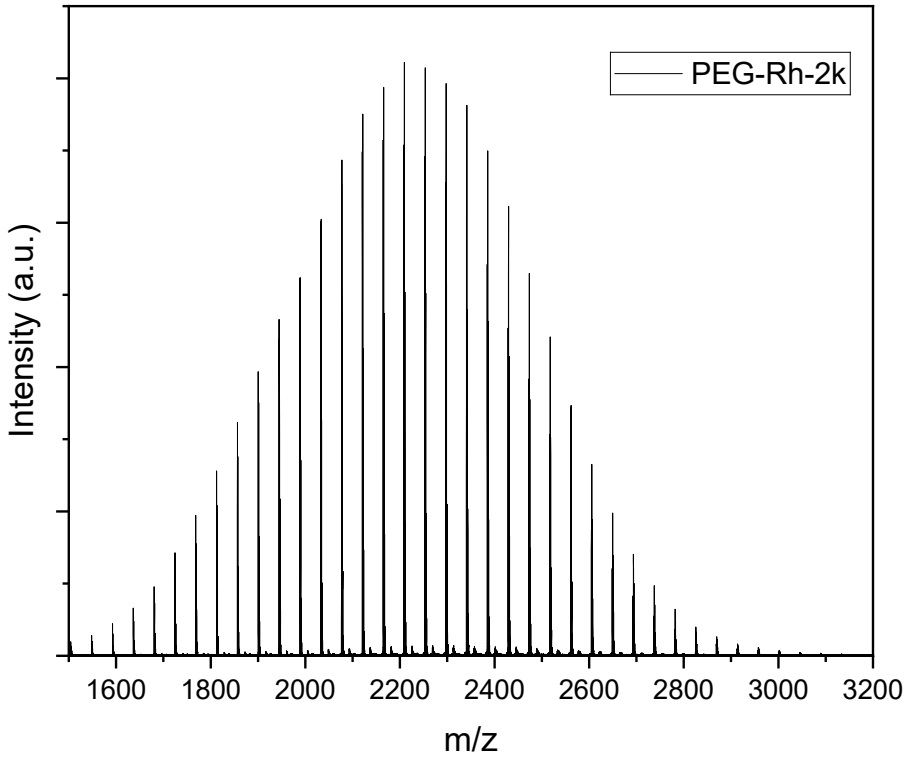

Molecular Weight Averages

Peak #	RT (min)	Mp (g/mol)	Mn (g/mol)	Mw (g/mol)	Mz (g/mol)	Mz+1 (g/mol)	PD
1	17.256	2865	2134	2664	3087	3609	1.248360

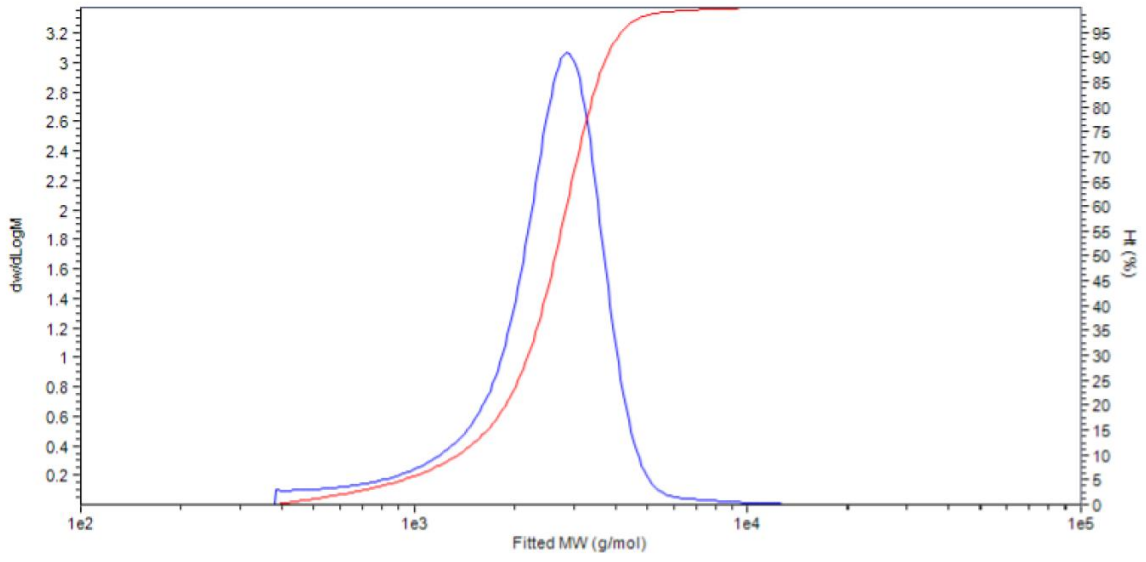

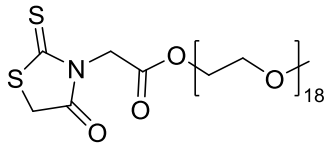

Preparation of PEG-Rh-750 Polyethylene glycol monomethyl ether (750, commercially available) (1500 mg, 2.00 mmol), 2-(4-oxo-2-thioxothiazolidin-3-yl)acetic acid (764 mg, 4.00 mmol), DMAP (48.9 mg, 0.40 mmol), DCC (825 mg, 4.00 mmol) and DCM (23 mL) were used. The crude product was purified by column chromatography (chloroform -> chloroform/ethanol 24/1) to yield the product as a white solid. (1159 mg, 77%). ^{1}H NMR (400 MHz, $CDCl_3$) δ 4.69 (s, 2H), 4.25 (dd, J = 5.8, 3.6 Hz, 2H), 4.04 (s, 2H), 3.81 – 3.37 (m, 68H), 3.31 (s, 3H). GPC ($CHCl_3$): M_n = 706 Da M_w = 866 Da

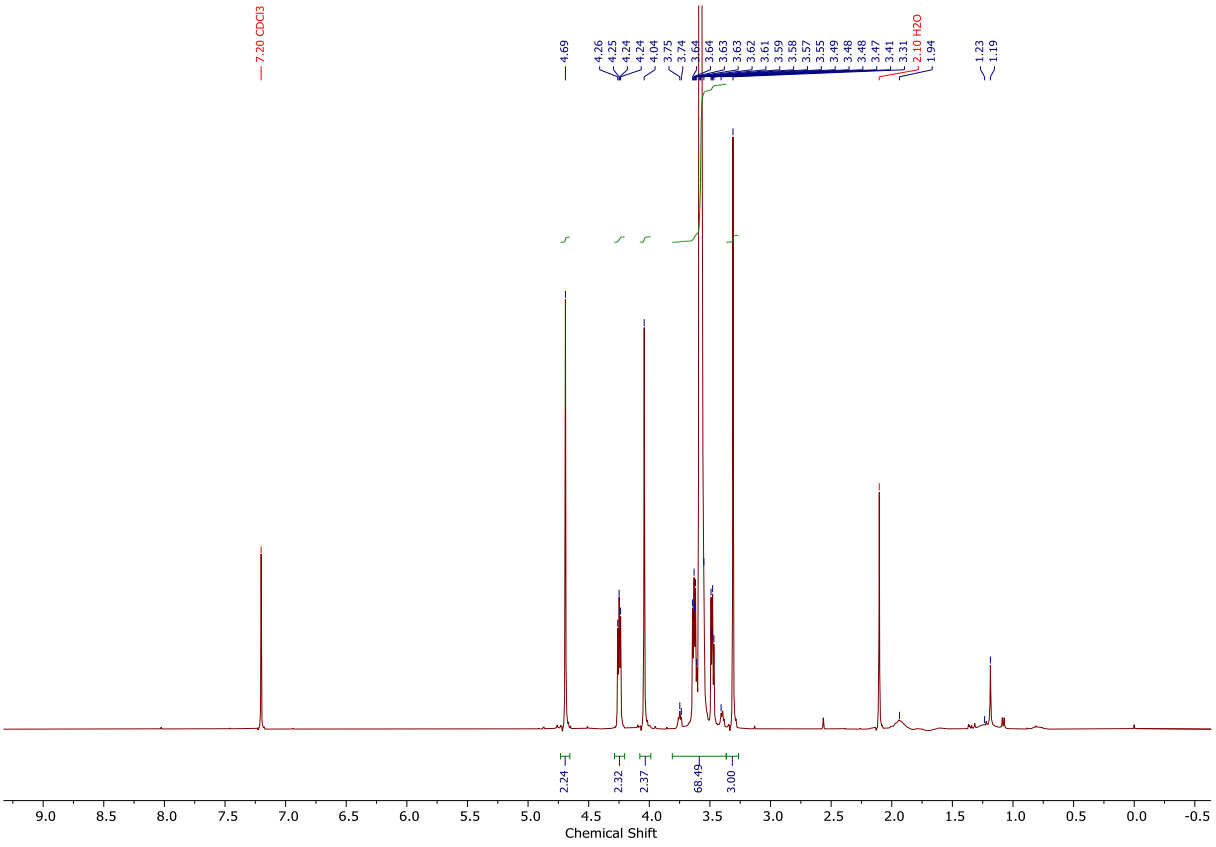

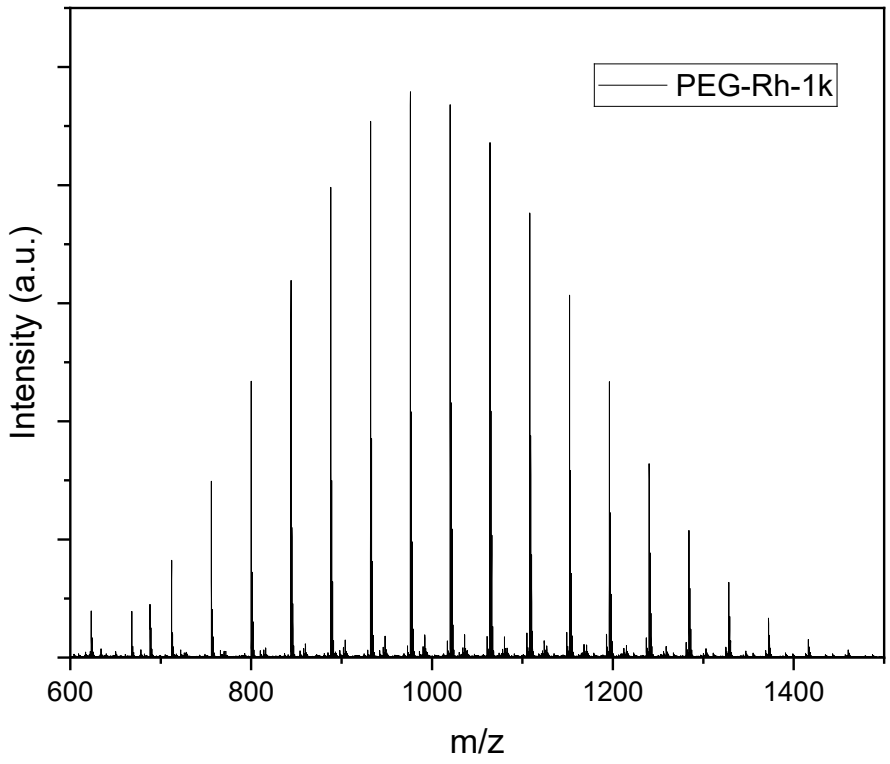

Molecular Weight Averages

Peak #	RT (min)	Mp (g/mol)	Mn (g/mol)	Mw (g/mol)	Mz (g/mol)	Mz+1 (g/mol)	PD
1	18.148	979	706	866	1001	1129	1.226629

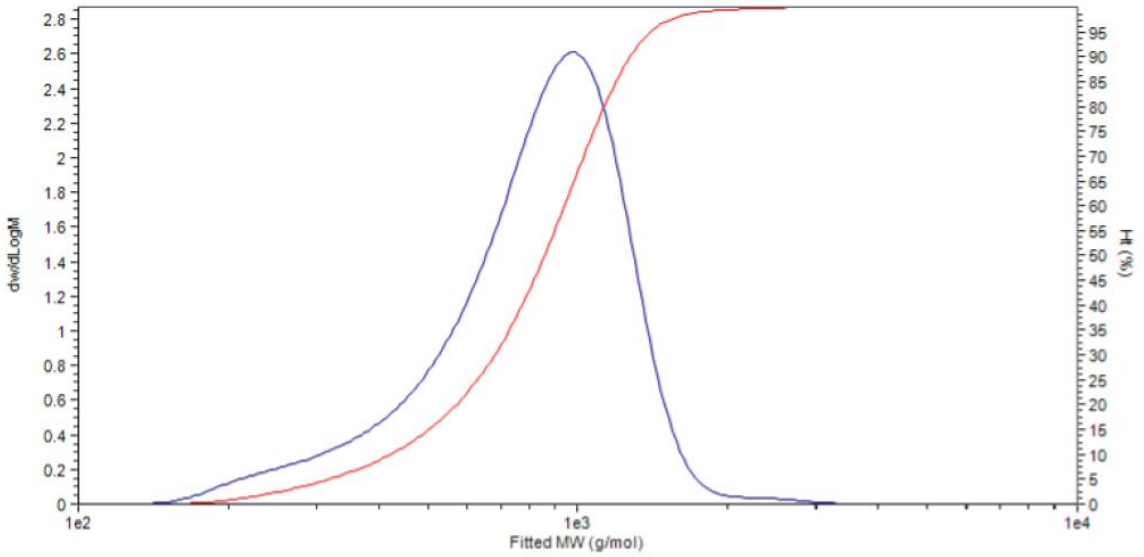

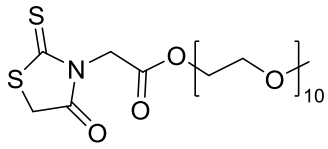

Preparation of PEG-Rh-450 Polyethylene glycol monomethyl ether (450, commercially available) (1200 mg, 2.54 mmol), 2-(4-oxo-2-thioxothiazolidin-3-yl)acetic acid (972 mg, 5.08 mmol), DMAP (62.0 mg, 0.51 mmol), DCC (1152 mg, 5.08 mmol) and DCM (19 mL) were used. The crude product was purified by column chromatography (chloroform -> chloroform/methanol 49/1) to yield the product as an orange oil. (1019 mg, 85%). ^{1}H NMR (400 MHz, CDCl3) δ 4.75 (s, 2H), 4.34 – 4.26 (m, 2H), 4.10 (s, 2H), 3.85 – 3.48 (m, 38H), 3.37 (s, 3H). GPC ($CHCl_3$): M_n = 525 Da, M_w =584 Da

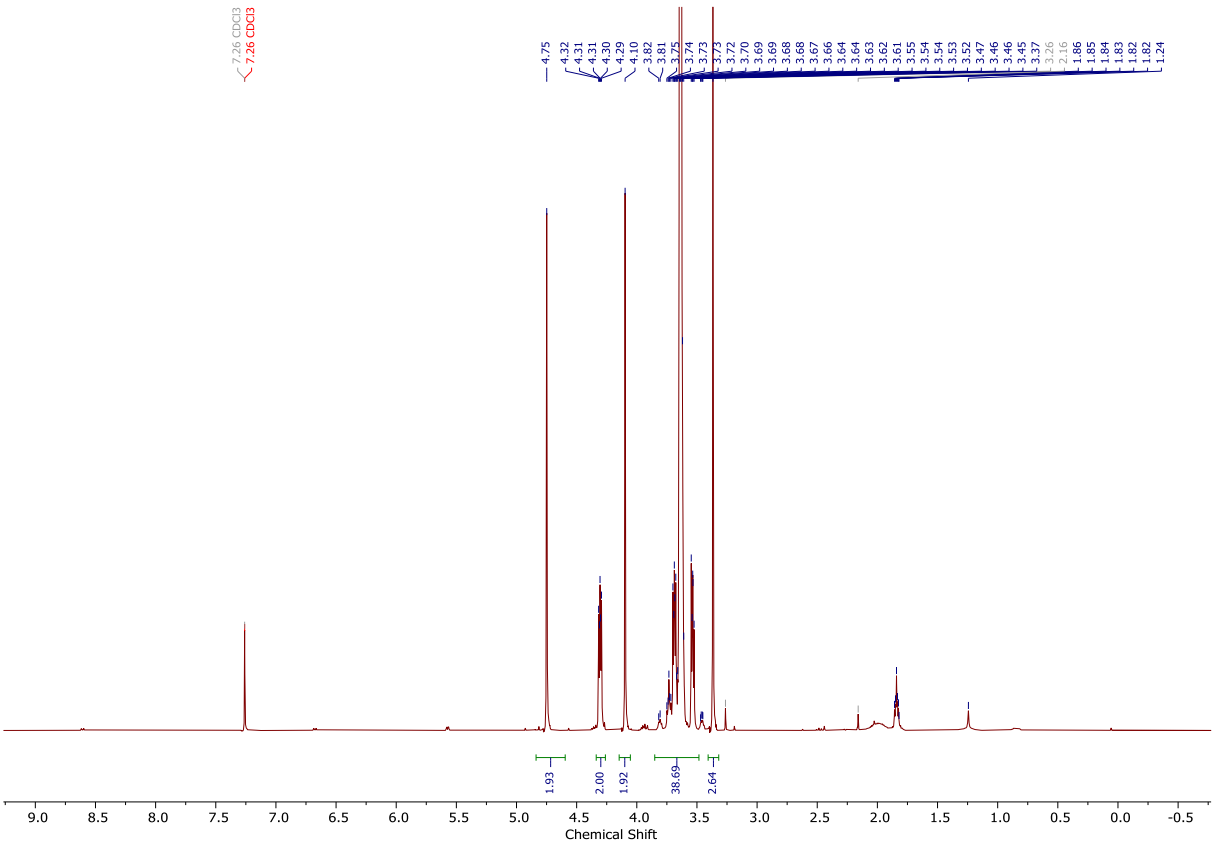

Molecular Weight Averages

Peak #	RT (min)	Mp (g/mol)	Mn (g/mol)	Mw (g/mol)	Mz (g/mol)	Mz+1 (g/mol)	PD
1	18.546	614	525	584	653	772	1.112381

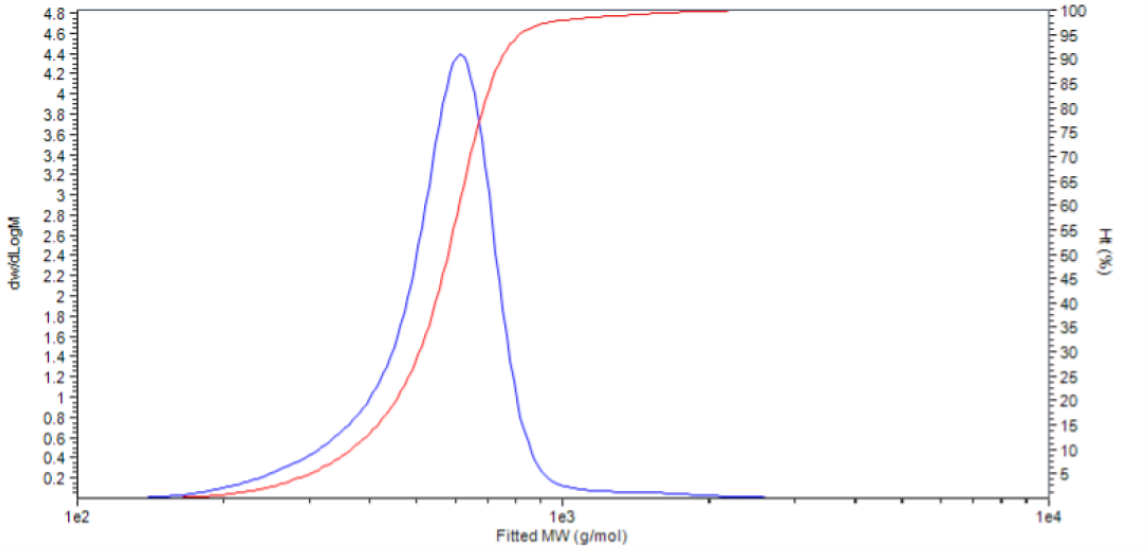

General Procedure C.2 for Synthesis of rhodanine-terminated polyesters

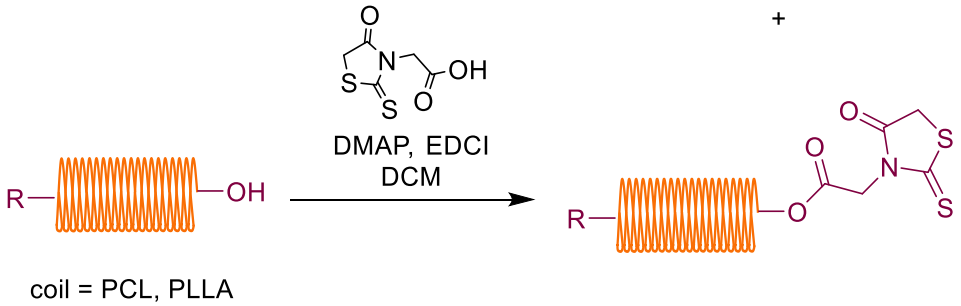

Benzyl-substituted PCL and PLLA were prepared according to prior literatures with $Sn(Oct)_2$ as a Lewis acid. General procedure B.2 is similar to B.1 except that upon completion, the reaction mixture is diluted with chloroform, then washed with saturated sodium bicarbonate solution, water, and then dried in vacuo, before being precipitated in cold diethyl ether to yield the rhodanine-terminated polyesters.

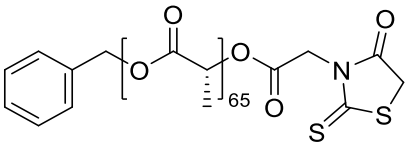

Example Procedure: Preparation of PCL-Rh-6k α-benzyl-ω-hydroxy-polycaprolactone (6k) (1000 mg, 0.165 mmol), 2-(4-oxo-2-thioxothiazolidin-3-yl)acetic acid (79.1 mg, 0.413 mmol) was dissolved in anhydrous DCM (20 mL). Then, DMAP (5.03 mg, 0.041 mmol) and EDCI (71.7 mg, 0.462 mmol) was added and the reaction mixture was stirred at room temperature overnight. Upon completion, the reaction mixture is diluted with chloroform (200 mL), then washed with saturated sodium bicarbonate solution (200 mL), water (200 mL x 2), and then dried in vacuo, before being precipitated in cold diethyl ether to yield PCL-Rh-6k as a white solid (723 mg, 72%). ^{1}H NMR (400 MHz, $CDCl_3$) δ 7.34 (d, J = 5.3 Hz, 5H), 5.11 (s, 2H), 4.06 (t, J = 6.6 Hz, 107H), 3.64 (t, J = 6.5 Hz, 4H), 2.30 (t, J = 7.5 Hz, 112H), 1.90 – 1.51 (m, 236H), 1.38 (qd, J = 9.2, 6.1 Hz, 114H). GPC ($CHCl_3$): M_n = 5.5 kDa, M_w = 8.8 kDa

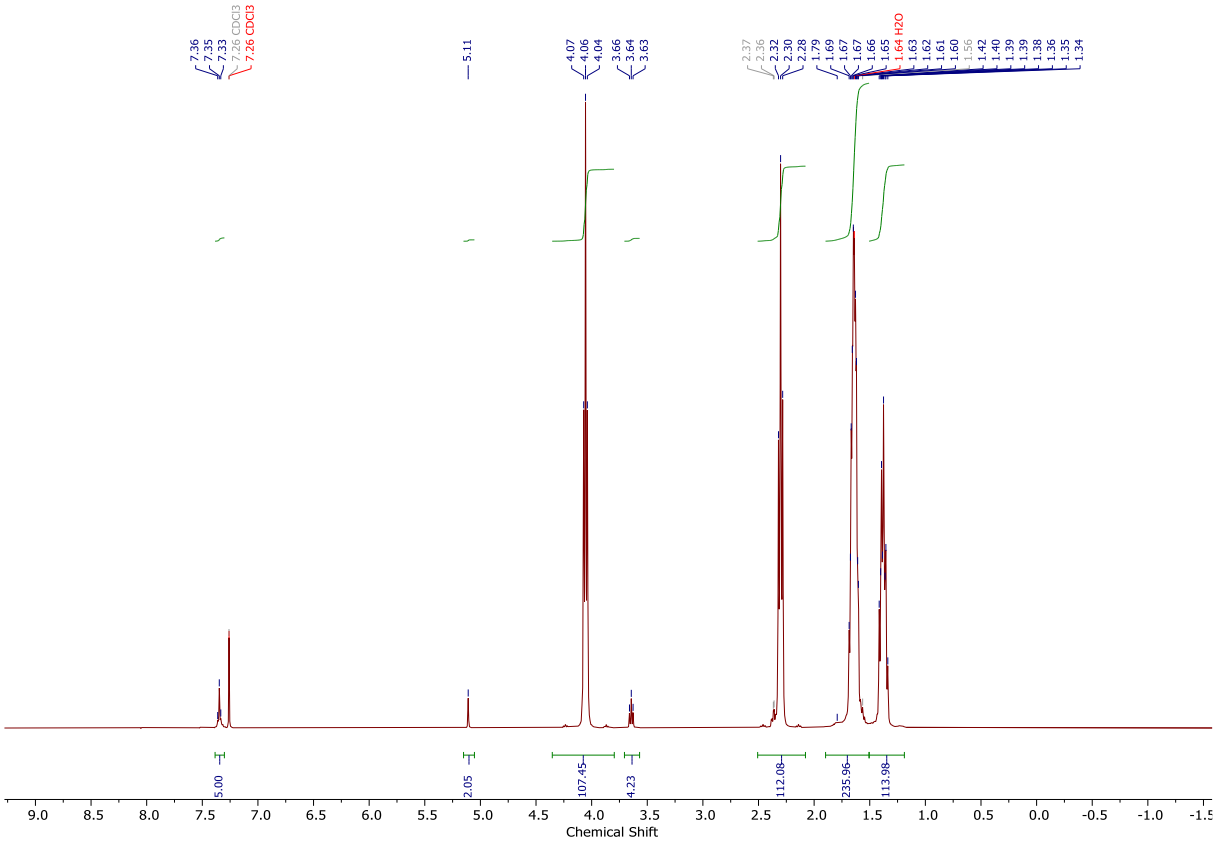

Molecular Weight Averages

Peak #	RT (min)	Mp (g/mol)	Mn (g/mol)	Mw (g/mol)	Mz (g/mol)	Mz+1 (g/mol)	PD
1	16.783	5183	5555	8761	13536	18935	1.577138

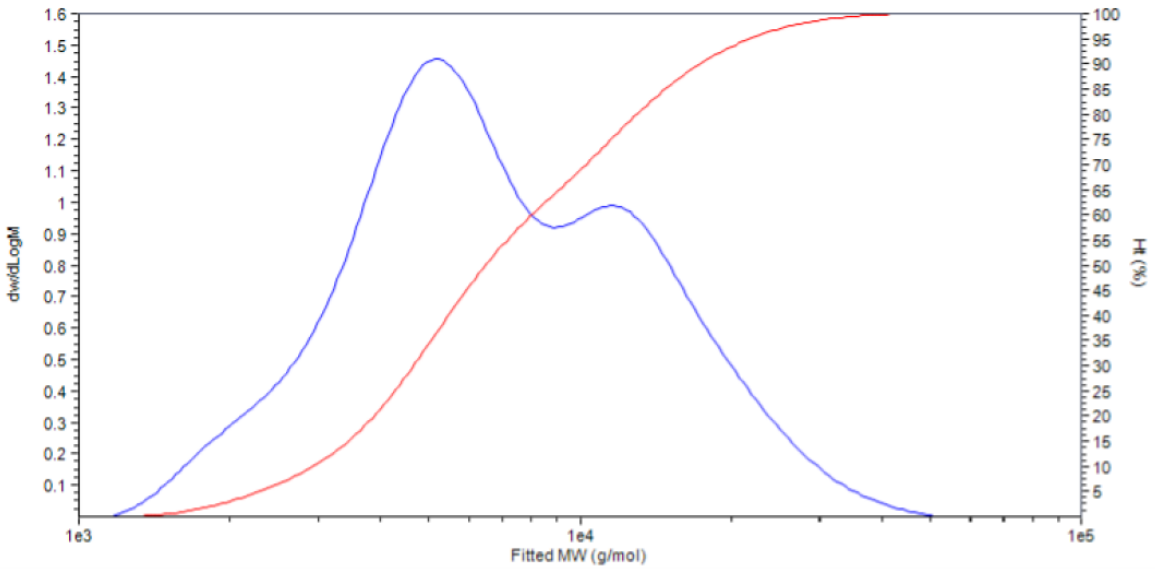

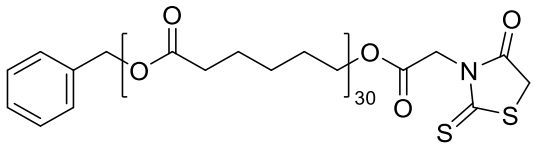

Preparation of PCL-Rh-3k α-benzyl-ω-hydroxy-polycaprolactone (3k) (800 mg, 0.234 mmol), 2-(4-oxo-2-thioxothiazolidin-3-yl)acetic acid (112 mg, 0.585 mmol), DMAP (7.14 mg, 0.0585 mmol), EDCI (101.7 mg, 0.655 mmol) and anhydrous DCM (16 mL) were used, yielding PCL-Rh-3k as a white solid. (401 mg, 50%). ^{1}H NMR (400 MHz, $CDCl_3$) δ 7.35 (s, 5H), 5.11 (s, 2H), 4.06 (t, J = 6.7 Hz, 58H), 3.65 (t, J = 6.5 Hz, 4H), 2.30 (t, J = 7.5 Hz, 59H), 1.64 (qt, J = 6.8, 3.8 Hz, 128H), 1.38 (ddd, J = 15.4, 9.1, 6.4 Hz, 61H). GPC ($CHCl_3$): M_n = 3.8 kDa, M_w = 5.3 kDa

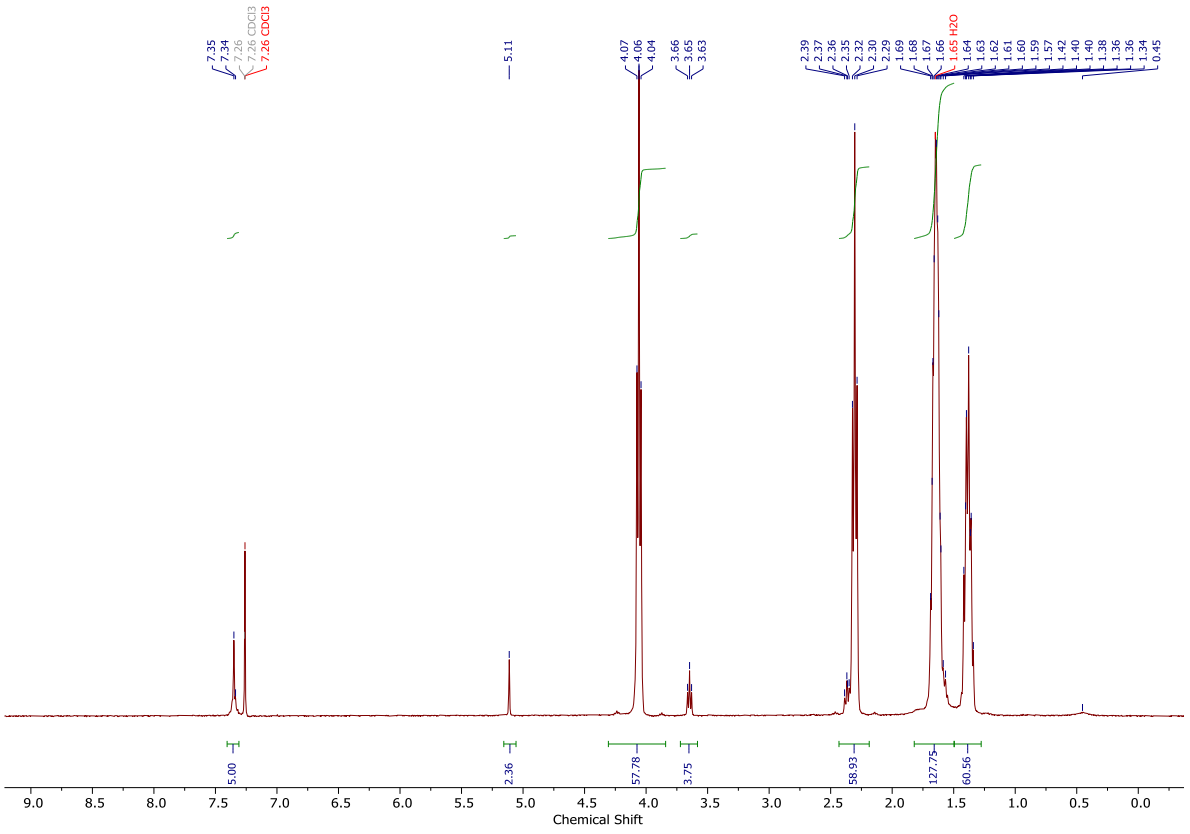

Molecular Weight Averages

Peak #	RT (min)	Mp (g/mol)	Mn (g/mol)	Mw (g/mol)	Mz (g/mol)	Mz+1 (g/mol)	PD
1	17.109	3456	3762	5333	7972	11182	1.417597

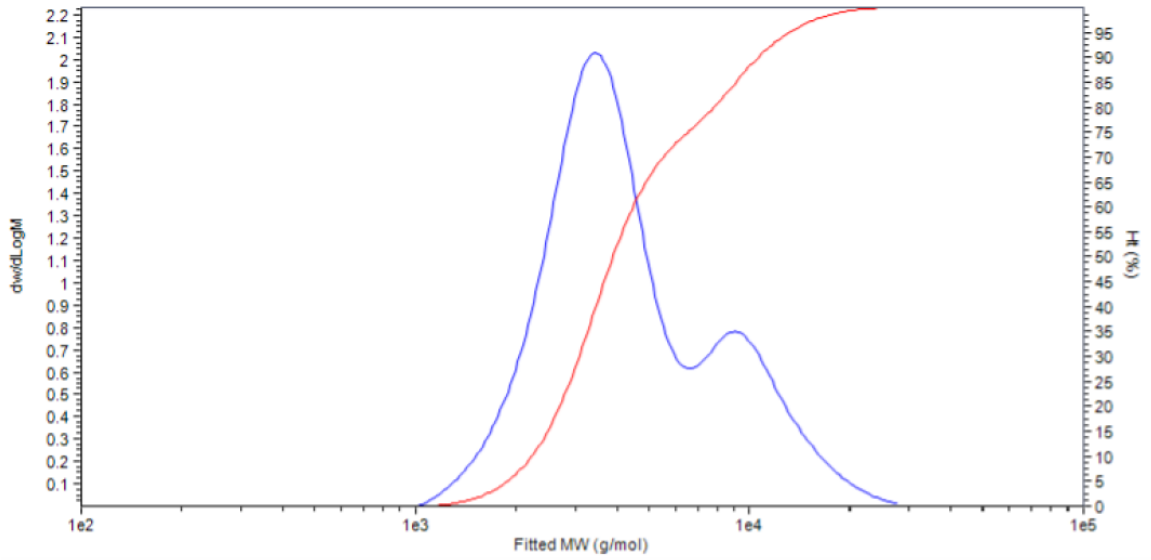

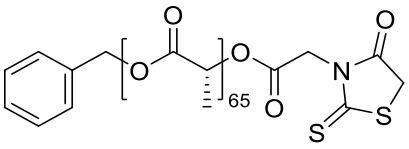

Preparation of PLLA-Rh-5k α-benzyl-ω-hydroxy-poly(L-lactide) (5k) (828 mg, 0.20 mmol), 2-(4-oxo-2-thioxothiazolidin-3-yl)acetic acid (95.5 mg, 0.50 mmol), DMAP (6.10 mg, 0.050 mmol), EDCI (86.9 mg, 0.56 mmol) and anhydrous DCM (16 mL) were used, yielding PLLA-Rh-5k as a white solid. (655 mg, 79%). ^{1}H NMR (400 MHz, $CDCl_3$) δ 7.34 (td, J = 7.5, 5.2 Hz, 5H), 5.16 (q, J = 7.1 Hz, 66H), 4.87 (s, 1H), 4.78 (s, 1H), 4.07 (s, 2H), 1.58 (d, J = 7.1 Hz, 224H). GPC ($CHCl_3$): M_n = 4.8 kDa, M_w =7.0 kDa

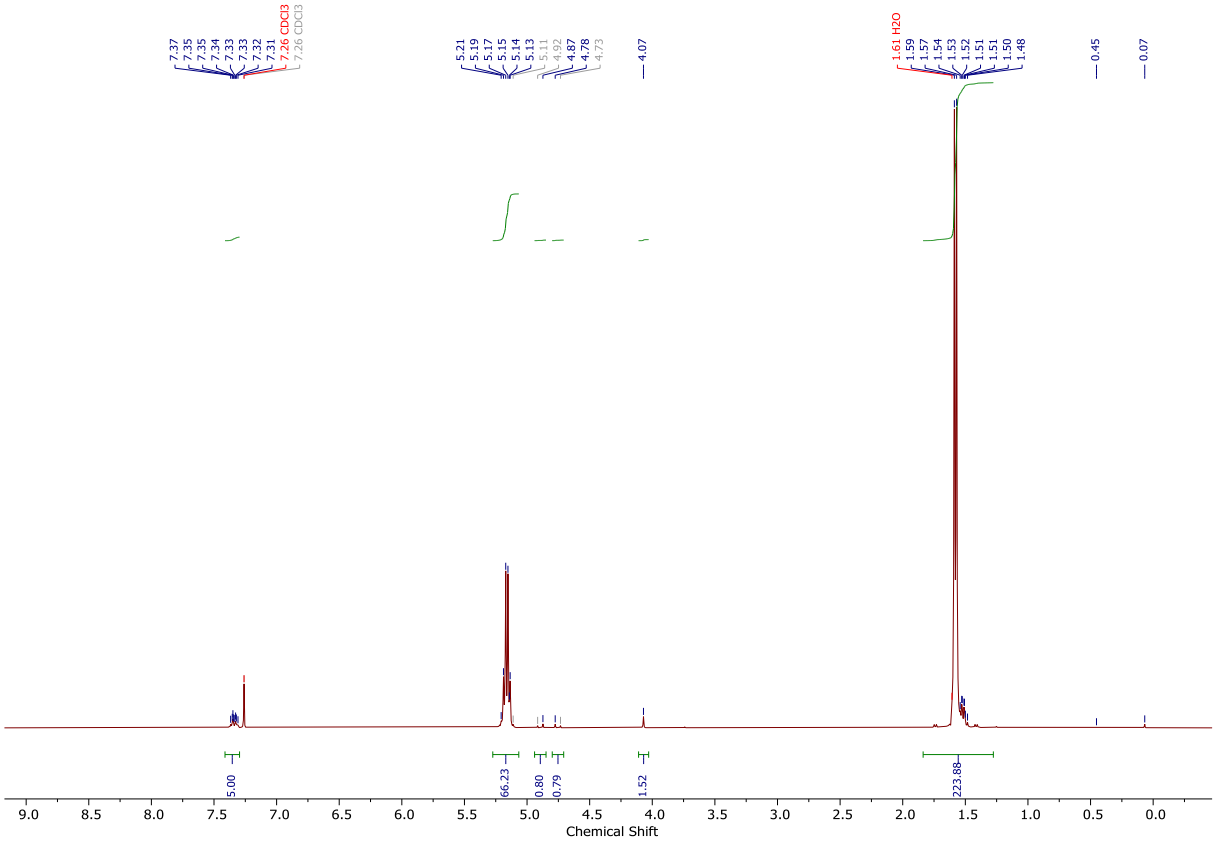

Molecular Weight Averages

Peak #	RT (min)	Mp (g/mol)	Mn (g/mol)	Mw (g/mol)	Mz (g/mol)	Mz+1 (g/mol)	PD
1	16.911	4485	4798	7042	10064	13242	1.467695

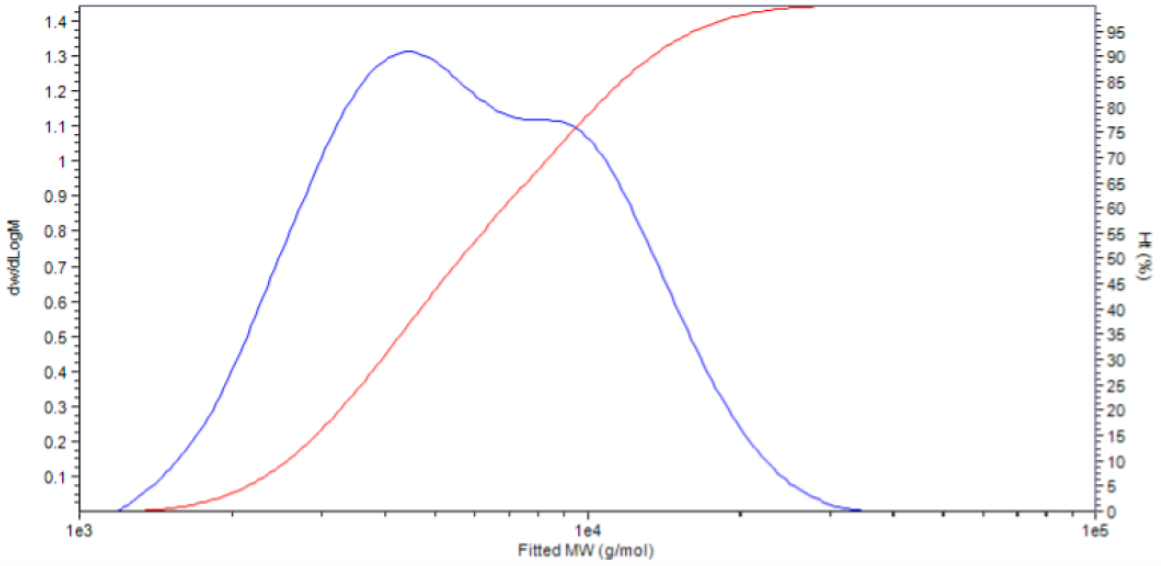

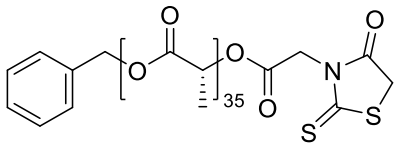

Preparation of PLLA-Rh-2k α-benzyl-ω-hydroxy-poly(L-lactide) (2k) (1012 mg, 0.40 mmol), 2-(4-oxo-2-thioxothiazolidin-3-yl)acetic acid (191 mg, 1.00 mmol), DMAP (12.20 mg, 0.10 mmol), EDCI (173 mg, 1.12 mmol) and anhydrous DCM (24 mL) were used, yielding PLLA-Rh-2k as a white solid. (687 mg, 68%). ^{1}H NMR (400 MHz, $CDCl_3$) δ 7.34 (td, J = 7.7, 5.3 Hz, 5H), 5.16 (q, J = 7.1 Hz, 37H), 4.89 (d, J = 17.0 Hz, 1H), 4.75 (d, J = 16.9 Hz, 1H), 4.07 (s, 2H), 1.58 (d, J = 7.1 Hz, 114H). GPC ($CHCl_3$): M_n = 2.8 kDa M_w =3.8 kDa

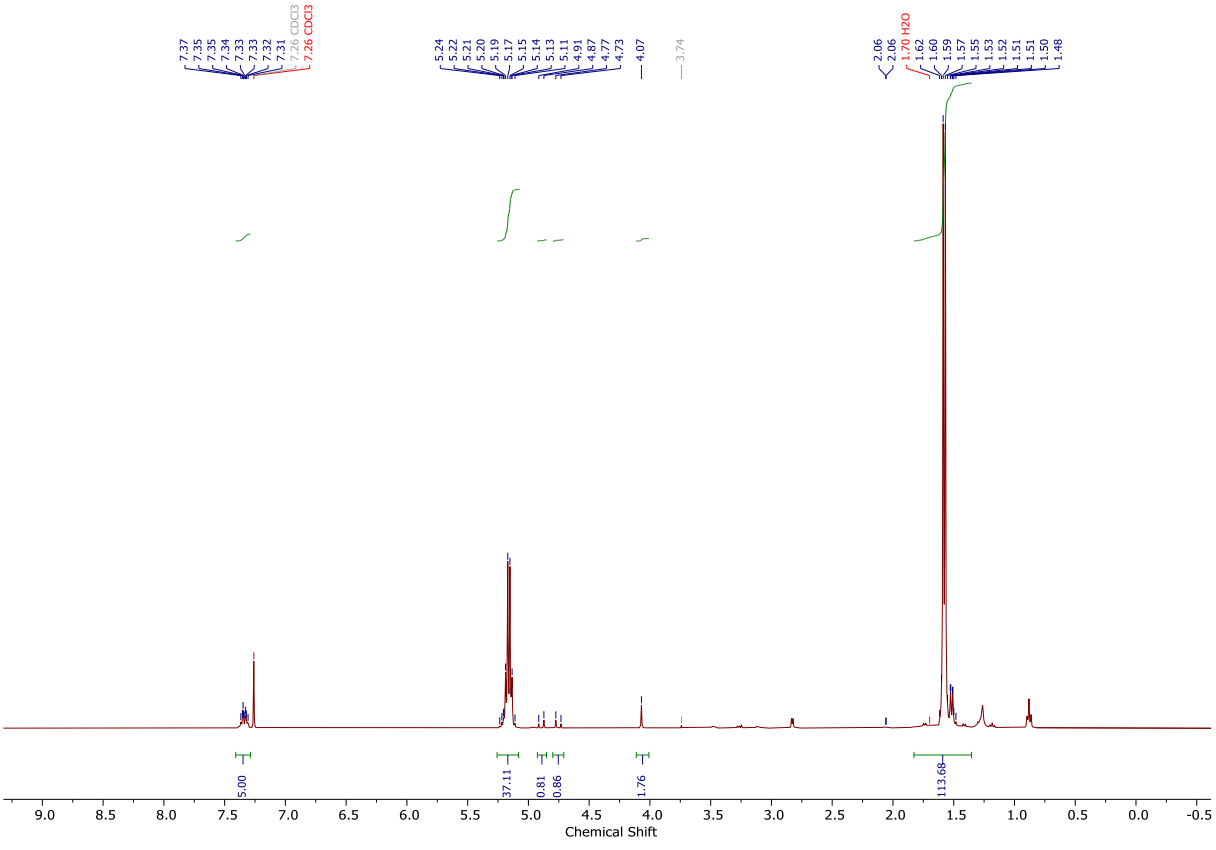

Molecular Weight Averages

Peak #	RT (min)	Mp (g/mol)	Mn (g/mol)	Mw (g/mol)	Mz (g/mol)	Mz+1 (g/mol)	PD
1	17.296	2741	2781	3842	5769	8709	1.381517

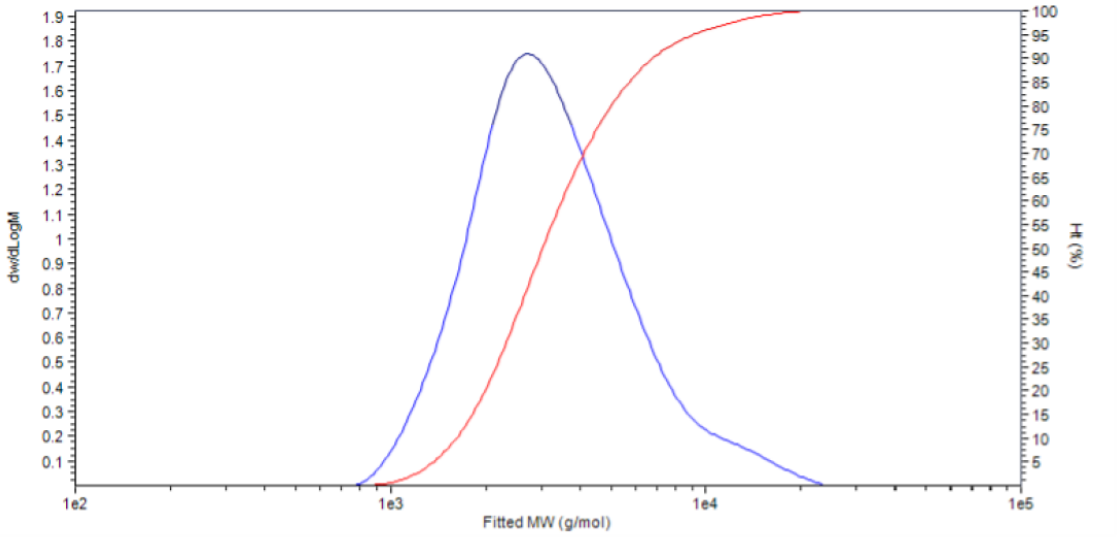

General Procedure D for Rod-coil block coupling

Example Procedure: Preparation of P3DOT-b-PEG-10

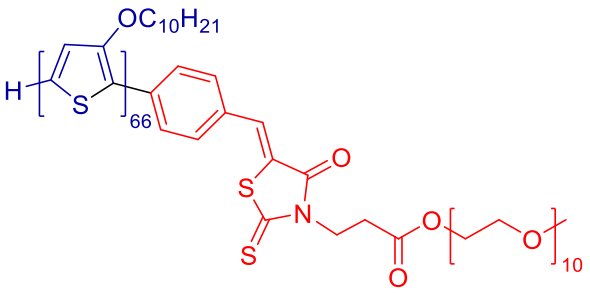

P3DOT H/PEG-10

Under N_2, P3DOT H/CHO (30 mg, 15.0 kDa, 0.002 mmol) and PEG-10-Rh (7.7 mg, 0.012 mmol) was added to a microwave vial. Then, anhydrous $CHCl_3$ (4.5 mL) and piperidine (0.060 mL, 0.60 mmol, 50 eq w.r.t. PEG) was added and the reaction mixture was warmed to reflux for 24 hours. Then, the reaction mixture is precipitated in methanol and further purified by Soxhlet extraction with acetonitrile, then chloroform. The chloroform layer was washed twice with water and concentrated, then re-precipitated in methanol to yield a dark blue solid (29 mg). ^{1}H NMR (400 MHz, $CDCl_3$) δ 6.92 (s, 30H), 4.16 (s, 80H), 3.65 (d, J = 4.0 Hz, 38H), 3.38 (s, 4H), 1.90 (s, 105H), 1.57 – 1.12 (m, 776H), 0.87 (tt, J = 7.0, 3.1 Hz, 221H). GPC (PhCl): M_n = 16.3 kDa, M_w = 20.1 kDa

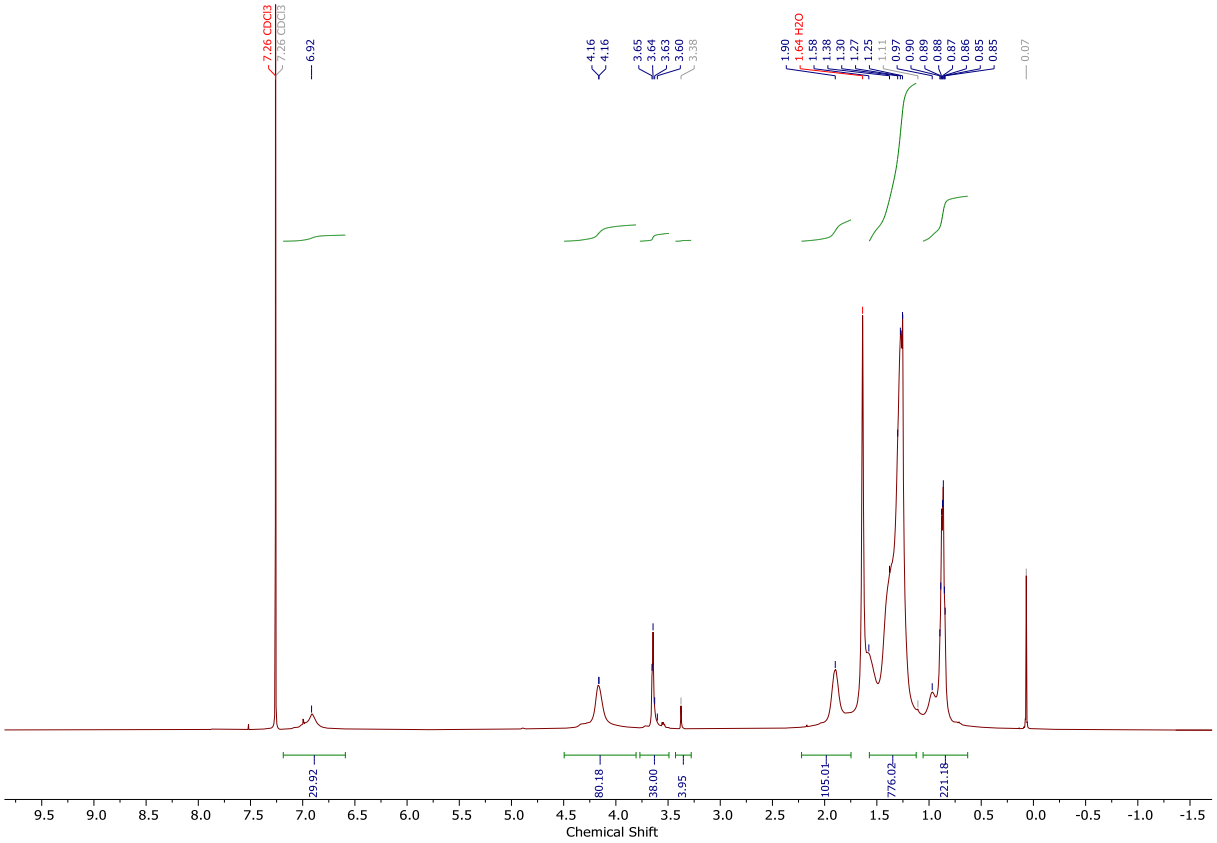

Molecular Weight Averages

Peak	Mp (g/mol)	Mn (g/mol)	Mw (g/mol)	Mz (g/mol)	Mz+1 (g/mol)	Mv (g/mol)
Peak 1	20627	16280	20122	23332	26248	19623

PD
1.236

Distribution Plot

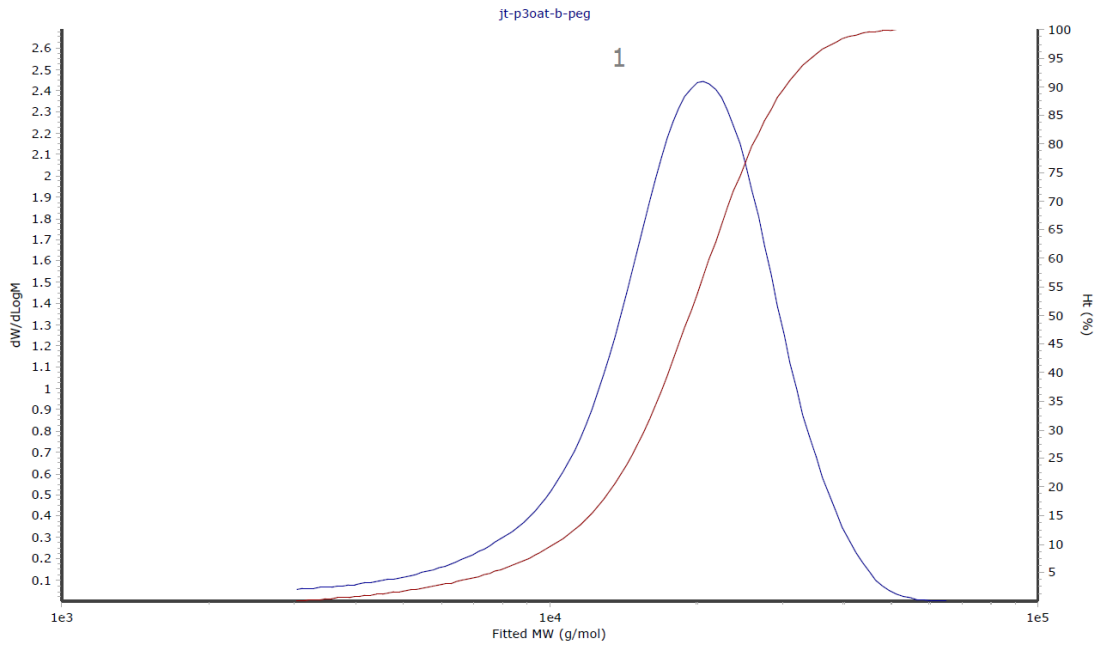

Preparation of P3DOT-b-PEG-18 P3DOT H/CHO (30 mg, 0.002 mmol), PEG-18-Rh (12 mg, 0.012 mmol), anhydrous $CHCl_3$ (4.5 mL) and piperidine (0.060 mL) was used, yielding a dark blue solid (30 mg). ^{1}H NMR (400 MHz, $CDCl_3$) δ 6.92 (s, 43H), 4.16 (s, 99H), 3.65 (d, J = 4.9 Hz, 68H), 3.38 (s, 5H), 2.06 – 1.75 (m, 126H), 1.56 – 1.08 (m, 909H), 0.87 (dd, J = 8.3, 5.0 Hz, 192H). GPC (PhCl): M_n =16.5 kDa, M_w = 25.0 kDa

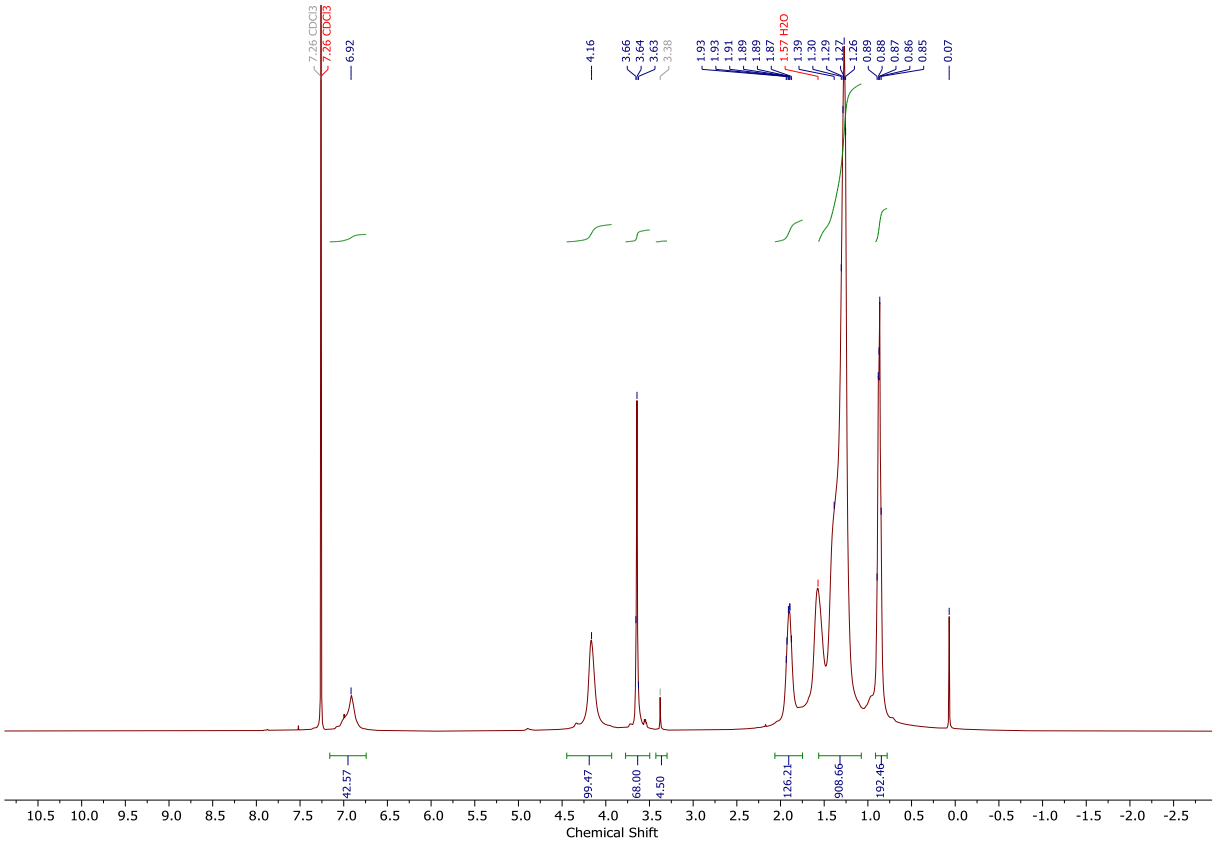

Molecular Weight Averages

Peak	Mp (g/mol)	Mn (g/mol)	Mw (g/mol)	Mz (g/mol)	Mz+1 (g/mol)	Mv (g/mol)
Peak 1	25254	16537	24981	31057	36961	24048

PD
1.511

Distribution Plot

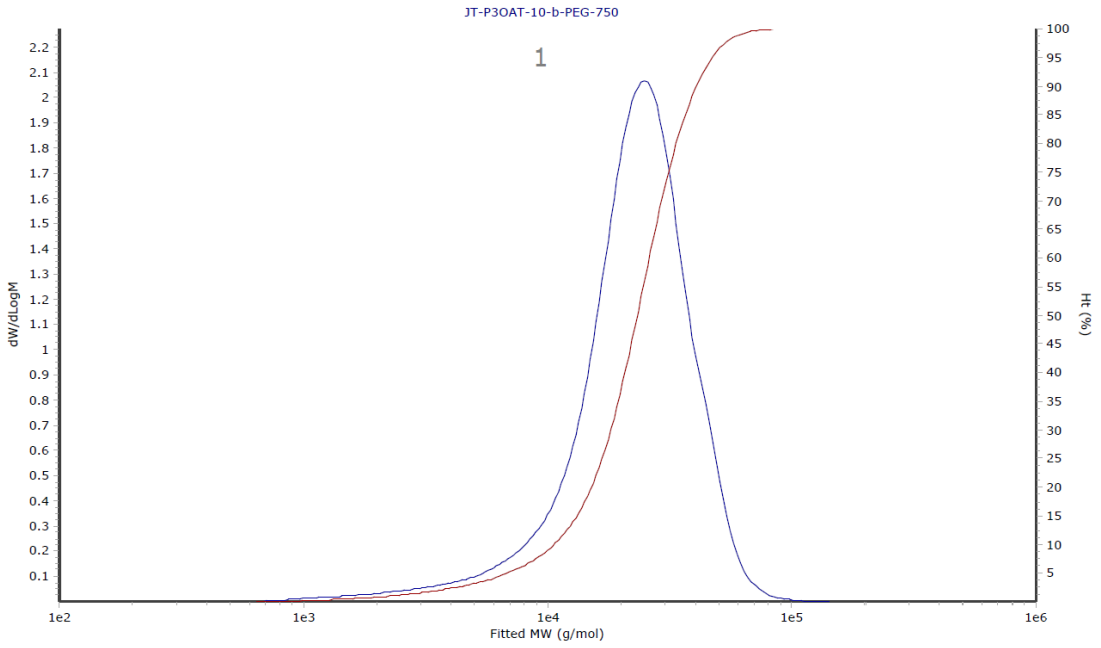

Preparation of P3DOT-b-PEG-40 P3DOT H/CHO (30 mg, 0.002 mmol), PEG-40-Rh (26 mg, 0.012 mmol), anhydrous $CHCl_3$ (4.5 mL) and piperidine (0.060 mL) was used, yielding a dark blue solid (29 mg). ^{1}H NMR (400 MHz, $CDCl_3$) δ 6.95 (s, 47H), 4.17 (s, 113H), 3.64 (s, 188H), 3.38 (s, 3H), 2.02 – 1.77 (m, 146H), 1.61 – 1.19 (m, 1087H), 0.98 – 0.73 (m, 235H). GPC (PhCl): M_n = 17.4 kDa, M_w = 25.2 kDa

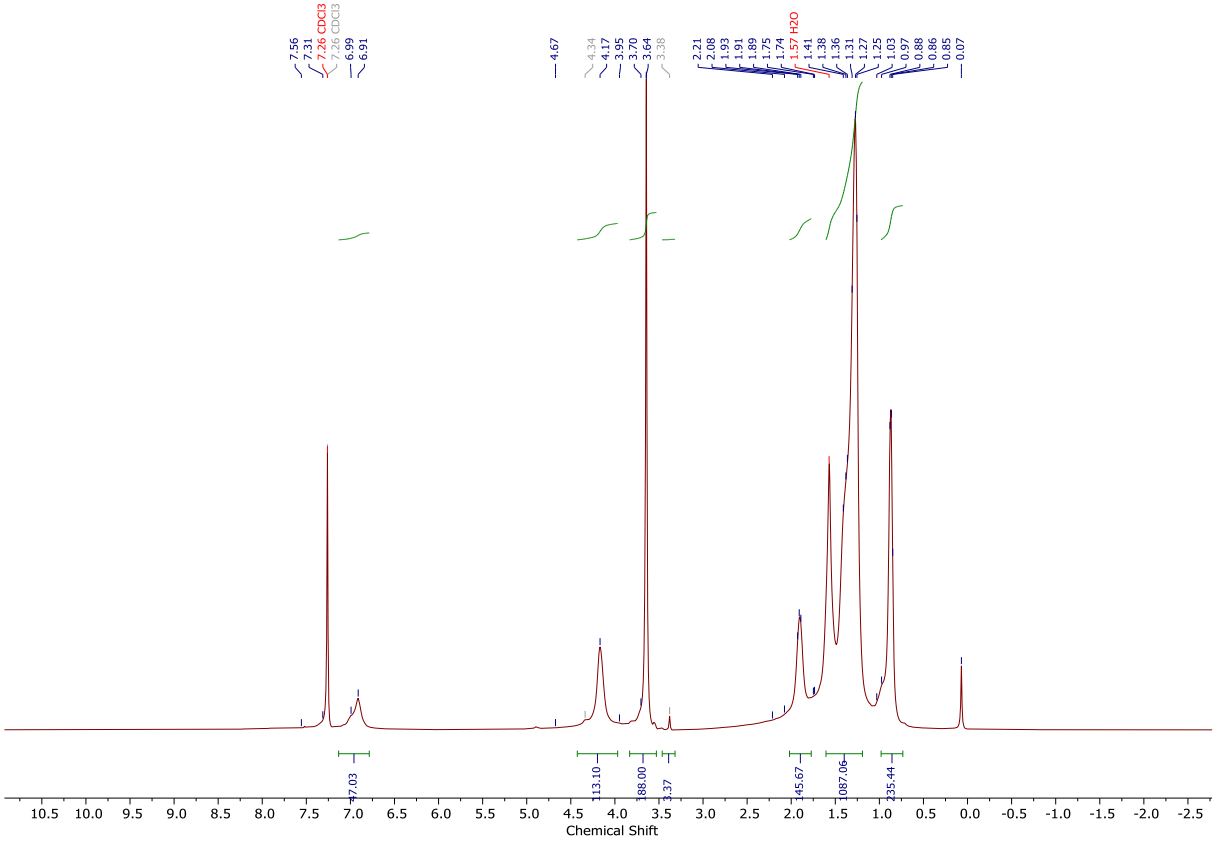

Molecular Weight Averages

Peak	Mp (g/mol)	Mn (g/mol)	Mw (g/mol)	Mz (g/mol)	Mz+1 (g/mol)	Mv (g/mol)
Peak 1	26392	17383	25231	30666	35662	24370

PD
1.451

Distribution Plot

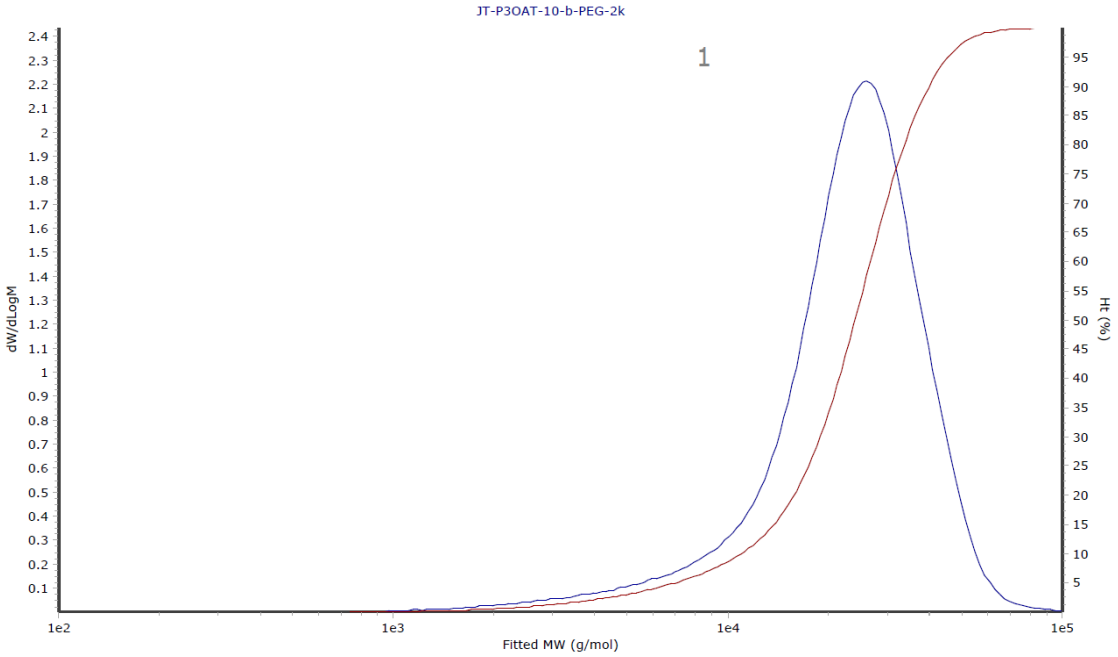

Preparation of P3DOT-53-b-PEG-80 P3DOT H/CHO (30 mg, 0.002 mmol), PEG-80-Rh (52 mg, 0.012 mmol), anhydrous $CHCl_3$ (4.5 mL) and piperidine (0.060 mL) was used, yielding a dark blue solid (32 mg). ^{1}H NMR (400 MHz, $CDCl_3$) δ 7.12 – 6.69 (m, 45H), 4.45 – 3.96 (m, 104H), 3.64 (s, 382H), 3.47 – 3.33 (m, 4H), 1.91 (dd, J = 14.2, 6.7 Hz, 124H), 1.62 – 1.13 (m, 1007H), 0.87 (td, J = 6.8, 2.9 Hz, 215H). GPC (PhCl): M_n = 19.5 kDa, M_w = 26.4 kDa

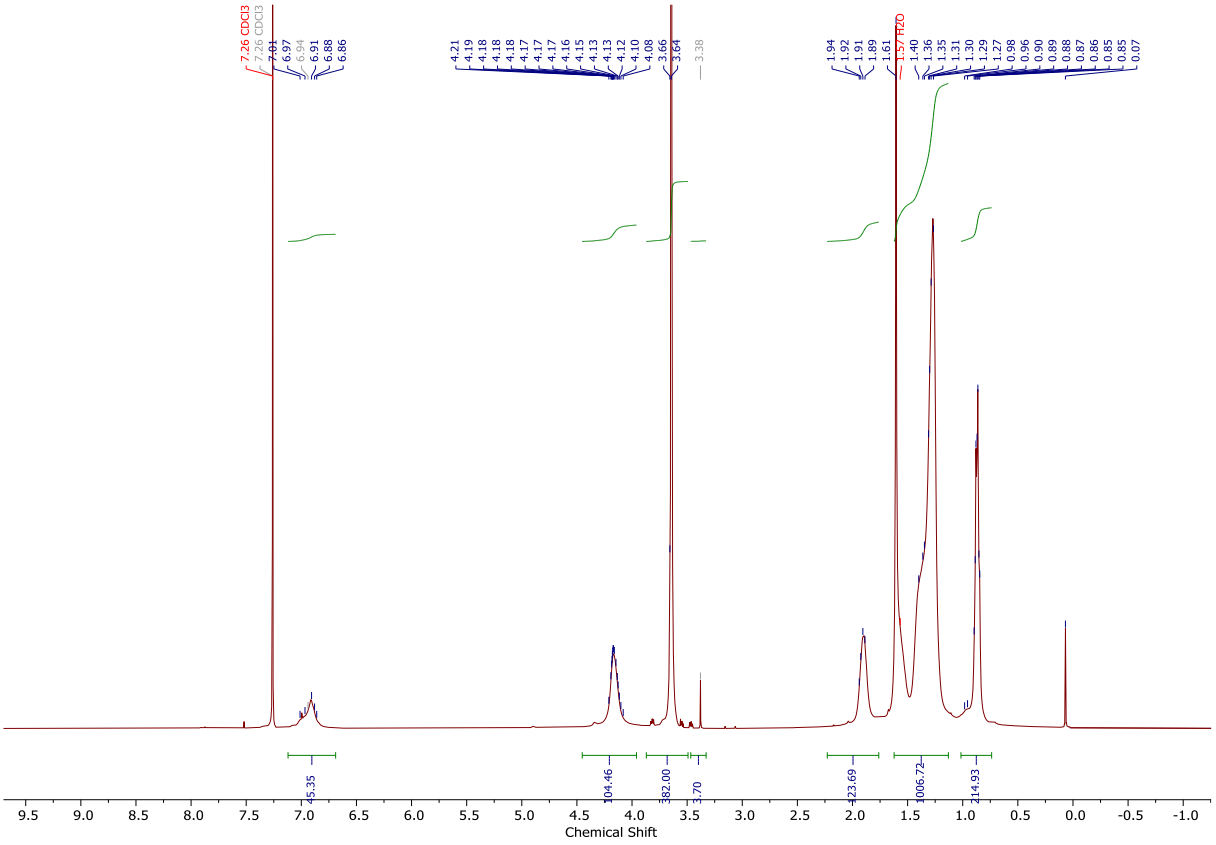

Molecular Weight Averages

Peak	Mp (g/mol)	Mn (g/mol)	Mw (g/mol)	Mz (g/mol)	Mz+1 (g/mol)	Mv (g/mol)
Peak 1	27590	19503	26463	32194	37941	25593

PD
1.357

Distribution Plot

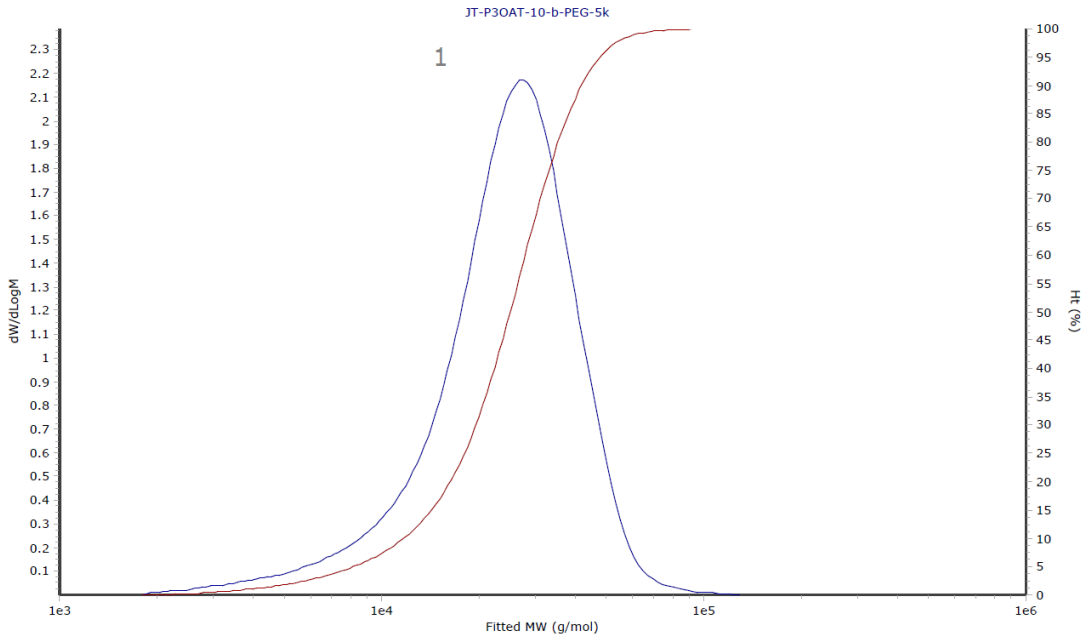

Preparation of P3DOT-53-b-PLLA-34 P3DOT H/CHO (30 mg, 15.0 kDa, 0.002 mmol) and PLLA-34-Rh (44 mg, 0.016 mmol) was added to a microwave vial. Then, anhydrous $CHCl_3$ (4.5 mL) and 2,2,6,6-tetramethylpiperidine (0.14 mL, 0.8 mmol, 50 eq w.r.t. PLLA) was added and the reaction mixture was warmed to reflux for 36 hours. Then, the reaction mixture is precipitated in methanol and further purified by Soxhlet extraction with acetonitrile, then chloroform, which was concentrated and re-precipitated in methanol to yield a dark blue solid (33 mg). ^{1}H NMR (400 MHz, $CDCl_3$) δ 6.91 (s, 32H), 5.16 (q, J = 7.1 Hz, 36H), 4.16 (s, 84H), 1.90 (s, 111H), 1.76 – 1.47 (m, 651H), 1.47 – 1.06 (m, 1294H), 0.89 (td, J = 17.1, 6.7 Hz, 413H). GPC (PhCl): M_n = 16.5 kDa M_w = 24.1 kDa

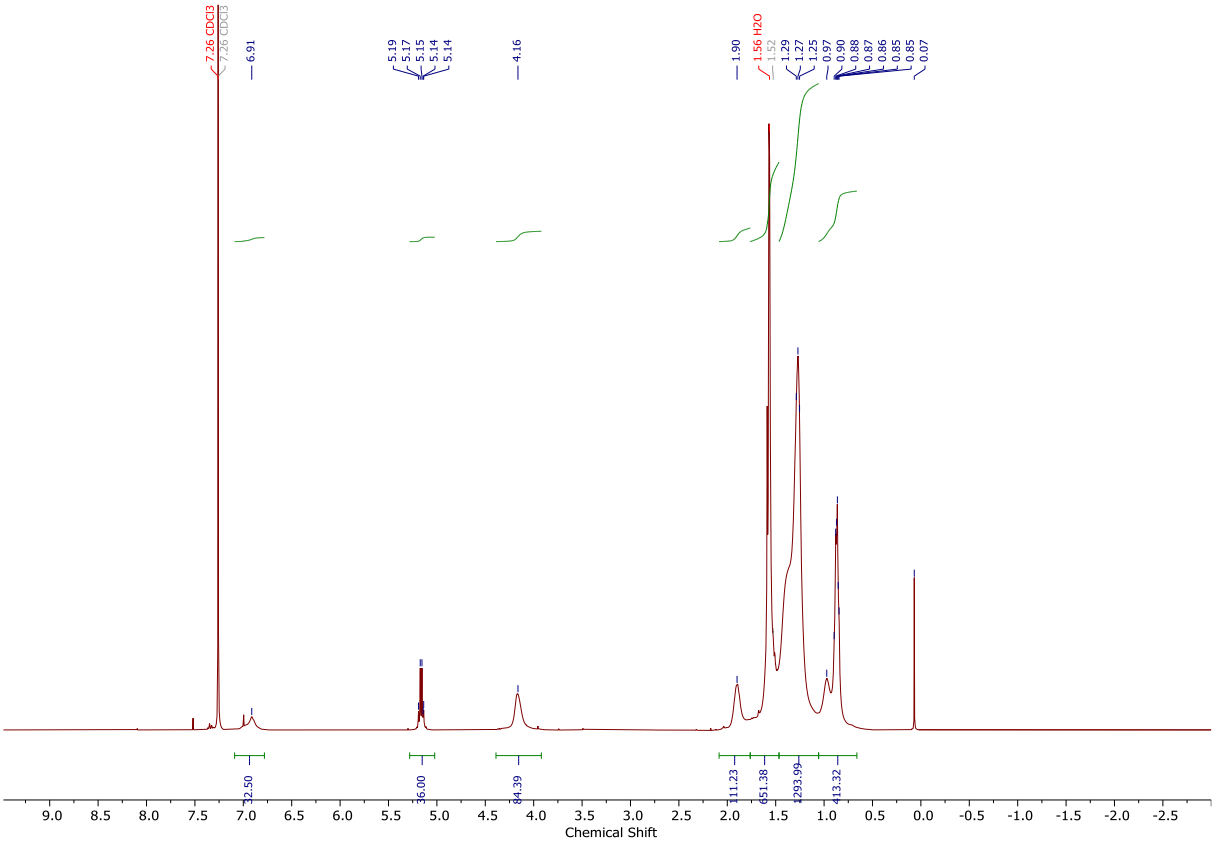

Molecular Weight Averages

Peak	Mp (g/mol)	Mn (g/mol)	Mw (g/mol)	Mz (g/mol)	Mz+1 (g/mol)	Mv (g/mol)
Peak 1	21842	16464	24061	31140	38688	23044

PD
1.461

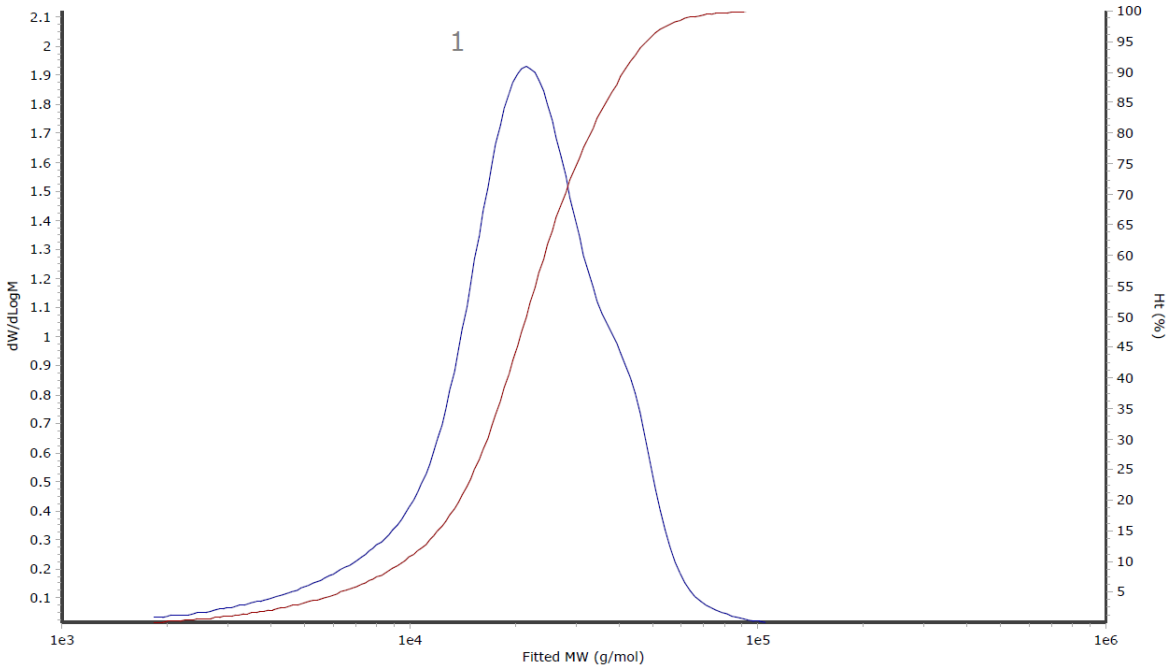

Preparation of P3DOT-53-b-PLLA-65 P3DOT H/CHO (30 mg, 0.002 mmol), PLLA-65-Rh (79 mg, 0.016 mmol), anhydrous $CHCl_3$ (4.5 mL) and 2,2,6,6-tetramethylpiperidine (0.14 mL) was used, yielding a dark blue solid (33 mg). ^{1}H NMR (400 MHz, $CDCl_3$) δ 7.40 – 7.30 (m, 6H), 6.91 (s, 30H), 5.16 (q, J = 7.1 Hz, 66H), 4.16 (s, 90H), 1.90 (s, 214H), 1.56 (s, 835H), 1.33 (d, J = 51.5 Hz, 1569H), 1.05 – 0.75 (m, 494H). GPC (PhCl): M_n = 18.3 kDa, M_w = 25.9 kDa.

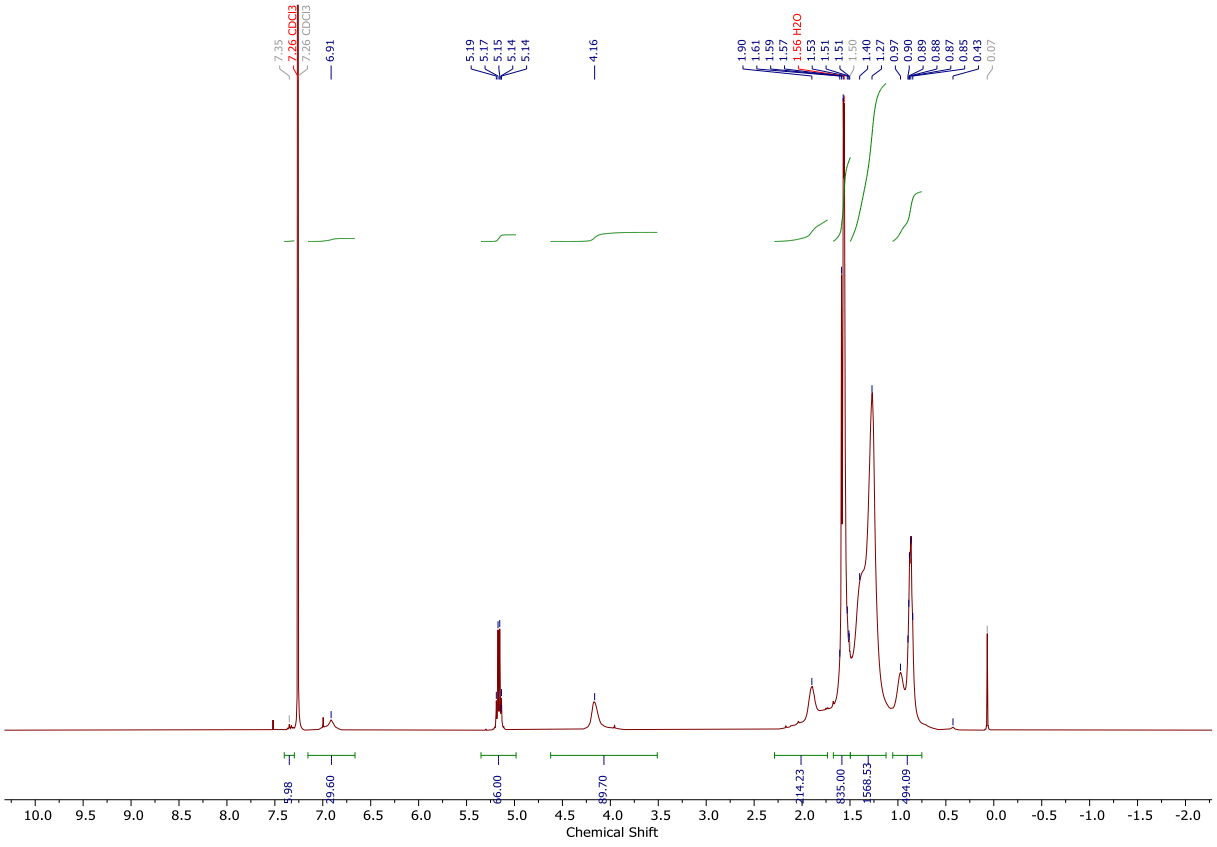

Molecular Weight Averages

Peak	Mp (g/mol)	Mn (g/mol)	Mw (g/mol)	Mz (g/mol)	Mz+1 (g/mol)	Mv (g/mol)
Peak 1	22808	18342	25906	34454	45592	24778

PD
1.412

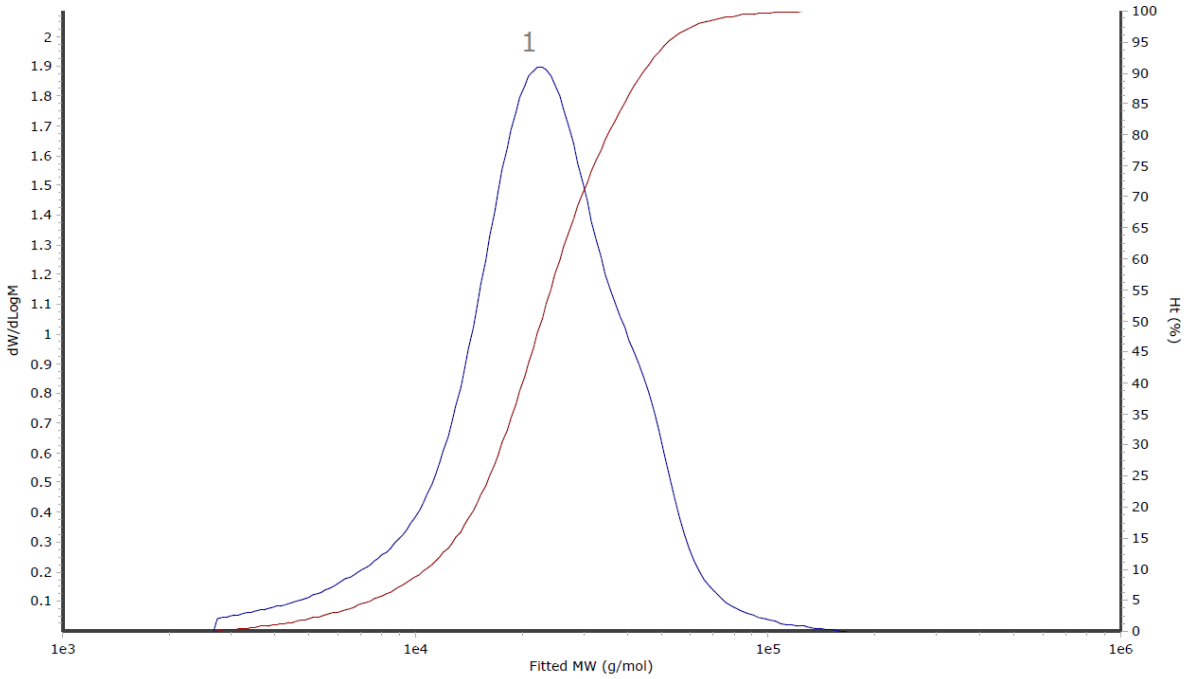

Preparation of P3AOT-G1C7-b-PEG-18 P3AOT-G$_1$C$_7$ H/CHO (34 mg, 0.003 mmol), PEG-18-Rh (18 mg, 0.018 mmol), anhydrous $CHCl_3$ (3.5 mL) and piperidine (0.090 mL) was used, yielding a dark blue solid. (26 mg). ^{1}H NMR (400 MHz, $CDCl_3$) δ 6.96 (s, 30H), 4.31 (s, 85H), 4.02 – 3.76 (m, 93H), 3.71 – 3.62 (m, 65H), 3.58 (dt, *J* = 15.1, 6.6 Hz, 61H), 3.38 (s, 5H), 1.63 (d, *J* = 11.6 Hz, 491H), 1.46 – 1.11 (m, 993H), 1.06 – 0.64 (m, 386H). GPC (PhCl): M_n = 13.6 kDa, M_w = 17.2 kDa

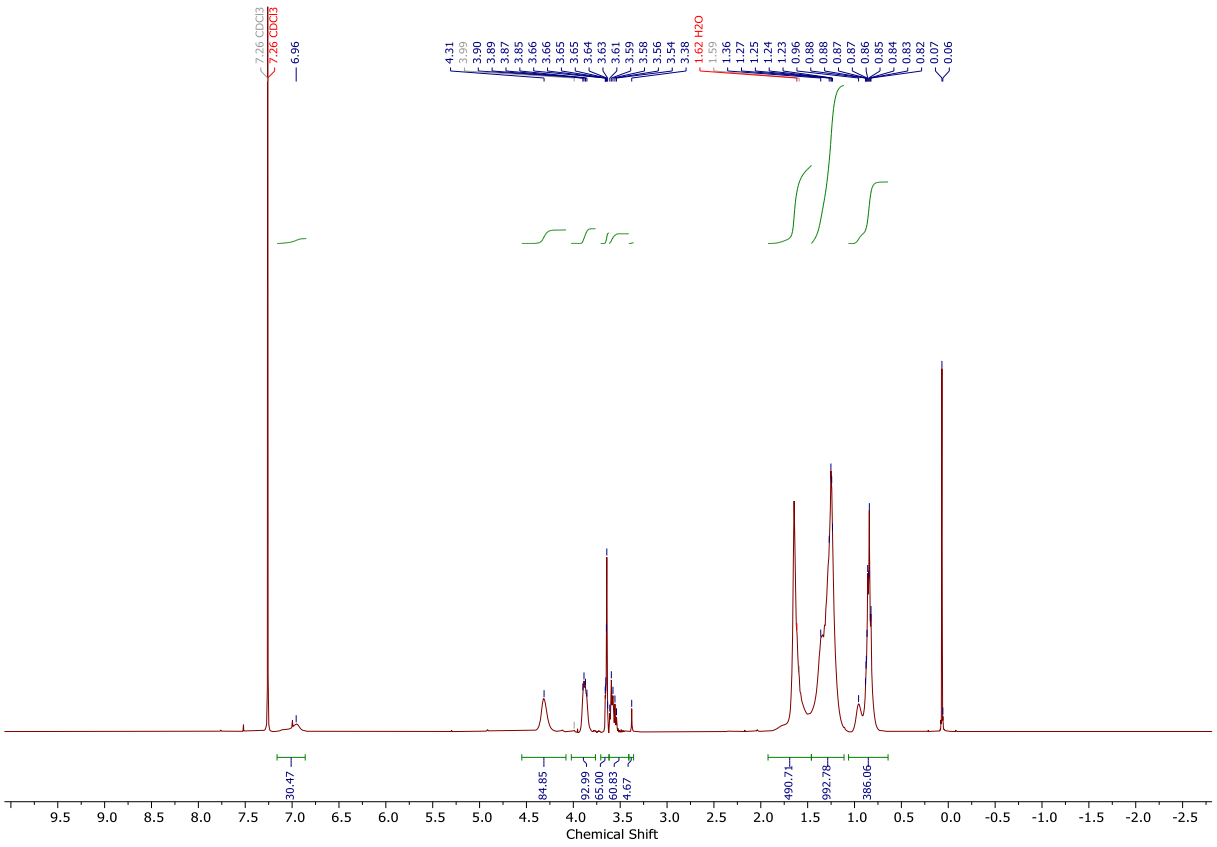

Molecular Weight Averages

Peak	Mp (g/mol)	Mn (g/mol)	Mw (g/mol)	Mz (g/mol)	Mz+1 (g/mol)	Mv (g/mol)
Peak 1	15154	13656	17243	22105	28862	16638

PD
1.263

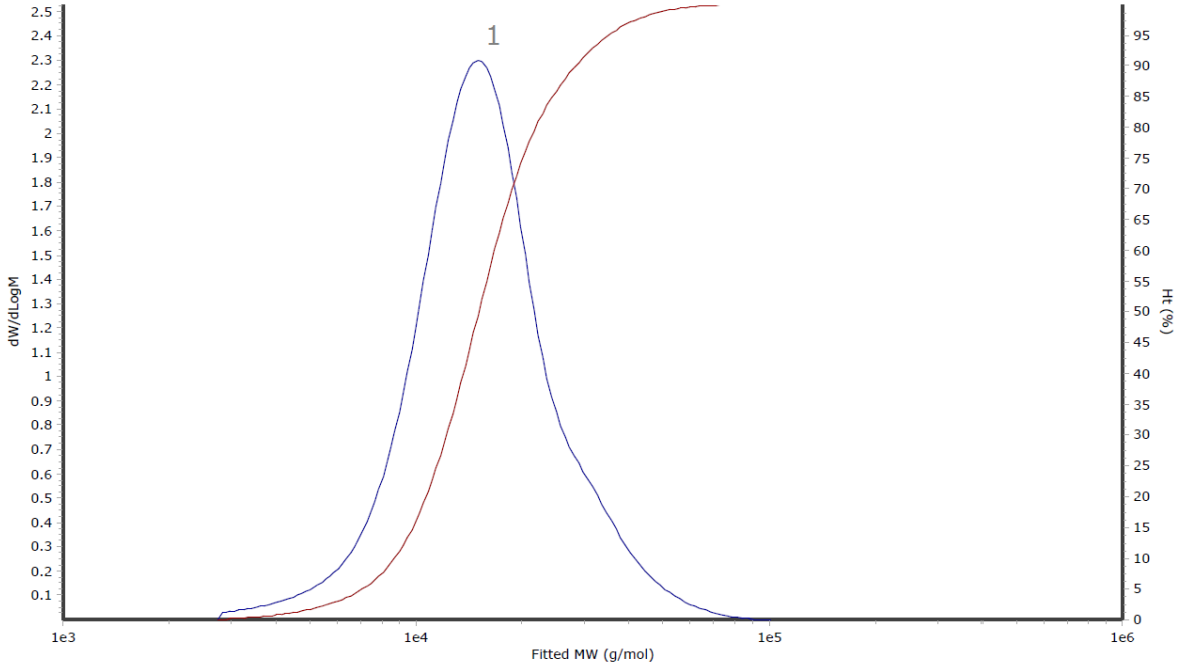

Preparation of P3AOT-C_2C_6-b-PEG-18 P3AOT-C_2C_6 H/CHO (53.4 mg, 0.004 mmol), PEG-18-Rh (24.0 mg, 0.024 mmol), anhydrous $CHCl_3$ (5.3 mL) and piperidine (0.12 mL) was used, yielding a dark blue solid (45 mg). ^{1}H NMR (400 MHz, $CDCl_3$) δ 6.92 (s, 9H), 4.18 (s, 19H), 3.65 (d, J = 5.4 Hz, 65H), 3.38 (s, 4H), 1.89 (s, 21H), 1.56 (s, 185H), 1.27 (d, J = 9.9 Hz, 213H), 0.87 (t, J = 5.4 Hz, 53H). GPC (PhCl): M_n = 16.8 kDa, M_w = 21.1 kDa

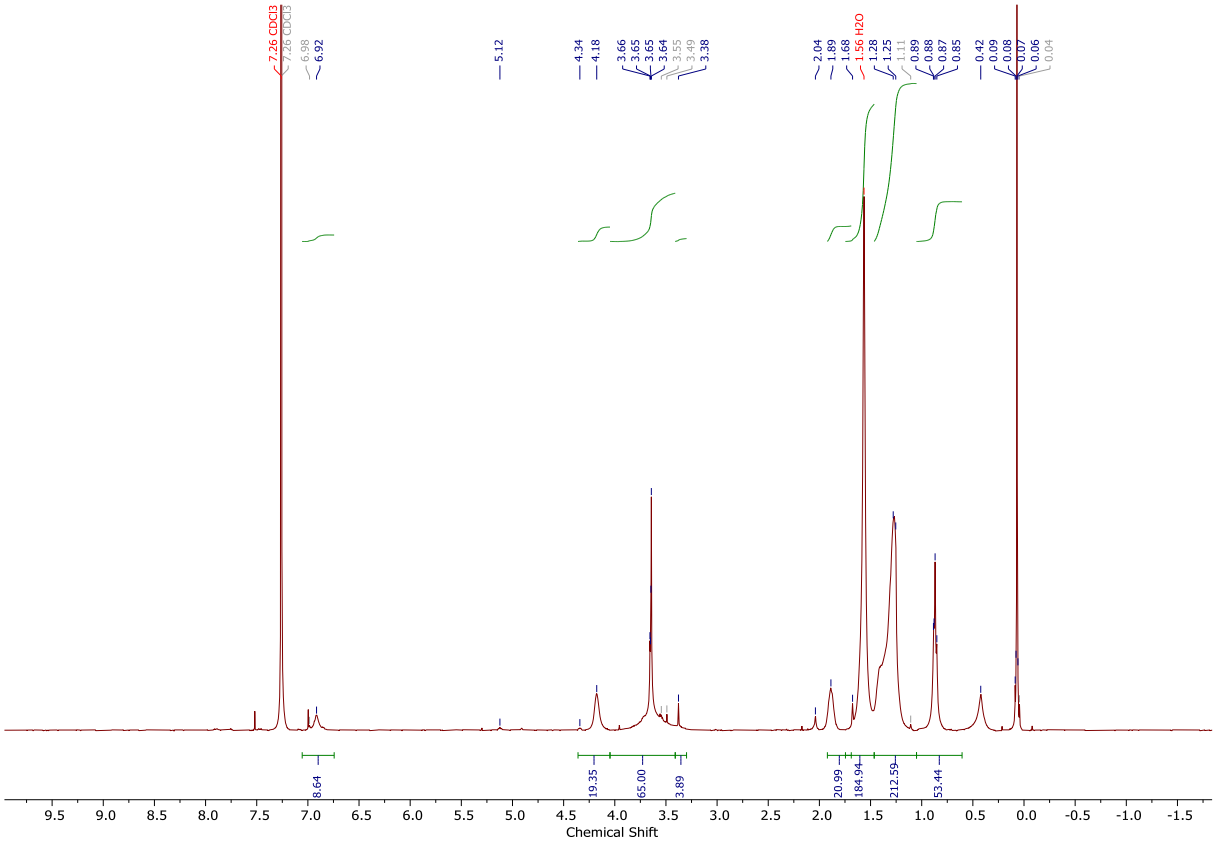

Molecular Weight Averages

Peak	Mp (g/mol)	Mn (g/mol)	Mw (g/mol)	Mz (g/mol)	Mz+1 (g/mol)	Mv (g/mol)
Peak 1	21225	16831	21138	25514	30496	20517

PD
1.256

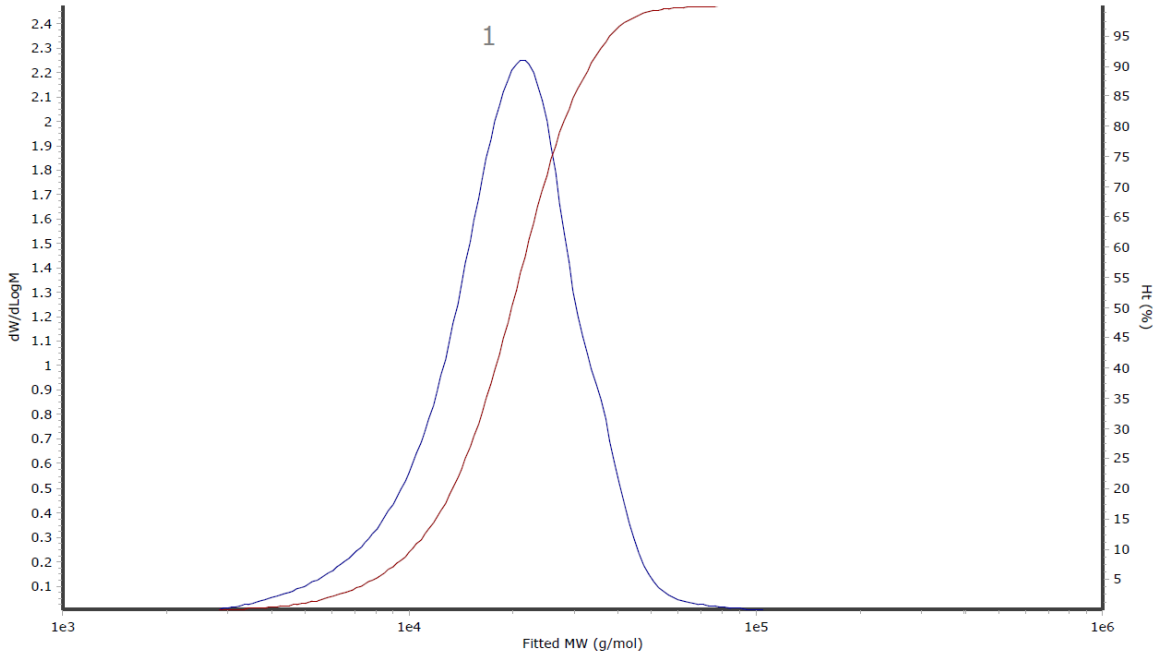

7.2.2 Synthetic Procedure for Chapter 4

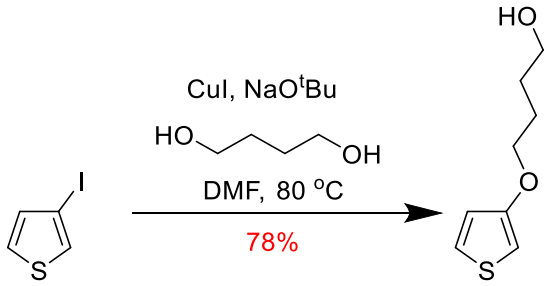

Preparation of 4-(thiophen-3-yloxy)butan-1-ol (https://pubs.rsc.org/en/content/articlelanding/2015/ra/c5ra12529d)

Under N_2, 3-iodothiophene (3.15 g, 15 mmol), 1,4-butanediol (4.06 g, 45 mmol), cuprous iodide (256 mg, 1.5 mmol) and sodium tert-butoxide (4.32 g, 45 mmol) were dissolved in anhydrous DMF (30 mL) and heated at 80 °C for 24 hours. Then, ethyl acetate (280 mL) and water (200 mL) were added. The aqueous phase was re-extracted with ethyl acetate (200 mL x 2), which was combined with the organic phase, concentrated to a volume of 300 mL under reduced pressure and washed with brine (300 mL). Then organic layer was then dried over anhydrous sodium sulphate and concentrated under reduced pressure. The product was further purified by column chromatography (hexane/ethyl acetate 1/1) to yield 4-(thiophen-3-yloxy)butan-1-ol as a pale yellow liquid (2.01 g, 78%). ^{1}H NMR (500 MHz, CDCl3) δ 7.16 (dd, J = 5.3, 3.1 Hz, 1H), 6.74 (dd, J = 5.2, 1.6 Hz, 1H), 6.23 (dd, J = 3.2, 1.5 Hz, 1H), 3.97 (t, J = 6.2 Hz, 2H), 3.68 (t, J = 6.4 Hz, 2H), 2.42 (s, 1H), 1.85 (dq, J = 8.3, 6.4 Hz, 2H), 1.72 (dq, J = 9.5, 6.4 Hz, 2H). ^{13}C NMR (126 MHz, CDCl3) δ 157.76, 124.70, 119.46, 97.32, 70.00, 62.37, 29.38, 25.79.

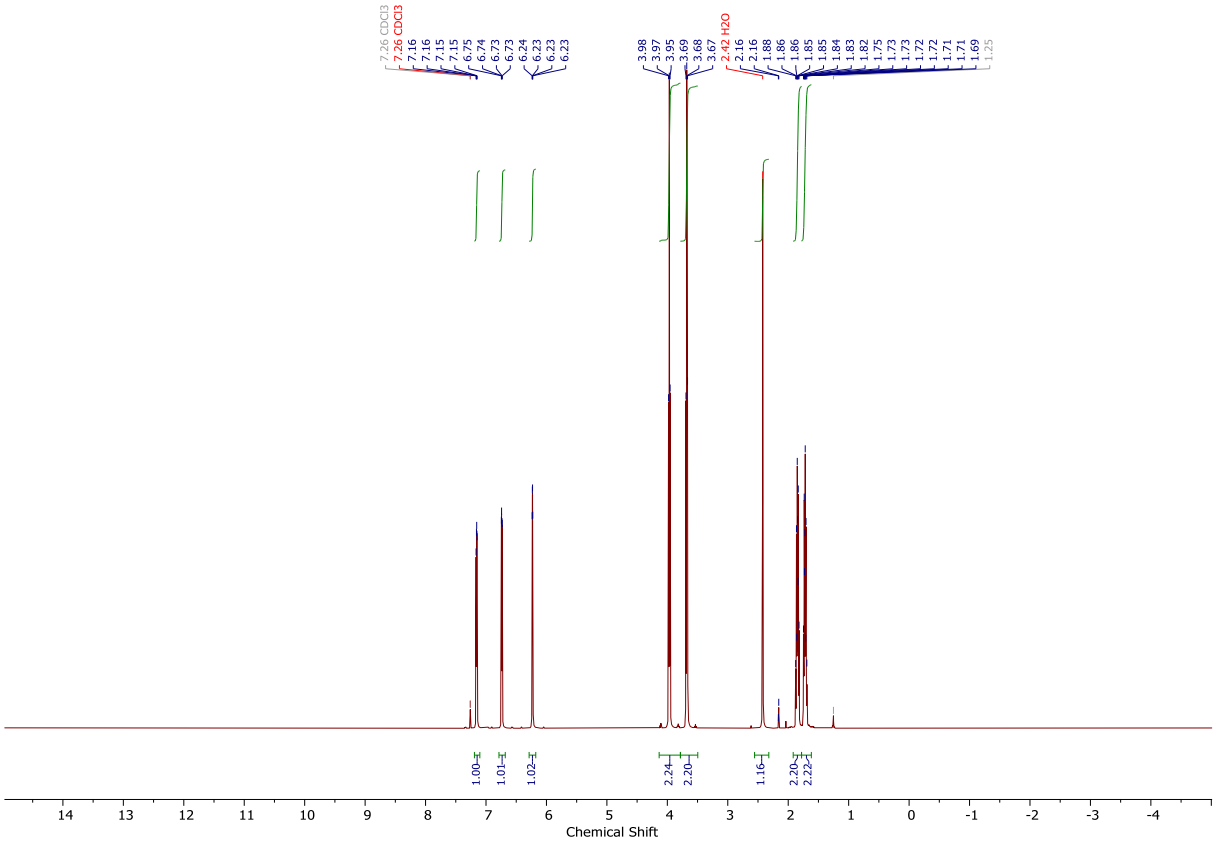
7.26 CDCl3
7.26 CDCl3
7.16
7.16
7.15
7.15
6.75
6.74
6.73
6.73
6.24
6.23
6.23
6.23
3.98
3.97
3.95
3.69
3.68
3.67
2.42 H2O
2.16
2.16
1.88
1.86
1.86
1.85
1.85
1.84
1.83
1.82
1.75
1.73
1.73
1.72
1.72
1.71
1.71
1.69
1.25
1.00
1.01
1.02
2.24
2.20
1.16
2.20
2.22
Chemical Shift

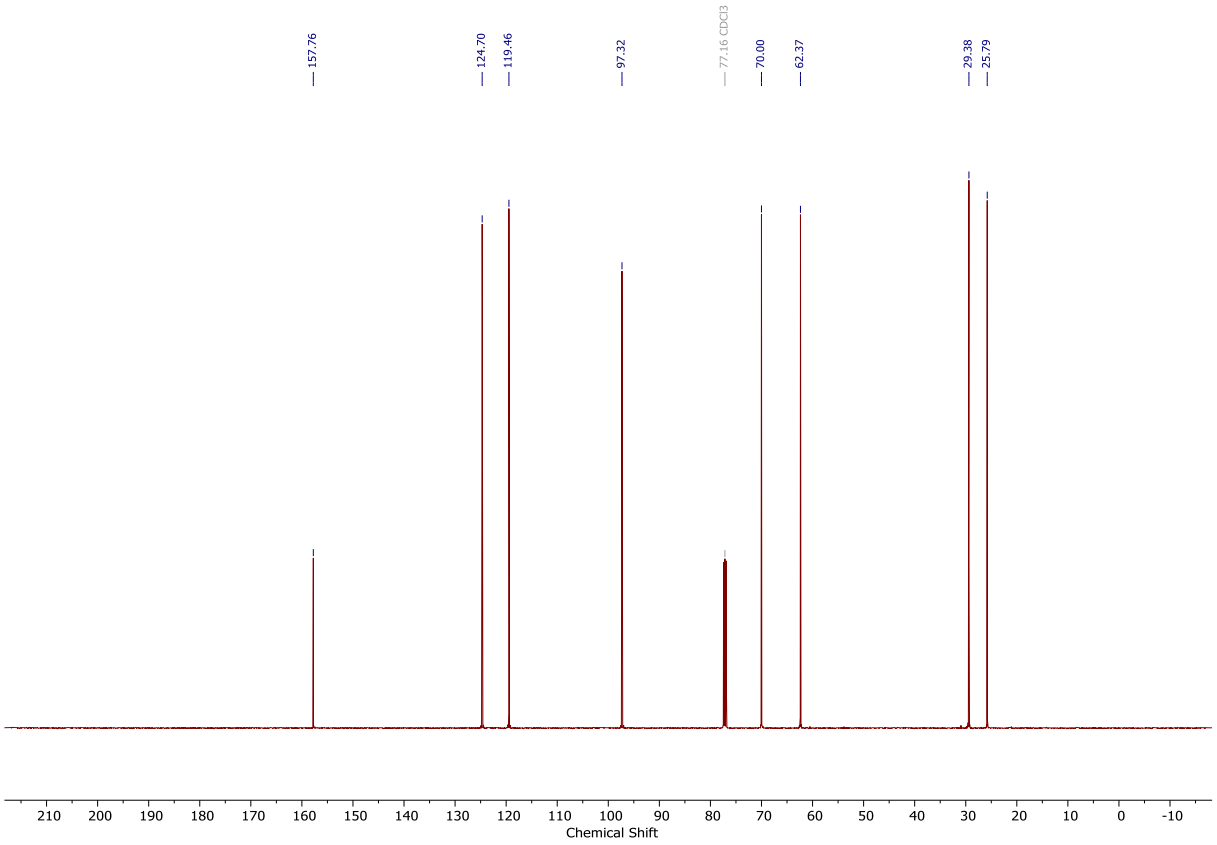
157.76
124.70
119.46
97.32
77.16 CDCl3
70.00
62.37
29.38
25.79
Chemical Shift

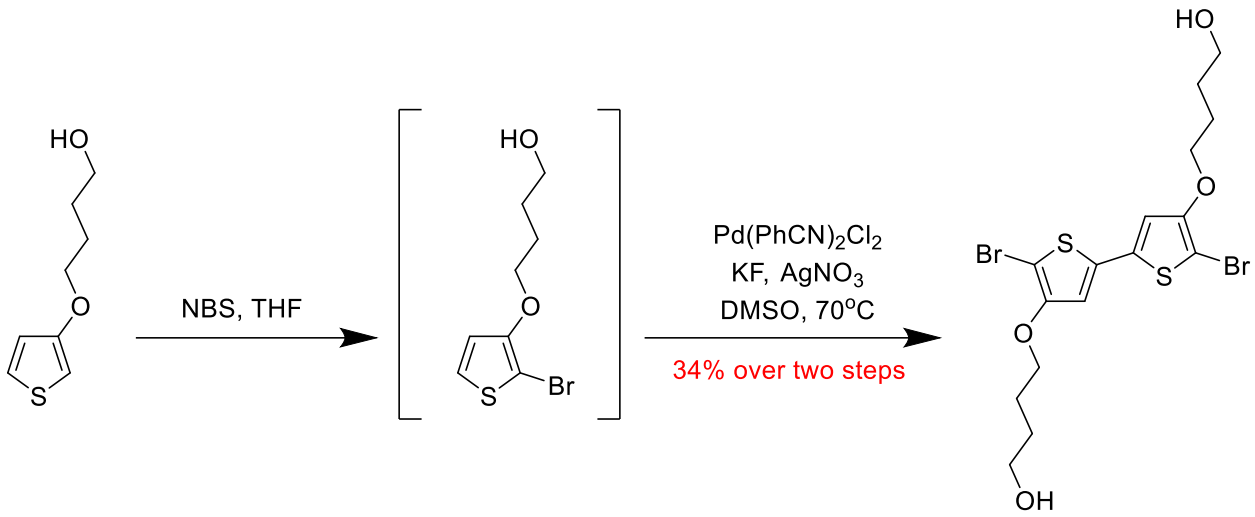

Preparation of 4,4'-((5,5'-dibromo-[2,2'-bithiophene]-4,4'-diyl)bis(oxy))bis(butan-1-ol) (T_2-OH_2-Br_2)

Under N_2, 4-(thiophen-3-yloxy)butan-1-ol (2.00 g, 11.7 mmol) was dissolved in anhydrous THF (23 mL) and cooled to 0 °C. Then, N-Bromosuccinimide (2.08 g, 11.7 mmol) was added in three portions and stirred at room temperature for 2 hours. Upon completion, the reaction mixture was quenched with water (100 mL) and then extracted thrice with ethyl acetate (100 mL x 3). The organic phase was washed with brine (200 mL) and then dried over anhydrous sodium sulphate before being concentrated under reduced pressure. The crude product was further purified through column chromatography (Hexane/ethyl acetate 1/1). The intermediate **must not be immediately dried.** Anhydrous DMSO (20 mL) was added before the volatile solvent removed under reduced pressure. Then, the reaction mixture was de-gassed with N_2 bubbling for 1 hour. Silver nitrate (3.97 g, 23.4 mmol, 2 eq), anhydrous potassium fluoride (1.36 g, 23.4 mmol, 2 eq) and bis(benzonitrile)palladium dichloride ($PdCl_2(PhCN)_2$) (134 mg, 0.351 mmol, 0.03 eq) was added and the reaction mixture was warmed to 70 °C for 3 hours. Upon completion, the reaction mixture was quenched with water (80 mL). The aqueous layer was extracted with ethyl acetate (100 mL x 3), which was similarly dried following brine wash (200 mL), anhydrous sodium sulphate

and column chromatography (ethyl acetate -> ethyl acetate/methanol 99/1) to yield a yellow solid (995 mg, 34%). ^{1}H NMR (500 MHz, CD_3CN) δ 7.01 (s, 2H), 4.11 (t, J = 6.5 Hz, 4H), 3.55 (td, J = 6.4, 5.3 Hz, 4H), 2.60 (t, J = 5.3 Hz, 2H), 1.77 (tt, J = 8.5, 6.3 Hz, 4H), 1.68 – 1.56 (m, 4H). ^{13}C NMR (126 MHz, CD_3CN) δ 155.83, 135.74, 115.17, 90.56, 73.05, 62.15, 29.79, 26.75. HRMS (ESI): calcd for $C_{16}H_{20}Br_2O_4S_2$, 497.9164; found 497.9183 (M^+, 3.8 ppm).

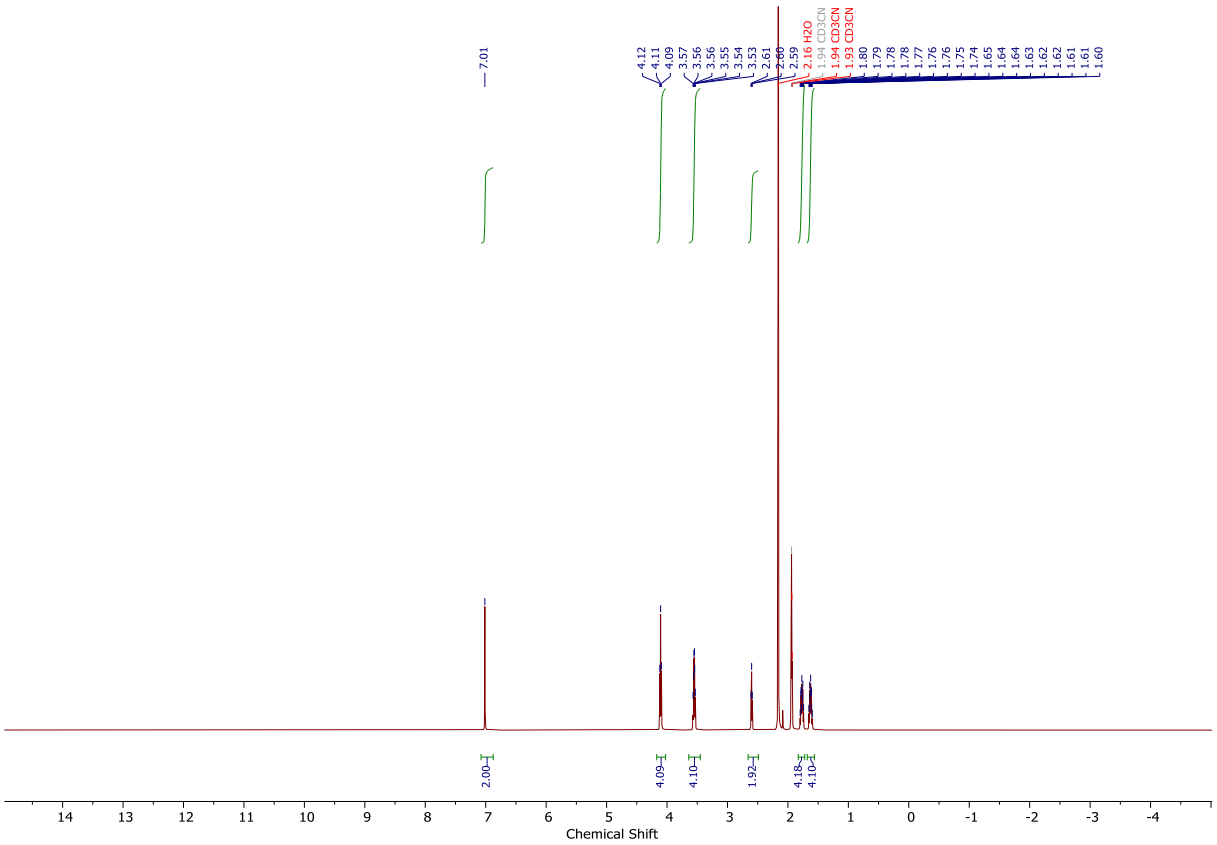
7.01
4.12
4.11
4.09
3.57
3.56
3.56
3.55
3.54
3.53
2.61
2.60
2.59
2.16 H2O
2.06 CD3CN
1.94 CD3CN
1.93 CD3CN
1.80
1.79
1.78
1.78
1.77
1.76
1.76
1.75
1.74
1.65
1.64
1.64
1.63
1.62
1.62
1.61
1.61
1.60
2.00
4.09
4.10
1.92
4.18
4.10
Chemical Shift

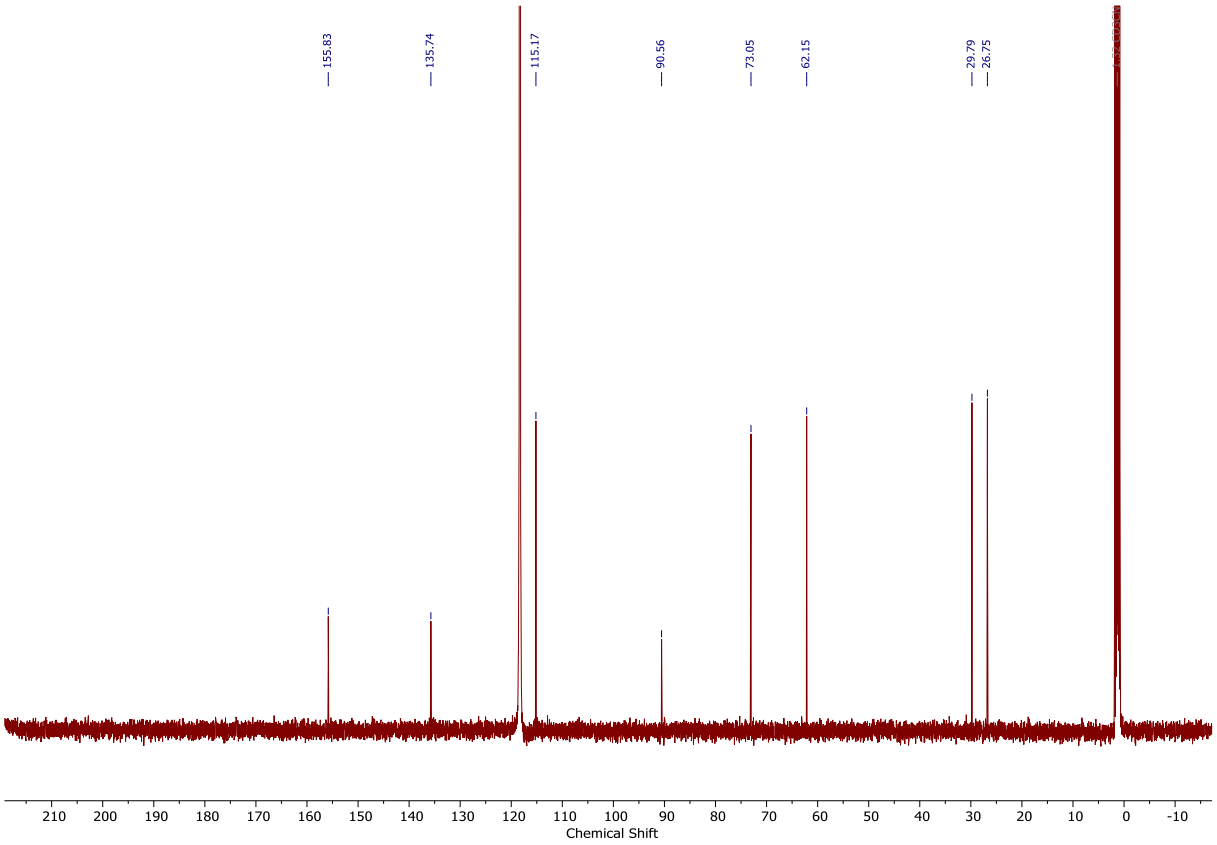
155.83
135.74
115.17
90.56
73.05
62.15
29.79
26.75
Chemical Shift

Expanded Spectrum RT 0.11, NL 400688, Peak [1], Target Mass 497.9164

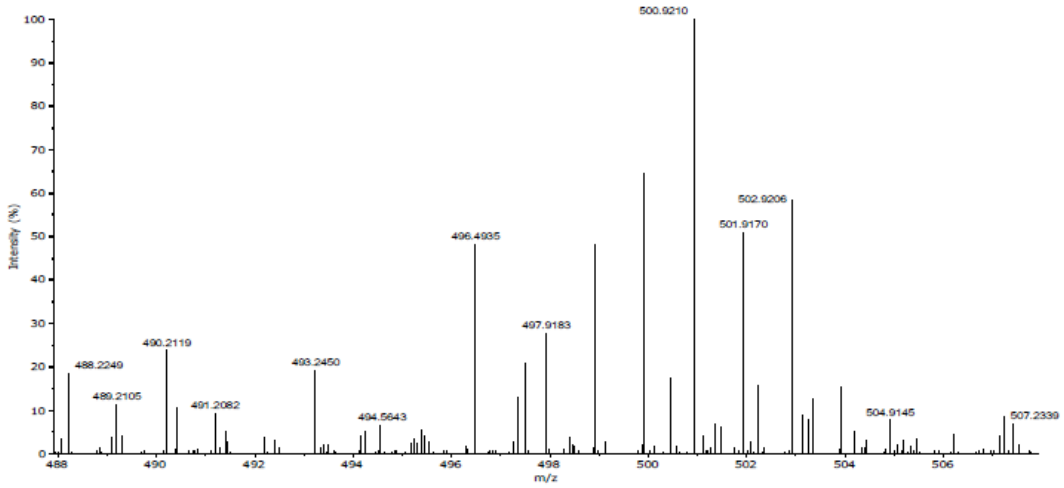

Theoretical Spectrum for C16H20Br2O4S2, Minimum Abundance 0.01%

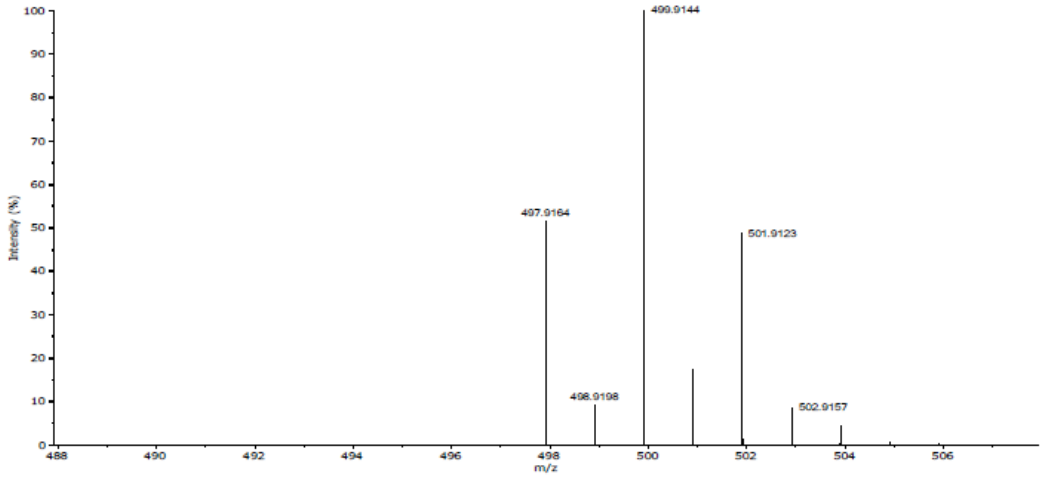

Measured Mass	Calculated Mass	Error (mDa)	Error (ppm)	Formula $[M]^+$	Response
497.9183	497.9164	1.87	3.76	$C_{16}H_{20}Br_2O_4S_2$	30108

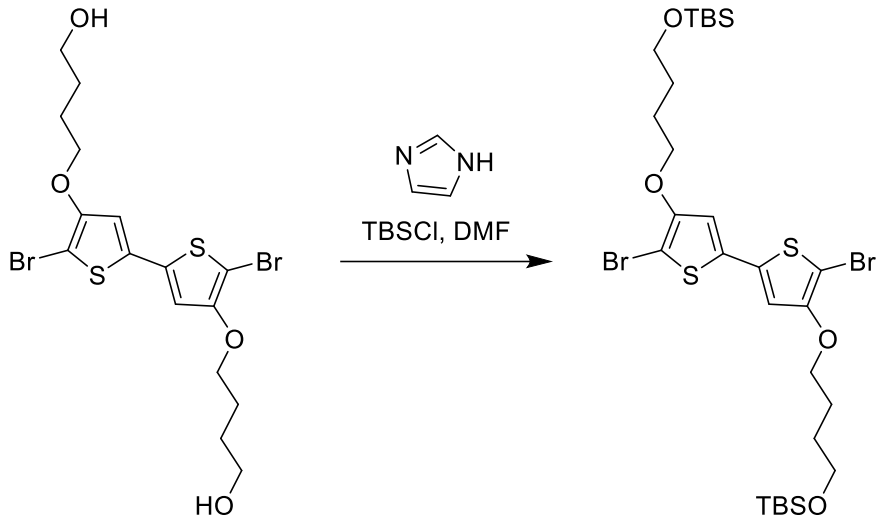

Preparation of T_2-$OTBS_2$-Br_2

T_2-OH_2-Br_2 (300 mg, 0.6 mmol) and TBSCl (217 mg, 2.4 eq) was added to anhydrous DMF and protected from light. Then, imidazole (102 mg, 2.5 eq) was added and the reaction mixture was stirred at room temperature overnight. The reaction mixture was diluted with water (100 mL) and extracted with dichloromethane (75 mL x 3), which is then washed with water (200 mL x 4) and further purified by column chromatography (hexane -> hexane/ethyl acetate 25/1) to yield the product as yellow powder. (390 mg, 89%) ^{1}H NMR (500 MHz, CD_2Cl_2) δ 6.80 (s, 2H), 4.08 (t, J = 6.5 Hz, 4H), 3.68 (t, J = 6.2 Hz, 4H), 1.82 (dq, J = 8.8, 6.6 Hz, 4H), 1.68 (dt, J = 9.3, 6.4 Hz, 4H), 0.89 (s, 18H), 0.06 (s, 12H). ^{13}C NMR (126 MHz, CD_2Cl_2) δ 155.08, 135.30, 113.99, 90.94, 72.72, 63.09, 29.54, 26.57, 26.10, 18.58, -5.21. HRMS (ESI): calcd for $C_{28}H_{48}Br_2O_4S_2Si_2Na$, 749.0792; found 749.0772 ($M+Na^+$, -2.6 ppm).

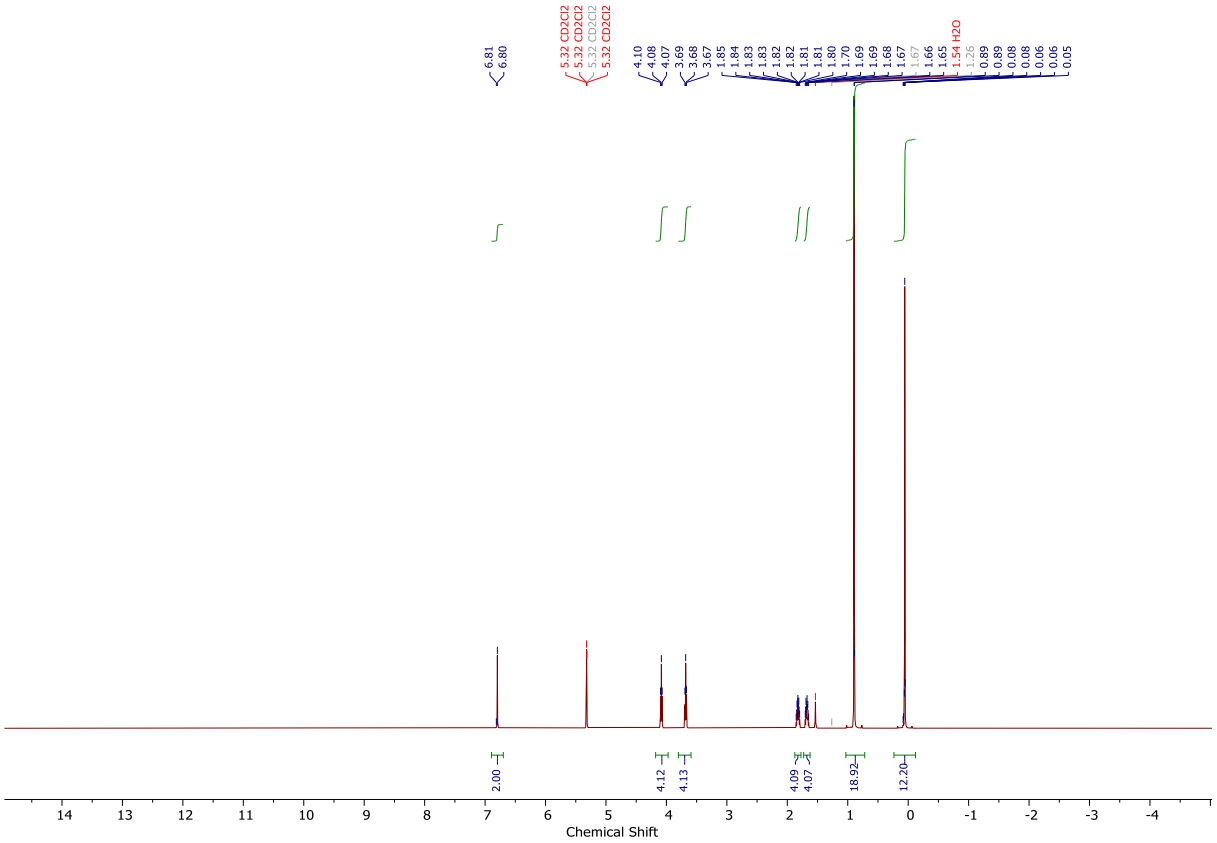
6.81
6.80
5.32 CD2Cl2
5.32 CD2Cl2
5.32 CD2Cl2
4.10
4.08
4.07
3.69
3.68
3.67
1.85
1.84
1.83
1.83
1.82
1.82
1.81
1.81
1.80
1.70
1.69
1.69
1.68
1.67
1.67
1.66
1.65
1.54 H2O
1.26
0.89
0.89
0.08
0.08
0.06
0.06
0.05
2.00
4.12
4.13
4.09
4.07
18.92
12.20
Chemical Shift

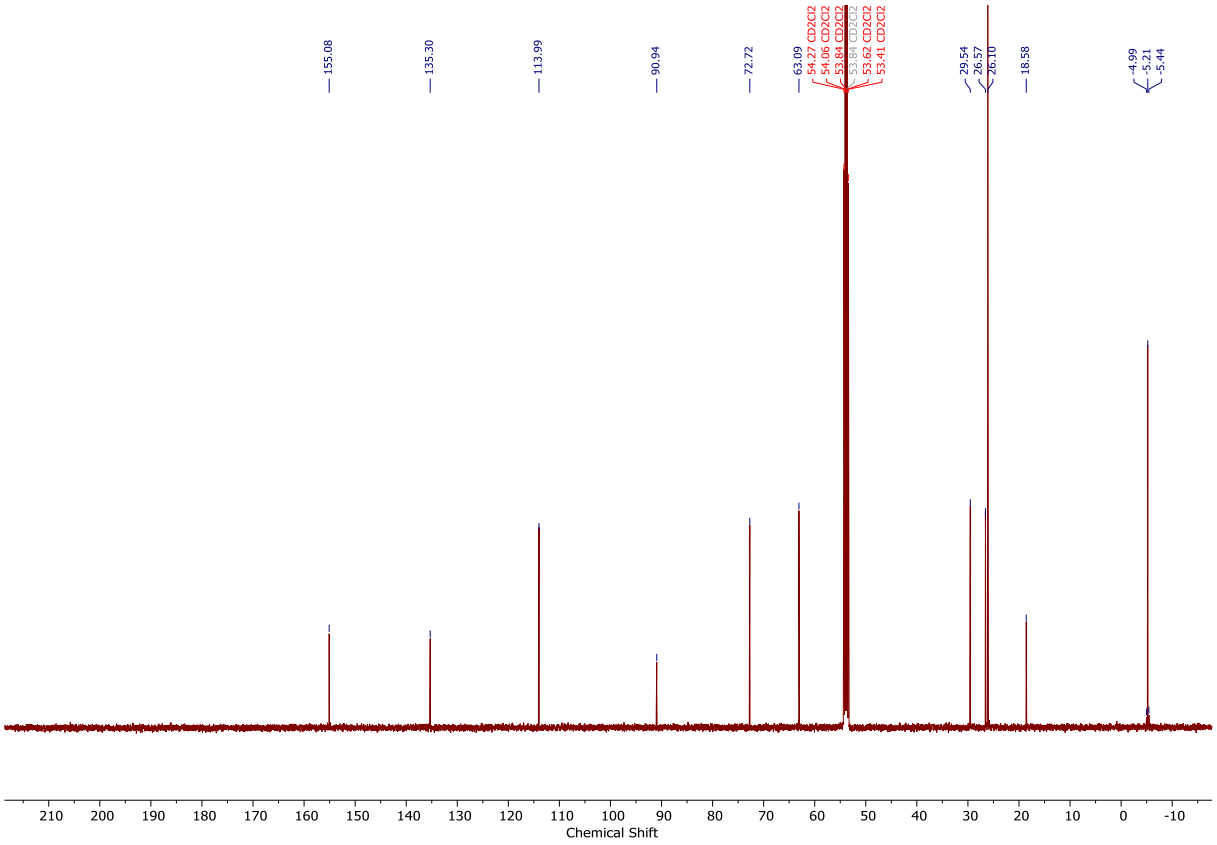
155.08
135.30
113.99
90.94
72.72
63.09
54.27 CD2Cl2
54.06 CD2Cl2
53.84 CD2Cl2
53.84 CD2Cl2
53.62 CD2Cl2
53.41 CD2Cl2
29.54
26.57
26.10
18.58
-4.99
-5.21
-5.44
Chemical Shift

Expanded Spectrum RT 0.09, NL 783423, Peak [1], Target Mass 749.0792

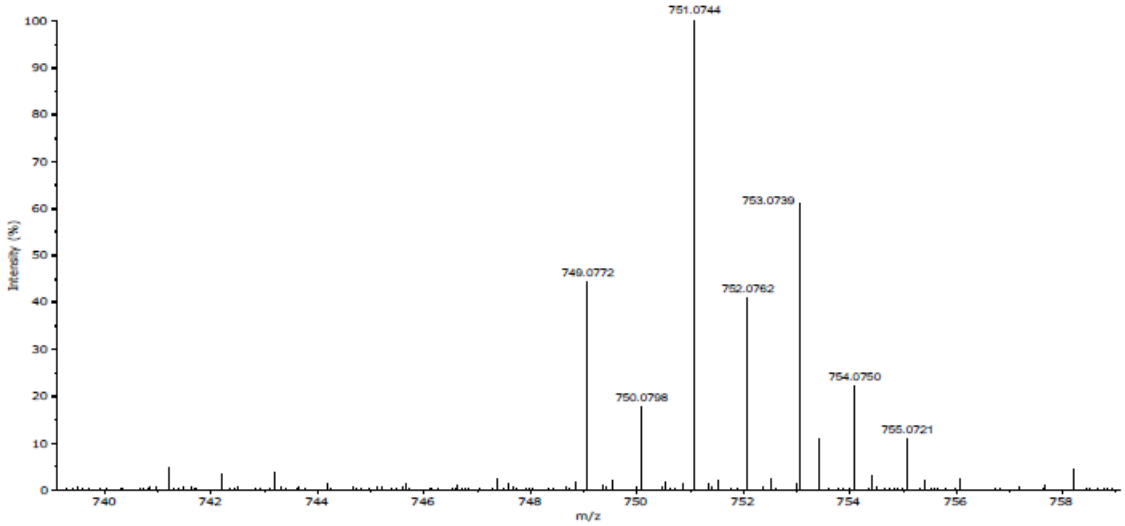

Theoretical Spectrum for C28H48Br2O4S2Si2Na, Minimum Abundance 0.01%

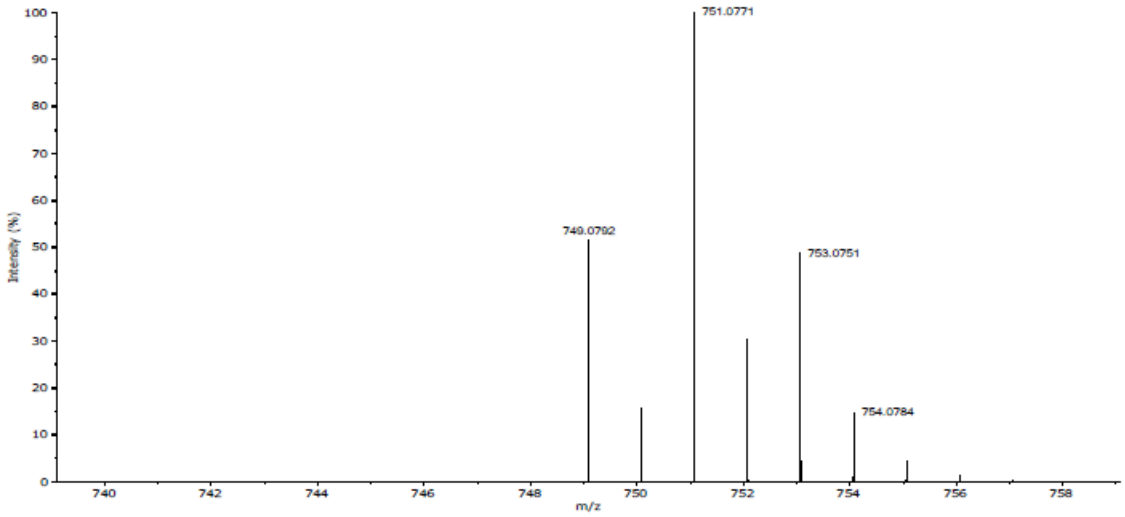

Measured Mass	Calculated Mass	Error (mDa)	Error (ppm)	Formula $[M+Na]^+$	Response
749.0772	749.0792	-1.95	-2.61	$C_{28}H_{48}Br_2O_4S_2Si_2Na$	37964

Preparation of PgBTTT-OTBS

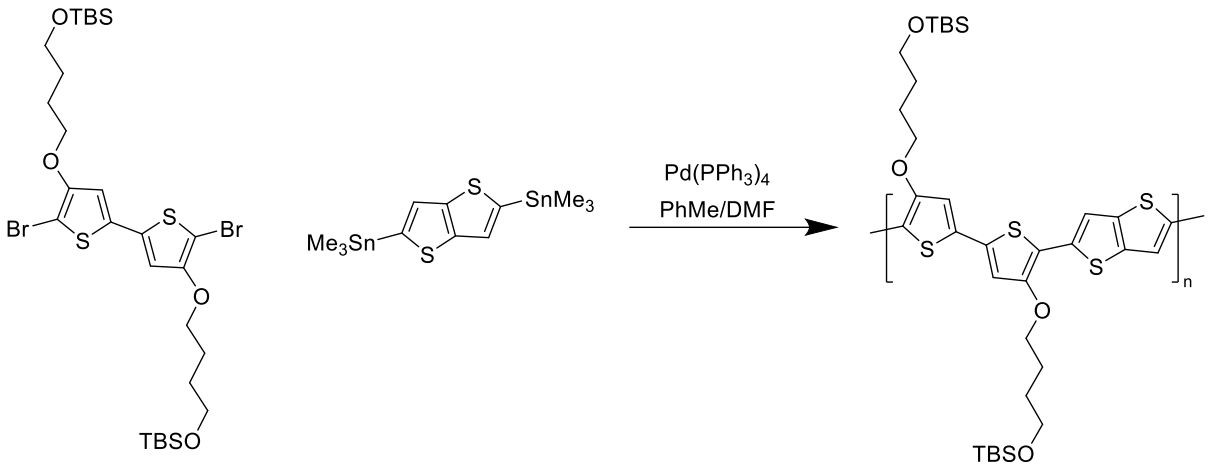

Under N_2, T_2-OH_2-Br_2 (145.6 mg, 0.2 mmol), 2,5-bis(trimethylstannyl)-thieno[3,2-b]thiophene (93.1 mg, 0.2 mmol) and $Pd(PPh_3)_4$ (5.78 mg, 0.005 mmol, 0.025 eq) was dissolved in a mixture of anhydrous toluene (2.4 mL) and DMF (1.6 mL). The reaction mixture was heated to 110 ºC for 24 hours, before being cooled to room temperature and precipitated in methanol. The crude polymer solid was further purified by Soxhlet extraction (methanol -> acetone -> hexane -> chloroform), concentrated and re-precipitated in methanol to yield a dark blue solid (103 mg, 70%). ^{1}H NMR (400 MHz, TCE-d_2) δ 6.41 (d, J = 148.2 Hz, 2H), 3.29 (m, 8H), 1.80 – 0.78 (m, 8H), 0.28 (s, 18H), -0.56 (s, 12H). GPC (PhCl): M_n = 3.9 kDa, M_w = 7.3 kDa

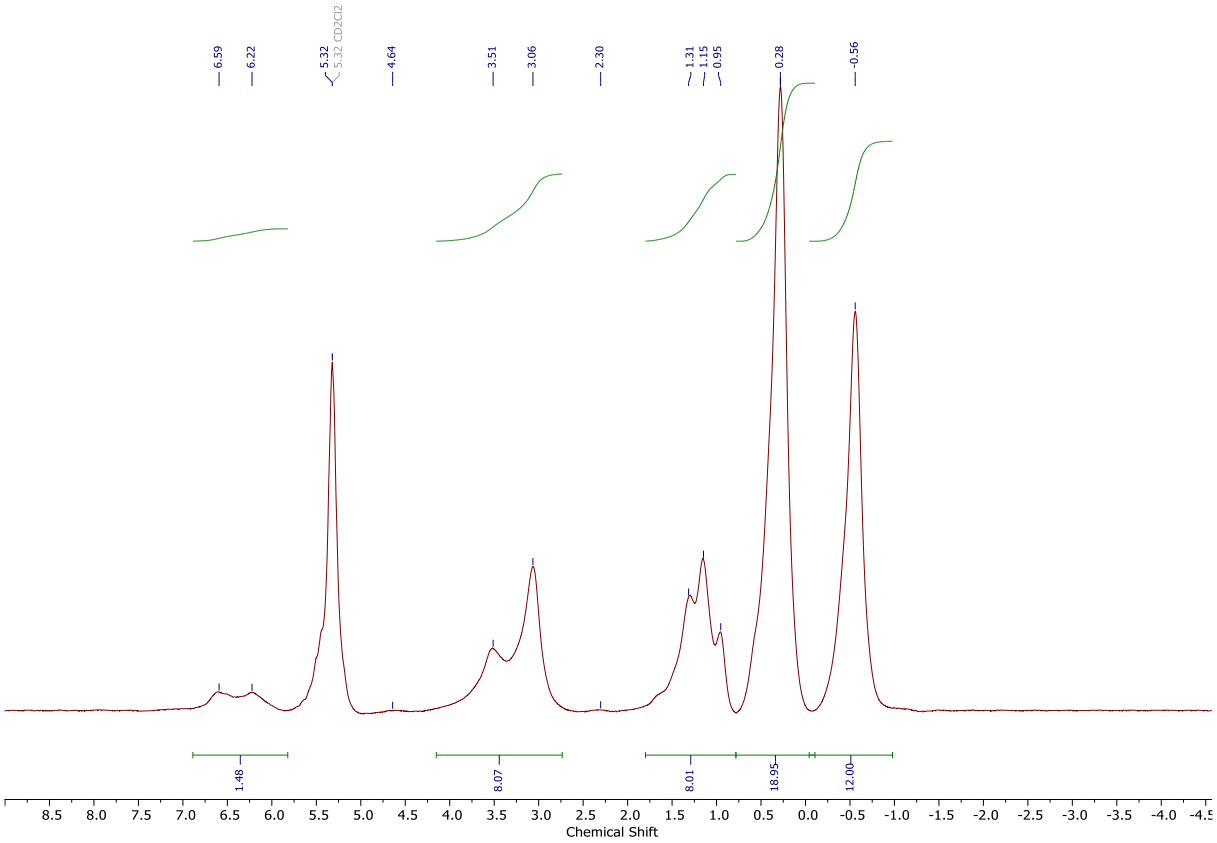

Molecular Weight Averages

Peak	Mp (g/mol)	Mn (g/mol)	Mw (g/mol)	Mz (g/mol)	Mz+1 (g/mol)	Mv (g/mol)
Peak 1	8264	3889	7347	11608	16798	6807

PD
1.889

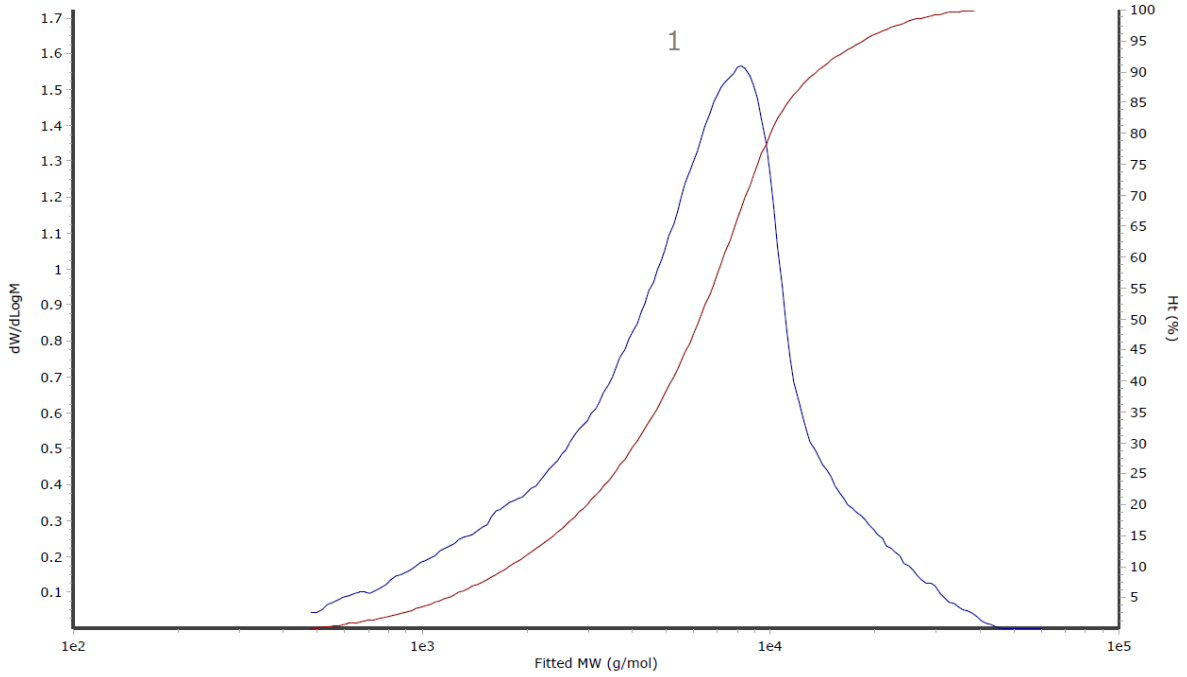

7.2.3 Synthetic Procedure for Chapter 5

Preparation of T-OC_{10}-Br-BDACO

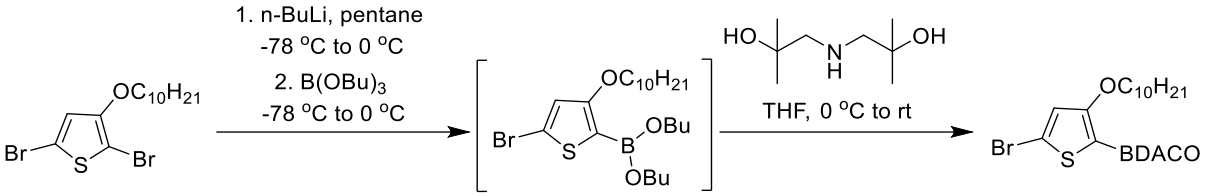

2,5-dibromo-3-(decyloxy)thiophene (3944 mg, 9.90 mmol) was dissolved in anhydrous pentane (100 mL) and cooled to -78 °C. Then, n-BuLi (6.80 mL, 1.6 M, 1.1 eq) was added dropwise and the reaction mixture was stirred at -78 °C for one hour, followed by 0 °C for another hour. Then, the reaction mixture was cooled again to -78 °C and $B(OBu)_3$ (3417 mg, 4.0 mL, 1.5 eq) was added, and the reaction mixture was stirred at -78 °C for 1 hour, followed by 0 °C for another hour, which the solution formed a viscous gel after about 30 minutes and anhydrous THF (10 mL) was added to dissolve the suspension. Then, DACO (3192 mg, 2 eq) was dissolved in anhydrous THF (90 mL) and added to the reaction mixture, which was stirred at room temperature overnight. Upon completion, the reaction mixture was dissolved in diethyl ether (200 mL) and washed with water thrice (300 mL x 3), then over anhydrous sodium sulphate and dried in vacuo, which a solid will likely precipitate. The solid is triturated with the diethyl ether and collected. The supernatant is dried in vacuo and triturated again with diethyl ether to collect more product. Then, the remaining liquid is further purified by C18 – column chromatography column chromatography and the products are combined to yield a white solid, 1450 mg, 2.97 mmol, 30%). ^{1}H NMR (400 MHz, CD_2Cl_2) δ 6.78 (s, 1H), 5.87 (s, 1H), 3.94 (t, J = 6.8 Hz, 2H), 3.25 (dd, J = 11.9, 7.9 Hz, 2H), 2.81 (dd, J = 11.9, 4.5 Hz, 2H), 1.78 – 1.69 (m, 2H), 1.33 (d, J = 41.0 Hz, 20H), 1.14 (s, 6H), 0.94 – 0.81 (m, 3H). ^{13}C NMR (101 MHz, CD_2Cl_2) δ 155.0, 119.7, 110.7, 76.7, 71.9,

62.6, 32.3, 30.2, 30.0, 30.0, 30.0, 29.8, 29.7, 29.5, 26.5, 23.1. ^{11}B NMR (128 MHz, CD_2Cl_2) δ 9.83. HRMS (ESI): calcd for $C_{22}H_{40}BBrNO_3S$, 488.2000; found 488.2003 ($M+H^+$, 0.7 ppm).

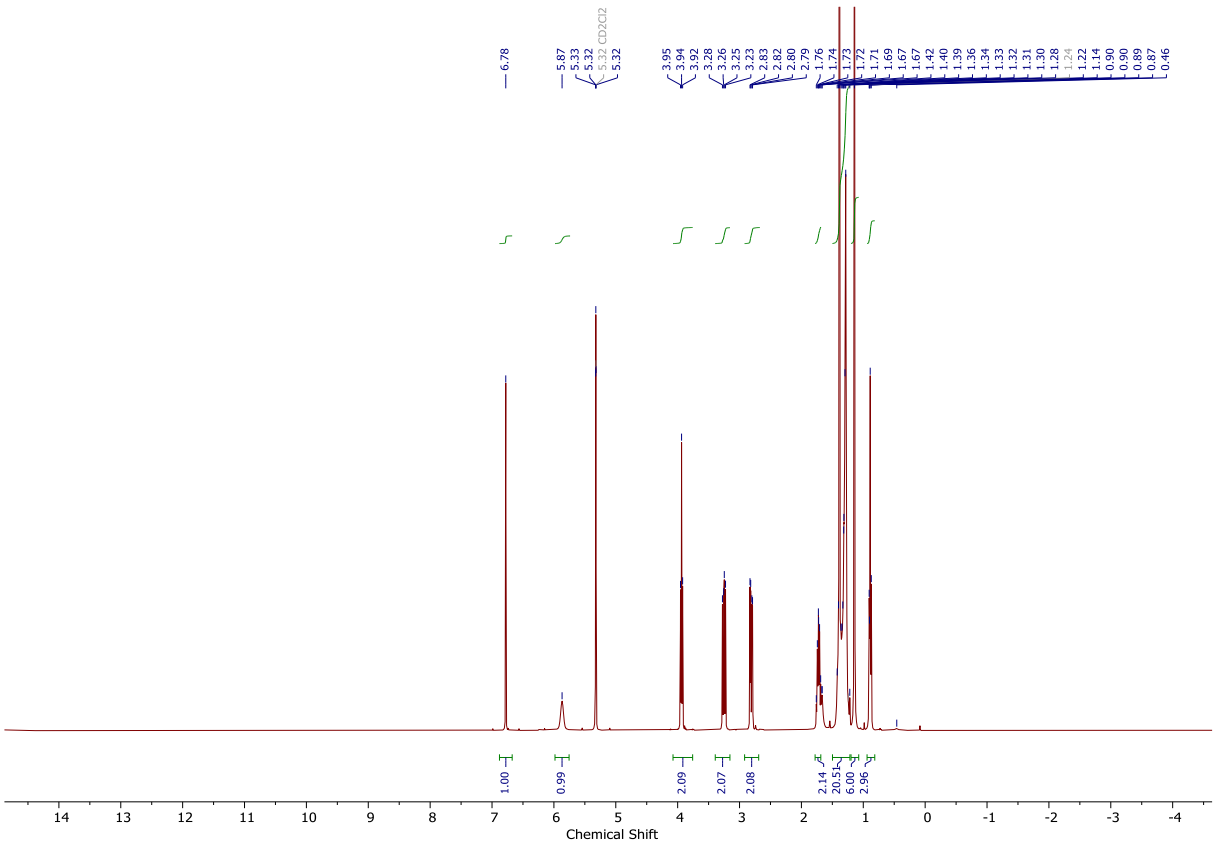

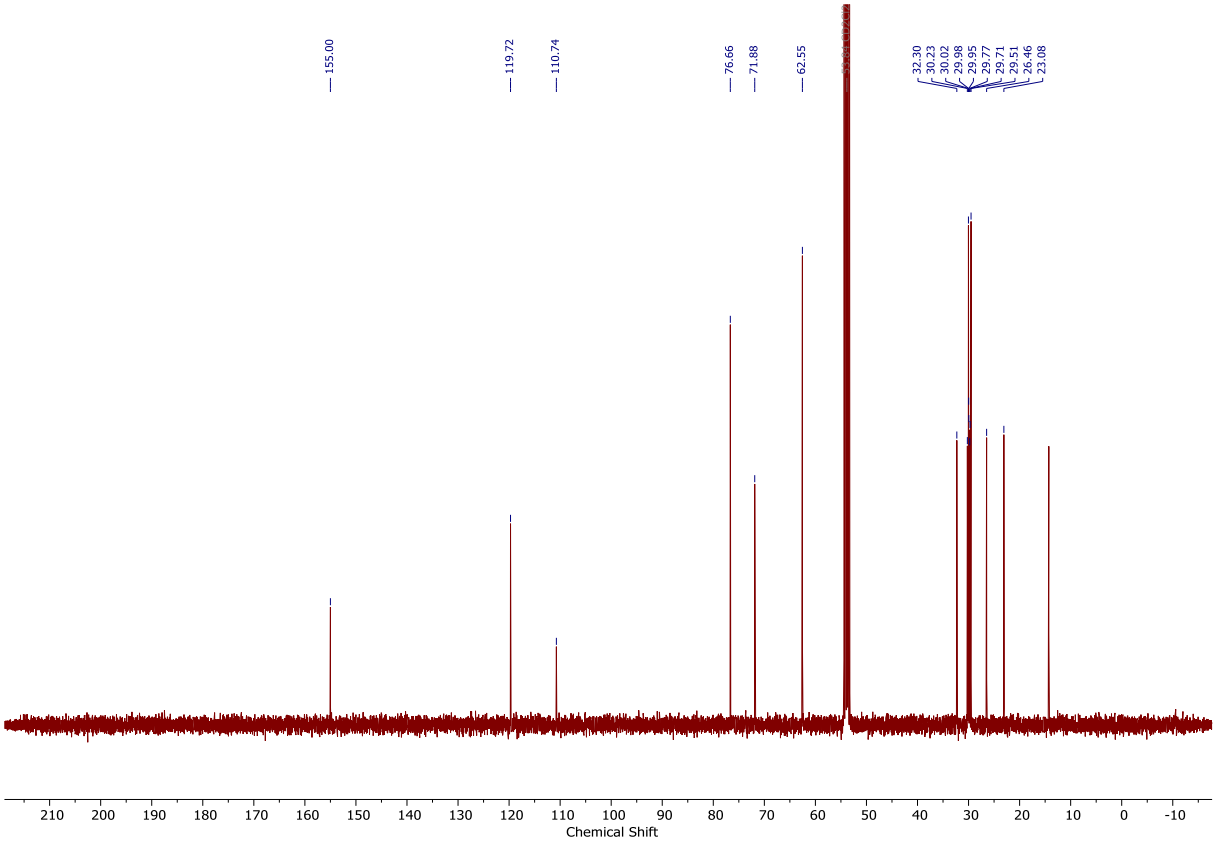
155.00
119.72
110.74
76.66
71.88
62.55
32.30
30.23
30.02
29.98
29.95
29.77
29.71
29.51
26.46
23.08
210 200 190 180 170 160 150 140 130 120 110 100 90 80 70 60 50 40 30 20 10 0 -10
Chemical Shift

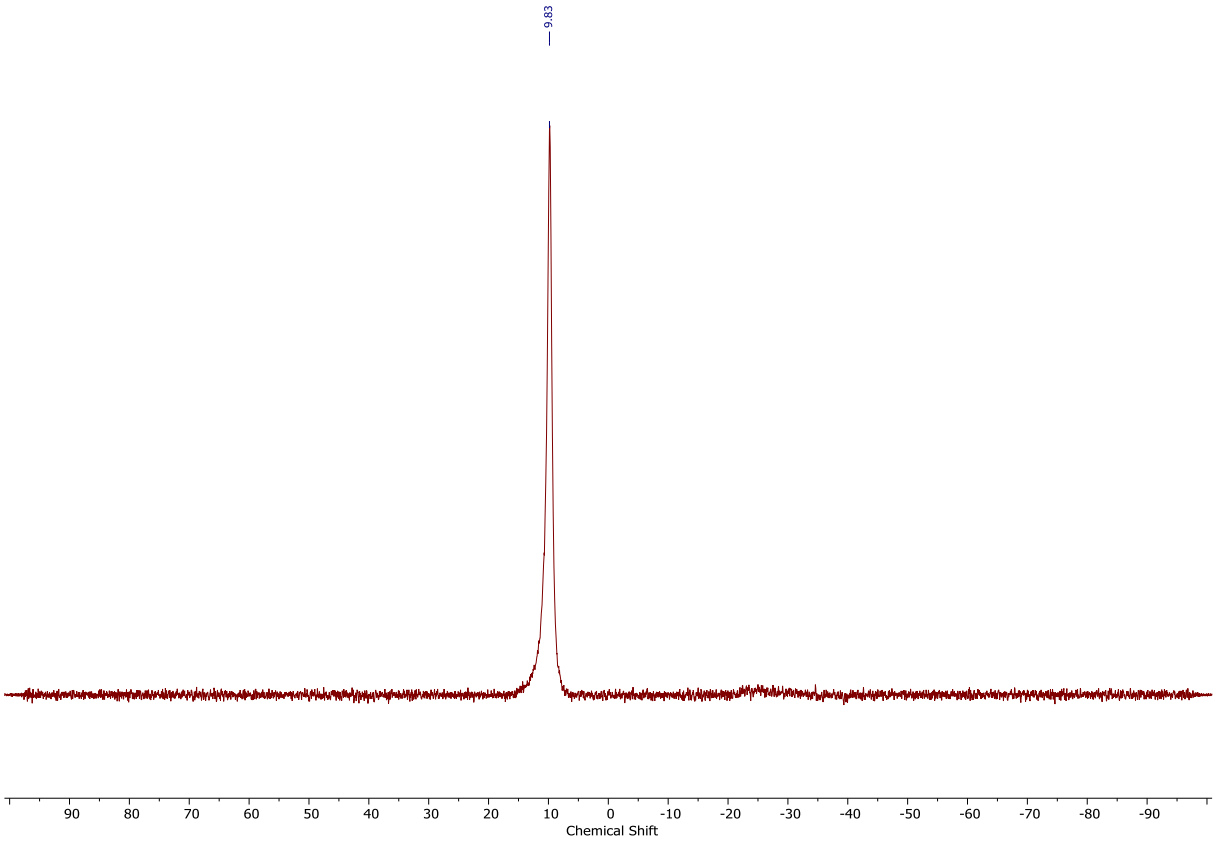
9.83
90 80 70 60 50 40 30 20 10 0 -10 -20 -30 -40 -50 -60 -70 -80 -90
Chemical Shift

Expanded Spectrum RT 0.12, NL 11054578, Peak [1], Target Mass 488.2000

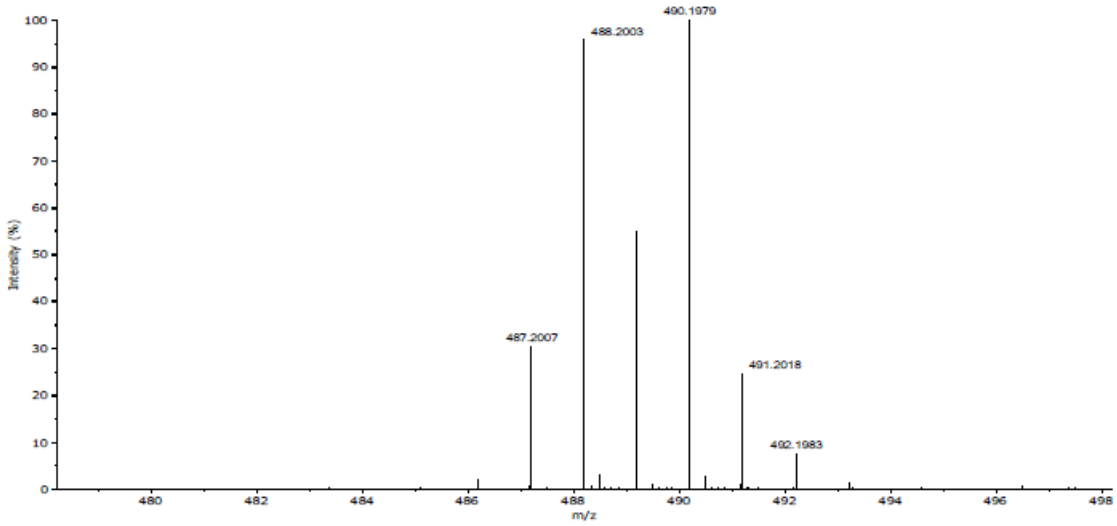

Theoretical Spectrum for C22H40BBrNO3S, Minimum Abundance 0.01%

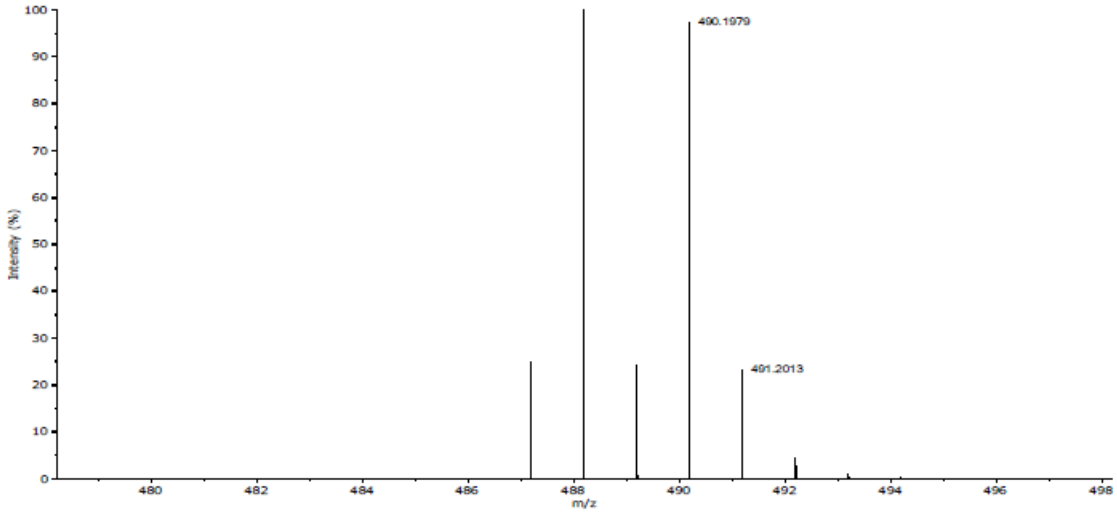

Measured Mass	Calculated Mass	Error (mDa)	Error (ppm)	Formula $[M+H]^+$	Response
488.2003	488.2000	0.32	0.65	$C_{22}H_{40}BBrNO_3S$	3202004

Preparation of T-G1OC7-Br-BDACO

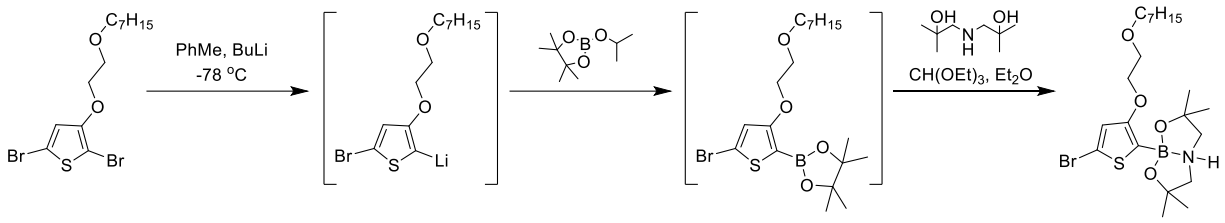

T-G_1C_7-Br_2 (4114 mg, 10.28 mmol) was dissolved in anhydrous toluene (102 mL) and cooled to -78 ºC. Then, BuLi (1.6 M, 6.4 mL, 1 eq) was added dropwise the reaction mixture was stirred at -78 ºC for an hour. Then, isopropyl pinacol boronic ester (3825 mg, 4.2 mL) was added and the reaction mixture was stirred at -78 ºC for 1 hour, followed by room temperature for another 2 hours. Then, the reaction mixture was diluted with diethyl ether (400 mL) and washed with water (400 mL x 3) then over anhydrous sodium sulphate and dried in vacuo at 70 ºC to remove all the volatile side-products. DACO (4143 mg, 2.5 eq) was added to the crude product. The mixture was evacuated under vacuum, then backfilled with N_2. Then, anhydrous diethyl ether (50 mL) was added, followed by anhydrous ethyl orthoformate (11426 mg, 7.5 eq, 12.8 mL), and then left to stir overnight. Upon completion of reaction, the reaction mixture was again diluted with diethyl ether (400 mL), then washed with water (400 mL x 3), dried over anhydrous sodium sulphate and dried in vacuo under high vacuum to remove ethyl orthoformate, which the reaction mixture should solidify to yield a brown solid, which was triturated with diethyl ether to yield a white fluffy solid (2.5 g). The supernatant was further purified by column chromatography over neutral alumina (20% PE/EA to elute the demetallated product and 50% to elute the desired product) to yield additional fluffy white solid (0.5 g). Total yield of T-G1OC7-Br-BDACO was 60% (3.0 g) over two steps. ^{1}H NMR (400 MHz, CD_2Cl_2) δ 6.77 (s, 1H), 6.61 (s, 1H), 4.10 – 4.03 (m, 2H), 3.68 – 3.62 (m, 2H), 3.50 (t, J = 6.9 Hz, 2H), 3.22 (dd, J = 11.8, 7.8 Hz, 2H),

2.76 (dd, J = 11.8, 4.4 Hz, 2H), 1.64 (s, 1H), 1.62 – 1.52 (m, 2H), 1.41 – 1.22 (m, 14H), 1.13 (s, 6H), 0.96 – 0.81 (m, 3H). ^{13}C NMR (101 MHz, CD_2Cl_2) δ 153.8, 120.7, 111.0, 76.4, 72.0, 71.2, 69.4, 62.5, 32.2, 30.1, 30.0, 29.6, 29.5, 26.3, 23.0, 14.2. ^{11}B NMR (128 MHz, CD_2Cl_2) δ 9.64. HRMS (ESI): calcd for $C_{21}H_{38}BBrNO_4S$, 490.1792; found 490.1805 ($M+H^+$, 2.6 ppm).

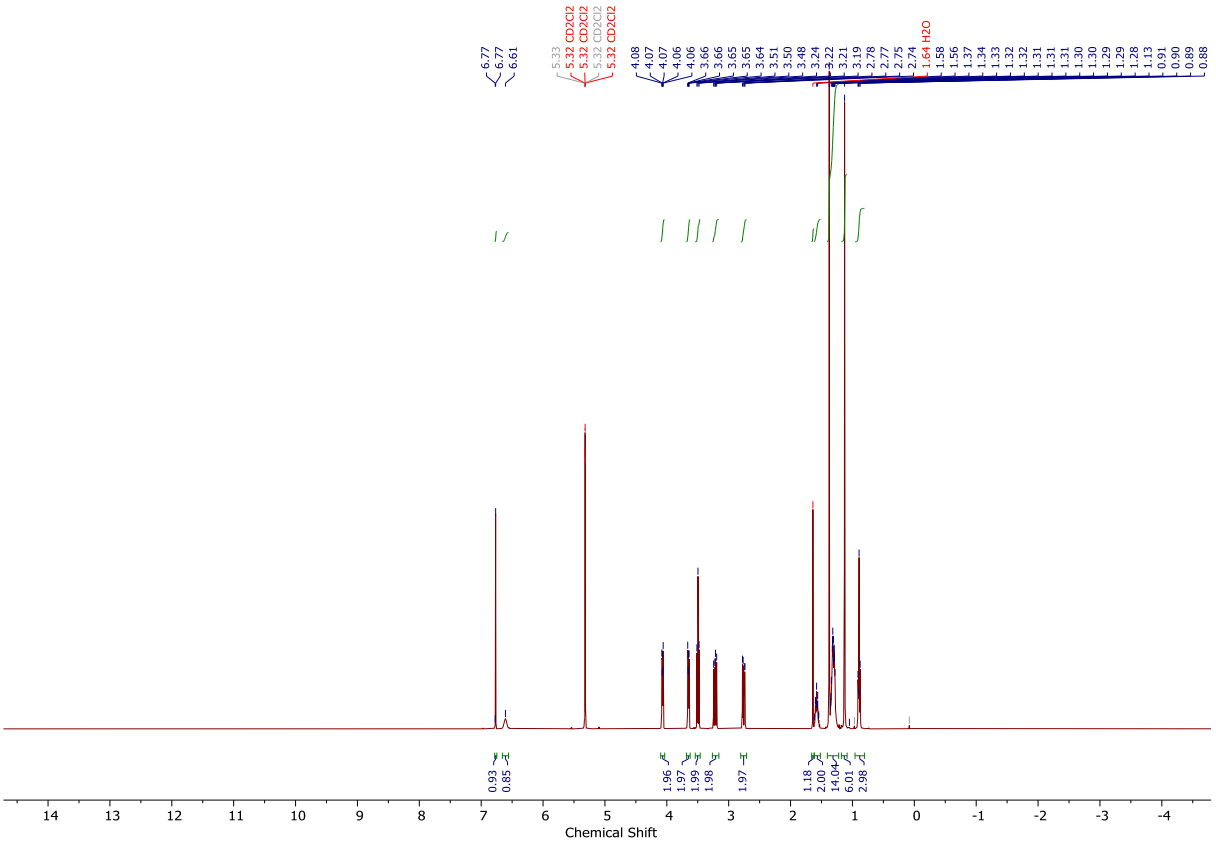

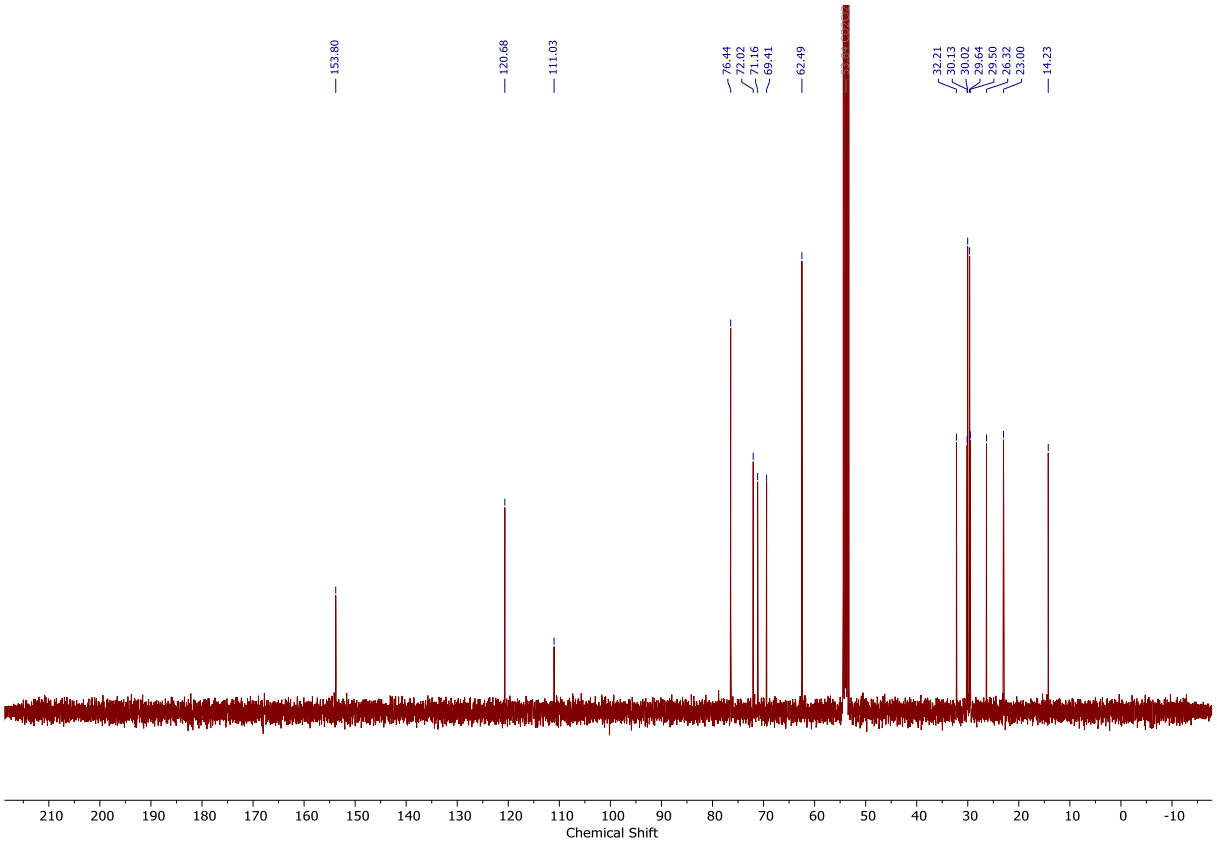
153.80
120.68
111.03
76.44
72.02
71.16
69.41
62.49
32.21
30.13
30.02
29.64
29.50
26.32
23.00
14.23
210 200 190 180 170 160 150 140 130 120 110 100 90 80 70 60 50 40 30 20 10 0 -10
Chemical Shift

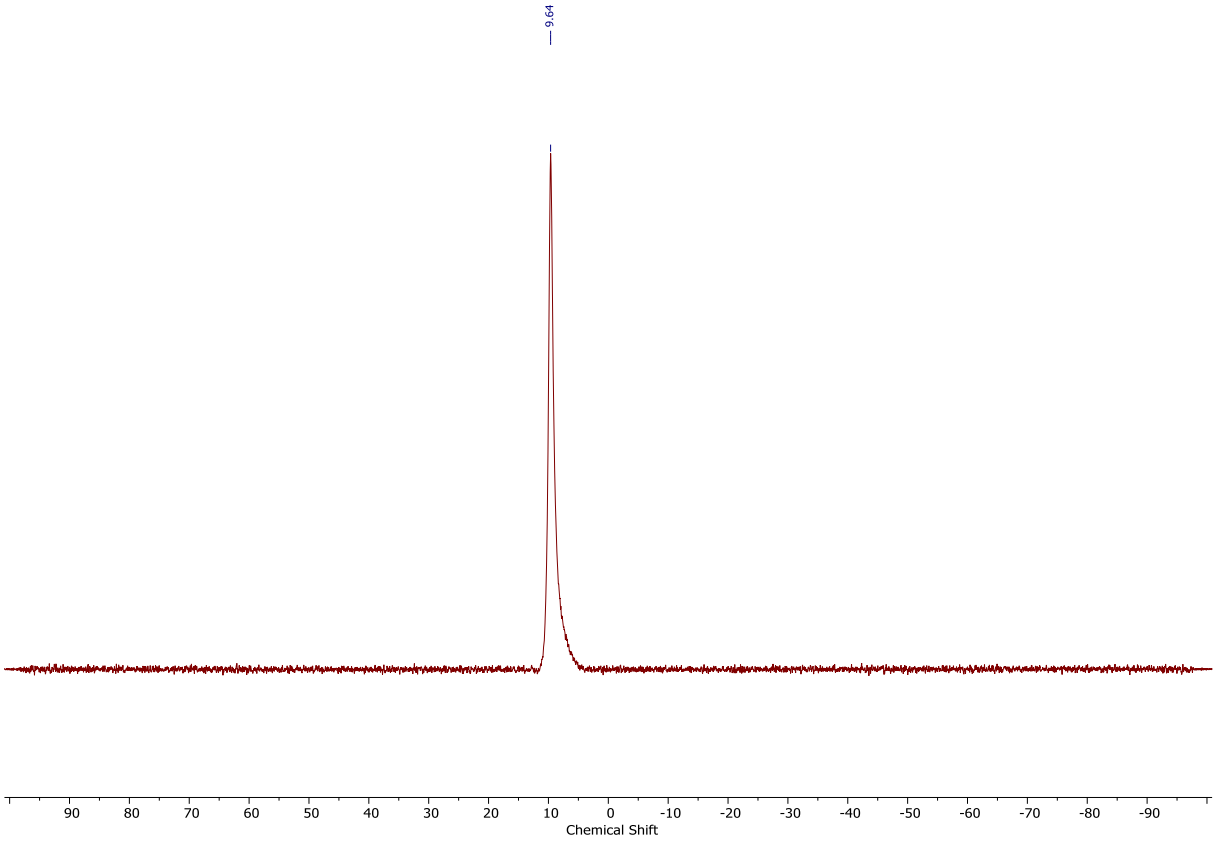
9.64
90
80
70
60
50
40
30
20
10
0
-10
-20
-30
-40
-50
-60
-70
-80
-90
Chemical Shift

Expanded Spectrum RT 0.11, NL 1589432.38101196, Peak [1], Target Mass 490.1792

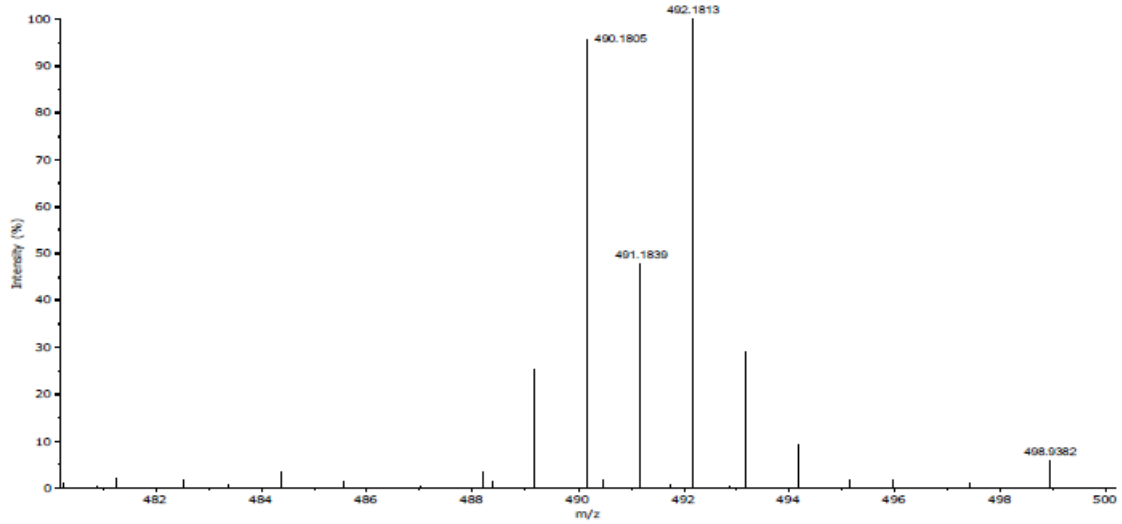

Theoretical Spectrum for C21H38BBrNO4S, Minimum Abundance 0.01%

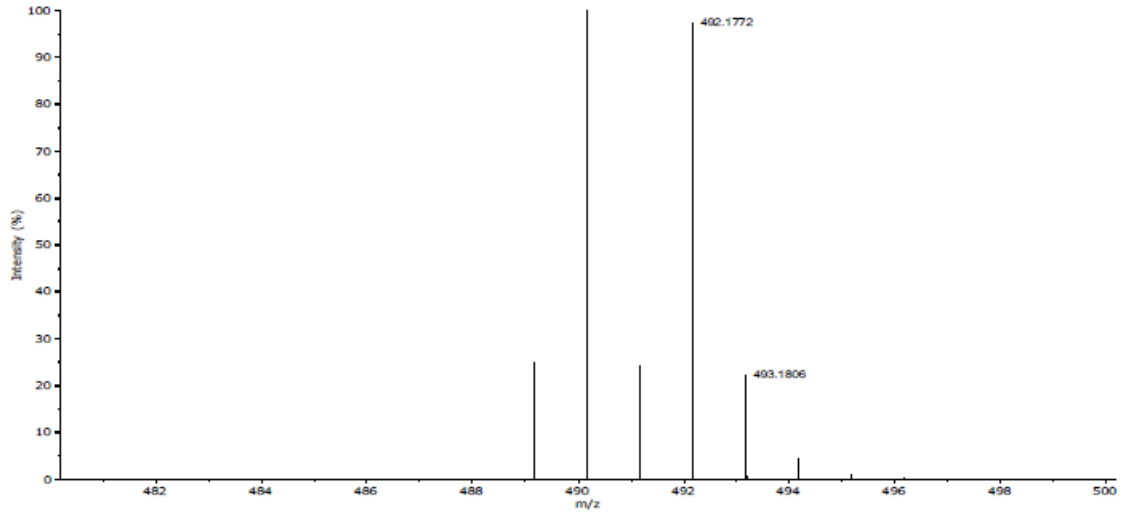

Measured Mass	Calculated Mass	Error (mDa)	Error (ppm)	Formula $[M+H]^+$	Response
490.1805	490.1792	1.25	2.55	$C_{21}H_{38}BBrNO_4S$	1185432

Preparation of T-G2OC4-Br-BDACO

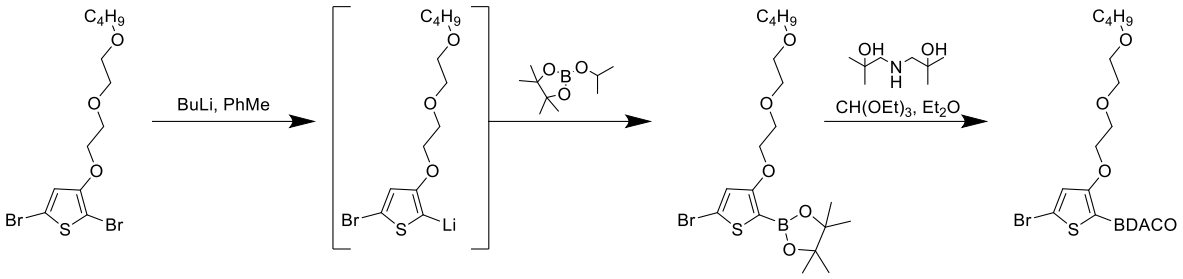

T-G2C4-Br_2 (4979 mg, 12.38 mmol) was dissolved in anhydrous toluene (120 mL) and cooled to -78 ºC. Then, n-BuLi (7.7 mL) was added dropwise and the reaction mixture was stirred at -78 ºC for one hour. Then, isopropyl pinacol boronate ester (4.6 mL, 4.21 g, 24.76 mmol, 2 eq) was added at -78 ºC, stirred for 30 minutes, before the reaction mixture is left at 0 ºC for 2 hours. The reaction mixture is then diluted with diethyl ether (300 mL) and washed thrice with water (300 mL x 3), before dried over anhydrous sodium sulphate and in vacuo. DACO (4.99 g, 2.5 eq) was added, then anhydrous diethyl ether (60 mL), then triethyl orthoformate (13.8 g, 7.5 eq, 15.5 mL) were added and stirred for 24h for complete reaction. The crude mixture is diluted with ethyl acetate (300 mL), washed thrice with water (300 mL x 3), then dried over anhydrous sodium sulphate, and dried in vacuo, over high vac to remove triethyl orthoformate. The crude product was triturated twice with 1:1 diethyl ether/hexane to yield the product as a white solid (2.5 g). The remaining solid was passed through neutral alumina plug (Hexane/EA 4:1 -> EA) to yield the product as an off-white solid (400 mg). Total yield of T-G2OC4-Br-BDACO was 49% (2.9 g) over two steps. ^{1}H NMR (400 MHz, CD_2Cl_2) δ 6.76 (s, 1H), 6.56 (d, *J* = 10.9 Hz, 1H), 4.11 – 4.02 (m, 2H), 3.76 – 3.68 (m, 2H), 3.68 – 3.62 (m, 2H), 3.59 – 3.52 (m, 2H), 3.43 (t, *J* = 6.7 Hz, 2H), 3.28 (dd, *J* = 11.8, 7.8 Hz, 2H), 2.75 (dd, *J* = 11.9, 4.3 Hz, 2H), 1.54 (dtd, *J* = 8.5, 6.9, 5.8 Hz, 2H), 1.37 (s, 8H), 1.12 (s, 6H), 0.92 (t, *J* = 7.4 Hz, 3H). ^{13}C NMR (101 MHz, CD_2Cl_2) δ 153.7, 120.7, 111.0, 76.4, 71.4, 71.3, 71.1, 70.3, 70.0, 62.5, 32.1, 30.0, 29.7, 19.7, 14.1. ^{11}B NMR (128 MHz,

CD_2Cl_2) δ 9.62. HRMS (ESI): calcd for $C_{20}H_{35}BBrNO_5SNa$, 514.1405; found 514.1404 ($M+Na^+$, -0.1 ppm).

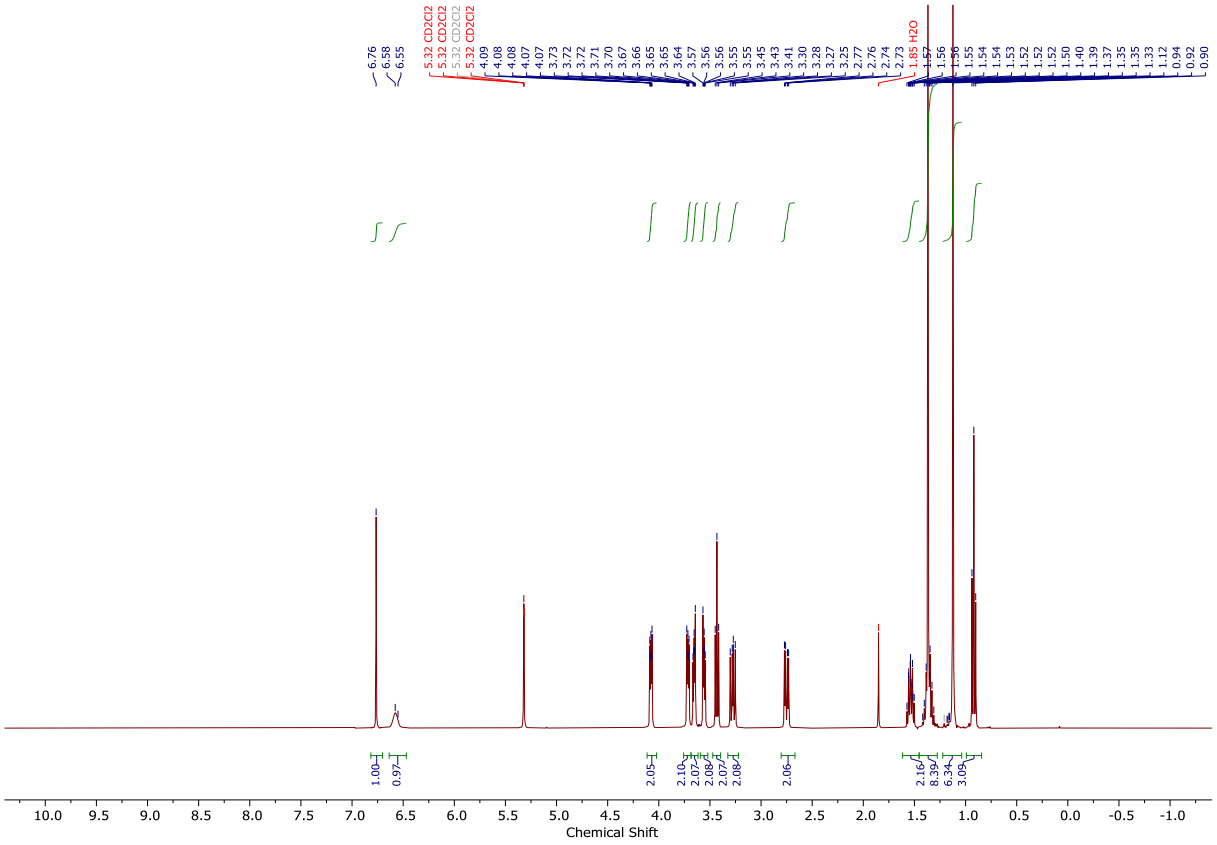

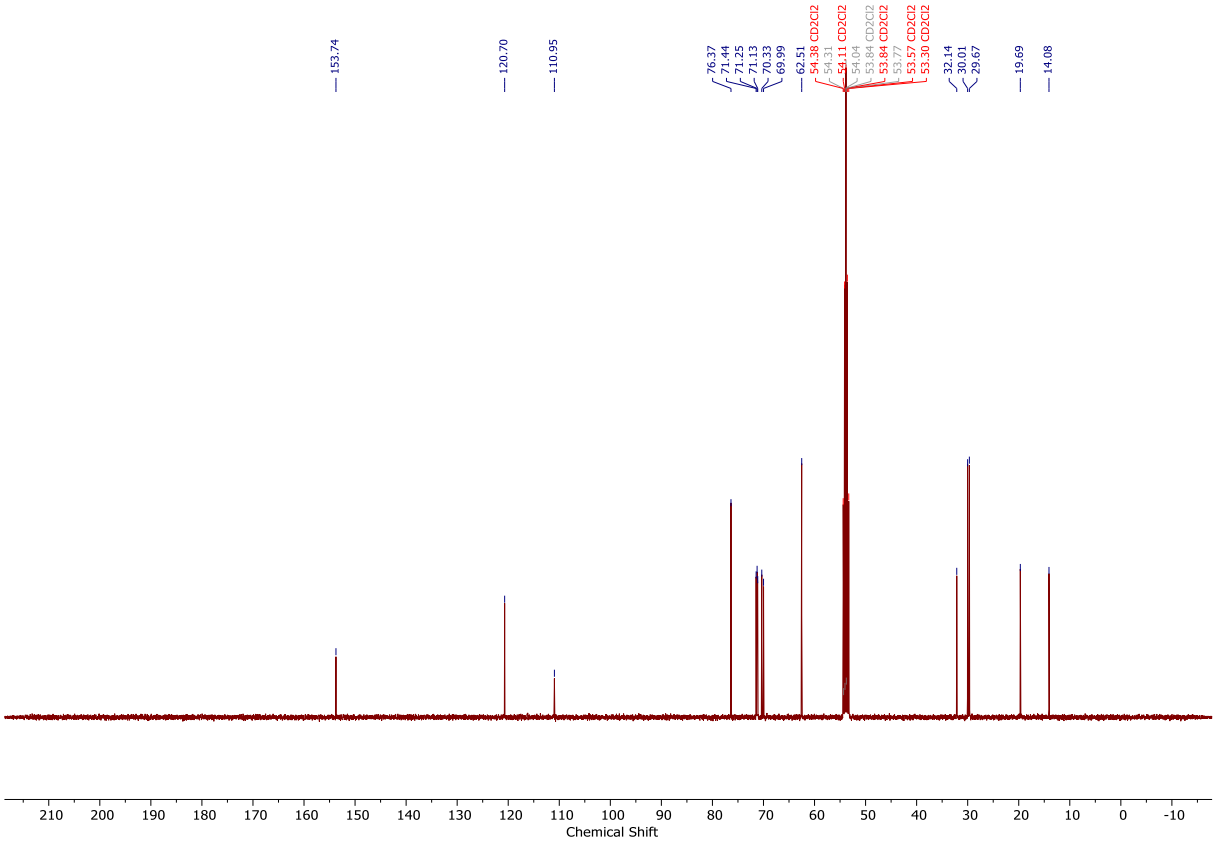
153.74
120.70
110.95
76.37
71.44
71.25
71.13
70.33
69.99
62.51
54.38 CD2Cl2
54.31
54.11 CD2Cl2
54.04
53.84 CD2Cl2
53.84 CD2Cl2
53.77
53.57 CD2Cl2
53.30 CD2Cl2
32.14
30.01
29.67
19.69
14.08
210 200 190 180 170 160 150 140 130 120 110 100 90 80 70 60 50 40 30 20 10 0 -10
Chemical Shift

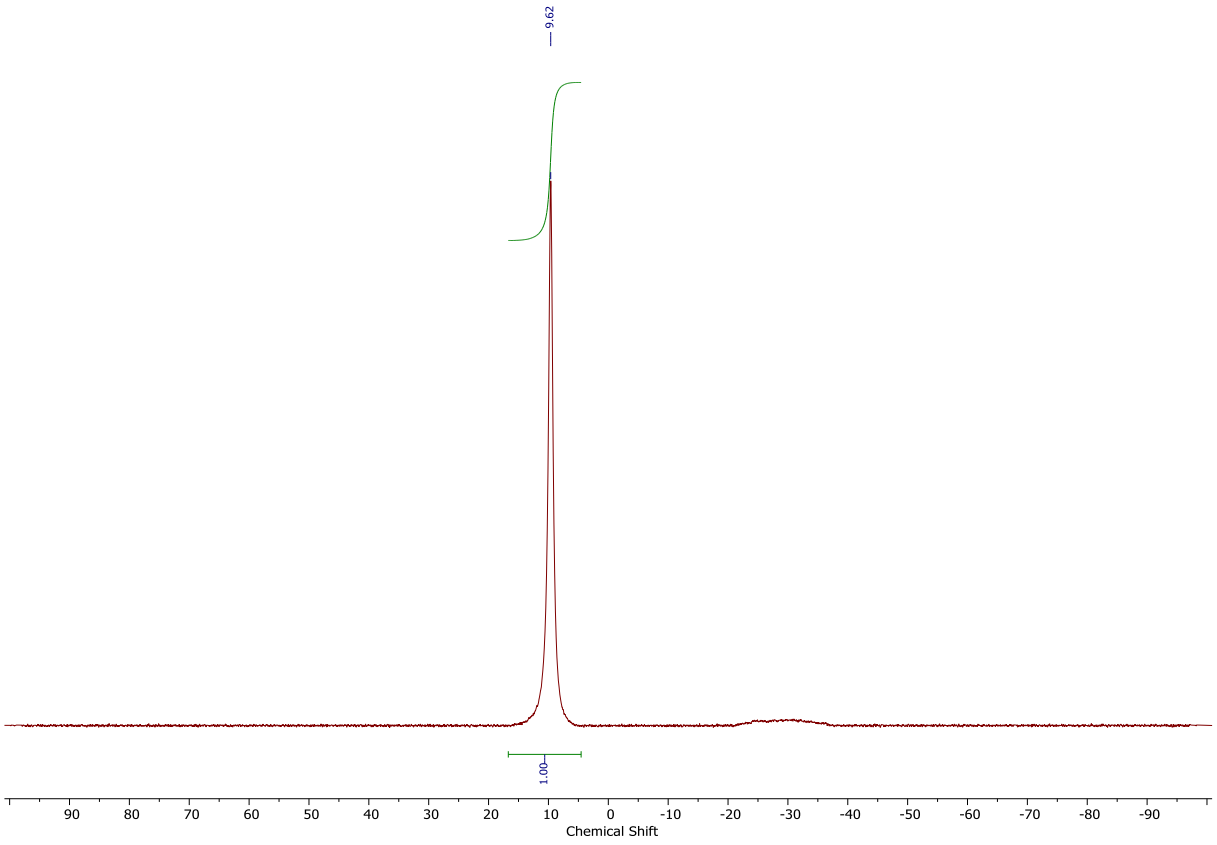
9.62
1.00
90 80 70 60 50 40 30 20 10 0 -10 -20 -30 -40 -50 -60 -70 -80 -90
Chemical Shift

Expanded Spectrum RT 0.12, NL 13928173, Peak [1], Target Mass 514.1405

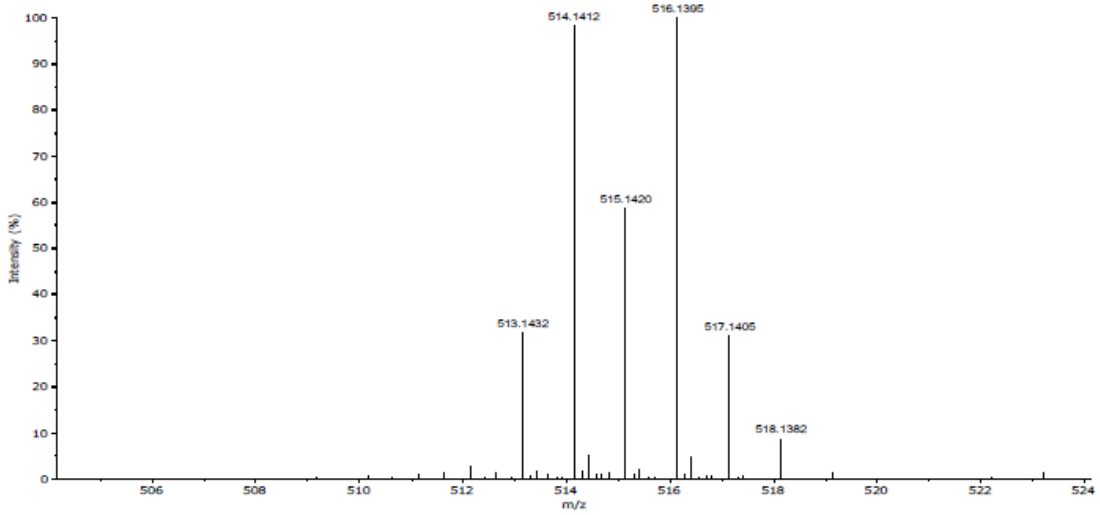

Theoretical Spectrum for C20H35BBrNO5SNa, Minimum Abundance 0.01%

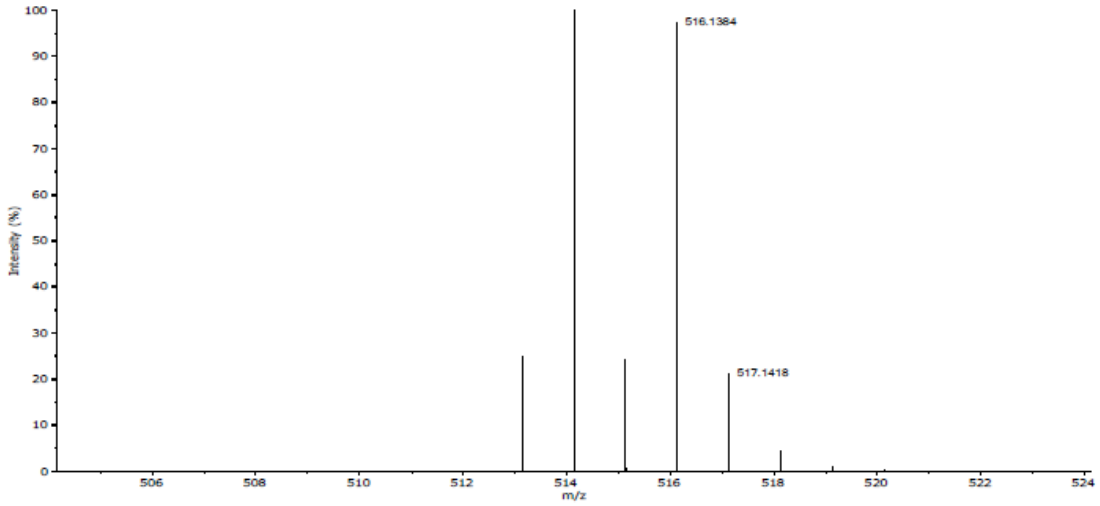

Measured Mass	Calculated Mass	Error (mDa)	Error (ppm)	Formula $[M+Na]^+$	Response
514.1404	514.1405	-0.06	-0.11	$C_{20}H_{35}BBrNO_5SNa$	57665842

Preparation of T-G3-Br-BDACO

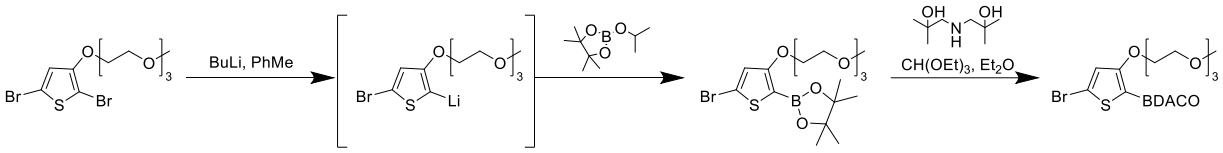

T-G_3-Br_2 (4968 mg, 12.29 mmol) was dissolved in anhydrous toluene (120 mL) and cooled to -78 ºC. Then, n-BuLi (7.7 mL) was added dropwise and the reaction mixture was stirred at -78 ºC for one hour. Then, isopropyl pinacol boronate ester (5.0 mL, 4.57 g, 2 eq) was added at -78 ºC, stirred for 30 minutes, before the reaction mixture is left at 0 ºC for 2 hours. The reaction mixture is then diluted with diethyl ether (300 mL) and washed thrice with water (300 mL x 3), before dried over anhydrous sodium sulphate and in vacuo. DACO (4.95 g, 2.5 eq) was added, then anhydrous diethyl ether (60 mL), then triethyl orthoformate (13.8 g, 7.5 eq, 15.5 mL) were added and stirred for 24h for complete reaction. The crude mixture is diluted with ethyl acetate (300 mL), washed thrice with water (300 mL x 3), then dried over anhydrous sodium sulphate, and dried in vacuo, over high vac to remove triethyl orthoformate. The crude product was triturated twice with 1:1 diethyl ether/hexane to yield the product as a white solid (1.1 g). The remaining solid was passed through neutral alumina plug (Hexane/EA 4:1 -> EA) to yield the product as an off-white solid (230 mg). Total yield of T-G3-Br-BDACO was 20% (1.3 g) over two steps. 1H NMR (500 MHz, CD_2Cl_2) δ 6.76 (s, 1H), 6.58 (s, 1H), 4.14 – 4.01 (m, 2H), 3.74 – 3.70 (m, 2H), 3.70 – 3.64 (m, 2H), 3.64 – 3.60 (m, 2H), 3.60 – 3.56 (m, 2H), 3.53 – 3.48 (m, 2H), 3.32 (s, 3H), 3.27 (dd, J = 11.9, 7.8 Hz, 2H), 2.78 (dd, J = 11.9, 4.4 Hz, 2H), 1.37 (s, 7H), 1.13 (s, 7H). ^{13}C NMR (126 MHz, CD_2Cl_2) δ 153.8, 120.7, 110.9, 76.4, 72.3, 71.2, 71.0, 70.9, 70.8, 70.1, 62.5, 59.0, 30.1, 29.7. ^{11}B NMR (161 MHz, CD_2Cl_2) δ 9.53. HRMS (ESI): calcd for $C_{19}H_{34}BBrNO_6S$, 494.1378; found 494.1379 ($M+H^+$, -0.1 ppm).

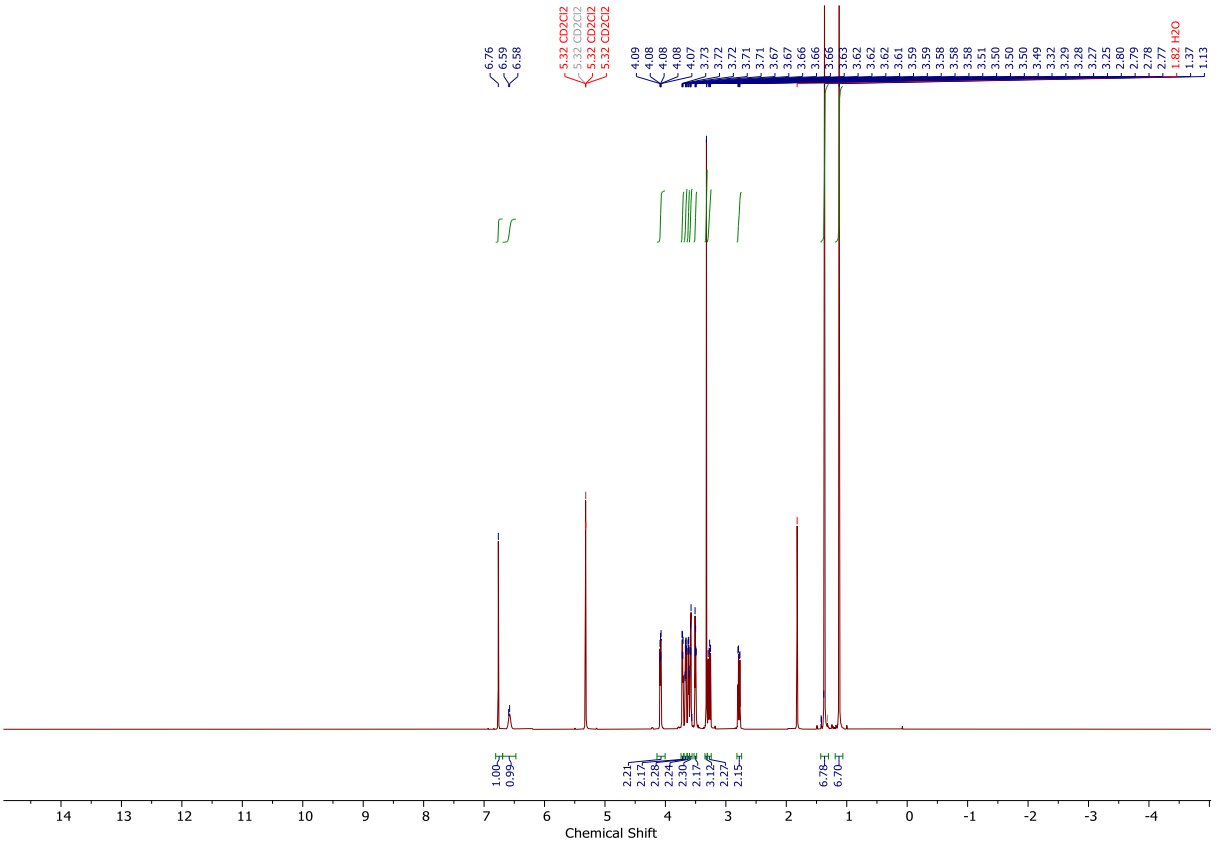
6.76
6.59
6.58
5.32 CD2Cl2
5.32 CD2Cl2
5.32 CD2Cl2
5.32 CD2Cl2
4.09
4.08
4.08
4.08
4.07
3.73
3.72
3.72
3.71
3.71
3.67
3.67
3.66
3.66
3.66
3.63
3.62
3.62
3.62
3.61
3.59
3.59
3.58
3.58
3.58
3.51
3.50
3.50
3.50
3.49
3.32
3.29
3.28
3.27
3.25
2.80
2.79
2.78
2.77
1.82 H2O
1.37
1.13
1.00
0.99
2.21
2.17
2.28
2.24
2.30
2.12
3.12
2.27
2.15
6.78
6.70
14 13 12 11 10 9 8 7 6 5 4 3 2 1 0 -1 -2 -3 -4
Chemical Shift

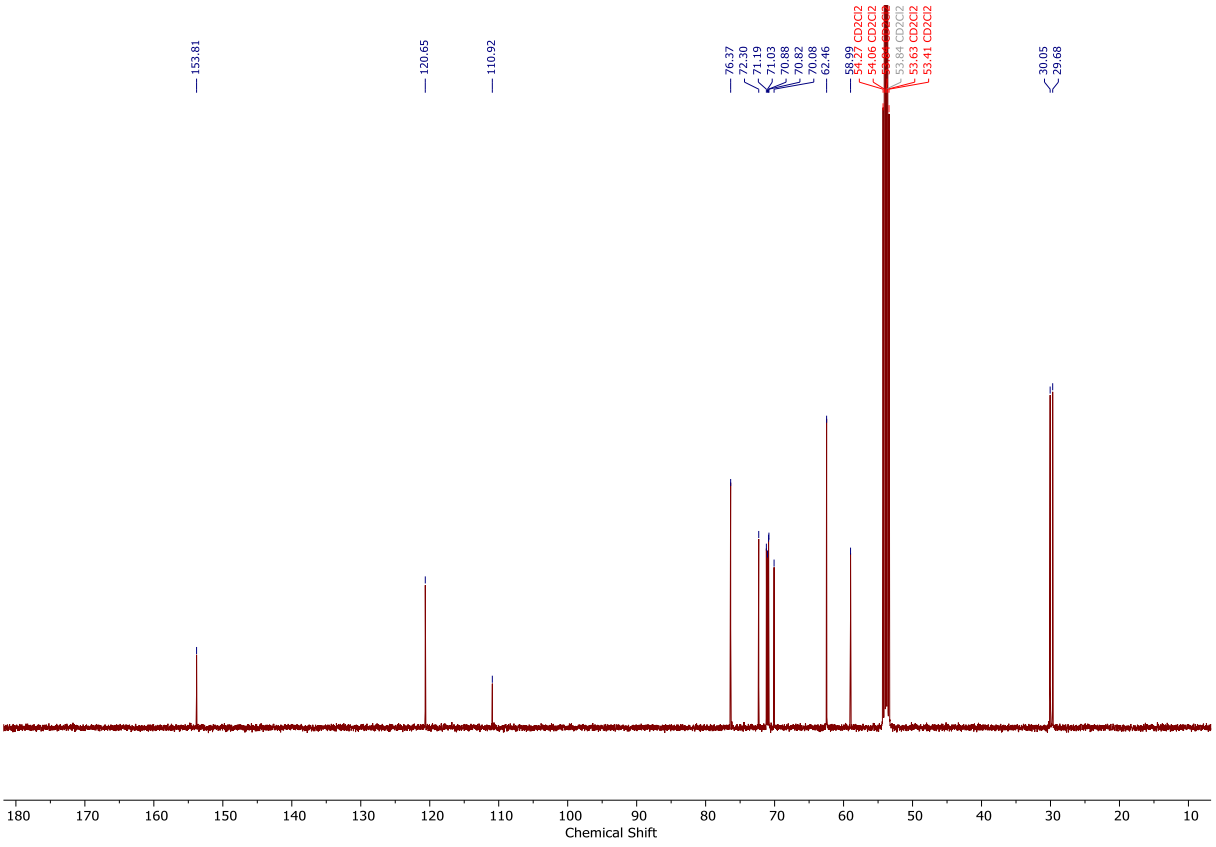
153.81
120.65
110.92
76.37
72.30
71.19
71.03
70.88
70.82
70.08
62.46
58.99
54.27 CD2Cl2
54.06 CD2Cl2
53.84 CD2Cl2
53.63 CD2Cl2
53.41 CD2Cl2
30.05
29.68
180 170 160 150 140 130 120 110 100 90 80 70 60 50 40 30 20 10
Chemical Shift

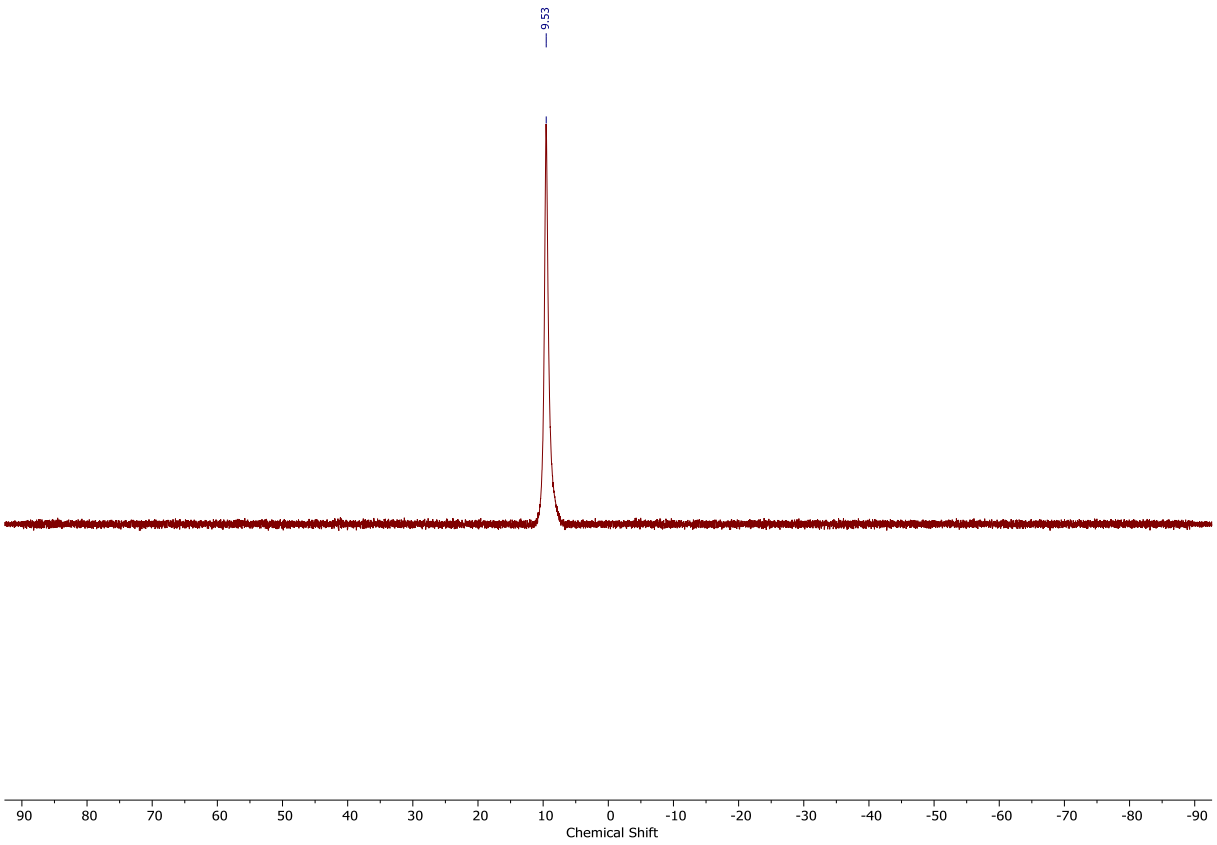
9.53
90
80
70
60
50
40
30
20
10
0
-10
-20
-30
-40
-50
-60
-70
-80
-90
Chemical Shift

Expanded Spectrum RT 0.11, NL 3355315.95880127, Peak [1], Target Mass 494.1378

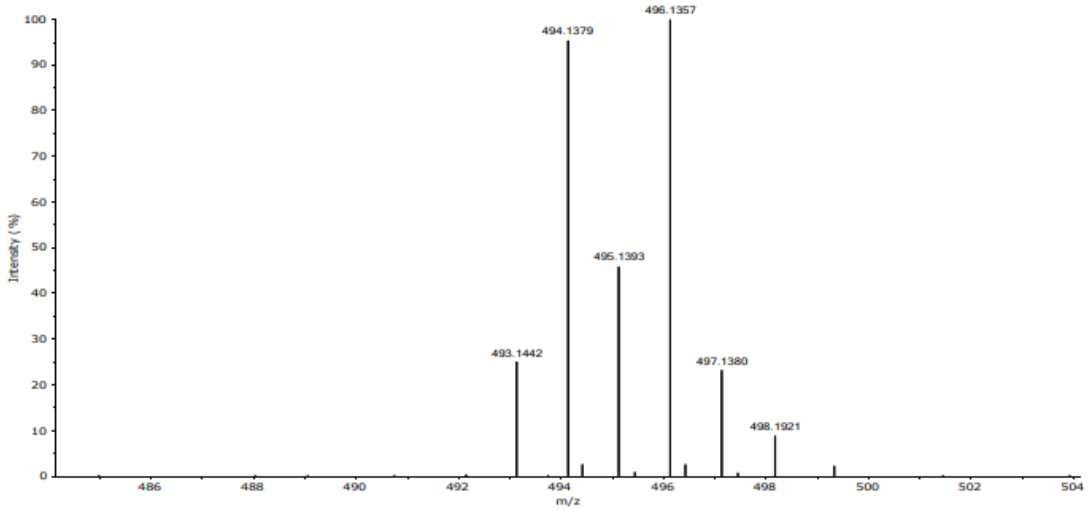

Theoretical Spectrum for C19H34BBrNO6S, Minimum Abundance 0.01%

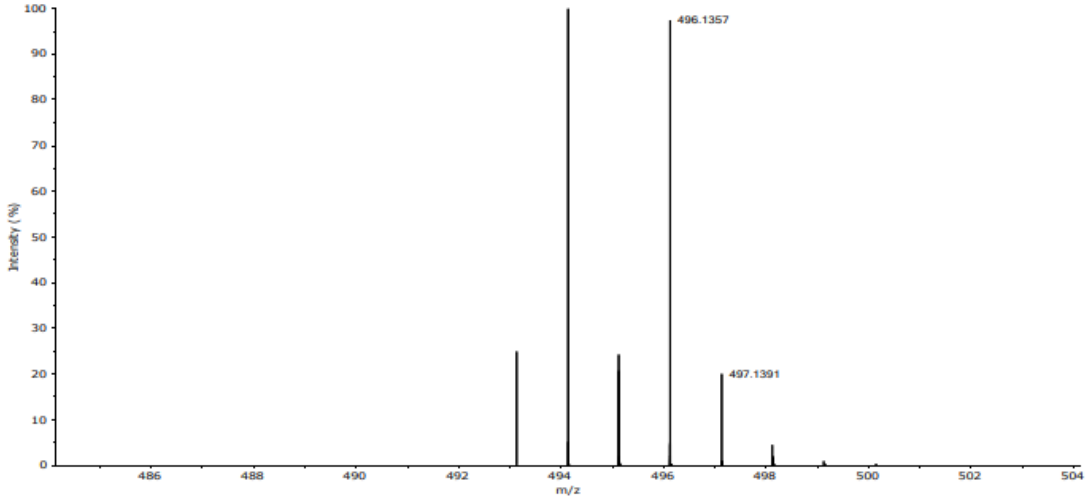

Measured Mass	Calculated Mass	Error (mDa)	Error (ppm)	Formula $[M+H]^+$	Response
494.1379	494.1378	0.12	0.25	$C_{19}H_{34}BBrNO_6S$	3897911

Preparation of 2-bromo-4-(tetradecyloxy)thiophene

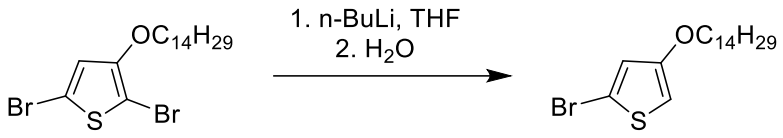

2,5-dibromo-(tetradecyloxy)thiophene (4086 mg, 9 mmol) was added to anhydrous pentane (120 mL) and cooled to -78 ºC. n-BuLi (1.6 M, 6.8 mL, 10.8 mmol, 1.2 eq) was added dropwise and the reaction mixture was further stirred at -78 ºC for an hour, then at 0 ºC for an hour, before H_2O (10 mL) added and the reaction quenched at room temperature for 30 minutes. The reaction mixture was diluted with dichloromethane (200 mL) and washed with water thrice (200 mL), then dried over anhydrous magnesium sulphate and further purified by column chromatography (hexane) to yield a white solid (2.70 g, 80%). ^{1}H NMR (400 MHz, $CDCl_3$) δ 6.73 (d, J = 1.8 Hz, 1H), 6.10 (d, J = 1.9 Hz, 1H), 3.88 (t, J = 6.5 Hz, 2H), 1.74 (dq, J = 8.3, 6.6 Hz, 2H), 1.48 – 1.37 (m, 2H), 1.26 (s, 20H), 0.94 – 0.81 (m, 3H). ^{13}C NMR (101 MHz, $CDCl_3$) δ 157.0, 122.8, 111.7, 98.7, 70.2, 32.1, 29.8, 29.8, 29.8, 29.7, 29.7, 29.5, 29.5, 29.2, 26.1, 22.8, 14.3. HRMS (ESI): calcd for $C_{18}H_{32}BrOS$, 375.1352; found 375.1350 ($M+H^+$, -0.5ppm).

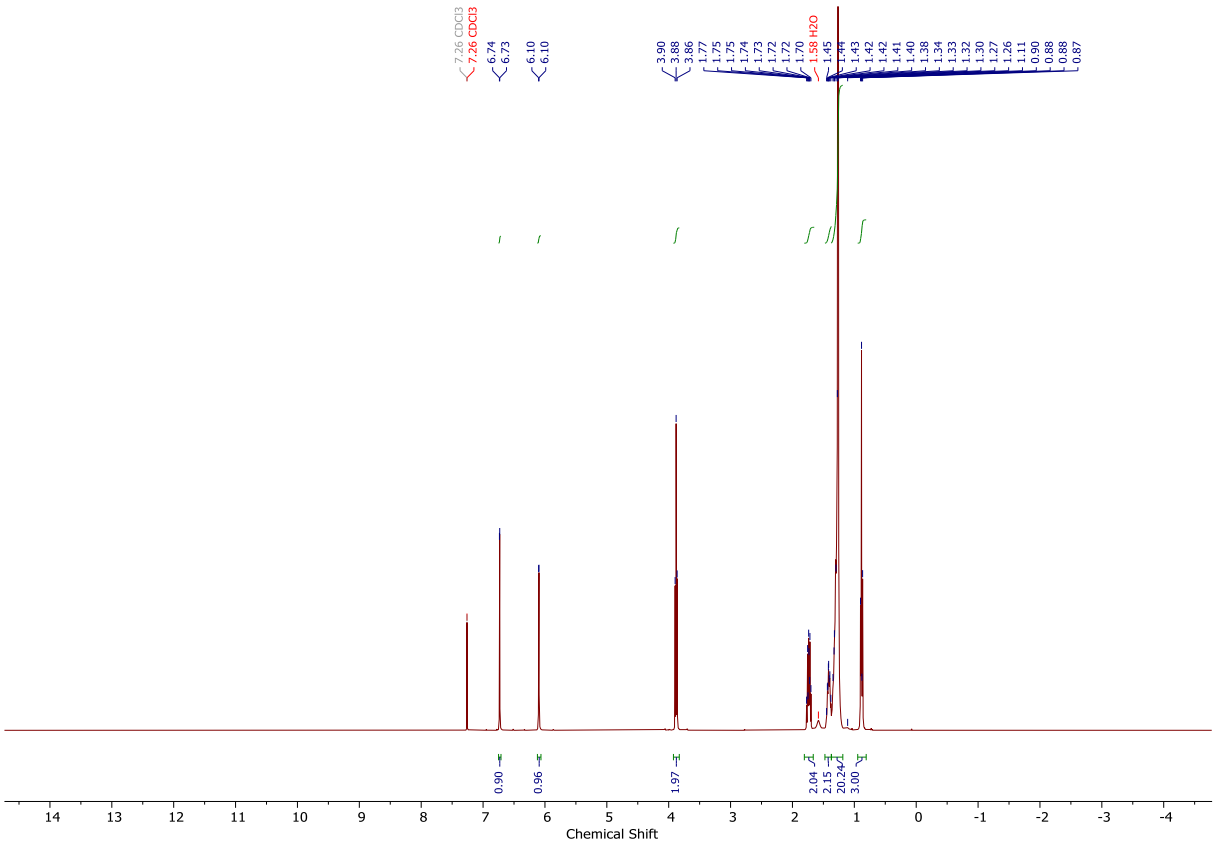
7.26 CDCl3
7.26 CDCl3
6.74
6.73
6.10
6.10
3.90
3.88
3.86
1.77
1.75
1.75
1.74
1.73
1.72
1.72
1.70
1.58 H2O
1.45
1.44
1.43
1.42
1.42
1.41
1.40
1.38
1.34
1.33
1.32
1.30
1.27
1.26
1.11
0.90
0.88
0.88
0.87
0.90
0.96
1.97
2.04
2.15
20.24
3.00
Chemical Shift

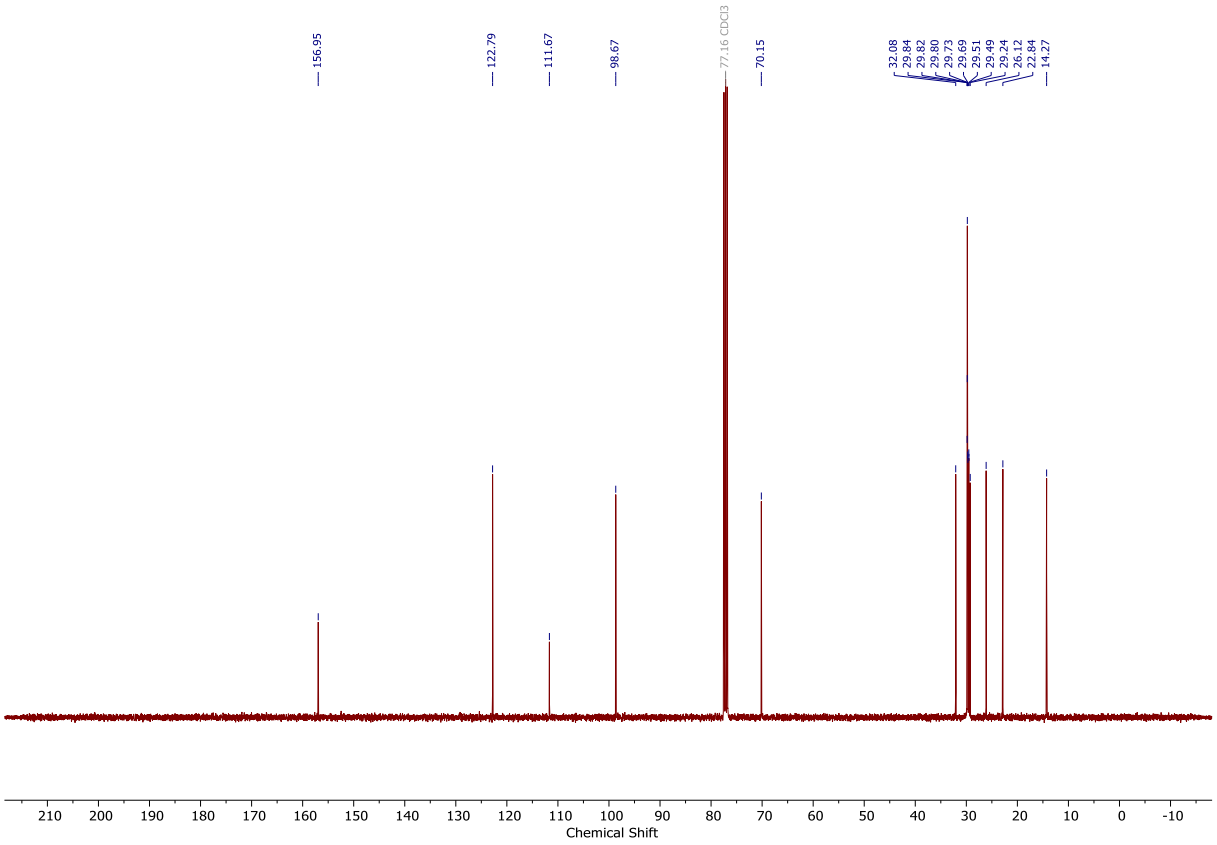
156.95
122.79
111.67
98.67
77.16 CDCl3
70.15
32.08
29.84
29.82
29.80
29.73
29.69
29.51
29.49
29.24
26.12
22.84
14.27
Chemical Shift

Expanded Spectrum RT 0.10, NL 346988, Peak [1], Target Mass 375.1352

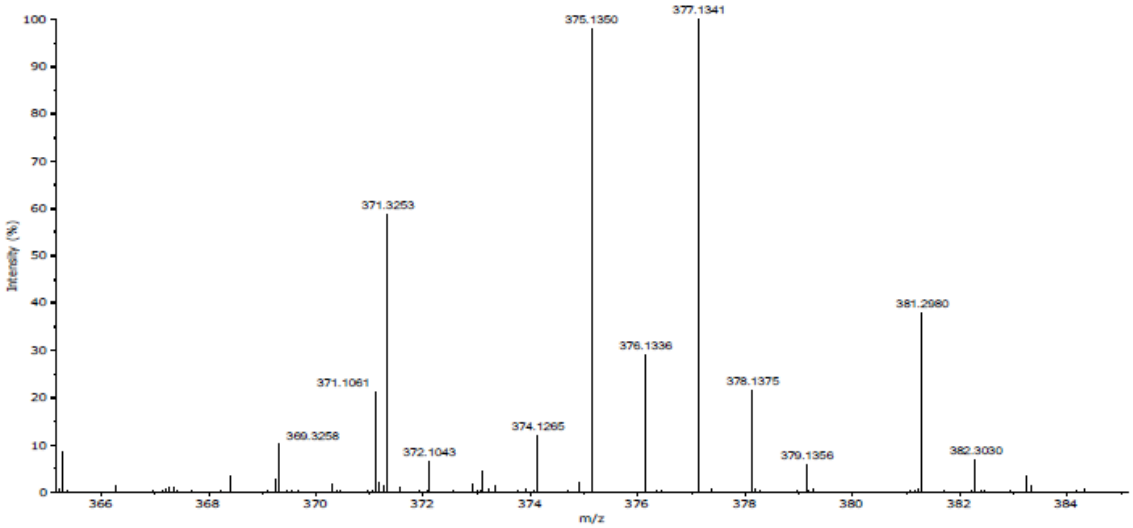

Theoretical Spectrum for C18H32BrOS, Minimum Abundance 0.01%

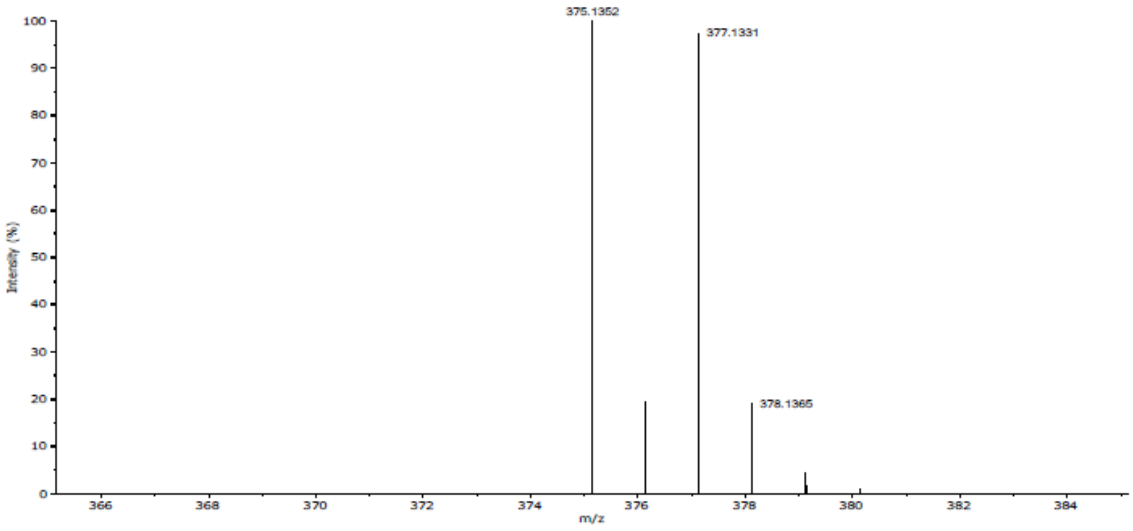

Measured Mass	Calculated Mass	Error (mDa)	Error (ppm)	Formula $[M+H]^+$	Response
375.1350	375.1352	-0.17	-0.46	$C_{18}H_{32}BrOS$	613663

Preparation of 4-(tetradecyloxy)-2,2'-bithiophene

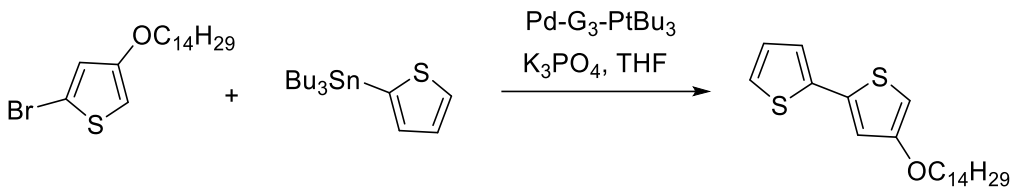

T-OC_{14}-3-Br (2500 mg, 6.7 mmol), 2-tributylstannylthiophene (2.4 mL, 1.05 eq), Pd-G3-$PtBu_3$ (158.4 mg), K_3PO_4 (1422 mg, 6.7 mmol, 1 eq) was added to a 2-neck round-bottom flask, evacuated under vacuum, then backfilled with N_2. Degassed THF (50 mL) was added and the reaction mixture was stirred at room temperature overnight. Upon completion, Pd black is removed by diluting the solution with DCM (200 mL) and filtered through celite. The celite cake is washed with an additional 80 mL of DCM and the organic layer is washed twice with H_2O, which is then dried over anhydrous magnesium sulphate and further purified by column chromatography over hexane as a pale-yellow solid. (2219 mg, 88%). ^{1}H NMR (400 MHz, $CDCl_3$) δ 7.20 (dd, J = 5.1, 1.2 Hz, 1H), 7.15 (dd, J = 3.6, 1.2 Hz, 1H), 7.00 (dd, J = 5.1, 3.6 Hz, 1H), 6.86 (d, J = 1.5 Hz, 1H), 6.12 (d, J = 1.7 Hz, 1H), 3.94 (t, J = 6.5 Hz, 2H), 1.77 (dq, J = 8.2, 6.6 Hz, 2H), 1.51 – 1.40 (m, 2H), 1.40 – 1.18 (m, 20H), 0.95 – 0.83 (m, 3H). ^{13}C NMR (101 MHz, $CDCl_3$) δ 157.7, 137.8, 135.9, 127.9, 124.7, 123.6, 96.3, 70.3, 32.1, 29.9, 29.8, 29.8, 29.8, 29.7, 29.5, 29.5, 29.4, 26.2, 22.9, 14.3. HRMS (ESI): calcd for $C_{22}H_{34}OS_2$, 378.2046; found 378.2029 (M^+, -4.4 ppm).

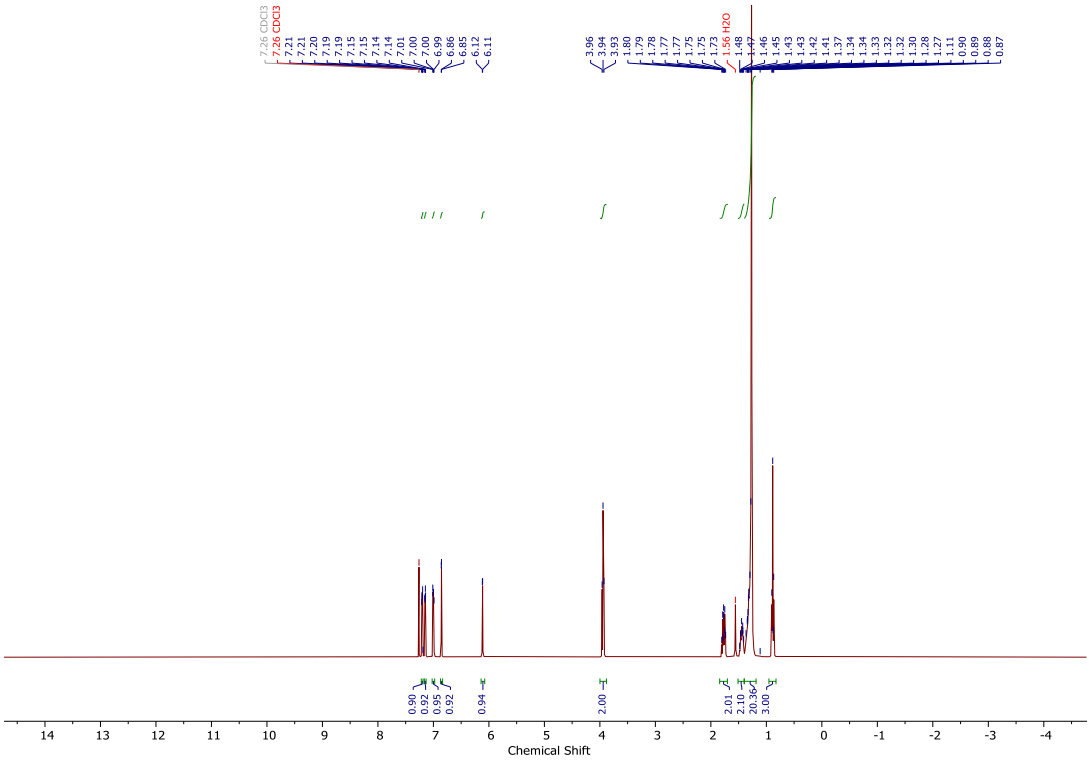
7.26 CDCl3
7.26 CDCl3
7.21
7.21
7.20
7.19
7.19
7.15
7.15
7.14
7.14
7.01
7.01
7.00
7.00
6.99
6.86
6.85
6.12
6.11
3.96
3.94
3.93
1.80
1.79
1.78
1.77
1.75
1.75
1.73
1.56 H2O
1.48
1.47
1.46
1.45
1.43
1.43
1.42
1.41
1.37
1.34
1.34
1.33
1.32
1.30
1.28
1.27
1.11
0.90
0.89
0.88
0.87
0.90
0.92
0.95
0.92
0.94
2.00
2.01
2.10
20.36
3.00
Chemical Shift

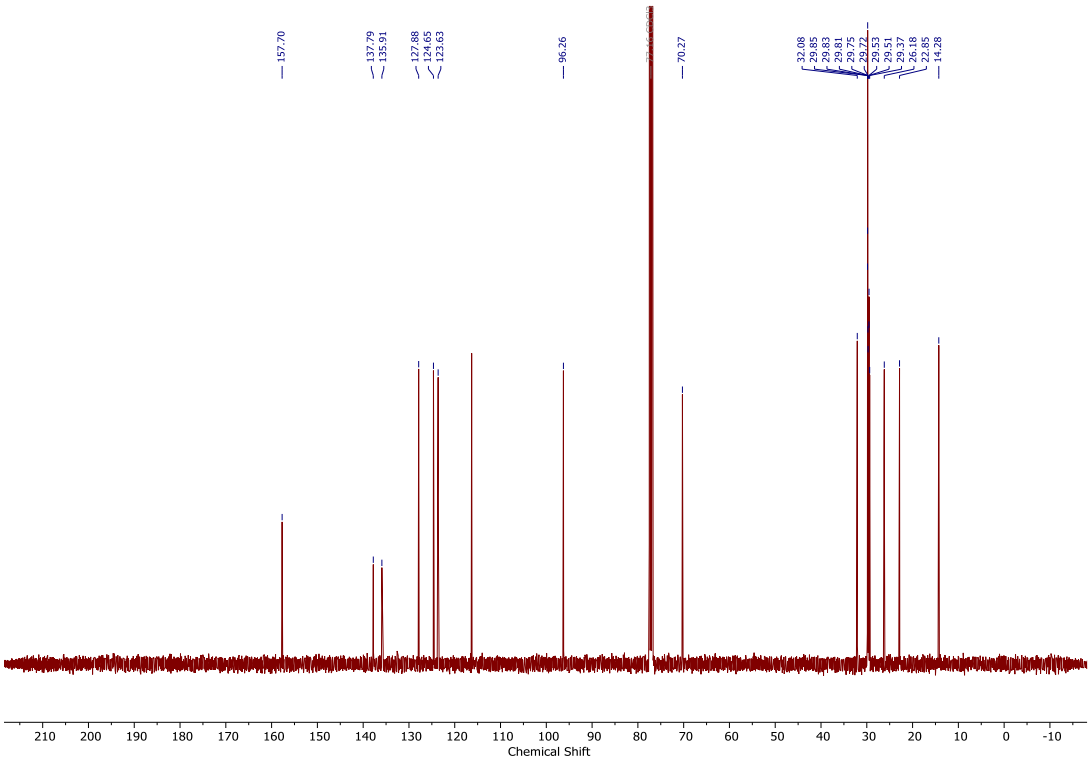
157.70
137.79
135.91
127.88
124.65
123.63
96.26
70.27
32.08
29.85
29.83
29.81
29.75
29.73
29.53
29.51
29.37
26.18
22.85
14.28
Chemical Shift

Expanded Spectrum RT 0.11, NL 1398741, Peak [1], Target Mass 378.2046

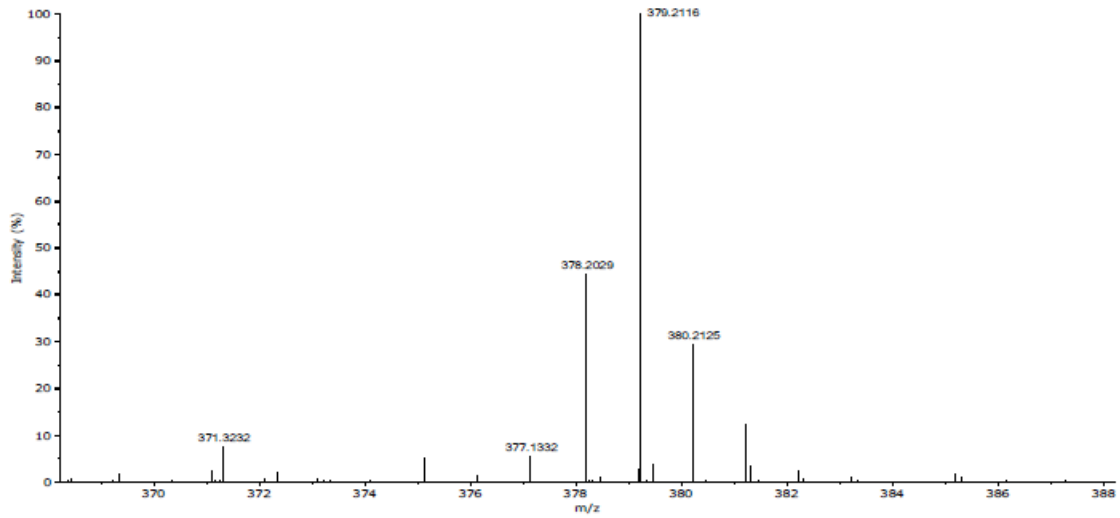

Theoretical Spectrum for C22H34OS2, Minimum Abundance 0.01%

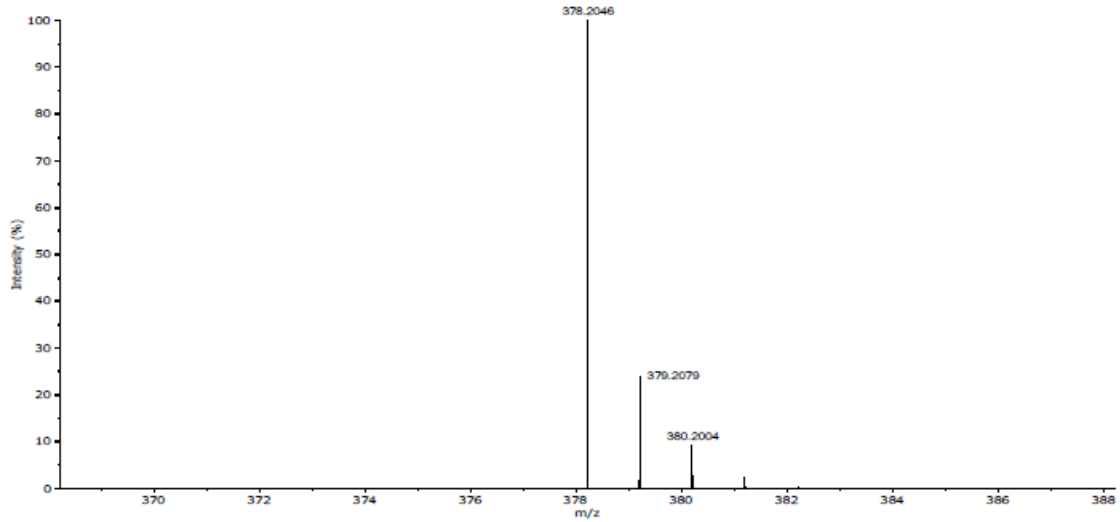

Measured Mass	Calculated Mass	Error (mDa)	Error (ppm)	Formula $[M]^+$	Response
378.2029	378.2046	-1.66	-4.39	$C_{22}H_{34}OS_2$	1923196

Preparation of 5,5'-dibromo-4-(tetradecyloxy)-2,2'-bithiophene

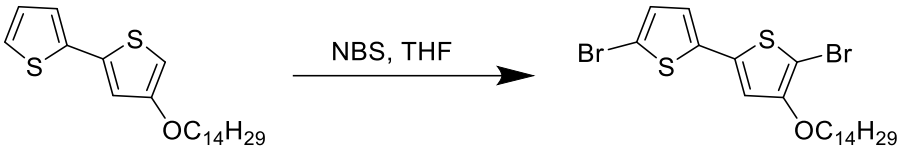

4-(tetradecyloxy)-2,2'-bithiophene (2150 mg, 5.68 mmol) was dissolved in anhydrous THF (55 mL) and cooled in a water bath. Then, NBS (2153 mg, 12.5 mmol, 2.2 eq) was added and the reaction mixture was stirred at room temperature overnight. Reaction was completed after 2 hours. The reaction mixture was then diluted with ethyl acetate (245 mL) and washed with water thrice (200 mL x 3), before being dried over anhydrous sodium sulphate and further purified by column chromatography. (Hexane, dry loaded) to yield a pale-yellow solid. (2.78 g, 91%). ^{1}H NMR (400 MHz, CD_2Cl_2) δ 6.99 (d, J = 3.9 Hz, 1H), 6.89 (d, J = 3.9 Hz, 1H), 6.80 (s, 1H), 4.04 (t, J = 6.6 Hz, 2H), 1.75 (dq, J = 8.2, 6.6 Hz, 2H), 1.50 – 1.40 (m, 2H), 1.27 (d, J = 6.5 Hz, 20H), 0.92 – 0.82 (m, 3H). ^{13}C NMR (101 MHz, CD_2Cl_2) δ 155.1, 138.8, 134.6, 131.3, 124. 2, 114.5, 111.8, 90.8, 72.9, 32.3, 30.1, 30.1, 30.1, 30.0, 30.0, 29.8, 29.8, 29.7, 26.2, 23.1, 14.3. HRMS (ESI): calcd for $C_{22}H_{33}Br_2OS_2$, 535.0334; found 535.0312 ($M+H^+$, -4.1 ppm).

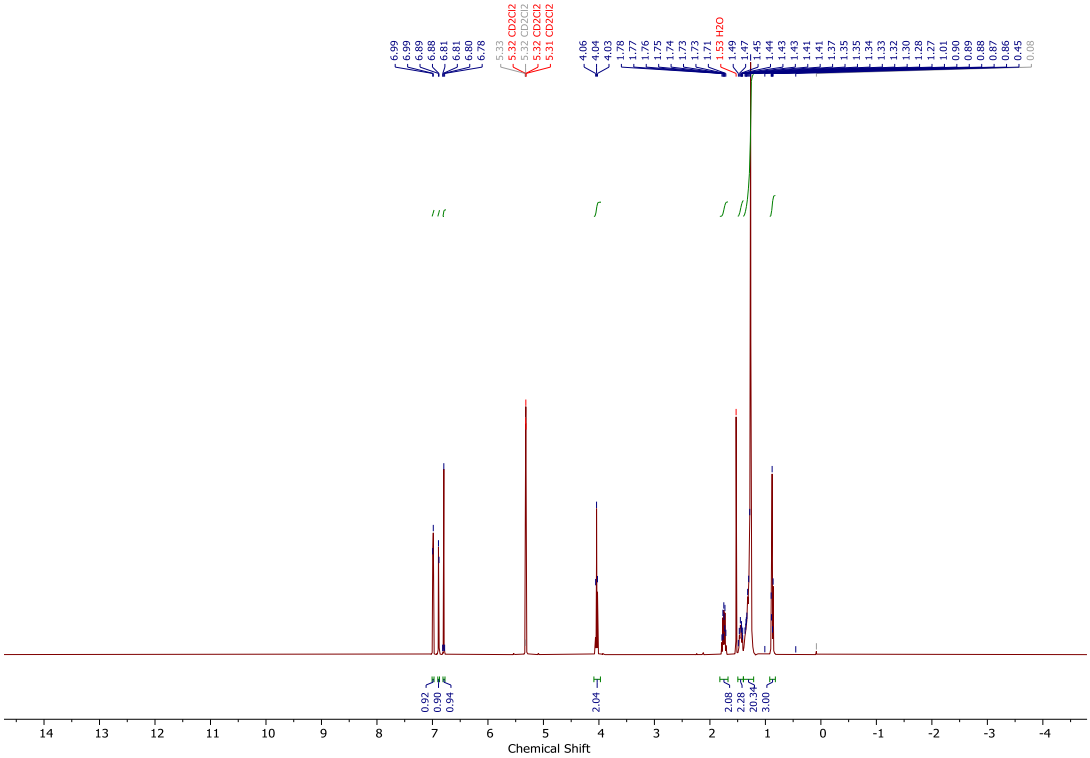
6.99
6.99
6.89
6.88
6.81
6.81
6.80
6.78
5.33
5.32 CD2Cl2
5.32 CD2Cl2
5.32 CD2Cl2
5.31 CD2Cl2
4.06
4.04
4.03
1.78
1.77
1.76
1.75
1.74
1.73
1.73
1.71
1.53 H2O
1.49
1.47
1.45
1.44
1.43
1.43
1.41
1.41
1.37
1.35
1.35
1.34
1.33
1.32
1.30
1.28
1.27
1.01
0.90
0.89
0.88
0.87
0.86
0.45
0.08
0.92
0.90
0.94
2.04
2.08
2.28
20.34
3.00
Chemical Shift

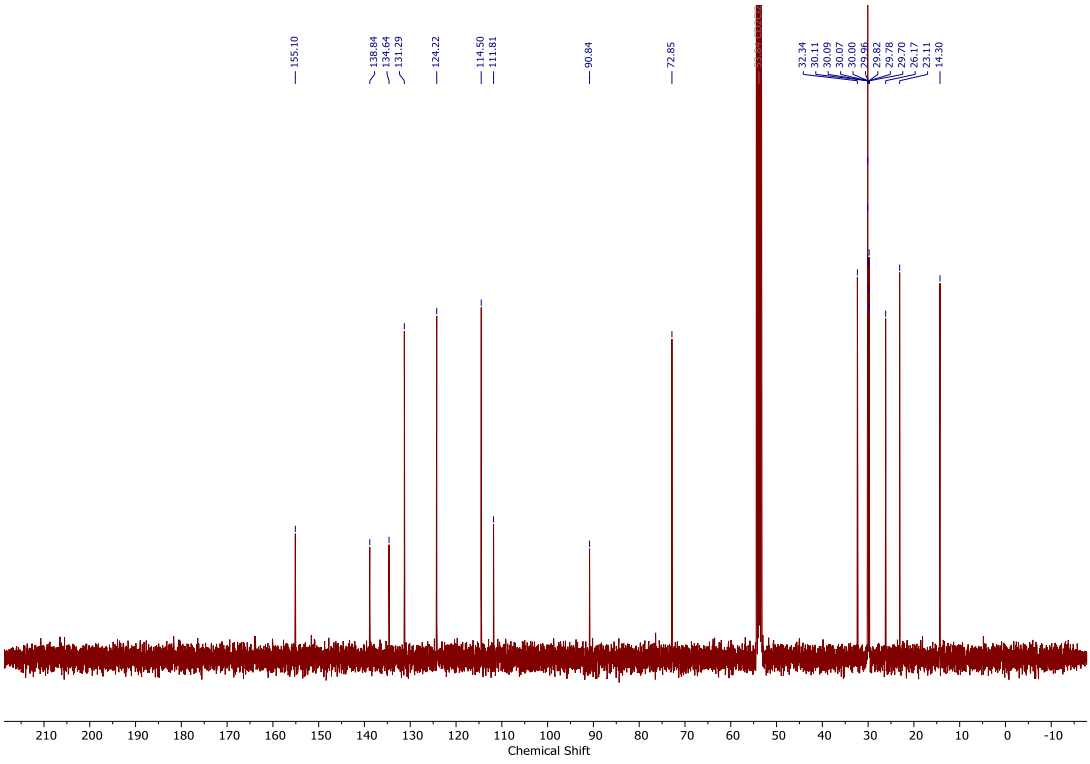
155.10
138.84
134.64
131.29
124.22
114.50
111.81
90.84
72.85
32.34
30.11
30.09
30.07
30.00
29.86
29.82
29.78
29.70
26.17
23.11
14.30
Chemical Shift

Expanded Spectrum RT 0.10, NL 185902, Peak [1], Target Mass 535.0334

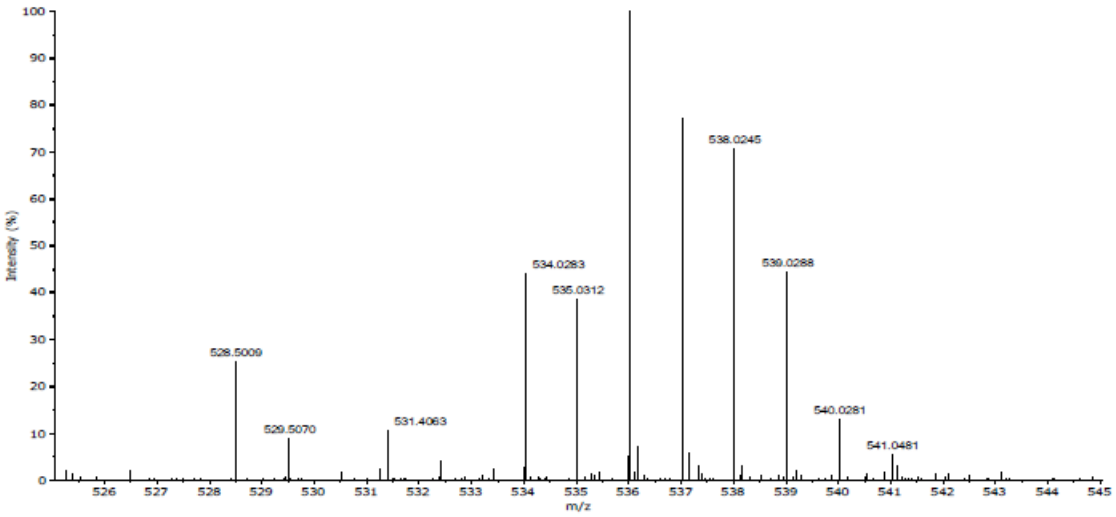

Theoretical Spectrum for C22H33Br2OS2, Minimum Abundance 0.01%

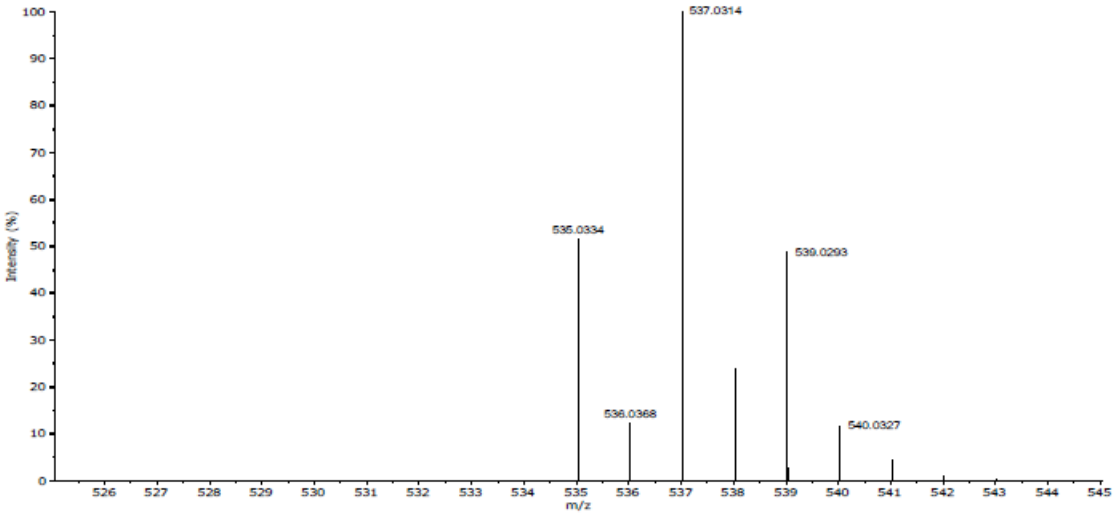

Measured Mass	Calculated Mass	Error (mDa)	Error (ppm)	Formula $[M+H]^+$	Response
535.0312	535.0334	-2.21	-4.13	$C_{22}H_{33}Br_2OS_2$	172172

Preparation of T-T-OC$_{14}$-Br-BDACO

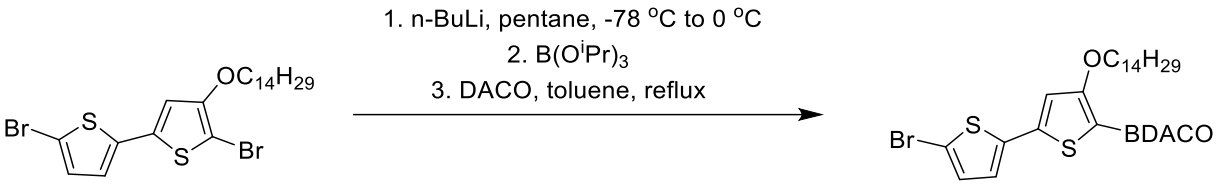

5,5'-dibromo-4-(tetradecyloxy)-2,2'-bithiophene (265.21 mg, 0.5 mmol) was dissolved in anhydrous pentane and cooled to -78 °C. Then, it is insulated from light with aluminium foil and BuLi (0.35 mL, 1.6 M, 0.55 mmol, 1.1 eq) was added dropwise and the reaction mixture was stirred at -78 °C for an hour, followed by 0 °C for an additional hour (ended up as a uniform orange solution). Then, B(OBu)$_3$ (0.20 mL, 1.5 eq) was added, washed and concentrated. Ligand (201.55 mg, 2.5 eq) was vacuumed and dissolved in anhydrous THF, then added and stirred for 2 hours at room temperature, passed through a quick normal phase column with ethyl acetate, then triturated with hexane to yield an off-white solid. (73 mg, 12%). ^{1}H NMR (500 MHz, CD$_3$CN) δ 7.00 (d, J = 3.8 Hz, 1H), 6.97 (s, 1H), 6.90 (d, J = 3.8 Hz, 1H), 6.03 (s, 1H), 3.97 (t, J = 6.7 Hz, 2H), 3.34 – 3.11 (m, 2H), 2.79 (dd, J = 12.1, 4.3 Hz, 2H), 1.84 – 1.66 (m, 2H), 1.29 (d, J = 31.1 Hz, 26H), 1.09 (s, 6H), 0.86 (d, J = 9.0 Hz, 5H). ^{13}C NMR (126 MHz, CD$_3$CN) δ 156.7, 140.8, 133.5, 131.1, 124.1, 122.4, 113.9, 108.8, 75.9, 70.9, 61.6, 31.7, 29.5, 29.4, 29.4, 29.3, 29.3, 29.3, 29.2, 29.1, 29.1, 28.7, 26.8, 25.8, 22.4, 13.4. ^{11}B NMR (161 MHz, CD$_3$CN) δ 9.67. HRMS (ESI): calcd for C$_{30}$H$_{50}$BBrNO$_3$S$_2$, 626.2503; found 626.2503 (M+H+, 0.0 ppm).

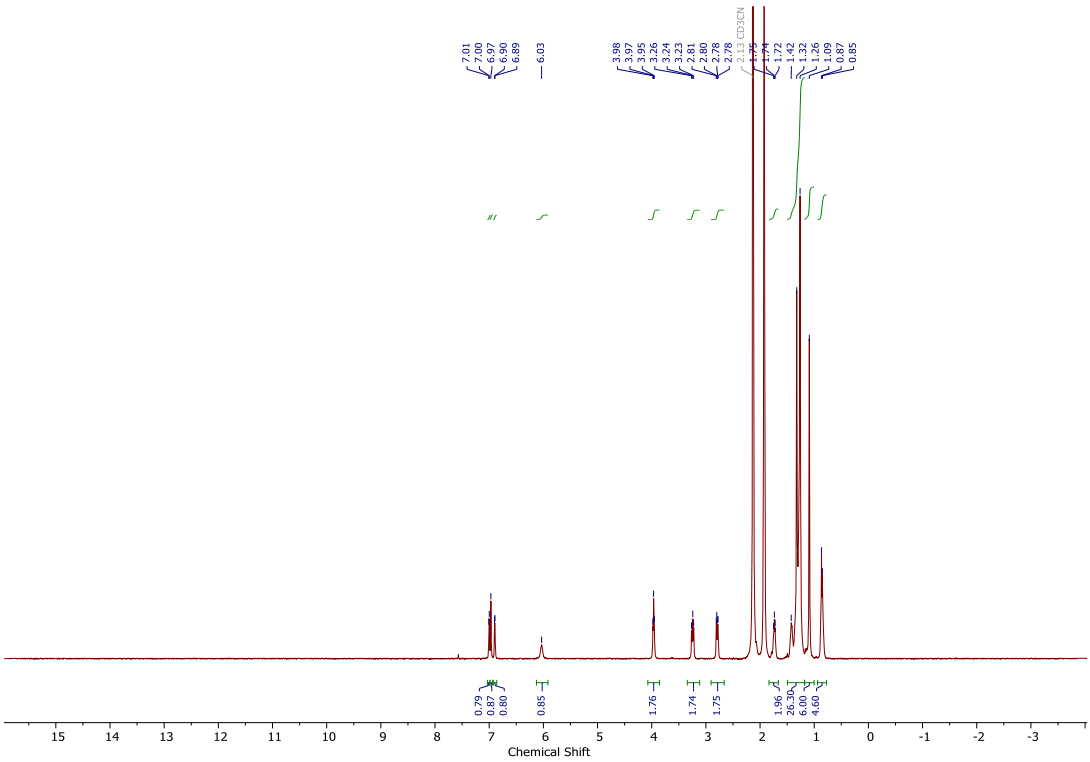
7.01
7.00
6.97
6.90
6.89
6.03
3.98
3.97
3.95
3.26
3.24
3.23
2.81
2.80
2.78
2.78
2.13 CD3CN
1.93
1.74
1.72
1.42
1.32
1.26
1.09
0.87
0.85
0.79
0.87
0.80
0.85
1.76
1.74
1.75
1.96
26.30
6.00
4.60
Chemical Shift

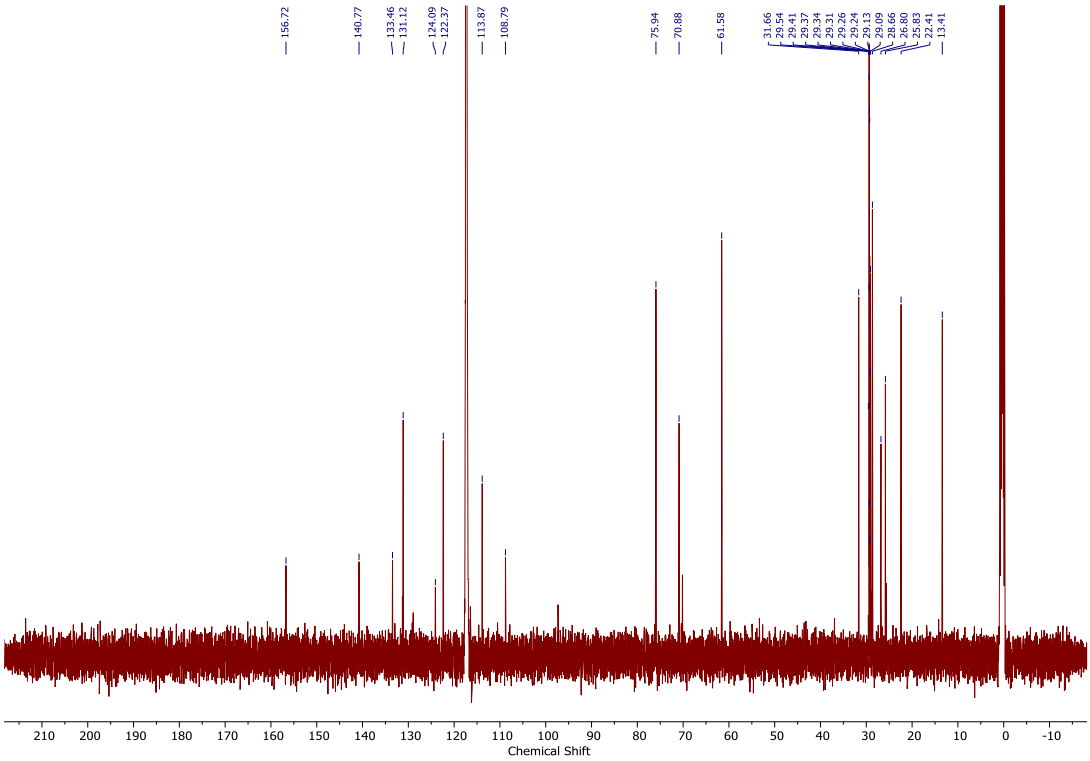
156.72
140.77
133.46
131.12
124.09
122.37
113.87
108.79
75.94
70.88
61.58
31.66
29.54
29.41
29.37
29.34
29.31
29.26
29.24
29.13
29.09
28.66
26.80
25.83
22.41
13.41
Chemical Shift

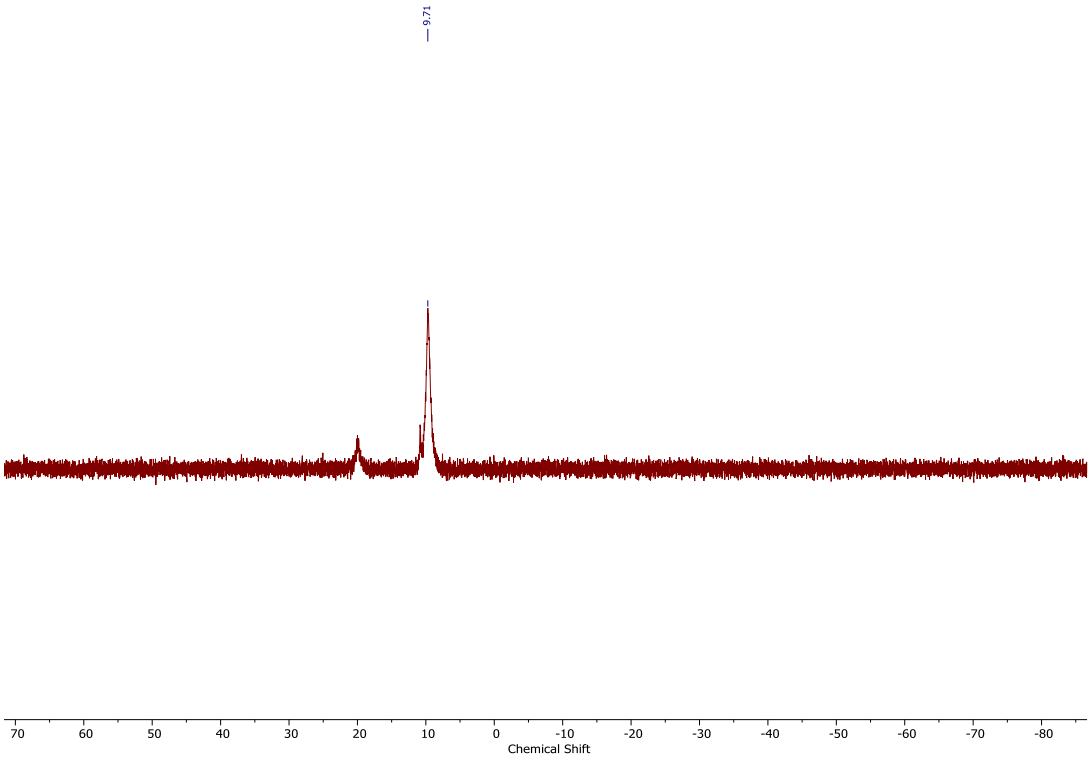
9.71
70
60
50
40
30
20
10
0
-10
-20
-30
-40
-50
-60
-70
-80
Chemical Shift

Expanded Spectrum RT 0.09, NL 262850.76171875, Peak [1], Target Mass 626.2503

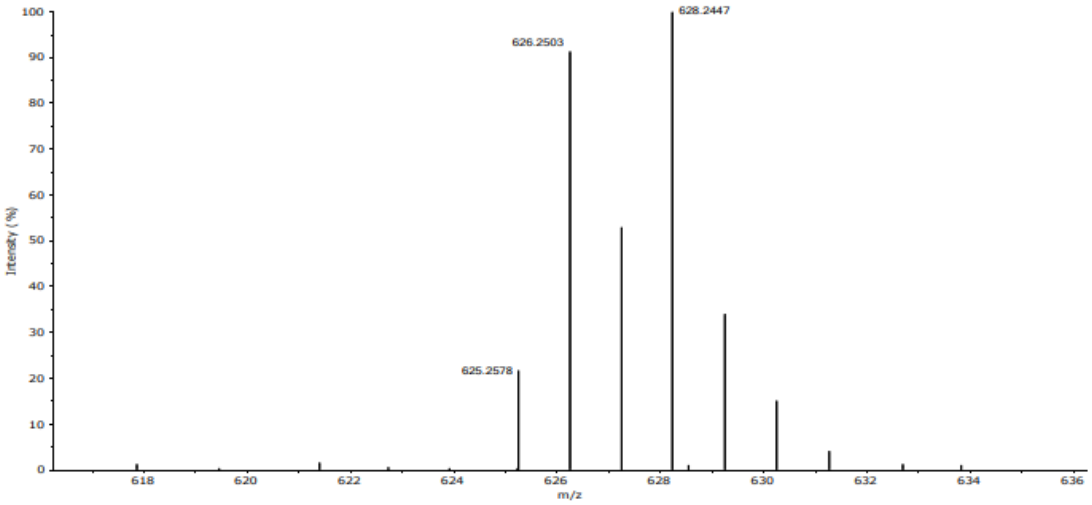

Theoretical Spectrum for C30H50BBrNO3S2, Minimum Abundance 0.01%

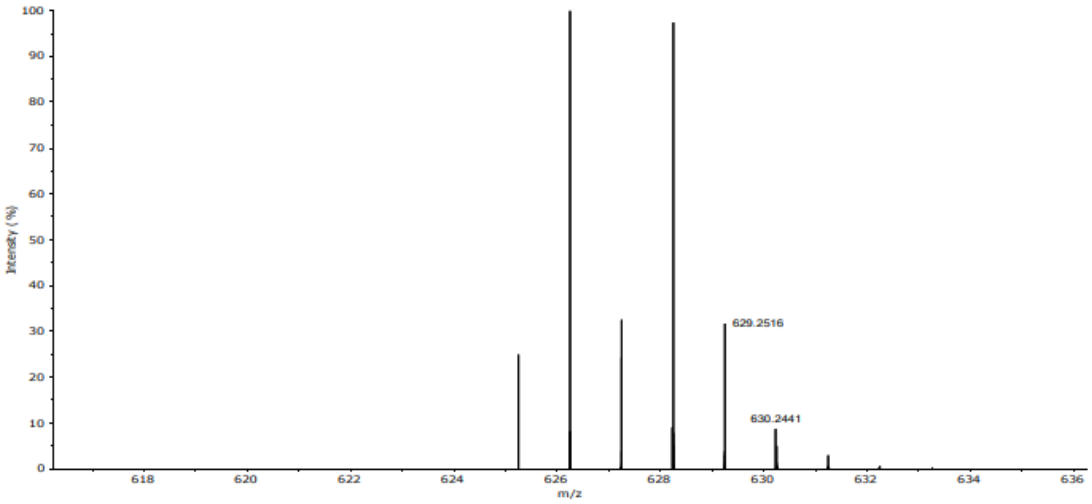

Measured Mass	Calculated Mass	Error (mDa)	Error (ppm)	Formula $[M+H]^+$	Response
626.2503	626.2503	-0.01	-0.01	$C_{30}H_{50}BBrNO_3S_2$	350834

Preparation of P3DOT-S

RuPhos Pd G3 precatalyst (20.07 mg, 0.024 mmol, 0.02 eq), RuPhos (67.20mg, 0.144 mmol, 0.12 eq), 4-iodobenzaldehyde (5.29 mg, 0.0228 mmol, 0.95 eq w.r.t. catalyst, a stock solution of 1 mg/mL, 0.86 mL is prepared) and K2CO3 (663.4 mg, 4.8 mmol, 4 eq) was added to a microwave vial, evacuated under vacuum and exchanged with N_2 thrice. Then, degassed THF (29.40 mL), followed by degassed H2O (0.60 mL) was added and the reaction mixture was warmed to 50 ºC for 30 min to prepare the precatalyst. T-OC_{10}-Br-BDABO (585.96 mg, M_r = 488.33 g/mol, 1.2 mmol) was dissolved in degassed (30 mL) and added to the previous reaction mixture and the reaction mixture was warmed to 45 ºC for 40 hours, which was then further purified by Soxhlet extraction (MeOH -> Acetone -> Hexane -> chloroform) to yield a dark blue solid (144 mg, 50.3%). ^{1}H NMR (400 MHz, $CDCl_3$) δ 9.93 (s, 1H), 6.92 (s, 29H), 4.18 (s, 78H), 1.89 (s, 64H), 1.27 (t, *J* = 5.8 Hz, 1267H), 0.99 – 0.71 (m, 389H). GPC (PhCl): M_n = 6.6 kDa, M_w = 9.5 kDa

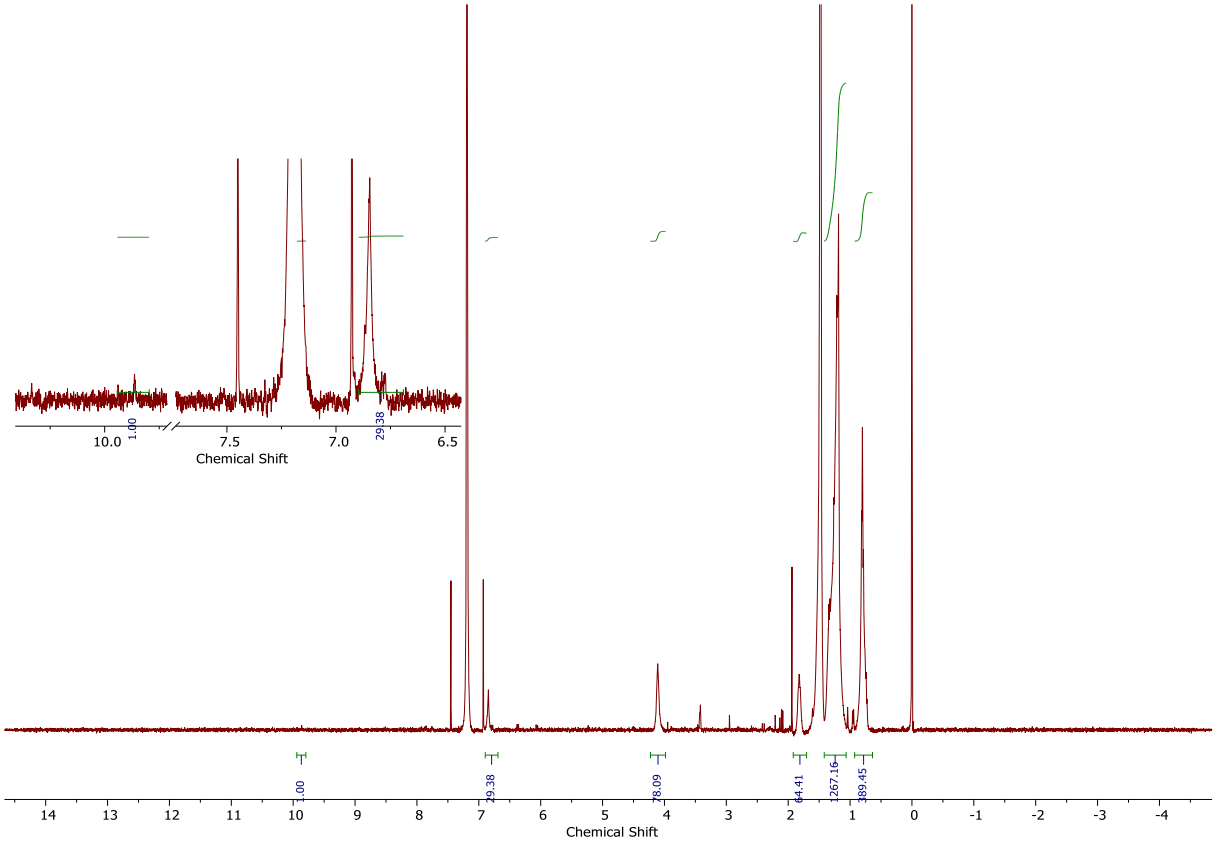
1.00
29.38
10.0
7.5
7.0
6.5
Chemical Shift
1.00
29.38
78.09
64.41
267.16
389.45
14
13
12
11
10
9
8
7
6
5
4
3
2
1
0
-1
-2
-3
-4
Chemical Shift

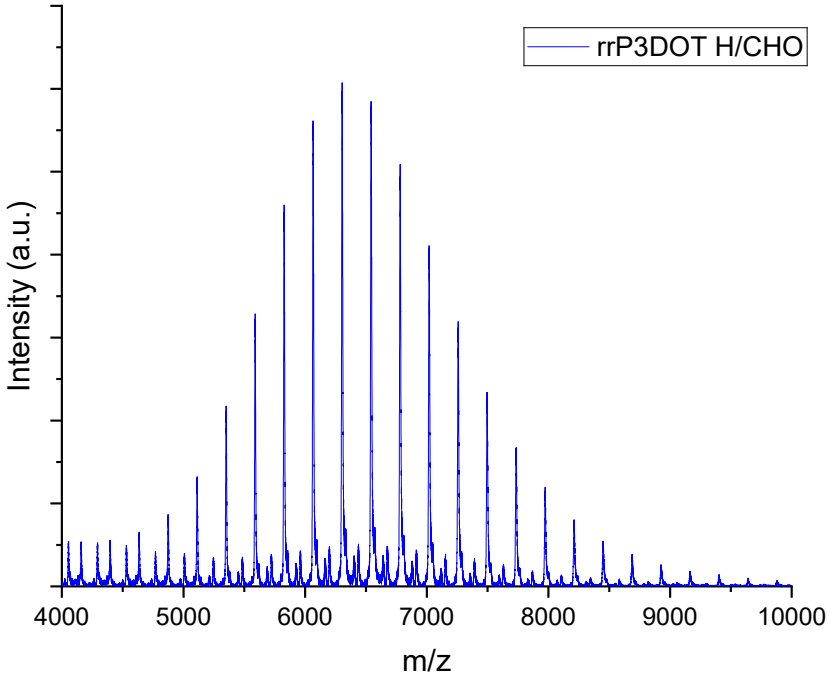

Molecular Weight Averages

Peak	Mp (g/mol)	Mn (g/mol)	Mw (g/mol)	Mz (g/mol)	Mz+1 (g/mol)	Mv (g/mol)
Peak 1	6865	6639	9511	12524	15556	9088

PD
1.433

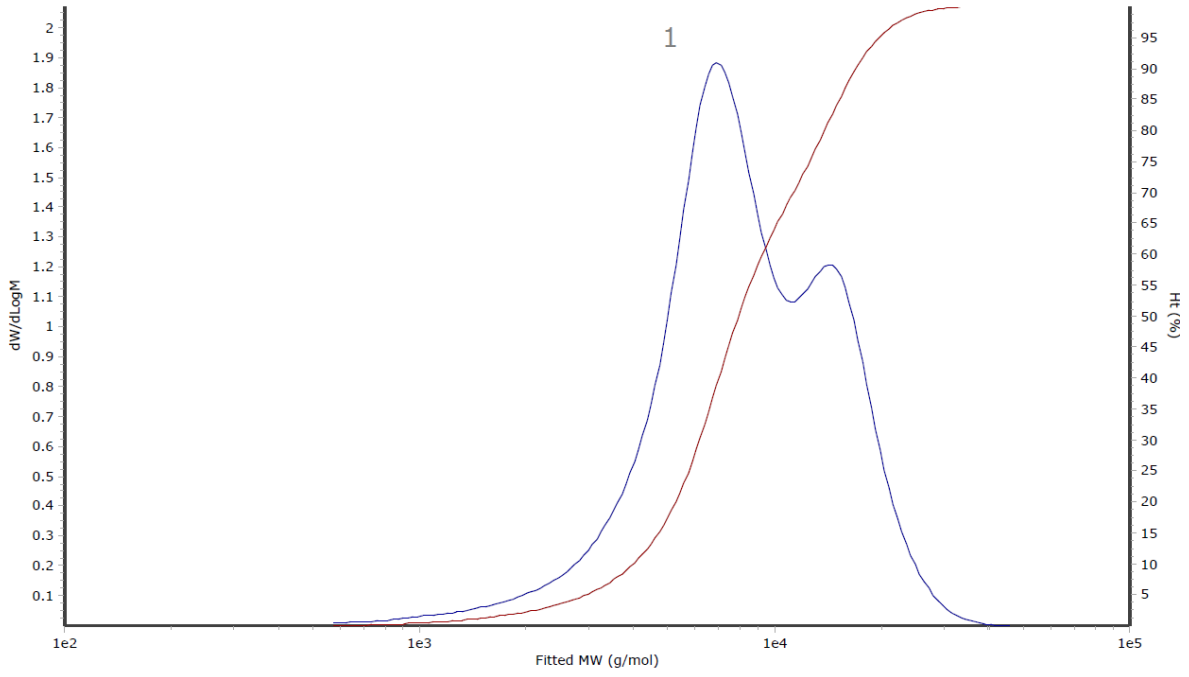

Preparation of F8BT Br/Br

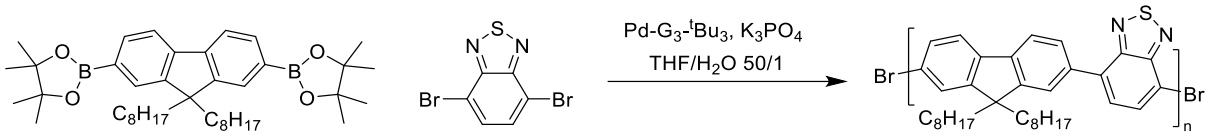

F_8-Bpin$_2$ (64.26 mg, 0.1 mmol), BT-Br$_2$ (29.40 mg, 0.1 mmol), Pd-G$_3$-PtBu$_3$ (2.29 mg, 4 mol%) and K_3PO_4 (212 mg, 10 eq) was added to a microwave vial, then evacuated under vacuum and backfilled with N_2. Then, anhydrous THF (1.5 mL) and H_2O (0.03 mL) was added and the reaction mixture was warmed at 40 ºC for 1 hour, before being precipitated in methanol and further purified by Soxhlet extraction (methanol -> hexane -> chloroform), before being concentrated and precipitated in methanol to yield an orange solid (45 mg, 66%). GPC (PhCl): M_n = 18.1 kDa, M_w = 55.9 kDa

Molecular Weight Averages

Peak	Mp (g/mol)	Mn (g/mol)	Mw (g/mol)	Mz (g/mol)	Mz+1 (g/mol)	Mv (g/mol)
Peak 1	20865	18062	55851	177878	330747	45843

PD
3.092

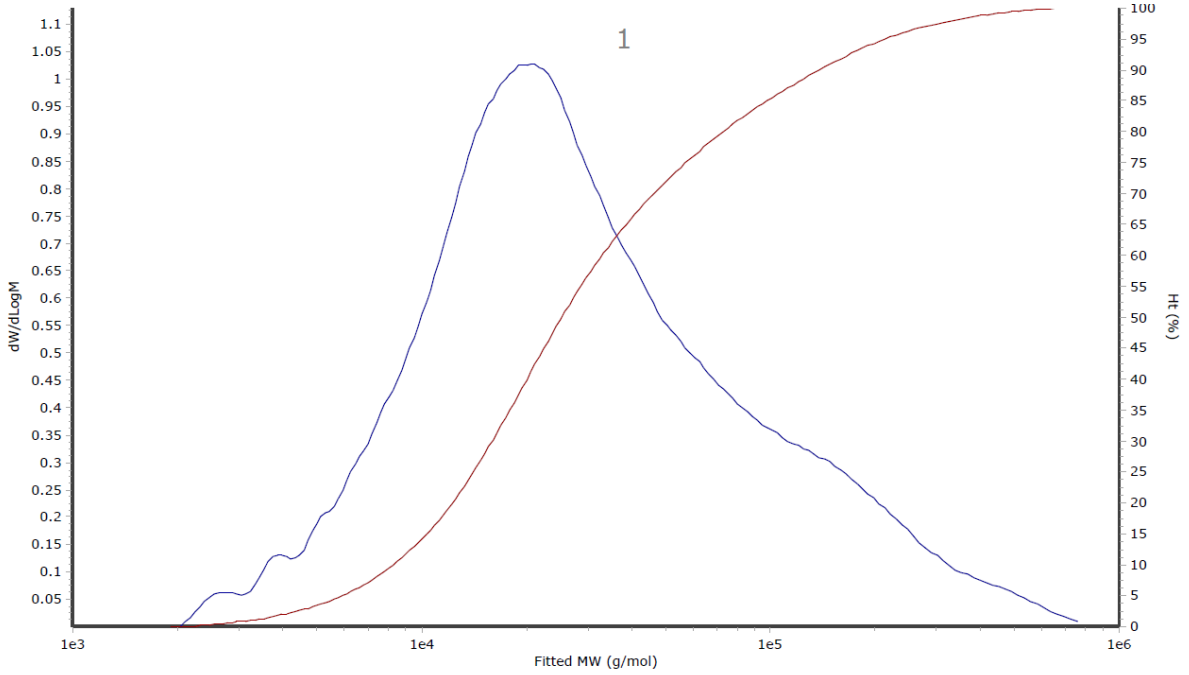

Preparation of F8BT Alkyne/Alkyne

Under N_2, F8BT Br/Br (40 mg, 2.2 umol), Pd-G_3-$PtBu_3$ (0.63 mg, 0.5 eq), anhydrous K_3PO_4 (4.67 mg, 10 eq) and ethynyltributylstannane (13.9 mg, 20 eq) was dissolved in anhydrous THF (2 mL) and stirred at room temperature for 48 hours. Then, the reaction mixture was diluted with chloroform (20 mL) and washed with water (20 mL x 2), before being concentrated and precipitated in methanol to yield an orange solid (31 mg, 78%), which is used in next step without further purification. GPC (PhCl): M_n = 23.3 kDa, M_w = 113 kDa

Molecular Weight Averages

Peak	Mp (g/mol)	Mn (g/mol)	Mw (g/mol)	Mz (g/mol)	Mz+1 (g/mol)	Mv (g/mol)
Peak 1	18668	23343	112563	458663	898507	86240

PD
4.822

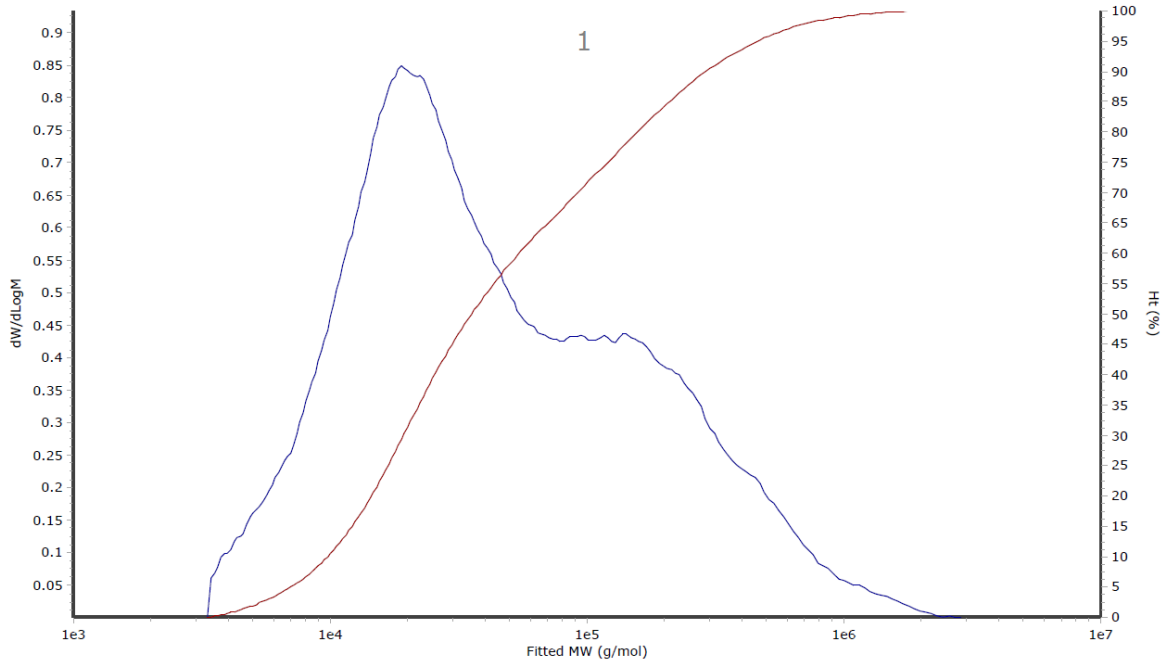

Preparation of PEG-b-F8BT-b-PEG

Under N_2, F8BT Alkyne/Alkyne (23 mg, 1.0 umol), azide-terminated PEG (15 mg, 3.0 umol) CuBr (0.29 mg, 1.5 eq), PMDETA (1.04 mg, 6 eq) was dissolved in anhydrous THF (2 mL) and stirred at 40 ºC for 24 hours. Then, the reaction mixture was diluted with chloroform (20 mL) and washed with water (20 mL x 2), before being concentrated and precipitated in methanol to yield an orange solid (19 mg, 50%). ^{1}H NMR (400 MHz, $CDCl_3$) δ 8.23 – 7.84 (m, 190H), 3.65 (s, 738H), 3.38 (s, 6H), 1.18 (d, J = 13.9 Hz, 643H), 0.81 (t, J = 6.6 Hz, 231H). GPC (PhCl): M_n = 39.1 kDa, M_w = 126 kDa

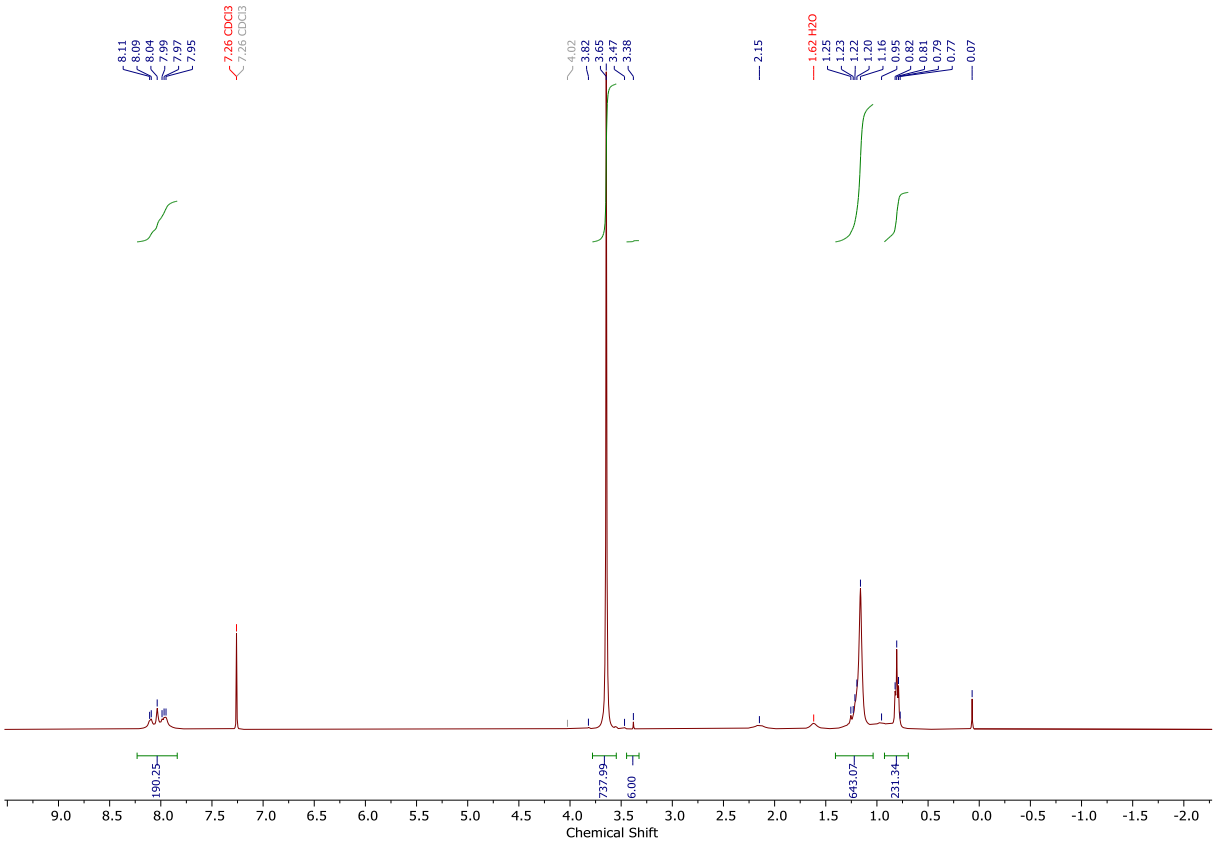

Molecular Weight Averages

Peak	Mp (g/mol)	Mn (g/mol)	Mw (g/mol)	Mz (g/mol)	Mz+1 (g/mol)	Mv (g/mol)
Peak 1	30128	39181	125609	489107	1018500	100608

PD
3.206

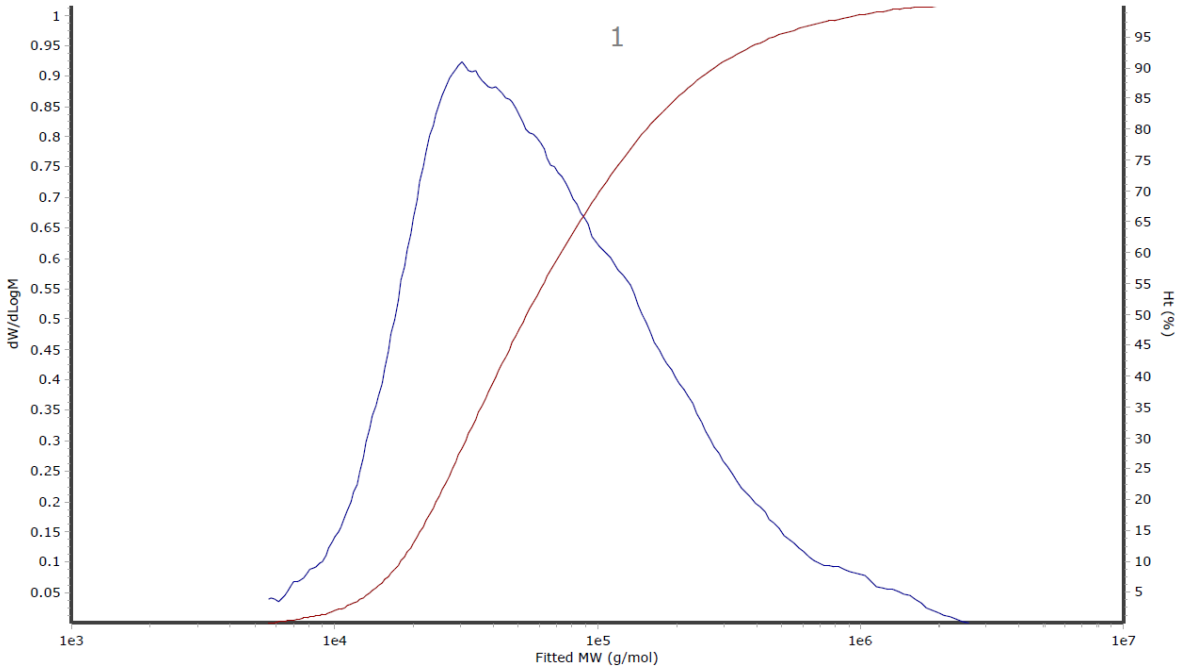

CHAPTER 8

References

(1) Peterson, D. Global Semiconductor Sales Increase 19.1% in 2024; Double-Digit Growth Projected in 2025. Semiconductor Industry Association.
(2) Semiconductor Market Size, Share, Growth & Forecast 2032.
(3) CHIPS and Science Act: Breaking down the law's impact 2 years later
(4) Organic Semiconductor Market Size, Share, Industry Forecast by 2032.
(5) Organic Semiconductor Market Growth Prospects, Insights, and Future Trends Report.
(6) Intelligence, C. B. Organic Semiconductor Market Size, Share, Growth, Trends and Forecast Report - 2031. Consegic Business Intelligence.
(7) Research, V. M. Organic Semiconductor Market Size, Share & Growth Forecast by 2035.
(8) Organic Semiconductor Market Size, Share, Scope & Forecast.
(9) Zou, S.-J.; Shen, Y.; Xie, F.-M.; Chen, J.-D.; Li, Y.-Q.; Tang, J.-X. Recent Advances in Organic Light-Emitting Diodes: Toward Smart Lighting and Displays. *Mater. Chem. Front.* **2020**, *4* (3), 788–820..
(10) Yadav, S.; Mittal, P.; Negi, S. Recent Advancements over a Decade for Organic Light-Emitting Diodes: From Structural Diversity, Role of Layers, Colour Emission, Material Classification, Performance Improvement, Fabrication to Applications. *Bull Mater Sci* **2022**, *45* (3), 109.
(11) OLED Market Size, Share, Growth & Trends Report, 2030.
(12) OLED Market Size, Share and Trends Analysis, 2024-2032. Global Market Insights Inc.
(13) The Paris Agreement
(14) Lin, W.-C.; Sun, Y.-E.; Zhuang, Y.-R.; Huang, T.-F.; Lin, K.-J.; Elsenety, M. M.; Yen, J.-C.; Hsu, H.-K.; Chen, B.-H.; Chang, C.-Y.; et al. Optimally Miscible Polymer Bulk-Heterojunction-Particles for Nonsurfactant Photocatalytic Hydrogen Evolution *J. Am. Chem. Soc.* **2025**, 147, 3, 2537–2548
(15) Kosco, J.; Gonzalez-Carrero, S.; Howells, C. T.; Fei, T.; Dong, Y.; Sougrat, R.; Harrison, G. T.; Firdaus, Y.; Sheelamanthula, R.; Purushothaman, B.; Moruzzi, F.; Xu, W.; Zhao, L.; Basu, A.; De Wolf, S.; Anthopoulos, T. D.; Durrant, J. R.; McCulloch, I. Generation of Long-Lived Charges in Organic Semiconductor Heterojunction Nanoparticles for Efficient Photocatalytic Hydrogen Evolution. *Nat Energy* **2022**, *7* (4), 340–351.

(16) Kosco, J.; Gonzalez-Carrero, S.; Howells, C. T.; Zhang, W.; Moser, M.; Sheelamanthula, R.; Zhao, L.; Willner, B.; Hidalgo, T. C.; Faber, H.; Purushothaman, B.; Sachs, M.; Cha, H.; Sougrat, R.; Anthopoulos, T. D.; Inal, S.; Durrant, J. R.; McCulloch, I. Oligoethylene Glycol Side Chains Increase Charge Generation in Organic Semiconductor Nanoparticles for Enhanced Photocatalytic Hydrogen Evolution. *Adv. Mater.* **2022**, 34, 2105007.

(17) Coropceanu, V.; Cornil, J.; da Silva Filho, D. A.; Olivier, Y.; Silbey, R.; Brédas, J.-L. Charge Transport in Organic Semiconductors. *Chem. Rev.* **2007**, *107* (4), 926–952.

(18) Giannini, S.; Blumberger, J. Charge Transport in Organic Semiconductors: The Perspective from Nonadiabatic Molecular Dynamics. *Acc. Chem. Res.* **2022**, *55* (6), 819–830.

(19) Yavuz, I. Dichotomy between the Band and Hopping Transport in Organic Crystals: Insights from Experiments. *Phys. Chem. Chem. Phys.* **2017**, *19* (38), 25819–25828.

(20) Sirringhaus, H.; Sakanoue, T.; Chang, J.-F. Charge-transport physics of high-mobility molecular semiconductors. *Phys. Status Solidi B* **2012***, 249*, No. 9, 1655–1676.

(21) Li, Y.; Lagowski, J. B. Charge Carrier Mobility in Conjugated Organic Polymers – Case Studies Using Multi-Step Computational Approach. *Polymer* **2011**, *52* (21), 4841–4850.

(22) Brédas, J.-L.; Beljonne, D.; Coropceanu, V.; Cornil, J. Charge-Transfer and Energy-Transfer Processes in π-Conjugated Oligomers and Polymers: A Molecular Picture. *Chem. Rev.* **2004**, *104* (11), 4971–5004.

(23) Chen, X.; Guo, J.; Peng, L.; Wang, Q.; Jiang, S.; Li, Y. Charge Transport in Organic Field-Effect Transistors. *Mater. Today Electron.* **2023**, *6*, 100077.

(24) Borchert, J. W.; R. Thomas Weitz; Ludwigs, S.; Klauk, H. A Critical Outlook for the Pursuit of Lower Contact Resistance in Organic Transistors. *Adv. Mater.* **2021**, *34* (2).

(25) Rivnay, J.; Inal, S.; Salleo, A.; Owens, R. M.; Berggren, M.; Malliaras, G. G. Organic Electrochemical Transistors. *Nat Rev Mater* **2018**, *3* (2), 1–14.

(26) Friedlein, J. T.; McLeod, R. R.; Rivnay, J. Device Physics of Organic Electrochemical Transistors. *Org. Electron.* **2018**, *63*, 398–414.

(27) McCulloch, I.; Heeney, M.; Bailey, C.; Genevicius, K.; MacDonald, I.; Shkunov, M.; Sparrowe, D.; Tierney, S.; Wagner, R.; Zhang, W.; Chabinyc, M. L.; Kline, R. J.; McGehee, M. D.; Toney, M. F. Liquid-Crystalline Semiconducting Polymers with High Charge-Carrier Mobility. *Nat Mater.* **2006**, *5* (4), 328–333

(28) Kim, S.; Kim, A.; Jang, K.-S.; Yoo, S.; Ka, J.-W.; Kim, J.; Yi, M. H.; Won, J. C.; Hong, S.-K.; Kim, Y. H. The Effect of Thermal Annealing on the Layered Structure of Smectic Liquid Crystalline Organic Semiconductor on Polyimide Gate Insulator and Its OFET Performance. *Synth. Met.* **2016**, *220*, 311–317

(29) Raghuwanshi, V.; Bharti, D.; Mahato, A. K.; Varun, I.; Tiwari, S. P. Effect of Thermal Annealing on Electrical Stability of TIPS-Pentacene Flexible OFETs. In *2017 IEEE 12th Nanotechnology Materials and Devices Conference (NMDC)*; 2017; pp 192–193.

(30) Ohayon, D.; Druet, V.; Inal, S. A Guide for the Characterization of Organic Electrochemical Transistors and Channel Materials. *Chem. Soc. Rev.* **2023**, *52* (3), 1001–1023.

(31) Inal, S.; Malliaras, G. G.; Rivnay, J. Benchmarking Organic Mixed Conductors for Transistors. *Nat Commun* **2017**, *8* (1), 1767.

(32) Kukhta, N. A.; Marks, A.; Luscombe, C. K. Molecular Design Strategies toward Improvement of Charge Injection and Ionic Conduction in Organic Mixed Ionic–Electronic Conductors for Organic Electrochemical Transistors. *Chem. Rev.* **2021**, *122* (4), 4325–4355.

(33) Li, C.-Y.; Jiang, G.-H.; Tomoya Higashihara; Lin, Y.-C. Interfacial Stabilization of Organic Electrochemical Transistors Conferred Using Polythiophene-Based Conjugated Block Copolymers with a Hydrophobic Coil Design. *ACS Appl. Mater. Interfaces* **2024**, *16*, 39, 52753–52765

(34) Cendra, C.; Giovannitti, A.; Savva, A.; Venkatraman, V.; McCulloch, I.; Salleo, A.; Inal, S.; Rivnay, J. Role of the Anion on the Transport and Structure of Organic Mixed Conductors. *Adv. Funct. Mater.* **2018**, *29* (5), 1807034

(35) Flagg, L. Q.; Giridharagopal, R.; Guo, J.; Ginger, D. S. Anion-Dependent Doping and Charge Transport in Organic Electrochemical Transistors. *Chem. Mater.* **2018**, *30* (15), 5380–5389.

(36) Flagg, L. Q.; Bischak, C. G.; Quezada, R. J.; Onorato, J. W.; Luscombe, Christine. K.; Ginger, D. S. P-Type Electrochemical Doping Can Occur by Cation Expulsion

in a High-Performing Polymer for Organic Electrochemical Transistors. *ACS Mater. Lett.* **2020**, *2* (3), 254–260.

(37) Meng, B.; Liu, J.; Wang, L. Oligo(Ethylene Glycol) as Side Chains of Conjugated Polymers for Optoelectronic Applications. *Polym. Chem.* **2020**, *11* (7), 1261–1270.

(38) Moro, S.; Siemons, N.; Drury, O.; Warr, D. A.; Moriarty, T. A.; Perdigão, L. M. A.; Pearce, D.; Moser, M.; Hallani, R. K.; Parker, J.; McCulloch, I.; Frost, J. M.; Nelson, J.; Costantini, G. The Effect of Glycol Side Chains on the Assembly and Microstructure of Conjugated Polymers. *ACS Nano* **2022**, *16* (12), 21303–21314.

(39) Moser, M.; Savagian, L. R.; Savva, A.; Matta, M.; Ponder, J. F. Jr.; Hidalgo, T. C.; Ohayon, D.; Hallani, R.; Reisjalali, M.; Troisi, A.; Wadsworth, A.; Reynolds, J. R.; Inal, S.; McCulloch, I. Ethylene Glycol-Based Side Chain Length Engineering in Polythiophenes and Its Impact on Organic Electrochemical Transistor Performance. *Chem. Mater.* **2020**, *32* (15), 6618–6628.

(40) Moser, M.; Hidalgo, T. C.; Surgailis, J.; Gladisch, J.; Ghosh, S.; Sheelamanthula, R.; Thiburce, Q.; Giovannitti, A.; Salleo, A.; Gasparini, N.; Wadsworth, A.; Zozoulenko, I.; Berggren, M.; Stavrinidou, E.; Inal, S.; McCulloch, I. Side Chain Redistribution as a Strategy to Boost Organic Electrochemical Transistor Performance and Stability. *Adv. Mater.* **2020**, *32* (37), 2002748.

(41) DiTullio, B. T.; Savagian, L. R.; Bardagot, O.; De Keersmaecker, M.; Österholm, A. M.; Banerji, N.; Reynolds, J. R. Effects of Side-Chain Length and Functionality on Polar Poly(Dioxythiophene)s for Saline-Based Organic Electrochemical Transistors. *J. Am. Chem. Soc.* **2023**, *145* (1), 122–134.

(42) Dong, B. X.; Nowak, C.; Onorato, J. W.; Strzalka, J.; Escobedo, F. A.; Luscombe, C. K.; Nealey, P. F.; Patel, S. N. Influence of Side-Chain Chemistry on Structure and Ionic Conduction Characteristics of Polythiophene Derivatives: A Computational and Experimental Study. *Chem. Mater.* **2019**, *31* (4), 1418–1429.

(43) Alsufyani, M.; Stoeckel, M.; Chen, X.; Thorley, K.; Hallani, R. K.; Puttisong, Y.; Ji, X.; Meli, D.; Paulsen, B. D.; Strzalka, J.; Regeta, K.; Combe, C.; Chen, H.; Tian, J.; Rivnay, J.; Fabiano, S.; McCulloch, I. Lactone Backbone Density in Rigid Electron-Deficient Semiconducting Polymers Enabling High N-type Organic Thermoelectric Performance. *Angew Chem Int Ed* **2022**, *61* (7).

(44) Giovannitti, A.; Maria, I. P.; Hanifi, D.; Donahue, M. J.; Bryant, D.; Barth, K. J.; Makdah, B. E.; Savva, A.; Moia, D.; Zetek, M.; Barnes, P. R. F.; Reid, O. G.; Inal, S.; Rumbles, G.; Malliaras, G. G.; Nelson, J.; Rivnay, J.; McCulloch, I. The Role

of the Side Chain on the Performance of N-Type Conjugated Polymers in Aqueous Electrolytes. *Chem. Mater.* **2018**, *30* (9), 2945–2953.

(45) Schmode, P.; Savva, A.; Kahl, R.; Ohayon, D.; Meichsner, F.; Dolynchuk, O.; Thurn-Albrecht, T.; Inal, S.; Thelakkat, M. The Key Role of Side Chain Linkage in Structure Formation and Mixed Conduction of Ethylene Glycol Substituted Polythiophenes. *ACS Appl. Mater. Interfaces* **2020**, *12* (11), 13029–13039.

(46) Maria, I. P.; Paulsen, B. D.; Savva, A.; Ohayon, D.; Wu, R.; Hallani, R. K.; Basu, A.; Du, W.; Anthopoulos, T. D.; Sahika Inal; Rivnay, J.; McCulloch, I.; Giovannitti, A. The Effect of Alkyl Spacers on the Mixed Ionic-Electronic Conduction Properties of N-Type Polymers. *Adv. Funct. Mater.* **2021**, *31* (14), 2008718–2008718.

(47) Yu, H.; Marks, A.; Tuladhar, S. M.; Siemons, N.; Anderson, I.; Bidinger, S.; Keene, S. T.; Quill, T. J.; Wu, R.; Gough, O.; Wu, G.; Eisner, F.; Salleo, A.; Rivnay, J.; Malliaras, G. G.; Piers; McCulloch, I.; Nelson, J. The Influence of Alkyl Spacers and Molecular Weight on the Charge Transport and Storage Properties of Oxy-Bithiophene-Based Conjugated Polymers. *Angew. Chem. Int. Ed.* **2025,** *64*, e202417897

(48) Tan, E.; Kim, J.; Stewart, K.; Pitsalidis, C.; Kwon, S.; Siemons, N.; Kim, J.; Jiang, Y.; Frost, J. M.; Pearce, D.; Tyrrell, J. E.; Nelson, J.; Owens, R. M.; Kim, Y.; Kim, J. The Role of Long-Alkyl-Group Spacers in Glycolated Copolymers for High-Performance Organic Electrochemical Transistors. *Adv. Mater.* **2022**, *34* (27).

(49) Jones, A. L.; Keersmaecker, M. D.; Savagian, L. R.; DiTullio, B. T.; Pelse, I.; Reynolds, J. R. Branched Oligo(Ether) Side Chains: A Path to Enhanced Processability and Elevated Conductivity for Polymeric Semiconductors. *Adv. Funct. Mater.* **2021**, *31* (35).

(50) Sun, H.; Mikhail Vagin; Wang, S.; Crispin, X.; Forchheimer, R.; Berggren, M.; Fabiano, S. Complementary Logic Circuits Based on High-Performance N-Type Organic Electrochemical Transistors. **2018**, *30* (9), 1704916–1704916.

(51) Sun, H.; Gerasimov, J.; Berggren, M.; Fabiano, S. N-Type Organic Electrochemical Transistors: Materials and Challenges. *J. Mater. Chem. C* **2018**, *6* (44), 11778–11784.

(52) Guo, J.; Flagg, L. Q.; Tran, D. K.; Chen, S. E.; Li, R.; Kolhe, N. B.; Giridharagopal, R.; Jenekhe, S. A.; Richter, L. J.; Ginger, D. S. Hydration of a Side-Chain-Free n-

Type Semiconducting Ladder Polymer Driven by Electrochemical Doping. *J. Am. Chem. Soc.* **2023**, *145* (3), 1866–1876.

(53) Wu, H.; Yang, C.; Li, Q.; Kolhe, N. B.; Strakosas, X.; Stoeckel, M.; Wu, Z.; Jin, W.; Savvakis, M.; Kroon, R.; Tu, D.; Woo, H. Y.; Berggren, M.; Jenekhe, S. A.; Fabiano, S. Influence of Molecular Weight on the Organic Electrochemical Transistor Performance of Ladder-Type Conjugated Polymers. *Adv. Mater.* **2021**, *34* (4), 2106235.

(54) Yang, C.-Y.; Stoeckel, M.-A.; Ruoko, T.-P.; Wu, H.-Y.; Liu, X.; Kolhe, N. B.; Wu, Z.; Puttisong, Y.; Musumeci, C.; Massetti, M.; Sun, H.; Xu, K.; Tu, D.; Chen, W. M.; Woo, H. Y.; Fahlman, M.; Jenekhe, S. A.; Berggren, M.; Fabiano, S. A High-Conductivity N-Type Polymeric Ink for Printed Electronics. *Nat Commun.* **2021**, *12* (1), 2354.

(55) Liu, T.; Heimonen, J.; Zhang, Q.; Yang, C.-Y.; Huang, J.-D.; Wu, H.-Y.; Stoeckel, M.-A.; van der Pol, T. P. A.; Li, Y.; Jeong, S. Y.; Marks, A.; Wang, X.-Y.; Puttisong, Y.; Shimolo, A. Y.; Liu, X.; Zhang, S.; Li, Q.; Massetti, M.; Chen, W. M.; Woo, H. Y.; Pei, J.; McCulloch, I.; Gao, F.; Fahlman, M.; Kroon, R.; Fabiano, S. Ground-State Electron Transfer in All-Polymer Donor:Acceptor Blends Enables Aqueous Processing of Water-Insoluble Conjugated Polymers. *Nat Commun* **2023**, *14* (1), 8454.

(56) He, Q.; Wang, J.; Xu, T.; Tam, T. L. D.; Wang, J.; Liu, N.; Chang, S.; Meng, H.; Xu, J. A Novel Solubilizing Fully π-Conjugated Ladder Polymer and Its Thermoelectric Properties. *ACS Macro Lett.* **2025**, *14* (5), 630–635.

(57) He, Q.; Tam, T. L. D.; Koh, X. Q.; Tham, N. N.; Meng, H.; Huang, W.; Xu, J. P- and N-Dopable Ambipolar Bulk Heterojunction Thermoelectrics Based on Ladder-Type Conjugated Polymers. *J. Mater. Chem. C* **2022**, *11* (1), 204–210.

(58) He, Q.; Zhang, X.; Tam, T. L. D.; Wang, J.; Chen, H.; Chien, S. W.; Tham, N. N.; Koh, X. Q.; Lee, J. J. C.; Lin, M.; Soh, P. X.; Meng, H.; Huang, W.; Xu, J. Balancing Solubility and Thermoelectric Performance in π-Extended Poly(Benzimidazoanthradiisoquinolinedione) Ladder-Type Conjugated Polymer. *ACS Appl. Electron. Mater.* **2024**, *6* (5), 2999–3005.

(59) He, Q.; Dexter Tam, T. L.; Lin, T.; Chien, S. W.; Lin, M.; Meng, H.; Huang, W.; Xu, J. π-Extended Poly(Benzimidazoanthradiisoquinolinedione) Ladder-Type Conjugated Polymer. *ACS Macro Lett.* **2022**, *11* (9), 1136–1141.

(60) Tam, D.; Lin, M.; Chien, S. W.; Xu, J. Facile Synthesis of Solubilizing a Group-Free, Solution-Processable *P*-Type Ladder Conjugated Polymer and Its Thermoelectric Properties. *ACS Macro Lett.* **2021**, *11* (1), 110–115

(61) Wu, X.; Tam, D.; Chen, S.; Salim, T.; Zhao, X.; Zhou, Z.; Lin, M.; Xu, J.; Loo, Y.-L.; Wei Lin Leong. All-Polymer Bulk-Heterojunction Organic Electrochemical Transistors with Balanced Ionic and Electronic Transport. *Adv. Mater.* **2022**, *34* (42).

(62) Wu, X.; He, Q.; Zhou, Z.; Tam, D.; Tang, C.; Lin, M.; Moser, M.; Griggs, S.; Marks, A.; Chen, S.; Xu, J.; McCulloch, I.; Leong, W. L. Stable *N*-Type Perylene Derivative Ladder Polymer with Antiambipolarity for Electrically Reconfigurable Organic Logic Gates. *Adv. Mater.* **2024**, *36* (31).

(63) Izuhara, D.; Swager, T. M. Poly(Pyridinium Phenylene)s: Water-Soluble N-Type Polymers. *J. Am. Chem. Soc.* **2009**, *131* (49), 17724–17725.

(64) Huang, Z.; Li, P.; Lei, Y.; Deng, X.; Chen, Y.; Tian, S.; Pan, X.; Lei, X.; Song, C.; Zheng, Y.; Wang, J.; Zhang, Z.; Lei, T. Azonia-Naphthalene: A Cationic Hydrophilic Building Block for Stable N-Type Organic Mixed Ionic-Electronic Conductors**. *Angew. Chem. Int. Ed.* **2023**, *63* (6).

(65) Stegerer, D.; Liu, T.; Xiong, M.; Wu, H.-Y.; Kang, M. G.; Woo, H. Y.; Fabiano, S.; Sommer, M. Molar Mass Improves the Performance of N-Type Organic Electrochemical Transistors. *Chem. Mater.* **2025**, *37* (14), 5226–5233.

(66) Li, P.; Sun, W.; Li, J.; Chen, J.-P.; Wang, X.; Mei, Z.; Jin, G.; Lei, Y.; Xin, R.; Yang, M.; Xu, J.; Pan, X.; Song, C.; Deng, X.-Y.; Lei, X.; Liu, K.; Wang, X.; Zheng, Y.; Zhu, J.; Shixian Lv. N-Type Semiconducting Hydrogel. *Science* **2024**, *384* (6695), 557–563.

(67) Li, J.-L.; Deng, X.-Y.; Chen, J.; Fu, P.-X.; Tian, S.-Y.; Wang, Y.; Gu, X.; Lei, T. Cationic Conjugated Polymers with Enhanced Doped-State Planarity for *N* -Type Organic Thermoelectrics. *CCS Chemistry* **2025**, *7* (5), 1449–1458.

(68) Sirringhaus, H. 25th Anniversary Article: Organic Field-Effect Transistors: The Path beyond Amorphous Silicon. *Adv. Mater.* **2014**, *26* (9), 1319–1335.

(69) McCulloch, I.; Heeney, M.; ML Chabinyc; DeLongchamp, D.; Kline, R.; M Coelle; Duffy, W.; Fischer, D.; Gundlach, D.; Hamadani, B.; Hamilton, R.; Richter, L.; A Salleo; M Shkunov; D Sporrowe; Tierney, S.; Zhong, W. Semiconducting Thienothiophene Copolymers: Design, Synthesis, Morphology, and Performance in Thin-Film Organic Transistors. *Adv. Mater.* **2009**, *21* (10-11), 1091–1109.

(70) Hopkins, J.; Ta, D.; Lauto, A.; Baker, C.; Daniels, J.; Wagner, P.; Wagner, K. K.; Kirby, N.; Cazorla, C.; Officer, D. L.; Damia Mawad. Impact of Side Chain Extension on the Morphology and Electrochemistry of Phosphonated Poly(Ethylenedioxythiophene) Derivatives. *Adv. Mater. Technologies* **2023**, *8* (19).

(71) Bates, C. M.; Bates, F. S. *50th Anniversary Perspective* : Block Polymers—Pure Potential. *Macromolecules* **2017**, *50* (1), 3–22.

(72) BATES, F. S. Polymer-Polymer Phase Behavior. *Science* **1991**, *251* (4996), 898–905.

(73) Bates, F. S.; Fredrickson, G. H. Block Copolymer Thermodynamics: Theory and Experiment. *Annu. Rev. Phys. Chem.* **1990**, *41* (1), 525–557.

(74) Mai, Y.; Eisenberg, A. Self-Assembly of Block Copolymers. *Chem. Soc. Rev.* **2012**, *41* (18), 5969–5985.

(75) Leibler, L. Theory of Microphase Separation in Block Copolymers. *Macromolecules* **1980**, *13* (6), 1602–1617.

(76) Nisticò, R. Block Copolymers for Designing Nanostructured Porous Coatings. *Beilstein J. Nanotechnol.* **2018**, *9* (1), 2332–2344.

(77) Lynd, N. A.; Hillmyer, M. A. Influence of Polydispersity on the Self-Assembly of Diblock Copolymers. *Macromolecules* **2005**, *38* (21), 8803–8810.

(78) Lynd, N. A.; Meuler, A. J.; Hillmyer, M. A. Polydispersity and Block Copolymer Self-Assembly. *Prog. Polym. Sci.* **2008**, *33* (9), 875–893.

(79) Bang, J.; Jeong, U.; Ryu, D. Y.; Russell, T. P.; Hawker, C. J. Block Copolymer Nanolithography: Translation of Molecular Level Control to Nanoscale Patterns. *Adv. Mater.* **2009**, *21* (47), 4769–4792.

(80) Xu, T.; Kim, H.-C.; DeRouchey, J.; Seney, C.; Levesque, C.; Martin, P.; Stafford, C. M.; Russell, T. P. The Influence of Molecular Weight on Nanoporous Polymer Films. *Polymer* **2001**, *42* (21), 9091–9095.

(81) Jeong, U.; Kim, H.-C.; Rodriguez, R. L.; Tsai, I. Y.; Stafford, C. M.; Kim, J. K.; Hawker, C. J.; Russell, T. P. Asymmetric Block Copolymers with Homopolymers: Routes to Multiple Length Scale Nanostructures. *Adv. Mater.* **2002**, *14*, No. 4, February 19

(82) Jeong, U.; Ryu, D. Y.; Kim, J. K.; Kim, D. H.; Wu, X.; Russell, T. P. Precise Control of Nanopore Size in Thin Film Using Mixtures of Asymmetric Block Copolymer and Homopolymer. *Macromolecules* **2003**, *36* (26), 10126–10129.

(83) Huang, W.-C.; Shastry, T.; Chen, P.-C.; A p, A.; Liu, K.-P.; Ho, R.-M. Controlled Orientation of Polystyrene-*b*-Poly(L-Lactide) Nanostructured Thin Films by Air Plasma Treatment *via* Thermal Annealing. *Giant* **2025**, *25*, 100367. https://doi.org/10.1016/j.giant.2025.100367.

(84) Yang, K.-C.; Yao, C.-T.; Huang, L.-Y.; Tsai, J.-C.; Hung, W.-S.; Hsueh, H.-Y.; Ho, R.-M. Single Gyroid-Structured Metallic Nanoporous Spheres Fabricated from Double Gyroid-Forming Block Copolymers via Templated Electroless Plating. *NPG Asia Mater.* **2019**, *11* (1).

(85) Tsai, H.-W.; Shao, S.-W.; Chiu, P.-T.; Chang, C.-Y.; Sung, Y.-C.; Li, G.-H.; Chen, Y.-C.; Kumagai, A.; Jinnai, H.; Hung, Y.-C.; Tsai, J.-C.; Ho, R.-M. Helically Deployed Au Nanoparticles Using Block Copolymer Templates as Chiral Plasmonic Monoliths. *Giant* **2025**, *21*, 100350.

(86) Zschech, D.; Kim, D. H.; Milenin, A. P.; Scholz, R.; Hillebrand, R.; Hawker, C. J.; Russell, T. P.; Steinhart, M.; Ulrich Gösele. Ordered Arrays of 〈100〉-Oriented Silicon Nanorods by CMOS-Compatible Block Copolymer Lithography. *Nano Lett.* **2007**, *7* (6), 1516–1520.

(87) Guarini, K.W., Black, C.T. and Yeung, S.H.I. (2002), Optimization of Diblock Copolymer Thin Film Self Assembly. *Adv. Mater,* 14: 1290-1294.

(88) Peña, S. I.; Borbolla-Jiménez, F. V.; Duarte-Peña, L.; Moreno, A.; Pérez-Caltzontzin, L. E.; Del, L.; Romero-Montero, A.; Maykel González-Torres; Hernán Cortés; Hernández-Parra, H.; Javad Sharifi-Rad; Leyva-Gómez, G. Repurposing Poloxamers as Antimicrobial Agents: A Comprehensive Review of Mechanisms and Applications. *Drug Development Research* **2025**, *86* (5)

(89) Lin, Q.; Owh, C.; Lim, J. Y. C.; Chee, P. L.; Yew, M. P. Y.; Hor, E. T. Y.; Loh, X. J. The Thermogel Chronicle─from Rational Design of Thermogelling Copolymers to Adv. Thermogel Applications. *Acc. Mater. Res.* **2021**, *2* (10), 881–894.

(90) Bertsch, P.; Diba, M.; Mooney, D. J.; Leeuwenburgh, S. C. G. Self-Healing Injectable Hydrogels for Tissue Regeneration. *Chem. Rev.* **2022**, *123* (2).

(91) Russo, E.; Villa, C. Poloxamer Hydrogels for Biomedical Applications. *Pharmaceutics* **2019**, *11* (12), 671.

(92) Loewe, R. S.; Ewbank, P. C.; Liu, J.; Zhai, L.; McCullough, R. D. Regioregular, Head-to-Tail Coupled Poly(3-Alkylthiophenes) Made Easy by the GRIM

Method: Investigation of the Reaction and the Origin of Regioselectivity. *Macromolecules* **2001**, *34* (13), 4324–4333.

(93) He, M.; Qiu, F.; Lin, Z. Conjugated Rod–Coil and Rod–Rod Block Copolymers for Photovoltaic Applications. *J. Mater. Chem.* **2011**, *21* (43), 17039–17048.

(94) Yang, C.; Lee, J. K.; Heeger, A. J.; Wudl, F. Well-Defined Donor–Acceptor Rod–Coil Diblock Copolymers Based on P3HT Containing C60: The Morphology and Role as a Surfactant in Bulk-Heterojunction Solar Cells. *J. Mater. Chem.* **2009**, *19* (30), 5416–5423.

(95) Lee, J. U.; Jung, J. W.; Emrick, T.; Russell, T. P.; Jo, W. H. Morphology Control of a Polythiophene–Fullerene Bulk Heterojunction for Enhancement of the High-Temperature Stability of Solar Cell Performance by a New Donor–Acceptor Diblock Copolymer. *Nanotechnology* **2010**, *21* (10), 105201.

(96) Yu, X.; Xiao, K.; Chen, J.; Lavrik, N. V.; Hong, K.; Sumpter, B. G.; Geohegan, D. B. High-Performance Field-Effect Transistors Based on Polystyrene-*B*-Poly(3-Hexylthiophene) Diblock Copolymers. *ACS Nano* **2011**, *5* (5), 3559–3567.

(97) Taniya M. S. K. Pathiranage; Ma, Z.; Chinthaka M. Udamulle Gedara; Pan, X.; Lee, Y.; Gomez, E. D.; Biewer, M. C.; Krzysztof Matyjaszewski; Stefan, M. C. Improved Self-Assembly of P3HT with Pyrene-Functionalized Methacrylates. *ACS Omega* **2021**, *6* (41), 27325–27334.

(98) Chiang, Y.-C.; Kobayashi, S.; Isono, T.; Shih, C.-C.; Shingu, T.; Hung, C.-C.; Hsieh, H.-C.; Tung, S.-H.; Satoh, T.; Chen, W.-C. Effect of a Conjugated/Elastic Block Sequence on the Morphology and Electronic Properties of Polythiophene Based Stretchable Block Copolymers. *Polym. Chem.* **2019**, *10* (40), 5452–5464.

(99) Wu, W.-N.; Tu, T.-H.; Pai, C.-H.; Cheng, K.-H.; Tung, S.-H.; Chan, Y.-T.; Liu, C.-L. Metallo-Supramolecular Rod–Coil Block Copolymer Thin Films for Stretchable Organic Field Effect Transistor Application. *Macromolecules* **2022**, *55* (23), 10670–10681.

(100) Hsu, L.-C.; Kobayashi, S.; Isono, T.; Chiang, Y.-C.; Ree, B. J.; Toshifumi Satoh; Chen, W.-C. Highly Stretchable Semiconducting Polymers for Field-Effect Transistors through Branched Soft–Hard–Soft Type Triblock Copolymers. *Macromolecules* **2020**, *53* (17), 7496–7510.

(101) Kang, S.; Kim, G.-H.; Park, S.-J. Conjugated Block Copolymers for Functional Nanostructures. *Acc. Chem. Res.* **2022**, *55* (16), 2224–2234.

(102) Kamps, A. C.; Cativo, Ma. H. M.; Fryd, M.; Park, S.-J. Self-Assembly of Amphiphilic Conjugated Diblock Copolymers into One-Dimensional Nanoribbons. *Macromolecules* **2014**, *47* (1), 161–164.

(103) Jin, X.-H.; Price, M.; Finnegan, J. R.; Boott, C. E.; Richter, J.; Rao, A.; S. Matthew Menke; Friend, R. H.; Whittell, G. R.; Manners, I. Long-Range Exciton Transport in Conjugated Polymer Nanofibers Prepared by Seeded Growth. *Science* **2018**, *360* (6391), 897–900.

(104) Patra, S. K.; Ahmed, R.; Whittell, G. R.; Lunn, D. J.; Dunphy, E. L.; Winnik, M. A.; Manners, I. Cylindrical Micelles of Controlled Length with a π-Conjugated Polythiophene Core via Crystallization-Driven Self-Assembly. *J. Am. Chem. Soc.* **2011**, *133* (23), 8842–8845.

(105) Cai, J.; Chua, X. W.; Li, C.; Grüne, J.; Ghosh, P.; Ding, Y.; MacKenzie, H. K.; Qiu, H.; Greenham, N. C.; Rao, A.; Manners, I. Uniform Conjugated Polymer Rectangular Platelets Exhibiting Long-Range Exciton Diffusion. *Nat. Mater.* **2025**, 1–8.

(106) Han, L.; Wang, M.; Jia, X.; Chen, W.; Qian, H.; He, F. Uniform Two-Dimensional Square Assemblies from Conjugated Block Copolymers Driven by π–π Interactions with Controllable Sizes. *Nat Commun* **2018**, *9* (1), 865.

(107) Yang, S.; Kang, S.-Y.; Choi, T.-L. Semi-Conducting 2D Rectangles with Tunable Length via Uniaxial Living Crystallization-Driven Self-Assembly of Homopolymer. *Nat Commun* **2021**, *12* (1), 2602.

(108) Sahika Inal; Rivnay, J.; Leleux, P.; Ferro, M.; Ramuz, M.; Brendel, J. C.; Schmidt, M. M.; Mukundan Thelakkat; Malliaras, G. G. A High Transconductance Accumulation Mode Electrochemical Transistor. *Adv. Mater.* **2014**, *26* (44), 7450–7455.

(109) Giovannitti, A.; Sbircea, D.-T.; Inal, S.; Nielsen, C. B.; Bandiello, E.; Hanifi, D. A.; Sessolo, M.; Malliaras, G. G.; McCulloch, I.; Rivnay, J. Controlling the Mode of Operation of Organic Transistors through Side-Chain Engineering. *Proc. Natl. Acad. Sci. U.S.A.* **2016**, *113* (43), 12017–12022.

(110) Kawan, M.; Hidalgo, T. C.; Du, W.; Pappa, A.-M.; Owens, R. M.; McCulloch, I.; Inal, S. Monitoring Supported Lipid Bilayers with N-Type Organic Electrochemical Transistors. *Mater. Horiz.* **2020**, *7* (9), 2348–2358.

(111) Gerasimov, J. Y.; Gabrielsson, R.; Forchheimer, R.; Stavrinidou, E.; Simon, D. T.; Berggren, M.; Fabiano, S. An Evolvable Organic Electrochemical Transistor for Neuromorphic Applications. *Adv. Sci.* **2019**, *6* (7), 1801339.

(112) Ding, B.; Jo, I.-Y.; Yu, H.; Kim, J. H.; Marsh, A. V.; Gutiérrez-Fernández, E.; Ramos, N.; Rapley, C. L.; Rimmele, M.; He, Q.; Martín, J.; Gasparini, N.; Nelson, J.; Yoon, M.-H.; Heeney, M. Enhanced Organic Electrochemical Transistor Performance of Donor–Acceptor Conjugated Polymers Modified with Hybrid Glycol/Ionic Side Chains by Postpolymerization Modification. *Chem. Mater.* **2023**, *35* (8), 3290–3299.

(113) Nicolini, T.; Jokubas Surgailis; Savva, A.; Scaccabarozzi, A. D.; Nakar, R.; Thuau, D.; Wantz, G.; Richter, L. J.; Dautel, O.; Georges Hadziioannou; Stingelin, N. A Low-Swelling Polymeric Mixed Conductor Operating in Aqueous Electrolytes. *Adv. Mater.* **2020**, *33* (2).

(114) Hungenberg, J.; Hochgesang, A.; Florian Meichsner; Mukundan Thelakkat. Self-Doped Mixed Ionic-Electronic Conductors to Tune the Threshold Voltage and the Mode of Operation in Organic Electrochemical Transistors. *Adv. Funct. Mater.* **2024**, *34* (44).

(115) Cobet, C.; Gasiorowski, J.; Farka, D.; Stadler, P. Polarons in Conjugated Polymers. *Springer Series in Surface Sciences* **2018**, 355–387.

(116) Griggs, S.; Marks, A.; Bristow, H.; McCulloch, I. N-Type Organic Semiconducting Polymers: Stability Limitations, Design Considerations and Applications. *J. Mater. Chem. C* **2021**, *9* (26), 8099–8128.

(117) Meisel, S. L.; Johnson, G. C.; Hartough, H. D. Polymerization of Thiophene and Alkylthiophenes. *J. Am. Chem. Soc.* **1950**, *72* (5), 1910–1912.

(118) Curtis, R. F.; Jones, D. M.; Thomas, W. A. The 'Trimer' and 'Pentamer' from the Polymerisation of Thiophen by Polyphosphoric Acid. *J. Chem. Soc. C* **1971**, No. 0, 234–238.

(119) Yamamoto, T.; Sanechika, K.; Yamamoto, A. Preparation of Thermostable and Electric-Conducting Poly(2,5-Thienylene). *J. Polym. Sci., Polym. Lett. Ed.* **1980**, *18* (1), 9–12.

(120) John; Dudek, L. P. Synthesis and Properties of Poly(2,5-Thienylene). *J. Polym. Sci.* **1980**, *18* (9), 2869–2873.

(121) Hajlaoui, R.; Fichou, D.; Horowitz, G.; Nessakh, B.; Constant, M.; Garnier, F. Organic Transistors Using A-octithiophene and α, Ω-dihexyl-α-octithiophene:

Influence of Oligomer Length versus Molecular Ordering on Mobility. *Adv. Mater.* **2004**, 9 557-561.

(122) Hajlaoui, R.; Horowitz, G.; Garnier, F.; Arce-Brouchet, A.; Laigre, L.; Kassmi, A. E.; Demanze, F.; Kouki, F. Improved Field-effect Mobility in Short Oligothiophenes: Quaterthiophene and Quinquethiophene. *Adv. Mater.* **2004**, 9 389-391.

(123) Dodabalapur, A.; Torsi, L.; Katz, H. E. Organic Transistors: Two-Dimensional Transport and Improved Electrical Characteristics. *Science* **1995**, *268* (5208), 270–271. https://doi.org/10.1126/science.268.5208.270.

(124) Riadh Hajlaoui; Fichou, D.; Horowitz, G.; Belkacem Nessakh; Constant, M.; Garnier, F. Organic Transistors Using α-Octithiophene and α, ω-Dihexyl-α-Octithiophene: Influence of Oligomer Length versus Molecular Ordering on Mobility. *Adv. Mater.* **1997**, *9* (7), 557–561.

(125) Fichou, D.; Marie-Paule te Ulade-Fichou; Horowitz, G.; Frédéric Demanze. Thermal and Optical Characterization of High Purity α-Octithiophenk. *Adv. Mater.* **1997**, *9* (1), 75–80.

(126) Katz, H. E.; Torsi, L.; Dodabalapur, A. Synthesis, Material Properties, and Transistor Performance of Highly Pure Thiophene Oligomers. *Chem. Mater.* **1995**, *7* (12), 2235–2237.

(127) Katz, H. E.; Bao, Z.; Gilat, S. L. Synthetic Chemistry for Ultrapure, Processable, and High-Mobility Organic Transistor Semiconductors. *Acc. Chem. Res.* **2001**, *34* (5), 359–369.

(128) Facchetti, A.; Mushrush, M.; Yoon, M.-H.; Hutchison, G. R.; Ratner, M. A.; Marks, T. J. Building Blocks for N-Type Molecular and Polymeric Electronics. Perfluoroalkyl- versus Alkyl-Functionalized Oligothiophenes (NT; $N = 2-6$). Systematics of Thin Film Microstructure, Semiconductor Performance, and Modeling of Majority Charge Injection in Field-Effect Transistors. *J. Am. Chem. Soc.* **2004**, *126* (42), 13859–13874.

(129) Ponomarenko, S.; Kirchmeyer, S. Synthesis and Thermal Behaviour of α,A′-Didecyloligothiophenes. *J. Mater. Chem.* **2003**, *13* (2), 197–202.

(130) Lin, P.; Yan, F. Organic Thin-Film Transistors for Chemical and Biological Sensing. *Adv. Mater.* **2012**, *24* (1), 34–51.

(131) Kilbinger, A. F. M.; Feast, W. J. Solution Processable Alternating Oligothiophene-PEO-Block-Co-Polymers: Synthesis and Evidence for Solvent Dependent Aggregation. *J. Mater. Chem.* **2000**, *10* (8), 1777–1784.

(132) Sandberg, H.; Henze, O.; Kilbinger, A. F. M.; Sirringhaus, H.; James Feast, W.; Friend, R. H. Oligoethyleneoxide Functionalised Sexithiophene Organic Field Effect Transistors. *Synth. Met.* **2003**, *137* (1), 885–886.

(133) Parr, Z. S.; Rashid, R. B.; Paulsen, B. D.; Poggi, B.; Tan, E.; Freeley, M.; Palma, M.; Abrahams, I.; Rivnay, J.; Nielsen, C. Semiconducting Small Molecules as Active Materials for P-Type Accumulation Mode Organic Electrochemical Transistors. *Adv. Electron. Mater.* **2020**, 6, 2000215

(134) McCullough, R. D.; Lowe, R. D. Enhanced Electrical Conductivity in Regioselectively Synthesized Poly(3-Alkylthiophenes). *J. Chem. Soc., Chem. Commun.* **1992**, No. 1, 70–72.

(135) Chen, T. A.; Rieke, R. D. The First Regioregular Head-to-Tail Poly(3-Hexylthiophene-2,5-Diyl) and a Regiorandom Isopolymer: Nickel versus Palladium Catalysis of 2(5)-Bromo-5(2)-(Bromozincio)-3-Hexylthiophene Polymerization. *J. Am. Chem. Soc.* **1992**, *114* (25), 10087–10088.

(136) Sirringhaus, H.; Brown, P. J.; Friend, R. H.; Nielsen, M. M.; Bechgaard, K.; Langeveld-Voss, B. M. W.; Spiering, A. J. H.; Janssen, R. a. J.; Meijer, E. W.; Herwig, P.; de Leeuw, D. M. Two-Dimensional Charge Transport in Self-Organized, High-Mobility Conjugated Polymers. *Nature* **1999**, *401* (6754), 685–688.

(137) Bao, Z.; Dodabalapur, A.; Lovinger, A. J. Soluble and Processable Regioregular Poly(3-Hexylthiophene) for Thin Film Field-Effect Transistor Applications with High Mobility. *Appl. Phys. Lett.* **1996**, *69* (26), 4108–4110.

(138) R Sugimoto, S Takeda, HB Gu, K Yoshino - *Chem. Express*, 1986.

(139) McCullough, R. D. The Chemistry of Conducting Polythiophenes. *Adv. Mater.* **1998**, *10* (2), 93–116.

(140) Liu, Y.; Nishiwaki, N.; Saigo, K.; Sugimoto, R. Polymerization of 3-Hexylthiophene with FeCl3 in Aromatic Solvents. *Polym. Bull.* **2015**, *72* (7), 1817–1826.

(141) Yaghoobi Nia, N.; Bonomo, M.; Zendehdel, M.; Lamanna, E.; Desoky, M. M. H.; Paci, B.; Zurlo, F.; Generosi, A.; Barolo, C.; Viscardi, G.; Quagliotto, P.; Di Carlo, A. Impact of P3HT Regioregularity and Molecular Weight on the Efficiency

and Stability of Perovskite Solar Cells. *ACS Sustainable Chem. Eng.* **2021**, *9* (14), 5061–5073.

(142) Sivaraman, P.; Mishra, S. P.; Bhattacharrya, A. R.; Thakur, A.; Shashidhara, K.; Samui, A. B. Effect of Regioregularity on Specific Capacitance of Poly(3-Hexylthiophene). *Electrochim. Acta.* **2012**, *69*, 134–138.

(143) Stein, P. C.; Botta, C.; Bolognesi, A.; Catellani, M. NMR Study of the Structural Defects in Poly(3-Alkylthiophene)s: Influence of the Polymerization Method. *Synth. Met.* **1995**, *69* (1), 305–306.

(144) Nawaz, A.; Kumar, A.; Hümmelgen, I. A. Ultra-High Mobility in Defect-Free Poly(3-Hexylthiophene-2,5-Diyl) Field-Effect Transistors through Supra-Molecular Alignment. *Org. Electron.* **2017**, *51*, 94–102.

(145) Noriega, R.; Rivnay, J.; Vandewal, K.; Koch, F. P. V.; Stingelin, N.; Smith, P.; Toney, M. F.; Salleo, A. A General Relationship between Disorder, Aggregation and Charge Transport in Conjugated Polymers. *Nat Mater* **2013**, *12* (11), 1038–1044.

(146) Nawaz, A.; Koehler, M.; Kumar, A.; Merces, L.; Abreu, A. B. R.; Bufon, C. C. B.; Serbena, J. P. M.; Hummelgen, I. A. Improvement of Poly(3-Hexylthiophene-2,5-Diyl) Electron Mobility through Complete Elimination of Regioregularity Defects. ChemRxiv October 8, 2021.

(147) Barbosa, N. M.; Marcia; Araujo, P. T.; Sampaio, R. N. Photoinduced Self-Assembled Nanostructures and Permanent Polaron Formation in Regioregular Poly(3-Hexylthiophene). *Adv. Mater.* **2018**, *30* (16).

(148) Ansari, M. A.; Mohiuddin, S.; Kandemirli, F.; Malik, M. I. Synthesis and Characterization of Poly(3-Hexylthiophene): Improvement of Regioregularity and Energy Band Gap. *RSC Adv.* **2018**, *8* (15), 8319–8328.

(149) Miyakoshi, R.; Yokoyama, A.; Yokozawa, T. Catalyst-Transfer Polycondensation. Mechanism of Ni-Catalyzed Chain-Growth Polymerization Leading to Well-Defined Poly(3-Hexylthiophene). *J. Am. Chem. Soc.* **2005**, *127* (49), 17542–17547.

(150) Leone, A. K.; Goldberg, P. K.; McNeil, A. J. Ring-Walking in Catalyst-Transfer Polymerization. *J. Am. Chem. Soc.* **2018**, *140* (25), 7846–7850.

(151) He, W.; Patrick, B. O.; Kennepohl, P. Identifying the Missing Link in Catalyst Transfer Polymerization. *Nat Commun* **2018**, *9* (1), 3866.

(152) Jeffries-El, M.; Sauvé, G.; McCullough, R. D. Facile Synthesis of End-Functionalized Regioregular Poly(3-Alkylthiophene)s via Modified Grignard Metathesis Reaction. *Macromolecules* **2005**, *38* (25), 10346–10352.

(153) Boudouris, B. W.; Frisbie, C. D.; Hillmyer, M. A. Polylactide−Polythiophene−Polylactide Triblock Copolymers. *Macromolecules* **2010**, *43* (7), 3566–3569.

(154) Boudouris, B. W.; Frisbie, C. D.; Hillmyer, M. A. Nanoporous Poly(3-Alkylthiophene) Thin Films Generated from Block Copolymer Templates. *Macromolecules* **2007**, *41* (1), 67–75.

(155) Lohwasser, R. H.; Thelakkat, M. Synthesis of Amphiphilic Rod–Coil P3HT-b-P4VP Carrying a Long Conjugated Block Using NMRP and Click Chemistry. *Macromolecules* **2012**, *45* (7), 3070–3077.

(156) Iovu, M. C.; Zhang, R.; Cooper, J. R.; Smilgies, D. M.; Javier, A. E.; Sheina, E. E.; Kowalewski, T.; McCullough, R. D. Conducting Block Copolymers of Regioregular Poly(3-Hexylthiophene) and Poly(Methacrylates): Electronic Materials with Variable Conductivities and Degrees of Interfibrillar Order. *Macromol. Rapid Commun.* **2007**, *28* (17), 1816–1824.

(157) Kim, H.; Lee, Y. J.; Hwang, S. S.; Choi, D. H.; Yang, H.; Baek, K. Synthesis of Multiarmed Poly(3-Hexyl Thiophene) Star Polymer with Microgel Core by GRIM and ATRP Methods. *J. Polym. Sci. A Polym. Chem.* **2011**, *49* (19), 4221–4226.

(158) Rajaram, S.; Armstrong, P. B.; Kim, B. J.; Fréchet, J. M. J. Effect of Addition of a Diblock Copolymer on Blend Morphology and Performance of Poly(3-Hexylthiophene):Perylene Diimide Solar Cells. *Chem. Mater.* **2009**, *21* (9), 1775–1777.

(159) Reichstein, P. M.; Gödrich, S.; Georg Papastavrou; Mukundan Thelakkat. Influence of Composition of Amphiphilic Double-Crystalline P3HT-*B*-PEG Block Copolymers on Structure Formation in Aqueous Solution. *Macromolecules* **2016**, *49* (15), 5484–5493.

(160) Han, J.; Kim, J.-S.; Shin, J. M.; Yun, H.; Kim, Y.; Park, H.; Kim, B. J. Rapid Solvo-Microwave Annealing for Optimizing Ordered Nanostructures and Crystallization of Regioregular Polythiophene-Based Block Copolymers. *Polym. Chem.* **2019**, *10* (36), 4962–4972.

(161) Pessoni, L.; De Winter, J.; Surin, M.; Hergué, N.; Delbosc, N.; Lazzaroni, R.; Dubois, P.; Gerbaux, P.; Coulembier, O. Synthesis of Polyphthalaldehyde-Based

Block Copolymers: Utilization of a Thermo-Sacrificial Segment for an Easy Access to Fine-Tuned Poly(3-Hexylthiophene) Nanostructured Films. *Macromolecules* **2016**, *49* (8), 3001–3008.

(162) Zhang, G.; Ohta, Y.; Tsutomu Yokozawa. Exclusive Synthesis of Poly(3-Hexylthiophene) with an Ethynyl Group at Only One End for Effective Block Copolymerization. *Macromol. Rapid Commun.* **2017**, *39* (3).

(163) Liu, J.; Loewe, R. S.; McCullough, R. D. Employing MALDI-MS on Poly(Alkylthiophenes): Analysis of Molecular Weights, Molecular Weight Distributions, End-Group Structures, and End-Group Modifications. *Macromolecules* **1999**, *32* (18), 5777–5785.

(164) Shi, C.; Yao, Y.; Yang, Y.; Pei, Q. Regioregular Copolymers of 3-Alkoxythiophene and Their Photovoltaic Application. *J. Am. Chem. Soc.* **2006**, *128* (27), 8980–8986.

(165) Koeckelberghs, G.; Marnix Vangheluwe; Samyn, C.; A. Persoons; Thierry Verbiest. Regioregular Poly(3-Alkoxythiophene)S: Toward Soluble, Chiral Conjugated Polymers with a Stable Oxidized State. *Macromolecules* **2005**, *38* (13), 5554–5559.

(166) Ma, T.; Dong, B. X.; Onorato, J. W.; Niklas, J.; Poluektov, O.; Luscombe, C. K.; Patel, S. N. Correlating Conductivity and Seebeck Coefficient to Doping within Crystalline and Amorphous Domains in Poly(3-(Methoxyethoxyethoxy)Thiophene). *J. Polym. Sci.* **2021**, *59* (22), 2797–2808.

(167) Zhao, X.; Alsufyani, M.; Tian, J.; Lin, Y.; Jeong, S. Y.; Woo, H. Y.; Yin, Y.; McCulloch, I. High Efficiency N-Type Doping of Organic Semiconductors by Cation Exchange. *Adv. Mater.* **2024**, *36* (47).

(168) Paterson, A. F.; Savva, A.; Wustoni, S.; Tsetseris, L.; Paulsen, B. D.; Faber, H.; Emwas, A. H.; Chen, X.; Nikiforidis, G.; Hidalgo, T. C.; Moser, M.; Maria, I. P.; Rivnay, J.; McCulloch, I.; Anthopoulos, T. D.; Inal, S. Water Stable Molecular N-Doping Produces Organic Electrochemical Transistors with High Transconductance and Record Stability. *Nat Commun* **2020**, *11* (1), 3004.

(169) Tokita, Y.; Uchida, T.; Kamigawara, T.; Hoka, K.; Nitto, R.; Ohta, Y.; Yokozawa, T. Tandem Kumada–Tamao Catalyst-Transfer Condensation Polymerization and Suzuki–Miyaura Coupling for the Synthesis of End-Functionalized Poly(3-Hexylthiophene). *Chem. Commun.* **2023**, *59* (88), 13139–13142.

(170) Holliday, S.; Ashraf, R. S.; Wadsworth, A.; Baran, D.; Yousaf, S. A.; Nielsen, C. B.; Tan, C.-H.; Dimitrov, S. D.; Shang, Z.; Gasparini, N.; Alamoudi, M.; Laquai, F.; Brabec, C. J.; Salleo, A.; Durrant, J. R.; McCulloch, I. High-Efficiency and Air-Stable P3HT-Based Polymer Solar Cells with a New Non-Fullerene Acceptor. *Nat Commun.* **2016**, *7* (1).

(171) Duan, T.; Tang, H.; Liang, R.-Z.; Lv, J.; Kan, Z.; Singh, R.; Kumar, M.; Xiao, Z.; Lu, S.; Laquai, F. Terminal Group Engineering for Small-Molecule Donors Boosts the Performance of Nonfullerene Organic Solar Cells. *J. Mater. Chem. A* **2019**, *7* (6), 2541–2546.

(172) Liu, J.; McCullough, R. D. End Group Modification of Regioregular Polythiophene through Postpolymerization Functionalization. *Macromolecules* **2002**, *35* (27), 9882–9889.

(173) Delbosc, N.; De Winter, J.; Moins, S.; Persoons, A.; Dubois, P.; Coulembier, O. Macrocyclic P3HT Obtained by Intramolecular McMurry Coupling of Linear Bis-Aldehyde Polymer: A Direct Comparison with Linear Homologue. *Macromolecules* **2017**, *50* (5), 1939–1949.

(174) Ku, S.-Y.; Brady, M. A.; Treat, N. D.; Cochran, J. E.; Robb, M. J.; Kramer, E. J.; Chabinyc, M. L.; Hawker, C. J. A Modular Strategy for Fully Conjugated Donor–Acceptor Block Copolymers. *J. Am. Chem. Soc.* **2012**, *134* (38), 16040–16046.

(175) Verduzco, R.; Botiz, I.; Pickel, D. L.; Kilbey, S. M. I.; Hong, K.; Dimasi, E.; Darling, S. B. Polythiophene-Block-Polyfluorene and Polythiophene-Block-Poly(Fluorene-Co-Benzothiadiazole): Insights into the Self-Assembly of All-Conjugated Block Copolymers. *Macromolecules* **2011**, *44* (3), 530–539.

(176) Lin, Y.-H.; Smith, K. A.; Kempf, C. N.; Verduzco, R. Synthesis and Crystallinity of All-Conjugated Poly(3-Hexylthiophene) Block Copolymers. *Polym. Chem.* **2012**, *4* (2), 229–232.

(177) Baskaran, M.; Hashim, R.; Sulaiman, O.; Awalludin, M. F.; Sudesh, K.; Arai, T.; Kosugi, A. Properties of Particleboard Manufactured from Oil Palm Trunk Waste Using Polylactic Acid as a Natural Binder. *Waste Biomass Valor* **2019**, *10* (1), 179–186.

(178) Vrandečić, N. S.; Erceg, M.; Jakić, M.; Klarić, I. Kinetic Analysis of Thermal Degradation of Poly(Ethylene Glycol) and Poly(Ethylene Oxide)s of Different Molecular Weight. *Thermochimica Acta* **2010**, *498* (1), 71–80.

(179) Xu, Z.; Li, W. Control the Self-Assembly of Block Copolymers by Tailoring the Packing Frustration. *Chin. J. Chem.* **2022**, *40* (9), 1083–1090.

(180) Thommes, M.; Kaneko, K.; Neimark, A. V.; Olivier, J. P.; Rodriguez-Reinoso, F.; Rouquerol, J.; Sing, K. S. W. Physisorption of Gases, with Special Reference to the Evaluation of Surface Area and Pore Size Distribution (IUPAC Technical Report). *Pure Appl. Chem.*. **2015**, *87* (9-10), 1051–1069.

(181) Yrjö Viisanen; Lbadaoui-Darvas, M.; Piedehierro, A. A.; Welti, A.; Athanasios Nenes; Laaksonen, A. Water Vapor Adsorption–Desorption Hysteresis due to Clustering of Water on Nonporous Surfaces. *Langmuir* **2024,** *40*, 38, 20311–20321

(182) Jin, Y.; Wang, W.; Su, Z. Spectroscopic Study on Water Diffusion in Poly(L-Lactide)−Poly(Ethylene Glycol) Diblock Copolymer Film. *Macromolecules* **2011**, *44* (7), 2132–2139.

(183) Huang, L.; Wang, Z.; Chen, J.; Wang, B.; Chen, Y.; Huang, W.; Chi, L.; Marks, T. J.; Facchetti, A. Porous Semiconducting Polymers Enable High-Performance Electrochemical Transistors. *Adv. Mater.* **2021**, *33* (14), 2007041.

(184) Chen, S. E.; Flagg, L. Q.; Onorato, J. W.; Richter, L. J.; Guo, J.; Luscombe, C. K.; Ginger, D. S. Impact of Varying Side Chain Structure on Organic Electrochemical Transistor Performance: A Series of Oligoethylene Glycol-Substituted Polythiophenes. *J. Mater. Chem. A* **2022**, *10* (19), 10738–10749.

(185) Flagg, L. Q.; Bischak, C. G.; Onorato, J. W.; Rashid, R. B.; Luscombe, C. K.; Ginger, D. S. Polymer Crystallinity Controls Water Uptake in Glycol Side-Chain Polymer Organic Electrochemical Transistors. *J. Am. Chem. Soc.* **2019**, *141* (10), 4345–4354.

(186) Schnitzer, T.; van den Bersselaar, B. W. L.; Lamers, B. A. G.; van Son, M. H. C.; Maessen, S. J. D.; de Graaf, F. V.; de Waal, B. F. M.; Trapp, N.; Vantomme, G.; Meijer, E. W. Crystal Lattice Analysis for 2D Nanomorphology Prediction of Phase-Separated Materials. *J. Am. Chem. Soc.* **2025**, *147* (2), 1991–1999.

(187) Botiz, I.; Darling, S. B. Self-Assembly of Poly(3-Hexylthiophene)-Block-Polylactide Block Copolymer and Subsequent Incorporation of Electron Acceptor Material. *Macromolecules* **2009**, *42* (21), 8211–8217.

(188) Yang, Z.; Fu, K.; Yu, J.; Shi, X.; Zhou, P.; Cheng, Z. Facile Preparation of Nanoporous C60/P3HT Thin Films from PLA-*b*-C60-*b*-P3HT Triblock Copolymers. *Appl. Surf. Sci.* **2018**, *458*, 70–76.

(189) Awaja, F.; Gilbert, M.; Kelly, G.; Fox, B.; Pigram, P. J. Adhesion of Polymers. *Prog. Polym. Sci.* **2009**, *34* (9), 948–968.

(190) Grujicic, M.; Sellappan, V.; Omar, M. A.; Seyr, N.; Obieglo, A.; Erdmann, M.; Holzleitner, J. An Overview of the Polymer-to-Metal Direct-Adhesion Hybrid Technologies for Load-Bearing Automotive Components. *Journal of Materials Processing Technology* **2008**, *197* (1), 363–373.

(191) Fan, C.; Shi, J.; Dilger, K. Water Uptake and Interfacial Delamination of an Epoxy-Coated Galvanized Steel: An Electrochemical Impedance Spectroscopic Study. *Prog. Org. Coat.* **2019**, *137*, 105333.

(192) Muangmeesri, S.; Baddigam, K. R.; Navare, K.; Apostolopoulou-Kalkavoura, V.; Witthayolankowit, K.; Håkansson, H.; Mathew, A. P.; Acker, K. V.; Samec, J. S. M. Recycling of Polyesters by Organocatalyzed Methanolysis Depolymerization: Environmental Sustainability Evaluated by Life Cycle Assessment. *ACS Sustainable Chem. Eng.* **2024**, *12* (10), 4114–4120.

(193) Jeung Gon Kim; Gue Seon Lee; Lee, A. Triazabicyclodecene: A Versatile Catalyst for Polymer Synthesis. *J. Polym. Sci.* **2023**, *62* (1), 42–91.

(194) Leibfarth, F.A., Moreno, N., Hawker, A.P. and Shand, J.D. (2012), Transforming polylactide into value-added materials. *J. Polym. Sci. A Polym. Chem.,* 50: 4814-4822.

(195) Chini, S. F.; Amirfazli, A. Understanding Pattern Collapse in Photolithography Process due to Capillary Forces. *Langmuir* **2010**, *26* (16), 13707–13714.

(196) Willner, B. J.; Aitchison, C. M.; Podjaski, F.; Lu, W.; Tian, J.; Durrant, J. R.; McCulloch, I. Correlation between the Molecular Properties of Semiconducting Polymers of Intrinsic Microporosity and Their Photocatalytic Hydrogen Production. *J. Am. Chem. Soc.* **2024**, *146* (45), 30813–30823.

(197) Moser, M.; Ponder Jr., J. F.; Wadsworth, A.; Giovannitti, A.; McCulloch, I. Materials in Organic Electrochemical Transistors for Bioelectronic Applications: Past, Present, and Future. *Adv. Funct. Mater.* **2019**, *29* (21), 1807033.

(198) Khodagholy, D.; Doublet, T.; Quilichini, P.; Gurfinkel, M.; Leleux, P.; Ghestem, A.; Ismailova, E.; Hervé, T.; Sanaur, S.; Bernard, C.; Malliaras, G. G. In Vivo Recordings of Brain Activity Using Organic Transistors. *Nat Commun.* **2013**, *4* (1).

(199) Liu, J.; Ye, G.; Hinderikus G. O. Potgieser; Koopmans, M.; Sami, S.; Mohamad Insan Nugraha; Diego Rosas Villalva; Sun, H.; Dong, J.; Yang, X.; Qiu, X.; Yao,

C.; Portale, G.; Fabiano, S.; Anthopoulos, T. D.; Baran, D.; Remco W. A. Havenith; Chiechi, R. C.; Anton, J. Amphipathic Side Chain of a Conjugated Polymer Optimizes Dopant Location toward Efficient N-Type Organic Thermoelectrics. *Adv. Mater.* **2020**, *33* (4).

(200) Wagner, J.; Song, Y.; Lee, T.; Katz, H. E. The Combined Influence of Polythiophene Side Chains and Electrolyte Anions on Organic Electrochemical Transistors. *Electrochem. Sci. Adv.* **2021**.

(201) Sun, Z.; Khau, B.; Dong, H.; Takacs, C. J.; Yuan, S.; Sun, M.; Mosevitzky Lis, B.; Nguyen, D.; Reichmanis, E. Carboxyl-Alkyl Functionalized Conjugated Polyelectrolytes for High Performance Organic Electrochemical Transistors. *Chem. Mater.* **2023**, *35* (21), 9299–9312.

(202) Toušek, J.; Toušková, J.; Ludvík, J.; Liška, A.; Remeš, Z.; Kylián, O.; Kousal, J.; Chomutová, R.; Heckler, I. M.; Bundgaard, E.; Krebs, F. C. Comparison of the Electron Work Function, Hole Concentration and Exciton Diffusion Length for P3HT and PT Prepared by Thermal or Acid Cleavage. *Solid-State Electron.* **2016**, *116*, 111–118.

(203) Søndergaard, R. R.; Kion Norrman; Krebs, F. C. Low-Temperature Side-Chain Cleavage and Decarboxylation of Polythiophene Esters by Acid Catalysis. *J. Polym. Sci. A Polym. Chem.* **2011**, *50* (6), 1127–1132.

(204) Hallani, R. K.; Paulsen, B. D.; Petty, A. J. I.; Sheelamanthula, R.; Moser, M.; Thorley, K. J.; Sohn, W.; Rashid, R. B.; Savva, A.; Moro, S.; Parker, J. P.; Drury, O.; Alsufyani, M.; Neophytou, M.; Kosco, J.; Inal, S.; Costantini, G.; Rivnay, J.; McCulloch, I. Regiochemistry-Driven Organic Electrochemical Transistor Performance Enhancement in Ethylene Glycol-Functionalized Polythiophenes. *J. Am. Chem. Soc.* **2021**, *143* (29), 11007–11018.

(205) Masui, K.; Ikegami, H.; Mori, A. Palladium-Catalyzed C−H Homocoupling of Thiophenes: Facile Construction of Bithiophene Structure. *J. Am. Chem. Soc.* **2004**, *126* (16),

(206) Takahashi, M.; Masui, K.; Sekiguchi, H.; Kobayashi, N.; Mori, A.; Funahashi, M.; Tamaoki, N. Palladium-Catalyzed C−H Homocoupling of Bromothiophene Derivatives and Synthetic Application to Well-Defined Oligothiophenes. *J. Am. Chem. Soc.* **2006**, *128* (33), 10930–10933.

(207) Luukkonen, A.; Jern, J.; He, Q.; Heeney, M.; Österbacka, R. Reversible Stress-Induced Doping and Charge Trap Generation in IDT-BT EGOFETs. *J. Mater. Chem. C* **2025**, *13* (8), 3815–3824.

(208) Shah, S. T. A.; Guiry, P. J. The Chemoselective and Efficient Deprotection of Silyl Ethers Using Trimethylsilyl Bromide. *Org. Biomol. Chem.* **2008**, *6* (12), 2168–2172.

(209) Navarro, O.; Marion, N.; Oonishi, Y.; Kelly, R. A.; Nolan, S. P. Suzuki−Miyaura, α-Ketone Arylation and Dehalogenation Reactions Catalyzed by a Versatile N-Heterocyclic Carbene−Palladacycle Complex. *J. Org. Chem.* **2006**, *71* (2), 685–692.

(210) Jiang, X.; Li, B.; Xiang, C.; Shi, C.; Yang, M.; Liu, D.; Dong, X.; Chen, J.; Wang, Z.; Yuan, J.; Chi, L.; Huang, L. Integrating Hydrophobic and Hydrophilic Building Blocks for High-Performance Organic Electrochemical Transistors and Biosensing. *Angew. Chem. Int. Ed.* **2025**, *64* (36). e202505141.

(211) Wu, Y.; Fan, Q.; Fan, B.; Qi, F.; Wu, Z.; Lin, F. R.; Li, Y.; Lee, C.-S.; Woo, H. Y.; Yip, H.-L.; Jen, A. K.-Y. Non-Fullerene Acceptor Doped Block Copolymer for Efficient and Stable Organic Solar Cells. *ACS Energy Lett.* **2022**, *7* (7), 2196–2202.

(212) Wu, Y.; Guo, J.; Wang, W.; Chen, Z.; Chen, Z.; Sun, R.; Wu, Q.; Wang, T.; Hao, X.; Zhu, H.; Min, J. A Conjugated Donor-Acceptor Block Copolymer Enables over 11% Efficiency for Single-Component Polymer Solar Cells. *Joule* **2021**, *5* (7), 1800–1815.

(213) Li, S.; Yuan, X.; Zhang, Q.; Li, B.; Li, Y.; Sun, J.; Feng, Y.; Zhang, X.; Wu, Z.; Wei, H.; Wang, M.; Hu, Y.; Zhang, Y.; Han Young Woo; Yuan, J.; Ma, W. Narrow-Bandgap Single-Component Polymer Solar Cells with Approaching 9% Efficiency. *Adv. Mater.* **2021**, *33* (32). 2101295.

(214) Kwon, N. Y.; Park, S. H.; Kang, H.; Takaloo, A. V.; Harit, A. K.; Woo, H. Y.; Kim, T. G.; Yoon, H. J.; Cho, M. J.; Choi, D. H. Rational Design of a Main Chain Conjugated Copolymer Having Donor–Acceptor Heterojunctions and Its Application in Indoor Photovoltaic Cells. *J. Mater. Chem. A* **2020**, *8* (38), 20091–20100.

(215) Park, S. H.; Kim, Y.; Kwon, N. Y.; Lee, Y. W.; Woo, H. Y.; Chae, W.; Park, S.; Cho, M. J.; Choi, D. H. Significantly Improved Morphology and Efficiency of Nonhalogenated Solvent-Processed Solar Cells Derived from a Conjugated Donor–Acceptor Block Copolymer. *Adv. Sci.* **2020**, *7* (4), 1902470.

(216) Park, C. G.; Park, S. H.; Kim, Y.; Nguyen, T. L.; Woo, H. Y.; Kang, H.; Yoon, H. J.; Park, S.; Cho, M. J.; Choi, D. H. Facile One-Pot Polymerization of a Fully Conjugated Donor–Acceptor Block Copolymer and Its Application in Efficient Single Component Polymer Solar Cells. *J. Mater. Chem. A* **2019**, *7* (37), 21280–21289.

(217) Gasperini, A.; Johnson, M.; Jeanbourquin, X.; Yao, L.; Rahmanudin, A.; Guijarro, N.; Sivula, K. Semiconducting Alternating Multi-Block Copolymers via a Di-Functionalized Macromonomer Approach. *Polym. Chem.* **2017**, *8* (5), 824–827.

(218) Robb, M. J.; Montarnal, D.; Eisenmenger, N. D.; Ku, S.-Y.; Chabinyc, M. L.; Hawker, C. J. A One-Step Strategy for End-Functionalized Donor–Acceptor Conjugated Polymers. *Macromolecules* **2013**, *46* (16), 6431–6438.

(219) United Nations. *The Climate Crisis – a Race We Can Win*. United Nations.

(220) Carrington, D. *Climate crisis: 11,000 scientists warn of "untold suffering."* the Guardian.

(221) *Global Market Outlook for Solar Power 2025-2029 - SolarPower Europe.*

(222) Harun Tüysüz. Alkaline Water Electrolysis for Green Hydrogen Production. *Acc. Chem. Res.* **2024**, *57* (4). 558–567

(223) Kosco, J.; Moruzzi, F.; Willner, B.; McCulloch, I. Photocatalysts Based on Organic Semiconductors with Tunable Energy Levels for Solar Fuel Applications. *Adv. Energy Mater.* **2020**, *10* (39), 2001935.

(224) Lyons, R. J.; Sprick, R. S. Processing Polymer Photocatalysts for Photocatalytic Hydrogen Evolution. *Mater. Horizons* **2024**, *11* (16), 3764–3791.

(225) Aitchison, C. M.; Sprick, R. S. Conjugated Nanomaterials for Solar Fuel Production. *Nanoscale* **2021**, *13* (2), 634–646.

(226) Sikiru, S.; Busari, Y.; Olutoki, J.; Mahat, M.; Kolawole, S. Recent Advances in Polymer-Based Photocatalysts for Environmental Remediation and Energy Conversion: A Review. *JPM* **2025**, *42* (1), 1–31.

(227) An, S.; Jeong, K.; Hassan, S. Z.; Ham, G.; Kang, S.; Lee, J.; Ma, H.; Kwon, J.; Jeong, S. Y.; Yang, J.; Woo, H. Y.; Cho, H.; Cha, H.; Son, C. Y.; Chung, D. S. Hydrophilic Photocrosslinkers as a Universal Solution to Endow Water Affinity to a Polymer Photocatalyst for an Enhanced Hydrogen Evolution Rate. *Adv. Sci.* **2024**, *11* (28). 2309786

(228) Zou, Y.; Guo, J.; Liu, Y.; Du, Y.; Pu, Y.; Wang, D. Process Intensified Synthesis of Luminescent Poly(9,9-Dioctylfluorene- *Alt* -Benzothiadiazole) and Polyvinyl Alcohol Based Shape Memory Polymeric Nanocomposite Sensors toward Cold Chain Logistics Information Monitoring. *Polym. Chem.* **2023**, *14* (11), 1275–1281.

(229) Troughton, J.; Neophytou, M.; Gasparini, N.; Seitkhan, A.; Isikgor, F. H.; Song, X.; Lin, Y.-H.; Liu, T.; Faber, H.; Yengel, E.; Kosco, J.; Oszajca, M. F.; Hartmeier, B.; Rossier, M.; Lüchinger, N. A.; Tsetseris, L.; Snaith, H. J.; Wolf, S. D.; Anthopoulos, T. D.; McCulloch, I.; Baran, D. A Universal Solution Processed Interfacial Bilayer Enabling Ohmic Contact in Organic and Hybrid Optoelectronic Devices. *Energy Environ. Sci.* **2020**, *13* (1), 268–276.

(230) Peng, W.; Dong, J.; Li, H.; Chow, C.; Hu, Q. Room Temperature Suzuki Cross-Coupling Polymerizations of Aryl Dihalides and Aryldiboronic Acid/Acid Esters with *T* -Bu $_3$ P-Coordinated 2-Phenylaniline-Based Palladacycle Complex as the Precatalyst. *J. Polym. Sci. A Polym. Chem.* **2019**, *57* (14), 1606–1611.

(231) Luke, J.; Speller, E. M.; Wadsworth, A.; Wyatt, M. F.; Dimitrov, S.; Lee, H. K. H.; Li, Z.; Tsoi, W. C.; McCulloch, I.; Bagnis, D.; Durrant, J. R.; Kim, J. Twist and Degrade—Impact of Molecular Structure on the Photostability of Nonfullerene Acceptors and Their Photovoltaic Blends. *Adv. Energy Mater.* **2019**, *9* (15), 1803755.

(232) Ma, B.; Shi, Q.; Ma, X.; Li, Y.; Chen, H.; Wen, K.; Zhao, R.; Zhang, F.; Lin, Y.; Wang, Z.; Huang, H. Defect-Free Alternating Conjugated Polymers Enabled by Room- Temperature Stille Polymerization. *Angew. Chem. Int. Ed.* **2022**, *61* (16). e202115969

(233) Goto, E.; Ando, S.; Ueda, M.; Tomoya Higashihara. Nonstoichiometric Stille Coupling Polycondensation for Synthesizing Naphthalene-Diimide-Based π-Conjugated Polymers. *ACS Macro Lett.* **2015**, *4* (9), 1004–1007.

(234) Doubina, N.; Paniagua, S. A.; Soldatova, A. V.; Alex; Marder, S. R.; Luscombe, C. K. Steric Effects of the Initiator Substituent Position on the Externally Initiated Polymerization of 2-Bromo-5-Iodo-3-Hexylthiophene. *Macromolecules* **2011**, *44* (3), 512–520.

(235) Howell, M. T.; Kei, P.; Anokhin, M. V.; Losovyj, Y.; Fronczek, F. R.; Nesterov, E. E. Suzuki–Miyaura Catalyst-Transfer Polymerization: New Mechanistic Insights. *Polym. Chem.* **2023**, *14* (37), 4319–4337.

(236) Yang, H.-S.; Choi, H.-N.; Lee, I.-H. Recent Progress on End-Group Chemistry of Conjugated Polymers Based on Suzuki-Miyaura Catalyst-Transfer Polymerization. *Giant* **2023**, *14*, 100152.

(237) Au-Duong, A.-N.; Wu, C.-C.; Li, Y.-T.; Huang, Y.-S.; Cai, H.-Y.; Jo Hai, I.; Cheng, Y.-H.; Hu, C.-C.; Lai, J.-Y.; Kuo, C.-C.; Chiu, Y.-C. Synthetic Concept of Intrinsically Elastic Luminescent Polyfluorene-Based Copolymers via RAFT Polymerization. *Macromolecules* **2020**, *53* (10), 4030–4037.

(238) Lee, J.; Kim, H.; Park, H.; Kim, T.; Hwang, S.-H.; Seo, D.; Chung, T. D.; Choi, T.-L. Universal Suzuki–Miyaura Catalyst-Transfer Polymerization for Precision Synthesis of Strong Donor/Acceptor-Based Conjugated Polymers and Their Sequence Engineering. *J. Am. Chem. Soc.* **2021**, *143* (29), 11180–11190.

(239) Thorley, K. J.; McCulloch, I. Why Are S–F and S–O Non-Covalent Interactions Stabilising? *J. Mater. Chem. C* **2018**, *6* (45), 12413–12421.

(240) Nishimura, R.; Hattori, Y.; Akazawa, M.; Jun-ichiro Kitai; Shinichiro Okude; Sakamoto, Y.; Seiji Yamazoe; Satoshi Yokojima; Nakamura, S.; Uchida, K. Autopolymerization of 2-Bromo-3-Methoxythiophene, Analysis of Reaction Products and Estimation of Polymer Structure. *Polymer Journal* **2020**, *53* (3), 429–438.

(241) Popescu, A.; Musteti, A. D.; Ferrer-Ugalde, A.; Viñas, C.; Núñez, R.; Francesc Teixidor. Influential Role of Ethereal Solvent on Organolithium Compounds: The Case of Carboranyllithium. *Chemistry - A European Journal* **2012**, *18* (11), 3174–3184.

(242) Seo, K.-B.; Lee, I.-H.; Lee, J.; Choi, I.; Choi, T.-L. A Rational Design of Highly Controlled Suzuki–Miyaura Catalyst-Transfer Polycondensation for Precision Synthesis of Polythiophenes and Their Block Copolymers: Marriage of Palladacycle Precatalysts with MIDA-Boronates. *J. Am. Chem. Soc.* **2018**, *140* (12), 4335–4343.

(243) Leone, A. K.; McNeil, A. J. Matchmaking in Catalyst-Transfer Polycondensation: Optimizing Catalysts Based on Mechanistic Insight. *Acc. Chem. Res.* **2016**, *49* (12), 2822–2831.

(244) Tokita, Y.; Katoh, M.; Ohta, Y.; Yokozawa, T. Mechanistic Investigation of Catalyst-Transfer Suzuki–Miyaura Condensation Polymerization of Thiophene–Pyridine Biaryl Monomers with the Aid of Model Reactions. *Chem. Eur. J.* **2016**, *22*, 17436.

(245) Bautista, M. V.; Varni, A. J.; Ayuso-Carrillo, J.; Carson, M. C.; Noonan, K. J. T. Pairing Suzuki–Miyaura Cross-Coupling and Catalyst Transfer Polymerization. *Polym. Chem.* **2021**, *12* (10), 1404–1414.

(246) Kosaka, K.; Uchida, T.; Mikami, K.; Ohta, Y.; Yokozawa, T. AmPhos Pd-Catalyzed Suzuki–Miyaura Catalyst-Transfer Condensation Polymerization: Narrower Dispersity by Mixing the Catalyst and Base Prior to Polymerization. *Macromolecules* **2018**, *51* (2), 364–369.

(247) Keene, S. T.; Michaels, W.; Melianas, A.; Quill, T. J.; Fuller, E. J.; Giovannitti, A.; McCulloch, I.; Alec, T. A.; Tassone, C. J.; Qin, J.; Troisi, A.; Salleo, A. Efficient Electronic Tunneling Governs Transport in Conducting Polymer-Insulator Blends. *J. Am. Chem. Soc.* **2022**, *144* (23), 10368–10376

(248) MacFarlane, L. R.; Zhao, C.; Cai, J.; Qiu, H.; Manners, I. Emerging Applications for Living Crystallization-Driven Self-Assembly. *Chem. Sci.* **2021**, *12* (13), 4661–4682.

(249) Xiao, L.; Parkinson, S.; Xia, T.; Edge, P.; O'Reilly, R. K. Enhancing the Scalability of Crystallization-Driven Self-Assembly Using Flow Reactors. *ACS Macro Lett.* **2023**, *12* (12), 1636–1641.